

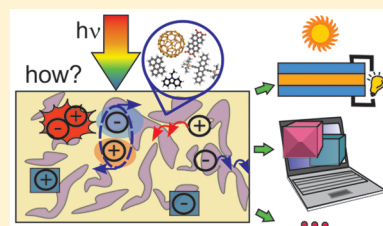
## Organic Optoelectronic Materials: Mechanisms and Applications

Oksana Ostroverkhova\*

Department of Physics, Oregon State University, Corvallis, Oregon 97331, United States

### S Supporting Information

**ABSTRACT:** Organic (opto)electronic materials have received considerable attention due to their applications in thin-film-transistors, light-emitting diodes, solar cells, sensors, photorefractive devices, and many others. The technological promises include low cost of these materials and the possibility of their room-temperature deposition from solution on large-area and/or flexible substrates. The article reviews the current understanding of the physical mechanisms that determine the (opto)electronic properties of high-performance organic materials. The focus of the review is on photoinduced processes and on electronic properties important for optoelectronic applications relying on charge carrier photogeneration. Additionally, it highlights the capabilities of various experimental techniques for characterization of these materials, summarizes top-of-the-line device performance, and outlines recent trends in the further development of the field. The properties of materials based both on small molecules and on conjugated polymers are considered, and their applications in organic solar cells, photodetectors, and photorefractive devices are discussed.



### CONTENTS

1. Introduction	B		
2. Exciton Physics	C		
2.1. Optical Properties of Molecules	C		
2.1.1. Optical Absorption	D		
2.1.2. Fluorescence and Phosphorescence	D		
2.2. Exciton Dynamics in Crystalline Materials	E		
2.3. Frenkel and Charge Transfer Excitons	G		
2.4. Molecular Aggregates	H		
2.4.1. H-Aggregates	H		
2.4.2. J-Aggregates	I		
2.4.3. HJ-Aggregates	I		
2.5. Energy and Charge Transfer	J		
2.6. Exciton Diffusion	K		
2.7. Exciton Physics That Enables Novel Material Design Paradigms	L		
2.7.1. Singlet Fission	L		
2.7.2. Thermally Activated Delayed Fluorescence	M		
2.7.3. FRET and CT Competition and FRET-Mediated CT in D–A Materials	N		
2.8. Summary	N		
3. Charge Carrier Photogeneration	O		
3.1. Analytical Models of Charge Generation	O		
3.2. Computational Efforts	R		
3.2.1. Methods Involving Electronic Structure Calculations	R		
3.2.2. Monte Carlo Simulations	T		
3.2.3. Device Modeling	T		
3.3. Experimental Evidence	X		
3.3.1. Ultrafast- vs Longer-Time-Scale Charge Carrier Generation	X		
3.3.2. Intrinsic or Extrinsic?	Y		
		3.3.3. Singlet Fission-Enabled Charge Generation	AC
		3.4. Summary	AC
		4. Charge Transport	AF
		4.1. General Considerations	AF
		4.2. Charge Transport Mechanisms: Theoretical Considerations	AH
		4.2.1. Band Transport	AH
		4.2.2. Polaron Transport	AH
		4.2.3. Origin of $d\mu/dT < 0$	AI
		4.2.4. Quantum Coherence and Charge Transport	AL
		4.2.5. Disorder Models	AM
		4.2.6. Charge Transport in D/A Materials and Mixed-Phase Blends	AN
		4.3. Experimental Evidence vs Models	AO
		4.3.1. Organic Crystals and Small-Molecule Crystalline Films	AO
		4.3.2. Polymers	AQ
		4.4. Summary	AS
		5. Charge Trapping and Recombination	AS
		5.1. Charge Trapping	AS
		5.1.1. Charge Traps in Photorefractive Organic Materials	AU
		5.2. Charge Recombination	AV
		5.2.1. Bimolecular Recombination	AV
		5.2.2. Trap-Assisted Recombination	AW
		5.3. Summary	AX
		6. Photorefractive Effect	AX
		6.1. Summary	AZ

Received: February 18, 2016

7. Experimental Methods for Probing Exciton and Charge Carrier Dynamics			
7.1. Macroscopic Scales	AZ	11.3.2. Laser-Based Ultrasound	CO
7.1.1. Time-Resolved Probes (fs–ns time-scales)	AZ	11.3.3. Ultrasound-Modulated Optical Tomography	CO
7.1.2. Longer Time-Scale and Steady-State Measurements of Charge Carrier Dynamics	AZ	11.3.4. Photonic Applications	CP
7.1.3. Techniques for Probing Longer Time-Scale Exciton Dynamics and Steady-State Behavior	BE	11.4. Other Optoelectronic Applications	CP
7.1.4. Photorefractive Properties Characterization	BG	11.5. Summary	CQ
7.2. Microscopic Scales	BH	12. Summary and Outlook	CQ
7.2.1. Scanning Probe Microscopy	BI	Associated Content	CR
7.2.2. Optical Absorption and PL Imaging	BI	Supporting Information	CR
7.2.3. Ultrafast Time-Resolved Microscopy	BK	Author Information	CR
7.2.4. Single-Molecule Fluorescence Spectroscopy	BL	Corresponding Author	CR
7.3. Summary	BL	Notes	CR
8. Importance of Comprehensive Physical Studies: Examples	BN	Biography	CR
8.1. Charge Carrier Dynamics on Various Time-Scales: From Ultrafast Dynamics to Device Performance	BN	Acknowledgments	CR
8.2. Optical vs Electronic Properties	BN	List of Abbreviations	CR
8.3. Macroscopic vs Microscopic Scales	BP	References	CT
9. Materials	BQ		
9.1. High-Mobility Small-Molecule Organic Semiconductors	BR		
9.2. High-Mobility Conjugated Polymers	BR		
9.3. Materials for Organic Solar Cells	BT		
9.3.1. Donor Materials	BU		
9.3.2. Acceptor Materials	BU		
9.3.3. High-Dielectric Constant Organic Materials	BV		
9.3.4. Ternary Blends	BW		
9.3.5. Kasha's Rule Breaking Materials	BW		
9.3.6. Hybrids with Graphene and Carbon Nanotubes	BX		
9.3.7. Organic–Inorganic Hybrid Materials and Interfacial Phenomena	BX		
9.4. Naturally Derived and Other H-Bonded Materials	BX		
9.5. Photorefractive Organic Amorphous Materials	BY		
9.6. Summary	CA		
10. Effects of Structure and Morphology, Fabrication, and Processing	CD		
10.1. Structure and Morphology	CD		
10.1.1. Crystalline Small-Molecule Materials	CD		
10.1.2. Polymers	CE		
10.1.3. Donor–Acceptor Bulk Heterojunctions	CE		
10.2. Fabrication and Processing	CF		
10.3. Summary	CH		
11. Applications	CI		
11.1. Organic Photovoltaic Cells (OPVs)	CI		
11.1.1. Undersanding the Limiting Factors	CI		
11.1.2. Optimization of Device Design	CK		
11.2. Organic Photodetectors and Phototransistors	CM		
11.3. Photorefractive Devices and Novel Effects	CN		
11.3.1. 3D Displays	CN		

## 1. INTRODUCTION

Organic optoelectronic materials (for example anthracene) have been known for almost a century, as the first studies of their optical and electronic properties have been reported in the 1910s.<sup>1</sup> In the 1960s and 1970s, interest in such materials was intensified by the discovery of electroluminescence in molecular crystals and of conducting polymers.<sup>2</sup> However, a real surge of interest in the field of organic (opto)electronics occurred during the past 20 years, due to major improvements in material design and purification that led to a significant boost in the materials performance. Currently, organic materials receive considerable attention due to their applications in electronic and optoelectronic devices, such as organic thin-film-transistors, light-emitting diodes (OLEDs), solar cells, sensors, photorefractive (PR) devices, and many others. Of particular technological interest are low-cost solution-processable thin films that can be deposited on large areas and/or flexible substrates.

There are two major classes of organic semiconductors that are discussed in this review: small-molecular-weight materials and photoconductive polymers with advanced (opto)electronic performance. Small-molecular-weight semiconductors are attractive because they can be efficiently purified, and their ability to form ordered structures has enabled high charge carrier mobilities. They have also served as model systems for a broad variety of fundamental studies of exciton and charge carrier dynamics. On the other hand, polymers are advantageous for large-area device fabrication; they have enabled not only high-performance single-component devices (such as polymer TFTs), but also devices that utilize blends of various components performing different functionalities, such as bulk heterojunction (BHJ) solar cells, PR devices, and small molecule:polymer-based TFTs. Recent advances in polymer design, synthesis, and processing enabled remarkable progress in polymer-based device performance, as discussed in this review.

The field of organic (opto)electronics has experienced a significant growth in the past 10 years, with more than 2,800 papers published on the subject in the year 2015. Table S1 provides a summary of selected recent *review articles*, *tutorials*, and *perspectives* focused on a specific topic in the field; these articles should be consulted for an in-depth analysis of a particular area within the field. The table reflects the high level of interest that organic (opto)electronics generated in the scientific community around the world. Additionally, a number

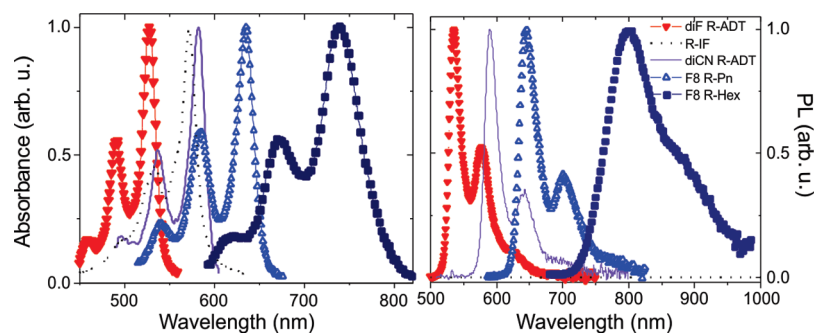


**Figure 1.** Absorption and PL spectra of functionalized pentacene (F8 R-Pn), hexacene (F8 R-Hex), anthradithiophene (diF R-ADT and diCN R-ADT), and indenofluorene (R-IF) derivatives in toluene. Adapted from ref 37. Copyright 2012 American Chemical Society.

of recent books covering various aspects of physics of organic semiconductors, characterization, materials design, and device performance are available and should be referred to for background material.<sup>2–6</sup>

The goal of this review is to provide a balanced assessment of the current understanding of the physical mechanisms that determine the optoelectronic properties of high-performance organic materials, to highlight the capabilities of various experimental techniques for characterization of these materials, to summarize top-of-the-line device performance, and to outline recent trends (since 2011, unless stated otherwise) in the further development of the field, as of June 2016. The focus of the review is on *photoinduced* processes and on electronic properties important for optoelectronic applications relying on charge carrier photogeneration. Therefore, detailed discussions of electronic applications (e.g., OFETs or spintronic devices) and of optoelectronic applications that do not rely on photoinduced charge generation (e.g., OLEDs), as well as photonic applications (e.g., those based on exciton-photon coupling in microcavities),<sup>7–10</sup> are beyond the scope of the review. Review papers on these subjects are available, and references to selected reviews are included in Table S1. Nevertheless, discussions of high-mobility materials (Sections 4.2, 9.1, 9.2, and 10) and of materials featuring particular photophysical processes (such as TADF materials, Sections 2.7 and 11.4, or J-aggregates, Section 2.4), as well as an overview of experimental methods and insights they enable (Section 7) could be useful for researchers working in these areas. Also beyond the scope of this review are efforts toward development of perovskites, graphene-based materials, and organic–inorganic hybrids whose optoelectronic response relies on plasmonic interactions. Even within the scope limitations, in spite of my best effort, there will surely be important articles that I neglect to cite; I apologize for this in advance.

One of the motivations behind contributing this review is to enhance cross-pollination across different areas of organic optoelectronics by creating a relatively compact resource outlining the most promising research efforts, points of controversy, effective solutions, and branching-out endeavors in various areas. Each of the pursuits discussed is then thoroughly referenced, encouraging the reader to seek further details in more focused reviews and representative case studies.

The structure of the paper is as follows. Sections 2–6 review the physical mechanisms behind exciton dynamics and charge carrier photogeneration and transport in high-performance materials and provide examples of experimental evidence pertaining to such mechanisms. Section 7 reviews various experimental techniques developed for characterization of

materials with a focus on photophysics and photoconductivity, illustrated by key insights that had been enabled by these techniques. Section 8 provides examples of cross-cutting studies of exciton and charge carrier dynamics that highlight the complexity of and connections between processes contributing to optoelectronic properties on various time and spatial scales. Section 9 briefly summarizes the best-performing organic optoelectronic materials, as well as outlining new pursuits in materials development. Abbreviated names of all the compounds are used throughout the paper; the full names of these compounds can be found in the List of Abbreviations. In describing donor (D)–acceptor (A) materials, the notations D:A and D/A refer to donor–acceptor blends (bulk heterojunctions) and planar heterojunctions, respectively. Section 10 highlights selected innovative approaches enabling systematic studies of structure–property relationships and advances in thin-film fabrication and processing. Section 11 summarizes selected applications and highlights best-performing devices, and Section 12 concludes, with challenges summarized and outlook provided.

## 2. EXCITON PHYSICS

The fundamentals of exciton physics in organic semiconductors can be found in books.<sup>1,2,4</sup> Recent comprehensive reviews of various aspects of exciton dynamics and their theoretical descriptions are also available (Table S1).<sup>11–24</sup> In this section, a brief background providing context for current research endeavors is provided, along with examples of recent results, which are then used in follow-up discussions throughout the review.

### 2.1. Optical Properties of Molecules

Organic molecular solids are composed of molecules that are weakly bonded by van der Waals forces. Because of the weak bonding, the properties of individual molecules are retained in a solid to a much greater extent compared to those of inorganic materials. Therefore, in order to understand the optical properties of an organic solid, it is important to understand the properties of the molecules themselves. The wave function describing the properties of the molecule  $\psi$  is a function of both the electronic variables ( $r$ ) and nuclear variables ( $R$ ). Since organic compounds involve complicated multielectron molecules, exact analytical solution of the Schrödinger equation is not feasible, and approximations must be used. One of the commonly used approximations is the adiabatic Born–Oppenheimer approximation, which assumes that large differences between electron and nuclear masses lead to instantaneous response of the electrons to any configurational change of nuclei. With this approximation, the total wave function ( $\Psi$ )

is a product of the electronic ( $\psi_e$ ) and nuclear ( $\psi_N$ ) wave functions, and  $\psi_e(r_i, R_k)$  (where indices  $i$  and  $k$  correspond to the  $i$ th electron and  $k$ th nucleus) is calculated using the instantaneous nuclear positions  $R_k$  as parameters. This approximation typically works well for rigid molecules (e.g., acene or acene-thiophene derivatives) and will be assumed to be valid in the discussion of optical absorption and fluorescence properties below. However, its applicability to other systems, such as electronically excited molecular aggregates, has been questioned, and the separability of the electronic and nuclear wave functions depends on the strength of the electronic coupling,<sup>25</sup> as detailed in a tutorial review by Chenu and Scholes.<sup>25</sup>

**2.1.1. Optical Absorption.** Optical absorption spectra of molecules often reflect coupling between the electronic excitation (exciton) and vibrational modes of the molecule (Figure 1), for example C–C stretching modes or C–H wagging modes of the benzene ring. The intensity of the absorption line is determined by the overlap of vibrational wave functions (Franck–Condon overlap integral). If the vibrational energy is considerably higher than the thermal energy (i.e.,  $\hbar\omega_m \gg k_B T$ ), the probability of the transition from the zeroth vibrational level of the ground state to the  $m$ th vibrational level of an  $i$ th vibrational mode of the excited state is described by the Poisson distribution in the form<sup>2</sup>

$$I_{0-m_i} = \frac{S_i^{m_i}}{m_i!} e^{-S_i} \quad (1)$$

where  $S_i$  is the Huang–Rhys parameter for the  $i$ th vibrational mode given by

$$S_i = \frac{1}{2} M_i \omega_{m_i} \frac{\Delta Q_i^2}{\hbar} \quad (2)$$

This expression assumes that the oscillation is treated as a harmonic oscillator with a reduced mass  $M_i$ , frequency  $\omega_{m_i}$ , and the change in equilibrium coordinate  $\Delta Q_i$ . The intensity distribution between the vibronic bands of eq 1 depends on the change in a nuclear arrangement ( $\Delta Q_i$  in eq 2) upon excitation. If no nuclear configurational change occurs (i.e.,  $\Delta Q_i = 0$ ), only a  $0 \rightarrow 0$  transition occurs. At  $\Delta Q_i \neq 0$ , the higher the Huang–Rhys parameter  $S_i$  is, the more intense are transitions to higher vibrational levels (e.g.,  $0 \rightarrow n$ ,  $n \geq 1$ ) as compared to  $0 \rightarrow 0$ . The Huang–Rhys parameter is related to the reorganization energy  $\lambda$  (which plays a significant role in charge transport, Section 4.1) by  $\lambda = \sum_i S_i \hbar \omega_{m_i}$ .

In the presence of several vibrational modes  $i$ , the normalized absorption spectrum is described by the following Franck–Condon expression<sup>2</sup>

$$I_{abs}(\hbar\omega) = n(\hbar\omega)\hbar\omega \sum_{m_i} \prod_i \frac{S_i^{m_i}}{m_i!} e^{-S_i} \Gamma \delta(\hbar\omega - (\hbar\omega_0 + \sum_i m_i \hbar\omega_{m_i})) \quad (3)$$

Here  $n$  is the refractive index at the transition energy  $\hbar\omega$ ,  $\hbar\omega_0$  is the energy of the  $0 \rightarrow 0$  transition, and  $\delta$  is the Delta-function. The summation is over  $m_i = 0, 1, 2, \dots$ , corresponding to vibrational levels with energy  $\hbar\omega_{m_i}$ . When a single vibrational mode dominates,  $i = 1$ , and the equation simplifies. For many organic semiconductor molecules, optical absorption spectra can be described by the vibronic progression of eq 1 due to a single “effective” mode at  $\sim 0.16$ – $0.18$  eV (which may represent a cluster of ring breathing/vinyl stretching modes),<sup>26</sup>

with dominant  $0 \rightarrow 0$  transition and  $S \leq 1$ .<sup>26–28</sup> However, assignment of specific vibrational modes that couple to the electronic excitation is not straightforward based on optical spectra, which necessitates the development of new experimental methodologies for this task, such as high-resolution photoelectron momentum mapping.<sup>29</sup>

The parameter  $\Gamma$  in eq 3 is a function describing the line shape, typically Gaussian, Lorentzian, or a combination of both. In the case of the Gaussian line shape,

$$\Gamma = \frac{1}{\sigma\sqrt{2\pi}} \exp(-(\hbar\omega - \hbar\omega_0)^2/2\sigma^2) \quad (4)$$

where  $\sigma$  is a measure of the line width. The origin of the inhomogeneous line broadening  $\sigma$  in organic semiconductors has been extensively studied, as it provides information on the energetic disorder. For example, in PPV and PPP oligomers, analysis of temperature-dependent spectra of solutions and films revealed that the line broadening is due to the interchain (polarization-induced) and intrachain (torsion-induced) disorder, with the former dominating in films.<sup>30</sup>

**2.1.2. Fluorescence and Phosphorescence.** After a molecule has absorbed an incident photon, it can relax back to the ground state by radiative and nonradiative processes. The nonradiative processes include energy dissipation as heat, collisions, molecular conformational changes, etc. The radiative ones include fluorescence (e.g.,  $S_1 \rightarrow S_0$ ), phosphorescence (e.g.  $T_1 \rightarrow S_0$ ), delayed fluorescence (e.g.,  $S_1 \rightarrow T_1 \rightarrow S_1 \rightarrow S_0$ ), etc. Fluorescence is typically preceded by internal conversion (i.e., relaxation within the states with the same spin multiplicity, such as  $S_n \rightarrow S_1$ ) that occurs on subpicosecond time-scales, whereas phosphorescence involves either intersystem crossing ( $S_1 \rightarrow T_1$ ) or singlet fission ( $S_0 + S_1 \rightarrow T_1 + T_1$ ). Since the internal conversion (IC) is a very fast process, fluorescence emission typically occurs from the lowest vibrational state of the excited electronic state (Kasha’s rule), and the  $S_1 \rightarrow S_0$  emission spectrum is a mirror image of the absorption spectrum (Figure 1). Measurements of the  $S_1 \rightarrow S_0$  emission spectrum allow one to probe the vibronic structure of the ground state  $S_0$ , with the photoluminescence (PL) emission described by eq 5, where all parameters are the same as in those in eq 3.<sup>2</sup>

$$I_{PL}(\hbar\omega) = (n(\hbar\omega)\hbar\omega)^3 \sum_{m_i} \prod_i \frac{S_i^{m_i}}{m_i!} e^{-S_i} \Gamma \delta(\hbar\omega - (\hbar\omega_0 - \sum_i m_i \hbar\omega_{m_i})) \quad (5)$$

Analysis of temperature-dependent PL spectra using eq 5 has been used, for example, to quantify aggregation properties of small molecules and polymer chains (Section 2.4).<sup>28,31</sup> The key parameters characterizing photon emission are the radiative lifetime ( $\tau_r$ ) and quantum yield ( $\Phi_f$  and  $\Phi_p$  in the case of fluorescence and phosphorescence, respectively). The radiative lifetime of an excited electronic state ( $\tau_{rad}$ ) is defined as the reciprocal of the radiative transition probability  $\tau_{rad} = 1/\sum_n A_{0n}$ , where  $A_{0n}$  is the Einstein coefficient describing spontaneous emission from the lowest vibrational state (0) of the excited electronic state to the  $n$ th vibrational level of the ground state. The actual excited-state lifetime ( $\tau$ ), however, also depends on the nonradiative transition probability, and in a simple description is given by

$$\tau = 1/(k_{rad} + k_{ISC} + k_{nr}) \quad (6)$$

where  $k_{rad}$  is the reciprocal of  $\tau_{rad}$ ,  $k_{ISC}$  is a rate constant describing intersystem crossing, and  $k_{nr}$  is a rate constant describing nonradiative transitions from the excited to the

Table 1. Electrochemical and Photophysical Properties of Selected Molecules

Molecule	HOMO <sup>a</sup> (eV)	LUMO <sup>a</sup> (eV)	E <sub>gap</sub> <sup>b</sup> (eV)	λ <sub>abs</sub> <sup>c</sup> (nm)	λ <sub>em</sub> <sup>c</sup> (nm)	E <sub>opt, gap</sub> <sup>d</sup> (eV)	Φ <sub>f</sub> <sup>e</sup>	τ <sub>f</sub> <sup>e</sup> (ns)	Φ <sub>B</sub> <sup>e</sup> 10 <sup>-6</sup>	N <sub>tot</sub> <sup>f</sup> 10 <sup>5</sup>
diF TES-ADT	-5.35	-3.05	2.30	525	532	2.33	0.7	9.4	1.1 ± 0.2	8.2
diCN TIPS-ADT	-5.55	-3.49	2.06	582	590	2.11	0.76	12.7	2.5 ± 0.5	3.6
TIPS-Pn	-5.16	-3.35	1.81	643	650	1.91	0.75	11.8	10 ± 1	
F8 TIPS-Pn	-5.55	-3.6	1.95	632	644	1.94	0.6	9.4	1.9 ± 0.5	4.2
F8 TCHS-Pn	-5.55	-3.59	1.94	635	644	1.93	0.61	8.7	1.0 ± 0.2	8.2
F8 TCHS-Hex	-5.3	-3.7	1.6	739	799	1.61				
IF-TIPS	-5.88	-4.0	1.88	572 <sup>g</sup>		2.16 <sup>g</sup>	<0.01			

<sup>a</sup>Values were obtained from differential pulse or cyclic voltammetry. From refs 36–38. <sup>b</sup>Calculated as the difference between the HOMO and LUMO energies. <sup>c</sup>Wavelengths of maximal optical absorption and fluorescence emission, as well as fluorescence quantum yields Φ<sub>f</sub> and lifetimes τ<sub>f</sub> measured in dilute toluene solution. From refs 36 and 35. <sup>d</sup>The optical gap calculated using the average value between the absorption and emission wavelengths. <sup>e</sup>Photobleaching quantum yields obtained for molecules incorporated in a PMMA host under 532 nm (ADT) or 633 nm (Pn) illumination; ref 35. <sup>f</sup>Total number of emitted photons obtained from the molecules incorporated in a PMMA host calculated using N<sub>tot</sub> = Φ<sub>f</sub>/Φ<sub>B</sub>, where Φ<sub>f</sub> is the fluorescence quantum yield for the molecules in PMMA. The N<sub>tot</sub> of the order of 10<sup>5</sup> is sufficiently high to enable fluorescence imaging of the molecules on the single-molecule level at room temperature; ref 35. <sup>g</sup>Corresponds to the S0–S2 transition; the S0–S1 transition is optically forbidden and is not observed in the absorption spectra (Figure 1).<sup>38</sup> The optical gap is calculated based on the wavelength of the maximum S0–S2 absorption.

ground state. The temperature dependence of the ISC and of the nonradiative rate in the form  $k_{ISC, nr} = k_1 + k_2 \exp(-E_a/k_B T)$  (where  $E_a$  is the activation energy and  $k_1, k_2$  are constants) has been utilized in, for example, obtaining the singlet–triplet energy splitting<sup>32</sup> and quantifying exciton diffusion,<sup>28,33</sup> respectively, in various organic films. Temperature-dependent radiative rates ( $k_{rad}$ ) have provided a measure for exciton coherence in, for example, Tc aggregates.<sup>34</sup>

The quantum yield (QY) of fluorescence from a particular state is given by

$$\Phi_f = \Phi^*(\tau/\tau_{rad}) \quad (7)$$

where Φ\* is the efficiency of forming of that state, which can usually be assumed to be close to unity. Another parameter of interest, which quantifies the molecule photostability, is the photobleaching QY, Φ<sub>B</sub>, which is the probability of photobleaching upon absorption of a photon (thus, low values of Φ<sub>B</sub> are desirable). For example, the best fluorophores for single-molecule fluorescence spectroscopy (Section 7.2.4) exhibit photobleaching QYs on the order of ~10<sup>-7</sup> or lower. Table 1 shows fluorescence and photobleaching QYs (Φ<sub>f</sub> and Φ<sub>B</sub>), along with other parameters obtained from several functionalized ADT and Pn derivatives. These materials have served as model systems in many physical studies and have been utilized in (opto)electronic devices (Section 9.1). Additionally, many of these molecules are sufficiently fluorescent and photostable to be imaged on the single-molecule level at room temperature and have been employed as single-molecule fluorophores in SMFS.<sup>35</sup>

## 2.2. Exciton Dynamics in Crystalline Materials

The simplest approach to describe optical excitation of crystalline organic materials is to consider a linear array of  $N$  identical molecules  $i$  ( $i = 1, \dots, N$ ) coupled via electrostatic interaction  $V_{ij}$ , so that the Hamiltonian describing the system is<sup>2</sup>

$$H = \sum_{i=1}^N (H_i + \Delta H_i) + \frac{1}{2} \sum_{\substack{i,j=1 \\ i \neq j}}^N V_{ij} \quad (8)$$

where  $H_i$  is the Hamiltonian of an individual molecule and  $\Delta H_i$  reflects molecule-to-molecule variation due to static and dynamic disorder. The wave function for the ground state

can be approximated by the product of the individual wave functions  $\psi_{i0}$  so that  $\Psi_{GS} = A \prod_{i=1}^N \psi_{i0}$ , where  $A$  is the antisymmetrization operator. The excited state wave function can be presented as

$$\Psi_E = \sum_{j=1}^N c_j \Psi_{jE} \quad (9)$$

where  $c_j$  are coefficients (obtained by solving the Schrödinger equation using the variational principle) and, in the case of local excitation (Frenkel exciton, FE), the wave function  $\Psi_{jE}$  is given by

$$\Psi_{jE}(FE) = \psi_j \prod_{\substack{i=1 \\ i \neq j}}^N \psi_{i0} \quad (10)$$

which represents the coupled array of the excited molecule  $j$  and  $N - 1$  molecules in the ground state. (Although Frenkel excitons comprise neutral states, they can have wave functions delocalized over  $N$  sites.<sup>12</sup>)

The electrostatic interaction  $V_{ij}$  gives rise to overall energy shifts of the ground-state energy  $D_{GS} = \langle \Psi_{GS} | (1/2) V_{ij} | \Psi_{GS} \rangle$  (gas-to-crystal shift) and excited state energy  $D_E = \langle \Psi_{jE} | (1/2) V_{ij} | \Psi_{jE} \rangle$  of the molecular assembly as compared to energies of noninteracting molecules. Additionally, splitting of energy levels occurs to yield  $N$  transition energies:  $E = E_j + \Delta D + 2J_0 \cos(ka)$ , where  $E_j$  is the excitation energy of the noninteracting molecule,  $\Delta D = D_{GS} - D_E$ ,  $a$  is the distance between nearest neighbors, and  $k = 0, \pm 2\pi/Na, \dots, \pm\pi/a$  (which assumes that the linear array of molecules has periodic boundary conditions). The parameter  $J_0$  quantifies the interaction energy (resonance energy) between neighboring molecules (i.e.,  $i$  and  $j$ ), and it is given by  $J_0 = \langle \Psi_{jE} | (1/2) V_{ij} | \Psi_{iE} \rangle$ . Therefore,  $N$  coupled molecules form a band of excited states (Frenkel exciton states) with a bandwidth  $W$  of  $4J_0$ . (In the case of the dimer,  $N = 2$ , the splitting between the two excited states is  $2J_0$ , with the factor of 2 difference from other values of  $N$  due to interactions with only one, as opposed to two, neighboring molecule.<sup>2</sup>) The selection rule for the excitation of this crystalline array comes from the momentum conservation, which requires that the photon with wavelength  $\lambda$  can only excite the excitonic state with wave vector  $k = 2\pi/\lambda$ . Given that the wavelength  $\lambda$  is several orders of magnitude

larger than the lattice constant  $a$ , this implies that only an exciton state close to the bottom (or top, depending on symmetry as discussed below) of the exciton band, typically corresponding to  $k = 0$ , can be populated. These selection rules govern the shape and the spectral range of the absorption and emission spectra of ordered molecular assemblies, such as H- or J-aggregates (Section 2.4).

If there are two molecules per unit cell, resonance interaction between translationally nonequivalent molecules gives rise to additional splitting (Figure 2(a)), commonly referred to as

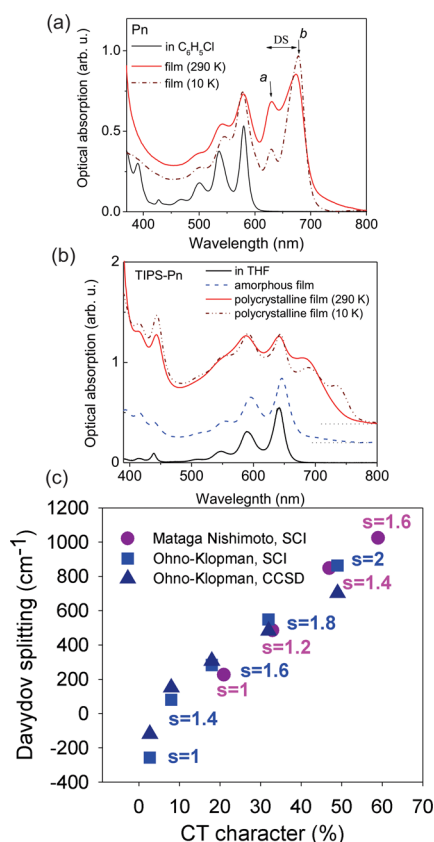


**Figure 2.** Absorption spectra of pentacene (Pn) (a) and TIPS-pentacene (TIPS-Pn) (b) in solution and in films. For polycrystalline films, data at 10 K are also included. In (b), the spectra are offset along the  $y$ -axis for clarity. In Pn (herringbone packing), the Davydov splitting (DS) is observed in film spectra. No Davydov splitting is observed in TIPS-Pn with 2D brick-work packing. Adapted with permission from ref 40. Copyright 2005 American Institute of Physics. (c) Davydov splitting calculated at the INDO/SCI and INDO/CCSD levels versus the CT character of the lowest eigenstate of a Pn unit cell dimer. Reproduced with permission from ref 80. Copyright 2013 American Physical Society.

Davydov splitting (DS). Davydov splitting in oligoacenes increases as the size of the molecule increases (from  $\sim 200\text{ cm}^{-1}$  in Ac to  $1100\text{ cm}^{-1}$  in Pn); it depends on morphology and crystallinity,<sup>39,40</sup> and it is a sensitive measure of the degree of mixing between Frenkel and CT excitons (Figure 2(c)),<sup>41</sup> as discussed in Section 2.3.

One illustrative example for the behavior of the exciton transfer integral  $J_0$  was provided in ref 42, in which  $J_0$  was calculated in the line-dipole approximation for two parallel or collinear conjugated polymer chains of length  $L$  separated by a distance  $R$ . It was found that  $J_0$  scales with  $L$  ( $J_0 \sim L$ ) when  $L < R$  and behaves as  $J_0 \sim 1/L^{1.8}$  or  $\sim 1/L^2$  when  $L > R$  for parallel

or collinear chains, respectively.<sup>42</sup> This implies, for example, that the Davydov splitting in aggregates and the probability of exciton transfer between the neighboring chains decreases as the chain length increases, when the chain lengths are larger than their separation. Comprehensive discussions of how various aspects of intermolecular interactions contribute to  $J_0$  can be found in refs 43 and 44.

Given the considerations above, there are several typical changes in absorption spectra measured in molecular solids compared to those of “isolated” (noninteracting) molecules (e.g., in solutions or incorporated in host matrices): (a) spectral shift, (b) splitting of the spectral lines, leading to absorption peak positions depending on polarization of light, (c) variation in the selection rules leading to differences in the oscillator strength of lines corresponding to different transitions, and (d) changes in molecular vibrational transitions and coupling to intermolecular (lattice) modes (Figure 2(a)–(b)). The existence of well-defined spin states (singlet and triplet excitons), similar to those of isolated molecules, is retained in the solid. Analysis of these trends and comparison with spectra of isolated molecules represents a powerful tool for assessment of the type and extent of intermolecular interactions in the solid, which determine the exciton dynamics. An assessment of the spectral shift and of the change in the ratio between the 0–0 and 0–1 absorption peaks (obtained from fits of the data to eq 3) can provide information on film crystallinity,<sup>40,45</sup> molecular packing,<sup>31,46</sup> trap distribution, and type and degree of disorder.<sup>26–28,47</sup> Examples of these studies are considered in Section 2.4.

Exciton properties depend on relative contributions of terms of eq 8. If  $V_{ij} > \Delta H_{ij}$ , the delocalized Frenkel exciton is described by a superposition of molecular exciton states (eq 9), which supports the coherent exciton transport. For example, largely coherent energy transport over distances of up to  $4.4\ \mu\text{m}$  was reported in H-aggregate-type fibers, in which 1D  $\pi$ -stacked assemblies were further enforced by hydrogen bonding.<sup>48</sup> If disorder is significant such that  $V_{ij} < \Delta H_{ij}$ , the absorption spectrum of the solid are similar to those of the noninteracting molecules, and the excited state is a localized excited state that transfers its energy to a neighboring molecule in an incoherent manner. If the interaction potential contains dipole-only terms, the energy transfer can be described in the framework of FRET; if exchange interactions dominate, the energy transfer is of Dexter-type (Section 2.5).

The disorder causing exciton localization can be of static (due to e.g. heterogeneity of site energies) or of dynamic (due to the electron–phonon coupling) origin. For example, Wang and Chan<sup>49</sup> observed a transition from coherent to incoherent exciton transport in ZnPc crystals at  $\sim 350\text{ fs}$  after photoexcitation and after about  $2\text{ nm}$  travel due to dynamic localization. Arag3 and Troisi<sup>50</sup> considered thermal fluctuations of  $J_0$  due to exciton coupling to low frequency intermolecular vibrations (dynamic disorder). They calculated time-dependent excitonic coupling for Ac and Tc crystals exhibiting the herringbone-type packing and determined that fluctuations in the exciton coupling are of the same order of magnitude as the coupling itself, which necessitates incorporation of exciton dynamic localization into exciton transport models, similar to the case of charge carriers (Section 4.2.3). Excellent discussions of electron–phonon coupling and of exciton localization and dispersion can be found in refs 51 and 13, respectively.

Coherence in various aspects of exciton and charge carrier dynamics, its meaning, and its importance for processes

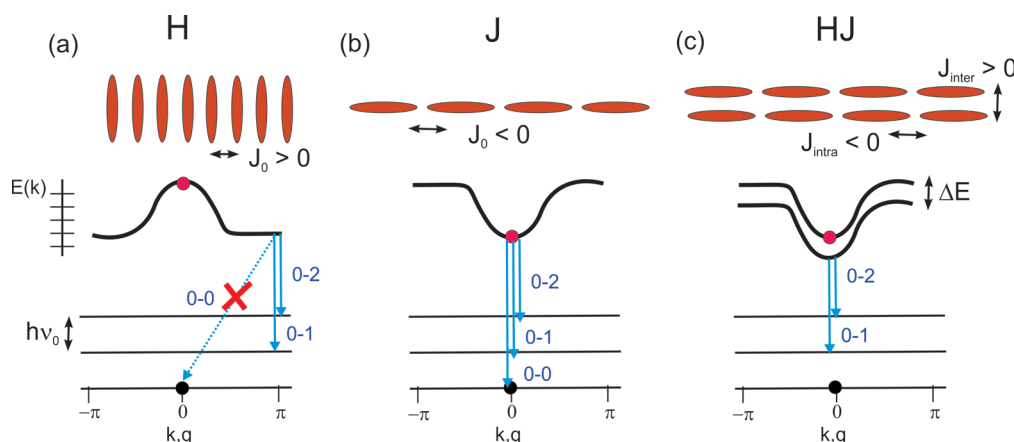


**Figure 3.** Schematics of (a) H-aggregates, (b) J-aggregates, and (c) HJ-aggregates, with the sign of the coupling constant  $J_0$  indicated. Also shown is the energy dispersion  $E(k)$  of the lowest vibronic band in each aggregate. The red dot indicates the  $k = 0$  exciton that is optically allowed from (i.e., can radiatively couple to) the ground state (black dot). The phonons with wave vector  $q$  derive from the intramolecular vibrations with energy  $h\nu_0$ . Arrows indicate emission pathways at low temperatures. In J-aggregates the 0–0 emission is allowed, and it leads to the superradiance. In H-aggregates with no disorder, the intraband relaxation populates the  $k = \pi$  state, and 0–0 emission is disallowed. In the HJ-aggregate, interchain interactions split each intrachain band into symmetric and antisymmetric bands separated by energy  $\Delta E$ . In both H- and HJ-aggregates, the 0–0 emission is thermally activated. For details, see ref 91.

relevant for optoelectronic devices have been debated, and it is a topic of considerable interest.<sup>4,14,24,49,52–62</sup> In the context of energy transfer, examples of coherent effects include a so-called “super-transfer”, which is the exceptional enhancement of the energy transfer rate (in spite of the incoherent nature of the transfer)<sup>63</sup> and a wave-like (rather than hopping-like) excitation transfer between the donor and acceptor which simultaneously realizes different energy transfer pathways, altering energy transport properties through quantum interference.<sup>64</sup> In the context of other important aspects of exciton physics, Chan et al.<sup>60</sup> and Bakulin et al.<sup>58</sup> showed (using TR-2PPE and 2DES, respectively) how coherent coupling enables efficient singlet fission in Tc and functionalized Pn films (Section 2.7.1). Jumper et al.<sup>65</sup> applied coherent 2DES (Section 7.1.1.3) with a 10 fs time resolution to a model dimer system (diacetylene-linked PDI dimer) and observed a sub-50-fs population transfer between the two exciton states. This was attributed to internal conversion, which prevented sustainment of long-lived exciton coherence in this system. Hildner et al.<sup>66</sup> used ultrafast SMFS (Section 7.2.4) to determine dephasing times in TDI single molecules embedded in PMMA. The experiments revealed a broad distribution of times ranging between 25 and 110 fs (peaked at 60 fs) due to the heterogeneous local environment. A quantitative description of exciton coherence and localization, which have been the subject of intense research in light-harvesting complexes,<sup>67,68</sup> illustrated by experiments probing this behavior, is available in refs 69 and 70. A discussion of classical versus quantum coherence in molecular systems can be found in ref 71.

### 2.3. Frenkel and Charge Transfer Excitons

In addition to the Frenkel excitons discussed above, possible excited species are charge transfer (CT) excitons. In contrast to Frenkel excitons that comprise neutral states, the CT excitons comprise ionic states (so that opposite charges reside on different molecules). In this case, the excited state wave function  $\Psi_{JE}$  in eq 9 is given by

$$\Psi_{JE}(CT) = \psi_j^+ \psi_{j+1}^- \prod_{i=1, i \neq j, j+1}^N \psi_{i0} \quad (11)$$

Just like Frenkel excitons, the CT excitons could be delocalized<sup>72,73</sup> or localized (forming, for example, an excimer<sup>74–77</sup>). Additionally, in real physical systems, Frenkel and CT excitons are not independent, and the Frenkel–CT exciton interaction (explicitly discussed in, for example, refs 41, 78, and 79) has important implications for exciton and charge carrier dynamics.<sup>80</sup> The nature of the excitations involved can be appreciated via the explicitly written electronic Hamiltonian of the system:<sup>81</sup>

$$H_{el} = \sum_{mn} (J_{mn} - U\delta_{mn}) c_m^\dagger d_n^\dagger c_n d_m + \sum_n (t_e c_n^\dagger c_{n+1} + t_h d_n^\dagger d_{n+1} + H. c. ) - \sum_{n,s \neq 0} V_{CT}(s) c_n^\dagger c_{n+s}^\dagger d_{n+s} d_n \quad (12)$$

which assumes a subspace consisting of a single electron and a single hole.<sup>81</sup> Here  $c_n^\dagger$  ( $c_n$ ) creates (annihilates) an electron in the LUMO and  $d_n^\dagger$  ( $d_n$ ) creates (annihilates) an electron in the HOMO of the  $n$ th molecule, whereas  $c_n^\dagger d_n^\dagger$  and  $c_n d_n$  create and annihilate, respectively, a local Frenkel excitation. The first term in eq 12 accounts for energy transfer between the  $n$ th and  $m$ th molecules, mediated by the Coulomb coupling  $J_{mn}$ , and it also includes the local exciton binding energy  $U$ . The second term describes the CT mediated by the electron ( $t_e$ ) and hole ( $t_h$ ) transfer integrals, which also couple Frenkel and CT excitons. The last term accounts for the Coulomb binding energy between the charges separated by the distance  $|s|d$ , where  $d$  is the distance between nearest neighbors, with

$$V_{CT}(s) = \frac{e^2}{4\pi\epsilon_0\epsilon|s|d} \quad (13)$$

The nature of low-energy excitations in molecular crystals has been a subject of several theoretical investigations.<sup>79,80,82,83</sup>

In acenes, coupling between the Frenkel and CT excitons has been theoretically shown to increase with molecular size<sup>41</sup> and to have a direct relation with the magnitude of the Davydov splitting (Figure 2(c)).<sup>46,80</sup> Importantly, large hybridization of Frenkel and CT excitons, resulting in the CT character of the lower Davydov component, has been cited as one of the reasons behind fast and efficient SF in Pn crystals<sup>80</sup> and as a factor promoting charge generation at D/A interfaces and singlet exciton diffusion.<sup>41</sup> The issue, however, is still debated.<sup>19,79</sup> For example, Qi et al.<sup>84</sup> observed the presence of both CT and Frenkel excitons near the onset of absorption of Pn crystals at energies as low as  $\sim 1.88$  eV, whereas Haas et al.<sup>85</sup> observed Frenkel-only excitons at  $\sim 1.8$ – $2.6$  eV in crystalline Pn films. Hestand et al.<sup>46</sup> proposed that, in Pn crystals, the lower (*b*-polarized) component of the Davydov band has a large (45%) admixture of the Frenkel and CT excitons, whereas the upper (mainly *a*-polarized) component has mostly Frenkel exciton character (15% of the CT content). To resolve the issue and to develop understanding of the Frenkel-CT mixing depending on the molecular structure and packing, systematic studies done on single crystals are desirable.<sup>79</sup> Also of importance is to establish how exciton character manifests into experimentally measured features. For example, Ishino et al.,<sup>86</sup> based on the analysis of transient absorption spectra (and their derivative-like features in particular) and time-resolved PL, reported optical excitation of *mixed* Frenkel and CT excitons in DNTT films and proposed that such excitons exert electric fields on the surrounding molecules, inducing a Stark shift. However, the theoretical analysis of Fujita et al.<sup>83</sup> suggests that the appearance of derivative-like features is more consistent with formation of *localized* Frenkel exciton upon photoexcitation and that the Stark effect occurs from CT states *after* the Frenkel-CT decoherence time.

## 2.4. Molecular Aggregates

A variety of high-performance small-molecule and polymeric materials owe their enhanced properties to particular  $\pi$ -stacking motifs that promote exciton and/or charge carrier delocalization and transport. Therefore, of particular interest is the exciton dynamics in H-, J-, and recently introduced HJ-type molecular aggregates<sup>87–89</sup> that are often formed in  $\pi$ -stacked arrangements. For example, H-aggregates are frequently found in materials with a face-to-face packing motif, whereas J-type behavior is expected from head-to-tail arrangements (Figure 3). Spectral features and PL QYs and lifetimes obtained as a result of different packing motifs can be appreciated from Figure 4.<sup>90</sup> The exciton coupling is determined by the values of  $J_{mn}$  in eq 12; if one considers a linear array of molecules with dominant nearest-neighbor interaction determined by the exciton coupling  $J_{n,n\pm 1} = J_0$ , then  $J_0 > 0$  for H- and  $J_0 < 0$  for J-aggregates, and the exciton bandwidth  $W$  is  $W = 4|J_0|$ .<sup>89</sup> A tutorial review of excitons in molecular aggregates and manifestation of their properties in the optical absorption and PL properties can be found in ref 91. For a comprehensive discussion of the various structural characteristics of the absorption and emission spectra, depending on the sign of  $J_0$  and the magnitude of the exciton-vibrational coupling, as well as temperature, see ref 11.

In a series of articles,<sup>26,34,45,47,92</sup> Spano provided a valuable guide to analyzing optical spectra of aggregates which allows one to determine the type of the aggregate and to extract information about intra- and interaggregate disorder, exciton

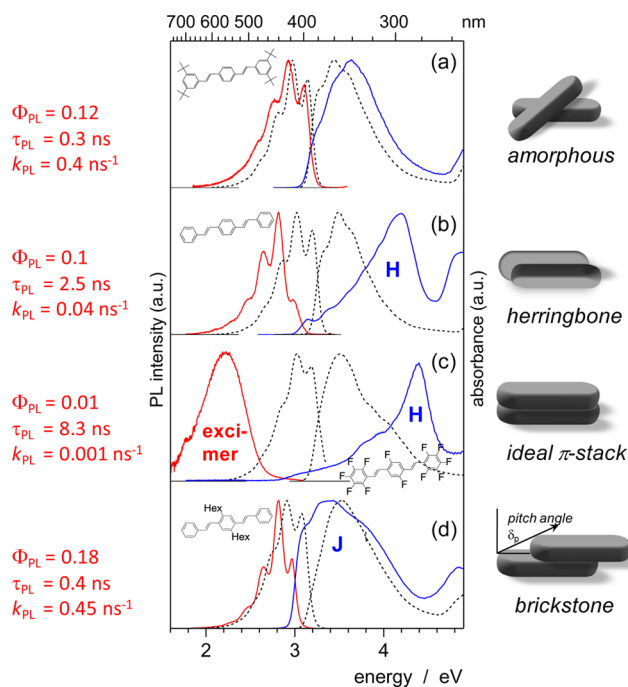


**Figure 4.** Optical absorption (right) and PL emission (left), as well as PL quantum yields, lifetimes and radiative rate constants, of DSB-based nanoparticles. Emission from excimers and H- and J-aggregates is indicated. Spectra obtained in solutions are also included (dashed lines). Reproduced with permission from ref 90. Copyright 2013 Royal Society of Chemistry.

bandwidth, correlation and coherence lengths, etc. The method relies on the analysis of the temperature dependence of the ratio of 0–0 and 0–1 intensities (eq 1) obtained from fits of the optical absorption and PL spectra with eqs 3 and 5 describing vibronic progression (Section 2.1). It is often necessary to perform this analysis even if the only goal is to determine the type of the aggregate, since in many cases relying on the solution-to-solid spectral shifts (expected to be blue for H- and red for J-aggregates, based on the selection rules) is not reliable due to large nonresonant shifts  $\Delta D$  (Section 2.2).

**2.4.1. H-Aggregates.** Optical absorption and PL properties of various organic semiconductors, both small-molecule (such as DSB<sup>90,93</sup> or diF TES-ADT<sup>28</sup>) and polymers (such as P3HT<sup>26,27,31</sup>), have been described in the framework of those of H-aggregates. In ideal H-aggregates (with no disorder), the emission from the bottom of the exciton band to the ground state (i.e.,  $0 \rightarrow 0$  transition) is strictly forbidden due to symmetry reasons; the  $0 \rightarrow 0$  emission is allowed only if it originates at the top of the exciton band, which holds most of the oscillator strength of the transition (Figure 3(a)). The strongly reduced transition dipole moment of the lowest-energy transition in H-aggregates has been cited to be potentially beneficial for achieving a stable charge-separated state (as there is no competition with, for example, superradiant emission in J-aggregates).<sup>48</sup> In contrast to  $0 \rightarrow 0$  emission, that from  $0 \rightarrow 1$  and  $0 \rightarrow 2$  transitions is not restricted and is allowed from any state within the exciton band.<sup>94</sup> At  $T = 0$  K, after a picosecond time-scale relaxation of the exciton to low-energy states, the top of the exciton band is thermally inaccessible, and the highest energy emission occurs to the first vibronic level of the ground state (i.e.,  $0 \rightarrow 1$  transition).<sup>26,95</sup> At  $T > 0$  K, some  $0 \rightarrow 0$  emission may occur due to thermal activation of the exciton to the top of the band. In the presence of disorder, the oscillator

strength is more evenly distributed within the exciton band,<sup>94</sup> and the  $0 \rightarrow 0$  emission can be significant even at low temperatures.<sup>26,95</sup> The strength of the  $0 \rightarrow 0$  emission serves as a probe of disorder and coherence of the emitting exciton. In contrast, emission from vibronic progressions,  $0 \rightarrow 1$  and  $0 \rightarrow 2$ , is mostly of incoherent origin and is considerably less sensitive to the presence of disorder.<sup>26,47,95</sup>

In the case of weakly coupled ( $W \ll \hbar\omega_0$ , where  $\omega_0$  is the effective or main intramolecular vibrational frequency) H-aggregate, the exciton bandwidth  $W$  ( $W = 4|J_0|$ ) can be extracted from the ratio of intensities of  $0 \rightarrow 0$  and  $0 \rightarrow 1$  absorption peaks (obtained from fits of the optical absorption spectra with eq 3).<sup>47</sup> For example, when the Huang–Rhys parameter  $S = 1$  (e.g., in P3HT),<sup>91</sup>

$$\frac{(I_{0-0}/I_{0-1})_{\text{abs}} \approx (1 - 0.24W/(\hbar\omega_0))^2}{(1 + 0.073W/(\hbar\omega_0))^2} \quad (14)$$

This relationship can be readily modified for other values of  $S$ .<sup>28,47,96</sup> The ratio  $(I_{0-0}/I_{0-1})_{\text{abs}}$  of eq 14 decreases as  $W$  increases, and it serves as a sensitive measure of intermolecular (or interchain) excitonic coupling.<sup>91</sup>

Similarly, analysis of the ratio of the  $0 \rightarrow 0$  and  $0 \rightarrow 1$  PL emission intensities (obtained from fits of the PL data with eq 5) yields the spatial correlation parameter  $\beta$  ( $0 \leq \beta \leq 1$ ), from which the correlation length  $l_0$  is determined using  $l_0 = 1/\ln(\beta)$ . For example, if the Huang–Rhys parameter  $S = 1$ , then

$$\frac{(I_{0-0}/I_{0-1})_{\text{PL}} = (1 - \beta)/(1 + \beta)(\sigma/W)^2(1 - 0.24W/(\hbar\omega_0))^2}{(1 - 0.39W/(\hbar\omega_0))^2} \quad (15)$$

where  $\sigma$  can be obtained from Gaussian fits to the PL spectral lines in accordance to eq 4. With such analysis, correlation lengths of 7.8 and 3.8–5 (corresponding to exciton delocalization over 7–8 and 4–5 molecules, respectively) were obtained in P3HT<sup>26</sup> and diF TES-ADT<sup>28</sup> crystalline films. Further analysis can be performed to yield the exciton coherence length.<sup>26</sup> Recently, the approach has been extended to two dimensions (2D), which enables quantifying exciton delocalization in 2D. For example, in high-molecular-weight P3HT  $\pi$ -stacked aggregates, the coherence length along the polymer backbone was determined to be about 2 nm, while the interchain coherence length was  $<1$  nm.<sup>97</sup> The  $(I_{0-0}/I_{0-1})_{\text{PL}}$  ratio of eq 15 grows with increasing disorder through increasing  $\sigma$  and/or decreasing  $\beta$  (or  $l_0$ ), which can manifest in the PL temperature dependence, as has been observed in various materials.<sup>26,28</sup> For example, from analysis of PL spectra in a broad temperature range (5–300 K), Panzer et al.<sup>31</sup> were able to distinguish between two types of H-aggregates forming in P3HT solutions due to subtle differences in temperature-dependent packing arrangements of P3HT chains.

The approach outlined above was also extended to include coupling to both fast (e.g., C–C stretching, 1400  $\text{cm}^{-1}$ ) and slow (e.g., torsional,  $<1000$   $\text{cm}^{-1}$ ) modes.<sup>98</sup> The results showed that coupling to the slow mode in H-aggregates increases the radiative QY, so that in the limit of strong electron–phonon coupling fluorescence is no longer quenched. This explains the experimental observations of strong emission reported in several H-aggregated systems (e.g., with fluorescence QY of 0.3 in hexaphenyl films).<sup>99</sup>

**2.4.2. J-Aggregates.** J-aggregate formation has been observed in a variety of small-molecule<sup>96,100–102</sup> and

polymer<sup>91,103,104</sup> materials, prominent examples of which include PDI derivatives, porphyrins, cyanine dyes, and PDA. Similar analysis of the PL spectra to that discussed above for the case of H-aggregates can be applied for J-aggregates.<sup>91</sup> Similar expressions to those of eqs 14 and 15 can be used by incorporating the change of the sign of  $J_0$  (so that  $J_0 < 0$ ) as a reversal of the signs of  $W$  in the numerator and denominator. Then, the opposite trends in the behavior of the intensities of the  $0 \rightarrow 0$  and  $0 \rightarrow 1$  transitions are predicted for J-aggregates, as compared to H-aggregates (Figure 3(b)). For example, the ratio of the  $0 \rightarrow 0$  and  $0 \rightarrow 1$  intensities in the absorption spectrum increases with increasing  $W$ , whereas the  $0 \rightarrow 0$  to  $0 \rightarrow 1$  intensity ratio in the PL spectrum decreases with increasing temperature or increasing disorder. In ideal aggregates,  $(I_{0-0}/I_{0-1})_{\text{PL}}$  is given by

$$(I_{0-0}/I_{0-1})_{\text{PL}} = N_{\text{coh}}/S \quad (16)$$

where  $N_{\text{coh}}$  is the exciton coherence number (and  $S$  is the Huang–Rhys parameter).<sup>104</sup> Equation 16 reflects coherent enhancement of the  $0-0$  intensity, which decreases with temperature as the exciton localizes (in contrast to that in H-aggregates). For aggregates containing two molecules per unit cell,  $N$  is the total number of molecules in the aggregate in the polarization direction of the lower Davydov component.<sup>96</sup> In the presence of disorder,  $N$  is replaced by  $N_{\text{coh}}$ , which is the number of coherently connected molecules in the emitting exciton; it decreases from  $N$  to 1 as the disorder or temperature increases.

The enhanced coherence number at low temperatures for J-aggregates leads to cooperative emission or superradiance, a phenomenon in which the radiative rate of the aggregate ( $k_{\text{rad}}$ ) exceeds that of the monomer ( $k_{\text{mon}}$ ) by a factor of  $N_{\text{coh}}$  so that  $k_{\text{rad}}/k_{\text{mon}} = \mathcal{F} N_{\text{coh}}$ , where  $\mathcal{F}$  is a generalized Franck–Condon factor.<sup>104</sup> For example, in Tc aggregates, a superradiant exciton delocalized over  $N_{\text{coh}}$  of  $\sim 10$  molecules was observed at sub-50-ps after photoexcitation.<sup>34</sup> Based on the sensitivity of the  $0 \rightarrow 0$  PL peak to coherence, a methodology to monitor exciton spatial coherence in time using time-resolved fluorescence spectroscopy was proposed. The approach was demonstrated to be robust for J-aggregates on any time-scales and applicable to H-aggregates at early times after photoexcitation.<sup>55</sup> As an example of experimental realization of such a methodology, Sung et al.<sup>105</sup> used the time evolution of the ratio of the  $0 \rightarrow 0$  and  $0 \rightarrow 1$  PL intensities measured via fluorescence upconversion spectroscopy in conjunction with eq 16 to determine the time-dependent exciton coherence number ( $N_{\text{coh}}$ ) in PBI  $\pi$ -stacked aggregates. They determined that, in columnar  $\pi$ -stacks, the Frenkel exciton is initially delocalized over at least three monomers and coherently moves along the stack for several tens of femtoseconds before forming an excimer. Enhanced radiative rates of J-aggregates have been extensively explored in photonic applications that rely on exciton–photon coupling resulting from interactions between excitons and cavity modes.<sup>7–9</sup>

**2.4.3. HJ-Aggregates.** An interplay of interference between Coulomb coupling which promotes H-aggregate behavior and CT-mediated coupling which promotes J-aggregate behavior results in so-called HJ-aggregate behavior (Figure 3(c)).<sup>88</sup> Such interplay manifests in the optical absorption spectra, reported, for example, in TAT nanopillars,<sup>87</sup> which were treated theoretically in ref 81. It was predicted that this phenomenon should be common for conjugated polymer chains which have intrachain J-like coupling and interchain H-

like coupling.<sup>104</sup> The PL  $0 \rightarrow 0$  to  $0 \rightarrow 1$  intensity ratio in HJ-aggregates exhibits an H-like thermally activated behavior up to temperature  $T \approx 1.3\Delta E/k_B$  (where  $\Delta E$  is shown in Figure 3(c)) followed by J-like behavior,  $\sim T^{-1/2}$ , at higher temperatures; see theoretical description in ref 88.

When the Frenkel exciton band is energetically well separated from the CT band, the electronic Hamiltonian responsible for exciton physics in the HJ-aggregate can be presented as follows:<sup>81</sup>

$$H_{\text{eff}} = \sum_{mn} (J_{mn} + J_{\text{SR}} \delta_{m,n\pm 1}) c_m^\dagger d_m^\dagger c_n d_n + \sum_n (\Delta_{\text{SR}} - U) c_n^\dagger d_n^\dagger c_n d_n \quad (17)$$

which incorporates the effective short-range (SR) coupling  $J_{\text{SR}}$  given by

$$J_{\text{SR}} = -\frac{2t_e t_h}{U - V_{\text{CT}}(1)}$$

and the second-order energy level shift  $\Delta_{\text{SR}}$  given by

$$\Delta_{\text{SR}} = -\frac{2(t_e^2 + t_h^2)}{U - V_{\text{CT}}(1)}$$

with all other parameters the same as those defined for eq 12.

The short-range CT coupling has been shown to be considerably more sensitive to sub-Angstrom slips between the neighboring molecules in a  $\pi$ -stack, in contrast to the long-range Coulomb coupling. Because such slips also affect electronic properties (e.g., charge carrier mobility),<sup>106,107</sup> it could be possible to screen for aggregates with high charge carrier mobility using the absorption spectrum that incorporates the exciton mobility. With these considerations, if the  $0 \rightarrow 0$  to  $0 \rightarrow 1$  intensity ratio in the optical absorption of the solid is similar to that of the noninteracting molecules (e.g., in solution), then the short- and long-range coupling are canceled, yielding a low mobility exciton. Aggregates in which this ratio strongly deviates from the monomer value are then expected to have the highest mobility. The concept of interfering couplings has been shown to remain robust in the presence of the static disorder and resistant to dynamic disorder in  $\pi$ -stacks.<sup>81</sup>

In spite of theoretical guidance outlined above, analysis of experimentally measured optical spectra in organic semiconductors and their interpretation are not straightforward, as illustrated below. Depending on polarization, spectra may reveal H- or J-character of aggregates.<sup>96</sup> For example, using polarized optical absorption spectra of Pn crystals, it was established that the lower (*b*-polarized) Davydov component behaves as a J-aggregate and has a 45% CT content, whereas the upper component (mainly *a*-polarized) has properties of an H-aggregate and a low (15%) CT content.<sup>46</sup> These findings are consistent with the different temperature dependences of the *a*- and *b*-polarized components that have been previously observed in Pn films (Figure 2(a)).<sup>40</sup> In polymers, interplay of interchain (promoting H-) and intrachain (promoting J-) coupling revealed hybrid HJ-character in, for example, PDA dimers. Based on the temperature dependence of the radiative decay rate and of the  $(I_{0-0}/I_{0-1})_{\text{PL}}$  ratio, the H- to J-transition, featuring thermally activated superradiance, was predicted.<sup>88</sup> Furthermore, H- or J-dominated behavior can be morphology-dependent. This is the case for P3HT spin-cast films exhibiting H-like behavior, in contrast to ordered P3HT nanofibers that

show J-like behavior.<sup>88</sup> Systematic studies of aggregate formation<sup>108</sup> and transient PL analysis are necessary to distinguish between the behavior of disordered H-aggregates<sup>28</sup> and of a combination of localized and delocalized exciton states<sup>109</sup> which manifest in similar temperature dependence of PL spectra. Other interesting exciton coupling types such as HH or JJ are also possible, as discussed in ref 81. Finally, exciton physics can be controlled via exciton–photon coupling in cavities. For example, enhancement of the exciton coherence length in J-aggregates and conversion from H- to J-aggregate-type behavior in microcavities were theoretically predicted in ref 110 and are awaiting experimental verification.

## 2.5. Energy and Charge Transfer

An exciton can move from an excited “donor” molecule (D) to an “acceptor” molecule (A) via a nonradiative process of energy transfer, after which the donor molecule is in the ground state and the acceptor molecule is in the excited state. Two processes of energy transfer are typically considered: Förster resonant energy transfer (FRET) and Dexter energy transfer. FRET is based on a dipole–dipole interaction, and because it involves fields rather than direct electron exchange, it is a long-range process. FRET is typically relevant only for the singlet exciton transport, although, in some phosphorescent materials, FRET for triplet states was also reported.<sup>16</sup> The FRET transfer rate in 3D materials scales with the D–A distance  $r$  as follows

$$k_{\text{FRET}}(r) = (1/\tau)(R_0/r)^6 \quad (18)$$

where  $\tau$  is the intrinsic exciton lifetime (not limited by any type of quenching) and

$$R_0^6 = \frac{9\Phi_f \kappa^2}{128\pi^5 n^4} \int \lambda^4 F_D(\lambda) \sigma_A(\lambda) d\lambda \quad (19)$$

where  $0 \leq \kappa^2 \leq 4$  is the dipole-dipole orientation factor,  $\Phi_f$  is the fluorescence QY of the donor,  $n$  is the refractive index at the wavelength where the spectral overlap integral is maximized,  $\lambda$  is the wavelength,  $F_D$  is the normalized donor fluorescence, and  $\sigma_A$  is the acceptor absorption cross-section. (In 2D cases, such as in the case of interaction between a molecule and graphene, the distance dependence of the FRET rate changes to  $k_{\text{FRET}} \sim 1/r^4$ .<sup>111,112</sup>) The Förster (or FRET) radius  $R_0$  is a measure for a maximal D–A distance at which significant FRET occurs; it corresponds to the D–A distance at which the FRET efficiency is 1/2 of the maximal FRET efficiency, and it is in the 1–10 nm range,<sup>15,35</sup> which is considerably larger than the intermolecular spacings (<1 nm) in organic solids. From eq 18, the FRET efficiency relies on the overlap between the emission spectrum of the donor and the absorption spectrum of the acceptor, donor fluorescence QY, acceptor absorptivity, and mutual D–A molecular orientation.

The expression of eq 18 is obtained using a point-dipole approximation and is based on only the dipole–dipole interaction. As such, it does not account for the localized/delocalized character of the excited-state wave functions pertinent to conjugated systems in the solid state. A generalization of the Förster theory was proposed,<sup>63</sup> which introduced a Förster critical distance defined as

$$R_G = \eta R_0$$

where  $\eta$  is the electronic coupling correction factor. For example, for the bridged poly(para-phenylenes),  $\eta$  was found to be in the range between 1.1 and 1.6 for the head-to-head and in the range between 0.2 and 0.8 for the cofacial configurations.

At shorter D–A distances (<1 nm), the dipole approximation breaks down, so that higher order multipole contributions play a role in the intermolecular Coulomb interactions. Additionally, a short-range Dexter energy transfer, which relies on the overlap of molecular orbitals and proceeds via direct exchange of electrons, may occur. The Dexter mechanism applies both to singlet and triplet excitons, and its efficiency exponentially decreases with the D–A distance  $r$ , yielding the transfer rate

$$k_{\text{DET}}(r) = KJ \exp(-2r/L) \quad (20)$$

where  $K$  is related to specific orbital interaction,  $J$  is a normalized spectral overlap integral, and  $L$  is the van der Waals radius.<sup>15</sup> In organic crystals, the Dexter transfer occurs most efficiently in the direction of  $\pi$ – $\pi$  stacking.

In contrast to FRET, Dexter transfer does not rely on the QY of the donor emission or on the absorption cross-section of the acceptor, and it is, therefore, considered to be the dominant mechanism of triplet exciton migration. In amorphous solids, the Dexter-type triplet transfer was described as a correlated transfer of two electrons utilizing Marcus (eq 21) or Miller–Abrahams (eq 31) rates which proceeded via multiphonon hopping and single-phonon-assisted tunneling at high and low temperatures, respectively.<sup>113</sup> In particular, at higher temperatures the triplet transfer was mainly governed by the changes in molecular configurations, whereas at low temperatures it was dominated by the energetic disorder.

If the differences in the donor and acceptor LUMO energies, the  $\Delta\text{LUMO}$  values, are large enough to overcome the exciton binding energy, the electron transfer from donor to acceptor becomes a competing process with the energy transfer.<sup>114</sup> (Hole transfer is also possible if donor and acceptor HOMO levels are properly aligned.<sup>115</sup>) This is a short-range interaction (<1 nm) that relies on the spatial overlap of D and A wave functions, and the result of this interaction is a positively charged donor and negatively charged acceptor molecule. The most common description of electron transfer (ET) is provided by the Marcus theory, with the following expression for the transfer rate:<sup>116,117</sup>

$$k_{\text{ET}} = \frac{(J_{\text{DA}})^2}{\hbar} \sqrt{\frac{\pi}{\lambda k_{\text{B}}T}} \exp\left[-\frac{(\lambda + \Delta G)^2}{4\lambda k_{\text{B}}T}\right] \quad (21)$$

where  $J_{\text{DA}}$  is the electronic coupling,  $\lambda$  is the reorganization energy, and  $\Delta G$  is the total Gibbs energy change for the CT reaction.

When describing charge carrier or exciton dynamics in the solid state, a simpler Miller–Abrahams expression (eq 31) is often used (Section 3.1). Examples include description of charge hopping in polymers,<sup>118</sup> charge trapping/detrapping in PR polymers<sup>119</sup> and polycrystalline films,<sup>120</sup> and triplet exciton diffusion in disordered materials.<sup>121</sup>

More recently, to describe charge carrier hopping in high-mobility crystalline small-molecule materials and polymers,<sup>122,123</sup> an ET rate that incorporates the quantum-mechanical nuclear tunneling effect has been utilized, which is given by<sup>122</sup>

$$k_{\text{ET,QM}} = \frac{(J_{\text{DA}})^2}{\hbar} \int_{-\infty}^{\infty} dt \exp\left[-\sum_j S_j(2\bar{n}_j + 1) - \bar{n}_j e^{-i\omega_j t} - (\bar{n}_j + 1)e^{i\omega_j t}\right] \quad (22)$$

where  $\bar{n}_j = 1/[\exp(\hbar\omega_j/k_{\text{B}}T) - 1]$  is the occupation number for the  $j$ th vibrational mode with frequency  $\omega_j$  and  $S_j$  is the Huang–Rhys factor for the  $j$ th mode. In the limits of strong electron–phonon coupling ( $\sum_j S_j \gg 1$ ), short time-scales, and high temperature ( $\hbar\omega_j/k_{\text{B}}T \ll 1$ ), eq 22 transforms into eq 21 with  $\lambda = \sum_j S_j \hbar\omega_j$ .

## 2.6. Exciton Diffusion

Exciton transport in organic semiconductors is important for many optoelectronic applications, including OPVs and OLEDs. Exciton quantum transport was studied theoretically;<sup>61</sup> for example, several studies in light-harvesting systems<sup>124</sup> and in 1D molecular assemblies<sup>125</sup> focused on the effects of traps and dynamic disorder on the coherent transport. Pelzer et al.<sup>124</sup> modeled the efficiency of exciton quantum transport in light-harvesting systems and demonstrated that, in the presence of a trap, quantum transport is most sensitive to changes in spatial correlation in the region near the trap. Moix et al.<sup>125</sup> applied the Haken–Strobl–Reineker model to numerical studies of coherent quantum exciton 1D transport in disordered systems in the presence of thermal fluctuations and determined that the static disorder promotes localization, while dynamic disorder induces transport. In particular, at short time-scales, a nondiffusive motion of a free particle bounded by Anderson localization length-scales was obtained. This was then followed by the environment-induced dephasing (which destroys the phase coherence responsible for Anderson localization), leading to diffusive transport at longer time-scales. In a weak dephasing regime, the diffusion constant was found to be proportional to the square of the localization length, which significantly enhanced the exciton diffusion rate for the quantum coherent transport as compared to the classical case.

In amorphous and polycrystalline organic materials, coherent exciton transport over long distances is not readily realized; instead, it mostly occurs by incoherent hopping, which is facilitated by Förster or Dexter energy transfer described above. Comprehensive recent reviews of exciton diffusion are available.<sup>15,16</sup> An excellent summary of methods of measuring diffusion lengths suitable for various sample geometries and morphology, along with a survey of diffusion coefficients in various materials, can be found in ref 16. A new method based on time-resolved transient absorption spectroscopy which utilizes a time-of-flight-type methodology for obtaining diffusion coefficients was also recently proposed.<sup>126</sup> Methods for numerical simulations of exciton diffusion were reviewed in ref 17.

Exciton diffusion models that translate nanoscale energy transfer rates of eq 18 into mesoscopic-level transport vary in complexity.<sup>17</sup> In a simple case, exciton diffusion can be described in the framework of random walk,<sup>16</sup> and it is modeled as a simple differential equation:

$$\frac{dn}{dt} = D\nabla^2 n - \frac{n}{\tau} + G \quad (23)$$

Here  $n$  is the exciton density,  $\tau$  is the exciton lifetime,  $D$  is the diffusion coefficient, and  $G$  is the exciton generation rate.

Once the exciton is created (with a certain energy), it starts a downhill migration via energy transfer toward the lower energy sites. For singlet excitons, this process takes  $\sim 100$  ps and can be observed by the bathochromic shift of the PL spectrum during this time. In disordered materials at room temperature, the downhill migration proceeds to a quasi-equilibrium level at  $-\sigma^2/k_{\text{B}}T$  below the center of the Gaussian DOS (see Section

4.2.5),<sup>2</sup> which can be monitored by observing the position of the PL maximum.<sup>28</sup> After this, thermally activated hopping typically occurs, which can be described by the diffusion equation (e.g., eq 23) and characterized by the diffusion length

$$L_D = (ZD\tau)^{1/2} \quad (24)$$

where  $Z = 1, 2,$  or  $3$  depending on whether diffusion occurs in 1D, 2D, or 3D space,  $D$  is the diffusion coefficient, and  $\tau$  is the exciton lifetime. When hopping is mediated by FRET,  $D = (A/\tau)(R_0^6/6r^4)$ , where  $R_0$  is the Förster radius of eq 19 and  $A$  is a constant that accounts for the distribution of molecular separations  $r$  (which ranges between the  $\pi$ - $\pi$ -stacking distance of  $\sim 3$ – $4$  Å and  $R_0$  of  $\sim 3$ – $5$  nm). Typical values for the diffusion coefficient  $D$  are  $10^{-4}$ – $10^{-2}$  cm<sup>2</sup>/s for singlet excitons and  $10^{-6}$ – $10^{-3}$  cm<sup>2</sup>/s for triplet excitons. Typical diffusion lengths  $L_D$  are  $\sim 5$ – $20$  nm for singlets (with polymers on the lower end and small molecule materials on the higher end) and  $\sim 30$ – $300$  nm for triplets, although  $>100$  nm diffusion lengths for singlets and  $>1$   $\mu$ m (and even  $>10$   $\mu$ m in several single crystals) for triplets have also been reported.<sup>16,127,128</sup> At lower temperatures (below  $\sim 150$ – $250$  K, depending on the material),<sup>16,28</sup> excitons cannot reach the quasi-equilibrium level, as their energy is insufficient for the downhill migration. In this regime, thermally activated hopping does not occur and  $D$  and  $L_D$  become temperature dependent and rely on particular characteristics of the DOS.

Exciton diffusion is isotropic in amorphous films and anisotropic in organic crystals.<sup>129</sup> The source of such anisotropy is the low degree of symmetry of organic crystals and the strong dependence of the FRET rate on the mutual orientations of the molecules and/or of the Dexter rate on the spatial overlap of the wave functions of the neighboring molecules. Given the mechanisms involved in energy transfer, the routes for optimized singlet and triplet exciton diffusion have been identified.<sup>15</sup> These involve maximizing fluorescence QY and reducing the index of refraction for the singlet exciton diffusion and improving molecular order via templating, crystallization, or self-assembly for the triplet exciton diffusion. In both cases, it is also important to design interfaces between grains or phases such that exciton trapping and quenching are minimized.

High exciton densities and diffusion increase the probability of two excitons interacting during their lifetimes, which may result in exciton–exciton annihilation.<sup>130</sup> Exciton quenching can also occur by defects, metal interfaces, etc., which manifests in the reduction of PL decay lifetimes and QY (which could be systematically studied to determine the exciton diffusion lengths).<sup>131</sup> It was recently discussed that the exciton quenching sites that limit exciton diffusion have the same origin as traps for charge transport in many polymeric and small-molecule materials.<sup>132</sup> Therefore, optimization of exciton transport could lead to optimal charge transport as well. Indeed, an increase in exciton diffusion coefficients due to reduced disorder has been correlated with similar improvements in charge carrier mobility in materials ranging between amorphous polymers<sup>133</sup> and crystalline small-molecule films.<sup>134</sup> Another exciton quenching channel is exciton–polaron annihilation, which is detrimental for OLED operation at larger currents<sup>135</sup> and for the fill factor (FF) in planar HJ solar cells;<sup>136</sup> however, this mechanism is relatively unexplored. Another unexplored area is exciton diffusion in n-type materials, as most exciton diffusion studies have been done on p-type materials (mostly because of the availability of fullerene derivatives as efficient PL quenchers).<sup>16</sup> Also of interest are systematic studies of exciton

diffusion in new generation OLED materials such as those based on TADF (Section 2.7.2), which may reveal interesting phenomena. For example, recently, transport of the electron–hole pair of the CT state in TADF materials was directly observed, and “inchworm”-like motion over 5–10 nm was demonstrated.<sup>137</sup>

## 2.7. Exciton Physics That Enables Novel Material Design Paradigms

**2.7.1. Singlet Fission.** A process of singlet fission (SF), in which excitation of one singlet exciton results in formation of two triplet excitons, recently attracted considerable attention due to the potential of utilizing this process in obtaining solar cells with up to 200% internal quantum efficiency (IQE). Comprehensive reviews of the SF process are available.<sup>18–21,24</sup> Briefly, the process starts with a noninteracting combination of molecules in  $S_0$  and  $S_1$  states, and the SF is induced by the interaction Hamiltonian  $H_{\text{int}} = H_{\text{el}} + H_{\text{spin}}$ , where  $H_{\text{el}}$  describes spin-independent electrostatic interactions and  $H_{\text{spin}}$  comprises spin-dependent interactions.<sup>19</sup> The action of  $H_{\text{el}}$  represents the internal conversion and produces a pair of coherently coupled triplet states  $^1(\text{TT})$  (also known as multiexciton ME states<sup>60,138</sup>). The exact mechanism of the  $^1(\text{TT})$  formation is still under debate, with the main contenders being a one-step mechanism (via direct  $S_0S_1$  and  $^1(\text{TT})$  coupling), a two-step (CT-mediated) mechanism, and the quantum interference between these two pathways, all of which have been extensively studied theoretically.<sup>139–143</sup> The magnitude of  $H_{\text{spin}}$  with respect to the energies of other coupled triplet states configurations (e.g.,  $^3(\text{TT})$  and  $^5(\text{TT})$ ) determines whether the coupled triplets would diffuse apart.<sup>19</sup>

The SF process,  $S_0 + S_1 \rightarrow ^1(\text{TT}) \rightarrow T_1 + T_1$ , is spin-allowed and thus can occur on subpicosecond time-scales. To be competitive with other processes, it proceeds most efficiently if  $E(S_1) \geq 2E(T_1)$ . Based on the nature and alignment of excited states, Smith and Michl<sup>20</sup> categorized SF-exhibiting materials into three classes. The best-studied class is molecules in which the  $S_1$  excitation is dominated by the HOMO–LUMO transition and is separated energetically from  $S_2$ . This is the case for acene derivatives, which have served as a model system for systematic studies of the intermolecular SF. These include Pn<sup>23,140,144</sup> and functionalized Pn derivatives such as TIPS-Pn,<sup>76,145,146</sup> DTP-Pn,<sup>58</sup> or halogenated R-Pn,<sup>147</sup> Tc<sup>60,148–152</sup> and TIPS-Tc,<sup>149</sup> and Hex<sup>153</sup> and TCHS-Hex.<sup>154</sup> Particularly instructive are comparisons between the SF properties in Pn and Tc, in which the exothermic and endothermic scenarios for the SF process, respectively, are realized.<sup>60,150,155</sup> One recent observation is that although the endothermic nature of the SF in Tc leads to a slower fission process (as compared to Pn or TIPS-Pn), the triplet excitons in Tc experience a singlet-mediated enhancement in their diffusion coefficients by more than an order of magnitude on the picosecond–nanosecond time-scales,<sup>156</sup> whereas such enhancement is not realized in TIPS-Pn. This observation then prompts an additional energy consideration for SF-based optoelectronics that considers not only the efficiency of the SF process itself but also the subsequent exciton dynamics.

On the fundamental physics level, the questions under debate include the role of coherence and of the states with a CT character in determining the SF efficiency.<sup>18</sup> One particular controversy concerns the strength of coupling between the  $S_1S_0$  and  $^1(\text{TT})$  states. Recent theoretical work predicts insignificant coupling, which suggests that coherence is not important for

achieving high SF efficiency.<sup>157</sup> This is consistent with 200% triplet yields achieved via the SF process in TIPS-Pn solutions,<sup>76</sup> in which formation of excimers was determined to be the key factor, thus supporting the CT-mediated formation of  $^1(\text{TT})$ . This experimental observation supports a hypothesis of a fast two-step formation of  $^1(\text{TT})$  (rather than a one-step process via direct coupling), which has been put forward in theoretical work in refs 80, 139, and 150. In particular, while the direct coupling between the  $\text{S}_1\text{S}_0$  and  $^1(\text{TT})$  states is weak, the coupling mediated by the intermediate CT states could be strong. Yao<sup>158</sup> incorporated local and nonlocal electron–phonon coupling (see Section 4.1) into the Frenkel–CT mixing model and revealed that the CT-mediated SF was facilitated by quantum coherence and controlled by nonlocal coupling. Aryanpour et al.<sup>143</sup> found that the intermolecular CT plays a strong role in the SF not only in acenes, but also in polyenes. In the CT-mediated mechanism for the SF, the CT properties determine the SF efficiency; for example, if the CT character is too weak (e.g. for high-energy CT states), the  $^1(\text{TT})$  formation is thought to proceed via a superexchange mechanism (through virtual CT states), the efficiency of which scales inversely with the energy mismatch between Frenkel and CT states. However, if the CT character is too strong, stable excimer states can form which could prevent triplet generation.<sup>143,159</sup>

On the other hand, temperature-independent SF in crystalline Tc (in spite of the endothermic scenario with  $E(\text{S}_1) - 2E(\text{T}_1) = -0.2$  eV) has been observed and attributed to the strong electronic coherent coupling, invoking entropic gain for the triplet exciton generation.<sup>60</sup> In this case, strong coherent coupling was considered to be the reason behind the appearance of the  $^1(\text{TT})$  state at <20 fs (limited by the experimental resolution of TR-2PPE) simultaneously with the  $\text{S}_1$  exciton formation, whereas the separated triplets  $\text{T}_1$  were observed at 10–100 ps time-scales. The contribution of coherent coupling to SF in several Pn derivatives was also emphasized by Bakulin et al.<sup>58</sup> However, in that case it was the coherent coupling between *vibronic states* in the  $^1(\text{TT})$  manifold, and *not the electronic coupling* between the  $\text{S}_1\text{S}_0$  and  $^1(\text{TT})$ , which was deemed important for the SF, as directly confirmed using 2DES (Section 7.1.1.3).

Theoretical investigations examined the role of molecular packing<sup>160,161</sup> in determining the SF in the solid state. A packing motif yielding efficient SF has been identified to be a slip-stack arrangement with the slip in the direction of the HOMO–LUMO transition moment. For example, in perylene derivatives, packing motifs such that  $dX = 3.5\text{--}4$  Å and  $dY = 0\text{--}0.5$  Å (where  $dX$  and  $dY$  are the shifts along the long and short molecular axes, respectively) were predicted to exhibit the most efficient SF.<sup>161</sup> Using nonadiabatic molecular dynamics simulations, Wang et al.<sup>160</sup> examined various Pn dimer conformations and obtained SF time-scales and triplet yields for various configurations. They observed the importance of the thermal fluctuations, concluded that the large CT character of the photoexcited state is not necessary for the efficient SF, and found a direct relation between the SF time constant and the instantaneous triplet yield. They also established that slip-stacked configurations with a shift of one ring along the transverse direction and an offset of one or two rings along the longitudinal axis of the molecule yielded the best SF efficiencies. Renaud and Grozema<sup>142</sup> examined the effects of exciton–phonon coupling on SF in PDI dimers, found that intermolecular vibrational modes can significantly affect the SF

rate, and identified conditions under which the SF rate increased by up to an order of magnitude.

Morphology has also been cited as an important factor in determining the SF efficiency, following the dynamics of the resulting triplet excitons in the solid state.<sup>152,155</sup> For example, in comparative studies of SF in Tc single crystals and films, faster SF rates were observed in polycrystalline films.<sup>12</sup> Burdett et al.<sup>148</sup> observed quantum beats in delayed fluorescence from Tc single crystals due to triplet fusion of the triplet pair in the coherent superposition state; such beats were considerably less pronounced in films.<sup>24,162</sup>

Although it is clear that molecular solids with proper energetics and character of excited states can produce triplet states via a highly efficient SF, a significant problem of efficient separation followed by transport of triplets (and potentially their separation into a pair of mobile charge carriers, as often required by applications) remains.<sup>24,163</sup> Toward solution of this problem, the first obstacle to overcome is triplet–triplet annihilation, which suggests that triplet excitons must be separated on the time-scale competitive with this process. One strategy<sup>163</sup> utilized *intramolecular* SF (iSF) to generate the  $^1(\text{TT})$  state and then used *intermolecular* interactions to separate the triplet excitons. A proof of principle demonstration was reported in oligoenes; this study also identified the need for theoretical work on molecular design principles that would maximize intramolecular biexciton formation upon optical excitation and efficient intermolecular Dexter energy transfer.

The iSF has been demonstrated in a variety of small molecules (e.g., bipentacenes<sup>164</sup> and quinodal bithiophene<sup>165</sup> with triplet yields of ~200% and 180%, respectively) and conjugated polymers (e.g., PDA, PPV, P3TV,<sup>166,167</sup> and D–A copolymers<sup>168</sup>). Sanders et al.<sup>169</sup> studied iSF in phenylene-spaced Pn–Tc heteromers depending on the spacer length. Higher iSF efficiencies were observed in heteromers with shorter spacers, which was attributed to higher singlet exciton delocalization, deemed important for the iSF in this system. Zhai et al.<sup>167</sup> examined iSF in luminescent (DOO-PPV) and nonluminescent (PDA) conjugated polymers. They found a hot exciton-mediated SF in DOO-PPV films, but not solutions, which suggests the *interchain* nature of the process. In contrast, *intra*chain SF was operational in the PDA. The iSF is advantageous because the relevant energy levels can be tuned through chemical modifications.<sup>166</sup> Based on the design principles for the intermolecular SF, Busby et al.<sup>168</sup> proposed design criteria for the materials with strong iSF: a reduced singlet–triplet gap (so that  $E(\text{S}_1) \geq 2E(\text{T}_1)$ ) and a strong CT character of the lowest-lying excitation. Following these criteria, they designed D–A small molecules and copolymers and demonstrated up to 170% triplet yields. However, understanding the mechanisms of intramolecular SF, and in particular that in polymers, and how they differ from intermolecular ones in acenes is still incomplete, requiring more studies. A recent theoretical treatment of photoexcitations in D–A copolymers<sup>170</sup> suggested that, in contrast to homopolymers, in the D–A copolymers the intramolecular (TT) states are optically allowed. Experimental verifications of this prediction and assessment of the role it plays in high PCEs achieved in solar cells with D–A copolymer donors (Table 8) are in order.

**2.7.2. Thermally Activated Delayed Fluorescence.** Thermally activated delayed fluorescence (TADF) process proceeds by reverse ISC from triplet to singlet excited states. This process is the basis for third-generation OLEDs (Section 11.4), and it relies on relatively small (e.g., < 0.2 eV) energy

differences between singlet ( $S_1$ ) and triplet ( $T_1$ ) states  $\Delta E_{ST}$ .<sup>171</sup> The internal efficiency of electroluminescence (EL) involving TADF is given by

$$\Phi_{EL}(\text{int}) = \eta_S \Phi_f + \eta_S \Phi_{TADF} + \eta_T \Phi_{TADF} / \Phi_{ISC} \quad (25)$$

where  $\eta_S = 0.25$ ,  $\eta_T = 0.75$ , and  $\Phi_f$ ,  $\Phi_{TADF}$ , and  $\Phi_{ISC}$  are the fluorescence QY, TADF QY, and ISC efficiency, respectively.

Based on this process, IQEs of nearly 100% and external QEs (EQEs) nearing 20% have been demonstrated in the blue, green, yellow, and orange-red wavelength regions.<sup>172–174</sup> These efficiencies are considerably higher than those achievable in fluorescence-based OLEDs (with theoretical EQEs of only 5%), and without the need for expensive phosphorescent materials that involve rare metals. With a combination of TADF emitters, WOLED operation was also demonstrated, with EQE of >17% and CIE (0.30, 0.38).<sup>175</sup>

The well-known TADF materials include eosin, fullerene, and porphyrin derivatives.<sup>171</sup> The molecular design such that small  $\Delta E_{ST}$  and large radiative rates are achieved simultaneously has been a subject of intensive research,<sup>176</sup> as summarized in a recent review article.<sup>171</sup> Examples of molecules with small  $\Delta E_{ST}$  include those with electron-donating and electron-accepting groups such that the spatial overlap between the HOMO and LUMO is decreased. These requirements have been realized, for example, in triazine (CC2TA), spiro- (spiro-CN), spiro-acridine, phenoxazine, and CDCB (e.g., 4Cz-TPN) derivatives. Another design strategy utilized exciplex (i.e., intermolecular D-A) states, which also have small  $\Delta E_{ST}$  as their HOMO and LUMO are spatially separated, for example m-MTDATA:t-Bu-PBD.

In addition to the use of the TADF for emitters in OLEDs, a double-dopant OLED system, which combines a wide-energy-gap host, a TADF-assistant dopant, and a fluorescent emitter dopant was proposed. In this system, triplet excitons created on the TADF-assistant dopant via electrical excitation are upconverted to the  $S_1$ (TADF) state of the TADF molecule, and then these singlet excitons are transferred to the  $S_1$ (Em) state of a fluorescent emitter molecule via FRET, followed by the radiative decay from  $S_1$ (Em) of the fluorescent emitter. Blue, green, yellow, and red OLEDs with EQE in the 13.5–18% range were demonstrated using this approach, with the emission wavelength region determined by the fluorescent emitter molecule.<sup>172</sup>

**2.7.3. FRET and CT Competition and FRET-Mediated CT in D–A Materials.** Several methods of exciton dynamics manipulation have been proposed that enhance solar cell performance. These include cascade energy relay for long-range energy transfer,<sup>177–180</sup> guiding exciton diffusion using exciton gates,<sup>181</sup> use of FRET for extending the optical absorption to longer wavelengths<sup>182</sup> and charge generation,<sup>183,184</sup> and various schemes that utilize combinations of charge and energy transfer.<sup>185,186</sup>

Coffey et al.<sup>187</sup> observed that trilayer devices such as P3HT/CuPc/ $C_{60}$  with efficient FRET toward the charge-generating CuPc/ $C_{60}$  interface exhibited a better efficiency than bilayer devices. Menke et al.<sup>178</sup> incorporated SubPc molecules in a wide-energy-gap material and showed that optimization of the molecular separation that controls intermolecular interactions and reduces exciton quenching allows for improved exciton diffusion lengths ( $L_D$ ). With this scheme, higher PL QYs, higher lifetimes, and a resulting Förster radius  $R_0$  were observed as compared to those of a pristine SubPc film. Using the improved exciton transport, the PCE of 4.4% was achieved in

planar HJ OPVs, which is higher than that in SubPc-based BHJs.<sup>178</sup> In a follow-up work, the authors introduced exciton permeable interfaces in the planar HJ devices, which break the symmetry in energy transfer and enable directional exciton transport.<sup>181</sup>

Cnops et al.<sup>179</sup> designed a trilayer  $\alpha$ -6T/SubNc/SubPc system where amorphous SubNc and SubPc served as acceptor layers with a large Förster radius of 7.5 nm. This boosted exciton transport and improved charge generation via a FRET-mediated mechanism, leading to the PCE of 8.4%, one of the best performances from small-molecule nonfullerene solar cells (Table 8).<sup>179</sup>

Griffith and Forrest<sup>180</sup> incorporated three layers of donor materials (DPT/rubrene/DBP) to create an energy cascade system combined with the acceptor ( $C_{60}$ ) layer, achieving the PCE of 7.1% (Table 8). They investigated exciton blocking, transfer, and quenching properties and analyzed contributions of the photocurrent from each layer to the device performance. It was concluded that the primary factor responsible for improved performance of this cascading system as compared to earlier ones is the efficient exciton blocking in the widest energy gap layer near the anode, which reduced the quenching.

FRET and CT competition in D:A blends, as well as their contribution to charge photogeneration, has been a subject of many studies.<sup>114,182,183,188</sup> Shepherd et al.<sup>114</sup> observed the transition from dominant FRET to CT state formation (exciplex) in small-molecule D:A combinations of functionalized ADT derivatives. When D and A molecules were separated by a neutral spacer (PMMA), FRET was the dominant process. As the spacer was eliminated, a strongly emissive CT state formation was observed; the presence of such tightly bound states subsequently was linked to inefficiency of diF TES-ADT:diCN TIPS-ADT BHJs and ternary blends based on these materials and P3HT.<sup>188</sup>

Synergistically designed exciton and charge carrier dynamics for improved device performance has been realized in organic ternary BHJs, in which an additional donor or acceptor molecule is introduced into the standard, binary blends of donor and acceptor, thus creating  $D_1:D_2:A$  or  $D:A_1:A_2$  blends. These are designed to utilize FRET, cascade CT, and/or parallel-like CT to enhance charge generation (Section 9.3.4).<sup>185,186,189–193</sup> For example, PCE of 9.2% was recently achieved in ternary blends PID2:PTB7-Th:PC<sub>71</sub>BM (Table 8) utilizing a combination of FRET and hole relay.<sup>185</sup>

Control of the exciton dynamics in blends and heterostructures is important not only for organic optoelectronics, but also for organic photonics; see the recent review in ref 194. For example, morphology-dependent FRET efficiency was recently used to reversibly switch fluorescence emission<sup>195</sup> between the red, green, and blue channels (RGB) in blends containing two types of fluorescent molecules.

## 2.8. Summary

Significant progress has been made in understanding of fundamental photophysics in molecular materials, in designing materials that enable specific features of exciton physics, and in manipulating exciton dynamics to achieve enhanced optoelectronic device performance. However, there are several aspects that warrant further exploration. The role of exciton delocalization and various coherences (electronic, vibrational, or mixed) in energy transport, singlet fission, and CT dynamics is a highly debated topic in need of systematic studies, especially by experimental techniques uniquely sensitive to

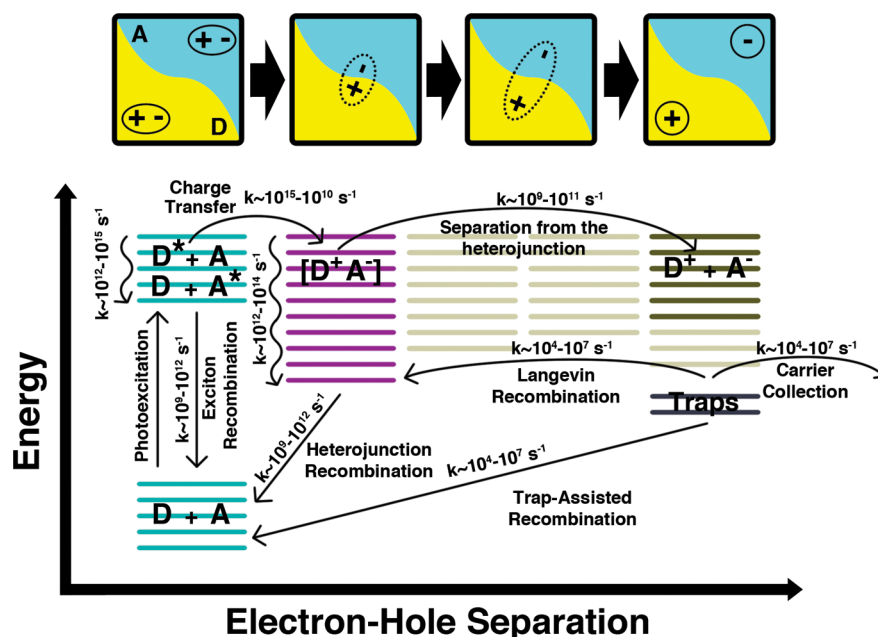


**Figure 5.** Schematics of exciton relaxation, charge generation, and charge recombination in a photoexcited organic D/A material. The notations are ground state (D + A), exciton manifolds (D\* + A, D + A\*), CT states ([D<sup>+</sup>A<sup>-</sup>]), and charge separated states (D<sup>+</sup> + A<sup>-</sup>). Representative rates are also indicated. Triplet dynamics have been omitted for clarity. Reproduced from ref 205. Copyright 2014 American Chemical Society.

coherent processes. The nature of low-energy excitons and how it manifests in the photophysical properties of the material are necessary to establish depending on the molecular structure and packing; particular systems of interest are ultrapure single crystals and high-performance D–A copolymers. Finally, developing a predictive understanding of how molecular structure and packing enable particular photophysical properties (e.g., coherent energy transfer, enhanced radiative rates, efficient iSF, etc.) and how robust these are with respect to dynamic and static disorder is important for design of next-generation optical materials with properties on demand.

### 3. CHARGE CARRIER PHOTOGENERATION

The nature of primary photoexcitations in organic semiconductors has been under debate for many years.<sup>196</sup> Of particular importance for optoelectronic applications are mechanisms of charge carrier photogeneration. A considerable amount of research has addressed under what conditions it would be possible to generate mobile charge carriers in pristine organic semiconductors directly, for example via a band-to-band excitation similar to that in inorganic semiconductors, and whether charge carrier generation necessarily proceeds via a multistep process that starts with a formation of a tightly bound exciton (with binding energies  $E_b$  of  $\sim 0.5$ – $1$  eV).<sup>40,74,197–204</sup> The most effective strategy to increase charge carrier photogeneration in organic materials has been to create donor–acceptor (D–A) heterojunctions (HJs), at which the energy offset at the D/A interfaces would provide a driving force for charge separation. The basic idea, illustrated in Figure 5,<sup>205</sup> is that photons absorbed by the donor or acceptor molecules generate excitons that diffuse to the interface, where the exciton dissociates. For efficient dissociation, the energy gain for this electron or hole motion should be higher than the exciton binding energy.<sup>206</sup> However, the exact mechanisms behind this basic understanding have been a subject of intense debate, driven by observations of nearly 100% IQEs in many polymer/fullerene D/A HJs, which is seemingly incompatible

with high exciton binding energies.<sup>207</sup> Considerable progress has been made both in theoretical modeling and in understanding of structure–property relationships in regard to the effects of the HOMO and LUMO energies of the D and A, the morphology of the D and A domains and of the D/A interfaces, and other properties specific to the molecular structures of D and A and intermolecular interactions. Questions pertaining to the importance of excess energy, entropy, delocalization, etc. for charge carrier generation, depending on the material, its crystallinity, and other parameters have been investigated, as discussed in Section 3.3.

Detailed discussions of pre-2010 developments in charge photogeneration models can be found in earlier review papers.<sup>208–210</sup> Gao and Inganäs<sup>211</sup> summarized the current understanding of charge generation in polymer:fullerene solar cells. Few et al.<sup>212</sup> reviewed recent advances in theoretical modeling of charge photogeneration in organic HJs. Here, a brief overview of earlier developments provides context for and is followed by discussion of the most recent results.

#### 3.1. Analytical Models of Charge Generation

The common view of charge generation in organic materials is that photon absorption leads to formation of an electron–hole pair (exciton) in which the electron and the hole are bound by the Coulomb attraction with a potential

$$V = \frac{e^2}{4\pi\epsilon\epsilon_0 r} \quad (26)$$

Here  $e$  is the charge of the electron,  $\epsilon$  is the dielectric constant of the organic medium,  $\epsilon_0$  is the dielectric permittivity of vacuum, and  $r$  is the electron–hole separation. In order to generate free charge carriers, this attraction must be overcome, which is considerably more difficult to achieve in organic materials ( $\epsilon = 2$ – $4$ ) as compared to inorganic materials (e.g.,  $\epsilon = 11$  in GaAs). An additional complication is introduced by the localized nature of electronic states in organic materials (small  $r$  in eq 26). Otherwise, the electron–hole pair recombines,

radiatively or nonradiatively. This is the process of geminate recombination, which competes with charge carrier separation.

A quantitative theory of geminate recombination was first proposed by Onsager<sup>213</sup> in 1938, who studied geminated recombination of a Coulombically bound cation–anion pair undergoing Brownian motion in solutions. He obtained the probability that the pair initially separated by a distance  $r$  overcomes the Coulomb attraction and generates free charge carriers (i.e., autoionization). In this model, the autoionization of the excited state creates (with efficiency  $\eta_0$ ) a positively charged parent ion and a hot electron with excess kinetic energy. This is followed by a thermalization process, during which the hot electron loses its initial excess energy due to inelastic scattering, leading to formation of an intermediate charge pair (CP) state of carriers bound by the Coulomb potential. The final stage is the dissociation of the CP state (with a probability  $P_{\text{diss}}$ ) which proceeds more efficiently at higher applied electric fields ( $F$ ) and temperatures ( $T$ ). The relevant length scales are the mean thermalization length ( $r_{\text{th}}$ ) (or the initial CP separation) and the critical Coulomb radius  $r_C$  of thermal dissociation of the CP state (also called the Onsager radius) given by

$$r_C = \frac{e^2}{4\pi\epsilon\epsilon_0 k_B T} \quad (27)$$

At low electric fields, the dissociation probability is  $P_{\text{diss}}(r_{\text{th}}, F, T) = \exp(-r_C/r_{\text{th}})(1 + \delta r_C)$  with  $\delta = eF/(2k_B T)$ .<sup>214</sup> The quantum efficiency of free charge carrier generation  $\eta$  is then a product of  $\eta_0$  and  $P_{\text{diss}}$ . The parameter  $\eta_0$  is generally considered to be independent of applied electric field, but this has been questioned in several studies.<sup>215–217</sup> The Onsager model also predicts a strong dependence of  $\eta$  on the wavelength (or frequency  $\nu$ ) of excitation, with photogeneration efficiency<sup>218</sup> increasing at  $h\nu > E_{\text{th}}$  approximately described (near  $E_{\text{th}}$ ) by  $\eta \sim (h\nu - E_{\text{th}})^{5/2}$ . Here  $E_{\text{th}}$  is a threshold energy (that has been used as a measure of the bandgap of the material) above which intrinsic charge photogeneration can be observed. For example, in Pn the bandgap of 2.25 eV was derived from the steady-state photocurrent dependence on the photon energy ( $h\nu$ ).<sup>219</sup>

Despite its earlier success in describing charge generation in a wide variety of materials, including molecular crystals and photoconductive polymers,<sup>218,220</sup> in many reports the observed photogeneration efficiencies modeled by the Onsager model produced unrealistically high thermalization lengths, in part due to unrealistic boundary conditions with a zero reaction radius. Noolandi and Hong<sup>221</sup> solved the problem with more realistic boundary conditions, incorporating a finite recombination rate; their exciton dissociation rates were, for example, shown to be in agreement with those obtained from kinetic Monte Carlo simulations of 1:1 P3HT:PCBM blends.<sup>222</sup> Sano and Tachiya<sup>223</sup> incorporated a finite intrinsic recombination rate  $p = k_{ET}R$  where  $R$  is the separation between the electron and hole and  $k_{ET}$  is the electron transfer rate. Several empirical models have been proposed that take into account nonzero reaction radius and a finite recombination rate.<sup>224,225</sup> Such approaches typically assume that the dissociation probability is given by

$$P_{\text{diss}} = k_d / (k_{\text{rec}} + k_d) \quad (28)$$

where  $k_d$  and  $k_{\text{rec}}$  are dissociation and geminate recombination rates, respectively, and  $k_d$  depends on the initial separation  $R$  and electric field  $F$ . In Braun's formulation,<sup>226</sup> often referred to

as the Onsager–Braun theory, the exciton dissociation rate is given by

$$k_d(F) = \frac{3Dr_C}{R^3 \exp(r_C/R)} J_1[2\sqrt{-2b}]/\sqrt{-2b} \quad (29)$$

Here  $D$  is the sum of the diffusion coefficients of the cation and anion,  $r_C$  is the Coulomb radius of eq 27,  $J_1$  is the first-order Bessel function, and

$$b = \frac{e^3 F}{8\pi\epsilon\epsilon_0 (k_B T)^2}$$

The expression above also assumes that  $\exp(r_C/R) \gg 1$ , which is valid for nonpolar systems.<sup>225</sup> The Onsager–Braun theory has been extensively used in modeling photocurrents in organic solar cells and other optoelectronic devices.<sup>120,227–231</sup> Kinetic Monte Carlo simulations of dissociation rates in disordered D:A blends showed a reasonable agreement with this theory at intermediate electric fields.<sup>232</sup> However, in order to fit experimental OPV  $J$ – $V$  data in the framework of this model, typically unrealistic assumptions about mobility or CT state lifetimes are required.<sup>233–236</sup>

Wojcik and Tachiya<sup>225</sup> pointed out that the expression (28) assumes that both dissociation and geminate recombination follow the exponential kinetics, so that it implies that the probability that the electron–hole pair survives recombination until time  $t$  is

$$W(t) = P_{\text{diss}} + (1 - P_{\text{diss}}) \exp(-(k_{\text{rec}} + k_d)t)$$

where  $P_{\text{diss}}$  is given by eq 28. However, it was shown by Sano and Tachiya<sup>223</sup> that  $W(t)$  follows more complicated power-law dynamics given by

$$W(t) \sim 1 + \frac{1}{1 - \exp(-r_C/R) + (Dr_C/pR^2) \exp(-r_C/R)} \frac{r_C}{(\pi Dt)^{1/2}}$$

One particular assumption of eq 29 questioned by Wojcik and Tachiya was that eq 29 relies on the electric field-dependent dissociation rate derived by Onsager in 1934 for the case of *reversible equilibrated* bulk recombination, which is not applicable to the situation of geminate recombination. Instead, they proposed exact extension of the Onsager theory of geminate recombination. At low electric fields ( $<10^5$  V/cm), the exact dissociation probability matched well with that of eq 28 with the  $k_d$  similar to that of eq 29 but with the factor of 3 eliminated from the numerator (which is referred to as the “modified Braun theory”). (Physically, the elimination of the factor of 3 from eq 29 was explained by redefining the recombination volume.) At higher electric fields, however, the modified Braun theory overestimated the dissociation probability as compared to the exact theory, with a progressively worse agreement at the increased initial electron–hole separation and/or dielectric constant of the medium. In the same work,<sup>225</sup> recombination over a range of distances (rather than at a set distance  $R$ ) was also explored, which made the model more flexible and potentially applicable to charge generation in conjugated polymers. The case of reversible equilibrated bulk recombination in the context of charge generation was recently discussed by Burke et al.,<sup>237</sup> who argued that, in most organic solar cells, free carriers are in equilibrium with the CT states from which they are created. In this formulation, the charge generation rate is determined by

the density of CT states and the average CT recombination rate constant ( $k_{r,CT}$ ) and the CT state dissociation rate constant is directly related to  $k_{r,CT}$  and the Langevin reduction factor  $\gamma/\gamma_{\text{Lan}}$  (see Section 5.2.1).

Falkowski et al.<sup>216</sup> considered various distributions of the initial electron–hole pair separation distances and found that charge photogeneration is significantly enhanced, especially for lower electric fields, in the case of broader initial separation distributions and smaller recombination velocities. Rubel et al.<sup>238</sup> calculated analytically the probability of electron–hole pair dissociation on a 1D chain in the presence of static disorder due to the Gaussian distribution of local transition rates and site energies. They arrived at the dissociation probability given by<sup>239</sup>

$$P_{\text{diss}} = \frac{k_d}{k_d + k_{\text{rec}}} = \frac{\tau_0}{\tau_0 + \sum_{n=1}^{N-1} a_{n \rightarrow n+1}^{-1} \exp\left(\frac{E_n - E_1}{k_B T}\right)} \quad (30)$$

where  $a_{n \rightarrow n+1}$  is the Miller–Abrahams's hopping rate for the hole given by

$$a_{n \rightarrow n+1} = \nu_0 \exp(-2\gamma r) \begin{cases} \exp\left(-\frac{E_{n+1} - E_n}{k_B T}\right), & E_{n+1} > E_n \\ 1, & E_{n+1} \leq E_n \end{cases} \quad (31)$$

Here  $\nu_0$  is the attempt-to-jump frequency,  $\gamma$  is a measure for the electronic coupling, and  $E_n$  is the hole energy on site  $n$ . As an example, the authors calculated the probability of exciton dissociation at the D/A interface as a function of applied electric field, and it was established that the disorder promotes exciton dissociation at low electric fields and suppresses it at higher fields.

Given the importance of charge generation in D/A HJs, several models were developed that specifically addressed the presence of the HJ. Wojcik and Tachiya<sup>240</sup> developed an analytical model for geminate recombination in D/A HJs based on the Smoluchowski equation. They derived the electron-pair survival probability  $W(t)$  that decays as  $t^{-1}$  at longer times ( $t$ ) and argued that the 3D system with a HJ is mathematically equivalent to a 4D anisotropic system without a HJ. It was then emphasized that increasing the dimensionality promotes charge generation and, thus, introduction of the HJ increases the charge carrier escape probability. The effect of the system dimensionality on charge generation efficiency was also discussed from the standpoint of entropy (Section 3.3.2.2).<sup>241</sup>

Petersen et al.<sup>227</sup> argued that the Onsager–Braun formalism assumes an isotropic active material with the exciton dissociation rate  $k_d$  being an even function of the electric field  $F$ , and that this assumption is not valid for CT states in planar HJs. An alternative model was introduced, which considers a temperature ( $T$ ) dependent dissociation rate  $k_d$  and introduces an electric field- and temperature-dependent term  $B_{CT}(F, T)$  into eq 28, which yields

$$P_{\text{diss}} = \frac{1}{1 + \frac{k_r}{k_d(T)B_{CT}(F, T)}} \quad (32)$$

with  $B_{CT}(F, T) = \frac{(1 - \exp[-F r_s / k_B T]) k_B T}{F r_s}$ , where  $r_s$  is the effective electron–hole separation distance. The same work also introduced the field-dependent tunneling model for the case when charge generation is limited by the dissociation of the

initial Frenkel exciton rather than that of the CT state. In this case a functional form of the  $P_{\text{diss}}$  was similar to that of eq 32, but instead of  $B_{CT}(F, T)$  it featured a temperature-independent factor  $B_{FE}(F)$  such that  $B_{FE}(F) = \frac{(1 - \exp[-F \gamma \alpha / e]) e}{F \gamma \alpha}$ , where  $\gamma$  and  $\alpha$  are the inverse localization radius and excited state polarizability in the direction of the applied field, respectively. These models were then used to simulate the  $J$ – $V$  characteristics of a merocyanine dye/ $C_{60}$  planar HJ. The authors were able to reproduce the photocurrent dependence on the electric field and on the film thickness with the CT state dissociation model and weak temperature dependence of the photocurrent with the field-dependent tunneling model.

Servaites et al.<sup>233</sup> built on the hot exciton dissociation model originally developed by Arkhipov et al.<sup>242</sup> for conjugated polymers, incorporating vibrationally assisted hot dissociation in the exciton dissociation probability. The model addressed experimental evidence for the importance of ultrafast charge separation (at time-scales similar to those defined by vibrational frequencies) for high-performance solar cell materials.<sup>243,244</sup> In Arkhipov et al.'s model, external field lowers the energetic barrier for geminate pair dissociation, and the model assumes a thermally assisted mechanism and a Boltzmann rate of dissociation, which implies long enough time-scale for a local thermal distribution to be reached. Servaites et al. modified the Arkhipov's expression for the dissociation probability by replacing the excess energy  $h\nu - E_g$  with  $\Delta G_{CS}$ , which is the offset between the energies of the  $S_1$  exciton and of charge separated states (CS) at the D/A interface ( $\Delta G_{CS} = E_{g,D} - (IP_D - EA_A)$ ), where  $E_{g,D}$  is the optical bandgap of the donor,  $IP_D$  is the ionization potential of the donor, and  $EA_A$  is the electron affinity of the acceptor). Additionally, the integration was limited to the  $[k_B T, k_B T + \langle E_{CS} \rangle]$  region, where  $\langle E_{CS} \rangle \geq \alpha \Delta G_{CS}$  with  $\alpha = k_B / C$  ( $C$  is the local heat capacity). With these modifications, the dissociation probability is given by

$$P_{\text{diss}} = 1 - \exp\left[-\frac{\nu_0}{\beta} \int_{k_B T}^{\langle E_{CS} \rangle + k_B T} dE_{\text{phon}} \exp\left(-\frac{E_{GP}}{E_{\text{phon}}}\right) + \frac{e}{E_{\text{phon}}} \sqrt{\frac{eFz}{\pi \epsilon \epsilon_0}}\right] \quad (33)$$

where  $\nu_0$  is the attempt to jump frequency,  $\beta$  is the first-order decay constant of the excess thermal energy,  $E_{\text{phon}}$  is the local phonon energy available for dissociation,  $E_{GP}$  is the geminate pair binding energy,  $F$  is the electric field, and  $z$  is the cosine of the angle between the electric field and the dissociation direction. This model was then used to calculate PCE as a function of  $\Delta G_{CS}$ . It was able to reproduce the high PCEs achieved with moderate bandgap polymers ( $E_{g,D} \sim 1.6$ – $1.7$  eV) and to explain the reduced charge separation efficiency in systems with low  $\Delta G_{CS}$ .

While the Onsager model and its extensions are premised on a point charge approximation, such approximation is not readily applicable to conjugated systems with a more delocalized excited state, exemplified by conjugated polymers.<sup>245,246</sup> Arkhipov et al.<sup>247</sup> explicitly introduced conjugation effects by considering the effective mass of a hole on a polymer chain. This was motivated by the need to better describe experimentally observed weak temperature dependence of the photocurrent in, for example, MeLPPP, which was not supported by Onsager approach-based models. In this model,

after photoexcitation of the polymer donor, the electron is transferred to the acceptor (which in pristine polymers could be provided by an inadvertent impurity),<sup>248</sup> while the hole, still bound to the electron by Coulomb interaction, remains on the polymer chain and is delocalized within the effective conjugation length. This delocalization was described as zero-point quantum oscillations in the Coulomb potential of the electron, which are associated with an energy that depends on the effective mass of the hole ( $m_{\text{eff}}$ ) and ultimately assists the hole in overcoming the Coulomb potential. This model was applied to two physical situations: low concentration of acceptors randomly distributed in a polymer matrix (dopant-assisted charge photogeneration<sup>248</sup>) and extended D/A interface such as in a bilayer system (interfacial dipole-assisted charge photogeneration<sup>247</sup>).

In the dopant-assisted charge photogeneration model, the dissociation probability at a site with a polymer chain-isolated acceptor separation  $r$  is<sup>248</sup>

$$P_{\text{diss}}(r) = \frac{1}{1 + (\nu_0\tau_0)^{-1} \exp(-2\gamma r)} \frac{1}{1 + \exp(-2\gamma r) \exp\left(\frac{U_{\text{max}} - E_{\text{min}}}{k_{\text{B}}T}\right)} \quad (34)$$

Here  $\nu_0$  is the attempt-to-jump frequency,  $\tau_0$  is the exciton lifetime, and  $\gamma$  is a measure for the electronic coupling.  $E_{\text{min}}$  is the energy of the hole, and  $U_{\text{max}}$  is the maximum value of the total potential given by the sum of the Coulomb potential and that created by the applied electric field. Then,  $P_{\text{diss}}(r)$  is combined with a Poisson distribution function accounting for a random distribution of distances  $r$  and integrated over space to produce the overall dissociation yield.<sup>248</sup>

The Arkhipov et al.'s interfacial dipole-assisted charge photogeneration model<sup>247</sup> presumes that there is a partial charge separation at the D/A interface in the dark, which creates an array of immobile interfacial dipoles formed by the holes on the donor ( $+\alpha e$ ) and electrons on the acceptor ( $-\alpha e$ ). Here the parameter  $\alpha$  is a measure of the dipole strength and  $e$  is the elementary charge. Immediately after exciton dissociation, the hole is considered to be delocalized along the polymer chain, which is described by the effective mass  $m_{\text{eff}}$  whereas the electron is localized at the acceptor molecule. Interaction between the hole and the discrete partial positive charges from the interfacial dipoles leads to quantization effects and supplies the hole with the kinetic energy dependent on  $m_{\text{eff}}$ . The model predicted a dramatic increase in the dissociation probability as the dipole strength  $\alpha$  increased and/or the hole effective mass decreased. However, in the range of electric fields ( $\leq 10^5$  V/cm) relevant for optoelectronic devices, high exciton dissociation efficiencies were predicted only for  $m_{\text{eff}} \leq 0.3 m_e$  (where  $m_e$  is the electron mass), which are unrealistic for organic disordered materials.

The theory was further developed by Baranovskii and colleagues,<sup>249–251</sup> showing that unrealistically small effective masses were not necessary. They considered two situations: the presence of discrete interfacial dipoles (a similar assumption to that of Arkhipov et al.<sup>247</sup>), with several modifications of the model as discussed below, and the presence of the dipole smeared along the polymer chain. The former model (Figure 6(a)) led to the relaxed requirements for the effective mass  $m_{\text{eff}}$  so that high dissociation efficiencies could be obtained with  $m_{\text{eff}} = m_e$  (Figure 6(b)). The main modifications with respect to

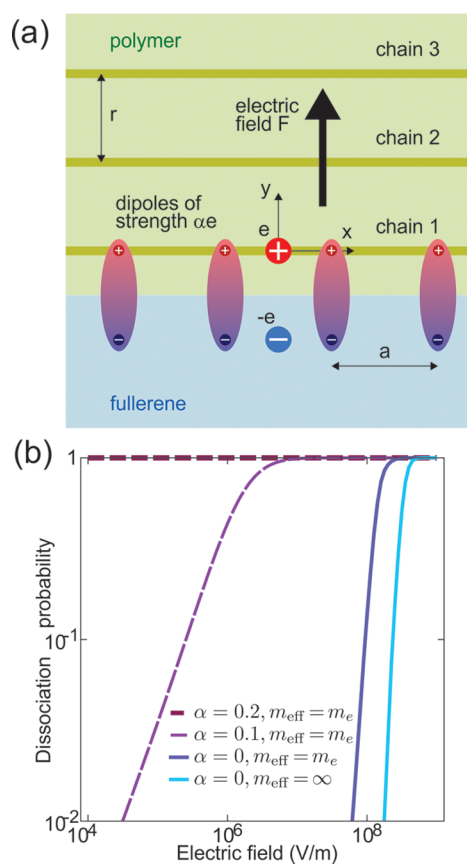


**Figure 6.** (a) Schematics of a charge photogeneration model incorporating interaction between the delocalized hole on a polymer chain and a large set of the discrete interfacial dipoles. The magnitude of  $\alpha$  represents a dipole strength. (b) Electric field-dependence of the dissociation probability of the electron–hole pair obtained for different effective masses of the hole ( $m_{\text{eff}}$ ) and dipole strengths  $\alpha$ . Reprinted from ref 249. Copyright 2012 American Chemical Society.

Arkhipov et al.'s original model concerned the initial placement of the hole with respect to the dipoles, inclusion of the interaction between the hole and up to 100 dipoles on each side of the hole (and not only nearest dipoles), and the redefined criterion for dissociation.<sup>249</sup> This model, in conjunction with Arkhipov's dopant-assisted charge generation model,<sup>248</sup> was successful in explaining the electric field dependence of the charge photogeneration efficiency in a variety of polymer/ $C_{60}$  planar HJs.<sup>245</sup> More recently, it was also used to show that hole delocalization (quantified by  $m_{\text{eff}}$ ) was responsible for the reduced CT state binding energies in polymer/ $C_{60}$  bilayers, eliminating the need for the excess energy.<sup>252</sup>

### 3.2. Computational Efforts

**3.2.1. Methods Involving Electronic Structure Calculations.** Although the analytical models discussed above incorporate the effects of many physical parameters on charge generation, they do not capture the differences in performance of various materials caused by the differences in their chemical structure and the physical properties of the interfaces. Theoretical efforts that incorporate such effects, as well as the pros and cons of various methods, were recently reviewed in ref 212. These include the DFT and Hartree–Fock methods for predictions of structure–electronic property relationships,<sup>253</sup> TDDFT for modeling excited states of molecules,<sup>254</sup> con-

strained DFT (CDFT) and many-body methods (such as Green's function GW and Bether–Salpeter (BSE) approaches) for computing charge transfer state properties,<sup>255,256</sup> and QM/MM calculations for incorporating the effects of microscopic polarization of the medium. Recent advances in the DFT methods enabling theoretical predictions of the ground and excited states of organic materials were summarized in ref 253.

The particular properties under investigation include effects of donor and acceptor molecular alignment on the CT state energy and dynamics, of the local dielectric environment and disorder on the energetic landscape at the interface and its effect on charge separation, and of the dynamics of molecules at the interface on charge separation. Several examples of insights obtained from such studies on small molecules, polymers, and their D–A HJs are given below; for a detailed discussion, see ref 212 and relevant references in Table S1.

Poelking et al.<sup>257</sup> developed an approach that includes a long-range charge–quadrupole interaction in calculations of hole and electron energies for the high-performance HJs of the dicyanovinyl-substituted oligothiophenes (DCVnTs) (which have an ADA molecular structure) as the donor and C<sub>60</sub>. They demonstrated that long-range electrostatic effects fostered by mesoscale structural order determine the energy levels at the D/A interfaces. The authors further discussed that their findings are applicable to a wide variety of ADA materials (for example, high-performance small-molecule solar cell materials patented by Heliatek).

Troisi<sup>258</sup> considered crystalline donor and acceptor materials, modeled as 2D lattices separated by a defect-free interface, and included multielectron states (DAA instead of DA, so that possible CT states are D<sup>+</sup>AA<sup>-</sup> and D<sup>+</sup>A<sup>-</sup>A) in calculations. The initial state was a delocalized Frenkel exciton (FE) (Section 2.2), the final states were the CT states, and the Hamiltonian included coupling between the FE and CT states as a perturbation. The study concluded that the charge separation relies on the electronic coupling between the donor and acceptor orbitals (i.e., on the corresponding bandwidths, because they increase the effective coupling between the initial FE and the final CT state). It was also emphasized that the process of charge separation is an electronic process, so that nuclear motions are not important.

On the other hand, Bedard-Hearn et al.<sup>259</sup> found nuclear dynamics to be important for exciton dissociation in pristine conjugated polymers. They performed mixed quantum/classical simulations focusing on the nonadiabatic excited state dynamics of single and  $\pi$ -stacked PPV oligomers of varying length and found evidence of charge photogeneration at various time-scales depending on the excitation relaxation pathways. Such pathways were determined by the nuclear dynamics that induced nonadiabatic coupling to the excited electronic states, which was in turn influenced by the electric field and conjugation length of the polymer and/or by interchain coupling.

Various extensions of the Su–Schrieffer–Heeger (SSH) model sought to take into account effects of electric field, temperature, and impurities on exciton dissociation in conjugated polymers.<sup>260,261</sup> For example, it was found that in cis-polyacetylene, the presence of impurities and higher temperature reduced the critical electric field necessary for subpicosecond exciton dissociation. Liu et al.<sup>262</sup> included the electron–electron correlation effects in the SSH model by using a multiconfigurational time-dependent Hartree–Fock formalism. They modeled singlet and triplet dissociation in

polyacetylene in the presence of the applied electric field and found that electron–electron correlation impeded dissociation of both exciton types, and more so in the case of triplet excitons. Shin and Lin<sup>263</sup> incorporated interchain  $\pi$ – $\pi$  interactions and dynamical electron–phonon coupling into the SSH Hamiltonian and probed photoinduced CT at the PPV/C<sub>60</sub> interfaces. They found that the CT proceeded via a nonadiabatic mechanism with an associated phonon relaxation energy of 0.3 eV, which coincides with the common energy offset contributing to the  $V_{oc}$ .<sup>209</sup> Gao et al.<sup>264</sup> applied the SSH model to polymer/polymer D/A HJs and found that the critical energy offset for the CT is determined not only by the Frenkel exciton binding energy, but also by that of the CT state.

Caruso and Troisi<sup>265</sup> calculated a long-range electron transfer rate in a polymer:fullerene system (exemplified by the P3HT:PCBM). They hypothesized that the electron can tunnel at long distances if the barrier for tunneling is sufficiently low and concluded that such tunneling enables long-range exciton dissociation, when excitons are away from the D/A interface by tens of angstroms. Vázquez and Troisi<sup>266</sup> examined effects of static disorder at the D/A interfaces in a 1D system of N donor and N acceptor molecules and obtained the exponential dependence of exciton dissociation rates on the exciton–interface separation with the disorder-dependent decay constant. They concluded that the final states are hot CT states with well-separated electrons and holes. Lee et al.<sup>267</sup> used semiclassical quantum dynamics at <100 fs and Redfield theory at 10–100 ps to probe dissociation and relaxation of CT states. They considered a fixed point charge (hole) on the donor and treated the acceptor as a finite 1D lattice. They found that CT states can evolve to charge separated (CS) states on <100-fs time-scales due to quantum diffusion, without the need for formation of hot/delocalized CT states. On picosecond time-scales, the CS states relaxation to the low-energy CT states was observed due to the interaction with the thermal bath.

Bittner and Silva<sup>53</sup> applied a fully QM/finite temperature exciton-lattice model to study electron dynamics of primary photoexcitations in polymer/fullerene HJs that included effects of  $\pi$ -stacking, energetic disorder, and phonon relaxation. They found that as the energy offset between the donor and acceptor increased, an increasing density of long-range CT states (polarons) became isoenergetic with the photoexcited exciton state, which facilitated resonant tunneling. In polymer/fullerene HJs, resonant tunneling enabled by environmental fluctuations generated “current-producing” states at 35 fs and pinned CT (exciplex) states at 43 ps after ultrafast excitation.

Yao et al.<sup>268</sup> applied the Wigner function formalism to solving hierarchy equations of motion to take into account effects of phonons, or dynamic disorder, on exciton dissociation in D/A HJs. Considerable deviations from the Onsager–Braun theory were found in the presence of phonons, and the inclusion of electron–phonon coupling increased the photocurrent. In a follow-up work, Yao<sup>54</sup> studied how ultrafast coherent dynamics and delocalization could contribute to the process of charge photogeneration using the framework of the spin-boson model and employing the time-dependent density matrix renormalization group algorithm. Energy conversion efficiencies of more than 90% were predicted if the quantum coherence is fully utilized, in the absence of incoherent loss such as nongeminate recombination. Large enhancements in efficiencies due to quantum effects (such as coherent superposition of states) have been predicted in other studies as well. For example, an efficiency boost by 25%–40%,

depending on the temperature, was obtained in the presence of coherent electronic coupling between the donor states.<sup>269</sup>

**3.2.2. Monte Carlo Simulations.** Kinetic Monte Carlo approaches enabled valuable insights into the types of morphology<sup>270–275</sup> that promote charge photogeneration and explored the effects of excess energy, local mobility,<sup>222</sup> conjugation length,<sup>232</sup> and disorder<sup>234</sup> on charge separation.<sup>212</sup> Pre-2011 work was summarized in ref 276. Examples of more recent studies and the insights they offered are given below; a more comprehensive discussion can be found in ref 277.

Lyons et al.<sup>274</sup> examined the relative effect of domain size, purity, and quality of the interface on the OPV performance. This study established the need to control the interaction parameter  $\chi$  between the two components of the D:A blend, which quantifies the interfacial width between the domains (scaling as  $\sim\chi^{-0.5}$ ) in the framework of the Cahn–Hilliard model. (This parameter can be controlled, for example, by using additives in solvents or solvent mixtures.<sup>278</sup>) The  $0.05 \leq \chi \leq 0.08$  range was explored, and it was concluded that when the interfaces between the domains are sharp, up to 30% improvement in the photocurrent can be achieved even in morphologies with impure domains and poor electrode connectivity.

Jones et al.<sup>235</sup> studied CT separation dynamics depending on the energetic disorder and BHJ morphology. They modeled charge carrier hopping using Marcus rates (eq 21) and determined the CT separation and recombination dynamics at various electric fields. The simulations revealed a multi-exponential geminate recombination rate which was analyzed using the Wojcik and Tachiya model (Section 3.1).<sup>225</sup> Two recombination pathways were identified, which incorporated field-independent (intrinsic) and field-activated exciton dissociation.

Heiber and Dhinojwala<sup>279</sup> considered the effects of excess vibrational energy and delocalization on charge separation in a bilayer D/A system (exemplified by P3HT/PCBM). They found a significant decrease in geminate recombination as the exciton interaction radius increased. Additionally, it was concluded that the hot charge carriers must hop 100–1000 times faster than the relaxed carriers in order for the excess vibrational energy to contribute to charge separation (thus outcompeting energy dissipation). In the subsequent study,<sup>270</sup> the authors simulated exciton–exciton annihilation using conditions close to those used in transient absorption experiments in P3HT:PCBM blends. The range for the values of the exciton delocalization radius was estimated based on the comparison of the simulated exciton concentration dependence on the pump intensity with experimental data. Next, exciton dissociation and recombination were simulated, depending on morphology. The exciton delocalization radius yielded only 1–2 nm, and it was concluded that exciton delocalization could not be the dominant factor behind efficient charge separation in these blends.

Heitzer et al.<sup>275</sup> explored the effects of initial exciton delocalization on charge separation in BHJs (exemplified by various high-performance polymer:fullerene, small molecule:fullerene, and polymer:polymer blends) with different domain sizes and 10 different morphologies that included mixed and pure domains. They established that up to 40% of excitons that undergo subpicosecond dissociation exhibit this behavior even in the absence of delocalization, due to solely geometrical factors (such as high surface to volume ratio and high fractal dimensionality of the domains). The remaining 60% of ultrafast

dissociation could be equivalently explained by impure domains or exciton delocalization, thus questioning whether exciton delocalization is indeed essential for efficient exciton dissociation. Jones et al.<sup>280</sup> explored the importance of CT state delocalization and concluded that hot CT state delocalization cannot be the sole reason behind the high efficiency achieved in polymer:fullerene OPVs. Instead, they emphasized spatial variation in energy levels due to, for example, aggregation, as the major contributing factor to charge generation.

Maqsood et al.<sup>281</sup> considered exciton migration, followed by dissociation or recombination, in 3D by FRET using 10 different geometries representing planar HJs or various BHJ morphologies. They found that, at low energetic disorder (DOS width  $\sigma < 50$  meV), the exciton transport depended on the mesoscopic ordering, average domain size, and energetic disorder. In contrast, at high disorder ( $\sigma > 50$  meV), the exciton dissociation probability was independent of morphology-related factors and was determined only by disorder.

Van Eersel et al.<sup>234</sup> analyzed the  $J$ – $V$  characteristics measured in pristine MDMO-PPV, PCBM, and MDMO-PPV:PCBM BHJs in the hole-only SCLC regime. They applied a fitting procedure of ref 282 and a framework of the extended Gaussian disorder model (EGDM)<sup>283</sup> (Section 4.2.5) to extract parameters pertaining to hopping transport: the attempt-to-hop frequency  $\nu_0$ , the width of the Gaussian DOS  $\sigma$ , and the nearest-neighbor distance  $a_{nn}$ . Then, these parameters served as an input for kinetic Monte Carlo modeling that used Miller–Abrahams hopping rates to calculate exciton dissociation and recombination yields. It was concluded that exciton dissociation proceeds via a two-step process: CT state formation driven by the band offset followed by charge separation driven by the relaxation in the DOS. This process was found to be weakly temperature and electric field dependent, and the majority of excitons dissociated into free charge carriers at all fields. The small fraction of polaron pairs that instead recombined exhibited a strong electric field dependence of the recombination yield, which led to the conclusion that the field dependence of the polaron pair recombination yield cannot be a relevant measure for the exciton dissociation yield.

**3.2.3. Device Modeling.** Device modeling efforts focused on simulations of  $J$ – $V$  characteristics in solar cells<sup>229,231,284–294</sup> or SCLC-regime diodes<sup>295,296</sup> and time-resolved photocurrents<sup>120,297–303</sup> using various modifications of the semiconductor drift-diffusion model adapted for a particular material and device geometry. A comprehensive review of device modeling of organic BHJ solar cells can be found in ref 304.

The main considerations in organic optoelectronic device modeling can be summarized as follows. Continuity equations for hole and electron densities coupled with the Poisson's equation and with drift-diffusion equations, which describe drift and diffusion of charge carriers, the effect of space charge, and charge carrier generation and loss in semiconductor devices, serve as a foundation. Then, features specific to organic materials are incorporated into the equations. These include the electric field and temperature dependence of charge generation and mobility,<sup>236,284,305,306</sup> properties of charge traps and DOS distribution,<sup>119,307,308</sup> and various nongeminate recombination mechanisms.<sup>290,307,309</sup> Also important is to take into account optical effects such as a nonuniform optical absorption profile and interference (that determine the exciton generation rate and resulting exciton diffusion).<sup>310–312</sup> Finally, a major step is the explicit incorporation of the microstructure of organic films

Table 2. Ultrafast Charge Carrier Separation in Pristine Organic Materials

Material	Expt Technique (time-scale) <sup>a</sup>	Wavelength, light intensity ( $\mu\text{J}/\text{cm}^2$ ) or incident photon density, electric field (kV/cm)	Efficiency <sup>c</sup>	Notes <sup>d</sup>	Refs
<b>Small molecules</b>					
Pn	THz (<0.4 ps)	400, 500, 0	$\mu\eta$ ( $\text{cm}^2/(\text{Vs})$ ): (0.3)	Ultrapur; $\tau^{-b}$ , $b = 0.6$	365
	THz	400, 120–830, 0	$\mu\eta$ ( $\text{cm}^2/(\text{Vs})$ ): (0.2)		202
	THz	266 or 400, 370–2000, 0		Ultrapur; carrier coupling to 1.1 THz mode	360
	THz	400–680, 1000, 0	$\mu\eta$ ( $\text{cm}^2/(\text{Vs})$ ): 0.02	$\lambda$ -and T-independent $\eta$ (5–300 K)	201
	THz	580, 900–1500, 0	$\mu\eta$ ( $\text{cm}^2/(\text{Vs})$ ): 0.02–0.04	$\mu\eta$ correlated with the grain size	40
	THz gen. (<0.1 ps)	580, 700, 21		Max emission at 0.6 THz; Max frequency 1.7 THz	40
TIPS-Pn	F-TAS (<2 ps)	490, $10^{18}$ $\text{cm}^{-3}$ , 200	$\eta$ : 10% of $T_1$ via SF	$E_b = 0.32$ eV	342
	THz	800, 2500, 0	$\mu\eta$ ( $\text{cm}^2/(\text{Vs})$ ): (0.2)	$\tau^{-b}$ , $b = 0.6$	198
	THz	400–800, 500–1000, 0	$\mu\eta$ ( $\text{cm}^2/(\text{Vs})$ ): (0.2)	$\lambda$ -and T-independent $\eta$ (5–300 K); $\tau^{-b}$ , $b = 0.6$ ; $\eta_{\text{max}}/\eta_{\text{min}} = 1.7$	201, 365, 413
	THz	400–800, 1000, 0	$\mu\eta$ ( $\text{cm}^2/(\text{Vs})$ ): 0.02	$\lambda$ -and T-independent $\eta$ (5–300 K)	201
TES-Pn	THz	580, 900–1500, 0	$\mu\eta$ ( $\text{cm}^2/(\text{Vs})$ ): <0.01–0.06	$\mu\eta$ correlated with the grain size; $\tau^{-b}$ , $b = 0.53$	40
	TPC (<30 ps)	400, 30, 12	$\mu\eta$ ( $\text{cm}^2/(\text{Vs})$ ): 0.022	T-independent $\eta$ (290–350 K); $\tau^{-b}$ , $b = 0.52$	347
	THz	400 or 580 or 800, 500, 0	$\mu\eta$ ( $\text{cm}^2/(\text{Vs})$ ): (0.06)	$\eta_{\text{max}}/\eta_{\text{min}} = 2$	413
	THz	400, 500, 0	$\mu\eta$ ( $\text{cm}^2/(\text{Vs})$ ): (0.03)	T-independent $\eta$ (5–300 K)	365
diF TIPS-ADT	TPC (<100 ps)	400 or 266 or 200, 33–264, 83	$\eta$ : (>5%)	$\lambda$ -independent, T-independent $\eta$ (180–375K)	346
	TPC (<30 ps)	400, 30, 12	$\mu\eta$ ( $\text{cm}^2/(\text{Vs})$ ): 0.025	T-independent $\eta$ (290–350 K); $\tau^{-b}$ , $b = 0.66$	347
	TPC (<30 ps)	400, 5, 40	$\mu\eta$ ( $\text{cm}^2/(\text{Vs})$ ): 0.025	$\tau^{-b}$ , $b = 0.45$	36, 322
	TPC (<30 ps)	400, 5, 40	$\mu\eta$ ( $\text{cm}^2/(\text{Vs})$ ): 0.025	$\tau^{-b}$ , $b = 0.2$	36, 322, 414
diF TES-ADT	TPC (<500 ps)	355, 0.4, 120	$\mu\eta$ ( $\text{cm}^2/(\text{Vs})$ ): 0.002	T-independent $\eta$ (98–200 K); $\tau^{-b}$ , $b = 0.2$ (98 K), 0.3 (300 K);	28
	TPC (<500 ps); simulations	355, 0.18, 40	$\eta_{\text{SSC}} = 3.5\%$	$\eta_{\text{SSC}}$ : spatially separated carriers on subs time-scales	120
	TPC (<500 ps); simulations	532, 2, 50	$\eta_{\text{SSC}} = 3.6\%$	$\eta_{\text{SSC}}$ : spatially separated carriers on subs time-scales; higher crystallinity = higher $\eta_{\text{SSC}}$ ( $\eta_{\text{SSC}} = 20\%$ in diF TES-ADT; PCBM (10 wt %))	300
	THz	400, 500, 0	$\mu\eta$ ( $\text{cm}^2/(\text{Vs})$ ): (0.05)	T-independent $\eta$ (5–300 K)	365
Rubrene	THz (<0.2 ps)	400, $2 \times 10^{17}$ ph/cm <sup>2</sup> , 0	$\eta$ : (0.08%)	Ultrapur; Coupling to 15.5 THz mode	361
	THz, TAS	400, (0.2–3.5) $\times 10^{19}$ cm <sup>-3</sup> , 0		$\eta$ ultrafast charge generation; Coupling to 72–78 cm <sup>-1</sup> mode	200
		562, < $10^{-3}$ photon/molecule, 0	$\mu\eta$ ( $\text{cm}^2/(\text{Vs})$ ): 0.002 (at 430 nm and 480 nm); 0.0004 (at 620 nm)	sub-200 ps generation via self-trapped exciton dissociation; $E_b = 35$ meV	366
	TPC (<50 ps)	430 or 480 or 620, 2–4, 30		T-independent $\eta$ (80–300 K); at 620 nm: Exciton–exciton collision	415
C <sub>60</sub>	THz, TAS (<0.5 ps)	400, $5 \times 10^{13}$ photons/pulse, 0		Time-dependent mobility <20 ps	416
	F-TAS, Stark (<0.2 ps)	390, 350, 600–1500	$\eta$ : 13%	F-assisted, time-independent mobility at 0.2–10 ps, time-dependent mobility at >10 ps	417
PCBM	TAS (mid-IR) (<0.1 ps)	617 and 800, 11–1217, 0	$\eta$ : 100%	WEG film; band-edge recombination (CT state formation): 53% (47%) of free carriers	203
Polymers MEH-PPV	THz (<0.3 ps)	266 or 400, $10^{16}$ photons/cm <sup>2</sup> , 0	$\eta$ : <1%	( $\eta$ : 2X at 266 nm as compared to 400 nm); hot exciton dissociation	343
	THz generation	400, 225, 10	$\eta$ : 0.05%	Time-dependent mobility (0–6 ps)	418
	IRAV (<0.1 ps)	200–620, $10^{19}$ photons/cm <sup>3</sup> , 0	$\eta$ : 10%	T-independent $\eta$ (90–300 K), $\lambda$ -independent $\eta$ (200–600 nm)	419

Table 2. continued

Material	Expt Technique (time-scale) <sup>a</sup>	Wavelength, light intensity ( $\mu\text{J}/\text{cm}^2$ ) or incident photon density, electric field (kV/cm)	Efficiency <sup>c</sup>	Notes <sup>d</sup>	Refs	
Polymers						
	PPV (stretched oriented films)	800 (via TPA), -, 175 200–620, $10^{19}$ photons/cm <sup>3</sup> , 0 400, 1–59, 330 400, 0.1, 50–250	$\eta$ : 35% $\eta$ : 10%	Max emission at 0.5 THz $\lambda$ -independent $\eta$ (350–600 nm), $\eta$ : 2X at 200–300 nm as compared to 350–600 nm T-independent $\eta$ (100–300 K)	420 419 301 421	
	BAMH-PPV nPVP	400, $2 \times 10^{18}$ photons/cm <sup>3</sup> , 50–600 390, 160–1600, 0–1000 400, 200, 330	$\mu\eta$ (cm <sup>2</sup> /Vs): 0.24 $\eta$ : 10%; $\eta$ : 15%	F-independent, linear intensity dependence Hot exciton dissociation; S <sub>1</sub> exciton dissociation Fast recombination	345 422 423	
OTV	400, 200, 330				423	
P3HT		500, 310–840, 0 400 and 800, (0.5–2.5) $\times 10^{15}$ photons/cm <sup>2</sup> , 0 400, $5 \times 10^{15}$ cm <sup>-2</sup> , 0 500, 0.4–59, 0 375, <10, 1300	$\eta$ : 24% $\eta$ : 0.8% at 400 nm; $\eta$ : 1.5% at 800 nm $\eta$ : <1% $\eta$ : 15% $\eta_{\text{SSC}}$ : 25%; $\eta$ (<1 ns): 10%; $\eta$ (>ns): 10%	T-independent $\eta$ (40–300 K) Long-lived carriers 2nd-order processes at $>0.7 \mu\text{J}/\text{cm}^2$ SSC: spatially separated carriers at subps time-scales; CT character; T-independent $\eta$ (80–300 K); < 1 ns: T-independent $\eta$ (80–300 K); >ns: T-activated $\eta$ Time-dependent mobility (ps– $\mu\text{s}$ ); t <sup>-b</sup> , b = 0.74–0.84	424 348 426 427 349	
	PSF-BT	F-TAS (<0.15 ps) TR-SHG, TOF				428
	Pt-DTBTBD	THz	400, $2 \times 10^{15}$ photons/cm <sup>2</sup> , 0	$\eta$ : 1–2%	Hot exciton dissociation	429
m-LPPP	F-TAS	390, 240–1200, 50–150			430	
POMEPT	F-TAS	345 and 500, 20, 0–2000	$\eta$ : 13% (F = 0) $\eta$ : 24% (F = 2 MV/cm)	Exciton dissociation (not hot) $\eta \sim F^2$	431	
PFO	TAS (<0.3 ps)	390, $6 \times 10^{13}$ and $4 \times 10^{14}$ photons/cm <sup>2</sup> , 0		Intrachain generation; hot exciton dissociation	432	

<sup>a</sup>Experimental technique used to perform observations. THz = optical pump–THz probe spectroscopy; IRRAV = infrared-active vibrational mode spectroscopy; TPC = time-resolved photocurrent; F-TAS = electric field-assisted transient absorption spectroscopy; TR-SHG = time-resolved second harmonic generation. A brief description of these experimental techniques can be found in section 7.1.1. The value in parentheses is a time resolution of the measurement. When deconvolution of the data is performed by numerical modeling, it is indicated as “simulations”. <sup>b</sup>The numbers separated by commas are excitation wavelength in nm, excitation pulse fluence in  $\mu\text{J}/\text{cm}^2$  when reported (or photon densities with units indicated), and applied electric field F in kV/cm. <sup>c</sup>Efficiency of charge generation  $\eta$  when available or  $\mu\eta$  (where  $\mu$  is the sum of electron and hole mobilities) extracted from the peak value of photoconductivity (limited by the time resolution of the experiment), at room temperature. The values in parentheses are for single crystals; others are for films. When multiple charge generation pathways are revealed, efficiencies of several pathways are included, with brief explanation under “Notes”. TPA = two-photon absorption. <sup>d</sup>Notes on the wavelength, temperature (T), electric field (F), dependence, or anisotropy of the charge generation efficiency, as well as the charge generation mechanism proposed by the authors. Comments on the carrier dynamics (such as power-law time dependence,  $\sim t^{-b}$  with the exponents b indicated) are also included when available. WEG = weak epitaxy growth. E<sub>b</sub> = binding energy.

into modeling (in contrast to effective medium approaches).<sup>271,272</sup> Below, selected examples illustrating some of these aspects are provided.

Giebink et al.<sup>315,314</sup> extended the “ideal diode” (or Shockley) equation, which describes recombination at (and diffusion to) p–n junctions, to organic (excitonic) semiconductors. They developed an analytical formalism describing  $J$ – $V$  characteristics in an OPV, which incorporated the voltage dependence of the photocurrent due to electric field-dependent polaron pair dissociation in the framework of Onsager–Braun theory (eq 29). The model was able to reproduce the double exponential character of a forward-biased dark current, the HJ ideality factor, the S-kink behavior,<sup>315</sup> and the voltage dependence of the photocurrent in planar HJs.

Arnab and Kabir<sup>316</sup> proposed an analytical model for  $J$ – $V$  characteristics in organic BHJs that incorporated exciton dissociation (described by the modified Braun model, Section 3.1), optical effects, and voltage-dependent dark current. They were able to reproduce data from P3HT:PCBM and PCPTBT:PCBM solar cells, without accounting for bimolecular recombination. Ibrahim et al.<sup>317</sup> incorporated bimolecular recombination in their analytical model assuming a uniform recombination rate. Neher et al.<sup>318</sup> considered the effect of low charge carrier mobility on the  $J$ – $V$  characteristics (with otherwise “ideal conditions”, that is the absence of electric field-dependent charge generation, of space charge field formation due to unbalanced electron and hole mobilities, and of surface recombination). They introduced a dimensionless parameter ( $\alpha$  of eq 58, Section 11.1.1.1) into the Shockley equation that accounts for transport-limited photocurrents and proposed it as a new figure of merit for organic solar cells (Section 11.1.1.1).

MacKenzie et al.<sup>307</sup> modeled the TPV data obtained from P3HT:PCBM solar cells by solving the drift-diffusion equations that explicitly incorporated DOS and carrier density-dependent mobility into nongeminate recombination rates. They considered a Gaussian DOS, an exponential DOS, and a superposition of the two and concluded that exponential DOS was essential in reproducing experimental  $J$ – $V$  characteristics. Wheeler et al.<sup>309</sup> included surface recombination into the model. They compared  $J$ – $V$  characteristics experimentally measured in PCDTBT:PCBM solar cells with untreated NiO (workfunction of 4.85 eV) and O<sub>2</sub> plasma-treated NiO (workfunction of 5.3 eV) interlayers with simulations and quantified large changes in the  $V_{oc}$  due to surface recombination.

Many studies emphasized the need to include injected (“dark”) charge carriers in the photocurrent simulations due to their contribution to the space-charge distribution, providing an additional bimolecular recombination channel (i.e., due to recombination between photogenerated and injected carriers),<sup>120,319</sup> and potentially producing photocurrent multiplicity effects.<sup>292,294</sup> The effects of non-negligible dark currents on optoelectronic device characteristics have been experimentally observed in solar cells, photodetectors, and PR devices. For example, Li et al.<sup>320</sup> observed that dark leakage currents were detrimental to  $V_{oc}$  in small-molecule planar HJs. General discussions of contributions of effects imposed or facilitated by electrodes (including injection of dark carriers) to the experimentally observed photoresponse can be found in refs 321–325.

Street et al.<sup>326</sup> showed that the photocurrent in PCDTBT:PCBM solar cells was reduced at a forward bias when the series resistance was large. They provided an

analytical expression that allows for determination of the series resistance from dark diode characteristics, which then enables calculation of the “internal” photocurrent from the experimentally measured photocurrent values.

Several studies incorporated dopants into their model,<sup>231,327</sup> which either could be intentionally introduced to tune the conductive properties of the material<sup>328</sup> or could be unintentional due to, for example, charged defects.<sup>329</sup>

Many device modeling studies utilized an effective medium approach,<sup>284</sup> in which the complex morphology of the D:A blend is neglected and effective parameters (such as effective mobility, DOS, etc.) are used. This approach was used to examine the effects of injection barriers, selective contacts, different charge generation and recombination mechanisms, and series resistance on the  $J$ – $V$  and time-dependent photocurrent characteristics.<sup>120,292,294</sup> However, given that morphology is of critical importance for optoelectronic properties of organic devices, considerable effort has been devoted to incorporating information on the microstructure into device modeling. Maturová et al.<sup>271</sup> solved the drift-diffusion, continuity, and Poisson equations on the 2D grid,<sup>330</sup> on which donor and acceptor phases were defined by mapping the 3D morphology on 2D. The geometry of various phases was obtained from AFM, TEM, and STM of polymer:PCBM blends, and each phase was characterized by its own set of parameters (charge generation rate, mobilities, dielectric constant, etc.). The simulated  $J$ – $V$  characteristics were then compared with experimentally measured ones. The authors concluded that phase-separated morphologies with sub-50-nm features yielded the best performance. Ray et al.<sup>331,332</sup> explicitly incorporated the effects of morphology by using the Cahn–Hilliard model to generate various morphologies followed by solving drift-diffusion equations to obtain solar cell  $J$ – $V$  characteristics. They showed that the PCE of random-morphology BHJs is reasonably close to that of the perfectly ordered fin-like (interdigitated) structure, so that the intrinsic randomness of solution-deposited BHJs does not represent an intrinsic limitation to the PCE. They also concluded that the short-circuit current  $J_{sc}$  is considerably more sensitive to morphology than the open-circuit voltage  $V_{oc}$ .<sup>332</sup>

Simulations of time-resolved photocurrents have been utilized in deconvolution of contributions of charge photo-generation efficiency, mobility, trapping, and recombination rates to the photocurrent, depending on the time-scales.<sup>120,297–303</sup> MacKenzie et al.<sup>333</sup> modeled ~100 ns to 100  $\mu$ s transient photocurrents in P3HT:PCBM solar cells by incorporating a discretized DOS into a time-domain drift-diffusion model. With a DOS consisting of several energy-offset Gaussians, the authors were able to reproduce both the photocurrent dynamics and the steady-state solar cell characteristics with the same set of parameters. Johnson et al.<sup>120</sup> incorporated several charge generation and recombination pathways into modeling of nanosecond time-scale photocurrents in pristine diF TES-ADT films and several ADT-based blends in devices with planar electrode geometry. They were able to model the electric field dependence<sup>120</sup> and light intensity dependence<sup>334</sup> of photocurrent dynamics with one set of parameters and quantified changes in charge generation and transport characteristics depending on the acceptor and on the film morphology and crystallinity.<sup>300,335</sup> In the subsequent study, Paudel et al.<sup>300</sup> used a similar approach to establish that ultrafast charge generation efficiency ( $\eta_{SSC}$  in Table 2) in ADT-based small-molecule D:A blends was promoted by crystallinity.

In addition to the time domain, modeling of frequency-dependent (photo)conductivity has been carried out, providing information on trap DOS,<sup>336,337</sup> carrier concentration-dependent mobility,<sup>338</sup> and recombination rates.<sup>339</sup>

Given the complexity of the models that involve a considerable number of parameters (pertaining to charge generation, transport, recombination, and trapping/detrapping), many of which cannot be determined experimentally, a robust validation procedure is desirable. Many studies relied on a good agreement between the modeling results and the experimental data, including additional mechanisms if a satisfactory agreement was not produced with existing formulations.<sup>120,228,284,307</sup> Some studies clarified roles of various parameters through analytical modeling<sup>293,340</sup> and sensitivity analysis.<sup>341</sup> Johnson et al.<sup>120,334</sup> modeled time-resolved photocurrents by introducing constraints on selected parameters available from other experiments and fitting several data sets (e.g., photocurrents at various electric fields and/or light intensities) simultaneously, with one set of parameters subject to particular laws. Set et al.<sup>288</sup> studied which parameters can be reliably extracted from solar cell  $J$ - $V$  characteristics and argued that while the charge generation rate can be reliably extracted from the  $J$ - $V$  measurements alone, the effective DOS and built-in electric field, as well as the mobility and recombination factor, are clustered pairs that can only be decoupled using other characterization techniques. More work is needed to determine the appropriate constraints for the models and reliable standardized procedures of their validation.

### 3.3. Experimental Evidence

The questions pertinent to charge photogeneration that have been discussed in the literature include intrinsic versus extrinsic charge generation, driving forces behind charge generation, and relevant time-scales, pathways, and efficiencies of charge generation. In this section, examples of experimental evidence addressing these questions are discussed. Additional examples are given in Section 7.1 as an illustration of experimental capabilities and of unique insights they provide.

**3.3.1. Ultrafast- vs Longer-Time-Scale Charge Carrier Generation.** Charge generation on subpicosecond time-scales has been reported in various molecular crystals and films,<sup>198,200,201,342</sup> conjugated polymers,<sup>197,343</sup> and their HJs<sup>344</sup> using various modalities of ultrafast spectroscopies and fast time-resolved photocurrents in device structures.<sup>300,345–347</sup> Table 2 provides examples of observations of ultrafast charge generation in pristine materials, along with conditions under which experiments were carried out and with other pertinent observations (such as temperature and/or excitation wavelength dependence).

Charge generation via several pathways has been observed in many materials, both pristine and D-A, with each pathway associated with its time-scale, efficiency, and dependence on external parameters.<sup>120,348,349</sup> For example, in small-molecule D:A blends based on the diF TES-ADT donor, ultrafast charge separation with  $\sim 4$ – $20\%$  efficiency ( $\eta_{\text{SSC}}$  in Table 2) was observed, depending on the acceptor and on the applied electric field. In addition, up to a  $\sim 20$ – $50\%$  ( $\sim 10\%$ ) charge generation efficiency was observed due to the donor (CT) exciton dissociation at nanosecond time-scales.<sup>120,300</sup> Multiple charge generation pathways involving dissociation of donor- or acceptor-only excitons and D/A CT excitons have also been reported in the D-A copolymer PSF-BT films,<sup>349</sup> P3HT:PCBM BHJs,<sup>350</sup> SubPc/C<sub>60</sub> planar HJs,<sup>351,352</sup> etc.

Gehrig et al.<sup>353</sup> observed subpicosecond charge generation in a low-bandgap polymer PBDTTT-C:PCBM BHJ, which was followed by a subnanosecond triplet state formation due to nongeminate carrier recombination (Figure 7). The charge

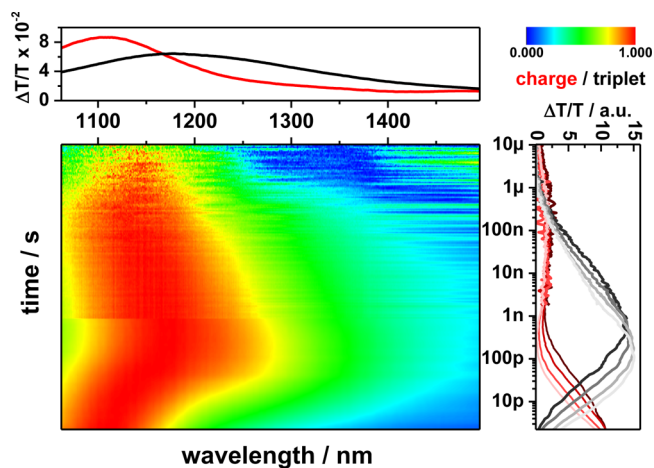


**Figure 7.** Normalized contour plot of the picosecond to millisecond near-IR transient absorption data obtained in PBDTTT-C:PC<sub>60</sub>BM blends. The top panel shows the spectra due to charged species (red) and triplet states (black) in the polymer. Charge carriers created on subpicosecond time-scales recombine nongeminately on the subnanosecond time-scales, creating a triplet state population (right panel). The triplet states undergo triplet–triplet annihilation, recreating a significant population of charge carriers at the nanosecond–microsecond time-scales. Reproduced from ref 353. Copyright 2015 American Chemical Society.

carrier population then increased again on the nanosecond–microsecond time-scales due to triplet–triplet annihilation that formed higher energy excited states prone to efficient charge separation.

In P3HT:PCBM blends, Cooke et al.<sup>344</sup> observed a sub-40-fs generation of mobile carriers which localized within  $\sim 120$  fs followed by recombination, possibly into an exciton, within  $\sim 1$  ps. Singh et al.<sup>204</sup> also studied P3HT:PCBM blends and observed that excitons reached the D/A interface within picoseconds, forming the CT excitons. Then, the CT excitons dissociated into mobile carriers on the nanosecond–microsecond time-scales, with the CT binding energy depending on the D/A interface area (the larger the area, the lower the binding energy).

One interesting question is whether the ability of the material to generate mobile charge carriers on ultrafast time-scales is absolutely necessary for the optoelectronic device performance that relies on the response to the cw excitation. Considerable evidence has been generated demonstrating that high-performance BHJs do exhibit ultrafast charge generation.<sup>73,244</sup> For example, Jin et al.<sup>354</sup> found good correlation between ultrafast photoconductivity assessed by time-resolved THz spectroscopy and OPV device performance. Therefore, materials exhibiting ultrafast charge generation, which outcompetes other processes such as unproductive (here meaning “not promoting charge generation”) FRET or strongly bound exciplex formation, represent a good starting point as optoelectronic materials. However, slower charge carrier generation mechanisms may also contribute to the device performance. For example, Kaake et al.<sup>355</sup> found that, in high-performance OPV blends p-DTS(PTTh<sub>2</sub>)<sub>2</sub>:PC<sub>71</sub>BM and PCDTBT:PC<sub>71</sub>BM with IQEs

approaching 100%, 70% of charge carriers were generated on the subpicosecond time-scales and the other 30% on the 1–100-ps time-scales. This suggests that both processes are important for achieving high IQEs. Additionally, other processes, such as carrier transport and nongeminate recombination, need be optimized simultaneously with charge generation, which renders the best blends from the standpoint of ultrafast charge generation not necessarily the best-performing blends in devices under cw illumination.<sup>37,302,356</sup>

**3.3.2. Intrinsic or Extrinsic?** Intrinsic charge generation, exemplified by generation of free carriers via a band-to-band transition in inorganic semiconductors, does not require driving force, and conditions under which it occurs in organic materials have been under debate for decades. For example, using mid-IR transient absorption spectroscopy, He et al.<sup>203</sup> recently reported *intrinsic, band-to-band* generation of free carriers, followed by band-edge radiative recombination (with 53% efficiency) or CT state formation (47%) on picosecond time-scales, in highly crystalline ZnPc films grown by weak epitaxy (Table 2). The observation was attributed to the highly ordered molecular packing with a short  $\pi$ – $\pi$  stacking distance of 3.4 Å, which favored the bandlike over the excitonic picture, supporting generation of delocalized free carriers. A tight  $\pi$ – $\pi$  stacking was also invoked to explain temperature- and polarization-dependent power-law decay of PL in TAT crystals by Labastide et al.,<sup>357</sup> from which *intrinsic, directional* charge-separated state formation in the  $\pi$ – $\pi$  stacking direction was inferred. In this case, however, the observations were attributed to the *strong CT coupling* along the  $\pi$ -stacking axis and described in the framework of the excitonic picture of HJ-aggregates (Section 2.4.3). More studies are needed to quantify how exactly the molecular packing drives charge separation and under what circumstances the fully delocalized picture of band-to-band charge generation, which requires no driving force, is appropriate.

In contrast to intrinsic generation, extrinsic charge generation requires driving force. Many factors may contribute to the necessary driving force, which include excess energy, entropy, static and dynamic disorder, local electrostatic environment, particular aspects of crystallinity (e.g., HOMO or LUMO bandwidths<sup>258</sup> or packing motifs), the dynamics of particular competing relaxation channels, external conditions (such as electric field or temperature), etc. There has been considerable experimental evidence that the relative importance of each of the factors above is material-dependent,<sup>206</sup> and criteria for what factor takes an optimization priority depending on the material class are necessary.

All of the factors above can promote ultrafast charge photogeneration, and not only in D–A materials, but also in pristine single-component systems (Table 2). Paquin et al.<sup>358</sup> used time-resolved PL spectroscopy to show that, in pristine P3HT films, the origin of the carriers generated on the picosecond time-scales is extrinsic, and *energy* driven, due to dissociation at the boundaries between ordered (aggregate) and amorphous domains. Mróz et al.<sup>359</sup> applied ultrafast spectroscopy to demonstrate that, in disordered porphyrin polymer films, excitons in amorphous regions dissociated with 2 orders of magnitude higher rates than those in aggregated regions. They concluded that *disorder* promotes subpicosecond generation of polaron pairs. Kandada et al.<sup>342</sup> observed a subpicosecond dissociation of the nascent triplet state (produced by a 80 fs *singlet fission*) into charge carriers in Pn films.

It has been suggested that electron–phonon coupling (*dynamic disorder*) plays a considerable role in the ultrafast carrier dynamics in Pn and rubrene crystals, either leading to carrier localization detrimental to charge transport<sup>360,361</sup> or promoting charge transport<sup>362</sup> depending on the model (Section 4.1). In the context of charge generation, Smith and Chin<sup>363</sup> theoretically demonstrated that both lattice and molecular vibrations may *assist* in ultrafast charge separation. In particular, they considered nanoscale PCBM aggregates and showed that the PCBM triple-band structure<sup>364</sup> supports an ultrafast charge separation at the D/A interface by a noise-assisted mechanism.

Questions regarding the origin of photoexcited mobile carriers have not been completely resolved even in model molecular materials, such as Pn and rubrene.<sup>127,321,365–368</sup> For example, Najafov et al.<sup>369</sup> argued that photoconductivity in rubrene crystals is mostly due to surface effects and is due to *singlet fission* followed by triplet exciton diffusion to the surface where they dissociate. However, Tao et al.<sup>366</sup> observed charge carrier generation on sub-100-fs time-scales and discussed that unrealistically high exciton diffusion coefficients would be necessary if the surface-mediated mechanism was behind these observations. Instead, they argued that photogenerated carriers are mostly generated in the bulk, either by *impurity-facilitated* exciton dissociation or *direct self-trapped* exciton dissociation with a small (0.035 eV) binding energy. (For example, an increase in photocurrent has been previously observed in oxidized rubrene due to formation of the oxygen-related band gap state that acts as an acceptor.<sup>370</sup>) Yada et al.,<sup>200</sup> based on their broadband THz spectroscopy results, proposed several processes contributing to generation of mobile carriers in rubrene at subpicosecond to ~50-ps time-scales, with the fast (sub-500-fs) generation of mobile holes enabled by fast electron trapping. Irkhin et al.<sup>367</sup> developed a method that can separate between surface and bulk contributions to steady-state photoconductivity in rubrene and can reversibly switch between these two contributions. Along with the surface conductivity being about 2 orders of magnitude higher than the bulk one, differences in light intensity dependence of the surface and bulk photocurrent were observed. In particular, a strongly nonlinear behavior for the surface-mediated photogeneration characterized by a power-law intensity-dependence ( $I_{\text{ph}} \sim I^a$ ) was obtained, with the parameter  $a$  changing from 1 to 1/3 to 1/4, depending on the dominant mechanism of charge carrier recombination in the particular intensity range.

The current understanding of charge generation in pristine polymers was recently summarized by Reid et al.<sup>371</sup> Several questions have been raised including the importance (or not) of chain folds for charge generation and the effects of excimer or other interchain species formation<sup>74</sup> on the solar cell performance. The need to understand the key similarities and differences in photophysics for homopolymers and D–A copolymers was also emphasized. Many of the issues discussed in the context of polymers (such as the effects of excimer/aggregate formation and of the CT character of low-energy excitations on charge carrier dynamics) are also pertinent to small-molecule crystalline materials.

**3.3.2.1. Energy Considerations.** The main energy considerations pertaining to charge photogeneration can be summarized by the two most commonly addressed questions: (i) whether extra photon energy helps promote charge generation and (ii) how large the D/A energy offset must be in D/A HJs to efficiently generate mobile charge carriers.<sup>206</sup> In

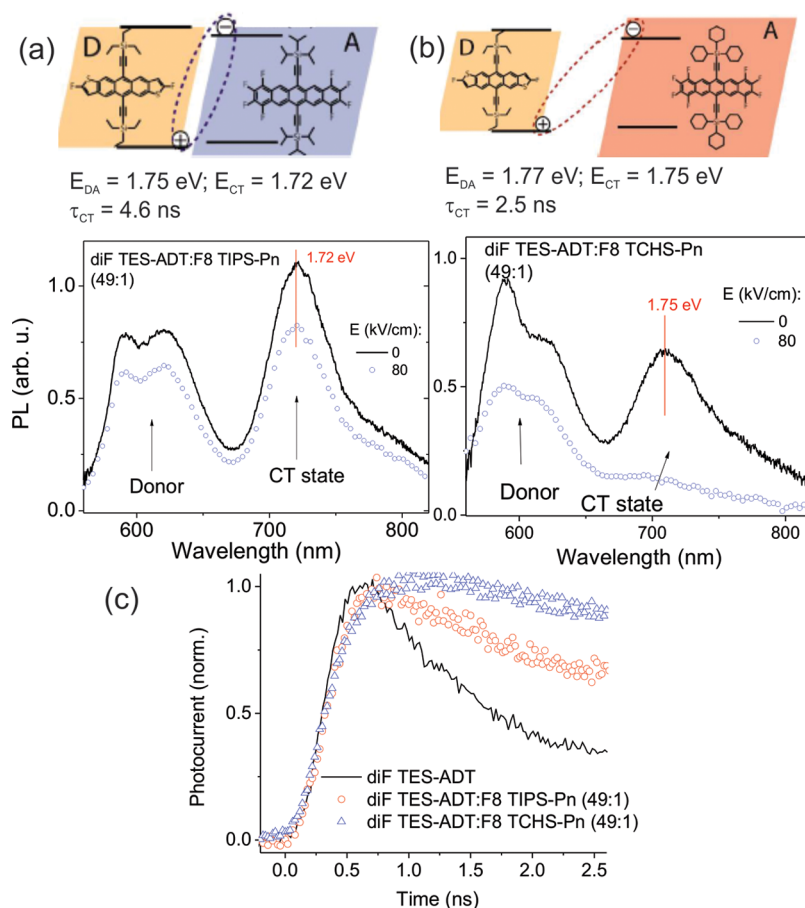


**Figure 8.** Photoluminescence of CT states formed in 49:1 diF TES-ADT blends with F8 TIPS-Pn (a) and F8 TCHS-Pn (b), in the absence and presence of an applied electric field  $E$ . The  $E_{DA}$  is the difference in energy between the LUMO of the F8 R-Pn acceptor and the HOMO of the diF TES-ADT donor,  $E_{CT}$  is the CT state energy determined from the PL spectra, and  $\tau_{CT}$  is the CT state lifetime. (c) Normalized photocurrent obtained under 355-nm 500-ps excitation of pristine diF TES-ADT films and diF TES-ADT:F8 R-Pn (49:1) blends at the applied electric field of 40 kV/cm, illustrating the effect of CT states on time-resolved charge carrier dynamics. A larger TCHS side group on the acceptor, as compared to TIPS, leads to a larger D–A separation, resulting in a less emissive CT state (which is also considerably more dissociative under applied electric field) and in the slow charge carrier recombination dynamics (c). Higher charge generation efficiency and slower recombination in the blend with the TCHS-containing acceptor, as compared to that with TIPS, enables up to a factor of  $\sim 3$  higher photocurrent in these blends (Figure 23). Adapted from ref 37. Copyright 2012 American Chemical Society.

many cases, however, there are additional energy considerations that play a role. For example, raising the energy of triplet excitons, to minimize back transfer from the CT state to a low-lying triplet state of the donor, was proposed as one of the guidelines for organic solar cell material design.<sup>372</sup> However, low-lying triplet states do not always represent a problem, and the kinetics of various processes can be as important as the thermodynamics.<sup>373</sup> Both energetics and kinetics determine whether formation of the donor singlet ( $S_1$ ) or donor CT exciton (D-CT)<sup>374</sup> results in their dissociation in the donor domain, radiative or nonradiative recombination, diffusion to the D/A interface resulting in charge or energy transfer to the acceptor, generation of triplet excitons via ISC or SF, etc.

Early work on molecular crystals indicated that intrinsic charge photogeneration in bulk materials proceeds with more efficiency at higher photon energies following the auto-ionization mechanism<sup>218</sup> (Section 3.1) and does not occur at wavelengths within the  $S_0$ – $S_1$  transition.<sup>2</sup> Indeed, an increase in steady-state photoconductivity by several orders of magnitude was observed in Pn crystals as the photon energy increased above the optical bandgap of  $\sim 2.2$  eV (which is about 0.4 eV higher than the lowest energy  $S_0$ – $S_1$  transition).<sup>218,219</sup>

However, in subpicosecond- through nanosecond-time-scale time-resolved measurements on acene crystals and films, such enhancement of the photoresponse has not been observed (Table 2). Therefore, it is important to understand what drives the ultrafast charge separation in pure and highly crystalline materials<sup>365</sup> and under what conditions the ultrafast intrinsic generation would become dominant over other mechanisms. This necessitates studies of ultrafast charge carrier dynamics in ultrapure crystals in an expanded wavelength range and highlights the importance of several charge generation pathways that proceed on different time-scales and follow different mechanisms.<sup>120,259,353</sup>

The original idea behind hot exciton dissociation in conjugated polymers developed by Arkhipov and co-workers was that the extra photon energy results in a higher energy electron, which promotes a larger electron–hole separation, thus reducing geminate recombination.<sup>375</sup> Recent work on steady-state photocurrents in PCPDTBT and PCDTBT pristine polymer diodes, however, emphasized the importance of the wave function delocalization.<sup>246</sup> In particular, in a higher-lying state, electron and hole are more delocalized and escape each other's attraction via a ballistic rather than thermalization

process. This makes the photogeneration process similar to that of autoionization in molecular crystals, which is more efficient upon excitation of a higher electronic state but does not improve with an additional vibrational excitation.

Based on the wavelength dependence of steady-state photocurrent in polymer/fullerene D/A bilayer solar cells, Hahn et al.<sup>246</sup> concluded that dissociation of higher electronic states proceeds more efficiently. However, excess vibronic energy did not matter, so that the increase in the photon energy up to  $\sim 0.5$  eV above the  $S_0-S_1$  0–0 transition did not enhance exciton dissociation, a conclusion similar to the authors' findings in pristine PCPDTBT and PCDTBT polymers.

Jailaubekov et al.<sup>244</sup> studied CuPc/fullerene bilayers using TR-2PPE and concluded that charge separation must occur within  $\sim 1$  ps after photoexcitation, during the hot CT exciton cooling time, because the relaxed CT state is tightly bound and cannot efficiently dissociate. This study emphasized the importance of electron delocalization, either intra- or intermolecular, which is in agreement with studies of various BHJs using pump–push spectroscopy (Section 3.3.2.4). As discussed in Section 3.2.2, the picture of CT excitons efficiently dissociating while relaxing in the DOS was also supported by Monte Carlo simulations.<sup>234</sup> Deotare et al.<sup>137</sup> probed CT exciton relaxation in the spatial, rather than time, domain. They used PL imaging to demonstrate that bound electron–hole pairs that form tightly bound CT states in D:A BHJs may be able to move over 5–10 nm distances, driven by energetic disorder and diffusion to lower energy states, before settling into a low-energy CT state. The electron–hole pair transport proceeded via “inchworm”-like motion, which was hypothesized to potentially be important for charge photogeneration.

Inefficient charge photogeneration from relaxed CT states was also reported in various small molecule D:A BHJs with a functionalized ADT donor and other functionalized ADT or functionalized Pn acceptors. In these materials, formation of highly emissive CT excitons (exciplexes) was observed, with the CT state properties dependent upon the D–A LUMO offset, as well as on the D–A separation (Figure 8) and on the packing motif (both of which were varied by changing the side groups on the acceptor molecule).<sup>37,356</sup> For example, Kendrick et al.<sup>37</sup> observed that the CT emission decreased as the D–A  $\Delta$ LUMO increased, with no emission observed at  $\Delta$ LUMO  $> 0.6$  eV. At a fixed  $\Delta$ LUMO, the D–A separation (controlled by the size of the side groups on the acceptor) determined the CT properties: the D–A exciplexes were less emissive and more prone to electric field-induced dissociation when the acceptor had larger side groups (enabling larger D–A separation) (Figure 8). Paudel et al.<sup>356</sup> reported that the relative packing motifs of the donor and acceptor affected the CT state formation: more efficient CT was observed in D/A combinations in which donor and acceptor molecules had similar  $\pi$ -stacking motifs. However, the exciplex contribution to charge generation was small,<sup>120,300</sup> and its formation was detrimental for solar cell performance based on these materials.<sup>188</sup> Exciplex formation is a common phenomenon occurring at D/A interfaces formed by polymer or small-molecule donor and nonfullerene acceptors.<sup>377,378</sup> However, in order to utilize these tightly bound CT states in charge generation, a mechanism is needed to reduce the binding energy. Examples of this include energy alignment enabling regeneration of the initial exciton by the back transfer (which could then have a lower binding energy), as has been realized in TFB:F8BT blends,<sup>378</sup> or molecular structure- or morphology-

controlled D/A separation, as has been observed in small-molecule blends.<sup>37</sup>

Grancini et al.<sup>379</sup> employed ultrafast spectroscopy to show that, in PCPDTBT:PCBM blends, both free polarons and CT states were generated at sub-100-fs time-scales from singlet excitons, but extra energy improved dissociation yields, possibly due to higher delocalization. Dimitrov et al.<sup>380</sup> arrived at similar conclusions about excess energy for the BTT-DPP:PCBM blend. They applied ultrafast pump–push spectroscopy to show that the photon energy  $\sim 0.2$  eV above the optical band gap doubled the quantum yield of photogenerated charges.

In contrast to the observations above, Lee et al.,<sup>381</sup> based on measurements of temperature-dependent IQE in P3HT:PCBM and PPV:PCBM BHJs, reported that exciton dissociation was independent of the photon energy, and the thermally relaxed CT excitons dissociated with the same efficiency as hot CT excitons. Similar conclusions were reached by Albrecht et al.,<sup>382</sup> who measured IQE in polymer:fullerene solar cells with various fullerene acceptors and observed similar photocurrents upon direct excitation of the CT states and of singlet donor or acceptor excitons. Vandewal et al.<sup>383</sup> expanded the study to include polymer:polymer, small molecule:fullerene, and polymer:fullerene blends and showed that IQEs of up to 90% can be achieved without relying on excess electronic or vibrational energy. Vandewal<sup>384</sup> further argued that the experimentally observed temperature dependence of  $V_{oc}$  extrapolation of which to 0 K is in good agreement with  $E_{CT}/q$  (where  $E_{CT}$  is the energy of the CT state and  $q$  is the electron charge),<sup>385,386</sup> provides another confirmation of carrier generation occurring via relaxed CT states. Pensack and Asbury<sup>387</sup> observed temperature-independent CT exciton dissociation in P3HT:PCBM blends using ultrafast vibrational spectroscopy and also concluded that excess energy does not assist charge separation in this system.

As of now, the consensus on the importance of excess energy and on the dominant driving force behind dissociation of relaxed CT excitons has not yet been reached, and reconciliation between results from various measurements on similar systems is needed. One particular concern is whether different methods probe different populations of CT states, of which only one population is relevant for the device performance. Based on the available experimental evidence, it is also clear that the excess energy requirement is material- and film morphology/crystallinity-dependent (e.g., crystallinity has been known to reduce requirements for energy).<sup>206</sup> In BHJs utilizing high-mobility donor polymers (such as DPP derivatives) the D–A energy offset needed to drive charge separation approaches zero (corresponding to D–A  $\Delta$ LUMO = 0.3 eV, assuming the exciton binding energy of 0.3 eV).<sup>388</sup> The photon energy dependence of charge generation also depends on the D–A energy offset and tends to be more pronounced at smaller energy offsets. In this case it would also be reasonable to expect that the charge separation must proceed on time-scales faster than exciton thermal relaxation. For an extensive summary of recent literature results on charge generation proceeding via hot vs relaxed CT excitons, refer to the review paper by Gao and Inganäs.<sup>211</sup> A recent review of properties of CT states and their role in charge generation and recombination can be found in ref 384.

Dimitrov and Durrant<sup>206</sup> summarized material design strategies necessary to achieve the highest possible charge separation efficiencies, with as small as possible D–A energy offset. These include the use of polymers with a high-degree of

D–A character, acceptors with high electron mobility/delocalization, as well as morphologies with different degrees of order in which the energy offset could be provided by differences in aggregate properties and charge separation may proceed via entropy-driven mechanisms.

**3.3.2.2. Entropy Considerations.** Gregg<sup>241</sup> discussed partial screening of the Coulomb potential in the 2D and 3D geometry due to the degeneracy of electronic states and associated with it change in entropy  $\Delta S$ . He argued that, in 1D materials,  $\Delta S = k_B \ln 1 = 0$ , and the activation energy for charge separation is high (0.27 eV for a 1D case such as that of ZnOOEP). For a 2D system,  $\Delta S = k_B \ln(2\pi/a)$ , where  $a$  is the lattice constant, and the activation energy is reduced (e.g., 0.13 eV for a 2D case such as that of P3HT). Finally, for a 3D system (e.g., C<sub>60</sub>),  $\Delta S = k_B \ln(4\pi(r/a)^2)$ , where  $r$  is the distance between charges and the activation energy is only 0.054 eV. Based on these considerations, one would expect about 4 orders of magnitude stronger charge photogeneration efficiency in 3D materials, as compared to that in 1D. Because most polymers and small molecules used in OPVs are  $\pi$ -stacked materials of dimensionality between 1D and 2D, this low symmetry may present an inherent impediment to charge generation, and the success of fullerene acceptors could partially be attributed to their 3D symmetry. From this perspective, amorphous polymers and glasses offer advantages over low-dimensional systems, especially if high charge carrier mobility can be achieved in such materials.<sup>389</sup>

Several reports in the literature specifically discussed the contribution of entropy to charge separation. For example, Gao et al.<sup>390</sup> attributed temperature-dependent  $V_{oc}$  in several polymer:fullerene and polymer:polymer blends to temperature-dependent charge separation, which they related to entropy. In particular, the entropy contribution to free energy decreased with decreasing temperature, leading to a requirement of a larger electron–hole pair initial distance for the charges to separate at low temperatures. Monahan et al.<sup>391</sup> were able to observe the dynamics of entropy-driven spontaneous delocalization of the CT exciton in crystalline Hex films. They showed that the process was temperature-independent and it drove the electron–hole separation from 14 to 52 nm within 100 fs.

However, Hahn et al.<sup>246</sup> found that the entropy was not a significant contributor to charge photogeneration in polymer donor/fullerene bilayer solar cells. They measured steady-state photocurrent as a function of applied electric field and considered the electric field at which the photocurrent saturated,  $F_{sat}$ , to be a measure of the electron–hole pair binding (so that  $eV = eF_{sat}r_0$ , where  $V$  is given by eq 26,  $r_0$  is the initial pair separation, and  $r_0 \sim 1/F_{sat}^{1/2}$ ). They found that  $F_{sat}$  was lower ( $r_0$  higher) in systems with polymers exhibiting higher hole delocalization in the polymer chain (i.e., with a stronger 1D character), which is opposite of what would be expected based solely on the entropy arguments.

**3.3.2.3. Effects of Local Interfacial Environment.** There has been increasing evidence of the critical importance of the D/A interfacial landscape for charge separation, which necessitates its theoretical modeling and experimental assessment.<sup>392</sup> Apart from energy and entropy considerations brought about by interfaces, another parameter of importance is a *local* dielectric constant. The importance of the dielectric constant for charge separation, as expected from eq 26, has been experimentally demonstrated,<sup>72</sup> and one of the material design strategies has been development of higher dielectric constant materials<sup>393,394</sup>

and composites<sup>395</sup> (Section 9.3.3). For example, polymers<sup>393</sup> and fullerene derivatives<sup>394</sup> with bulk dielectric constants of up to  $\sim 6$  were reported.

However, as pointed out by Baranovskii et al.,<sup>249</sup> the assumption of a low dielectric constant in organic materials may not be valid near the D/A interfaces, where electrostatic landscapes are highly inhomogeneous, and the molecular orientations, particulars of their stacking, etc. could contribute to large variations in the dielectric constant. Assessment of a local, position-dependent dielectric constant in small-molecule and polymer films has been the subject of several theoretical<sup>396</sup> and experimental<sup>397</sup> investigations. For example, dielectric constants between 3.4 (perpendicular to the plane of the molecule) and 15 (parallel to the plane of the molecule) were obtained from ab initio calculations on CuPc.<sup>396</sup> Hess et al.<sup>397</sup> employed quasi-single-molecule fluorescence microscopy to obtain maps of dielectric constants  $\epsilon$  in films of PMMA and PVDF, showing an *order of magnitude* variation of  $\epsilon$  across the PVDF film due to a distribution of structural phases in this polymer.

**3.3.2.4. Delocalization.** Recent experimental evidence suggests that charge carrier and/or exciton delocalization may play a significant role in ultrafast charge separation, with some of the reports discussed in the preceding sections. Bakulin et al.<sup>73</sup> used ultrafast pump–push photocurrent spectroscopy combined with DFT calculations to show that charge separation in polymer:PCBM and polymer:polymer BHJs occurs via hot-state charge delocalization rather than via energy-driven hopping. In polymer:PCBM BHJs, the electron was found to be delocalized on the fullerene molecule and could be further delocalized if additional fullerene molecules were available. Delocalization of the hole in the band states of the polymer, promoted by excess energy (provided by the IR push pulse), was found to enhance long-range charge separation. (If a polymer acceptor was used, a qualitatively similar effect was observed.) On the other hand, Guo et al.<sup>398</sup> observed that, in PBDTTT:PCBM BHJs, hole delocalization in the polymer, driven by polymer crystallinity, was detrimental for charge separation due to an enhanced probability of excimer and other low-energy trap state formation. Gélinas et al.<sup>399</sup> argued that delocalized band-like states in fullerene were the key factor for charge separation in polymer:fullerene and small molecule:fullerene BHJs. Their modeling revealed that charge separation proceeded either via incoherent transitions from *localized* donor to delocalized acceptor states or via a fully coherent wavepacket propagation across the interface, as both mechanisms were consistent with experimentally observed charge separation by  $\sim 4$  nm within  $\sim 40$  fs after excitation without the need for the excess energy. In the absence of electron delocalization, modeling revealed fast formation of a tightly bound CT exciton which would not be expected to dissociate on the ultrafast time-scales and thus was inconsistent with experimental observations.

Bernardo et al.<sup>72</sup> observed that in small-molecule:fullerene BHJs the delocalized CT state dissociation depended on the nanoscale fullerene crystallinity, and the strength of intermolecular electronic coupling within the crystallites was established to be of key importance. Jailaubekov et al.<sup>244</sup> pointed out that electronic delocalization can be intermolecular (due to local crystallinity) or intramolecular (due to long conjugation length in a donor polymer). Vandewal et al.<sup>383</sup> determined that the morphology of BHJs has to be controlled to promote delocalized CT states; however, Burke et al.<sup>237</sup>

warned that enhanced delocalization is likely to limit the  $V_{oc}$  due to increased recombination.

Kaake et al.<sup>56,355,400</sup> argued (based on the ultrafast transient absorption results) that the initial excited state in small-molecule:fullerene and polymer:fullerene BHJs is already delocalized, so that the CT state is comprised of mobile electrons and holes in the acceptor and donor domains, respectively, and it localizes at decoherence time-scales. It was observed that a large fraction ( $\sim 70\%$ ) of mobile charge carriers were produced on the ultrafast time-scales, as compared to that ( $\sim 30\%$ ) created following the exciton diffusion. The authors also noted that excited-state delocalization is sufficient but not necessary for efficient charge generation, and it is possible to achieve high photogeneration efficiency from a localized exciton diffusing to the D/A interface. Finally, it was concluded that the process of creating a delocalized coherent superposition of states via photoexcitation is universal, and it is rooted in the Heisenberg uncertainty principle. This conclusion was critically commented on by Mukamel,<sup>62</sup> who emphasized the difference between exciton delocalization (longer-lived coherence due to eigenstates spread over many molecules) and short-lived coherence between the eigenstates (e.g., a superposition of states with well-defined phases prepared by the incoming light). He further argued that the latter process, as well as the invoked uncertainty principle, cannot be relevant to the authors' experiments and that the Marcus theory when formulated in the delocalized basis can account for ultrafast charge transfer. The authors then clarified<sup>401,402</sup> that the property under discussion is the exciton delocalization. They further reported<sup>400</sup> on the excited state localization in pristine p-DTS(PTTh<sub>2</sub>)<sub>2</sub> films via 1.1 THz (intra- or intermolecular vibration) and 2.7 THz (torsion) modes. These were quenched in the presence of PCBM, instead giving rise to a 2.1 THz mode (assigned to the torsional mode frequency-shifted due to the presence of charge), the amplitude of which increased with the PCBM concentration and correlated with  $J_{sc}$  in p-DTS(PTTh<sub>2</sub>)<sub>2</sub>:PCBM solar cells. Because of these observations, the authors concluded that the CT occurs *before* the excited state localizes and that the coupling to the torsional mode is a part of the charge generation process.

The effects of vibrational coherence on charge photogeneration in polymer:fullerene BHJs have also been discussed. Falke et al.<sup>59</sup> concluded that coherent vibronic coupling between electronic and nuclear degrees of freedom promoted charge delocalization in P3HT:PCBM BHJs. Song et al.<sup>403</sup> performed 2DES on P3HT:PCBM blends and demonstrated that the vibrational coherence was directly transferred from the P3HT exciton to the P3HT hole polaron with the same spatial extent. They concluded that the driving force for electron transfer originated in the strong coupling between the photoexcited singlet states and a manifold of hot CT states, and was *not* due to a favorable electron affinity of the acceptor.

**3.3.3. Singlet Fission-Enabled Charge Generation.** Singlet fission (SF), a process of creating two triplet excitons from one singlet exciton (Section 2.7.1), has generated tremendous interest due to its potential to enable up to 200% IQEs in solar cells. However, in contrast to an impressive number of fundamental studies of the SF process,<sup>18–20</sup> reports demonstrating SF-enabled enhanced charge generation resulting in IQEs  $> 100\%$  in solar cells are limited. The successful device architectures making use of the SF involve planar D/A HJs with the SF-efficient donor (cast in a film with thickness within the triplet exciton diffusion length) and an acceptor with

the energy levels favoring triplet exciton ionization.<sup>404</sup> Examples of such systems include TIPS-Pn/PbS,<sup>23</sup> Pn or Tc/ $C_{60}$ ,<sup>405</sup> and Pn/Pc (where Pc represents various phthalocyanine derivatives).<sup>406</sup>

In Pn, the most well-studied SF material, ultrafast triplet dissociation into charge carriers observed via ultrafast spectroscopy was reported;<sup>342</sup> however, Pn/ $C_{60}$  devices exhibited strong triplet exciton-charge annihilation, which limited the EQE to about  $\sim 102\%$  in multilayer Pn/ $C_{60}$  devices.<sup>407</sup> To confine triplet excitons and minimize the triplet exciton losses, the P3HT layer was introduced in the device structure (i.e., ITO/PEDOT:PSS/P3HT/Pn/ $C_{60}$ /BCP/Ag), which led to the IQEs of 160% and EQEs of up to 109%.<sup>408</sup> Jadhav et al.<sup>409</sup> demonstrated up to  $\sim 71\%$  efficient SF in Tc-based multilayer devices, but the overall EQE was below 50%. Wu et al.<sup>405</sup> found that thicker layers of Tc were required to compete with singlet exciton dissociation and achieved 153% triplet yield and an IQE of 127% in Tc/ $C_{60}$  planar HJs. Ehrler et al.<sup>410</sup> demonstrated EQEs of up to 80% and PCE of 4.7% in Pn/PbSe HJs. Yang et al.<sup>411</sup> combined a solution processable functionalized Pn derivative TIPS-Pn with PbS nanocrystals with a bandgap allowing for triplet ionization in a single-junction device to demonstrate IQEs of up to 160% and EQEs of up to 60%, resulting in a PCE of 4.8%. Other venues for multiple exciton generation were also explored. For example, a functionalized Hex derivative, in which  $E(S_1) \geq 3E(T_1)$  (thus, potentially supporting creation of three triplet excitons out of a singlet exciton), was used as the donor in a planar HJ. However, the EQE was limited to  $< 1\%$ . No studies thus far reported enhanced PCEs based on SF-enabled charge generation in BHJs.

### 3.4. Summary

There has been tremendous progress in understanding the mechanisms of charge generation in organic materials, which drove the design of high-performance materials reaching unprecedented charge photogeneration efficiencies. New analytical models, such as those explicitly incorporating delocalization effects and vibrationally assisted hot CT exciton dissociation, have emerged. Computational studies have elucidated how electronic coupling between Frenkel and CT excitons, molecular and lattice vibrations, delocalization, and quantum coherence can drive ultrafast charge separation. Many factors that promote charge generation have been experimentally established.

However, understanding of the relative importance of various contributions to charge separation depending on the material is still lacking. In pristine materials, reports on intrinsic charge generation have been limited, and further studies of how the nature of low-energy excitons and particular aspects of crystallinity and morphology (e.g., molecular packing and mixed-phase structure in small-molecule solids, intra- and interchain interactions in polymers, etc.) contribute to charge generation are necessary. Of special interest is the case of D–A copolymers and how their distinct from homopolymers photophysics<sup>170</sup> and low disorder affect the underlying mechanisms for charge separation.

In D–A HJs, the importance of excess energy and the main driving force behind efficient dissociation of relaxed CT excitons are still under debate. Computational studies have identified possible mechanisms driving efficient charge separation without relying on extra energy, which includes spatially varying the energy landscape at the D/A interfaces,

Table 3. High-Mobility Materials and Their Characteristics

Type	Material	Mobility <sup>a</sup>	Packing <sup>b</sup>	Notes <sup>c</sup>	Ref		
Small-molecule materials							
hole	Pn	5.5	herringbone	$g_{\pi-\pi} = 2.5\%$	518		
		11 (Hall)		$\lambda = 95$ meV	519		
		21 (THz)		$J_{\pi-\pi} = 61$ meV	520		
		(40)		$J_{\text{tilted}} = 69$ meV	517		
	Rubrene	(20)	(29) (THz)	herringbone	$\sigma = 68$ meV	533	
					$J_1 = 77$ meV		200
		(40) <sup>d</sup> (4-probe)			$J_2 = 47$ meV	567	
					$J_3 = 33$ meV		568
		t-bu Rubrene	(12)		herringbone	$g_{\pi-\pi} = 1.5\%$	
						$\lambda = 160$ meV	569
		D-rubrene	(15)		herringbone	$J_{\pi-\pi} = 71$ meV	
		C10-DNTT	7.6ave, 7.9		herringbone	$J_{\text{tilted}} = 9$ meV	
		DNTT	(6.5ave, 6.8max)		herringbone	$\sigma = 53$ meV	570,536
						$W$ (HOMO) = 0.4 eV 3.74 Å	
diF TES-ADT	(6)		2D $\pi$ -stacking	$\sigma_{\text{vibr}} = 0.08$ Å	571		
				$J_1 = 83$ meV			
diF TES-ADT:PS	6.7			$J_2 = 14$ meV	572		
				$J_3 = 1.2$ meV			
diF TEG-ADT	2.3ave, 5.4max			$J_1 = 113$ meV	573		
				$\sigma_{\text{vibr}} = 0.12$ Å			
C6-DNT-VW	(6.2ave, 9.5max)		herringbone	$J_1 = 102$ meV	574		
				$\lambda = 136$ meV			
Bistetracene	(3.9ave, 6.1max)		2D $\pi$ -stacking	$J_1 = 68$ meV	575		
				$J_2 = 44$ meV			
TIPS-Pn	(8.1ave, 11max)		2D $\pi$ -stacking; specific metastable polymorph	$J_3 = 39$ meV	527		
				$J_1 = 76$ meV			
ditBu-BTBT	(7.1ave, 17max)		herringbone	$J_2 = 35$ meV	441		
				$\lambda = 138$ meV			
C8-BTBT:PS	2.5ave, 4.3max <sup>d</sup>			$J_1 = 34$ meV	576		
				$J_2 = 54$ meV			
Ph-BTBT-10	11.7ave, 13.9max		herringbone	$g_{\pi-\pi} = 0.9\%$	577		
				$3.34$ Å, $3.41$ Å			
DAT	16		herringbone	$\sigma_{\text{vibr}} = 0.09$ Å	437		
				$\lambda = 250$ meV; $J = 53$ – $60$ meV; Almost isotropic J			
				Aligned crystalline grains			
				$\sigma_{\text{vibr}} = 0.024$ Å			
				$\lambda = 85$ meV			
				$J_1 = 102$ meV			
				$J_2 = 60$ meV			
				$J_3 = 69$ meV			
				$J_1 = 85$ meV			
				$J_2 = 67$ meV			
				$J_3 = 38$ meV			

Table 3. continued

Type	Material	Mobility <sup>a</sup>	Packing <sup>b</sup>	Notes <sup>c</sup>	Ref	
Small-molecule materials						
electron	C10-DNBDT	(14)	herringbone	$\mu$ increases with strain	537	
	[9]phenacene	(10.5ave, 17.9max)	herringbone		578	
	Picene-(C <sub>14</sub> H <sub>29</sub> ) <sub>2</sub>	14.4ave, 20.9max			579	
	NDI	7.5	2D $\pi$ -stacking	Low humidity	580	
	PDIF-CN2	(6)		$\lambda = 280$ meV $J_1 = 95$ meV $J_2 = 65$ meV $J_3 = 0.1$ meV	581	
ambipolar	C <sub>60</sub>	6		Correlated with crystal grain size	582	
	F2-TCNQ	(7)	2D $\pi$ -stacking	W (LUMO) = 0.8 eV	583	
	1:1TIPS-Pn:a-Meo	3.2 ave, 6.8 max		doping	584	
	Fm-rubrene	(4.8h, 4.2e)		Au/CNT electrodes	585	
Polymer						
hole	DPP-DTT	10.5max		3.43 Å; crystallites 40 nm × 1 $\mu$ m	586	
	DPPDBTE	8.5ave, 10.5max		3.62 Å	587	
	DPPDTSE	9.8ave, 12.0max		3.58 Å	587	
	DPP-SVS1	6.6ave, 7.7max (drop); 9.8ave, 10.3max (sheared)		3.61 Å	588	
	DPP-SVS2	6.5ave, 7.4max(drop), 11.6ave, 13.9max (sheared) (17.8 at higher V)		3.60 Å	588	
	PTPP-DTTE	6.8ave, 7.4max		3.47 Å	589	
	PDVT-10	8.2max		3.66 Å	590	
	PDVT-10/B-CNT (1 wt %)	5ave, 7.2max			556	
	electron	PCDTPT	23.7 <sup>cd</sup>		3.5 Å	562
			21.3ave, 25.4max <sup>cd</sup>		oriented	591
			36.3max			
	ambipolar	CDT-BTZ	18.5, 22.2max <sup>cd</sup>		oriented	591
			7.0			592
ambipolar	PTDPPSe1	8.8h, 4.3e <sup>cd</sup>		3.6 Å; 3D conduction	593	
		2.8h, 6.3e			594	
		6.2h, 3.1e <sup>cd</sup>			593	

<sup>a</sup>Room-temperature mobility measured in OFETs unless stated otherwise (e.g., Hall effect, THz spectroscopy, or 4-probe configuration). Values in parentheses are for single crystals; otherwise for films. When available, both average (ave) over many devices and maximal (max) values are given. For ambipolar transport, electron (e) and hole (h) mobilities are indicated. When mobility is available in films made by different deposition methods (e.g., drop cast or shear-deposited), the method is indicated. <sup>b</sup>Packing motif as determined from crystal structure. <sup>c</sup>Additional information on the material, including  $\pi$ - $\pi$  stacking distances, transfer integrals ( $J$ ), reorganization energies ( $\lambda$ ), HOMO or LUMO bandwidths ( $W$ ), and paracrystallinity parameters ( $g$ ). The set of parameters  $g_{\pi-\pi}$  (paracrystallinity parameter for the  $\pi$ -stacking direction),  $\lambda$  (reorganization energy),  $J_{\pi-\pi}$  (modulus transfer integral for  $\pi$ -stacking for ideal crystal morphology),  $J_{\text{tilted}}$  (modulus transfer integral for face-to-edge stacking for ideal crystal morphology), and  $\sigma$  (energetic disorder) is obtained from theoretical investigations in ref 438. The energetic disorder is due to structural disorder caused by intermolecular rearrangements, molecular deformations, and polarization effects. The parameter  $\sigma_{\text{vibr}}$  is the amplitude of long-axis vibration at room temperature, taken as a measure for the extent of dynamic disorder; ref 536. The parameters  $J_1$ ,  $J_2$ , and  $J_3$  are nearest-neighbor transfer integrals taken either from corresponding references in the table or from ref 122. <sup>d</sup>In ref 565, Bittle et al. argued that the I-V characteristics used to extract peak mobilities in these references may need a more extensive analysis to account for the non-ohmicity of contacts and resulting nonideal I-V characteristics. With that taken into account, Bittle et al. obtained a factor of  $\sim 2$ – $5$  reduction in the mobility values (thus yielding values in the 1–10 cm<sup>2</sup>/(Vs) range) as compared to those reported in the original references.

microscopic-level electrostatics, and quantum-coherent effects. Reconciling experimental findings produced by different techniques (especially those that are done on the ultrafast time-scales versus in the steady state) performed on the same system is necessary (i) to rule out the possibility that these experiments assess different populations of excited states, only one of which matters for device performance, and (ii) to establish which theoretically predicted mechanism dominates the observed behavior. This also ties to the existence of various charge generation pathways (including ultrafast charge separation, exciton diffusion/relaxation followed by dissociation at longer time-scales, and equilibrated carrier recombination into an exciton followed by its dissociation) in organic

materials, which were confirmed in both computational and experimental studies. Their relative contribution to optoelectronic device performance, depending on the material and on the type of the device, needs elucidation.

Computational studies have revealed that delocalization of the initial donor exciton or of the CT exciton is not a necessity for efficient charge generation, and morphology (such as fractal domain structure and aggregation) can promote ultrafast charge separation without relying on any delocalization. On the experimental side, the importance of initial exciton delocalization for charge generation is under debate, but there has been consistency in reports that electron delocalization in the acceptor material promotes ultrafast charge separation. The role

of the hole delocalization in the donor material appears to be material dependent and needs further clarification.

Several experimental studies established the importance of vibrations and vibrational coherence for charge generation. However, the exact interplay of localized and delocalized states and the role of various types of coherence in charge separation is yet to be established. Theoretical studies on the topic produced mixed results, and better understanding of how nuclear motion contributes to charge generation is needed.

Overall, clearer guidelines that identify dominant factors (such as particular kinetics and thermodynamics of the donor and acceptor molecules, excess energy, delocalization, or favorable gradients of the interfacial energy or dielectric permittivity landscape) depending on the material are desirable. Theoretical models of charge generation that incorporate the effects of delocalization, spin-dependent dynamics, and the microscopic characteristics of the HJs are necessary. Experimental studies that utilize methods that are uniquely sensitive to coherent processes, that can quantify various charge generation pathways, and that enable monitoring charge carriers from their creation to extraction are also needed. Finally, with the established techniques there are important considerations pertaining to measurements of photoexcited charge carrier dynamics that affect data interpretation, as summarized in Section 7.3.

## 4. CHARGE TRANSPORT

In optoelectronic applications, device performance relies on the ability of the material to conduct charge carriers. The key characteristic that describes the charge transport properties of semiconductors is charge carrier mobility, which depends on the intrinsic properties of the material (such as molecular structure and packing), on the extrinsic properties (such as the nature of defects and their concentration), and on the external parameters (such as electric field and temperature). For background on charge transport in organic semiconductors, the reader is referred to excellent books on the topic<sup>2,433</sup> and comprehensive reviews (Table S1).<sup>434,435</sup>

### 4.1. General Considerations

The nature of charge transport in organic semiconductors depends on the interplay of electronic coupling among the constituent molecular units, the coupling to intra- and intermolecular vibrations, and the static intra- and intermolecular disorder. Depending on the system under study (e.g., molecular crystals or polymers, polycrystalline or amorphous films), these contributions vary considerably. For a qualitative understanding of parameters that determine charge transport, a convenient classification scheme for various contributions to charge transport can be obtained by considering the following one-electron Hamiltonian:<sup>2</sup>

$$H = H_0 + H_1 + H_2 + H_3 + H_4 \quad (35)$$

with each term describing the following contributions:

$$H_0 = \sum_n E_n a_n^\dagger a_n + \sum_l \hbar\omega_l (b_l^\dagger b_l + 1/2)$$

electronic and vibrational excitation

$$H_1 = \sum_n J_{mn} a_n^\dagger a_m \quad \text{electron transfer}$$

$$H_2 = \sum_n \sum_l g_{nl}^2 \hbar\omega_l a_n^\dagger a_n (b_{-l}^\dagger + b_l)$$

electron–phonon coupling (diagonal, local)

$$H_3 = \sum_{n,m} \sum_l f_{nml}^2 \hbar\omega_l a_n^\dagger a_m (b_{-l}^\dagger + b_l)$$

electron–phonon coupling (off-diagonal, non-local)

$$H_4 = \sum_n \Delta E_n a_n^\dagger a_n + \sum_{n,m} \Delta J_{mn} a_n^\dagger a_m$$

static disorder (diagonal and off-diagonal)

Here  $a_n^\dagger(a_n)$  is the creation (annihilation) operator for an electron in an orbital of energy  $E_n$  at the molecular site  $n$  and  $b_l^\dagger(b_l)$  is the creation (annihilation) operator for a vibrational mode with energy  $\hbar\omega_l$ .  $J_{mn}$  and  $E_n$  are the transfer integral and the energy, respectively, in a perfectly ordered lattice, and  $\Delta J_{mn}$  and  $\Delta E_n$  are their respective variations due to static disorder. The parameters  $g_{nl}^2$  and  $f_{nml}^2$  are dimensionless coupling constants for the electron–phonon coupling. The Hamiltonian of eq 35 assumes a low carrier density and ignores electron correlation and Coulomb interaction effects.<sup>2</sup> Nevertheless, it is useful for illustrating various contributions and limiting cases, pertaining to the discussion below.

In eq 35,  $H_0$  yields the total energy of the electronically and vibrationally excited molecular system (excluding coupling between electronic and vibrational modes), respectively.  $H_1$  describes the transfer of an electron from site  $m$  to site  $n$ , with the magnitude of electronic coupling (and probability of transition) incorporated in the transfer integral  $J_{mn}$ . The latter can be calculated<sup>435</sup> using  $J_{mn} = \langle m|H_0|n \rangle$  where  $|m\rangle$ ,  $|n\rangle$  are relevant HOMO (LUMO) orbitals of the isolated molecules in the case of hole (electron) transport, and its typical values are in the 10–200 meV range (see, for example, Tables 3 and 5).<sup>436</sup> It is determined by the wave function overlap, and on the molecular level it is strongly dependent upon intermolecular distances, orientations, and packing arrangements (such as longitudinal displacements). The larger transfer integral promotes charge delocalization, and maximizing the transfer integral has been one of the strategies behind rational design of high-mobility organic semiconductors.<sup>437</sup> Another important consideration for achieving high charge carrier mobility is a transfer integral that is as isotropic as possible.<sup>438–441</sup> For example, Yavuz et al. computationally studied 22 conjugated oligomers and observed that weak but multidimensional electronic coupling yielded a considerably higher hole mobility than strong, but low-dimensional coupling.<sup>438</sup> Also important is that a 2D transport is less affected by the presence of defects (thus, static disorder) as compared to 1D transport.<sup>440</sup>

$H_2$  and  $H_3$  describe the polaronic effects arising from interactions between the electronic excitation and intra- and intermolecular vibrations, which are commonly referred to as *dynamic disorder*. The coupling to the vibrational mode of energy  $\hbar\omega_l$  described by  $H_2$  manifests in the modulation of site energies  $E_n$ , and the coupling constant  $g^2$  defines the magnitude of this interaction and is directly related to the Huang–Rhys parameter  $S$  used in spectroscopy (Section 2.1).<sup>434</sup>  $H_2$  is the key interaction in Holstein-type polaron models, and it implicitly includes the intra- and intermolecular contributions to the reorganization energy  $\lambda$ . The reorganization energy

Table 4. Experimental Observations of  $d\mu/dT < 0$ 

Material	Single Crystal (SC) or film	RT mobility, <sup>a</sup> cm <sup>2</sup> /(Vs)	Max mobility, <sup>b</sup> cm <sup>2</sup> /(Vs) (T, K)	$\mu(T)^c$	T range ( $d\mu/dT < 0$ ) <sup>d</sup>	Method <sup>e</sup>	Notes <sup>f</sup>	Ref		
<b>Small molecules</b>										
Nph	SC	1h ( <i>a</i> -axis)	400h ( <i>a</i> -axis) (10K)	$T^{-n}$ $n = 2.9$	30–300 20–300	TOF	Ultrapure	506		
		0.65e ( <i>a</i> -, <i>b</i> -)	25e ( <i>a</i> -, <i>b</i> -axis) (40K)	$n = 1.47$ – $1.48$	30–100					
		0.3e ( <i>c</i> -axis)	2e ( <i>c</i> -axis) (30 K)	$n = 1.48$						
Tc	SC	0.1h (350 K)	1h (180 K)		180–350	SCLC, TOF		595,596		
		0.03 ( $\mu\eta$ )	0.1 ( $\mu\eta$ ) (10K)		10–300				THz	365
		0.7h (assumed)	1.8h (180 K)	$T^{-n}$ , $n = 2.09$	180–375				TPC	346
Rubrene	SC	0.05 ( $\mu\eta$ )	0.2 ( $\mu\eta$ ) (20K)		20–300	THz		365		
	SC	29h	140h (50K)		50, 300 K	THz		200		
	SC	8h ( <i>a</i> -axis)	12h ( <i>a</i> -axis) (175 K)		175–300	FET	higher $\mu$ correlates with $d\mu/dT < 0$	533		
	SC	20h ( <i>b</i> -axis)	30h ( <i>b</i> -axis) (175 K)		175–300	Hall		511		
	SC	10h	22h (175 K)							
		0.29h ( <i>c</i> -axis)	0.7h ( <i>c</i> -axis) (180 K)	$T^{-n}$ , $n = 1.6$ – $1.9$	180–300	TOF		507		
Pn	SC	15h	45h (90K)	$T^{-n}$ , $n = 0.9$ – $1.2$	90–300	FET (4-probe)	Deuterated	546		
	SC	35h	58h (225 K)	$T^{-n}$ , $n = 2.38$	225–310	SCLC	Ultrapure	508		
	SC	0.3 ( $\mu\eta$ )	2 ( $\mu\eta$ ) (5K)		5–300	THz	Ultrapure	365		
	SC	0.2 ( $\mu\eta$ )	0.4 ( $\mu\eta$ ) (10K)	$T^{-n}$ , $n = 0.27$	5–300	THz		202		
	film	0.02 ( $\mu\eta$ )	0.07 ( $\mu\eta$ ) (10K)	$T^{-n}$ , $n = 0.32$	5–300	THz		201		
TIPS-Pn	film	11h	45h (210 K)		210–290	Hall		519		
	SC	0.2 ( $\mu\eta$ )	4 ( $\mu\eta$ ) (10K)		10–300	THz		365		
	SC	0.2 ( $\mu\eta$ )	1.6 ( $\mu\eta$ ) (10K)		10–300	THz		198		
	SC	0.2 ( $\mu\eta$ )	2–3 ( $\mu\eta$ ) (10K)	$\exp(-\alpha T)$	10–300	THz		201		
	Film	0.02 ( $\mu\eta$ )	0.06 ( $\mu\eta$ ) (20K)		20–300	THz	$\mu\eta$ – crystallinity correlation	40		
	Film	1.3h	6h (4K)		4–300	FET	At high $V_D$ ; $V_D$ -dependent	513		
	Film	0.8	1.7 (125 K)		125–350	TR-SHG		597		
DNTT	SC	6.8h	9.9h (270 K)		270–300	FET	Vacuum-gap	514		
TMTSF	SC	4h	6h (160 K)	$T^{-n}$ , $n = 2$	160–300	FET		598		
C8-BTBT	SC	3.2h (9.1h max)	8.8h (80K)	$T^{-n}$ , $n = 1.1$	80–300	FET		599		
C10-DNBDT	SC	14h	28h (200 K)		200–320	FET (4-probe)	$\mu$ increases with strain	537		
PDIF-CN2	SC	3e	4e (225 K)		225–300	FET	vacuum gap	581		
		5.1e	10.8e (230 K)		230–290		(dielectric-dependent)			
F2-TCNQ	SC	6e	25e (150 K)		150–300	FET	Vacuum-gap; No $\mu$ vs $d\mu/dT$ correlation	583		
<b>Polymers</b>										
MEH-PPV	film			20% increase in $\sigma$ at 30 K	30–300	THz	amorphous	343		
P3HT	film	$2 \times 10^{-4}$ h (390 K)	$10^{-3}$ h (300 K)		300–390	FET	Polycrystalline	27		
		33 (THz)		30% increase in $\sigma$ at 40 K		THz		425		
2DPP-TEG	film	1.5e	2e (210 K)		210–300	FET	Polycryst., ambipolar; $\mu$ correlated with $d\mu/dT$	560		
					250–300	Hall				
CDT-BTZ-C16	film	5.6h	6.5h (240 K)		240–300	FET (4-probe)	>3 $\mu$ m long fibers; $d\mu/dT < 0$ only at high gate voltage	564		
P8T2Z-C12	film	1h (330 K)	1.8h (290 K)		290–330	FET	Low trap density; $d\mu/dT < 0$ only at high gate voltage	561		

<sup>a</sup>Room-temperature (RT) mobility unless stated otherwise. Hole or electron mobility is indicated by “h” or “e”, respectively. When the product “ $\mu\eta$ ” is reported, where  $\mu$  is the sum of the hole and electron mobility and  $\eta$  is the charge generation efficiency, it is assumed that the temperature dependence is due to that of the mobility of the dominant carrier. When the mobility was measured along a particular axis in the single crystal, the axis is indicated. <sup>b</sup>The highest mobility achieved, with the corresponding temperature indicated in parentheses. See also comments for <sup>a</sup>.

Table 4. continued

<sup>c</sup>Quantitative description of the temperature dependence of mobility when reported. In THz experiments on polymers, the reported  $\sigma$  is the photoconductivity and the temperature dependence is assumed to be due to that of the mobility. <sup>d</sup>The temperature range at which the  $d\mu/dT < 0$  behavior was observed. <sup>e</sup>Experimental method used for observations. FET = field effect transistor; Hall = Hall effect measurements; SCLC = space-charge-limited currents; THz = optical pump-THz probe spectroscopy; TOF = time-of-flight; TR-SHG = time-resolved second harmonic generation. Some of these methods are described in Section 7. <sup>f</sup>Additional comments pertaining to film morphology, device geometry, and correlation between the value of mobility and  $d\mu/dT$  (when data from multiple devices are available).

accounts for the change in the geometries of the molecules involved in charge transfer and the change in the polarization of the surrounding medium; it is responsible for charge localization and is related to the polaron binding energy by  $E_{\text{pol}} = \lambda/2$ . Typical values for the reorganization energy are in the range 0.07–0.18 eV, and minimization of the reorganization energy  $\lambda$  (in particular, its intramolecular part, which is dominant in organic solids) has been employed in computational screening of candidate high-mobility materials,<sup>437</sup> along with maximization of the transfer integrals.

$H_3$  describes the nonlocal coupling and is responsible for modulation of the transfer integral  $J_{mn}$  due to the electron–phonon interactions. This is the key interaction in, for example, Peierls-type models (such as the SSH Hamiltonian for conducting polymers).<sup>442</sup>  $H_4$  describes static disorder effects that manifest as changes to the site energy or transfer integral. These are not related to vibrations, but rather are determined by the structure of the molecular solid.

The mechanism of charge transport is determined by the magnitudes of different contributions to the overall Hamiltonian of eq 35.  $H_1$  favors coherent transport and charge delocalization (band transport). Simple criteria of whether the band transport can occur are based on the comparison between the energy bandwidth  $W$  and either the energy change due to scattering of the charge carrier<sup>443</sup> or the uncertainty of the charge carriers' site energy.<sup>2</sup> These criteria dictate that band transport can occur if charge carrier mobility  $\mu > ea^2/(2\hbar)$  or  $\mu > ea_0^2W/(\hbar k_B T)$ , respectively, where  $e$  is the elementary charge,  $a$  is the intermolecular distance,  $a_0$  is the lattice constant, and  $k_B T$  is the thermal energy. For  $a = 3\text{--}4 \text{ \AA}$ ,  $a_0 = 6 \text{ \AA}$ , and  $W = 10 k_B T$ , these estimates yield room-temperature mobilities of  $>1$  and  $>5 \text{ cm}^2/(\text{Vs})$ , respectively. Therefore, a considerable number of high-performance materials (Table 3) could potentially exhibit band transport at room temperature.

$H_2$  and  $H_3$  promote polaronic transport, and  $H_4$  is responsible for static disorder-controlled transport. In many high-mobility materials such as organic crystals,  $H_4$  is relatively small, and the competition between  $H_1$ ,  $H_2$ , and  $H_3$  determines charge transport characteristics, which makes theoretical description of charge transport in these materials difficult. In amorphous and mixed-phase materials,  $H_4$  is generally thought to dominate charge transport. However, this may not be the case in high-mobility polymers.<sup>389</sup> For example, Troisi<sup>444</sup> argued that there is a maximal value of charge carrier mobility compatible with a hopping mechanism that relies on the charge transfer from molecule to molecule in independent events. He established that such maximal hopping mobility could be as low as  $\sim 0.1 \text{ cm}^2/(\text{Vs})$ , thus requiring descriptions beyond the hopping mechanism for high-mobility organic materials.

## 4.2. Charge Transport Mechanisms: Theoretical Considerations

**4.2.1. Band Transport.** If the transport is dominated by  $H_1$  of eq 35 (thus requiring that the transfer integral is considerably higher than the reorganization energy), the charge carrier

delocalizes to form a propagating Bloch wave that is occasionally scattered by lattice vibrations. In this case, the charge carrier mobility is given by

$$\mu = e\tau/m_{\text{eff}} \quad (36)$$

where  $\tau$  is the mean scattering time and  $m_{\text{eff}}$  is the band effective mass that can be evaluated from the electronic band dispersion  $E_k$  using  $1/m_{\text{eff}} = (1/\hbar^2)|d^2E_k/dk^2|$ . The mobility of eq 36 is expected to be anisotropic (due to anisotropic effective mass) and have the power-law temperature dependence  $\mu \sim T^{-n}$ , with  $n = 0\text{--}3$  depending on the scattering mechanism (acoustic phonons, impurities, electron interactions).<sup>2</sup> Discussion of the effects of electron–phonon coupling on the effective mass  $m_{\text{eff}}$  and on the scattering time  $\tau$  can be found in ref 445.

Because of experimental observations of  $d\mu/dT < 0$  (commonly referred to as “bandlike” behavior, the terminology which will be used throughout this review) and mobility anisotropy in a variety of molecular crystals (Table 4), considerable theoretical effort has been devoted to establishing whether band transport does occur in these materials and which other mechanisms enable such observations, as discussed below. A formal definition of “bandlike” transport is discussed, for example, in ref 218 in the context of the Boltzmann theory of carrier transport. The applicability of this theory is determined by the Landau–Peierls criteria requiring that  $l \gg a_0$  (where  $l$  is the carrier mean free path and  $a_0$  is the lattice constant) and  $\hbar/\tau \ll k_B T$  (where  $\tau$  is the carrier relaxation time). Because these criteria are typically not satisfied by organic semiconductor materials in a wide temperature range, modifications of eq 36 that consider a narrow-band limit<sup>434</sup> or polaron renormalization (e.g., eq 37, Section 4.2.2) have been used to describe coherent charge transport in organic crystals.<sup>446,447</sup> An additional consideration is that, in high-mobility organic semiconductors, carriers exhibiting coherent band and incoherent hopping transport could potentially coexist, which prompted an introduction of a “carrier coherence factor” and a treatment that includes contributions of both types of carriers to experimentally measured mobility,<sup>448,449</sup> as discussed in Section 4.3.1.

**4.2.2. Polaron Transport.** If the  $H_2$  and  $H_3$  contributions to charge transport compete with that of  $H_1$  (while the  $H_4$  contribution is minimal), the charge propagation considerably depends on the strength of the electron–phonon coupling.

In the case of local electron–phonon coupling (described by  $H_2$ ), the mobility is a sum of two contributions arising from coherent electron tunneling and incoherent hopping,<sup>434</sup> the interplay of which is determined by the coupling constants  $g^2$  of eq 35. As the strength of the electron–phonon coupling increases, the contribution of the tunneling part to the overall mobility decreases. When  $H_2$  and  $H_3$  contributions dominate that of  $H_1$  (so that the reorganization energy is considerably higher than the transfer integral), a small (or lattice) polaron<sup>218</sup> forms that propagates by hopping. (In the earlier literature,<sup>218</sup> the concept of a “nearly-small” (or molecular) polaron was also

proposed. Such a polaron would form as a result of interaction of a charge carrier either with intramolecular vibrations of the molecule on which it was localized during its residence time or with the polar IR-active vibrational modes of the nearest-neighbor molecules. The molecular polaron propagates by “stepping via tunneling”, which is described by the temperature-dependent effective mass leading to  $d\mu/dT < 0$ .<sup>201</sup> In this description, the polaron type (electronic, molecular, or lattice) is determined by the carrier residence (or localization) time with respect to electronic polarization, vibronic relaxation, and lattice polarization times, respectively.) For a comprehensive discussion of the polaron size and how it determines charge transport characteristics, see ref 450.

For a small polaron, the hopping part of mobility in a classical limit (assuming that the phonon energy is small compared to the thermal energy, i.e.  $\hbar\omega \ll k_B T$ ) relies on a hopping rate  $k_{\text{hop}}$  described by the semiclassical Marcus theory for electron transfer reactions, and for a 3D system it is given by

$\mu_{\text{hop}} = \frac{e}{k_B T} \frac{a^2}{6} k_{\text{ET}}$  where  $k_{\text{ET}}$  is the electron transfer rate of eq 21 (with  $\Delta G = 0$ ) and  $a$  is the distance between the lattice sites.<sup>2</sup> This expression predicts the temperature dependent incoherent mobility contribution in the form  $\mu \sim T^{-3/2} \exp(-E_{\text{pol}}/2k_B T)$  (where  $E_{\text{pol}}$  is the polaron binding energy that is half of the reorganization energy  $\lambda$ , i.e.  $E_{\text{pol}} = \lambda/2$ ), which in the cases of  $E_{\text{pol}} \geq 70$  meV yields the Arrhenius-type thermally activated mobility at around room temperature. The temperature dependence of the coherent tunneling part of the mobility under the assumption of narrow bands incorporates that of the relaxation time (given by  $1/(2k_{\text{ET}})$  in the lowest-order approximation in a 1D model) and of the transfer integral.<sup>434</sup> This results in a complicated function describing the temperature dependence of mobility exhibiting  $d\mu/dT < 0$  behavior. In a more recent work, the theory was generalized to remove the narrow-band limit, which yielded the coherent part of mobility in the form<sup>446</sup>

$$\mu_{\alpha\beta, \text{coh}} = \frac{\sqrt{\pi} e \tau}{2N_c k_B T} \sum_k n_k (1 - n_k) \tilde{v}_\alpha(k) \tilde{v}_\beta(k) \quad (37)$$

where  $\tilde{v}_\alpha(k) = (1/\hbar)(\partial \tilde{E}(k)/\partial k_\alpha)$  is the polaron band velocity ( $\tilde{E}$  is the polaron band energy),  $n_k$  is the Fermi–Dirac distribution,  $\tau$  is the polaron lifetime, and  $N_c$  is the carrier concentration. The expression of eq 37 has a similar form to that for the band mobility derived from the Boltzmann equation, but the quantities  $\tilde{v}$ ,  $\tilde{E}$  reflect the electron–phonon coupling, which makes  $\tilde{E}$  temperature-dependent. Overall, the model predicts tunneling-dominated transport (with  $d\mu/dT \leq 0$ ) at low temperatures followed by Arrhenius-type hopping-dominated thermally activated transport at intermediate temperatures that changes into a  $\sim T^{-3/2}$  scattering-dominated behavior at high temperatures, with the crossover temperature dependent upon  $E_{\text{pol}}$ . Cheng and Silbey<sup>451</sup> (who studied 1D transport, explicitly incorporating electron–phonon coupling into the 1D Holstein model) pointed out that the crossover from band to hopping transport is not necessarily accompanied by thermally activated mobility. Instead, temperature-independent mobility could be obtained.

The applicability of the polaron transport model described above to crystalline organic semiconductors has been questioned in the literature<sup>436,452</sup> for several reasons. Troisi<sup>436</sup> argued that when the reorganization energy ( $\lambda$ ) is smaller than twice the transfer integral ( $2J$ , taken to be a measure of

intermolecular coupling), small polarons do not form, and the hopping rate cannot be defined at any temperature. He further discussed that even if the polarons do form, their hopping should be adiabatic, as the intermolecular coupling in crystalline materials is too strong for a nonadiabatic description associated with the Marcus rate.

Another aspect under discussion has been the semiclassical nature of the Marcus rate, which treats nuclear motion classically.<sup>453</sup> It has been emphasized that the vibrations have to be treated quantum mechanically and, in particular, incorporate the case of zero point energy being larger than the electron transfer reaction barrier. For example, the hopping mobility  $\mu_{\text{hop}}$  above assumes the low-energy “effective” mode (for which the approximation  $\hbar\omega \ll k_B T$  is valid), which excludes effects of coupling due to high-frequency intramolecular vibrations.

**4.2.3. Origin of  $d\mu/dT < 0$ .** In most high-performance organic crystalline semiconductors, the intermolecular electronic coupling ( $2J$ ) is comparable to the reorganization energy  $\lambda$  (Table 3), which places them in the intermediate charge transport regime.<sup>453</sup> Because the temperature dependence of the mobility ( $\mu(T)$ ) is readily obtained from experiments, and it can serve as a sensitive probe of the charge transport mechanism, considerable theoretical research effort focused on accurate description of  $\mu(T)$  and, in particular, the physical mechanisms behind observations of  $d\mu/dT < 0$  (Table 4) that address the issues outlined above.

The effects of nonlocal electron–phonon coupling (described by  $H_3$ ) on charge transport have been under extensive theoretical research.<sup>51</sup> Munn and Silbey<sup>454</sup> found that the nonlocal coupling can increase hopping and decrease band contributions to mobility. Hannewald et al.<sup>455,456</sup> used a mixed Holstein–Peierls approach to take into account both local and nonlocal coupling. They calculated the temperature dependence of polaron band narrowing and predicted an interplay between band and hopping regimes. With this approach, the temperature dependence of conductivity scales as  $\sim T^{-1}$  at low temperatures, which changes to  $T^{-1/2}$  at high temperatures, with or without a crossover region exhibiting thermally activated transport. They also observed conductivity anisotropy due to anisotropic phonon-assisted currents resulting from nonlocal electron–phonon interactions. In their subsequent work,<sup>446</sup> the authors removed the restriction of the narrow-band limit (allowing the bandwidth to be larger than  $k_B T$ ) in the coherent part of the total mobility, which removed the divergence (due to  $T^{-1}$  behavior) at low temperature, instead yielding a finite mobility as  $T \rightarrow 0$ . The theory was able to predict the  $\sim T^{-n}$  ( $2.5 < n < 3$ ) temperature dependence of mobility in Nph crystals, consistent with experiments, and showed a reasonable agreement with experiments for mobility anisotropy.

Troisi and Orlandi<sup>457</sup> applied a semiclassical approach (solving the time-dependent Schrodinger equation with classical treatment of vibrations) to study the effects of nonlocal-only coupling. They determined that thermal fluctuations in the transfer integral that are of the same order of magnitude as the transfer integral itself lead to carrier localization. In this picture, at room temperature, electronic states are localized due to dynamic disorder (and *not* due to the formation of small polaron), mostly due to interactions with the low-frequency modes (20–200  $\text{cm}^{-1}$ ) that were found to be most effective in modulating the transfer integrals.<sup>436</sup> (It has also been shown that sub-1-Å translations of acene molecules

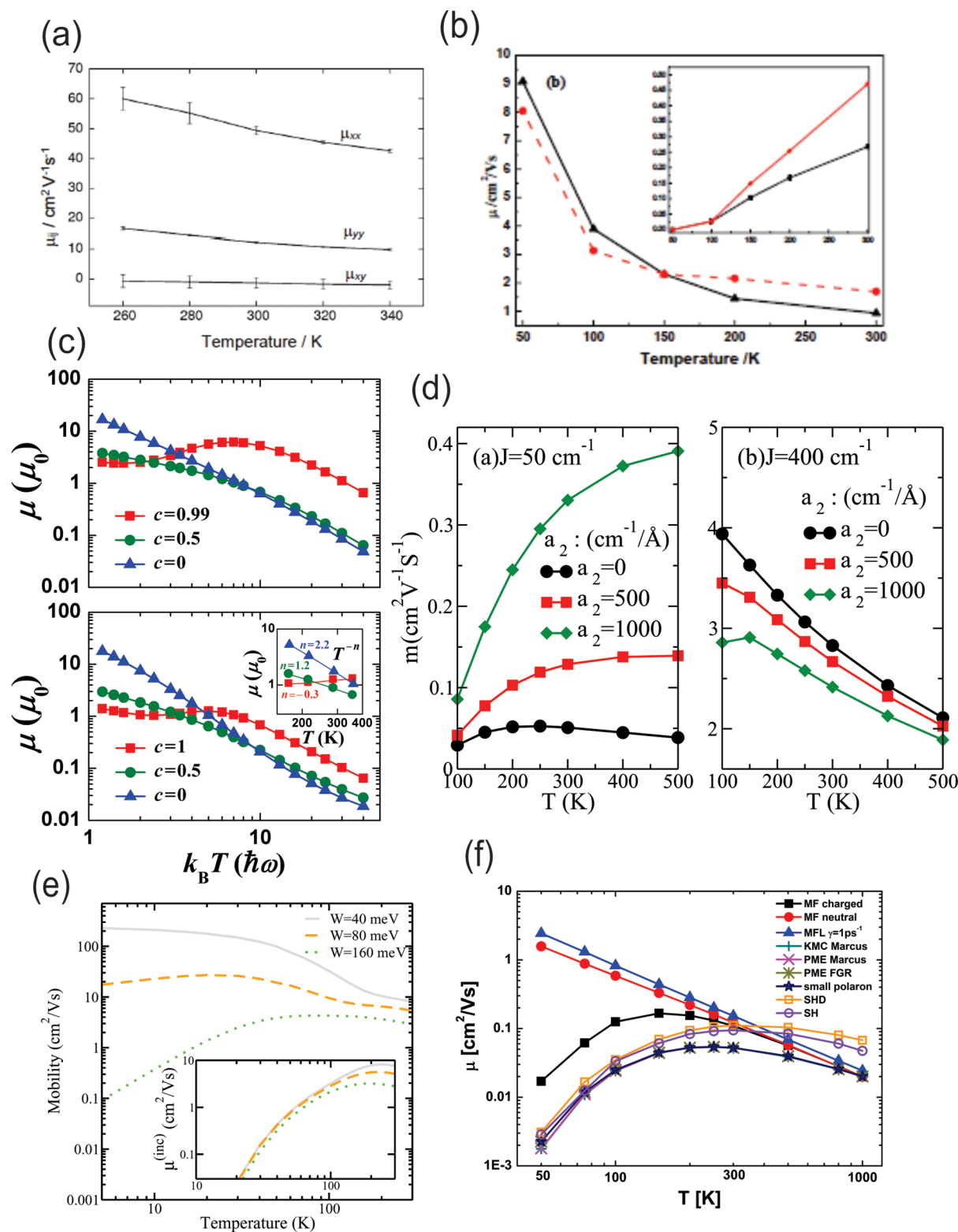


**Figure 9.** Temperature dependence of mobility calculated using different models. (a) Three components of the mobility tensor in a 2D molecular crystal (exemplified by rubrene) that is temperature-dependent due to dynamic disorder. Reproduced with permission from ref 459. Copyright 2011 American Institute of Physics. (b) Mobility in TIPS-Pn calculated using a fully QM approach, temperature dependent due to quantum effects of the intramolecular high-frequency vibrations within the localized charge picture in the absence (solid line) and in the presence (dashed line) of dynamic disorder. The inset shows temperature dependent mobility calculated using Marcus rates. Reproduced with permission from ref 468. Copyright 2012 Wiley-VCH. (c) Mobility calculated using Boltzmann theory (top) and the Kubo formula (bottom) for a crystalline organic semiconductor due to nonlocal electron–phonon coupling to symmetric ( $c = 1$ ), to antisymmetric ( $c = 0$ ), and equally to both ( $c = 0.5$ ) modes. The inset shows power-law temperature dependence at around room temperature. Reproduced with permission from ref 469. Copyright 2012 American Physical Society. (d) Mobility in organic molecular crystals for the Holstein–Peierls model with different nonlocal electron–phonon couplings  $\alpha_2$  ( $\alpha_2 = 0$  corresponds to the Holstein model) and different intermolecular couplings  $J$ . Reproduced with permission from ref 463. Copyright 2015 American Institute of

Figure 9. continued

Physics. (e) Total mobility (incorporating coherent and incoherent parts) with temperature dependence due to polaron quantum transport in disordered 3D crystals for several disorder strengths  $W$ . The inset shows the incoherent part of the mobility. Reproduced with permission from ref 472. Copyright 2011 American Physical Society. (f) Mobility in molecular stacks obtained from the mean-field (MF) theory starting from charged and neutral geometries without system-bath interaction, the MF theory with system-bath interaction, kinetic Monte Carlo (KMC) and Pauli master equation (PME) approaches with Marcus charge transfer rate, the PME with the Fermi Golden Rule (FGR) rate, the small polaron model, and the flexible surface hopping (FSH) with and without decoherence. Only local electron–phonon coupling was considered. Reproduced with permission from ref 474. Copyright 2013 American Institute of Physics.

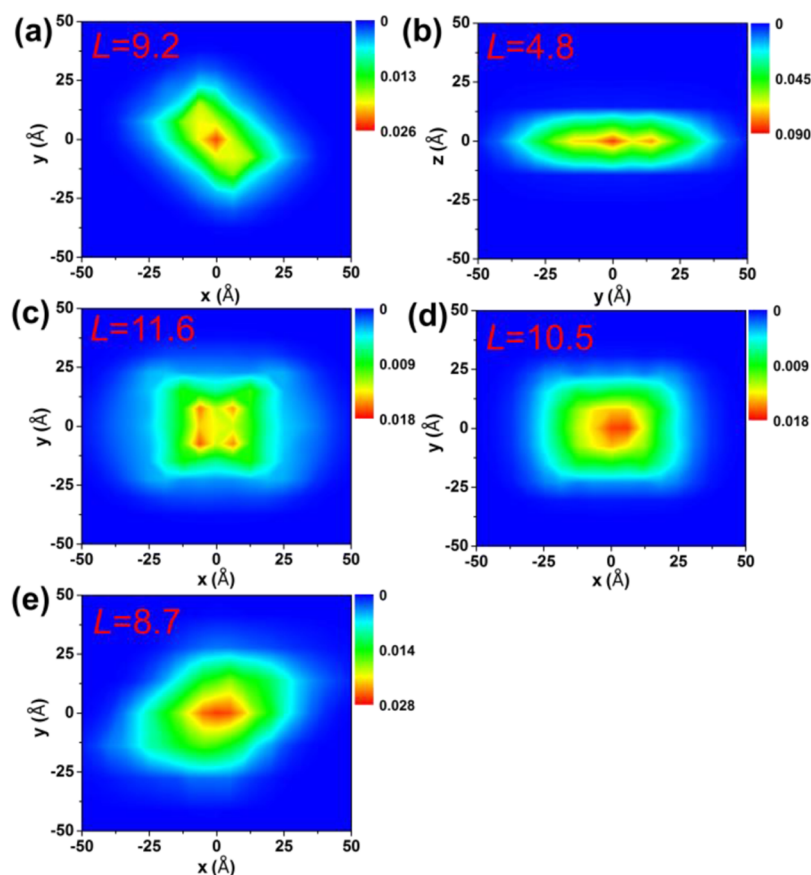


**Figure 10.** Electronic delocalization at 24 fs (corresponding to the characteristic time for loss of electronic coherence) in Pn (a), rubrene (b), DNTT (c), DATT (d), and PDIF-CN2 (e). The 2D delocalization length  $L$  shown in each image is calculated using  $L = 1/\sqrt{\sum_i |c_i|^4}$ . Reprinted with permission from ref 122. Copyright 2016 Royal Society of Chemistry.

along their long axis resulted in more than an order of magnitude change in transfer integrals.<sup>458</sup>) The temperature dependent mobility for a 1D molecular crystal calculated using this approach recovered a power-law dependence  $\mu \sim T^{-2}$  in a broad temperature range. Similar arguments were later applied to a 2D case of rubrene, in which the behavior intermediate between  $\mu \sim T^{-2}$  and  $\mu \sim T^{-1}$  was obtained, depending on the crystallographic direction (Figure 9(a)),<sup>459</sup> and the nature of charge transport was found to be unaffected by the reorganization energy (although the latter was important to obtain quantitative agreement with experimental mobility values).<sup>460</sup> The calculation was also able to reproduce experimentally obtained room-temperature mobility values along the  $a$ - and  $b$ -axes of  $\sim 8$  and  $\sim 20$   $\text{cm}^2/(\text{Vs})$ .<sup>461</sup>

Fratini and Ciuchi<sup>462</sup> calculated a nonlocal Green's function for a 1D molecular chain and observed the coexistence of the band states and the states localized by dynamic disorder. The temperature dependence of mobility calculated using the Kubo

formula showed a crossover from polaronic band transport ( $\sim T^{-3/2}$ ) to incoherent diffusion ( $\sim T^{-1/2}$ ) due to dynamic localization, *without* small polaron formation.

Song and Shi<sup>463</sup> employed an imaginary time path integral Monte Carlo simulation to show that while local coupling always localizes the charge carriers and reduces mobility, the nonlocal electron–phonon coupling decreases the band mobility but increases the hopping mobility (Figure 9(d)). Ribeiro and Stafström<sup>464</sup> applied the Holstein–Peierls approach to numerically examine the effects of the applied electric field, temperature, and dimensionality of the crystal (1D vs 2D) on polaron stability. They found that mobility was improved in the system with reduced dimensionality; in a 1D system the carrier velocity increased with temperature, and the electric field dependence of carrier velocity was nonmonotonic at low electric fields (e.g., at 50 kV/cm) but became closer to linear (corresponding to electric field-independent mobility) at higher fields (e.g., at 250 kV/cm).

The effects of coupling to intramolecular vibrations on charge carrier mobility and its temperature dependence were explored by Shuai and co-workers.<sup>362,453,465–468</sup> In particular, they used a quantum mechanical charge transfer rate<sup>452</sup> that includes quantum nuclear tunneling in kinetic Monte Carlo simulations of Brownian motion of charge carriers, from which mobility was calculated. The temperature dependence of mobility characterized by  $d\mu/dT < 0$  was obtained in a large temperature range (50–300 K) (Figure 9(b)), without invoking either delocalization in the extended states or dynamic disorder. Instead, it was attributed to hopping of a localized charge coupled to high-frequency intramolecular vibrations. The authors concluded that when the reorganization energy  $\lambda$  is much higher than the transfer integral, this formalism accurately described both the absolute values of mobilities and their temperature dependence, citing Pn, TIPS-Pn, Tc, rubrene, PDI, NDI, and similar derivatives as examples. Moreover, it was found that dynamic disorder did not limit transport but, on the contrary, enhanced the mobility by a phonon-assisted mechanism.

In their subsequent work, Jiang et al.<sup>122</sup> calculated mobility and mobility anisotropy in Pn, rubrene, DATT, DNNT, and PDIF-CN2 using four methods that rely on the following: (a) the Boltzmann transport equation coupled with the deformation potential (DP) theory; (b) semiclassical Marcus theory (eq 21); (c) quantum nuclear tunneling theory (eq 22); and (d) the time-dependent wave packet diffusion (TDWPD) approach. These methods describe fully delocalized bandlike transport (a), hopping without (b) and with (c) nuclear tunneling, and transport incorporating nuclear tunneling together with electronic delocalization and coherence (d). In (d), the time-dependent electronic properties are described by the wave function  $\psi(t) = \sum_i^N c_i(t)|i\rangle$ , and the measure of the electron delocalization length is given by  $L = 1/\sqrt{\sum_i |c_i|^4}$ , whereas the measure of the electron coherence length is provided by the correlation function  $\langle c_i c_j \rangle$ . The mobilities  $\mu_{\text{DP}} > \mu_{\text{TDWPD}} > \mu_{\text{quantum}} > \mu_{\text{Marcus}}$  were obtained in all materials, with  $\mu_{\text{quantum}}/\mu_{\text{Marcus}}$  of  $\sim 2$ – $5$  and average  $\mu_{\text{quantum}}$  and  $\mu_{\text{TDWPD}}$  values closer to the experimentally measured values than  $\mu_{\text{DP}}$  and  $\mu_{\text{Marcus}}$  (which overestimated and underestimated the measured values, respectively). In all systems studied, the electron coherence was found to be lost within several tens of femtoseconds, and differences between  $\mu_{\text{quantum}}$  and  $\mu_{\text{TDWPD}}$  were attributed to electron delocalization. Figure 10 shows the charge population distribution, along with electron delocalization length  $L$ , obtained in the high-mobility systems under study. Interestingly, the lowest  $L$  (accompanied by  $\mu_{\text{TDWPD}} \approx \mu_{\text{quantum}}$ ) was found in rubrene, which was attributed to strong mobility anisotropy, resulting in a 1D-like charge transport. This led the authors to conclude that the hopping model with the inclusion of nuclear tunneling is sufficient to describe charge transport in rubrene. In contrast, in Pn, DATT, DNNT, and PDIF-CN2, the electronic delocalization was considerably stronger ( $\mu_{\text{TDWPD}}/\mu_{\text{quantum}} \sim 1.2$ – $2.1$ ) and necessary to incorporate into the charge transport model.

Li et al.<sup>469</sup> extended the SSH formalism to investigate contributions of antisymmetric electron–phonon coupling, for which a displacement of the molecule  $n$  results in the increase of the transfer integral between this molecule and its neighbor molecule on one side and in the decrease on the other side, to mobility. (The standard SSH formulation considers only symmetric coupling, with both transfer integrals changing the

same way.) They applied the model to oligoacenes and bimolecular D/A crystals and determined that the temperature dependence of mobility depends on the type of coupling, thus emphasizing the importance of including coupling not only to optical phonons,<sup>436,470</sup> but also to acoustic phonons. For example, in the 150–350 K temperature region, they predicted a power-law dependence of mobility  $\mu \sim T^{-n}$  with  $n = 2.2$  for the symmetric coupling-only,  $-0.3$  for antisymmetric coupling-only, and  $1.2$  for the coupling to an equal mix of both types of modes (Figure 9(c)).

Zhong et al.<sup>471</sup> considered the effects of both static and dynamic disorder using the time-dependent wave packet diffusion method in 1D and showed that, in the presence of strong dynamic disorder, carriers move by hopping even in the absence of static disorder. Ortmann and Roche<sup>472</sup> incorporated static disorder into the Kubo theory and modeled the temperature dependence of polaron transport in 3D disordered crystals, showing a crossover from the  $d\mu/dT < 0$  to  $d\mu/dT \geq 0$  behavior as the static disorder increased (Figure 9(e)).

Wang and Beljonne<sup>473,474</sup> developed a flexible surface hopping algorithm to study a crossover between the band and hopping 1D charge transport. They observed a change in temperature dependence of mobility from thermally activated at small values of electronic coupling of  $\leq 100 \text{ cm}^{-1}$  (which were taken to be considerably smaller than the reorganization energy of  $1000 \text{ cm}^{-1}$ ), to temperature independent behavior in the intermediate range, and to a monotonic decrease with temperature at large coupling ( $\geq 400 \text{ cm}^{-1}$ ) (Figure 9(f)). They also argued that dynamic disorder can either impede or enhance charge transport, depending on the intrinsic (i.e., in the absence of thermal disorder) localization strength of charge carriers.

Ciuchi and Fratini<sup>475</sup> developed a theoretical framework that relates the time-dependent quantum dynamics of charge carriers to frequency-dependent conductivity. They generalized the treatment obtained in a classical hopping limit to high-mobility materials by addressing the interplay between mobile states in the band and localized states in the band tails. They concluded that intrinsic transport is due to the diffusive spread of localized wave functions rather than scattering of delocalized waves by phonons and disorder. In this case, a power-law behavior of mobility with temperature ( $\mu \sim T^{-n}$ ) originates from the reduction of the transient localization length as the thermal disorder increases. Extrinsic disorder changes the temperature dependence from power-law to thermally activated; however, an increase in the carrier concentration enhances mobility and suppresses thermally activated behavior.

**4.2.4. Quantum Coherence and Charge Transport.** Coherence-mediated quantum transport has been intensively studied in light-harvesting complexes that harvest light with quantum efficiency of nearly 1.<sup>68</sup> In these systems, higher-order quantum master equation approaches (which go beyond the Marcus (for electron transfer) and Förster (for energy transfer) approximations for electronic coupling, which are exact to the second order) need to be used.<sup>476</sup> An example of relevant mechanisms is quantum mechanical superexchange (which involves rates that are fourth-order in the electronic coupling), whose interplay with hopping determines the primary electron transfer in photosynthesis. The superexchange mechanism has been invoked in the description of ambipolar charge transport in D/A crystals,<sup>477,478</sup> and so incorporation of both incoherent hopping and superexchange kinetics into transport models for

organic semiconductors is another potential challenge for theoretical description of charge carrier dynamics.

Picon et al.<sup>52</sup> considered decoherence as the primary conduction mechanism in 2D ultrapure molecular crystals. They discussed that decoherence is driven by the coupling of the electron to the lattice through polarization and emphasized that phonons localize coherent states but assist the motion of less coherent ones. Using this approach, the authors were able to reproduce mobility values consistent with experiments and obtained the temperature dependence  $\mu \sim T^{-n}$  with  $n = 1.7$  at  $T > 50$  K.

Cao and co-workers<sup>125</sup> predicted that a disordered system coupled to a quantum harmonic bath would exhibit diffusion constants with a nonmonotonic temperature dependence, with a well-defined maximum. The effect of system dimensionality on quantum transport has shown that 3D structures characterized by centrosymmetric Hamiltonians are considerably more efficient than a random network.<sup>479</sup>

**4.2.5. Disorder Models.** In the case when  $H_4$  dominates over all other contributions to the Hamiltonian of eq 35, charge transport is governed by static disorder and is described as a random walk by incoherent hopping between molecular sites.<sup>2</sup> Comprehensive recent reviews of charge transport in organic disordered medium are available (Table S1).<sup>480–484</sup> For analytical theories that describe charge carrier mobilities and their dependence on carrier concentration, temperature, and electric field in systems with various DOS energy profiles, see the excellent reviews by Baranovskii and colleagues.<sup>480,481</sup> For a discussion of numerical algorithms enabling drift-diffusion simulations of charge transport in disordered organic semiconductors, see ref 485. Analysis of the conditions under which the continuum drift-diffusion description of charge transport fails can be found in ref 486.

The most widely used model, the Gaussian disorder model (GDM),<sup>2,480</sup> has successfully described charge carrier mobility in many polymers (including PPV and P3HT)<sup>481</sup> and organic glasses, PR polymer composites, and molecularly doped polymers.<sup>220</sup> In this model, charge transport occurs by hopping within a manifold of sites with Gaussian-distributed energy and a Gaussian distribution of intersite spacing. In this case, the density of states (DOS) is given by

$$g(E) = N/(\sigma(2\pi)^{1/2}) \exp(-E^2/2\sigma^2) \quad (38)$$

where  $\sigma$  is the DOS width, or energetic disorder, and  $N$  is the concentration of localized sites. Typical values for  $\sigma$  are  $\sim 0.05$ – $0.15$  eV,<sup>487</sup> and those for  $N$  are  $\sim 10^{20}$ – $10^{21}$  cm<sup>-3</sup>.<sup>480</sup> In the absence of polaronic effects (i.e., with minimal contribution of  $H_2$  and  $H_3$  in eq 35), the hopping rate is described by the Miller–Abrahams expression of eq 31, in which  $E_n$  and  $E_{n+1}$  are the carrier energies on sites  $n$  and  $n + 1$ , respectively, and  $\nu_0$  is the attempt-to-jump frequency (typically  $10^{10}$ – $10^{12}$  s<sup>-1</sup>). The model predicts that while the charge carrier hops from site to site, relaxing toward the quasi-equilibrium energy  $E_\infty = -\sigma^2/k_B T$ , its mobility is time-dependent (dispersive transport), after which it is time-independent. At low carrier densities, carriers occupy sites with a mean energy  $E_\infty$  relative to the center of the DOS distribution and have to be thermally activated to reach the transport energy where transport occurs, so that mobility increases with temperature. In particular, numerical simulations predict the temperature dependence of the drift mobility in the form  $\mu \sim \mu_0 \exp(-(C\sigma/k_B T)^2)$  with  $C \approx 2/3$ , slightly dependent on  $N$ .<sup>480</sup> The hopping mobility  $\mu$  also depends on the applied electric field ( $F$ ), as the field lowers the activation energy for

jumps in the field direction, with numerical simulations yielding a Poole–Frenkel-type dependence,  $\mu \sim \exp(\beta F)^{1/2}$ , with the parameter  $\beta$  dependent on the DOS width  $\sigma$ , temperature, and positional disorder responsible for the variation in the intersite distance  $a$  in eq 31. The effect of charge traps with energy  $E_{\text{trap}}$  and relative trap concentration  $c$  can be incorporated into the mobility prefactor<sup>2</sup> as  $\mu_0/(1 + c \exp(-E_{\text{trap}}/k_B T))$ .

Baranovskii and co-workers recently summarized developments of analytical theories describing charge transport in disordered organic semiconductors.<sup>480,481</sup> The variable range hopping (VRH) and its limiting case of nearest-neighbor hopping (NNH) (e.g., occurring when  $k_B T > \sigma$  in GDM) were discussed in detail in the framework of percolation theory, both for the exponential and for the Gaussian DOS. The authors also emphasized the concept of the transport energy  $E_t$  introduced by analogy to the mobility edge in the multiple-trapping (MT) model. (The MT model assumes that there is a defined energy (the mobility edge) in the DOS that separates extended states, enabling efficient charge transport from localized states.) Physically, this means that even though most carriers equilibrate at the energy  $E_\infty$  (in particular, at room temperature), charge transport occurs at a higher energy  $E_t$ , thus requiring thermal activation. For the Gaussian DOS of width  $\sigma$ , one of the proposed analytical expressions for mobility at low carrier densities ( $n \ll n_c$  with the critical density  $n_c$  determined by  $E_F(n_c) = E_\infty$ , where  $E_F$  is the Fermi energy) is given by<sup>480,481</sup>

$$\mu = \mu_0 \exp \left[ \frac{-2r(E_t)}{\alpha} - \frac{E_t}{k_B T} - \frac{1}{2} \left( \frac{\sigma}{k_B T} \right)^2 \right] \quad (39)$$

where  $r(E_t)$  is the distance between the localized states with energies below  $E_t$  and  $\alpha$  is the wave function decay length. In this regime, the mobility is independent of carrier density  $n$ , which allows one to experimentally distinguish between the charge transport in the Gaussian versus the exponentially distributed DOS, as in the latter case the mobility is carrier density-dependent at any  $n$ . At higher carrier densities,  $n > n_c$  (corresponding to  $n > 10^{17}$  cm<sup>-3</sup> in PPV and P3HT), the DOS is partially filled, and a quasi-Fermi level is established above  $E_\infty$ . This reduces the activation energy for charge transport and increases mobility,<sup>283</sup> gradually changing the temperature dependence of mobility from  $\mu \sim \exp(-1/2(\sigma/k_B T)^2)$  to the Arrhenius-type  $\mu \sim \exp(-\Delta/k_B T)$  with  $\Delta = E_t - E_F(n)$ . Different regimes of charge transport in a Gaussian DOS depending on the temperature and carrier density are schematically shown in Figure 11.

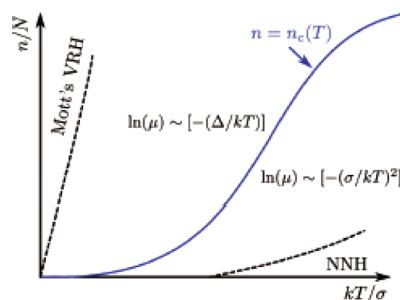


**Figure 11.** Regions depending on the carrier density  $n$  and temperature  $T$  corresponding to different conduction regimes for hopping in the Gaussian DOS. Reproduced with permission from ref 118. Copyright 2014 Wiley-VCH.

Charge transport in the exponential DOS has also been extensively studied analytically, with several models for the VRH transport available based on various approximations;<sup>480,481</sup> the exact solution has also been proposed.<sup>488</sup> One such model, the Vissenberg–Matters model,<sup>489</sup> has been utilized in several studies of current–voltage characteristics in organic FETs (Section 4.3.2).<sup>490,491</sup>

If there is a large-scale variation in site energy in addition to local site energy fluctuations, the extension of the GDM known as the correlated disorder model (CDM) has been utilized.<sup>492</sup> The GDM and CDM converge at high electric fields, but at low electric fields, and in polar materials, the effects of correlations may become important. The contribution of correlations to charge transport in various systems is under debate;<sup>118,493</sup> for example, it was proposed that they would be more important for small-molecule disordered films than for polymers.<sup>484</sup> The GDM and CDM that specifically incorporate the dependence of mobility on carrier concentration (in addition to temperature and electric field dependence) have been referred to as extended GDM (EGDM) and extended CDM (ECDM), respectively. In ECDM, the carrier density dependence of mobility is less pronounced, but the electric field dependence of mobility is stronger, than in EGDM.<sup>493</sup> For an overview of the EDGM and ECDM models and their applicability to various materials, see a review article by Coehoorn and Bobbert.<sup>484</sup>

In many cases of disordered systems, polaron effects (due to  $H_2$  and  $H_3$  in eq 35) cannot be neglected and have to be considered together with the static disorder effects of  $H_4$ . In this case, Marcus rates instead of Miller–Abrahams rates are used to describe hopping in computational studies<sup>494</sup> and the mobility temperature dependence is modified to include both the polaron binding energy  $E_{\text{pol}} = \lambda/2$  and the energetic disorder  $\sigma$ :<sup>495</sup>

$$\mu \sim \exp(-E_{\text{pol}}/(2k_{\text{B}}T) - (C\sigma/k_{\text{B}}T)^2) \quad (40)$$

Here, the interplay of polaronic and disorder effects is determined by  $E_{\text{pol}}$  and  $\sigma$ . At temperatures  $T < T_{\text{c}}$ , where  $T_{\text{c}} = 2(C\sigma)^2/(k_{\text{B}}E_{\text{pol}})$  ( $C$  is a parameter ranging between 0 and 1 that depends on  $\sigma/E_{\text{pol}}$ ), the transport is disorder-controlled, whereas at  $T > T_{\text{c}}$  it is polaron-controlled. At  $\sigma = 0.1$  eV and  $E_{\text{pol}} = 50$ – $100$  meV, the critical temperature is  $T_{\text{c}} = 600$ – $1500$  K, which renders charge transport to be mostly disorder-controlled in typical conjugated polymers. (The situation is, however, reversed for transport of triplet excitons, for which this model predicted polaron-controlled transport in PPP derivatives at temperatures above 20–140 K, depending on the derivative.<sup>495</sup>) Whether  $E_{\text{pol}}$  affects the concentration dependence of mobility or not is a subject of debate. It is important to note, however, that, at high carrier densities, the mobility temperature dependence in disordered semiconductors is Arrhenius even without polaronic effects (Figure 11), which makes it difficult to differentiate between the two contributions solely based on temperature dependence in that regime.<sup>480</sup>

To address the need for modeling charge transport in crystalline, yet disordered organic materials, Salleo et al.<sup>496</sup> applied a mobility edge, or MT model, which had been widely used for inorganic amorphous and polycrystalline materials, to organic films. The authors argued that fully Gaussian DOS would not be applicable to crystalline systems. Instead, an exponential approximation to an unknown-shaped DOS was used, and it was assumed that trapped carriers can become temporarily mobile by thermal excitation to the mobile states.

This model was used, for example, to describe charge carrier transport in crystalline polythiophene films<sup>496</sup> and, more recently, to extract mobility, trap density, and trap distribution from SCLCs in rubrene crystals<sup>295,497</sup> and from transient photocurrents in polymer:fullerene blends.<sup>498</sup> Mehraeen et al.<sup>499</sup> performed kinetic Monte Carlo simulations of carrier density-dependent conductivity, mobility, and Fermi level both using the MT model (localized states do not contribute to transport) and the hopping model (all states contribute to transport), and assuming a composite DOS that consists of a superposition of the Gaussian and exponentially distributed states. The approach was then applied to interpret the experimental data for n-doped  $C_{60}$  films.<sup>500</sup> The authors concluded that both models were able to reproduce experimental data, yielding, however, different densities and distribution widths of trap states. Such discrepancies arise from different charge transport pictures used by these models and suggest that additional data (e.g., measurements of Hall effect, thermoelectric transport, ESR, etc.) would be necessary to unambiguously quantify the DOS. Kwiatkowski et al.<sup>501</sup> proposed a Boltzmann-weighted hopping model that incorporates the effects of microstructure (and, in particular, the presence of crystalline and amorphous regions) into charge transport. They applied it to directionally crystallized P3HT films and quantified contributions of morphology-related defects to mobility and mobility anisotropy.

**4.2.6. Charge Transport in D/A Materials and Mixed-Phase Blends.** Many optoelectronic devices that rely on charge photogeneration, such as solar cells and PR devices, utilize blends of two or more types of molecules and/or have mixed-phase morphology. Therefore, it is of interest to discuss the dominant charge transport mechanisms in such systems, particularly those involving crystalline phases. Zhu et al. investigated the electronic properties of various mixed-stack D/A crystals and found that several crystals supported a 2D ambipolar charge transport with effective masses as low as  $\sim 0.2m_{\text{e}}$ .<sup>478</sup> The ambipolar nature of charge transport was attributed to a superexchange-controlled electronic coupling, similar for hole and electron transport. This behavior was recently studied in detail in ref 477. It was determined that such equivalent coupling is achieved when the coupling is dominated by the interaction between donor HOMO and acceptor LUMO and is not affected by disorder; in the absence of this interaction, a unipolar transport was obtained. An example of experimental study of the optical and electronic properties of D/A cocrystals can be found in ref 502.

Charge transport in D/A blends has been extensively studied by Monte Carlo simulations to determine the effects of morphology, domain size, energetic disorder, and electric field on mobility and/or overall device performance (Section 3.2.2). Koster<sup>503</sup> numerically solved the Pauli master equation to determine the effects of carrier density and electric field on charge transport characteristics in disordered blends. He found that in contrast to mobility in a pristine material, mobility in a blend may strongly decrease with the electric field at low carrier densities, and factorization of the electric field and carrier density dependence,<sup>283</sup> often employed in pristine materials, is not possible for blends.

Woellner et al.<sup>504</sup> used a similar approach to examine charge transport in a two-phase system in the low carrier density limit. They introduced an energy offset  $E_{\text{offset}}$  between the average energies of two phases, each with a Gaussian-distributed DOS (less energetic phase being more ordered). The study showed

that if  $E_{\text{offset}} \rightarrow 0$ , the transport was determined by the more disordered phase, whereas if the  $E_{\text{offset}} \rightarrow \infty$ ,<sup>503</sup> the transport was restricted to the less energetic phase. If  $E_{\text{offset}}$  had intermediate values, even a low amount (e.g., 20%) of ordered domains, which could be realized in amorphous–crystalline mixtures, could considerably improve the overall mobility of the disordered material.

Fischer et al.<sup>505</sup> modeled transport in ZnPc:C<sub>60</sub> (1:1) blend layers using a drift-diffusion model and concluded that even in unipolar (e.g., hole-only) devices the contribution of local “minority” (in this case electron) transport must be taken into account in order to describe the experimentally measured  $J$ – $V$  characteristics.

### 4.3. Experimental Evidence vs Models

**4.3.1. Organic Crystals and Small-Molecule Crystalline Films.** Given a variety of factors that play a role in charge transport in high-mobility organic semiconductors and the availability of theoretical descriptions discussed in the previous section, it is instructive to examine experimental evidence that would help in deciding for or against a particular model. As discussed above, typical experimental observables characterizing “bandlike” transport include mobilities of at least 1 cm<sup>2</sup>/(Vs),  $d\mu/dT < 0$  (e.g.,  $\mu \sim T^{-n}$  with  $0 < n < 3$ ), mobility anisotropy, and low charge carrier effective mass. These observations were made using time-of-flight,<sup>506,507</sup> SCLC,<sup>508</sup> time-resolved or frequency-resolved photoconductivity,<sup>198,201,346,365,413,509,510</sup> the Hall effect,<sup>435,511</sup> FET characteristics,<sup>512–514</sup> and ARPES.<sup>515,516</sup> Table 4 summarizes experimental observations of  $d\mu/dT < 0$  in various systems. Most of the observations of “bandlike” behavior have been made on single crystals, but some aspects of this behavior were also observed in polycrystalline films (e.g., Pn and R-Pn).<sup>201,513</sup> Several examples of “bandlike” and/or a “bandlike to hopping crossover” behavior revealed by various experiments are discussed below.

Pentacene crystals and polycrystalline films exhibited room-temperature hole mobilities of up to 40 cm<sup>2</sup>/(Vs) in crystals<sup>517</sup> and values ranging from 5.5 cm<sup>2</sup>/(Vs) (in TFTs)<sup>518</sup> to ~11 cm<sup>2</sup>/(Vs) (from Hall effect)<sup>519</sup> and to 21 cm<sup>2</sup>/(Vs) (from THz spectroscopy)<sup>520</sup> in films. Observations of “bandlike”  $d\mu/dT < 0$  behavior were made in optical pump–THz probe experiments,<sup>201,202,360,365</sup> in Hall effect measurements,<sup>519</sup> and in devices (Table 4).<sup>508</sup> Mobility anisotropy of up to a factor of 3.5 was observed in single-crystal FETs.<sup>521</sup> ARPES experiments on ultrathin Pn films produced somewhat conflicting results in regard to the HOMO bandwidth and resulting hole effective mass values.<sup>515,516,522,523</sup> For example, Ohtomo et al.<sup>515</sup> studied a single-crystal-quality monolayer at 130 K and found isotropic effective mass in the  $a$ – $b$  plane with values of 0.8–1  $m_e$  (where  $m_e$  is the electron mass). Similar effective mass (<0.8  $m_e$ ) was estimated from room-temperature THz experiments on Pn films.<sup>520</sup> On the other hand, Hatch et al.<sup>516</sup> observed strong temperature-dependent anisotropy of the effective mass, with the effective masses of 14  $m_e$  and 3  $m_e$  along the  $a$  and  $b$  axes at 75 K, which increased by an order of magnitude along the  $a$ -axis while staying almost the same along the  $b$ -axis at 300 K. The authors concluded that band structure plays a role in charge transport even at room temperature.

Germes et al.<sup>524</sup> inferred a “bandlike” to hopping transition at ~250 K from the temperature- and gate voltage-dependent Seebeck coefficient in Pn TFTs. The authors modeled the mobility using a combination of the mobility edge (or multiple

trapping) and variable range hopping models and emphasized the importance of both static and dynamic disorder. In the same devices, the FET mobility exhibited thermally activated behavior throughout the entire temperature range studied (200–340 K) and no dependence on the carrier density. This led the authors to conclude that the temperature and carrier density dependences of the FET mobility are not sufficient to evaluate the applicability of charge transport models. The importance of applying several experimental techniques to unambiguously determine physical mechanisms has been emphasized in the literature<sup>435,448,499</sup> (also see Section 8). For example, Lee et al.<sup>525</sup> observed anisotropy in surface conductivity in rubrene and Tc crystals using FET characteristics. Similar observations were made using the Hall effect in rubrene, but no Hall effect was observed in Tc. This led to the conclusion that the origin of such anisotropy was related to “bandlike” intrinsic properties in rubrene and to anisotropic incoherent hopping in Tc.

Zhang et al.<sup>526</sup> observed a crossover from thermally activated ( $d\mu/dT > 0$ ) to “bandlike” ( $d\mu/dT < 0$ ) behavior in epitaxially grown Pn layers, depending on the number of layers and on the carrier density (controlled by the FET gate voltage). In a one-layer film, thermally activated behavior was observed at all gate voltages, whereas in the two-layer film, the  $d\mu/dT < 0$  behavior emerged in the temperature range dependent upon the gate voltage. Room-temperature mobilities up to 3 cm<sup>2</sup>/(Vs) were observed in the two-layer film, about an order of magnitude higher than those in the one-layer film. The behavior was explained by strong modulation of the molecular packing by interfacial van der Waals interactions.

Functionalized Pn (i.e., R–Pn with R = TIPS, TES, TMTES) crystals and polycrystalline films also exhibited high mobilities (up to 11 cm<sup>2</sup>/(Vs) in TIPS–Pn crystals),<sup>527</sup>  $d\mu/dT < 0$  (Table 4), and molecular packing-dependent mobility anisotropy both in the optical pump–THz probe experiments<sup>198,201,365,413</sup> and in FETs.<sup>528,529</sup> For example, in optical pump–THz experiments, in-plane mobility anisotropy of ~3.5 and ~12 was observed in single crystals of TIPS–Pn and TES–Pn that exhibit 2D “brick-work” and 1D “slip-stack”  $\pi$ – $\pi$  stacking, respectively.<sup>413</sup> In FETs utilizing films of the same derivatives, similar trends were observed, with mobility anisotropy reaching ~3–10 in TIPS–Pn and ~21–47 in TES–Pn, depending on the spin-casting speed.<sup>528</sup>

Rubrene crystals exhibited mobilities of up to 43 cm<sup>2</sup>/(Vs) (Table 3), along with  $d\mu/dT < 0$  in ultrafast THz spectroscopy,<sup>200,365,530</sup> Hall effect measurements, and FETs (see a recent review by Podzorov<sup>531</sup>). Mobility anisotropy in FETs and in the Hall effect, with the mobility along the  $b$ -axis exhibiting a factor of ~3.5 higher values than those along the  $a$ -axis, was also demonstrated.<sup>525,532,533</sup> The ARPES experiments showed a HOMO dispersion up to 0.4 eV, with an estimated hole effective mass of 0.65  $m_e$ , which led to the conclusion that band transport is the dominant mechanism of charge transport in rubrene.<sup>534</sup> Frequency-dependent optical conductivity measurements<sup>510</sup> also yielded low effective masses, consistent with band structure calculations and not consistent with polaron formation. Inspired by this study, Li et al.<sup>445</sup> calculated “optical effective mass”  $m^*$  (to be distinguished from “band effective mass”  $m_{\text{eff}}$  of eq 36) that is accessible in the measurements of frequency-resolved photoconductivity<sup>510</sup> as a function of electron–phonon coupling strength and temperature. The authors argued that optical effective mass  $m^*$  should decrease as the electron–phonon strength increases and that

the presence of light carriers with small  $m^*$  is not a conclusive test for the band charge transport. It was further emphasized that, at room temperature, the charge transport in rubrene is of an incoherent nature (which is similar to the conclusions of Jiang et al.<sup>122</sup> discussed in Section 4.2.3). The authors also commented that the ARPES results on both Pn and rubrene indicate that the lifetime of the quasiparticle states was too short to support delocalized carriers and predicted that the electron–phonon coupling should strongly affect the carrier relaxation time  $\tau$ . This prediction is awaiting experimental verification.

The charge modulation spectroscopy (CMS) performed on a variety of R–Pn derivatives and on rubrene suggests that charge carriers are localized on the ultrafast time-scales.<sup>513</sup> The reconciling between “bandlike” features discussed above (such as  $d\mu/dT < 0$ ) and the localization features has been obtained in the framework of dynamic disorder.<sup>435</sup> Dynamic localization due to coupling of the charge carrier to intermolecular vibrations ( $H_3$  in eq 35) offers a satisfactory qualitative picture, supported by direct observation of strong coupling of the carriers to a low-frequency vibration mode at  $40\text{ cm}^{-1}$  (1.1 THz) in Pn crystals<sup>360</sup> and at  $\sim 75\text{ cm}^{-1}$  in rubrene crystals<sup>200</sup> using optical pump–THz probe spectroscopy. These modes are in the frequency range ( $20\text{--}200\text{ cm}^{-1}$ ) deemed to be most important for charge transport affected by dynamic disorder.<sup>436</sup>

Eggeman et al.<sup>107</sup> probed molecular motion in R–Pn and diF TES-ADT crystalline films using thermal diffuse electron scattering and quantified displacement along the long axis of the molecule due to thermal lattice fluctuations, which they described in the framework of a frozen-phonon model. In TIPS-Pn, they obtained an intermolecular displacement of the center-of-mass of  $0.13 \pm 0.02\text{ \AA}$  at 300 K and  $0.08 \pm 0.02\text{ \AA}$  at 100 K, arguing that such large fluctuations in the intermolecular distances can lead to large fluctuations in the transfer integrals, in agreement with dynamic disorder models.<sup>436</sup> Yamane and Kosugi<sup>535</sup> used ARPES to directly observe the dependence of the transfer integral on the intermolecular distances in the  $\pi$ – $\pi$  stacks in crystalline films of various metal–Pc derivatives and derived a linear relation between these parameters, with transfer integral decreasing with distance with a  $75 \pm 5\text{ meV/\AA}$  rate.

The description of charge transport in the presence of dynamic disorder also addresses the question of why some materials exhibit similar FET behavior with comparable FET mobilities, but drastically different Hall effect characteristics.<sup>435</sup> For example, in TMTES-Pn the wave function localization length was deemed large enough to allow observation of the ideal Hall effect but small enough to explain features of localized charge carriers detected by the CMS. For discussion of reconciliation between results from the Hall effect, Seebach, and ESR experiments, refer to an excellent review by Sirringhaus.<sup>435</sup> However, processes other than localization due to dynamic disorder (such as nuclear tunneling) have also been invoked as a possible explanation of the same trends (Section 4.2).<sup>453,466</sup>

Illig et al.<sup>536</sup> quantified the room-temperature long-axis vibration ( $\sigma_{\text{vibr}}$  in Table 4) predicted to dominate the dynamic disorder in rubrene and several R-Pn and R-ADT, DNNT, and C8-BTBT derivatives. They obtained a significantly reduced  $\sigma_{\text{vibr}}$  in C10-DNNT and C8-BTBT as compared to all other derivatives and proposed a conjugated core with side chains along the long molecular axis as a new molecular design strategy that minimizes dynamic disorder. Also, lower  $\sigma_{\text{vibr}}$  was correlated with higher mobility in C10-DNNT as compared to

DNNT. However, no particular correlation between mobility and  $\sigma_{\text{vibr}}$  was observed in rubrene, R-Pn, and R-ADT derivatives, which suggests that low dynamic disorder is not the dominant factor behind high mobility in rubrene and that  $\sigma_{\text{vibr}}$  alone cannot serve as a predictor of mobility.

Interestingly, Kubo et al.<sup>537</sup> observed a 50–60% increase in mobility in C10-DNBDT single-crystal nanowires (which exhibited room-temperature mobilities of up to  $14\text{ cm}^2/(\text{Vs})$ ,  $d\mu/dT < 0$ , and according to the design rule above should have low dynamic disorder) upon a 3% lattice strain, which the authors attributed to strain-induced suppression of thermal fluctuations. If strain can efficiently suppress dynamic disorder, considerably larger gains in mobility should be possible to obtain in materials with higher  $\sigma_{\text{vibr}}$  such as Pn, TIPS-Pn, or rubrene. Indeed, about a factor of 6 increase in mobility was observed in TIPS-Pn under strain;<sup>538</sup> however, the findings (including up to a factor of 39 increase in mobility if the strain is properly engineered) were described in the framework of strain-induced changes in transfer integrals without invoking thermal fluctuations.<sup>539</sup> Clearly, more studies are needed to understand the role of dynamic disorder in mobilities and their temperature dependence.

Given a large number of recent studies in organic materials relying on observations of the Hall effect, it is of major importance to stress that interpretation of Hall effect-derived mobility, charge carrier density, and a sign of the Hall coefficient depends on the nature of charge transport. Theoretical treatment of Hall-effect characteristics in the case of band transport and adiabatic and nonadiabatic polaron transport can be found in ref 540. Yi et al.<sup>448</sup> considered contributions of bandlike and hopping charge carriers (with densities  $n_1$  and  $n_2$  and mobilities  $\mu_1$  and  $\mu_2$ , respectively) to the Hall effect. They derived simple criteria that relate Hall effect- and FET-derived mobilities ( $\mu_{\text{Hall}}$  and  $\mu_{\text{FET}}$ , respectively) and densities ( $n_{\text{Hall}}$  and  $n_{\text{FET}}$ , respectively) depending on the combinations of  $n_1$ ,  $n_2$ ,  $\mu_1$ , and  $\mu_2$ , thus distinguishing among strong (high  $n_2$  and  $\mu_2$ ), intermediate, and weak (low  $n_2$  and  $\mu_2$ ) hopping contributions. In particular, when  $\mu_1/\mu_2$  is smaller (larger) than  $1 + \sqrt{n/n_1}$ , corresponding to the case of strong (weak) hopping contribution, the Hall carrier density  $n_{\text{Hall}}$  is higher (lower) than  $n_{\text{FET}}$  and the Hall mobility  $\mu_{\text{Hall}}$  is lower (higher) than  $\mu_{\text{FET}}$ . (Here  $n$  is the total carrier density.) In the intermediate case,  $\mu_1/\mu_2 = 1 + \sqrt{n/n_1}$  and  $n_{\text{Hall}} = n_{\text{FET}}$  and  $\mu_{\text{Hall}} = \mu_{\text{FET}}$ , a situation which mimics a simple picture with only bandlike carriers present. Importantly, in all three cases, the Hall and FET mobilities ( $\mu_{\text{Hall}}$  and  $\mu_{\text{FET}}$ ) are lower than the intrinsic band mobility  $\mu_1$ . The authors then demonstrated how the “intermediate hopping” case is realized in tetracene and oxidized rubrene crystals with various defect concentrations and both Hall and FET mobilities in the range of  $0.4\text{--}4\text{ cm}^2/(\text{Vs})$ .

The ratio of  $n_{\text{FET}}$  and  $n_{\text{Hall}}$  ( $n_{\text{FET}}/n_{\text{Hall}} = \mu_{\text{Hall}}/\mu_{\text{FET}} = \alpha$ , which can also be expressed in terms of  $\mu_1/\mu_2$  and  $n_1/n$  defined above),<sup>448</sup> coined a “carrier coherence factor”  $\alpha$ , was also used to quantify an interplay of “bandlike” and hopping charge transport in Pn single crystals and films.<sup>541,542</sup> The factor  $\alpha$  was found to increase as the temperature decreased (e.g., from  $\alpha = 0.7$  at 300 K to  $\alpha = 1$  at 200 K, at 1 GPa) and pressure increased (e.g., from  $\alpha = 0.5$  at 0.2 GPa to  $\alpha = 0.7$  at 1 GPa, at 300 K). The authors attributed the findings to the reduced dynamic disorder at low temperature and high pressure (quantified by fluctuations in the transfer integral,  $\Delta t/t$ ), leading to  $\alpha = 1$  at  $\Delta t/t \sim 0.11$ , which was interpreted as a

signature of “fully coherent transport”. However, given that the highest achieved mobility was only  $\sim 2.5 \text{ cm}^2/(\text{Vs})$ , considerably below values expected for band transport in Pn crystals, it appears that the observation of  $\alpha = 1$  would be more consistent with the “intermediate hopping” case discussed above.

In addition to coupling to low-frequency modes, the importance of coupling to high-frequency intramolecular modes has been emphasized in theoretical work<sup>362,452,453,465</sup> and established experimentally. For example, a broad-band THz spectroscopy on rubrene crystals demonstrated electron coupling to an intramolecular mode at 15.5 THz ( $\sim 520 \text{ cm}^{-1}$ ).<sup>361</sup> Bakulin et al.<sup>543</sup> applied pump–push photocurrent spectroscopy, combined with DFT calculations, to Pn/ $C_{60}$  photoresistors. The authors were able to quantify coupling of charge carriers to several intramolecular vibrational modes. They observed a factor of 2–5 stronger coupling to the stretching deformation along the long Pn axis (in the 1400–1650  $\text{cm}^{-1}$  range), as compared to that along the short axis (in the 1200–1400  $\text{cm}^{-1}$  range). The coupling was accompanied by an increase in the photocurrent (Figure 12), which was explained in the framework of the phonon-assisted hopping.

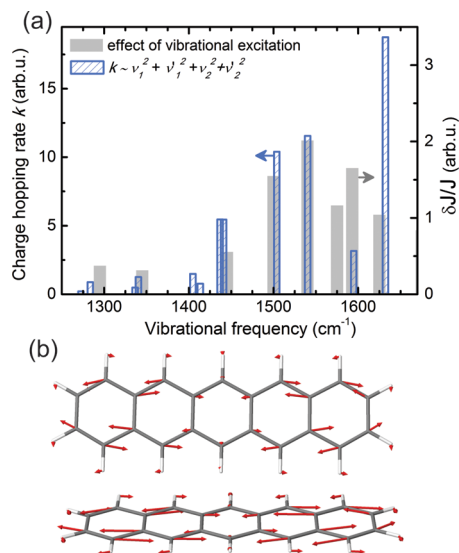


**Figure 12.** (a) Vibration-induced hopping rates for different modes calculated for a Pn crystal (left axis). Experimentally observed enhancement in the photocurrent due to vibrational excitation of the same modes (right axis). (b) Eigendisplacements of the 1,632  $\text{cm}^{-1}$  mode, which is one of the modes with a large transition dipole moment. Adapted with permission from ref 543. Copyright 2015 Nature Publishing Group.

The role of intramolecular vibrational modes in charge transport was theoretically investigated by comparison of the charge transport characteristics in unsubstituted and isotope-substituted derivatives (so-called isotope effect).<sup>544,545</sup> For example, when quantum nuclear tunneling is important for promoting charge transfer, the derivatives substituted with heavier nuclei (via, e.g., deuteration or  $^{13}\text{C}$ -substitution) are expected to exhibit lower carrier mobilities. The substitution position for a large isotope effect is determined by involving the vibrations with strong contributions to the reorganization energy and electron–phonon coupling. Via this mechanism, up to 20% electron mobility reduction was theoretically predicted for NDI-C6 derivatives with all-deuteration.<sup>544</sup> In acenes, 3–5%

(7–9%) hole (electron) mobility reduction was predicted for  $^{13}\text{C}$  replacement of all  $^{12}\text{C}$  atoms on the backbone due to the major contribution of  $\text{C}=\text{C}$  stretching to the reorganization energy, with larger effect expected for smaller molecules (e.g.,  $\sim 3\%$  in Pn versus 5% in Nph). On the other hand, deuteration (i.e., replacement of all H atoms on the acene backbone with D) was expected to produce a smaller effect (0.3–1% for holes and 4–6% for electrons).<sup>545</sup> This is consistent with an experimental study of Xie et al.,<sup>546</sup> who reported no effect of deuteration on the charge transport characteristics of rubrene crystals. However, a similar conclusion could also be reached if band transport was the dominant transport mechanism (as is often considered to be the case in rubrene), as no isotope effect would be expected in the band picture.<sup>545</sup> Therefore, experiments on derivatives with substitutions specifically targeting larger isotope effects are necessary to validate theoretical predictions. One example is TIPS-Pn, for which a relatively large change in the hole and electron mobility ( $\sim 15\%$  and 16%, respectively) was predicted upon backbone deuteration.

Clear understanding of the relationship between the mobility values and the temperature dependence  $d\mu/dT$ , and what it indicates about the charge transport mechanism, has also not been reached yet. For example, Xie et al.<sup>514</sup> observed no correlation between these  $\mu$  and  $d\mu/dT$  in DNNT single crystals, whereas Podzorov et al.<sup>533</sup> found that higher mobilities corresponded to more negative  $d\mu/dT$  in rubrene crystals. Moreover, Xie et al.<sup>547</sup> reported that Hall mobility and its temperature dependence in rubrene crystals were strongly dependent on the hole density  $p$ , with a well-defined peak mobility of  $\sim 4 \text{ cm}^2/(\text{Vs})$  at  $p \sim 0.15$  holes/molecule ( $\sim 2.6 \times 10^{13} \text{ cm}^{-2}$ ). (The authors were able to achieve hole densities  $p$  of up to 0.32 holes per molecule by using the electric double layer transistor geometry.) The authors observed temperature-independent mobility ( $\sim 4 \text{ cm}^2/(\text{Vs})$ ) at  $p \sim 0.15$  holes/molecule, whereas thermally activated mobility was observed at both lower and higher densities (e.g., with activation energies of 14 and 48 meV at  $p \sim 0.11$  and 0.26, respectively). To explain the differences in temperature-dependent resistance obtained at various hole densities, they invoked variable range hopping at low hole densities ( $< 0.15$  holes/molecule), strongly correlated 2D metal behavior at intermediate hole densities (corresponding to the peak mobility), and multiphonon hopping at high hole densities ( $> 0.15$  holes/molecule). Goetz et al.<sup>548</sup> observed a transition from thermally activated mobility (230–300 K) to temperature-independent (and considerably lower) mobility at lower temperatures in STB-TCNQ crystals. The observation was explained by the reduction in the STB librational motion (at 279 and 285  $\text{cm}^{-1}$ ) at low temperatures which froze-in the static orientational disorder, resulting in a tunneling mechanism of charge transport.

**4.3.2. Polymers.** For polymers with mobilities below  $\sim 0.1 \text{ cm}^2/(\text{Vs})$ , disorder models (Section 4.2.5) are typically adequate to describe experimental observations, and electric field-assisted and thermally activated behavior of mobility is commonly observed. Brondijk et al.<sup>490</sup> observed the reduced temperature dependence of FET transfer characteristics in monolayer polymer (of P3HT, PTV, or MDMO-PPV) films as compared to those in thicker ( $> 80 \text{ nm}$ ) films; these observations were described in the framework of 2D and 3D transport, respectively, in the exponential DOS using the Vissenberg-Matters VRH model. Kronemeijer et al.<sup>491</sup> established a 2D nature of charge carrier distribution in a variety of

top-gate polymer FETs and found a correlation between Urbach energies extracted from the sub-bandgap Urbach absorption tails and the DOS width obtained from modeling of FET characteristics using the Vissenberg–Matters model (see Section 8.2, Figure 24).

Dispersive transport characterized by time-dependent mobility was observed using THz spectroscopy,<sup>418,549</sup> transient photocurrent measurements,<sup>301,345</sup> photo-CELIV,<sup>550</sup> and other methods<sup>417</sup> in various polymers (e.g., PPV derivatives or PFO) and their BHJs. (Some reports of time-dependent mobility obtained from photo-CELIV have been questioned in the literature due to ambiguity in data interpretation.<sup>551</sup> The importance of experiments at as low intensities as possible in THz spectroscopy was also emphasized to differentiate between the time-dependent mobility and time-dependent photo-generated carrier density.<sup>552</sup>) On the other hand, Philippa et al.<sup>553</sup> observed time-independent and electric field-independent mobility ( $<10^{-3}$  cm<sup>2</sup>/(Vs)) in PCDTBT:PCBM and PTB7:PCBM solar cells.

At low carrier densities (e.g.,  $10^{15}$ – $10^{17}$  cm<sup>-3</sup>), which are typical for organic optoelectronic devices, the mobility measured in annealed P3HT:PCBM blends exhibited carrier density ( $n$ ) dependence  $\mu \sim n^{\delta}$  with  $\delta$  between 0.3 and 0.7,<sup>554</sup> depending on the crystallinity, which was explained in a framework of the multiple trapping model.<sup>555</sup> Yu et al.<sup>556</sup> observed a reduction in the thermal activation energy of the mobility from 42 to 7.4 meV, accompanied by an order of magnitude increase in mobility upon addition of 1 wt % of boron-doped CNTs to P3HT, due to increased P3HT crystallite sizes in the doped samples.

However, a number of observations were reported that are not readily described by the disorder models. Contrary to expectations of thermally activated charge carrier mobility in the disorder-dominated regime, charge transport in MEH-PPV films at subpicosecond time-scales yielded  $d\mu/dT < 0$ : in particular, a  $\sim 20\%$  mobility increase from 300 to 30 K,<sup>343</sup> which was attributed to freezing-out molecular torsions that decreased the disorder at low temperatures. Such observations are not limited to ultrafast time-scales. For example, Andersson et al.<sup>557</sup> also observed  $d\mu/dT < 0$ , and drastically different temperature dependence of electron and hole FET mobilities, in amorphous low-mobility ( $<10^{-3}$  cm<sup>2</sup>/(Vs)) D–A copolymer TQ1 films. Using DFT calculations, these observations were linked to conformational dependencies of frontier orbital delocalization. In electrochemically gated P3HT transistors, the Hall effect was observed at high hole densities ( $<0.15$  holes/monomer), with the hole mobility of  $\sim 0.8$  cm<sup>2</sup>/(Vs) at 190 K.<sup>558</sup> The authors attributed this observation to a crossover from the nonadiabatic VRH to a “bandlike” transport at hole densities of about  $6 \times 10^{20}$  cm<sup>-3</sup>.

Asadi et al.<sup>559</sup> examined charge transport in various semiconducting polymers (e.g., P3HT, PPV derivatives, etc.) at high carrier densities. They argued that the semiclassical description of hopping using either Miller–Abrahams or Marcus rates is insufficient, which led them to include effects of nuclear tunneling. (This formalism yields the Marcus rate at high temperatures, when  $k_{\text{B}}T \gg \hbar\omega_{\text{c}}$ , where  $\omega_{\text{c}}$  is a characteristic frequency taken to be a high-frequency stretching vibration.) This approach yielded a power-law dependence of the current ( $I$ ) on the temperature in the low-voltage ( $V$ ) Ohmic regime (so that  $I \sim T^{\alpha}V$ ) and a temperature-independent but power-law-voltage dependent current in a high-voltage regime ( $I \sim V^{1+\alpha}$ ). Experimentally, the authors

performed measurements at high charge carrier densities to suppress energetic disorder, which would allow them to observe intrinsic hopping. Using this formalism, they were able to describe the power-law dependence of FET source-drain currents on voltage and temperature in a variety of pristine and doped polymers (including P3HT, PPV, PTAA, PBTT, and PEDOT:PSS). Subsequently, van der Kaap et al. extended the approach to describe  $I$ – $V$  characteristics in a wide range of charge carrier densities, temperatures, and applied electric fields.<sup>123</sup>

The rigidity of the polymer core as well as chain alignment have been cited to be behind observations of high charge carrier mobility ( $>1$  cm<sup>2</sup>/(Vs)) in high-performance D–A copolymers (Table 3).<sup>389,560,561</sup> Extraordinary low disorder, characterized by Urbach energy comparable to that of inorganic crystals, was observed in some of these polymers, even in their amorphous phase, and attributed to torsion-free backbones.<sup>389</sup> For an excellent discussion of charge transport in high-mobility D–A polymers, see the review article by Sirringhaus.<sup>529</sup> In most high-mobility polymers, mobility is thermally activated (with  $\sim 10$ – $50$  meV activation energies) and is typically described within a framework of disorder models discussed in Section 4.2.5. For example, even in highly aligned polymer fibers with room-temperature mobilities up to  $\sim 24$  cm<sup>2</sup>/(Vs), FET mobility was thermally activated with  $\sim 30$  meV activation energy at 85–180 K and with higher activation energies at around room temperature (which was attributed to bias stress and/or moisture).<sup>562</sup> In DPP-DTT copolymer FETs, the CMS revealed the 2D delocalized polaronic signatures, similar for electrons and holes. However, combination of these effects with those of energetic disorder resulted in an imbalance in electron and hole mobilities, so that the FET mobilities were governed by disorder and yielded  $\sim 0.4$  and  $1.7$  cm<sup>2</sup>/(Vs) for electron and hole transport, respectively.<sup>563</sup>

In DPP-based polymer films (which exhibited mobilities on the order of  $1$  cm<sup>2</sup>/(Vs)), the  $d\mu/dT < 0$  with a  $\sim 25\%$  increase in FET mobility between 300 and 220 K was observed and was attributed to transport through interconnected aggregates with low disorder.<sup>560</sup> In this study, higher mobility values were correlated with the negative  $d\mu/dT$ . Lee et al.<sup>561</sup> studied FET mobilities (on the order of  $1$  cm<sup>2</sup>/(Vs)) in a D–A copolymer P8T2Z-C12. They observed Poole–Frenkel electric field-dependent mobility ( $\mu \sim \exp[\beta F^{1/2}]$ ) and electric field-dependent temperature dependence of mobility, with a crossover from  $d\mu/dT > 0$  to  $d\mu/dT < 0$  at higher electric fields. Similar observations were made in films of D–A copolymer CDT-BTZ derivatives with room-temperature mobilities of  $\sim 5$ – $10$  cm<sup>2</sup>/(Vs).<sup>564</sup> This behavior was attributed to the electric field-assisted removal of the energy barrier responsible for carrier localization, which enabled transport in the extended states. On the molecular level, this observation was related to the highly planarized backbone of the polymers that yielded polycrystalline films with ultralow trap density in the case of P8T2Z-C12 (see Figure 14) and ordered fibers in the case of CDT-BTZ. In the latter case, the authors also observed the Hall effect and calculated the “carrier coherence factor”  $\alpha$  (discussed in Section 4.3.1), obtaining  $\alpha \sim 0.4$  at 300 K,  $0.5$  at 240 K, and  $0.3$  at 200 K. The relatively high values of  $\alpha$ , comparable to those in molecular crystals, were interpreted as evidence for carrier delocalization and bandlike transport.<sup>564</sup> This description, along with other recent observations related to charge transport in high-mobility polymers, are awaiting theoretical validation.

#### 4.4. Summary

Understanding of charge transport in high-mobility organic materials is far from complete and over the past several years has been further challenged by extraordinarily high mobilities achieved in polymers with no long-range crystalline order. It has been clearly demonstrated theoretically that the “bandlike” behavior of mobility ( $d\mu/dT < 0$ , Table 4), as well as mobility anisotropy, does not provide a unique identification of the charge transport mechanism. Therefore, additional criteria that would help differentiate between various mechanisms in high-mobility materials (e.g., those with  $J < \lambda < 2J$ , where  $J$  is the highest transfer integral and  $\lambda$  is the reorganization energy, Table 3) and that would rely on experimentally accessible quantities are desirable.

Understanding of the role of electron–phonon interactions in charge transport and in the resulting mobility needs refining; experimental studies that probe effects of coupling to particular vibrational modes (both intramolecular and lattice) on charge transport are necessary. A clear picture of how charge delocalization, charge coupling to low- and high-frequency vibrational modes, and static disorder contribute to charge transport characteristics depending on the molecular structure, packing, and external factors (carrier concentration, temperature, electric field) has not yet been developed. Even in the case of well-studied rubrene, agreement on the coherent band transport versus incoherent hopping as the dominant transport mechanism at room temperature has not yet been reached. There is also conflicting evidence, both computational and experimental, on the contribution of dynamic disorder to charge transport.

More work is also needed to adequately describe charge transport characterized by high mobilities,  $d\mu/dT < 0$ , and other behavior (such as mobility electric field dependence, anisotropy, Hall effect, etc.) in D–A copolymers. In disordered materials, a better understanding of the applicability of the GDM versus CDM description of charge transport to various materials and of the relative importance of the polaron contribution to charge transport is necessary. Given the importance of the coexistence of amorphous and crystalline regions for optoelectronic properties of blends, charge transport models that specifically take into account this structural complexity are needed.

Remarkable mobilities have been reported in recent years, both in small-molecule materials and in polymers (Table 3), along with “bandlike” transport. However, care should be taken, for example, when extracting mobility values from nonideal FET characteristics (which may lead to up to an order of magnitude mobility overestimation),<sup>565</sup> when interpreting comparisons between mobilities and carrier densities extracted from Hall effect and FET characteristics (which may skew conclusions regarding the charge transport mechanism),<sup>448</sup> and when determining the effects of lattice strain on intrinsic mobility (which need to be disentangled from other effects, such as strain-induced change in the work function).<sup>566</sup>

Overall, quantitative descriptions of many observations pertaining to charge transport in high-mobility materials are awaiting, and the questions about the speed limit for charge hopping<sup>444</sup> and about the attainable limit for charge carrier mobility in organic materials remain open.

## 5. CHARGE TRAPPING AND RECOMBINATION

### 5.1. Charge Trapping

Charge trapping dramatically affects charge carrier dynamics, reducing charge carrier mobilities and causing a space-charge build-up. The nature of charge traps and their effect on charge transport have been intensively studied; for a brief insightful review, see ref 600. For a comprehensive review of defects, their characterization, and mitigation in OPVs, see ref 601. An excellent tutorial on trap characteristics, their experimental assessment, and their effect on device performance can be found in ref 602. Traps could be of structural<sup>106</sup> or chemical origin, and they contribute gap energy states that may reduce charge carrier mobility, serve as recombination centers, and/or lead to a space charge field formation.<sup>603</sup> The effect of traps on the device characteristics depends on the trap density and depth (the energy difference between the trap energy and the band edge). For example, in FETs “shallow” traps (i.e., those with depth on the order of several  $k_B T$ ) reduce the mobility and manifest as a gradual transistor turn-on. In contrast, “deep” traps (i.e., those with depth  $\gg k_B T$ ) shift the threshold voltage, but do not affect the mobility or the subthreshold behavior.<sup>602</sup> In OPVs, shallow traps impede carrier transport whereas deep traps enhance carrier recombination (Section 5.2.2). In PR devices, the presence of shallow traps reduces the speed of PR grating formation, whereas deep traps lead to illumination history-dependent device performance.<sup>119</sup> Intrinsic, or structural, traps in crystalline materials may be related to point defects or dislocations in crystalline domains, grain boundaries, and molecular displacements within the crystalline lattice; an even more complicated picture is realized in polymers.<sup>600</sup> Chemical origin (or extrinsic) traps include intentional or unintentional dopants, biproducts of synthesis such as quinones in Pn,<sup>508</sup> oxidation products as a result of reactions with oxygen,<sup>370,604–606</sup> hydrated oxygen complexes formation<sup>607</sup> or other products occurring as a result of reactions with water,<sup>608,609</sup> and products resulting from reactions with organic solvents.<sup>600</sup> For example, Nasrallah et al.<sup>610</sup> exposed diF TES-ADT FETs to ozone and observed oxidation via quinone and carboxyl formation; the former was found to serve as traps responsible for the FET hysteresis. Additionally, traps can be induced by bias stress, photoexcitation, or thermal annealing.<sup>219,338,611–613</sup> In PR polymer composites that use a small concentration (<2 wt %) of a sensitizer (e.g., C<sub>60</sub>, PCBM, and TNFM; see Table 6), the accumulation of sensitizer anions (e.g., C<sub>60</sub><sup>-</sup>) under illumination and bias has been directly linked to formation of hole traps.<sup>220</sup> It is possible that traps of this origin also exist in OPVs with morphologies with small acceptor domains.

Kalb et al.<sup>614</sup> quantified trap DOS in single crystals and/or thin films of several materials (including Pn, rubrene, C<sub>60</sub>, and 6T) using FET and SCLC measurements. They concluded that, in single-crystal FETs, the dipolar disorder due to the presence of the gate dielectric and adsorbed water is the main source of traps, observing that a hydrophobic fluoropolymer gate dielectric yielded the best performing trap-free devices. Lee et al.<sup>525</sup> deposited an inert fluoropolymer PFPE on the molecular crystal (rubrene or Tc) surface, which reduced the shallow trap density via Coulomb interactions between the local PFPE dipoles and trapped charges. Such interactions converted shallow traps into filled deep traps (that do not contribute to charge transport), thus enabling observations of intrinsic transport. Such treatment of Tc crystals resulted in an increased

mobility, conductivity, and conductivity anisotropy (Figure 13). Rubrene crystals had low trap densities and exhibited intrinsic

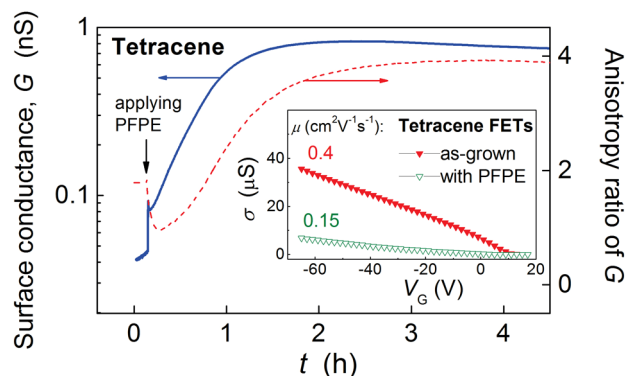


**Figure 13.** Time evolution of surface conductance ( $G = I/V$ , where  $I$  is the current and  $V$  is the voltage) and its anisotropy (defined as the ratio of the conductivities in the  $a$ - $b$  and orthogonal to the  $a$ - $b$  plane directions) in a Tc single crystal due to the “trap-healing effect” induced by the PFPE treatment. The inset shows the trap-healing effect in Tc FETs, leading to a factor of  $\sim 2.7$  increase in mobility. Adapted with permission from ref 525. Copyright 2013 Nature Publishing Group.

properties even without any treatment; nevertheless, the PFPE deposition dramatically reduced the noise in the Hall effect measurements. Gorgolis et al.<sup>337</sup> applied modulated photocurrent spectroscopy to determine the trap DOS in Pn films. They found a deep exponential trap distribution and a metastable Gaussian trap distribution, which they attributed to structural disorder and adsorbed water molecules, respectively. Dacuña et al.<sup>296</sup> intentionally introduced traps into rubrene crystals using UV ozone exposure and X-ray irradiation and measured temperature-dependent  $I$ - $V$  characteristics combined with numerical modeling. Both treatments were shown to increase trap concentration, which reduced the currents in the hole-only diodes. However, the trap energies and their spatial distribution considerably differed, with the UV ozone (X-ray irradiation) treatment increasing the density of surface (bulk) traps with a localized distribution centered at 0.35 eV (with broadly distributed) energy. Lee et al.<sup>561</sup> obtained trap DOS by simulating FET transfer characteristics in several D-A copolymers and compared them to those in benchmark polymers (such as P3HT) and organic crystals (DNNT and PDIF-CN2) and films (Pn on various gate dielectrics). They concluded that low trap densities in the P8T2Z-C12 polymer (Figure 14), similar to those achieved in organic single crystals, are behind observations of the  $d\mu/dT < 0$  regime (Table 4) in this material.

Ando et al.<sup>612</sup> showed that charge trapping in Pn films can lead to a polymorphic phase transition, causing changes in the transfer integral and serving as a potential source of variability in device-to-device performance. The relationship between the defect nature and whether it would serve as a charge trap is complicated, and not all defects serve as traps. For example, there has been experimental evidence<sup>615–617</sup> that, contrary to expectations, grain boundaries in polycrystalline films do not necessarily trap charges: in particular, the charges are trapped by the grain boundaries, and not on the grain boundaries.<sup>600</sup>

Dispersive transport has been discussed in the literature from the standpoint both of time-dependent mobility due to relaxation of charge carriers within the DOS and of time-

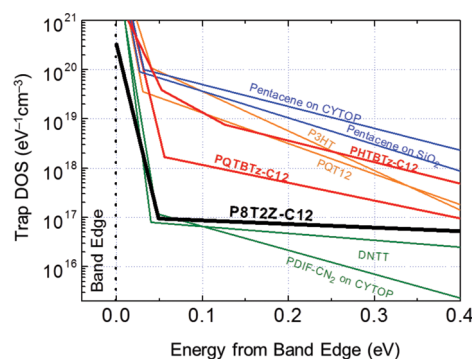


**Figure 14.** Trap DOS extracted from modeling the FET transfer characteristics in molecular crystals (DNNT, PDIF-CN2), small-molecule films (Pn) on various gate dielectrics, and polymer films. The low trap density in P8T2Z-C12 enabled observation of  $d\mu/dT < 0$  in TFTs at high gate voltages. Reprinted from ref 561. Copyright 2015 American Chemical Society.

independent mobility with a progressive carrier loss to trap states.<sup>553,555,618</sup> Manifestation of dispersive transport in the time-resolved carrier dynamics is a power-law time dependence of photocurrents and/or excited states populations ( $\sim t^{-b}$  with  $0 < b \leq 1$ ), which has been observed on time-scales as early as picoseconds after excitation, and over many orders of magnitude in time (Section 8.1).<sup>40,347,414,555,619</sup> Such behavior is ubiquitous in organic semiconductors, and it has been observed in molecular crystals,<sup>198,365</sup> polycrystalline films,<sup>40</sup> and polymers and their D/A blends.<sup>619</sup> Tachiya and Seki<sup>618</sup> theoretically considered recombination of the electron and hole under conditions that at least one of the carriers is mobile. They used the multiple trapping framework and incorporated energetic disorder assuming the exponential DOS ( $g(E) \sim \exp(E/E_0)$ ). They obtained analytical solutions for the cases of (i) equal and (ii) considerably slower recombination rate as compared to the trapping rates and derived the power-law kinetics of the carrier density ( $n$ ) decay in time. The model predicted  $n \sim t^{-b}$  with  $b = k_B T/E_0$  (so that the power-law exponent  $b$  scales linearly with temperature), and such behavior was experimentally observed in polymer:fullerene blends.<sup>555,620</sup> (However, considerably weaker temperature dependence of  $b$  was reported in molecular crystals and crystalline films.<sup>28,198,365</sup>) Hofacker et al.<sup>621</sup> extended this approach to include nonequilibrium carrier relaxation and provided a theoretical description of charge recombination accompanied by energy relaxation of carriers in materials with exponential and Gaussian DOS. They modeled the time dependence of the trapped and mobile charge carriers and established that recombination is much more pronounced in the Gaussian DOS as compared to the exponential DOS. For example, at longer times (e.g.,  $>10^6 \nu_0^{-1}$ , where  $\nu_0$  is the attempt-to-escape frequency, taken to be  $10^{12} \text{ s}^{-1}$ ) the free (trapped) carrier density decreased by  $>4$  ( $>5$ ) and 2 orders of magnitude over the same period of time in the case of the Gaussian DOS (with  $\sigma/k_B T = 5$  (4), where  $\sigma$  is the width of the Gaussian DOS) and exponential DOS (with  $E_0/k_B T = 5$  (4), where  $E_0$  is the energy scale in the exponential DOS), respectively.

Modeling of charge trap effects on time-resolved charge carrier dynamics with the goal of obtaining quantitative information on trap densities and distribution, as well as of their effect on charge carrier mobility and other characteristics such as PR grating dynamics, is not straightforward. The problem is often reduced to the inclusion of one or two trap

energy levels into the model,<sup>120,297,301,603</sup> which does not capture the power-law-distributed dynamics. Christ et al.<sup>619</sup> reproduced power-law decays in the nanosecond photo-response from P3HT:PCBM blends by incorporating nine exponentially distributed in energy trap states (ranging between 46 and 380 meV) into drift-diffusion simulations. Once trapping effects were accounted for, it was found that trap-free charge carrier mobilities were more than 3 times higher than the typically measured effective mobilities. MacKenzie et al.<sup>333</sup> included 80 electron trap and 80 hole trap levels, 10 meV width each, thus discretizing the DOS. The model was able to reproduce steady-state  $J$ - $V$  characteristics as well as transient photocurrent and photovoltage dynamics in P3HT:PCBM solar cells. The modeling extracted the DOS that consists of a set of Gaussians offset in energy, which were attributed to energetic disorder. Street<sup>622</sup> measured the time-resolved photocurrent  $I_{ph}(t)$  in polymer:PCBM solar cells and extracted the DOS ( $g(t)$ ) by analyzing photocurrent dynamics at times longer than the carrier transit time using

$$g(t) = \frac{I_{ph}(t)t}{evfk_B T}$$

where  $e$  is the electron charge,  $v$  is the device volume, and  $f$  is the fraction of the states filled at each energy level. The time  $t$  at which the carrier is extracted and the trap depth  $E$  were related by the following expression

$$E = k_B T \ln(\nu_0 t)$$

where  $\nu_0$  is the attempt-to-escape frequency. MacKenzie et al.<sup>623</sup> applied a similar approach and established that in order to extract the “true DOS” from the  $I_{ph}(t)$  in solar cells, the measurements should be performed over a range of negative voltages to ensure that DOS does not change with voltage.

Nicolai et al.<sup>607</sup> modeled single-carrier  $J$ - $V$  characteristics in various polymer films (including P3HT, PPV derivatives, F8BT, PF10TBT, and PCPDTBT) and observed that electron transport in all polymers was similar, and limited by traps with density of  $\sim 10^{17} \text{ cm}^{-3}$ , energy of  $\sim 3.6 \text{ eV}$  below the vacuum level, and a typical distribution width of  $\sim 0.1 \text{ eV}$  (Figure 15). They concluded that these electron traps must be of the same origin, and unrelated to structural defects, but rather have chemical origin and be caused by formation of hydrated oxygen complexes (e.g.,  $(\text{H}_2\text{O})_2\text{-O}_2$ ). In this case, the average trap depth decreases as the polymer LUMO deepens (e.g., from  $\sim 0.7$ – $0.8 \text{ eV}$  in PPV derivatives to  $\sim 0.6 \text{ eV}$

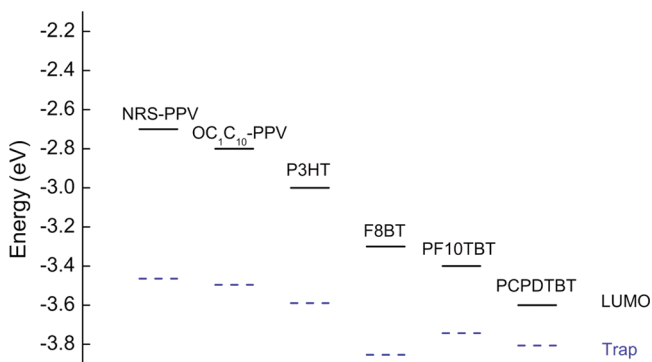


**Figure 15.** LUMO energies (solid line) and center of the electron trap distribution (dashed lines) in various polymers. Reproduced with permission from ref 607. Copyright 2012 Nature Publishing Group.

in P3HT and to  $\sim 0.2 \text{ eV}$  in PCPDTBT), as shown in Figure 15. In the follow-up work,<sup>624</sup> strong suppression of electron trapping in a low-bandgap semiconducting polymer was demonstrated when the polymer was blended with another, high-bandgap polymer. This was accompanied by reduction in losses due to nonradiative recombination (between free holes and trapped electrons), which boosted the efficiencies of polymer LEDs.

### 5.1.1. Charge Traps in Photorefractive Organic

**Materials.** Traps have been extensively studied in photorefractive (PR) materials,<sup>603,625–627</sup> as in these materials traps are a critical part of the materials design (Section 6).<sup>220,628,629</sup> In particular, they determine the capability of the material to store charge, which establishes the material’s utility for particular PR applications. Therefore, charge traps have to be incorporated into modeling of PR properties, and in many high-performance PR polymers at least two trap levels are needed to explain the PR performance.<sup>603</sup> PR polymer composites typically include a small amount of a sensitizer to promote charge generation, conductive polymer to promote charge transport, NLO chromophore to promote electric field-dependent refractive index change, and a plasticizer to lower the glass transition temperature. As such, the PR composites are highly disordered, and high trap densities, as well as large material-to-material variability, would be expected. However, most high-performance PR materials exhibit PR trap densities on the order of  $10^{17} \text{ cm}^{-3}$ ,<sup>630,631</sup> which suggests that only a particular subset of traps of all possible origins serves as a PR trap.

Most high-performance PR materials utilize a sensitizer, and accumulation of its anion (e.g.,  $\text{C}_{60}^-$ ) that forms under continuous excitation (and facilitated by the presence of applied electric field) has been determined to be one of the key factors affecting the hole trap density.<sup>632</sup> It is also responsible for the illumination history dependence of the PR response which is detrimental for devices. However, the degree to which the sensitizer anions accumulate, as well as the charge trapping and detrapping dynamics and effective trap densities, strongly depend on the HOMO energies of other constituents of the PR polymer composite (such as NLO chromophore and/or plasticizer), which act as compensating traps.<sup>603,633</sup> For example, in PR polymer composites containing  $\text{C}_{60}$  sensitizer ( $I_p = 6.4 \text{ eV}$ , where  $I_p$  is the ionization potential), 7-DCST NLO chromophore (5.9 eV), DBDC plasticizer (5.62 eV), and either PATPD (5.43 eV) or PVK (5.92 eV) as the charge-transporting polymer, a considerably more stable performance was achieved with PATPD as compared to PVK.<sup>634</sup> This observation was explained by an increased trap density in PVK-based composites, in which both the NLO chromophore and the plasticizer served as hole traps (as their  $I_p$  values are lower than that of PVK), that led to illumination history-dependent performance that degraded in time. These components did not serve as traps in the PATPD-based composite, so that no long-time evolution of the PR performance was observed. Also important is that the effective trap densities evolve dynamically depending on the illumination and electric field, which must be accounted for in modeling the PR characteristics and in designing materials for PR applications. Finally, depending on the material, for the best performance (which relies on unbalanced hole and electron transport, Section 6), it could be necessary to manipulate the relative densities of hole and electron traps. For example, addition of a low concentration of  $\text{Alq}_3$  to a PATPD-based PR polymer composite increased the

electron trap densities, which improved the PR gain and response time, as well as reduced the material's susceptibility toward dielectric breakdown.<sup>635</sup>

## 5.2. Charge Recombination

Nongeminate recombination involves charge carriers generated by different absorption events (in contrast to geminate recombination, which was discussed in Section 3.1). Nongeminate recombination has been extensively studied in D/A HJs and has been considered as one of the key factors responsible for the  $V_{oc}$  losses and a reduced FF in polymer:fullerene BHJs,<sup>289,291,636–639</sup> as well as for nonradiative losses in polymer LEDs.<sup>640</sup> Recent comprehensive reviews of nongeminate charge recombination in organic BHJs and OLEDs are available (Table S1).<sup>640–642</sup>

**5.2.1. Bimolecular Recombination.** Langevin theory has been used in many studies of organic optoelectronic materials to account for bimolecular recombination.<sup>641</sup> In this model, the bulk recombination rate constant  $\gamma_{Lan}$  was calculated from the flow rate of electrons into the infinite depth of the Coulomb potential of the hole, which recombine when electron and hole are infinitely close to each other. With this description, the rate constant is given by

$$\gamma_{Lan} = \kappa e(\mu_p + \mu_n)/\varepsilon\varepsilon_0 \quad (41)$$

so that the recombination rate is  $R_{Lan} = \gamma_{Lan} np$ , where  $n$  and  $p$  are electron and hole densities, respectively, and the prefactor  $\kappa = 1$ . The assumptions of the model are that the mean free path of the charge carriers is smaller than the Coulomb radius  $r_C$  of eq 27 and that the charge transport is homogeneous throughout the device; that is, electron and hole densities are nonfluctuating and uncorrelated.<sup>641</sup> This assumption might be valid for crystalline materials (including small-molecule BHJs),<sup>638</sup> for which such fluctuations could average out over the relatively long mean free path, but it breaks down in low-mobility disordered polymers and their D:A blends. As a result, in these systems Langevin rates tend to be overestimated as compared to experimentally measured ones by up to 3 orders of magnitude.<sup>638,639,643,644</sup> Hilczler and Tachiya<sup>645</sup> presented a unified theory of geminate (Section 3.1) and nongeminate recombination, arriving (in the absence of electric field) at the rate constant

$$\gamma = \frac{\gamma_{Lan}}{1 - \exp(-r_C/R)(1 - Dr_C/pR^2)} \quad (42)$$

Here  $p$  is a parameter given by the product of the back transfer rate and the electron–hole separation  $R$ ,  $D$  is the diffusion coefficient, and  $r_C$  is the Coulomb radius. Equation 42 recovers the Langevin expression when  $R = 0$  and can be extended to incorporate the dependence on the external electric field. The model also predicts that if  $Dr_C/pR^2 > 10^3$ , the recombination loss is suppressed by increasing the electric field. Burke et al.<sup>237</sup> applied this model to the case of recombination involving multiple events of CT state formation and splitting into free carriers in organic solar cells. They suggested that the Langevin reduction factor ( $\gamma/\gamma_{Lan}$ ) is a measure for the fraction of free carrier encounters that lead to recombination, with the factor approaching 1 if the CT state recombination is much faster than the CT state splitting into free carriers and with it approaching 0 if the CT states and free carriers are in equilibrium. They concluded that, in most organic solar cell materials, the reduction factor is at or below  $\sim 0.2$ , suggesting a close-to-equilibrium situation, which was then used to quantify

the relationship between  $V_{oc}$  and the properties of CT states (Section 11.1.1.1).

Various modifications of the Langevin rate constant  $\gamma_{Lan}$  of eq 41, specific to D–A systems, were proposed. For example, polarization effects were introduced by using a prefactor  $\kappa = |(\varepsilon_2 - \varepsilon_1)/(\varepsilon_2 + \varepsilon_1)|$ , where  $\varepsilon_{1,2}$  are the dielectric constants of the donor and acceptor, respectively. Accounting for charge spatial profiles and energetic disorder introduced a prefactor  $\kappa = 2\pi\Delta E/k_B T \exp(-2\Delta E/k_B T)$ , where  $\Delta E$  is the difference in the D–A HOMO or LUMO energies. Incorporation of only the motion of the slower charge carrier in the rate (which replaces  $\mu_n + \mu_p$  in eq 41 with the lower value out of  $\mu_n$  and  $\mu_p$ , i.e.  $\min(\mu_n, \mu_p)$ ) has also been proposed.<sup>641</sup>

Heiber et al.<sup>646</sup> showed through Monte Carlo simulations that the recombination rate dependence on a particular combination of electron and hole mobilities depends on the domain size. They proposed the following rate:

$$\gamma = \frac{2e}{\varepsilon\varepsilon_0} f(d) \left( \frac{\mu_e^g + \mu_h^g}{2} \right)^{1/g(d)} \quad (43)$$

where  $f(d)$  is a domain size-dependent prefactor and  $g(d)$  is the domain size-dependent exponent, both of which monotonously decrease as the domain size ( $d$ ) increases. For a very small domain ( $d \rightarrow 0$ ),  $f = 1$  and  $g = 1$ , recovering the Langevin expression. In the follow-up study,<sup>647</sup> eq 43 was generalized to replace the dependence on  $d$  with that on the dimensionless ratio  $d/d_s$ . Here  $d_s$  is the average charge carrier separation distance estimated using  $d_s = \Gamma(4/3)(3/(4\pi(n+p)))^{1/3}$ , where  $\Gamma$  is the gamma function and  $n$  ( $p$ ) is electron (hole) concentration.

Distinguishing between geminate and nongeminate recombination experimentally is not straightforward, and it has been shown theoretically<sup>240,648</sup> and experimentally<sup>649</sup> that it should be done at low light intensities. Experimentally, the bimolecular recombination efficiency has been obtained via time-resolved and steady-state measurements of photocurrents and excited state populations (e.g., in transient absorption experiments).<sup>120,289,291,300,555,637,650,651</sup> In the absence of other contributions, dominant bimolecular recombination would be expected to yield time-resolved power-law decays of charge carrier population scaling as  $\sim t^{-b}$  with  $b = 1$  and light intensity ( $I$ ) dependence of the photocurrent amplitude ( $I_{ph}$ ) scaling with intensity as  $I_{ph} \sim I^a$  with  $a = 0.5$ . However, often values of  $a < 1$  and  $b$  assuming any value in the range of  $0 < b < 1$  are observed.<sup>347,620</sup> Seki et al.<sup>620</sup> argued that  $b < 1$  is expected when the deep traps inside the bandgap are described by an exponential trap energy distribution and considered a case with  $b < 0.5$ . They analyzed light-induced electron spin resonance (LESR) data obtained under pulsed and continuous excitation of P3HT:PCBM and P3OT:PCBM BHJs in the framework of the multiple trapping model. It was established that the charge density power-law decay ( $\sim t^{-b}$ ) in time-resolved experiments (0.1–100 s in their case) could be related to trap distribution leading to intensity dependence of the steady-state photocurrent  $I_{ph} \sim I^a$  with  $a = b/1 + b$ .

The exponent  $a$  in the light intensity dependence with values  $0.5 < a < 1$  has been observed in various materials including polymer:fullerene BHJs,<sup>340</sup> PR polymers,<sup>220</sup> amorphous glasses (e.g., DCDHF), and small-molecule polycrystalline films such as R-Pn or diF R-ADT.<sup>347</sup> The values between 0.5 and 1 are typically described by varying contributions of shallow traps to charge transport,<sup>220</sup> described by space-charge field effects, or

related to the fraction of the charge carriers that are lost due to bimolecular recombination.<sup>340</sup> Evolution of the parameter  $a$  in  $I_{\text{ph}} \sim I^a$  depending on the time at which carriers are probed has been observed in frequency dependent (quasi-steady-state) photocurrent experiments in polycrystalline and amorphous films.<sup>347</sup> In these experiments, cw excitation was chopped at various chopper frequencies  $f$  and the photocurrent was detected with a lock-in amplifier. Values of  $a$  between  $\sim 0.7$  and  $0.9$ , depending on the material, were observed at  $f = 20$  Hz, increased with  $f$ , and approached  $1$  at  $f = 1$  kHz. In organic solar cells,  $a = 1$  was attributed to effective sweep-out of carriers prior to recombination.<sup>638</sup> Koster et al.<sup>340</sup> proposed that loss of carriers due to bimolecular recombination ( $\eta_{\text{BR}}$ ) in P3HT:PCBM BHJs could be obtained using  $\eta_{\text{BR}} = 1/a - 1$ , where  $a$  is determined from the light intensity ( $I$ ) dependence of the short-circuit current ( $J_{\text{sc}} \sim I^a$ ).

Wetzelaer et al.<sup>651</sup> proposed a method of obtaining bimolecular recombination efficiency from steady-state measurements of SCLCs in single-carrier and double-carrier devices (as controlled by carrier injecting or blocking electrodes) and arrived at the prefactor for the Langevin formulation ( $\kappa$  in eq 41) in the form

$$\kappa = \frac{16\pi}{9} \frac{J_p J_n}{J_D - (J_p + J_n)^2} \quad (44)$$

where  $J_p$  ( $J_n$ ) are hole-only (electron-only) SCLCs and  $J_D$  is the double-carrier current. This relationship was derived from combining the two limits of slow and infinite recombination, and it assumes trap-free electron and hole transport. The model was used, for example, to quantify the competition between charge recombination and extraction in various polymer:fullerene, polymer:polymer, and small molecule:fullerene BHJs, which was determined to be responsible for the FF achieved in these solar cells (Section 11.1.1.3).<sup>639</sup>

**5.2.2. Trap-Assisted Recombination.** Another important recombination mechanism is trap-assisted recombination, often referred to as Shockley–Read–Hall (SRH) recombination, which involves recombination between a mobile charge and a stationary charge of the opposite sign, immobilized in a deep trap. Kuik et al.<sup>652</sup> showed that, in disordered materials, this process is governed by diffusion of free carriers (typically holes) to the trapped carrier (typically electron). The SRH rate is given by

$$R_{\text{SRH}} = \frac{C_n C_p}{C_n(n + n_1) + C_p(p + p_1)} N_t p n \quad (45)$$

where  $N_t$  is the electron trap density,  $p$  ( $n$ ) is the mobile hole (electron) density,  $C_p$  ( $C_n$ ) are the hole (electron) capture cross-sections, and  $p_1 n_1 = N_C N_V \exp(-(E_C - E_V)/k_B T)$  (where  $N_C$  ( $N_V$ ) and  $E_C$  ( $E_V$ ) are conduction (valence) band DOS and energies). The SRH rate is linear with free carrier density (in contrast to the Langevin rate  $R_{\text{Lan}}$ , which is quadratic with carrier density) and thus is considered to be of a monomolecular character. This makes the SRH a first-order process, in contrast to the bimolecular second-order process represented by the Langevin model and its extensions. The total recombination rate is then a sum of the Langevin and of the SRH rates. (Note that sometimes the term “bimolecular recombination” includes both Langevin and SRH mechanisms and refers to recombination between two distinct species, irrespective of the order of the reaction.<sup>637</sup> For a detailed

discussion of the meaning of reaction order in the context of different recombination mechanisms, see ref 653. In the present review, “bimolecular” assumes the Langevin-type recombination, concerning recombination of mobile electrons and holes.) Analytical descriptions of charge recombination that include various recombination processes have been developed.<sup>618,621</sup>

Shuttle et al.<sup>554,654,655</sup> used a combination of experimental techniques and intensity-dependent  $V_{\text{oc}}$  measurements in a variety of polymer:fullerene and small molecule:fullerene BHJs to show that the kinetics of the charge carrier density can be described by  $dn/dt \sim -\gamma n^2 \sim n^{\delta+2}$ , where  $\delta > 0$ . This demonstrated that the rate  $\gamma$  is not a constant, but a parameter dependent upon carrier concentration that incorporates competition between bimolecular and SRH recombination mechanisms.

Several studies utilized the light intensity dependence of  $V_{\text{oc}}$  to quantify the interplay of bimolecular and SRH recombination, with the logarithmic dependence of  $V_{\text{oc}}$  on light intensity with the slope of  $k_B T/e$  in the case of bimolecular recombination-only and a higher slope in the presence of the SRH.<sup>638,642,656</sup> However, Proctor and Nguyen<sup>657</sup> pointed out that when the leakage current is not negligible ( $R_{\text{sh}}$  is finite in eq 46), the slope can appear to be higher than  $k_B T/e$  even in devices with purely bimolecular recombination, as described by the following expression:

$$V_{\text{oc}} = \frac{E_{\text{gap}}}{e} - \frac{k_B T}{e} \ln \left( \frac{(1-P)\gamma N_c^2}{PG - V_{\text{oc}}/eLR_{\text{sh}}} \right) \quad (46)$$

Here  $E_{\text{gap}}$  is the band gap,  $e$  is the elementary charge,  $P$  is the dissociation probability of a bound electron–hole pair,  $\gamma$  is the bimolecular recombination rate coefficient,  $N_c$  is the effective density of states,  $L$  is the active layer thickness, and  $G$  is the photogeneration rate. (At large shunt resistance values  $R_{\text{sh}}$ , the eq 46 simplifies to the expression proposed by Koster et al.<sup>658</sup> used for ideal systems with negligible leakage currents, and assuming Langevin bimolecular recombination mechanism to be the only loss mechanism.)

Tzabari and Tessler<sup>649</sup> observed the transition from bimolecular to monomolecular (SRH) recombination using measurements of EQE as a function of light intensity over  $\sim 4$  orders of magnitude in P3HT:PCBM solar cells. In their follow-up work, Tzabari et al.<sup>659</sup> used similar experiments to conclude that exciton–polaron recombination is a more competitive recombination channel than Langevin-type recombination, and it is the interplay of the SRH and exciton–polaron annihilation that determines recombination losses in P3HT:PCBM solar cells. (Exciton–polaron annihilation is also an important loss channel in OLEDs.<sup>640</sup>) Contributions of bimolecular and trap-assisted recombination to time-resolved photocurrents have also been quantified via drift-diffusion modeling of experimental data.<sup>120,303</sup>

Spin-dependent recombination in OPVs has not been studied as extensively as that in OLEDs, and the importance of spin of recombining charge carriers for recombination losses in OPVs has recently been emphasized.<sup>412,424,641</sup> Pertinent fundamental physics was explored, for example, by Devir-Wolfman et al.<sup>660</sup> who examined spin-mixing processes<sup>661</sup> that govern spin-dependent recombination in various P3HT:PCBM blends. Through measurements of photocurrent as a function of magnetic field in OPV devices, they demonstrated that hyperfine interactions within the polaron pairs and the “ $\Delta g$  mechanism” (where  $\Delta g$  is the difference in the  $g$ -factors of the

electron and hole), both in polaron pairs and in the CT excitons, are dominant spin-mixing processes at lower and higher magnetic fields, respectively.

### 5.3. Summary

Considerable progress in understanding charge trapping and recombination processes in organic materials and their role in determining key (opto)electronic device characteristics has been made in the recent years. Nevertheless, several aspects require further explorations. Quantitative description of traps resulting from structural defects (dislocations, polymorphs, etc.) and from extrinsic defects (such as chemical impurities) and of their relative contributions to charge transport and recombination characteristics is still lacking. Studies that include microscopic structure in considerations of trapping and recombination properties (rather than relying on macroscopic parameters) are also limited thus far. Mechanisms of trap reduction have been proposed, but better understanding of underlying processes and their relevance to various materials systems is needed. Advances in analytical and computational description of nongeminate recombination and its manifestation in experimentally accessible quantities have been made. However, further developments that incorporating charge delocalization and spin-dependent effects into formulations for charge recombination efficiencies<sup>641</sup> and experimental validations of these contributions depending on the system are necessary.

## 6. PHOTOREFRACTIVE EFFECT

The photorefractive (PR) effect refers to spatial modulation of the index of refraction under nonuniform illumination via space charge field formation and electric field-dependent refractive index change. The effect arises when charge carriers, photo-generated by a spatially modulated light intensity, separate by drift and diffusion processes and become trapped to produce a nonuniform space charge distribution. The resulting internal space-charge electric field then modulates the refractive index to create a phase grating, or hologram, which can diffract a light beam. Because of charge carrier motion over approximately micrometer distance, the incident light intensity pattern and the refractive index modulation are phase-shifted (displaced) in space. An important consequence of this phase shift is energy transfer between two interfering light beams in a PR medium, called asymmetric two-beam coupling (2BC). If the coupling is sufficiently strong, the 2BC gain may exceed the absorption and reflection losses of the sample, and optical amplification can occur. Many of the applications that have been proposed for PR materials rely on the 2BC gain, including coherent image amplification, novelty filtering, self-phase conjugation, beam fanning limiters, and simulations of neural networks and associative memories. Other applications, such as holographic data storage or 3D holographic displays,<sup>662,663</sup> rely on the ability of the hologram to diffract light, quantified by diffraction efficiency.

On the materials side, the photoconductive properties and electric field-dependent refractive index, as required by the PR effect, are generally provided by a combination of functional components in the composite that include a sensitizer, a transporting medium, trapping sites, and NLO chromophores. Comprehensive review of pre-2004 work on PR organic materials can be found in ref 220, with a more recent work reviewed in refs 628 and 629. A short tutorial-level overview of the PR effect, materials, and applications is available in ref 5; a

recent book on the subject is also available.<sup>664</sup> Here, a brief account of the mechanisms involved and outstanding issues are discussed, with the goal of promoting further research in this area that builds on achievements in understanding of relevant physical mechanisms and material design in organic solar cells and high-mobility polymers.

Figure 16 illustrates the microscopic processes required to produce a hologram by the PR mechanism. Two intersecting

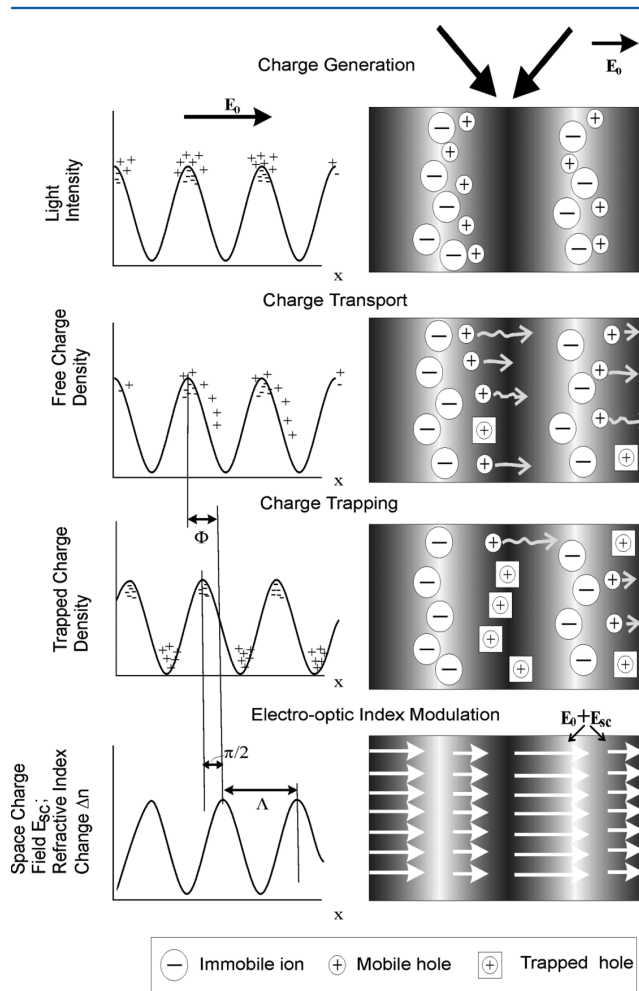


**Figure 16.** Photorefractive grating formation: (a) charge generation; (b) charge transport; (c) charge trapping; (d) space-charge field formation and refractive index modulation. Reprinted from ref 220. Copyright 2004 American Chemical Society.

coherent beams of light produce an interference pattern with a grating wavelength

$$\Lambda = \frac{\lambda}{2n \sin[(\theta_2 - \theta_1)/2]}$$

Here  $n$  is the index of refraction of the material,  $\lambda$  is the optical wavelength in vacuum, and  $\theta_1$  and  $\theta_2$  are the internal angles of incidence of the two writing beams relative to the sample normal. For normally accessible opening angles between the two light beams and visible optical wavelengths,  $\Lambda$  is in the range 0.3–20  $\mu\text{m}$ . The direction normal to the light and dark planes defines the direction of the grating wavevector  $K$ , the magnitude of which is given by  $K = 2\pi/\Lambda$ . If one denotes the  $x$ -axis as the direction of the grating wavevector, the optical intensity follows the sinusoidal pattern shown in Figure 16(a).

The first physical process required for the PR effect is the generation of mobile charge in response to the spatially varying illumination. Photoinduced charge generation is in most cases assisted by a sensitizer molecule that absorbs light and then becomes reduced, injecting a hole into the material (e.g., semiconducting polymer). Charge generation in PR materials is strongly electric field-dependent and is typically described in the framework of an Onsager or Onsager–Braun model;<sup>220,629</sup> however, newer models (Section 3.1) that, for example, explicitly include the effect of polymer conjugation in the formulation for photogeneration efficiency<sup>248</sup> may become more appropriate for new and improved PR materials. Inefficient charge generation has been cited as one of the factors limiting the rate of hologram formation, and the search for better and preferably nonfullerene sensitizers is ongoing (Section 9.5, Table 6).

The second element for the PR effect is transport of the generated charges, with one carrier being more mobile than the other. In Figure 16(b), the holes are shown to be more mobile, which is the more common case for organics, although several electron and bipolar transporting PR organic materials were reported.<sup>220,635</sup> (Note that having one type of charge carriers more mobile than the other is necessary since charge separation is essential for the space-charge field formation.) Charge transport mostly occurs by drift under applied electric field and is commonly described as hopping quantified in the GDM framework (Section 4.2.5). Charge transporters are typically conjugated polymers (e.g., PVK, PPV, PATPD) or small-molecule glasses (e.g., DCDHF, 2BNM), and low charge carrier mobility has been considered as one of the key factors limiting the rate of hologram formation.

The third element for the PR effect, which is critical for applications such as 3D holographic displays when long grating lifetimes are desired, is the presence of trapping sites which temporarily hold the charge carrier. Because trapping is an important part of the space-charge field formation in PR polymers, a considerable research effort has been devoted to understanding the origin and properties of PR traps (Section 5.1.1) and to identifying the desirable charge trap characteristics. For example, Monte Carlo simulations of space-charge field formation predicted that the optimal trap depth depends on the energetic disorder and trap concentration.<sup>665</sup>

After separation of charge carriers occurs, the resulting space-charge density is shown in Figure 16(c). Poisson's equation of electrostatics dictates that such a charge distribution produces a sinusoidal space-charge electric field as shown in Figure 16(d), with the resulting internal electric field shifted in space by 90° relative to the trapped charge, or one-quarter of the grating wavelength.

The final requirement for photorefractivity is that the optical index of refraction of the material must change in response to the local electric field, which includes contributions both from the applied electric field ( $E_0$ ) and from the space-charge field ( $E_{sc}$ ).<sup>666</sup> This is typically achieved by inclusion of a high concentration of NLO chromophores into the PR composite, for which the following figure of merit (FOM) has been identified:

$$\text{FOM} = \frac{1}{M} \left[ 9\mu_g \beta + \frac{2\mu_g^2 \Delta\alpha}{k_B T} \right] \quad (47)$$

Here  $M$  is the molar mass,  $k_B$  is the Boltzmann constant, and  $T$  is the temperature, and the requirements for the molecule are

determined by a combination of the ground state dipole moment ( $\mu_g$ ), polarizability anisotropy ( $\Delta\alpha$ ), and first hyperpolarizability ( $\beta$ ). The mechanism behind the refractive index change can be provided by the Pockels effect and orientational Kerr effect. Most high-performance PR materials have low glass transition temperature (achieved by inclusion of a plasticizer in the composite, Table 6), in which the latter mechanism dominates, resulting in a quadratic field dependence of the refractive index ( $\Delta n \sim (E_0 + E_{sc}(x))^2$ ). Due to the sinusoidal space charge electric field, a spatial modulation of the index of refraction results as shown in Figure 16(d). This is a grating or hologram that can diffract light. If the sample is much thicker than the grating wavelength, the grating is a volume hologram and readout of the grating occurs only when the Bragg condition is satisfied on the readout beam angle and frequency. The total spatial phase shift between the peaks of the optical intensity pattern in Figure 16(a) and the peaks of the index of refraction modulation in Figure 16(d) is denoted  $\Phi$ . When the phase shift is nonzero, the index grating is a *nonlocal* grating, and this property is one of the most important special properties of PR materials, which leads to the 2BC effect and 2BC-enabled applications.

The basic molecular model that describes space-charge field formation was introduced by Schildkraut and Buettner,<sup>305</sup> who adapted the model developed by Kukhtarev for inorganic crystals to the case of organic materials and associated electric field-dependent charge generation, transport, and trapping dynamics. The model involves solving a set of coupled nonlinear equations that describe time- and position-dependent free and trapped carrier densities produced as a result of nonuniform light excitation (Figure 16), which are solved in conjunction with the Poisson equation to determine the dynamics of the space-charge field formation. For several limiting cases, analytical description of the steady-state and dynamics of space-charge field formation was also developed.<sup>667</sup> Ostroverkhova and Singer<sup>603</sup> modeled the contributions of both shallow traps and deep traps into PR performance, with the latter responsible for effects such as the illumination history dependence of PR dynamics and of steady-state PR characteristics. They used a Fourier decomposition to separately consider spatially uniform (zeroth order) and spatially varying (first order) parameters and developed a procedure to extract parameters from time-resolved photocurrents and use them in predicting space-charge field dynamics. Kulikovskii et al.<sup>668</sup> further developed the analysis and were able to independently determine more parameters (e.g., separately assess trapping rates and trap densities) from time-resolved photocurrents and to explain the effects of time-gating on the PR performance.<sup>669</sup> Subsequently,<sup>670,671</sup> a photo-EMF technique was used to obtain a complete set of parameters necessary for space-charge field modeling. Oh et al.<sup>625</sup> explicitly included trap density-dependent mobility into trapping, detrapping, and recombination rates. Samiullah<sup>672</sup> incorporated exciton diffusion into the model and argued that a space-charge field can be produced by drift of holes even without traps at a particular combination of exciton diffusion rates and DOS. Most recently,<sup>673</sup> a phenomenological model was proposed that differentiates between the “single event” of excitation, transport, and trapping and “multiple events” (such as multiple trapping and releasing of the charge carrier) before the space-charge field is established. The need for a new model was dictated by experimental observations of diffraction efficiency dependence on the pulse width of pulsed writing beams, in a broad range of

pulse widths of the same pulse energy. Theoretical description of this effect and of the time-evolution of diffraction efficiency is now awaiting. Additional opportunities for theoretical modeling are presented by observations of the strong dependence of the PR performance on the presence of the buffer layer,<sup>673</sup> the origin of which would be important to understand for further optimization of the PR device architecture.

The main figures of merit for PR performance are gain coefficient ( $\Gamma$ ) and diffraction efficiency ( $\eta_{\text{FWM}}$ ), which relate to the refractive index modulation ( $\Delta n$ ) as follows:<sup>220</sup>

$$\Gamma = \frac{4\pi}{\lambda} \frac{\Delta n}{m} \sin \Phi \quad (48)$$

$$\eta_{\text{FWM}}^{\text{ext}} = e^{-\alpha L} \sin^2\left(\frac{\pi \Delta n L}{\lambda} \hat{e}_1 \cdot \hat{e}_2\right) \quad (49)$$

Here  $\lambda$  is the wavelength,  $m$  is the modulation depth of the interference pattern,  $\Phi$  is the phase shift,  $\eta_{\text{FWM}}^{\text{ext}}$  is the external diffraction efficiency,  $\alpha$  is the absorption coefficient,  $L$  is the effective interaction length  $L = d/\sqrt{\cos \theta_1 \cos \theta_2}$  ( $d$  is the sample thickness), and  $\hat{e}_1$  and  $\hat{e}_2$  are unit vectors along the electric field of the incident and diffracted beams, respectively. For the configuration with  $p$ -polarized readout,  $\hat{e}_1 \cdot \hat{e}_2 = \cos(\theta_1 - \theta_2)$ , while, for  $s$ -polarized readout, the dot product is unity. The dynamics of PR grating build-up, erasure, and dark decay are also of critical importance, and are governed both by processes participating in the space-charge field formation (charge photogeneration, transport, trapping, detrapping, and recombination)<sup>603</sup> and by the ability of the NLO chromophores to reorient in the electric field.<sup>674,675</sup> These are parameters that can be obtained from experiments, which provide quantitative information on the space-charge field formation.

The gain coefficient of eq 48, which quantifies the energy transfer between the two beams involved in grating formation, relies on  $\Phi \neq 0$ , and no energy coupling occurs at  $\Phi = 0$ . In PR materials,  $\Phi \neq 0$  is achieved by charge transport over macroscopic distances (Figure 16), which distinguishes the nonlocal PR mechanism from local mechanisms of grating formation such as photochromism or thermochromism. Given that both charge generation and transport in PR organic materials are electric field-dependent, high performance is typically achieved at high electric fields (Table 7), which limits their practical applications. Therefore, there has been an effort to reduce the fields<sup>676,677</sup> and/or find alternative mechanisms which, for example, would produce gains in the absence of electric field.<sup>678,679</sup> An example of such a mechanism is nonlocal photoisomerization,<sup>680</sup> which relies on the cooperative motion of azobenzene moieties in polymers or sol-gels under polarized excitation, resulting in spatially shifted domains with various orientations of chromophores. Materials with enabled photoisomerization-related mechanisms do not require applied electric fields and have been recently utilized in dynamic holographic recording.<sup>680–684</sup> The quantitative descriptions of mechanisms of creating *nonlocal* gratings that are *not* produced by charge carrier transport (or motion of interference patterns), however, are still under investigation, and only the PR materials relying on photoconductivity-enabled space-charge field formation and their applications will be considered in this review, in Sections 9.5 and 11.3 respectively.

## 6.1. Summary

The complexity of the PR mechanism dictates stringent requirements for the components of the PR composite. For

example, improving of charge generation efficiency by increasing the sensitizer concentration typically cannot be achieved, limiting concentrations to <2 wt %, because of increased trap densities (that limit the phase shift  $\Phi$  and inhibit charge transport) and undesirable enhanced optical absorption. Achieving enhanced carrier mobility by relying on a long-range order (e.g., film crystallinity) is also suboptimal, as the presence of crystallites reduces film optical quality. Low glass transition temperatures are needed for efficient NLO chromophore orientation, but they also promote phase separation and reduce the stability of the material. The existence of a trade-off between achieving fast dynamics of PR grating formation and strong steady-state performance (such as diffraction efficiency) is also a well-known issue, as exemplified by studies of PR performance depending on the sensitizer concentration.<sup>685,686</sup> Nevertheless, high 2BC gains and diffraction efficiencies together with submillisecond response times have been demonstrated (Table 7), enabling exciting applications (Section 11.3). Recent developments in the material design (Section 9), such as high-mobility polymers with torsion-free backbones, D–A copolymers that promote charge delocalization that minimizes the need for the driving force needed for charge generation in D:A blends, as well as considerably improved understanding of the intricacies of morphologies enabling efficient charge generation and transport in OPVs (Section 3.3, 9.2, 10), represent an exciting opportunity to further boost the PR performance. The recently reported capability to study PR grating formation under pulsed excitation varying over 9 orders of magnitude<sup>673</sup> has the potential to generate valuable insights into the underlying physics which were not previously accessible. There are also opportunities for further development of theoretical models of the PR effect that could guide further PR material design depending on the application.

## 7. EXPERIMENTAL METHODS FOR PROBING EXCITON AND CHARGE CARRIER DYNAMICS

In this section, selected methods that probe charge carrier and exciton dynamics are outlined, with a focus on insights they provided into electronic processes occurring in organic optoelectronic materials. The purpose of this section is (i) to highlight capabilities of experimental methodologies that probe specific aspects related to (or relying on) molecular photo-physics, charge generation, transport, trapping, and recombination, (ii) to promote further experimental studies of these processes, enabling new insights, by using novel combinations of methods, and (iii) to inspire development of new techniques. Books discussing basic implementations of various techniques at the tutorial-level are available.<sup>2,6,530,687,688</sup> References in Table S1 should be consulted for comprehensive reviews of experimental methods focused on other properties, such as characterization of film structure and morphology.

### 7.1. Macroscopic Scales

#### 7.1.1. Time-Resolved Probes (fs–ns time-scales).

**7.1.1.1. Pump–Probe Techniques.** The most prominent methodology that enables time-resolved measurements of excited states and charge carrier dynamics is time-resolved pump–probe spectroscopy. In a basic configuration, two pulsed beams (a pump and a probe) are incident on a sample, and the time delay between the pulses is controlled with a delay line. The transmission or reflection of the probe beam is monitored as a function of time delay with respect to the pump beam. The pump beam is often an optical beam in the UV–visible range,

and the wavelength of the probe beam depends on the technique, as discussed in this section. Detection schemes and data analysis are also technique-dependent. However, all techniques in this section can be classified as “optical excitation–optical probing” methods. The main advantage of the pump–probe techniques is their subpicosecond time resolution. Also, most of these techniques are noncontact, which makes them attractive for studies of intrinsic charge carrier dynamics, not confounded by effects occurring at or imposed by electrodes.

**7.1.1.1.1. All-Optical Pump–Probe Spectroscopy.** In this technique, both the pump and the probe beams are within the UV/visible to near-IR wavelength range ( $\sim 300$  nm to  $2 \mu\text{m}$ ). The pump is typically a sub-100-fs pulse at a set wavelength of excitation. The probe beam either originates from a tunable laser source or has a white-light supercontinuum spectrum. The change in the intensity and spectrum of the probe beam transmitted through or reflected from the sample ( $\Delta T/T_0$  or  $\Delta R/R_0$ , respectively) is measured as a function of the time delay between the pump and the probe pulses. This is the most widely used pump–probe technique, which has enabled mapping out energies and dynamics of excited states and probing processes such as excited state absorption ( $S_1 \rightarrow S_n$ ,  $T_1 \rightarrow T_n$ ), intersystem crossing ( $S_1 \rightarrow T_1$ ), spontaneous emission, etc. The time resolution of the all-optical pump–probe technique is limited by the pulse width of the laser beams used, which is typically around  $\sim 100$  fs, although measurements with a sub-5-fs resolution have also been reported.<sup>689</sup> The technique is very efficient in probing the populations of the excited states; however, it does not readily differentiate between the neutral and charged states, which necessitates additional measurements to unambiguously distinguish between such states and aid in interpretation of complicated excited state spectra. To address this issue, a modification has been suggested (F-TAS), which involves probing the difference in the transmission of the probe beam through the sample with and without applied electric field ( $F$ ).<sup>417</sup> In this case, the measured quantity is  $(\Delta T/T_0)(F) - (\Delta T/T_0)(F = 0)$ , and this modification has enabled probing dynamics of charged states in devices (e.g., in OLEDs<sup>690</sup>); see Table 2 for selected results. Recently, a technique based on time-resolved photoinduced absorption was proposed for measurements of singlet exciton diffusion.<sup>126</sup> Transient absorption microscopy, which combines time resolution of the pump–probe methodology with spatial resolution of diffraction-limited microscopy, has also been developed, as discussed in Section 7.2.3.

**7.1.1.1.2. Optical Pump–Terahertz (THz) Probe Spectroscopy.** In this experimental method (see a tutorial in ref 530), a sub-100-fs laser beam at an optical wavelength ( $\sim 400$ – $800$  nm) is used as a pump and the beam at far-infrared wavelengths (i.e. in the THz region: 1 THz corresponds to a wavelength of  $\sim 300 \mu\text{m}$ ) is used as a probe. The THz pulse can be generated using an 800-nm, sub-100-fs pulse from an amplified Ti:sapphire laser via optical rectification in a nonlinear optical crystal (e.g., ZnTe) or via transient photocurrent generation in a photoconductive switch (e.g., GaAs). Detection of the transmitted THz pulse occurs also using the linear electro-optic effect either in ZnTe or in a photoconductive switch geometry, with a typical time resolution of  $\sim 300$ – $500$  fs. Both geometries have been used for broadband THz spectroscopy;<sup>361,691</sup> for example, an 11- $\mu\text{m}$ -thick ZnTe crystal enabled detection in the 7–100 THz range.<sup>692</sup>

Optical pumping of the sample prior to probing with THz generally leads to two effects: a change in the THz amplitude and a phase shift. The most complete data acquisition involves measuring the THz waveform at each setting of the pump–probe delay (known as 2D scan). Then, the waveforms in the time-domain are Fourier-transformed into the frequency domain, and the data are analyzed using various models (e.g., Drude, Drude–Smith, Cole–Davidson, etc.)<sup>200,343,361,530</sup> to extract real and imaginary parts of photoconductivity ( $\sigma_{\text{ph}}$ ), as a function of frequency ( $\omega$ ). The real part of the photoconductivity is related to motion of the mobile charge carriers under the electric field of the THz wave, while the imaginary part probes polarization of the bound electron–hole pair (exciton). For example, in the thin-film approximation for the amplitude of the THz wave transmitted through a thin conducting film on a semi-insulating substrate with the refractive index  $n$ , assuming normal incidence, the transmission of the THz probe ( $T(\omega)$ ) is<sup>530</sup>

$$T(\omega) = \frac{E_t(\omega)}{E_i(\omega)} = \frac{2}{1 + n + Z_0 \sigma_{\text{ph}}(\omega) d} \quad (50)$$

where  $E_t$  ( $E_i$ ) is the Fourier transform of the transmitted (incident) amplitudes of the THz probe pulse,  $d$  is a film thickness, and  $Z_0$  is the impedance of free space ( $Z_0 = 377 \Omega$ ).

If there is no phase shift between the THz waveforms transmitted through the unexcited and photoexcited sample, it is possible to simplify measurements and data analysis by measuring only the *amplitude* of the THz pulse transmitted through the sample, as a function of pump–probe delay time (so-called 1D scans). In this case, a relative change in the amplitude of the transmitted THz probe pulse,  $-\Delta T/T_0$ , where  $T_0$  is the amplitude of THz transmission through unexcited sample, upon photoexcitation of the sample is measured. The  $-\Delta T/T_0$  is directly related to the real part of photoconductivity of the sample, and at small modulations  $|\Delta T/T_0| \ll 1$ , which is typically the case in organic semiconductors, the photoconductivity can be determined as<sup>198</sup>

$$\sigma_{\text{ph}} \approx \text{Re} \sigma_{\text{ph}} = -\frac{\Delta T}{T_0} \frac{1 + n}{Z_0 d} \quad (51)$$

The advantage of the technique is that real and imaginary parts of the conductivity can be obtained directly, without the need for Kramers–Kronig transformation. As a noncontact technique, it can be readily applied to studies of mobility and photogeneration efficiency anisotropy in organic crystals.<sup>361,413</sup>

The drawback is that charge carrier mobility ( $\mu$ , which is a sum of electron and hole mobilities) and photogeneration efficiency ( $\eta$ ) cannot be measured separately and are typically extracted as a  $\mu\eta$  product from the photoconductivity<sup>40,201</sup> or require additional information or analysis, often under assumptions of a particular model,<sup>530</sup> for their separation.

Measurements of transient photoconductivity using an optical pump–THz probe technique enabled observations of subpicosecond charge carrier photogeneration in a variety of organic single crystals and small-molecule and polymer films and their BHJs (Table 2, Section 8.1, Figure 22(a)).<sup>200,201,365</sup> They have also revealed “bandlike” behavior of charge transport,<sup>198,201</sup> enabled observation of power-law decay ( $\sim t^{-b}$ ) of photoconductivity on the picosecond time-scales in various crystals due to dispersive transport,<sup>40,198,201,365</sup> quantified crystal structure-dependent anisotropy in mobility,<sup>413</sup> established coupling of charge carriers to intermolecu-

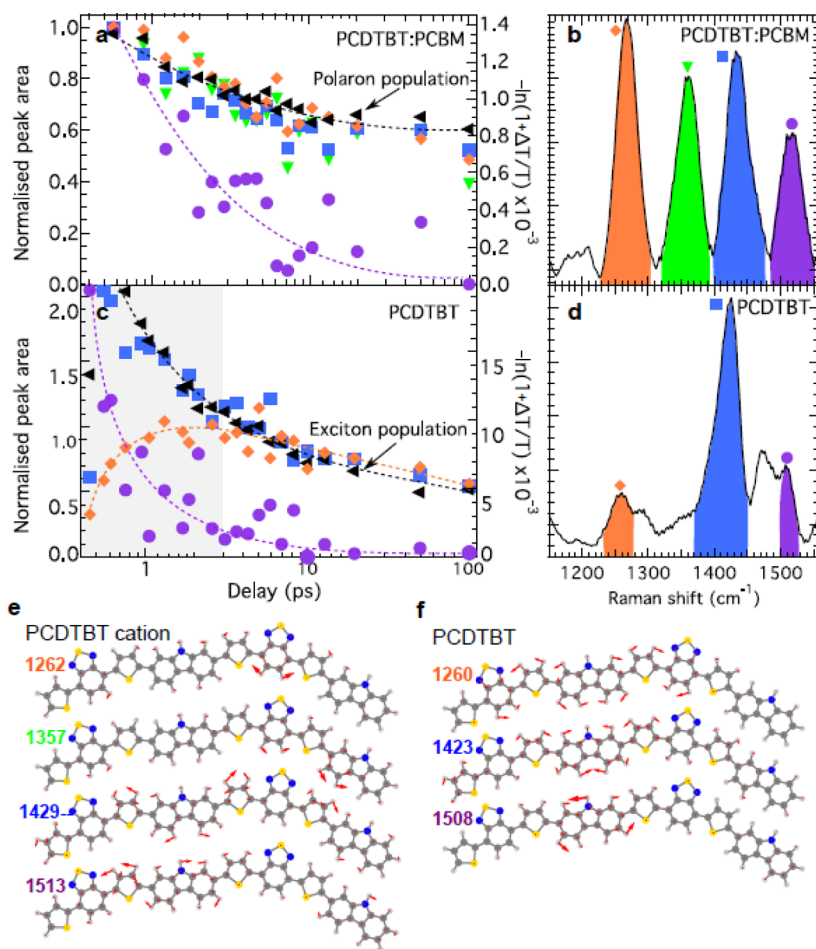


**Figure 17.** Dynamics of the stimulated Raman signals (obtained from Gaussian fits in (b) and (d), color-coded for different vibrational modes) obtained using FSRS and of the excited species population (black) obtained using TAS in a PCDTBT:PCBM blend (a) and in a pristine PCDTBT film (c). In the blend, the ultrafast CT leading to a sub-300-fs polaron formation is observed; no evolution of polaron vibrational signatures is then observed for the next  $\sim 50$  ps, indicative of hole-polarons free of the Coulomb interaction with electrons. In the pristine film, the exciton population evolves continuously over  $>100$  ps, indicative of ongoing structural evolution after the fast initial electron density redistribution. (e,f) Vibrational motion associated with the modes analyzed for the cation (e) and the neutral molecule (f). Reproduced from ref 376 under Creative Commons license 4.0 (<https://creativecommons.org/licenses/by/4.0>).

lar<sup>360</sup> and intramolecular<sup>361</sup> vibrational modes, and identified differences in charge trapping properties depending on crystal structure and film morphology (Tables 3 and 4).<sup>40,201,365</sup>

#### 7.1.1.1.3. Time-Resolved Microwave Conductivity (TRMC).

In this experiment, a sample is excited either with an optical pulse or with a highly energetic electron beam (in a so-called pulse radiolysis TRMC), and the transmission or reflection of the microwave probe pulse (i.e., at GHz frequencies) is monitored. This is a noncontact technique that allows one to probe real and imaginary parts of conductivity based on the decrease of the amplitude and/or a change in the phase of the electric field of the microwave probe, with nanosecond time resolution. An excellent overview of the technique was provided by Savenije et al.<sup>302</sup> Similar to the optical pump–THz probe spectroscopy, the technique measures photoconductivity, from which the product of charge carrier mobility (more precisely, a sum of electron and hole mobilities) and photogeneration efficiency then can be extracted, but it cannot separately measure these quantities. TRMC has provided valuable insights into nanosecond–microsecond charge carrier dynamics in polymers and polymer-based BHJs, as discussed throughout this review (e.g., Section 8.3).<sup>27,302</sup>

**7.1.1.1.4. Time-Resolved Vibrational Spectroscopy.** This comprises a variety of pump–probe techniques (including 2D techniques, such as 2D IR spectroscopy<sup>693</sup>), in which the probe is in the infrared (IR) wavelength region spanned by intramolecular vibrational modes ( $\sim 3$ – $10$   $\mu\text{m}$ ), and which measure time evolution of vibrational modes resulting from changes in the local environment. It provides information about molecular structure and charge carrier dynamics.<sup>694,695</sup> Various modalities of ultrafast time-resolved IR spectroscopy have been widely applied to studies of energy and charge transfer in photosynthetic systems,<sup>25,69,70,696</sup> of photoinduced dynamics in strongly correlated organic materials (e.g., CT complexes with strong electron–electron and electron–phonon interactions<sup>697</sup>), and of organic PV materials.<sup>693</sup>

In a technique that measures time-resolved photoinduced absorption by IR-active vibrational modes (IRAV), a sample is excited with a pump pulse at optical or near-IR wavelengths and is probed by a probe beam at wavelengths at which significant IRAV absorption occurs (e.g., at around  $10$   $\mu\text{m}$  in MEH-PPV). The IRAV absorption results from Raman-active vibrational modes that become infrared-active when the local symmetry is broken by self-localization of charges with associated changes in

the bond lengths (e.g., polaron formation).<sup>6</sup> The advantage of the IRAV measurements is in their ability to probe dynamics of exclusively charged excitations (as opposed to the convoluted response of charged and neutral excitations) with a sub-100-fs time resolution. Key insights obtained using IRAV spectroscopy include observations of wavelength- and temperature-independent ultrafast charge generation<sup>197,698</sup> in films of various PPV derivatives and polymer:fullerene blends and power-law ( $\sim t^{-b}$ ) carrier relaxation kinetics over many orders of magnitude in time in P3HT:PCBM.<sup>699</sup>

Jeong et al.<sup>694</sup> applied an approach called solvatochromism-assisted vibrational spectroscopy (SAVS), which utilizes the sensitivity of vibrational modes to their local electrostatic environments, to examine CT dissociation at D/A interfaces. They considered P3HT:PCBM and P3HT:BTBP-PDI blends and obtained time-scales (from time dependent vibrational frequency shifts) and energy barriers (from the temperature dependence of charge separation rates) for charge separation. Activationless CT was observed in the system with PCBM, whereas the activation energy of  $\sim 0.1$  eV was obtained with the nonfullerene acceptor. These observations were attributed to differences in delocalization of electronic wave functions, resulting in the lower CT state dissociation efficiency in the P3HT:BTBP-PDI blends.

Provencher et al.<sup>376</sup> applied time-resolved resonant Raman spectroscopy to study ultrafast charge photogeneration in PCDTBT:PCBM BHJs. They used the femtosecond stimulated Raman scattering (FSRS) method, in which a narrow-bandwidth Raman pulse stimulates scattering over various vibrational modes of the molecule and the broadband probe beam monitors Raman pulse-induced changes in the spectrum. By monitoring vibrational modes of the polymer that are sensitive to deformation of the molecular structure due to the presence of charge, at various time delays after ultrafast photoexcitation, they concluded that polarons formed within  $\sim 300$  fs (Figure 17). After that, the structural evolution was minimal, and the polymer conformation was similar to that in the equilibrium, which was interpreted as a signature of charge carriers being free from their mutual Coulomb interaction. In contrast, in pristine PCDTBT polymer, structural reorganization, accompanied by vibrational relaxation, persisted at least up to 100 ps after photoexcitation.

**7.1.1.1.5. Time-Resolved Two-Photon and X-ray Photoemission.** In a time-resolved two-photon photoemission (TR-2PPE) experiment, the pump beam excites an electron from the HOMO of the molecule into the excited states (e.g., into the free-electron-like image potential states (IPS) or CT states<sup>391,700</sup>). The time-delayed probe pulse ionizes these states, and the photoemission spectrum is measured as a function of pump–probe time delay. The technique provides insight into exciton dynamics and charge separation with a subpicosecond time resolution and is highly sensitive to surfaces ( $\sim 1$  nm), prompting its utility in studies of surfaces of pristine films and of organic–organic and organic–inorganic interfaces.<sup>49,701–704</sup>

Examples of important insights include determination of binding energies of the CT exciton in Pn films<sup>701</sup> and probing dynamics of hot CT states at CuPc/fullerene interfaces,<sup>244</sup> differentiation between IPS and CT states at surfaces of crystalline Pn and Tc,<sup>700</sup> and measurement of CT exciton delocalization dynamics in Hex films,<sup>391</sup> as well as observations of a sub-100-fs formation of excitons followed by self-trapping on the 400-fs time-scales in 6T films,<sup>702</sup> of the multiexciton

states in singlet fission in Pn,<sup>138</sup> of a sub-100-fs space charge field-assisted electron transfer from GaAs to C<sub>60</sub>,<sup>704</sup> and of a transition from coherent to incoherent exciton transport in ZnPc crystals (Section 2.1).<sup>49</sup> Dutton and Robey applied the TR-2PPE technique to examine exciton dissociation and recombination at CuPc/C<sub>60</sub>,<sup>705</sup> ZnPc/PTCDA, and H<sub>2</sub>Pc/C<sub>60</sub> interfaces.<sup>703</sup> In CuPc/C<sub>60</sub>, ultrafast charge separation, an excitation energy-dependent CT rate, and significant recombination to low-lying CuPc triplet states were observed. D/A systems with C<sub>60</sub> and PTCDA acceptors yielded comparable exciton dissociation rates, from which the authors concluded that the inherent features of the fullerene electronic structure are not a major factor in enhanced charge separation in HJs with fullerene acceptors. Instead, aggregation that enables carrier delocalization is of more importance, as has been emphasized in other studies as well.<sup>72,73,244</sup>

In time-resolved X-ray photoemission spectroscopy (TR-XPS), the optical probe pulse is replaced by the X-ray pulse train. For a comprehensive review of time-resolved X-ray spectroscopy, see ref 706. The TR-XPS can provide spatial selectivity of excited states, which can help probe the nature of the exciton dissociated state in OPVs.<sup>707</sup> For example, Arion et al.<sup>707</sup> applied the technique to CuPc/C<sub>60</sub> interfaces. They observed temporal evolution of the spectral signature of the charged C<sub>60</sub> state and concluded that the intermolecular CT in a CuPc domain is more than an order of magnitude slower than that in the C<sub>60</sub> domain.

**7.1.1.1.6. Time-Resolved Second-Harmonic Generation (SHG).** This technique relies on the measurement of electric-field-induced second harmonic generation (EFISHG) due to transient electric fields ( $E(0)$ ) created as a result of, for example, interfacial charge separation.<sup>138,708</sup> EFISHG is a four-wave mixing process, in which two optical fields of frequency  $\omega$  ( $E(\omega)$ ) mix with a quasi-dc field ( $E(0)$ ) to produce a resulting signal at  $2\omega$  with intensity

$$I(2\omega) \sim |\chi^{(3)}E(\omega)E(\omega)E(0)|^2 \quad (52)$$

where  $\chi^{(3)}$  is the third-order NLO susceptibility.

Examples of EFISHG utility in studies of organic optoelectronic materials include probing carrier lifetimes in organic solar cells<sup>709</sup> and molecular reorientation times in PR polymers,<sup>674</sup> typically with time resolution in the nanosecond to microsecond range. In an ultrafast version of the EFISHG measurement, a typical pump–probe experimental geometry is used, but the detected signal (e.g., reflected probe beam) is measured at the *doubled* frequency, as a function of pump–probe delay. This is an interface sensitive technique which, for example, enabled observations of ultrafast charge separation in CuPc/C<sub>60</sub> and Pn/C<sub>60</sub> HJs.<sup>138,708</sup>

**7.1.1.2. Other Time-Resolved Techniques Relying on Optical Detection.**

**7.1.1.2.1. Time-Resolved THz Emission.** In this technique, THz emission occurring as a result of charge carriers accelerated in an applied electric field is measured as a function of time, with subpicosecond time resolution.<sup>40,418,420</sup> The emitted THz field  $E_{\text{THz}}$  is proportional to the time derivative of the photocurrent ( $J$ ) in the far field,  $\partial J(t)/\partial t$ . The sample geometry is that of a photoconductive switch (e.g., a film on coplanar electrodes), one of the two most common methods to generate THz radiation (the other method being electro-optic rectification in a NLO material).<sup>530</sup> Using this method, ultrafast charge carrier generation in Pn<sup>40</sup> and oriented PPV<sup>420</sup> films was observed, and time-dependent picosecond

time-scales mobility in MEH-PPV films<sup>418</sup> was measured (Table 2).

**7.1.1.2.2. Pump–Push (or Dump)–Probe Spectroscopy.** Multiple ultrafast spectroscopy provides further insight into exciton and charge carrier dynamics and enables, for example, probing processes relying on coherence, such as coherent energy migration.<sup>14,25,64,69,70,696</sup>

In pump–push (or dump)–probe spectroscopy, the pump pulse generates singlet excitons, the “push” or “dump” pulse after a certain (typically fixed) time delay re-excites the sample, and the probe pulse detects the changes due to the “push” pulse as a function of the pump (or push)–probe time delay.<sup>710–712</sup> Using this technique, charge carrier generation with a yield of ~7% and 11% was observed upon promoting of the electron to a higher state with a ~0.5 eV or ~1 eV “push” pulse in pristine MeLPPP films<sup>713</sup> and P3HT<sup>710</sup> solutions, respectively, indicative of the importance of excess energy for charge generation in these materials.

Pump–dump–push spectroscopy has been extensively used in analysis of structural relaxation.<sup>711,714</sup> Busby et al.<sup>711</sup> examined the primary exciton relaxation mechanism in P3HT solutions and determined that torsional relaxation leading to excited-state self-trapping is the dominant mechanism. Clark et al.<sup>712</sup> studied oligofluorenes in solution and demonstrated that excitation to a specific higher-energy excited state (achieved by the “push” pulse) speeds up the torsional relaxation from ~10 ps to <0.1 ps due to efficient dumping of extra electronic energy into torsional modes. Musser et al.<sup>715</sup> examined the role of vibrational motion in ultrafast singlet exciton fission in TIPS-Pn films. In their experiments, a 10-fs pump pulse populated the first excited state and was followed by a ~650-fs “dump” pulse to remove a subpopulation of excitons by excitation into a higher-energy electronic state (here tuned to the T<sub>1</sub>–T<sub>2</sub> transition in TIPS-Pn). The comparison between differential transmittance of the white-light continuum probe beam with and without the “dump” pulse then provides information about residual vibrational coherence signatures of the triplet state. The authors concluded that singlet fission in TIPS-Pn is mediated by a conical intersection between the coupled electronic states.

**7.1.1.3. Techniques for Probing Exciton Coherence.** Review of various ultrafast spectroscopy modalities probing coherent processes can be found in ref 716. Coherence and its contribution to various aspects of exciton and charge carrier dynamics in organic optoelectronic materials and devices is one of the most intriguing current topics under investigation. For example, ultrafast photon–echo spectroscopy revealed that the initial (<200 fs) exciton relaxation in a benchmark material P3HT is highly correlated (not random) and the initial Stokes shift is driven by coherent low-frequency torsional excited-state self-trapping.<sup>717</sup> Two-dimensional electron spectroscopy (2DES) has emerged as an optical technique that can directly probe coherences, distinguish homogeneous and inhomogeneous line broadening, and detect correlations between excitonic states.<sup>69</sup> In this technique, three ultrafast laser pulses illuminate the sample, with controllable relative delays (coherence time  $t_1$  and waiting time  $t_2$ ). This pulse sequence creates a macroscopic third-order polarization (transient coherence) in the medium that generates the fourth pulse (which is the measured signal) in a unique phase-matched direction after some time delay (rephasing time)  $t_3$ .<sup>57</sup> A heterodyne detection performed by interfering the signal with the “load oscillator” pulse enables measurement of both the

amplitude and the phase of the signal electric field. (Detection of the signal using fluorescence, photocurrent, and electron emission has also been utilized.<sup>718–720</sup>) For a tutorial overview of phase-matching geometries utilized in various excitation-detection schemes, see ref 721.

The 2D spectrum contains the detected electric field as a function of excitation and emission (i.e., radiated FWM signal) frequencies at a given waiting time. Tutorial guides to 2D spectra interpretation can be found in refs 69 and 57, and a highlight is shown in Figure 18. The off-diagonal peak positions

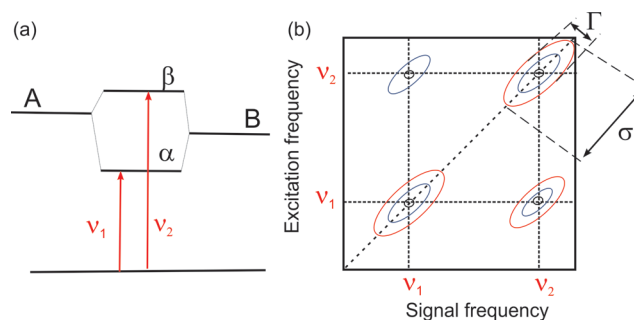


**Figure 18.** (a) Energy levels for a model dimer formed between two different chromophores A and B. (b) 2D spectrum of a dimer at a waiting time  $T$  between the pump and the probe pulses. The inhomogeneous ( $\sigma$ ) and homogeneous ( $\Gamma$ ) line widths are indicated. Off-diagonal peaks indicate that the states share a common ground state. The coherent superposition of states evolves in time with a phase factor  $\phi = i(E_\alpha - E_\beta)T/\hbar$ , where  $E_\alpha$  and  $E_\beta$  are the eigenenergies of the  $\alpha$  and  $\beta$  states (a)), which appear as oscillations in the amplitude of the off-diagonal peaks. The oscillations decay as the coherence dephases. Details can be found in ref 69.

provide information on the energy transfer pathways, whereas their dynamics probes coherent superpositions of exciton states which manifest in the oscillations of the peak amplitudes. However, distinguishing between electronic and vibrational coherences is a subject of current debate, as it is made complicated by the line broadening.<sup>69</sup> The 2DES has provided key insights into energy transfer mechanisms in light-harvesting complexes and is beginning to reveal important information on coherence in singlet fission,<sup>58</sup> charge transfer,<sup>403</sup> and exciton coupling,<sup>65</sup> as discussed in Section 2.2. A variety of multi-dimensional spectroscopy modalities, such as coherent photocurrent spectroscopy,<sup>720</sup> 2D fluorescence spectroscopy,<sup>722</sup> and 3D spectroscopy<sup>723</sup> are available and have been utilized in studies of biomolecules and inorganic semiconductor nanostructures; their applications to organic semiconductors are awaiting.

**7.1.1.4. Time-Resolved Photocurrent.** Techniques discussed in this section can be broadly classified as “optical excitation–electrical detection” techniques, which rely on measurements of time-resolved photocurrent under pulsed excitation. These experiments utilize short laser pulses for exciting a material and allow one to probe charge carrier dynamics with picosecond (ps) or better time resolution in devices.

**7.1.1.4.1. Pump–Push Photocurrent.** In this method, sub-100-fs pump (at visible wavelengths) and push (in the IR) pulses excite the sample, and the change in the photocurrent ( $J$ ) due to the push pulse (e.g.,  $dJ/J$  in Figure 12(a)) is measured with a photodiode as a function of the pump–push time delay.<sup>73</sup> This method was used in a variety of polymer- and small-molecule-based BHJs to demonstrate how charge

delocalization, facilitated by the push pulse excitation, promotes long-range charge separation<sup>73</sup> and to examine the dynamics of CT states created by hole or electron transfer in D:A BHJs,<sup>115</sup> in ternary polymer:polymer:fullerene blends,<sup>724</sup> and at organic–inorganic interfaces.<sup>725</sup>

**7.1.1.4.2. Auston Switch and Other Fast Photocurrent Probes.** In Auston switch configurations, electrodes are deposited on a glass substrate to form a microstrip transmission line with a back plane, and a film (crystal) is deposited (placed) on the top of two gaps: “injecting” and “sampling”. Short pulses of light, a pump and a probe, illuminate both gaps, and the time delay ( $\Delta t$ ) between the pulses is controlled by the optical delay line. One of the gaps (the “injecting” one) is biased, and the output signal generated in this gap by the photoexcited semiconductor under bias voltage serves as a bias for the second (“sampling”) gap. The quantity measured is the total charge ( $Q$ ) produced by the photoconductor in the “sampling” gap, as a function of the time delay ( $\Delta t$ ) between the pump and the probe optical pulses:

$$Q(\Delta t) \propto \int_{-\infty}^{\infty} v(t)v(t + \Delta t)dt \quad (53)$$

where  $v(t)$  is the signal produced by the biased photoconductor in the “injecting” gap. This approach is similar to NLO autocorrelation techniques utilized in measurements of duration of short laser pulses. From the photocurrent amplitude and dynamics, a product of mobility and photo-generated efficiency, as well as quantitative information on charge trapping and recombination, can be obtained.<sup>346,726</sup> The main advantage of the technique is in its time resolution, which can be as low as  $\sim 2$  ps,<sup>345</sup> and it can potentially be further improved by applying deconvolution algorithms.<sup>727</sup> This technique has been applied to demonstrate fast, electric field- and temperature-independent charge generation in a variety of polymer films and D:A blends.<sup>345,346,726</sup>

Fast oscilloscopes enable more direct measurements of time-resolved photocurrent, which is typically measured as a voltage across the load resistor. In this case, the transient photocurrent results from charge carriers generated by a short-pulsed illumination of a sample (e.g., a film deposited on a glass substrate with coplanar or interdigitated electrodes) that move under an applied electric field.<sup>729</sup> Under a 100-fs pulsed excitation and with a 50 GHz digital sampling oscilloscope detection, photocurrents with time resolution of  $< 30$  ps were measured in various functionalized ADT and Pn films.<sup>322,347,414</sup> In these experiments, the time resolution was limited by parasitic capacitance and inductance in the sample fixture and interconnects. An example of a photocurrent transient measured using this method in a TIPS-Pn thin film upon 100-fs, 400-nm laser pulse excitation is shown in Figure 22(b). From the peak amplitude, the product of charge carrier mobility ( $\mu$ ) and photogeneration efficiency ( $\eta$ ) can be calculated as  $\mu\eta = j_{\max}/(n_{\text{ph}}eF)$ , where  $j_{\max}$  is the peak photocurrent density,  $F$  is the electric field,  $e$  is the electron charge, and  $n_{\text{ph}}$  is the density of absorbed photons per pulse (Table 2).<sup>347,730</sup> However, given the complexity of processes contributing to the photocurrent (including different pathways of charge generation and different recombination processes), a considerably deeper insight is obtained by numerical modeling of the measured photocurrents.<sup>120,300,334</sup> Details on the procedure that enables extraction of various parameters pertaining to charge generation, transport, trapping, and recombination from time-resolved photocurrents can be

found in ref 120. A procedure based on the analysis of voltage-dependent transient photocurrents in solar cells that enables differentiation between geminate and nongeminate recombination was proposed in ref 731.

**7.1.2. Longer Time-Scale and Steady-State Measurements of Charge Carrier Dynamics.** Comprehensive reviews of well-established techniques for measuring charge carrier mobility using time-of-flight experiments, SCLC, (photo)CELIV, impedance spectroscopy, double-injection current, etc., along with discussions of their advantages and disadvantages, are available in refs 6, 732, and 733 and will not be considered here. An excellent tutorial review of experimental techniques assessing particular aspects of device physics can be found in ref 734. For new developments in the Hall effect measurements, see, for example, ref 735. Review of techniques specifically targeting properties of charge traps is also available.<sup>601</sup> Here a few selected methods, including less common, recently adapted, or newly developed techniques, are discussed.

**7.1.2.1. Techniques Relying on Optical Excitation–Electrical Detection.**  
**7.1.2.1.1. Photocurrent under Continuous Wave (cw) Illumination.** These experiments are performed on “sandwich”-type or “surface”-type samples (depending on the placement of the electrodes), and they involve measurements of photocurrent as a function of applied electric field, light intensity,<sup>347</sup> temperature,<sup>36,675,736,737</sup> magnetic field,<sup>660,738</sup> etc.<sup>37,356</sup> The experiment involves measurement of the total current under cw excitation of a sample ( $I_{\text{tot}}$ ), and the photocurrent ( $I_{\text{ph}}$ ) is then calculated as the difference between the total and the “dark” current ( $I_{\text{d}}$ ),  $I_{\text{ph}} = I_{\text{tot}} - I_{\text{d}}$ , from which the dark conductivity and photoconductivity ( $\sigma_{\text{d}}$  and  $\sigma_{\text{ph}}$ , respectively) can be calculated using, for example,  $\sigma_{\text{d (ph)}} = I_{\text{d (ph)}}/(FS)$ , where  $F$  is the applied electric field, and  $S$  (in the case of the sandwich sample geometry) is the electrode area. If the sample is highly absorbing, a more sophisticated scheme of extracting “intrinsic” photoconductivity values is necessary.<sup>739,740</sup> An excellent overview of the steady-state photocurrent behavior depending on the sample geometry, electrodes, and external parameters can be found in ref 741.

Results from the steady-state photocurrent measurements could be more difficult to interpret, as compared to those at ultrafast time-scales, as they incorporate a combination of many aspects of charge carrier dynamics in the material<sup>37,356</sup> and strongly depend on the properties of electrodes. An example of differences in the photoresponse measured from the same sample on the subnanosecond time-scales and in the steady state, depending on the electrode material, is discussed in ref 322. The steady-state photocurrent dependence on light intensity can provide information about charge trapping and recombination (Section 5.2.2).<sup>347</sup> The temperature dependence of the photocurrent has been used as a sensitive probe of glass transition temperature in PR polymers<sup>736</sup> and of phase transitions in PBI derivatives.<sup>737</sup> The magnetic field dependence of the photocurrent revealed the mechanisms of spin-mixing responsible for spin-dependent charge carrier recombination in polymer-based BHJs.<sup>660</sup>

The photocurrent can be measured as a function of time after the launch or cessation of the illumination, and parameters pertaining to charge photogeneration, trapping, and recombination properties can be extracted through numerical modeling. Numerical modeling of time-dependent cw photocurrents on the microsecond–second time-scales using drift-diffusion simulations enabled extraction of photoelectric parameters

that determine the dynamics of space-charge field formation in PR polymers,<sup>119,668</sup> quantifying trapping and recombination pathways in polymer BHJs,<sup>297,299,742</sup> and so on (Section 3.2.3). Studies of photocurrent dynamics beyond the ultrafast time-scales are important for characterization of materials with high density of deep traps and persistent photoconductivity, for understanding space-charge field effects resulting from charge accumulation in the bulk or at interfaces,<sup>743</sup> and for bridging the gap between charge carrier dynamics at ultrafast time-scales and performance of devices relying on photoresponse to cw excitation.

Frequency-dependent photocurrent under cw illumination, measured using lock-in detection, enables measurements of low-level signals and introduces another tunable parameter, the frequency (typically in the 0.001–10 kHz range), in the system. In these experiments, the lock-in amplifier is locked either to a chopper (or other modulator, such as an acousto-optic modulator) frequency when the light intensity is modulated<sup>347</sup> or to a frequency of an ac electric field applied to the sample.<sup>337,338</sup> For example, the latter measurement was employed to obtain trap distributions,<sup>337</sup> to establish a charge photogeneration mechanism,<sup>744</sup> and to separately determine photoexcited carrier concentration and mobility.<sup>338</sup> For a recent discussion of photocurrent spectroscopy and microscopy, see ref 321.

**7.1.2.1.2. Transient Photovoltage.** The transient photovoltage (TPV) technique<sup>622,654</sup> has been utilized in measurements of charge carrier dynamics in OPVs. In this method, solar cells are connected to the high-impedance terminal of an oscilloscope and illuminated with low-intensity white light ("light bias"), which controls the  $V_{oc}$ . Then, a nanosecond laser pulse creates a small optical perturbation which results in a voltage transient with an amplitude  $\Delta V_0 \ll V_{oc}$ , the dynamics of which is then related to the carrier lifetime as  $d\Delta V/dt \sim d\Delta n/dt = -\Delta n/\tau$ , where  $\Delta V$  is the photovoltage,  $t$  is the time,  $\Delta n$  is the change in the charge density due to the perturbing laser pulse, and  $\tau$  is the carrier lifetime. This technique has been applied to measurements of charge carrier lifetimes in organic solar cells and, in conjunction with charge extraction measurements, provided important insights into nongeminate recombination.<sup>636,637,745</sup>

**7.1.2.1.3. Time-Delayed Collection Field.** This technique is similar to pump–probe techniques, with an optical pump and electric probe, and it is sensitive to mobile and extractable charge carriers on time-scales of  $>0.1 \mu\text{s}$ .<sup>650</sup> The sample is illuminated by a nanosecond laser pulse (pump) while applying a constant prebias voltage  $V_{pre}$ . After a time delay  $\Delta t$ , a rectangular voltage pulse  $V_{coll}$  (probe) is applied to extract remaining free carriers. By varying  $V_{pre}$  and  $V_{coll}$ , one can separate field dependent charge generation and collection. The technique has been utilized, for example, in establishing field independent charge generation in P3HT:PCBM blends<sup>289</sup> and in probing the effect of additive solvent and molecular substitution in polymer:fullerene and polymer:polymer blends on charge carrier generation, recombination, and mobility.<sup>746,747</sup> Vandewal et al.<sup>383</sup> used this method to demonstrate that IQEs of  $>90\%$  in a variety of polymer-based and small-molecule-based BHJs can be achieved without the need for excess electronic or vibrational energy.

**7.1.2.1.4. Charge Extraction.** Charge extraction (CE) measurements, which were first applied to dye-sensitized solar cells<sup>748</sup> and subsequently adapted for use in OPVs,<sup>319</sup> enable determination of charge carrier concentrations. In conventional

charge extraction experiments,<sup>319</sup> a solar cell is initially held at a fixed point on the device  $J$ – $V$  characteristic either in the dark or under cw illumination. Then, it is switched to the zero bias (short circuit), with a simultaneous turning off the light (if any), which produces a current transient due to the charge carrier discharge at the electrodes. If the recombination losses during this time are small enough, the integral of this current transient with respect to time provides a measure for the excess charge in the cell under the  $J$ – $V$  condition specified before the switching. This technique, in conjunction with the TPV measurement, has been used to quantify recombination in solar cells and its effect on the open-circuit voltage ( $V_{oc}$ ) in a variety of polymer-based and small-molecule BHJs<sup>636,637</sup> and in planar HJs.<sup>745</sup>

A modification to the conventional CE technique, bias-amplified charge extraction (BACE), was recently proposed.<sup>749</sup> In BACE, charge extraction is accelerated by applying a reverse bias, to prevent losses due to charge trapping and recombination during the extraction (which are not accounted for by the conventional CE technique). The technique was applied to several polymer:fullerene blends (including P3HT:PCBM<sup>289,749</sup> and PCPDTBT:PCBM<sup>747</sup>) to quantify charge extraction depending on the polymer or fullerene derivative, film preparation conditions, and composition. Lange et al.<sup>750</sup> combined BACE with KFPM to quantify band bending at the polymer/electrode interfaces (F8BT, CN–ether–PPV, PFTBT, N2200 on Ag, Au, Al, Cr, Sm, MoO<sub>3</sub>, and conductive polymer electrodes), which was explained by CT from the electrodes to a small DOS that extends several hundreds of millielectronvolts into the band gap. The same states were found to govern charge carrier mobility in these polymers.

**7.1.2.2. Electro-optic Techniques.** Techniques discussed in this section utilize electrical excitation–optical probing for studies of charge carrier dynamics.

**7.1.2.2.1. Charge Modulation and Accumulation Spectroscopy.** Charge modulation spectroscopy (CMS) measures the change in the optical transmission spectrum of a FET or a diode upon application of a modulated electric field,<sup>563,751–753</sup> which can reveal optical signatures of localized and delocalized polarons.<sup>435,563</sup> In FET devices, a voltage bias consisting of the dc and a small ac component is applied to the gate to induce charge carriers, and the change in the transmitted probe light is detected using a photodetector and a lock-in amplifier locked to the frequency of the ac voltage. By changing the dc voltage component, the device can be operated in the accumulation or depletion regime. The CMS detects polaron-induced absorption and bleaching features related to injected charge carriers (i.e., in the absence of counterions, in contrast to chemical doping or photoexcitation). It allows for detection of polarons in the working FET device, in an accumulation  $\sim 1$  nm layer, and in a unipolar mode. It also enables discrimination between positive and negative polarons (which is a challenge in other techniques, such as optical pump–THz probe, TRMC, transient photocurrent measurements, etc.) that allows one to quantify charge carrier density.<sup>435</sup> The CMS spectra in the UV–visible range have been used in quantifying hole and electron delocalization<sup>563</sup> and in probing effects of the polymer chain conformation on polaron formation<sup>751</sup> in polymer FETs. In small-molecule FETs (e.g., rubrene and R-Pn), the CMS was used to establish temperature-dependent changes in charge delocalization.<sup>435</sup>

Chin et al.<sup>752</sup> extended the CMS technique to the mid-IR range, monitoring reflectance of the IR beam from working

P3HT FETs. In particular, they combined the mid-IR CMS with confocal FTIR microscopy to spatially map charge carrier density in FETs and observed polaronic and IRAG modes in the mid-IR CMS spectra (680–4000  $\text{cm}^{-1}$ ). The latter were related to charge oscillations along the polymer chain that have large oscillator strengths and serve as selective probes for polaron density and distribution. Through modeling their data, the authors were able to differentiate between oxidation-induced and electrostatically induced charge carriers. No polaron delocalization was observed at least up to  $3 \times 10^{16}$  holes/ $\text{cm}^2$  carrier density.

Spectroscopic determination of charged species has been instrumental for understanding the nature of charge traps and the source of degradation and/or illumination history dependence in device performance in PR organic materials.<sup>220,632</sup> For example, accumulation of fullerene anions (e.g.  $\text{C}_{60}^-$ ), which are generated in PR polymer composites with a fullerene sensitizer under cw illumination, can be quantified by monitoring formation of a characteristic spectral signature at  $\sim 1080$  nm.<sup>632</sup> A variant of this technique, charge accumulation spectroscopy (CAS), has been recently applied to studies of charge trapping and degradation pathways in n-type polymer FETs (e.g., p(NDI2OD-T2)).<sup>754,755</sup> The technique involves low-noise optical transmission measurement in FETs, concurrent with electrical measurements and atmosphere- and/or bias-stress measurements. It allows one to determine (independently) the concentration of polarons in the device from optical measurement of their associated charge-induced absorption. For example, this technique enabled quantitative description of degradation mechanisms due to oxygen and water exposure in p(NDI2OD-T2) FETs.<sup>755</sup>

**7.1.2.2.2. Nonlinear Optical Methods.** The nonlinear optical (NLO) techniques rely on optical detection of nonlinear polarization  $P_{\text{NL}} = \chi^{(2)}:E^2 + \chi^{(3)}:E^3 + \dots$  (where  $\chi^{(2)}$  and  $\chi^{(3)}$  are second- and third-order NLO susceptibilities and  $E$  represents optical or dc electric fields)<sup>756</sup> in working devices.<sup>757–759</sup>

Anglin et al.<sup>759</sup> applied vibrational sum frequency generation (SFG) spectroscopy to polymer TFTs to probe the relationship between interfacial polymer orientation and charge accumulation-related structural changes. In these experiments, visible ( $\omega_1$ ) and mid-IR ( $\omega_2$ ) pulses (tunable from 1000 to 2400  $\text{cm}^{-1}$ ) are spatially and temporally overlapped on the sample, and a reflected signal at frequencies  $\omega = \omega_1 + \omega_2$  is monitored. This is a coherent second-order ( $\chi^{(2)}$ ) NLO process that exploits selection rules of both Raman and IR spectroscopies, and it is highly interface-specific. This technique was used, for example, for detection of both hole and electron accumulation in a polymer PTAA in the absence of measurable source-drain currents<sup>759</sup> and for observation of the restructuring of P3HT/dielectric interfaces *in situ* during thermal annealing, which was linked to the device performance.<sup>760</sup> A model that allows one to extend the technique to probing multiple interfaces in stratified structures has also been proposed.<sup>761–764</sup>

An example of a third-order ( $\chi^{(3)}$ ) NLO process is EFISHG (Section 7.1.1.1), which was used to probe electric field distributions ( $E(0)$  in eq 52) in FET and in double-layer diode structures.<sup>757</sup> The ITO/PI/TIPS-Pn/Au diodes were excited with a nanosecond laser pulse at 1064 nm, and a step voltage was applied. A reflected SHG signal (at 532 nm) was observed at  $\sim 10$  ns to 25 ms after applying voltage. The time evolution of the SHG was related to charge injection from Au to TIPS-Pn, followed by charge transit through the TIPS-Pn layer and

subsequent charge accumulation at the TIPS-Pn/PI interface at  $<1$ -ms time-scales that completely screened the electric field in the TIPS-Pn layer.

**7.1.2.2.3. Other Electro-optic Methods for Monitoring Charge Carrier Dynamics.** Bittle et al.<sup>765</sup> measured frequency-dependent ( $<20$  kHz) mid-IR (700–1000  $\text{cm}^{-1}$ ) electro-reflectance in working TIPS-Pn FETs. The features observed in the IR spectra were attributed to Raman modes becoming IR-active due to polaronic distortions and were used to estimate mobility in TIPS-Pn crystals. Matsui and Hasegawa<sup>766</sup> developed a method of estimating spatiotemporal distribution of charge carriers in FETs using Fabri–Perot interference at an elastic polymer gate dielectric. This technique detects changes in the interference pattern due to modulation of the dielectric layer thickness induced by electrostatic forces between the accumulated charges. This method, for example, enabled spatial mapping of charging and discharging dynamics in the channel of working Pn TFTs with a parylene C gate dielectric.<sup>766</sup>

**7.1.3. Techniques for Probing Longer Time-Scale Exciton Dynamics and Steady-State Behavior.** Comprehensive descriptions of optical absorption and PL spectroscopy are available in books.<sup>687,767,768</sup> Here, recent efforts in measuring exciton dynamics on longer than ultrafast time-scales are briefly summarized.

Optical absorption and PL spectroscopy have been instrumental in obtaining information on intermolecular interactions (depending on the properties of molecules, molecular packing, and particular aspects of morphology and crystallinity) and their contributions to exciton dynamics.<sup>28,31,769,770</sup> Based on the theoretical description of spectra of molecular aggregates, a procedure was developed by Spano and co-workers<sup>91</sup> (Section 2.4) which enables extraction of the exciton bandwidth, static disorder, coherence length, etc. from spectra of aggregates formed in organic semiconductors (both small molecules<sup>28</sup> and polymers<sup>26,45</sup>). However, accurate modeling of the exciton coupling to vibrational modes is not simple, as both absorption and PL spectroscopy of organic materials suffer from experimental resolution limitations due to thermal fluctuations and static disorder. Several solutions that remedy these limitations have been proposed, including embedding the molecule into He droplets and single-molecule or quasi-single-molecule fluorescence spectroscopy. For example, Roden et al.<sup>771</sup> studied vibronic line shapes of PTCDA embedded in He droplets, and they were able to discern the contribution of several vibronic modes in the fluorescence emission spectrum.

High-sensitivity optical spectroscopy methods have also been developed. An example is photothermal deflection spectroscopy, which utilizes the heating effect produced in the process of nonradiative relaxation of the excited states. The heat generates a thermal gradient in the sample, which results in a refractive index gradient proportional to the absorbed light in the sample. This method has been utilized in high-precision measurements of an Urbach tail, over 3 orders of magnitude in absorbance, in polymer films (Figure 19),<sup>491</sup> as well as in detection of single metal nanoparticles<sup>772</sup> and nonfluorescent single molecules.<sup>773</sup>

Given the importance of CT states in optoelectronic materials, techniques that probe the CT nature of excited states are of importance. Electroabsorption spectroscopy, which measures a change in the optical absorption under a frequency-modulated electric field, is a common technique of choice. For example, Bernardo et al.<sup>72</sup> applied the technique to measure the polarizability of the CT exciton via the Stark effect in NPD:C<sub>60</sub>

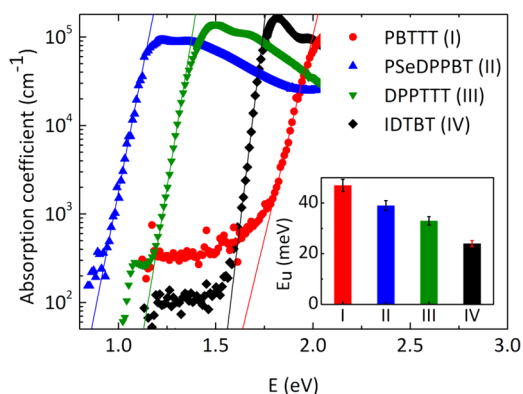


**Figure 19.** Normalized absorbance of polymer films measured using photothermal deflection spectroscopy (symbols). Solid lines show fits to the sub-bandgap region ( $E < E_g$ ) using  $a = a_0 \exp(E - E_g)/E_u$ , where  $E_g$  is the band gap and  $E_u$  is the Urbach energy (inset). For a variety of disordered polymers,  $E_u$  was found to correlate with the DOS width ( $k_B T_0$ ) obtained from modeling the FET characteristics ( $E_u \approx (k_B T_0)$ , Figure 24). Reproduced with permission from ref 389. Copyright 2014 Nature Publishing Group.

BHJs and established the link between CT exciton delocalization and the nanoscale-level crystallinity of fullerene domains.

With the current interest in the nature of low-energy excitons in molecular semiconductors (Section 2.3),<sup>79</sup> techniques that would unambiguously differentiate between Frenkel and CT excitons are desirable. Qi et al.<sup>84</sup> utilized high-resolution spectroscopic generalized ellipsometry, which measures changes in the amplitude and phase upon reflection of light from the sample, to obtain a polarization-dependent dielectric function in Pn single crystals. They were able to identify the admixture of Frenkel and CT excitons based on their distinct binding energy and the polarization dependence of the spectral features.

Time-resolved PL has been instrumental in quantitative assessments of energy and charge transfer characteristics,<sup>28,114</sup> probing of singlet fission and triplet fusion dynamics,<sup>148,152</sup> measurements of exciton diffusion coefficients,<sup>131</sup> differentiation between different photoexcited species,<sup>109</sup> and many others.<sup>687,767,768</sup> Labastide et al.<sup>357</sup> probed directional formation of charge-separated polaron pairs in TAT crystals using temperature- and polarization-dependent power-law decay of PL. An interesting example is detection of quantum beats in the time-resolved delayed PL in crystalline Tc due to coherent superposition of triplet states created by the singlet fission.<sup>148</sup> Tempelaar et al.<sup>55</sup> proposed a technique based on time-resolved PL measurements to probe the extent of spatial coherence, which involves measurement of the 0–0/0–1 PL intensity ratio (from fits to eq 5) as a function of time, which was recently realized by Sung et al.,<sup>105</sup> as discussed in Section 2.4.

Ward et al.<sup>130</sup> applied a transient grating technique to investigate exciton dynamics in rubrene crystals on the 20-ps to 10-ns time-scales. This method utilizes a FWM scheme (similar to that in Figure 20(b)), in which two optical pulses create an interference pattern leading to a spatially modulated excited state population that induces changes in the absorption or polarizability (“grating”). Then, the diffraction of the time-delayed probe pulse from the grating is detected. The method allows for a background-free detection of both absorption and refractive index change, which enabled, for example, observation of a power-law decay of the triplet states population due to bimolecular interactions.<sup>130</sup>

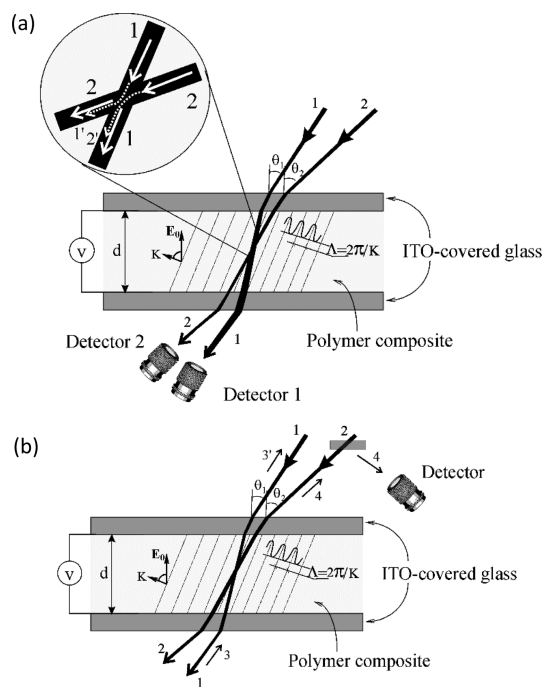


**Figure 20.** Experimental configuration used in characterization of PR materials: (a) two-beam coupling; (b) four-wave mixing geometry. Reprinted from ref 220. Copyright 2004 American Chemical Society.

Exciton diffusion length is an important parameter characterizing exciton dynamics in organic semiconductors. Measurements of this parameter using PL surface quenching, time-resolved PL bulk quenching combined with Monte Carlo simulations, spectrally resolved PL quenching, exciton–exciton annihilation (EEA), and TRMC, as well as by modeling of solar cell photocurrent spectra, have been reported. These measurements were reviewed in detail in refs 15, 16, and 131 and will not be considered here. Lin et al.<sup>131</sup> provided an overview of the pros and cons of the methods listed above for quantifying exciton diffusion and measured exciton diffusion lengths in DPP-based small-molecule films using six different experimental methods. They found very good agreement between different techniques when they were applied to amorphous films. However, it was established that in polycrystalline films the EEA-based method yielded a larger diffusion length than the techniques based on exciton quenching.

Techniques relying on PL imaging at microscopic spatial scales are summarized in Section 7.2.2.

#### 7.1.4. Photorefractive Properties Characterization.

The main mechanisms contributing to the PR effect are space-charge field formation (that relies on photoconductivity) and the electric field dependent refractive index change (Section 6). Therefore, techniques that probe charge carrier dynamics (Section 7.1) and the dynamics of the electric field-induced refractive index change (via that of birefringence<sup>675</sup> or EFISHG<sup>674</sup>) have been used to better understand the PR response of the material. For the PR device, the parameters of interest include PR grating formation, erasure, and dark decay times, two-beam coupling (2BC) gain coefficient  $\Gamma$ , and four-wave-mixing (FWM) diffraction efficiency  $\eta_{\text{FWM}}$ . Figures 20(a) and (b) show 2BC and FWM experimental geometries, respectively. A typical sample consists of two conductive but transparent indium tin oxide (ITO)-coated glass slides with a PR organic film of 30–100  $\mu\text{m}$  thickness in between. Optical

beams 1 (“probe” or “signal”) and 2 (“pump”) are incident at angles  $\theta_1$  and  $\theta_2$ , respectively, and interfere in the PR material, creating a nonlocal ( $\Phi \neq 0$ ) diffraction grating. Then the same beams 1 and 2 partially diffract from the grating they have just created (beams 1' and 2' in the inset of Figure 20(a)). Due to nonlocality of the grating, one diffracted beam (e.g., beam 1') interferes destructively with its companion beam 2, while the other diffracted beam 2' interferes constructively with beam 1. As a result, beam 1 is amplified (energy gain) while beam 2 is attenuated (energy loss). It should be emphasized that it is important that the energy transfer in PR materials persists in the *steady-state* because *transient* asymmetric energy exchange is known to occur in non-PR materials with local response (due to photochemistry, nonlinear optical susceptibility  $\chi^{(3)}$ , thermal modulation of the refractive index, etc.). The gain coefficient  $\Gamma$  can be determined from experimentally measured intensities as follows:

$$\Gamma = \ln(\beta_p I_1(\text{out})/I_2(\text{out}))/L \quad (54)$$

where  $\beta_p$  is the initial beam ratio (in the absence of coupling),  $\beta_p = I_2(\text{in})/I_1(\text{in})$ , and  $L$  is the interaction length  $L = d/\cos\theta_{1\text{int}}$  where  $d$  is a sample thickness. In some PR materials (such as DCDHF-based amorphous glasses) at  $\beta_p = 1$ , 2BC gain coefficients as high as  $400\text{ cm}^{-1}$  have been observed, so that almost complete energy transfer from beam 2 to beam 1 was achieved in a  $100\text{-}\mu\text{m}$ -thick film.<sup>675,740</sup>

The experimental geometry for the four-wave mixing (FWM) experiment is quite similar to that of 2BC; two writing beams, either cw or pulsed, are obliquely incident on the PR sample (Figure 20(b)). The difference is that, in the FWM experiment, in addition to writing beams 1 and 2, there is also a probe (reading) beam (beam 3 in Figure 20(b)) that is being partially diffracted from the grating created by the writing beams to create the fourth beam (beam 4). In the degenerate FWM geometry, which is common in PR measurements, beam 3 has the same wavelength as the writing beams and is usually chosen to be counter-propagating to one of the writing beams, as this results in a most efficient diffraction, as dictated by the Bragg condition,<sup>220</sup> and allows for background-free detection of very weak diffraction signals (beam 4). The diffracted beam intensity (i.e., that of beam 4) is typically measured as a function of time, applied electric field, writing beam intensities, etc. Then, the diffraction efficiency ( $\eta_{\text{FWM}}$ ), defined as the ratio  $\eta_{\text{FWM}}^{\text{ext}} = I_4/I_3$  (external diffraction efficiency) or  $\eta_{\text{FWM}}^{\text{int}} = I_4/(I_4 + I_3)$  (internal diffraction efficiency) is determined. Internal diffraction efficiencies of over 90% have been observed in a number of organic photorefractives (Table 7).<sup>220</sup>

## 7.2. Microscopic Scales

Understanding of exciton and charge carrier dynamics at micro- and nanoscales is necessary both from the device performance standpoint (as nanoscale morphology is one of the critical factors that determine BHJ performance<sup>774</sup>) and from the fundamental physics standpoint (enabling exploration of quantum coherence effects in molecular systems<sup>14</sup>). In this section, recent experimental efforts related to microscopy of organic optoelectronic materials are summarized.

**7.2.1. Scanning Probe Microscopy.** Scanning probe microscopy (SPM) methods have been utilized in measurements of current flows, resistance, capacitance, electrostatic forces, charge distribution, surface potential, PL, etc. with a sub-100-nm spatial resolution. Studies correlating morphology and charge generation, transport, and trapping properties at

microscopic scales in organic semiconductors have been performed using NSOM, conductive AFM/EFM (in some cases modified to study photoinduced carrier dynamics<sup>775–777</sup>), Kelvin probe scanning microscopy, etc. Information obtained from these experiments has been used to obtain insights into charge photogeneration,<sup>775–777</sup> identify bottlenecks in charge transport,<sup>778,779</sup> examine transport across grain boundaries,<sup>780</sup> probe the kinetics of charge trapping and detrapping,<sup>615,616,781</sup> etc. Reviews of SPM specifically applied to studies of photoinduced carrier dynamics can be found in refs 782 and 321. Comprehensive reviews of Kelvin probe force microscopy (KPFM),<sup>783–785</sup> as well as comparative reviews of different SPM techniques,<sup>786</sup> are available (Table S1). Below, a brief account of selected methods utilized in measurements relevant to charge carrier and exciton dynamics is provided.

**7.2.1.1. Kelvin Probe Force Microscopy.** The standard Kelvin probe force microscopy (KPFM) measures the electrostatic interaction between the sample and a vibrating (driven by an alternating bias  $V_{\text{ac}}$  with frequency  $\omega$ ) conductive probe mounted at the edge of a cantilever.<sup>783–785</sup> During the measurement, the Fermi levels of the probe and the sample align, causing an electrostatic force  $\mathcal{F}$  that depends on the surface potential difference  $\Delta_{\text{SP}}$  so that  $\mathcal{F}_{\omega}(t) = dC/dz(V_{\text{dc}} - \Delta_{\text{SP}})V_{\text{ac}} \sin(\omega t)$  (where  $dC/dz$  is the sample-probe distance dependent change in capacitance). Using a feedback circuit,  $V_{\text{dc}}$  is applied such that  $\mathcal{F}_{\omega}(t) = 0$ , in which case  $V_{\text{dc}} = \Delta_{\text{SP}}$  and, thus, a 2D map of  $\Delta_{\text{SP}}$  can be obtained. It is a noncontact technique that can be used to measure the work function and gain insight into bending and surface potential distribution even in poorly conducting films.<sup>749,784</sup> It can be employed in working devices such as FETs, and it can probe processes under illumination, such as charge photogeneration and detrapping.<sup>330</sup> For example, in P3HT-based BHJs, KPFM was utilized to observe charging and discharging dynamics of donor and acceptor domains in response to pulsed illumination.<sup>787</sup> The time resolution of this method is on the order of milliseconds, so faster processes (such as detrapping from shallow traps) cannot be probed. Data interpretation is not always straightforward and may require application of deconvolution algorithms.<sup>785</sup> Recent developments include multifrequency band excitation KPFM and 3D-KPFM techniques, which improve tip-sample deconvolution and bulk sensitivity.<sup>788</sup> For an overview of multifrequency force microscopy, see ref 789.

**7.2.1.2. Electric Force Microscopy.** Electric force microscopy (EFM) has the capacity to probe charge dynamics in organic semiconductors by measurements of the fluctuating electrical forces produced by these dynamics (e.g.,  $\mathcal{F}_{\omega}$  above).<sup>790</sup> An EFM employs a capacitatively charged AFM probe to sense electrical forces generated above the surface of a sample. Theoretical description of the two EFM observables, cantilever frequency fluctuations (related to low-frequency dynamics in the sample) and noncontact friction (related to high-frequency dynamics), can be found in ref 790. The method has been applied, for example, to studies of charge injection<sup>791</sup> and of charge traps in small-molecule (e.g., Pn, TIPS-Pn, and TES-ADT)<sup>615,616</sup> and polymer (e.g., PFB:F8BT or P3HT:PCBM)<sup>777</sup> films. Additionally, modeling of cantilever frequency noise over a working OTFT revealed the importance of including carrier-carrier Coulomb interactions into microscopic models of charge transport.<sup>792</sup>

Jaquith et al.<sup>615,616</sup> utilized time-resolved EFM in probing charge trap kinetics on the time-scales of 50 ms to tens of

seconds. The experiments revealed that traps in Pn and TIPS-Pn films were carrier concentration-dependent, and were created slowly by reactions of holes with a localized structural defect or impurity. Such reactions were not restricted to grain boundaries, and the traps could be cleared by illumination at wavelengths within the absorption spectrum of the film.<sup>793</sup> In contrast, in TES-ADT TFTs, traps were associated with grain boundaries, a similar finding to those in thin Pn films studied by KPFM.<sup>780,794</sup>

Ginger and co-workers demonstrated feedback-based time-resolved EFM operation with a 100- $\mu$ s time resolution,<sup>782</sup> which enabled time-resolved measurements of accumulation of photogenerated charges in OPVs.<sup>777,795</sup> These revealed single-exponential kinetics of charge accumulation with a rate directly proportional to local quantum efficiency and incident light intensity. An example of an important insight obtained in these measurements was that, in photoexcited PFB:F8BT blends, slower charging was observed near domain boundaries, indicating that most photocurrent was generated in the center of the domains, and not at D/A interfaces.<sup>777</sup> In a follow-up work,<sup>776</sup> a feedback-free scheme was proposed, with an  $\sim$ 100-ns time resolution and flexibility that enables its implementation in any experiments with a time-dependent force gradient. The improved time resolution enabled demonstration of the correlation between microsecond photocharging dynamics at nanoscales and variations in the OPV efficiency in a prototypical blend P3HT:PCBM.

**7.2.1.3. Conductive AFM.** Standard conductive AFM (c-AFM) involves scanning a conductive tip across a sample at a fixed voltage and recording a current map simultaneously with the topography;<sup>796</sup> for a brief recent review of c-AFM applications to studies of charge carrier dynamics in OTFTs and OPVs, see ref 797. Dante et al.<sup>798</sup> monitored changes in charge transport upon thermal annealing simultaneously with changes in film morphology of P3HT:PCBM blends. Pingree et al.<sup>799</sup> used photoconductive c-AFM to examine spatial variations in the photocurrent across various domains in P3HT:PCBM blends as a function of annealing. They found that, after annealing, the regions of the highest dark hole currents, highest dark electron currents, and highest photocurrents were each associated with different regions of the nanostructured films.

Although lateral spatial resolution down to  $\sim$ 5 nm has been demonstrated,<sup>800</sup> quantitative analysis of charge transport is complicated by the uncertainty in the tip-sample contact area.<sup>801,802</sup> To rectify this uncertainty, c-AFM was used to simultaneously map out mechanical and electrical properties (e.g., of P3HT films<sup>802</sup>). Using force-volume bias spectroscopy (FVBS), which generates an array of force-distance and current-voltage measurements, grain boundary-limited transport from room temperature to 110 °C was observed, and correlations between the sample stiffness and mobility suggestive of increased order in the film at higher temperatures were demonstrated.

Uttiya et al.<sup>801</sup> used c-AFM to screen microscopic single crystals of novel rubrene derivatives with enhanced photostability for their charge transport capabilities. Hourani et al.<sup>803</sup> observed anisotropy in charge transport in (3HT)<sub>8</sub> microcrystals. In small molecule:polymer films (e.g., TIPS-Pn:PTAA and diF TES-ADT:PTAA<sup>804</sup>), c-AFM studies established the existence of highly conductive grain boundaries, not present in pristine TIPS-Pn or diF TES-ADT films, which makes the device performance of such devices morphology-independent

(which is of important technological relevance) and improved with respect to that of pristine films.<sup>805</sup> Takacs et al.<sup>775</sup> used polarization-dependent photoconductive AFM to map out orientational order in BHJ solar cells. They were able to reconstruct the molecular director maps in p-DTS:PCBM BHJs comparable to those obtained via dark-field TEM imaging.

**7.2.1.4. Scanning Tunneling Microscopy.** Scanning tunneling microscopy (STM) relies on tunneling of charge carriers through a thin barrier between the biased tip and the sample which is typically deposited on a conductive surface. Because transmission through the barrier is ultrasensitive to the barrier width, STM images surface topography with atomic resolution; additionally, scanning tunneling spectroscopy (STS), in which the tunneling current ( $I$ ) is measured as a function of bias ( $V$ ), can be performed to obtain local DOS (which is proportional to  $dI/dV/(I/V)$ ). Also, measurements of  $d^2I/dV^2$  can provide information about the vibronic structure of a single molecule<sup>806</sup> and coupling of the electron with vibrational modes.<sup>807</sup>

STM has been utilized in imaging molecular arrangements at metal/organic interfaces<sup>808–813</sup> with a subnanometer precision, characterization of polymorphism in 2D self-assembled organic monolayers,<sup>814</sup> and visualization of assemblies of H-bonded materials.<sup>815–817</sup> Skomski et al.<sup>808</sup> imaged surface self-assembly of small molecules with an electron-deficient core and electron-rich units into a crystalline film. Wang and Dougherty<sup>818</sup> studied  $\alpha$ -6T films on C<sub>60</sub>/Au(111) substrates and showed that defects due to molecular sliding caused by intermolecular interactions modulated by the C<sub>60</sub> substrate did not affect the HOMO, pointing to extrinsic sources behind the electronic disorder. STM imaging in organic devices is complicated due to low intrinsic conductivity of organic semiconductors. Nevertheless, Roelofs et al.<sup>819</sup> demonstrated that STM/STS can be used on a working FET, and they were able to image Pn FET in the accumulation mode.

The sub-single-molecule spatial resolution of the STM enabled mapping of fluorescence<sup>820</sup> and vibrational<sup>821</sup> spectra from a single molecule, monitoring molecular conformations,<sup>822</sup> quantifying charging of single impurities in organic crystalline monolayers,<sup>823</sup> and inducing photon emission from a single molecule using an STM tip.<sup>824</sup> Recently, Ho and co-workers demonstrated rotational and vibrational spectroscopy on single molecules.<sup>825</sup>

STS was used to probe the electronic structure of small molecules<sup>826,827</sup> and conjugated polymers<sup>828</sup> on various surfaces, electronic coupling and surface reactivity at metal/organic interfaces,<sup>829–831</sup> the distribution of HOMO and LUMO levels in films depending on the position on the film,<sup>832</sup> intermolecular and molecule-defect interactions,<sup>833,834</sup> single-bond formation and dissociation,<sup>835</sup> and spin-splitting of single-molecule vibronic states under a magnetic field.<sup>836</sup>

Spin-polarized STS (SP-STs) that utilizes a ferromagnetic tip<sup>837</sup> has probed magnetization in molecular monolayers,<sup>838</sup> spin transport through a single molecule,<sup>839</sup> and tunneling magnetoresistance in molecular junctions.<sup>840</sup> Time-resolved STM methods have also been developed.<sup>841–843</sup> For example, Cocker et al.<sup>844</sup> demonstrated a THz-STM which enables measurements with sub-500-fs time resolution and sub-2-nm spatial resolution.

**7.2.1.6. Near-Field Scanning Optical Microscopy.** Near-field scanning optical microscopy (NSOM) (also referred to as SNOM) enables simultaneous assessment of surface topology and optical absorption, PL, and/or photoconductive properties, with a subdiffraction-limited spatial resolution.<sup>795,845,846</sup> In

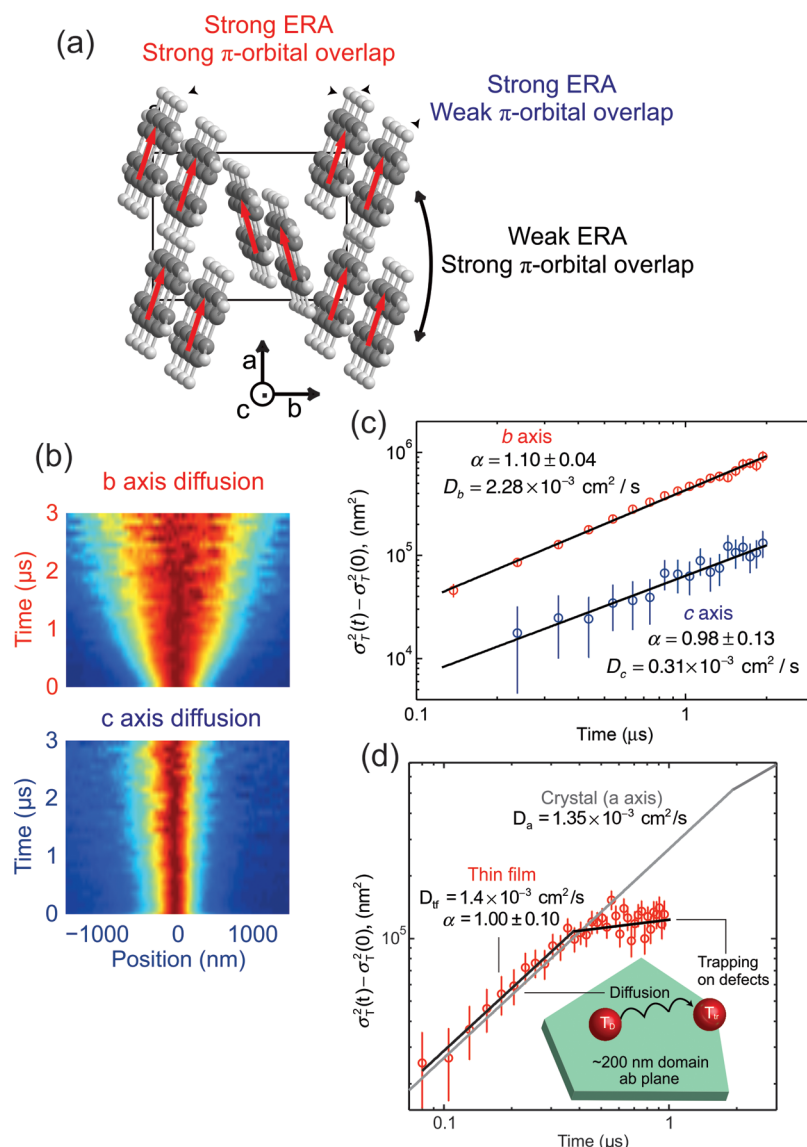


**Figure 21.** (a) Crystal structure of Tc. Red arrows indicate the optical transition dipole moment. The  $\pi$ - $\pi$  overlap is considerably higher in the  $a$ - $b$  plane than along the  $c$ -axis, resulting in large Dexter transfer anisotropy. (b) Normalized spatiotemporal maps of the emission intensity along the  $b$ -axis and the  $c$ -axis of the Tc crystal. (c,d) Time evolution of the triplet exciton mean square displacement along the  $b$ - and  $c$ -axes (c) and the  $a$ -axis (d) of the Tc crystal. Diffusion coefficients obtained from the data are also included. Data for a polycrystalline film are also included in (d), showing the transition to the subdiffusive regime due to exciton trapping at domain boundaries and defects. Adapted with permission from ref 852. Copyright 2014 Nature Publishing Group.

recent studies of organic semiconductors, NSOM was used to establish the effects of aggregation on the device performance;<sup>847</sup> it enabled domain spectroscopy in domains with different molecular order and crystallinity in oligomeric PQT-12 films<sup>848</sup> and in P3HT:p(NDI2OD-T2) copolymer blends,<sup>847</sup> and it revealed various polymorph phases in rubrene microcrystals.<sup>849</sup>

Materny and co-workers<sup>850,851</sup> developed a near-field pump-probe (PP-NSOM) spectroscopy, which they applied to PTCDA films. In PP-NSOM, pump and probe laser pulses, time-delayed with respect to each other, are collinear and are incident on the sample via a microscope objective. The probe pulse transmitted through the sample is collected with a NSOM tip, and it provides information on exciton dynamics with a nanoscale spatial resolution, and with a better image contrast than the conventional NSOM. The authors were able to map out the exciton-exciton annihilation rate in PTCDA films,

showing that it is overestimated in far-field experiments.<sup>850</sup> To obtain chemical specificity, NSOM-CARS was developed. This technique relies on contrast originating from vibrations of the nuclei and on high signal strength due to the coherent nonlinear interaction. In the CARS process, there are three incident laser fields. The frequency difference between the pump pulse ( $\omega_p$ ) and Stokes ( $\omega_s$ ) pulse is tuned to be in resonance with a vibrational mode of the molecule ( $\omega_p - \omega_s = \Omega_R$ ). The coherent excitation of the vibration makes the third probe pulse ( $\omega_{pr}$ ) scatter at the anti-Stokes frequency  $\omega_{as} = \omega_p - \omega_s + \omega_{pr}$ , which is the CARS signal. In a degenerate CARS scheme,  $\omega_p = \omega_{pr}$ . In the near-field CARS, the signal is detected through the NSOM tip. The authors were able to demonstrate NSOM-CARS imaging of P3HT films and surface-enhanced CARS in pyridine films.<sup>851</sup>

**7.2.2. Optical Absorption and PL Imaging.** Absorption and PL microscopy of organic semiconductors has been widely

utilized to visualize domains and D/A interfaces in D:A blends,<sup>188</sup> quantify exciton diffusion,<sup>128,137,852</sup> examine the nature of exciton states depending on the molecular order in crystalline films,<sup>109</sup> probe exciton delocalization,<sup>853</sup> and so on. Combinations of PL microscopy with Raman spectroscopy has enabled probing of the chemical composition of domains in organic films<sup>854,855</sup> and domain orientations in microcrystals.<sup>856</sup>

Irkhin and Biaggio<sup>128</sup> analyzed a spatial profile of steady-state PL emission from rubrene crystals, relative to that of the focused excitation, to probe anisotropy in exciton diffusion. They related spatial the exponential decay of the PL intensity away from the excitation position to formation of singlet excitons from fusion of triplet excitons (which had formed by singlet fission on picosecond time-scales) and inferred a triplet exciton diffusion length of 4  $\mu\text{m}$  along the *b*-axis of the crystal.

Akselrod et al.<sup>852</sup> imaged microsecond time-scale time-delayed fluorescence (TDF) resulting from triplet fusion to visualize and quantify triplet exciton transport in Tc. For that, they excited singlet excitons with a 100-fs laser focused to a diffraction-limited spot and obtained the image of TDF by scanning the sample with a small-area time-resolved SPAD to obtain a map of time-dependent singlet exciton density, which is then converted to that of triplet exciton density. From time-dependent triplet exciton density, the diffusion constant was calculated yielding  $1.35 \times 10^{-3} \text{ cm}^2/\text{s}$ ,  $2.28 \times 10^{-3} \text{ cm}^2/\text{s}$ , and  $0.31 \times 10^{-3} \text{ cm}^2/\text{s}$  along the *a*-, *b*-, and *c*-axes of Tc, respectively (Figure 21). From these constants, the diffusion lengths were obtained (yielding, e.g., 0.61  $\mu\text{m}$  along the *a*-axis). At times  $>2 \mu\text{s}$ , the transition from random walk diffusion to subdiffusion was observed in Tc films as excitons became trapped at or by the domain boundaries.

Deotare et al.<sup>137</sup> used a similar method (involving an optical microscope with a scanning detector) to characterize the physical diffusion of tightly bound CT states by imaging the transient PL. They used a TADF material (Section 2.7.2) (m-MTDATA:3TPYMB D:A blend) with long-lived CT states and monitored their diffusion over  $\sim 5\text{--}10 \text{ nm}$  before relaxing into lower-energy CT states.

Sharifzadeh et al.<sup>853</sup> combined spatially resolved, polarization-dependent optical absorption measurements with the *ab initio* excited-state calculations to determine relative grain orientations in polycrystalline TIPS-Pn films and their effect on the exciton dynamics. They established that the lowest-energy exciton is delocalized over  $\sim 3 \text{ nm}$ , which could play a role in the efficient singlet fission in this material, and is contained in the *a*-*b* plane of the crystal.

Rawat et al.<sup>109</sup> performed spatially-, temporally-, and polarization-resolved PL/linear dichroism microscopy on metal-free phthalocyanine ( $\text{H}_2\text{-OBPC}$ ) crystalline films. The measurements revealed the temperature-induced switching between localized and delocalized exciton states, which was related to the change in the molecular tilt with respect to the  $\pi\text{-}\pi$  stacking axis.

**7.2.3. Ultrafast Time-Resolved Microscopy.** Ultrafast pump-probe microscopy emerged as a powerful tool for investigations of exciton dynamics with a sub-100-fs time resolution and diffraction-limited spatial resolution.<sup>857–862</sup> This technique combines the advantages of an ultrafast time resolution enabled by a pump-probe methodology (Section 7.1.1) and  $\sim 150\text{--}250\text{-nm}$  spatial resolution enabled by confocal microscopy; see a comprehensive review in ref 860. Polli et al.<sup>857</sup> applied the technique to study the photophysics of PFO/PMMA interfaces. Grancini et al. mapped out the

electron transfer process across the P3HT/CdSe nanocrystal interface<sup>863</sup> and revealed an intercrystallite long-lived CT state at P3HT:PCBM interfaces.<sup>859</sup> Wong et al. observed a hot exciton vibrational relaxation followed by singlet fission and recombination with a kinetics depending on the domain<sup>862</sup> and revealed hidden interfaces<sup>861</sup> in polycrystalline TIPS-Pn films. Wan et al.<sup>156</sup> were able to visualize singlet and triplet exciton transport in single Tc crystals using polarization-dependent transient absorption microscopy. The authors demonstrated a coupled triplet and singlet exciton transport that led to a more than an order of magnitude enhancement in the diffusion constant for the triplet excitons on picosecond and nanosecond time-scales.

Recent advances in super-resolution microscopy<sup>864,865</sup> have laid foundations for various methods enabling subdiffraction limited optical imaging, which are now awaiting applications in high-resolution optical imaging of organic semiconductors. Toward this goal, for example, Penwell et al.<sup>866</sup> demonstrated fluorescence imaging of CN-PPV nanoparticles with a 90 nm resolution using stimulated emission depletion (STED) microscopy.

Voronine et al.<sup>719</sup> introduced a coherent 2D nanoscopy, which utilizes an ultrafast FWM methodology but with all 4 optical fields incident (in contrast to three incident and the fourth outgoing in a traditional FWM scheme, as in Figure 20(b)), with time delay between the pulses. The technique uses a wide-field illumination (thus 2D spectral information is collected simultaneously from a large area) but detects locally generated photoelectrons via photoemission electron microscopy (PEEM). This method overcomes the diffraction limit and provides resolution of about 50 nm, enabling imaging of nanoscale coherence.

Recently, ultrafast spectroscopy of individual molecules was demonstrated, as discussed in the following section.

**7.2.4. Single-Molecule Fluorescence Spectroscopy.** Single-molecule fluorescence spectroscopy (SMFS) has been widely utilized in probing nanoscale interactions and local nanoenvironment in a variety of media, including biological systems, polymers, and crystals. Comprehensive reviews of SMFS studies relevant for organic optoelectronics can be found in refs 867–873.

The requirements for the molecule that determine its suitability for studies using SMFS include high fluorescence QY ( $\Phi_f$ ) and high photostability. For the latter, the quantitative measures are the photobleaching QY,  $\Phi_B$  (Section 2.1), or the total number of photons the molecule emits before photobleaching,  $N_{\text{tot}}$ . For the best SMFS fluorophores,  $\Phi_B < 10^{-6}$  and  $N_{\text{tot}} > 10^6$ . The molecules of interest are typically incorporated in nonemissive solid hosts at ultralow concentrations, they are excited with a cw light, and their fluorescence is monitored using wide-field or confocal geometry (e.g., with an EMCCD or SPAD, respectively). The measurements can be done as a function of temperature, polarization of incident or emitted light, applied electric fields, etc. Many semiconducting polymers (such as PPV derivatives,<sup>874–878</sup> P3HT,<sup>879,880</sup> and PFO<sup>881,882</sup>) and small organic semiconductor molecules (such as Pn,<sup>868</sup> PDI,<sup>883–885</sup> and functionalized ADT and Pn derivatives<sup>35</sup>) have satisfied these requirements and have been subjected to SMFS studies. For example, single molecules of functionalized ADT (such as diF TES-ADT) and fluorinated Pn (such as F8 R-Pn) derivatives were imaged at room temperature in PMMA and BTBTB hosts, exhibiting  $\Phi_f$  of 0.7–0.9,  $\Phi_B$  of  $(1\text{--}2) \times 10^{-6}$ ,

and  $N_{\text{tot}}$  of  $(4-8) \times 10^5$  in PMMA, depending on the derivative (Table 1).

Single molecules can serve as sensitive probes of local changes in polarity, viscosity, the relaxation dynamics of the host, acoustic resonances, etc.<sup>397,886-889</sup> in various heterogeneous environments. The 2D or 3D rotational diffusion of a single-molecule probe introduced in a host polymer matrix can be analyzed to gain insights into polymer dynamics,<sup>890,891</sup> establish a degree of order in a host matrix,<sup>892</sup> and monitor electric-field-induced poling at the nanoscale.<sup>893</sup> Single-molecule probes have also provided information about defects,<sup>894</sup> temperature- and/or time-dependent structural dynamics,<sup>895,896</sup> and conduction.<sup>897</sup>

Analysis of the intermittency of fluorescence emission (i.e., blinking) may provide valuable insight into various conformational changes, reversible transitions to dark states, and interactions with a local environment.<sup>898,899</sup> For example, blinking statistics due to the intersystem crossing (ISC) to the triplet state is expected to be exponentially distributed,<sup>900</sup> whereas that due to photoexcited charge exchange between the molecule and a host results in more complicated distributions, such as power-law, log-normal, and Weibull, depending on the interaction.<sup>901</sup> In quantum dots and semiconductor nanocrystals,<sup>902-905</sup> blinking statistics were used to determine the energetic and kinetic properties of charge separated states. The origins of such distributions in organic molecules are less understood, and relating blinking statistics to the molecule's charge and energy exchange with the surrounding medium is of considerable interest,<sup>906-908</sup> especially in materials relevant for organic optoelectronic devices. Steiner et al.<sup>879</sup> analyzed the blinking dynamics of single P3HT chains, depending on the molecular weight and excitation intensity, and they demonstrated a dramatic decrease in fluorescence related to transformation from unfolded to folded chains, which was attributed to singlet-triplet annihilation (Section 8.3). Hoogenboom et al.<sup>909</sup> studied blinking dynamics in PDI trimers embedded in PMMA, which revealed the presence of dynamic charge tunneling between the PDI and PMMA. Wilma et al.<sup>910</sup> related spectral changes in a PBI molecule in PS during the blinking event to the diffusion of electrons in the PS matrix and calculated the distributions of local electron mobility in PS.

Another important property relevant for optoelectronic materials, which can be probed using SMFS, is exciton localization/delocalization characteristics. It has been demonstrated that SMFS with polarization-dependent excitation and emission enables estimation of the degree of exciton localization in the excited state.<sup>911</sup> Da Como et al.<sup>912</sup> established exciton delocalization over  $\sim 500$  repeat units in single PFO chains. Lippitz et al.<sup>913</sup> observed dynamic changes between localized and delocalized exciton states in biperyleneimide dimers, which were accompanied by line shape changes of the emission spectra, fluorescence intensity, and lifetime. In ref 914, spontaneous symmetry breaking in the excited state was observed in  $\text{Ir}(\text{piq})_3$ , a model OLED triplet emitter, which caused stochastic switching of the molecular dipole moment between the three ligands. Aggarwal et al.<sup>915</sup> demonstrated nondeterministic exciton localization in  $\pi$ -conjugated macromolecules. In a follow-up study, Thiessen et al.<sup>916</sup> established the effects of torsional relaxation in oligomers and cyclic structures on exciton localization. Adachi et al.<sup>917</sup> studied single chains of PFO, ensuring that only one chromophore on the single chain is photoactive at a time and used photon correlation spectroscopy. They observed differences in spectra,

emission dynamics, and photon statistics in "glassy" (with chromophores twisted with respect to each other) and  $\beta$ -phase (planarized) PFO. They concluded that the degree of structural relaxation in the excited state determines the exciton coherence length, which controls fluorescence lifetime. In particular, bending of single chains was correlated with increased fluorescence lifetime due to the decrease in exciton coherence length.

An important feature of the SMFS is that it can differentiate between dynamic and intra- and intermolecular disorder.<sup>880,918</sup> For example, Thiessen et al.<sup>880</sup> quantified interchromophoric disorder in P3HT responsible for the broad optical absorption spectrum. Stangl et al.<sup>75</sup> directly observed temporal fluctuations in the coupling of cofacial oligomers. Honmou et al.<sup>882</sup> observed EL and PL from a single PFO chain and established the keto defect-related origin of the unwanted green emission band that degrades the color purity, stability, and efficiency of PFO-based OLEDs. They were also able to observe charge-assisted formation of ground-state dimers.

Intra- and intermolecular interactions, important for optoelectronic devices, have also been studied using SMFS. Yoo et al.<sup>919</sup> quantified excitonic coupling as a result of interchromophore interactions in PDI trimers. Schindler and Lupton<sup>920</sup> were able to manipulate interchromophoric coupling (intrachain FRET) in single LPPP polymer chains by electrothermal modulation, which modulated the local dielectric environment. Intramolecular FRET in conformationally controlled dimers has also been extensively studied.<sup>75,921</sup>

Several studies addressed film-processing and working device-specific effects on the molecular photophysics. For example, Vogelsang et al.<sup>871,878</sup> established single MEH-PPV polymer chain dynamics during solvent vapor annealing. Nicolet et al.<sup>922</sup> used spectral lines of emission from single DBT molecules embedded as SM probes in a working Ac FET to probe the local electric field distribution due to charge injection in Ac. They observed trapping/detrapping events at the silica-Ac interface that were power-law distributed in time at 1.4 K.

New methodologies that enable high-accuracy 3D localization of molecules and determination of the rotational mobility of the molecule have been recently developed by the Moerner group.<sup>923-925</sup> Winterhalder et al.<sup>926</sup> proposed a three-photon fluorescence excitation scheme for extraction of chemically sensitive vibrational information for a single fluorescent molecule at room temperature. In this scheme, two simultaneous pump beams ( $\omega_1$  and  $\omega_2$ ) prepare the vibrational population (the vibrational hot band), which is then probed with a third pulse ( $\omega_3$ ) by converting the vibrational state population into a population of the fluorescent state. The resulting anti-Stokes fluorescence is blue-shifted with respect to  $\omega_3$  by vibrational energy. The intensity of this hot band fluorescence depends on the vibrational population, and by tuning  $\omega_1$  or  $\omega_2$ , one obtains spectroscopic information on the vibrational state of the molecule. The scheme has a similarity to CARS, but here only vibrational modes that strongly couple to the electronic transitions are addressed, which is necessary for a single-molecule level of sensitivity.

An exciting recent development in the SMFS field is the capability of performing ultrafast spectroscopy on single molecules, for example by combining time-resolved pump-dump spectroscopy with single-molecule-level detection capability. An excellent tutorial review of the subject is available in ref 869. With these approaches, the electronic and vibrational

dynamics of single molecules can be studied at room temperature. This enabled observations of electronic coherence/decoherence, vibrational wavepacket interference, and quantum control of single molecules.<sup>66,927</sup> One particular result is that the single-molecule approach enabled a more realistic assessment of coherence in particular units of complex molecules (such as light-harvesting complexes), as coherence times from bulk experiments are underestimated due to inhomogeneous averaging. Another important point is that the ergodicity principle (time-averaging equals ensemble averaging) does not hold for investigations on systems which engage into *functional* interactions with a structured environment, and therefore SMFS provides an opportunity to understand the functional characteristics of complex molecules.

Several methods (e.g., utilizing photothermal contrast) were developed for observation of a single molecule through absorption (rather than fluorescence) at room temperature.<sup>773,928,929</sup> Also, coupling of the single-molecule emission to plasmonic nanoantennas, which enables *directional* emission, has been demonstrated.<sup>930–932</sup> Efforts toward accessibility of SMFS have also been made—for example, a portable low-cost imaging system for fluorescence microscopy of single nanoscale objects using a smart phone was reported.<sup>933,934</sup>

### 7.3. Summary

The experimental capabilities discussed in this section illustrate a wide variety of modern techniques available for characterization of the optical and electronic properties of organic optoelectronic materials. Time-resolved methods enable probing ultrafast charge separation, exciton delocalization, coupling of charge carriers with molecular and lattice vibrations, and quantum-coherent effects. Various experimental protocols of material characterization in device structures have been proposed to probe nongeminate recombination and charge trapping properties. Techniques specifically sensitive to interfaces, grain boundaries, and structural inhomogeneities and the associated charge carrier dynamics are available. Methodologies that combine ultrafast time resolution with diffraction-limited spatial resolution and that are capable of real-time monitoring of processes such as exciton diffusion have also been developed. Microscopy methods have evolved to enable measurements of exciton localization/delocalization at nanoscales, to relate (opto)electronic properties with specific domain or polymer chain microstructure and molecular relaxation pathways, and to probe coherent effects in molecular assemblies and at the the single-molecule level.

Although this section was focused on successful application of methodologies, each technique has drawbacks, and it is important to understand technique-specific limitations. For example, a common important issue is that experimental techniques that provide insights into ultrafast charge carrier dynamics typically require high excitation densities to achieve good signal-to-noise ratio, which may produce nonlinear effects (such as exciton–exciton annihilation)<sup>935</sup> confounding the picture.<sup>371</sup> Therefore, it is desirable to keep excitation as low as possible (e.g., fluences of  $<1 \mu\text{J}/\text{cm}^2$  were deemed necessary at 500 nm excitation of P3HT<sup>427</sup>), establish the presence or absence of such effects, and account for them as necessary. Nonlinear optical methods and techniques probing coherent processes (such as 2DES) which also require high excitation densities, are difficult to perform on thin films due to film photodegradation and/or scattering, often requiring sample geometries that would minimize such effects (e.g., nano-

particles<sup>403</sup>). Many time-resolved techniques (such as THz spectroscopy, TRMC, and time-resolved photocurrent) which directly probe charge carrier dynamics measure photoconductivity, from which a product of the sum of the hole and electron mobilities and of charge photogeneration efficiency (referred to as  $\mu\eta$  in Table 2) can be obtained. However, the  $\mu$  and  $\eta$  separation, as well as contributions of electron and hole mobilities in  $\mu$ , is not straightforward. Scanning probe microscopies provide excellent spatial resolution, but their time resolution is limited, and practical solutions for achieving ultrafast time resolution combined with subdiffraction-limited spatial resolution and for nanoscale imaging of photoinduced exciton and charge carrier dynamics (e.g., *in situ* tracking of singlet exciton diffusion over 10–20 nm) are awaiting. Single-molecule spectroscopy is an excellent tool for studies of the molecular-level photophysics. However, it requires the fluorophores to be incorporated at ultralow concentrations in a nonfluorescent, typically high-bandgap matrix (e.g., PMMA or PS). This makes it difficult to apply the technique to studies of intermolecular interactions and of the nanoscale environment directly relevant to typical high-performance organic optoelectronic thin-film devices (such as BHJs).

Given the complexity of processes ultimately involved in organic (opto)electronic device performance, occurring both at the molecular level and at the molecular assembly level, it is often difficult to conclusively establish the underlying physical mechanisms based on results of one type of measurement. It is therefore important to characterize the optoelectronic material comprehensively by applying various experimental techniques and reconcile observations from these experiments. Some illustrations of this statement were provided in earlier sections (e.g., Section 4.3), and further examples are given in Section 8.

## 8. IMPORTANCE OF COMPREHENSIVE PHYSICAL STUDIES: EXAMPLES

### 8.1. Charge Carrier Dynamics on Various Time-Scales: From Ultrafast Dynamics to Device Performance

In order to establish bottlenecks in charge generation and transport, many studies have highlighted the importance of tracking charge carrier dynamics over multiple time-scales. Therefore, more understanding about underlying mechanisms is gained when charge carrier dynamics is assessed by combining ultrafast spectroscopy with other experimental and/or computational techniques applied to the same material and/or device. Examples of such combinations include high-resolution spectroscopy and/or time-resolved photocurrent measurements combined with cw photocurrent measurements or OPV device characteristics,<sup>37,346,347,356,724,936–939</sup> TRMC or time-resolved photocurrent measurements combined with FET studies,<sup>27,302</sup> and many others.<sup>940,941</sup> Such experiments revealed properties that persist over many orders of magnitude in time, which helps establish what aspect of carrier dynamics is ultimately important for the device performance. For example, power-law decays of transient photoconductivity ( $\sim t^{-b}$  with  $b = 0.52–0.53$ ) in crystalline TIPS-Pn films (Figure 22) were observed on the 1–100-ps time-scales in the optical pump-THz probe experiments<sup>40</sup> and from  $\sim 100$  ps to at least up to  $\sim 1 \mu\text{s}$  in transient photocurrent measurements in devices.<sup>36,347</sup> Similar behavior was observed in TIPS-Pn single crystals<sup>198,365</sup> and in diF R-ADT crystalline films,<sup>28,347,414</sup> in which weakly temperature-dependent power-law exponents  $b$  were obtained

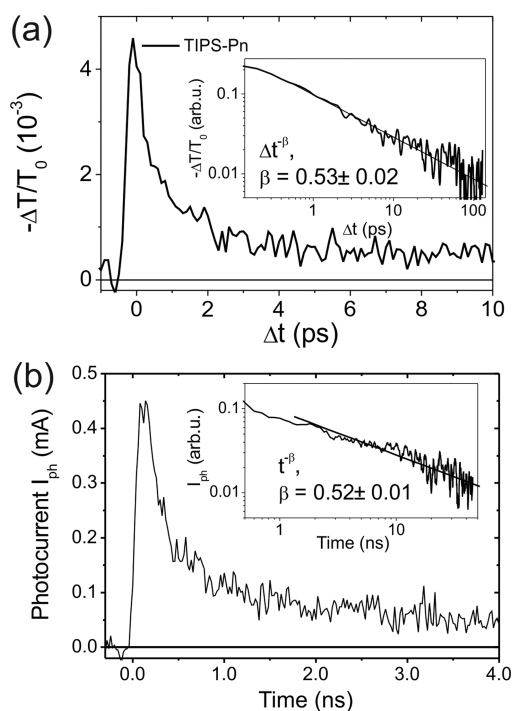


**Figure 22.** (a) Relative transmission of the THz probe beam measured in a polycrystalline TIPS-Pn film excited with a 100-fs, 580-nm pulse as a function of a pump–probe time delay ( $\Delta t$ ), reflecting the dynamics of photoinduced mobile charge carriers. The time resolution is  $\sim 0.4$  ps. The inset shows the longer time-scale dynamics, fit with the power-law function ( $\sim \Delta t^{-\beta}$ ). Adapted with permission from ref 40. Copyright 2005 American Institute of Physics. (b) Transient photocurrent measured under 100-fs, 400-nm excitation of a polycrystalline TIPS-Pn film in a thin-film device using a fast digital sampling oscilloscope. The time resolution is  $\sim 30$  ps. The inset shows decay dynamics at longer time-scales, fit with the power-law function ( $\sim t^{-\beta}$ ). Adapted with permission from ref 347. Copyright 2008 American Institute of Physics.

and attributed to charge carrier tunneling between the isoenergetic sites over many orders of magnitude in time. Among films of TIPS-Pn and diF R-ADT derivatives with various R-groups, lower power-law exponents  $b$  (corresponding to slower charge carrier recombination) correlated with higher cw photocurrents in devices.<sup>36</sup> Dimitrov et al.<sup>936</sup> used transient absorption spectroscopy to study charge photogeneration dynamics in several SiIDT-based polymer:fullerene blends on subpicosecond to millisecond time-scales and correlated these results with the OPV performance. They observed that the blend with a higher D–A energy offset exhibited efficient subpicosecond electric field-independent charge generation and a 3-fold higher short-circuit current  $J_{sc}$  as compared to a blend with a lower D–A energy offset, which instead underwent a singlet–triplet spin conversion at  $\sim 1$  ns after photoexcitation.

Although efficient charge photogeneration is a key factor in the performance of optoelectronic devices based on photo-response, nongeminate charge carrier recombination plays a significant role as well (Section 5.2). Therefore, many studies focused on monitoring charge carrier dynamics from photogeneration to extraction.<sup>289,294,637,639,724,747</sup> Kendrick et al.<sup>37</sup> chose the diF TES-ADT as the donor and added diCN TIPS-ADT, R-Pn, R-IF, R-Hex, or PCBM acceptors at small enough concentrations (2%) to prevent acceptor domain formation and to minimize changes in the hole mobility in the donor. The

choice of the acceptor molecules was dictated by the desirable range of the D–A  $\Delta$ LUMO (0.44–0.65 eV, depending on the acceptor) and of the average D–A separation (dictated by the R groups on the acceptors). They measured transient photocurrent under a  $\sim 500$  ps pulsed photoexcitation (with a sub-100-ps detection resolution) and the cw photocurrent, under applied electric field, in the same devices (Figure 8(c)). In all samples, the amplitude of the fast photocurrent, which is determined by the photogeneration efficiency,<sup>300</sup> was within a factor of 2 of that in pristine diF TES-ADT films (Figure 23(a)). In contrast, up to a factor of  $\sim 6$  enhancement was

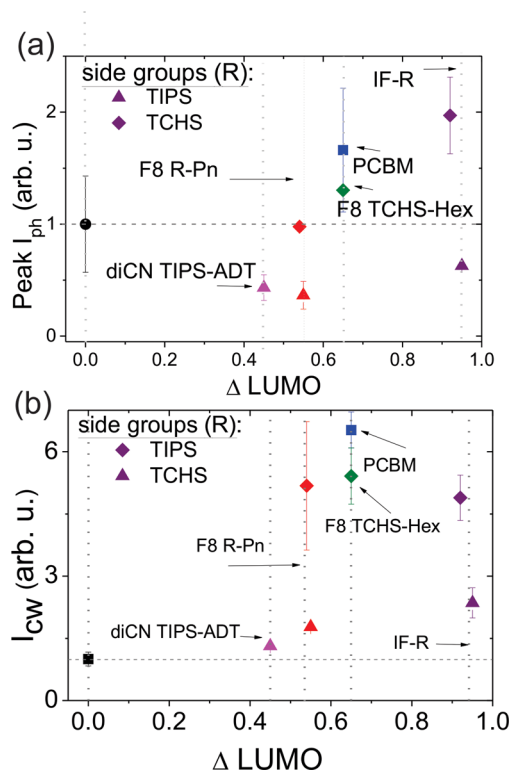


**Figure 23.** Peak transient (a) and cw (b) photocurrents observed upon pulsed and cw photoexcitation, respectively, of blends containing diF TES-ADT as the donor and 2 wt % of the acceptors (diCN TIPS-ADT, F8 TIPS-Pn, F8 TCHS-Pn, F8 TCHS-Hex, PCBM, TIPS-IF, and TCHS-IF), normalized by the values obtained in pristine ADT-TES-F films ( $\Delta$ LUMO = 0), as a function of  $\Delta$ LUMO. Symbols describing side group (R) designations are included in the plot. Up to a factor of 2 enhancement in charge photogeneration efficiency (a) is observed in blends with acceptors featuring large side groups TCHS enabling larger D–A spatial separation. The same blends exhibit up to a factor of  $\sim 6$  improvement in the cw photocurrent due to reduced charge carrier recombination. Adapted from ref 37. Copyright 2012 American Chemical Society.

observed in the cw photocurrent in several blends as compared to that in pristine diF TES-ADT (Figure 23(b)). It strongly depended on the D–A spacing controlled by the size of the side group R on the acceptor, with larger D–A spacings yielding higher photocurrents. This was attributed to inhibited charge carrier recombination (Figure 8(c)), and the higher cw photocurrents also corresponded to longer decays of the time-resolved photocurrent.

Burke and McGehee<sup>273</sup> established that a good BHJ cell should have a high local (e.g., measured at ps time-scales) mobility, whereas the bulk mobility commonly measured in

devices is not directly linked to charge generation. For example, Jin et al.<sup>354</sup> observed a factor of 1.8 higher ultrafast photoconductivity (measured using time-resolved THz spectroscopy) in PTB7:PCBM than in P3HT:PCBM blends, correlated with the solar cell performance of these blends. The local charge carrier mobility extracted from picosecond time-scale measurements in some polymers (such as PPV derivatives) can be up to several orders of magnitude higher than that in devices;<sup>345,418,549</sup> other polymers such as P3HT-based blends exhibited relatively time-independent mobility, at least over the  $\sim 1$ -ps to 100- $\mu$ s time-scales.<sup>552,942</sup> The local mobility may also exhibit considerably different temperature dependence than the “bulk” one,<sup>27,201,347</sup> having been governed by a different mechanism. In some cases (e.g., PPV,<sup>730</sup> PCDTBT:PCBM<sup>943</sup>), the charge carrier mobility became more thermally activated when it was probed at longer time-scales, for example due to the multiple-trapping carrier transport as the carriers relax into the deeper states.<sup>549</sup> In other systems, such as p-DTS:PCBM,<sup>943</sup> the activation energy did not change appreciably with time, at least through nanosecond time-scales, and charge transport proceeded via localized sites confined to a narrow energy range. Examples of such material-dependent behavior highlight that the best insight into the physics behind the photoexcited carrier dynamics is obtained by performing time-resolved experiments in conjunction with measurements of device characteristics, on the same system and on the same devices whenever possible.

## 8.2. Optical vs Electronic Properties

Given the importance of exciton dynamics for photogeneration of mobile charge carriers, as well as the similarity of factors contributing to exciton and charge carrier transport,<sup>728,944</sup> a question arises whether it would be possible to predict charge carrier dynamics based on optical measurements of exciton dynamics. A considerable amount of work focused on simultaneous studies of optical (e.g., via absorption and PL) and electronic (e.g., via photocurrents in devices) properties.<sup>27,28,36,356,368,945–947</sup> For example, PL quenching under applied electric fields and in the presence of acceptors has been used as a quantitative measure for Frenkel exciton dissociation into free carriers and D–A CT, respectively, see the excellent discussions in refs 206 and 946. However, the efficient D–A CT does not necessarily translate into efficient charge carrier generation.<sup>356,947–949</sup> For example, in diF TES-ADT blends with other ADT or R-Pn derivatives, efficient CT leads to the formation of tightly bound exciplexes, which deplete more efficient charge generation pathways<sup>300,356</sup> and do not yield significant improvements in  $J_{sc}$  of D:A BHJs as compared to that in pristine diF TES-ADT diodes,<sup>188</sup> rendering donor PL quenching irrelevant for understanding of the observed photocurrents.

Tvingstedt et al.<sup>947</sup> found a direct correlation between the electric field-assisted PL quenching of Frenkel excitons and extracted photocurrent in several pristine polymers. However, no such correlation was found with the PL quenching of the CT excitons in polymer:fullerene blends. In particular, considerably lower electric fields were required to generate photocurrents than to efficiently dissociate the CT states. Similar observations were made, for example, in the case of the CT excitons in polymer:nonfullerene small-molecule acceptor (MEH-PPV:HV-BT) blends<sup>946</sup> and Frenkel excitons in pristine polycrystalline diF TES-ADT<sup>28</sup> and oriented PPV<sup>421</sup> films. The origin of such discrepancies lies in the availability of alternative

channels for charge separation, which include nonemissive states that may or may not constitute precursor states for the emissive Frenkel or CT exciton formation. Therefore, the PL quenching is not a reliable predictor of charge generation efficiency, as discussed in detail in ref 206.

Optical absorption and PL spectra of organic solids contain information about exciton relaxation in a disordered energy landscape, exciton delocalization, etc. For example, the width of inhomogeneous broadening  $\sigma$  (eq 4) of the spectral lines provides a measure for the DOS for excitons, and at room temperature it describes the Stokes shift due to exciton relaxation ( $-\sigma^2/k_B T$ ) in amorphous and disordered polycrystalline films.<sup>2,28</sup> Analysis of the spectral shifts between the monomer and solid-state spectra enables differentiation between the amorphous and polycrystalline film structures (Figure 2).<sup>40</sup> The optical spectra analysis procedure developed by Spano and co-workers<sup>91</sup> (Section 2.4) has been utilized to determine exciton bandwidths and coherence lengths, establish types of molecular aggregates,<sup>87</sup> and distinguish between the aggregates of the same type but with different characteristics.<sup>31</sup>

It is of interest, however, to perform a side-by-side comparison of exciton and charge carrier dynamics and look for possible correlations.<sup>113</sup> Hoffmann et al.<sup>950</sup> combined measurements of PL and charge carrier mobilities (using TOF and OFET characteristics) with DFT calculations to show that, in conjugated A-B-type copolymers, the inhomogeneous DOS for excitons and charge carriers were very similar. They proposed that this is a characteristic feature of a broad range of conjugated polymers in which disorder results from variation in conjugation lengths rather than in chain coupling. They also discussed the possibility of predicting charge carrier mobility based on the optical absorption measurements, for example for a quick material screening in the industrial setting.

Kronemeijer et al.<sup>491</sup> examined the temperature dependent FET characteristics of a variety of top-gate polymer FETs, in conjunction with measurements of optical absorption using photothermal deflection spectroscopy. They found correlation between DOS (determined from temperature-dependent FET transfer characteristics) for charge carriers in FETs and the Urbach tail from the absorption spectra (Figure 24), which also supports the connection between optical measurements and charge transport characteristics in disordered materials.

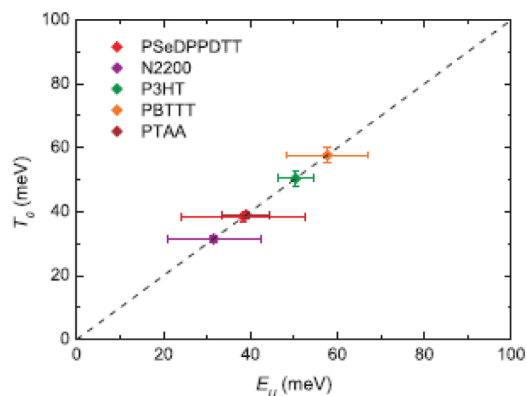


**Figure 24.** Correlation between the DOS width extracted from FET characteristics ( $T_0$ ) and the Urbach energy from the absorption spectra (see Figure 19), so that  $E_u \approx (k_B T_0)$ . Reproduced from ref 491. under Creative Commons license 4.0 (<https://creativecommons.org/licenses/by/4.0>).

Pingel et al.<sup>27</sup> and Platt et al.<sup>28</sup> looked for correlations between the exciton bandwidth  $W$  (extracted from absorption and/or PL spectra), which is a measure of intermolecular interactions (Section 2.2), and charge transport in polycrystalline P3HT and diF TES-ADT films, respectively. In both cases, absorption and emission properties were attributed to those of disordered H-aggregates, and exciton bandwidths  $W$  increased with temperature. The exciton bandwidth depends on the intermolecular  $\pi$ - $\pi$  stacking distance, the number of molecules in the aggregate, and the correlation length,<sup>44</sup> and it has served as a sensitive probe of the domain structure and quality of polycrystalline films.<sup>45,951</sup> In P3HT, an increase in  $W$  with temperature was dependent on the molecular weight of the polymer and attributed to a decreasing interaction length (i.e., shortening of the interacting conjugated segments) with temperature. Such decrease in the interaction length, however, did not negatively impact the nanosecond time-scale (“local” or intragrain) charge carrier mobility measured by TRMC and did not have a strong correlation with the behavior of the (macroscopic) OFET mobility dominated by the transport in the intergrain disordered regions. In diF TES-ADT, strongly temperature dependent  $W$  was attributed to dynamic disorder, and no correlation between the behavior of  $W$  and of the nanosecond time-scale photocurrents was observed. Instead, the nanosecond time-scale charge transport properties were dominated by static disorder. Although the exciton bandwidth was found to be highly sensitive to film morphology, no direct correlations between  $W$  and TRMC photocurrents or with FET mobilities were observed in other studies of P3HT films with systematically varying molecular weight<sup>951</sup> and casting solvent,<sup>45</sup> respectively. These observations suggest that the systems with low static disorder (such as aligned torsion-free polymer fibers or molecular crystals) and/or charge transport measurements at subpicosecond time-scales may be necessary to directly relate optical and electronic properties that originate from intermolecular coupling rather than structural defects, variations in polymer chain lengths, impurities, etc.

### 8.3. Macroscopic vs Microscopic Scales

Numerous studies identified the importance of grain boundaries, the presence of mixed phases, and nanoscale morphology for the optoelectronic properties of films. Insights obtained via various modalities of microscopy of organic semiconductors were discussed in Section 7.2. Comprehensive reviews of how the synergy of studies on the macroscopic and microscopic spatial scales promotes better understanding of the material design and device performance are available (Table S1).<sup>774,795,867</sup> Highlighted below are several recent examples of studies that obtained device performance-related insights using microscopy that directly probed (opto)electronic processes (rather than structural and morphological characteristics).

Lange et al.<sup>749</sup> applied KFPM in conjunction with the BACE measurements to several polymer:fullerene BHJs. The KFPM enabled quantifying energetic shifts in HOMO and LUMO depending on charge carrier density, film composition and thickness, and annealing, which were then related to the extracted charge in OPV measured with BACE. The authors concluded that the  $V_{oc}$  dependence on the blend composition and thermal history was determined by variations in the fullerene LUMO due to varying crystallinity.

Girdharagopal et al.<sup>776</sup> developed a conductive AFM-based method that enables measurements of the photoinduced charging with a  $\sim$ 100-ns time resolution, which was then

applied to studies of P3HT:PCBM BHJs annealed using different protocols. The photocharging rate, which is directly proportional to the local quantum efficiency, was then related to the EQE measured in the same OPV devices. A strong correlation between the two quantities was observed (with the rate increase from 20 to 45 kHz corresponding to the EQE increase from  $\sim$ 33 to 54%) due to changes in the nanoscale film structure as the annealing time increased.

Adachi et al.<sup>917</sup> used SMFS of single PFO chains to establish energetic heterogeneity in polymer charge trap levels of almost 1 eV due to an inhomogeneous local environment. They demonstrated that the well-known green emission band in PFO-based OLEDs is due to a distribution of spectrally discrete keto-defect-related emitters and argued that such large energetic heterogeneity should be a general property of charge traps in conjugated polymer films. Honmou et al.<sup>882</sup> were able to measure EL spectra from single BDOH-BF chains and proposed a mechanism based on the formation of interchain aggregates that describes variable EL in BDOH-BF-based OLEDs, depending on the polymer side chains.

A series of studies of functionalized ADT and Pn derivatives were performed on the macroscopic (device) level,<sup>37,300,356</sup> microscopic level,<sup>188</sup> and single-molecule level.<sup>35</sup> Time-resolved and cw photocurrents and PL were measured, in combination with numerical simulations,<sup>120</sup> in blends of diF TES-ADT as the donor and various small-molecule acceptors (including functionalized Pn derivatives). These studies quantified the properties of the emissive CT states and their contribution to the photocurrent, depending on the side groups of the acceptor.<sup>37,300,356</sup> The CT states were then used to image D/A interfaces in diF TES-ADT-containing binary and ternary solar cells, which linked the fine intermixture of donor and acceptor, resulting in the tightly bound CT state formation with a lower PCE.<sup>188</sup> Then, the same functionalized ADT and Pn derivatives as those used in devices (e.g., diF TES-ADT, diCN TIPS-ADT, F8 R-Pn) were imaged on the single molecule level, incorporated in PMMA or crystalline t-bu BTBTB hosts. The study revealed considerably higher photostability of molecules in a crystalline host, as compared to PMMA, and dependence of photostability and of orientational constraints upon the molecule incorporation into a crystalline host on the molecule's side groups R.<sup>35</sup>

Reid et al.<sup>371,951</sup> performed TRMC measurements on P3HT films of various molecular weight and observed saturation of the photocurrent at higher molecular weights in solution-cast films, with the photocurrents an order of magnitude higher than those in solid-state molded films in which the density of chain folds was reduced (Figure 25(a)). The authors hypothesized that two possible scenarios could be behind these observations, with the charge photogeneration either promoted by the interfaces between amorphous and crystalline domains or facilitated by chain folds acting as defects. The resolution between these two distinct pictures could be offered, for example, by the results of Steiner et al.<sup>879</sup> They performed PL spectroscopy on single P3HT chains of various molecular weight in solution and in a PMMA host, which enabled measurements on unfolded and folded chains, respectively (Figure 25(b)). In folded chains only, PL saturation was observed at higher molecular weights. This was explained by efficient funneling of the excitons (via energy transfer) to the acceptor chromophore (shown in red), which was followed by the triplet formation on the acceptor. The triplet exciton then quenched a singlet exciton within the range of exciton

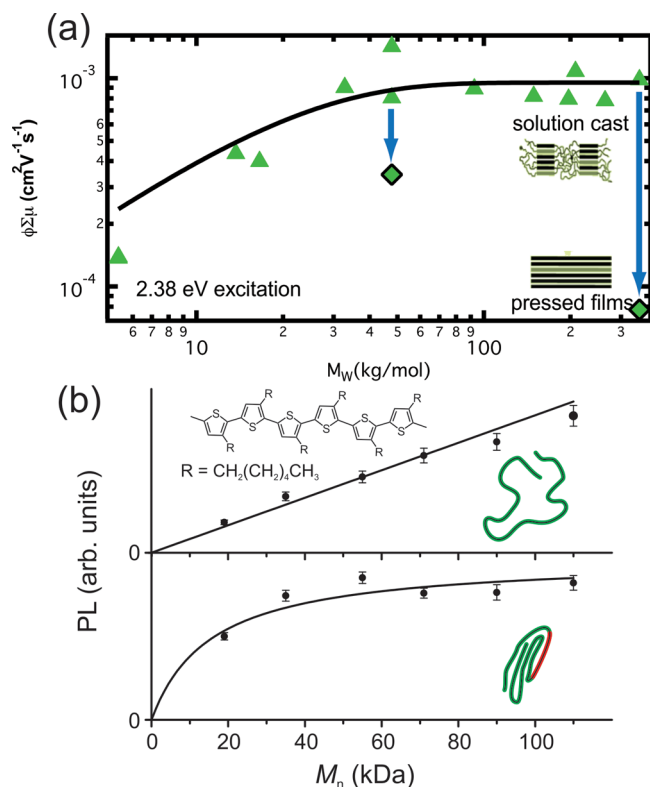


**Figure 25.** (a) Product of a charge photogeneration efficiency and a sum of hole and electron nanosecond-time-scale mobilities measured using TRMC in P3HT films with different molecular weights. Adapted with permission from ref 371. Copyright 2014 Wiley Periodicals. (b) PL from P3HT unfolded chains in solution (top) and folded single chains immobilized in a PMMA matrix (bottom) measured using fluorescence correlation spectroscopy and SMFS, respectively, as a function of the molecular weight of the polymer. Reproduced with permission from ref 879. Copyright 2014 American Physical Society.

migration (singlet–triplet annihilation). This process would prevent singlet exciton dissociation into free charge carriers, which suggests that the chain folds would be detrimental for charge generation, thus supporting the domain interface-driven charge generation picture. In spite of very different experiments (TRMC and SMFS) and observables employed in this example, the example illustrates how relating optical and electronic properties, at both the macroscopic and microscopic scales, could help identify deep connections between various observations and clarify underlying mechanisms.

## 9. MATERIALS

This section briefly summarizes best-performing organic materials in several categories: high-mobility materials, best solar cell materials, and best PR materials. For a detailed overview of material design, the reader is referred to comprehensive reviews focused on particular materials classes (Table S1). Also highlighted in this section are novel and/or nontraditional approaches to organic optoelectronic materials design.

### 9.1. High-Mobility Small-Molecule Organic Semiconductors

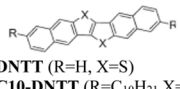
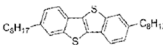
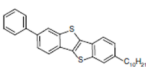
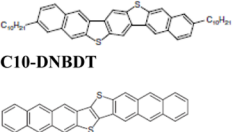
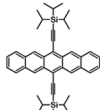
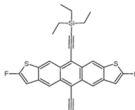
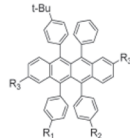
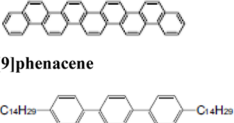
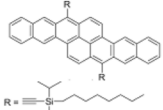
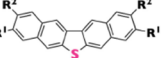
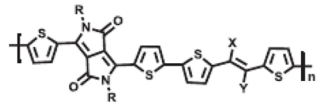
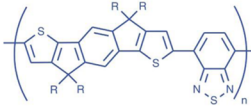
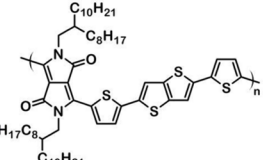
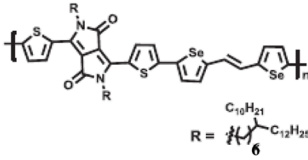
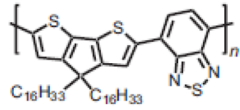
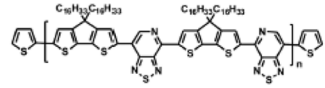
Tables 3 and 4 summarize the performance, and Figure 26 shows selected molecular structures of materials with the highest charge carrier mobilities to date. Room-temperature hole mobilities of up to  $\sim 40$  cm<sup>2</sup>/(Vs) were demonstrated in

Pn and rubrene crystals and in C8-BTBTB:PS blends. The enhanced performance of most small-molecule materials in Table 3 relies on their ability to form ordered crystalline structures, with herringbone and 2D  $\pi$ -stacking motifs favored over other packing motifs in achieving high OFET mobilities. As discussed in Section 4.1, low reorganization energies and large transfer integrals, as isotropic as possible (Table 3), have been identified as parameters necessary for achieving high mobilities in single-crystal OFETs. Based on these strategies, Sokolov et al.<sup>437</sup> developed a computational screening procedure using a combination of the QM and MM approaches that revealed a heteroacene compound DATT (Figure 26) as a potentially high-mobility organic semiconductor. The compound was then synthesized and characterized in single-crystal OFETs, revealing hole mobilities of up to 16 cm<sup>2</sup>/(Vs). For a comprehensive overview of material design strategies for small-molecule OFETs, see ref 952.

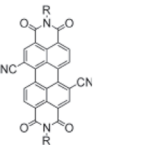
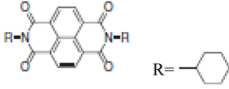
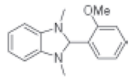
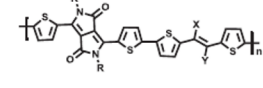
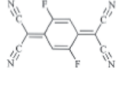
An instructive example can be drawn from studies of charge transport in various TIPS-Pn polymorphs (Table 5), in which mobility varied by 2 orders of magnitude depending on the molecular packing.<sup>527,953</sup> Molecular packing-dependent changes were also observed in the optical absorption spectra, consistent with previous studies of optical spectra in various functionalized Pn and ADT derivatives.<sup>36,40,356,954</sup> The highest hole mobility of up to 11 cm<sup>2</sup>/(Vs) was obtained in a polymorph with the highest hole transfer integrals achieved in two directions (in the *a-b* plane), which on the molecular level is enabled by relatively similar  $\pi$ - $\pi$  stacking distances in these directions (Table 5).<sup>527</sup> Notably, the TIPS-Pn polymorph I of Table 5 also exhibited *electron* mobilities of up to 6.8 cm<sup>2</sup>/(Vs) when doped with *o*-Meo-DMBI.<sup>584</sup>

Acene and acene-thiophene derivatives, in addition to their high mobilities, have been a model system for developing understanding of the optoelectronic properties of organic semiconductors, such as ultrafast photoinduced exciton and charge carrier dynamics (Table 3), as discussed in Sections 3.3 and 4.3), as well as for developing new device concepts. For example, recently, a *diffusion-based* Pn OFET on a flexible substrate, with a gain of  $>700$ , was demonstrated.<sup>955</sup> Pentacene (Pn), Tc, and functionalized acene derivatives (e.g., TIPS-Tc, TIPS-Pn, and TCHS-Hex) contributed most of the important insights into the mechanism of SF (due to their optimal energetics,  $E(S_1) \geq 2E(T_1)$ , Section 2.7.1) and the utility of the SF in devices (Section 3.3.3).<sup>22,157,406,407,409</sup> Solution-processable derivatives such as R-Pn or diF R-ADT functionalized with various side groups R enabled systematic studies that provided insights into the relationship between molecular packing and charge carrier mobility,<sup>952,956</sup> solar cell performance,<sup>957</sup> and properties of CT states in small-molecule D/A BHJs.<sup>37,356</sup> Crystalline films of Pn, functionalized Pn, and diF R-ADT derivatives exhibit photoconductive response<sup>36,321</sup> and photoconductive gains of  $\sim 15$ – $130$ , depending on the derivative,<sup>36,958,959</sup> which were exploited in photodetectors and photo-TFTs (Tables 10 and 11).<sup>960–962</sup> Fluorinated derivatives such as diF R-ADT, F8 R-Pn, and F8 R-Hex derivatives exhibit a considerably enhanced stability under illumination with respect to the corresponding nonfluorinated derivatives.<sup>35,963,964</sup> This makes them suitable for studies on the single molecule level using SFMS (Section 7.2.4), enabling systematic studies of nanoscale-level photophysics and interactions with the local nanoenvironment.<sup>35</sup> An acene-based molecule TTPO that resists decomposition until almost

## Hole transporters

 <b>Pentacene (Pn)</b>	 <b>DNTT</b> (R=H, X=S) <b>C10-DNTT</b> (R=C <sub>10</sub> H <sub>21</sub> , X=S)	 <b>C8-BTBT</b>	 <b>Ph-BTBT-10</b>
 <b>Rubrene</b>	 <b>C10-DNBDT</b> <b>DAT</b>	 <b>TIPS-Pn</b>	 <b>diF TES-ADT</b>
 <b>t-bu Rubrene</b> (R <sub>1</sub> =R <sub>3</sub> =H, R <sub>2</sub> =BU-t)	 <b>Picene</b> -(C <sub>14</sub> H <sub>29</sub> ) <sub>2</sub>	 <b>Bistetracene</b>	 <b>C6-DNT-VW</b> (R <sup>1</sup> =C <sub>6</sub> H <sub>13</sub> , R <sup>2</sup> =H)
 <b>PVDT-10</b> (R=C <sub>6</sub> C <sub>10</sub> , X=Y=H)	 <b>IDTBT</b> (R = C <sub>16</sub> H <sub>33</sub> )		
 <b>DPP-DTT</b>	 <b>DPPDTE</b>		
 <b>CDT-BTZ</b>	 <b>PCDTPT</b>		

## Electron transporters

 <b>PDIF-CN2</b> : R=CH <sub>2</sub> C <sub>3</sub> F <sub>7</sub>	 <b>NDI</b> R = 	 <b>C60</b>
 <b>o-MeO-DMBI</b> (with TIPS-Pn)	 <b>DPP-CNTVT</b> R=C <sub>10</sub> C <sub>14</sub> , X=CN, Y=H or X=H, Y=CN	 <b>F2-TCNQ</b>

## Ambipolar materials

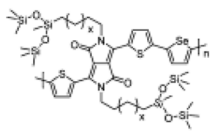
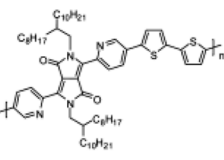
 <b>Fm-rubrene</b>	 <b>PTDPPSe</b> (x=2)	 <b>PDBPyBT</b>
--	---	--

Figure 26. Molecular structures of selected high-mobility materials. See Tables 3 and 4 and/or the discussion of their properties in the text.

Table 5. Structural, Electronic, and Optical Properties of Selected TIPS-Pn Polymorphs<sup>a</sup>

Polymorph	<i>a</i> (Å) <sup>b</sup>	<i>b</i> (Å) <sup>b</sup>	$\gamma$ (deg) <sup>b</sup>	$\pi$ - $\pi$ distance (Å) <sup>c</sup>	Hole transfer integrals (meV) <sup>d</sup>	Hole mobility (cm <sup>2</sup> /(Vs)) <sup>e</sup>	$\lambda_{\text{abs,max}}$ (nm) <sup>f</sup>
I	7.68	7.77	81.46	3.30; 3.89	10.6; 17.9	2.4 (3.8max)	~700
II	7.48	8.50	71.29	3.23; 3.65	34.3; -54.1	8.1 (11max)	~670
III	7.56	9.02	65.23	2.82; 3.75	1.3; 18.9	0.058 (0.09max)	~680

<sup>a</sup>Data from ref 527. <sup>b</sup>Crystal structure and molecular packing parameters determined experimentally using GIXD. <sup>c</sup>Obtained from molecular mechanics calculations for two pairs of molecules in the a-b plane. <sup>d</sup>Calculated using DFT with a B3LYP functional with a 6-31G\*\* basis for the same two pairs of molecules in the a-b plane as in b. <sup>e</sup>Average and maximal (in parentheses) hole mobility measured in TC/BG FETs (TC = top contact; BG = bottom gate). <sup>f</sup>Wavelength of maximal S0-S1 absorption.

its melting temperature of around 390 °C was also synthesized and characterized.<sup>811</sup>

Two-dimensional (2D) molecular structures are of interest due to their superior stability with respect to environmental influences and to chemical reactivity, as compared to linear molecules such as acenes.<sup>575,965</sup> For example, functionalized bis-tetracene derivatives exhibited hole mobilities of up to 6.1 cm<sup>2</sup>/(Vs), as well as a superior stability with respect to Diels-Alder reaction with fullerenes and a factor of ~200 longer half-life under continuous UV/vis excitation as compared to Pn.<sup>966</sup> The OFETs based on *peri*-xanthoxanthene (PXX) derivatives<sup>952,967-972</sup> with hole mobilities of up to ~0.8-0.9 cm<sup>2</sup>/(Vs)<sup>952,968</sup> (which were incorporated into flexible OFET-driven displays by Sony)<sup>973</sup> exhibited considerably better stability over time under exposure to oxygen, moisture, light, and heat as compared to similar Pn devices.<sup>968</sup>

Several molecular materials exhibited electron mobilities of 6-8 cm<sup>2</sup>/(Vs) (Table 3), which include NDI, PDI, fullerene, and TCNQ derivatives (Figure 26). For example, in single crystals of F2-TCNQ, room-temperature electron mobilities of 6-7 cm<sup>2</sup>/(Vs) were observed that increased to 16-25 cm<sup>2</sup>/(Vs), depending on the crystal and measurement technique, upon cooling the crystals down to 150 K (Table 4).<sup>583</sup> In contrast, mobility in TCNQ and F4-TCNQ crystals was lower (0.1-0.2 cm<sup>2</sup>/(Vs)) and thermally activated, in agreement with other studies on TCNQ derivatives.<sup>548</sup> The observations were related to "bandlike" transport enabled by a large LUMO bandwidth obtained for F2-TCNQ of 0.8 eV, which is twice as large as the HOMO bandwidth for rubrene.

Sirringhaus<sup>529</sup> summarized the design criteria for small-molecule organic semiconductors with high mobility: a high degree of crystallinity, short  $\pi$ - $\pi$  stacking distances with an extended  $\pi$ - $\pi$  overlap in more than one spatial direction, reduced formation of lattice defects, and suppression of thermal lattice fluctuations. For the latter, the molecular design strategy has been identified: the conjugated molecular core with side chains along the long axis of the molecule was predicted to be least susceptible to thermal fluctuations of the transfer integral, leading to dynamic disorder.<sup>536</sup> Driven by the recent success of D-A copolymers, in which mobilities of over >10 cm<sup>2</sup>/(Vs) have been demonstrated (Table 3), charge transport in FETs based on D-A polar small molecules was also investigated. For example, hole mobilities of up to 0.18 cm<sup>2</sup>/(Vs) were obtained in 2D stacks of merocyanine dyes, with potentially higher mobilities possible if larger crystalline grains were obtained.<sup>974</sup> Polar photoconductive small-molecule materials have been previously utilized in high-performance monolithic PR materials,<sup>220</sup> for which the requirement of high optical quality was satisfied by utilizing amorphous glass phases formed by such molecules (e.g., DCDHF or ATOP derivatives).<sup>347,740,975,976</sup> Crystalline phases of such materials could

potentially serve as a resource for high-mobility polar small-molecule materials.

## 9.2. High-Mobility Conjugated Polymers

A successful approach to achieving charge carrier mobilities above ~0.01 cm<sup>2</sup>/(Vs) in polymers has utilized semicrystalline lamellar microstructures with edge-on polymer orientations, an example of which are the benchmark polymers P3HT and PBTTT with mobilities of up to ~1.1 cm<sup>2</sup>/(Vs).<sup>529</sup> However, a breakthrough in achieving mobilities approaching those in molecular crystals (Table 3) was brought by the development of D-A polymers. These are typically copolymers with alternating electron deficient and electron rich units along the polymer backbone, which exhibit a low bandgap due to an intramolecular CT transition between the donor and acceptor moieties. This makes such polymers attractive both for OFET and for solar cell applications. For reviews of D-A polymer design, see refs 977-979.

Many successful D-A polymers are based on the electron-deficient unit of diketopyrrolopyrrole (DPP), which is a highly photostable red pigment widely utilized in paints. Hole mobilities of >10 cm<sup>2</sup>/(Vs) have been demonstrated in many DPP-based derivatives (Table 3). The key factor behind the success of DPP polymers has been identified to be a coplanar backbone conformation with minimal backbone torsion and steric hindrance between the donor and acceptor conjugated units.<sup>980</sup> Several other aspects, however, need further studies.<sup>529</sup> The outstanding questions include whether the electronic interactions between the donor and acceptor units promote closer  $\pi$ - $\pi$  stacking, whether the face-on or edge-on orientation of the backbone with respect to the substrate plane is important, and how to predict design of the flexible solubilizing chains to form low-energy, space-filling structures.

Other promising D-A copolymer classes include isoindigo(IID) and indacenodithiophene (IDT)-based copolymers.<sup>978,980</sup> For example, in PCDTPT and CDT-BTZ D-A copolymers aligned using nanogrooved substrates, room-temperature TFT hole mobilities of up to ~22 and 53 cm<sup>2</sup>/(Vs), respectively, were reported, depending on the channel length and molecular weight of the polymer.<sup>591</sup>

In optoelectronic applications such as PR devices, which rely on the optical quality of relatively thick (~100  $\mu$ m) films, the utility of polycrystalline materials is limited. Additionally, in any application, the level of morphology control necessary for reproducible performance of polycrystalline films may limit their technological feasibility (prompting, for example, an extensive research<sup>804,805,981</sup> into the electronic properties of blends of high-mobility small-molecule materials with amorphous conjugated polymers). This makes high-performance organic amorphous materials highly desirable. An interesting example of such material is IDTBT (Figure 26).<sup>389</sup> Because of its planarized backbone, even in an amorphous phase, it exhibited low energetic disorder (0.031 eV), which is

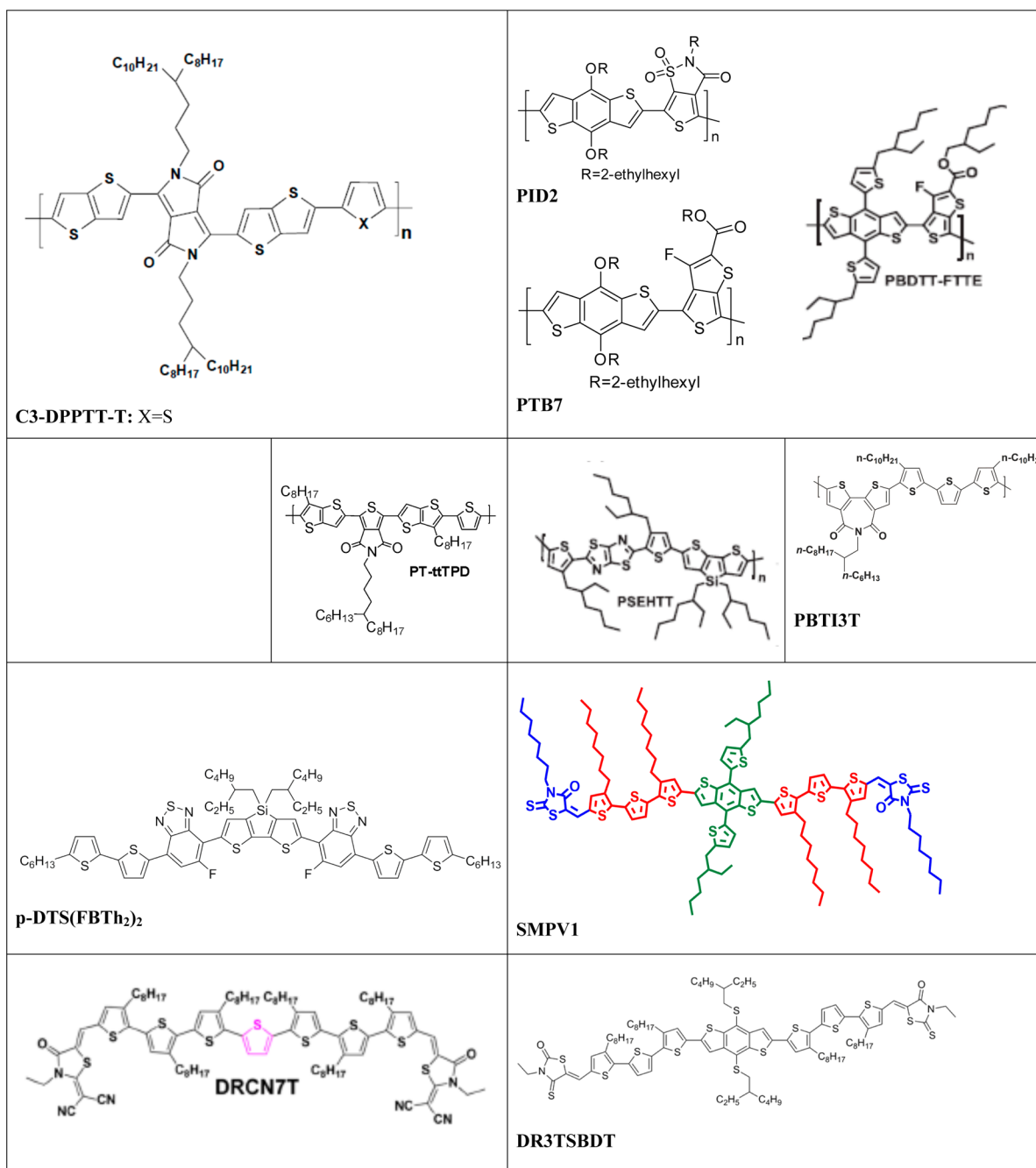


**Figure 27.** Donor materials for high-performance organic solar cells. See Table 8 and the discussion of their properties in the text.

comparable to that in the crystalline phase (0.026 eV), FET mobility of 1.5–2.5 cm<sup>2</sup>/(Vs), and near-ideal TFT current–voltage characteristics.

### 9.3. Materials for Organic Solar Cells

**9.3.1. Donor Materials.** Desirable characteristics of donor materials include absorption over a broad wavelength range, high hole mobility, and suitable energy levels (such as high triplet state energy). (For example, recently it was proposed that materials with small singlet–triplet energy splitting such as TADF materials, Section 2.7.2, offer enhancement in OPV performance due to reduced recombination.<sup>372</sup>) Among most successful donor materials for organic solar cells to date are low-bandgap D–A copolymers (Table 8). With several blends exhibiting PCEs of >10%, the requirement of the D–A

character as one of the key design guidelines for an OPV donor has been established.<sup>206</sup> In contrast to earlier polymer donor materials such as P3HT, which required the D–A energy offsets of >0.5 eV (corresponding to the D–A  $\Delta$ LUMO of >0.8 eV, assuming the exciton binding energy of 0.3 eV) to drive charge separation, the required energy offsets are considerably reduced in blends with D–A copolymers, approaching 0 (corresponding to  $\Delta$ LUMO of 0.3 eV) in, for example, DPP-based copolymers.<sup>206</sup> Comprehensive reviews of design of D–A copolymers and of their structure–property relationships are available (Table S1).<sup>977–979</sup>

Hachmann et al.<sup>982</sup> introduced a computational screening approach, based on the Schockley–Queisser model adapted for OPVs.<sup>983</sup> They identified building blocks promising for donor materials, which include [1,2,5]-thiadiazolo[3,4-C]pyridine,

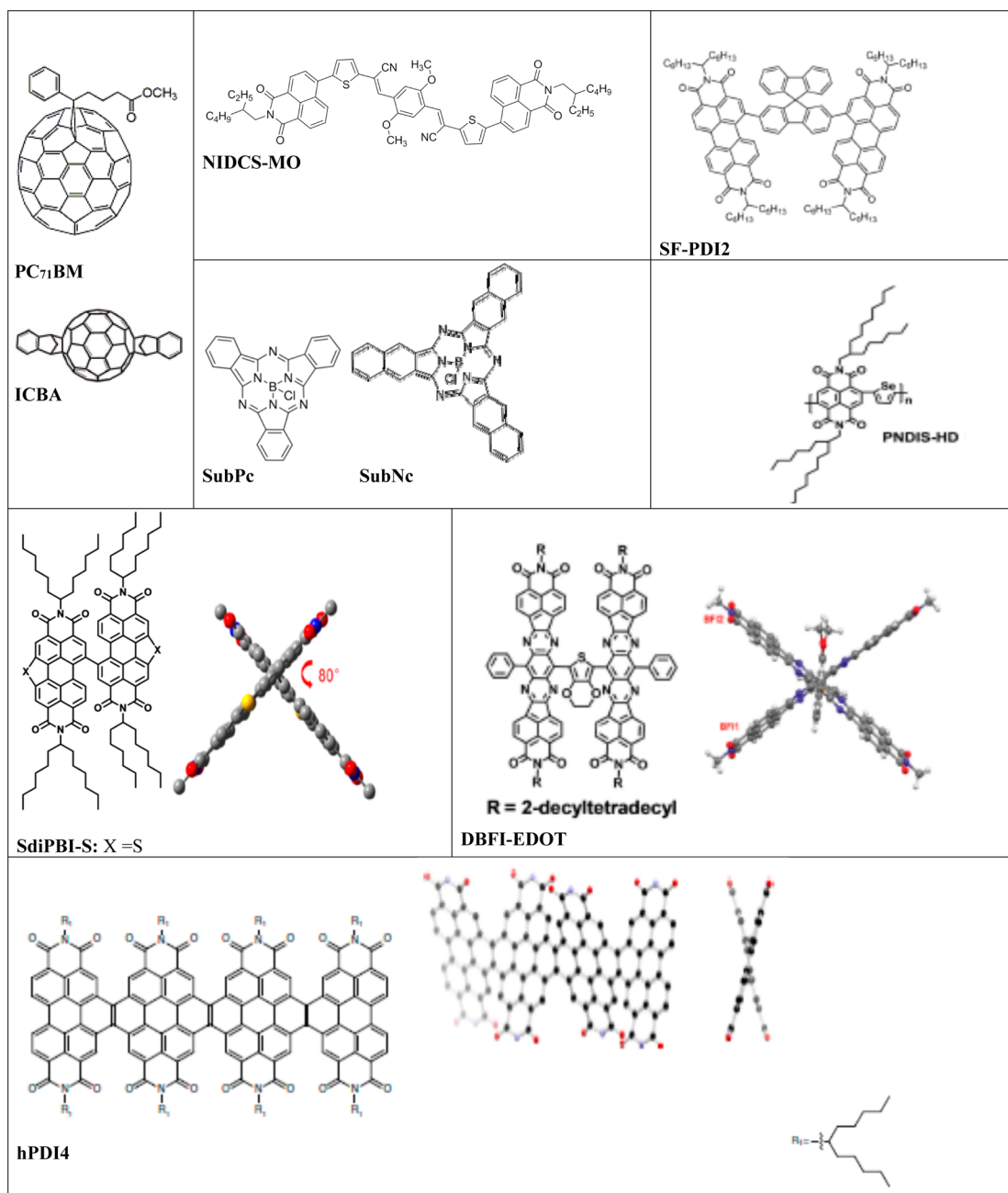


**Figure 28.** Acceptor materials for high-performance organic solar cells. See Table 8 and the discussion of their properties in the text.

pyridine, benzothiadiazole, silacyclopenta-2,3-diene, and 2H-2-silaindene.

Small molecules have advantages of high purity, definite molecular weight, tunable electronic structures, and better device reproducibility. PCEs of above 9% and around ~7% were achieved in several small-molecule BHJs and planar HJs, respectively (Table 8). Small-molecule donors explored include T-DPP-T-containing molecules, squaraine derivatives, oligothiophenes, acenes, phthalocyanines, various push–pull molecules,<sup>984–986</sup> and molecules with a complicated D–A architecture; see ref 987 for a recent review. Most successful small-molecule donors for BHJs (Table 8, Figure 27) have structures with alternating donor (D) and acceptor (A) groups. For example, DRCNnT donors (exhibiting PCEs of up to 10.1% in BHJs with fullerene acceptors) feature an A-D-A architecture (Figure 27). Another successful molecule p-

DTS(FBTTh<sub>2</sub>)<sub>2</sub> (which served as the donor in BHJs with fullerene and nonfullerene acceptors reaching PCEs of 9% and 5.4%, respectively) has a D<sup>1</sup>AD<sup>2</sup>AD<sup>1</sup> architecture in which D<sup>1</sup> (thiophene) and D<sup>2</sup> (dithienosilole, DTS) are electron-rich and A (fluorobenzothiadiazole) is an electron-poor fragment. In planar HJs, PCEs of over 7% have been obtained in several cases (Table 8). For example, an energy cascade system was realized in a multilayer structure with three donor layers (DPT, DBP, and rubrene) and a C<sub>60</sub> acceptor layer, yielding a PCE of 7.1%.<sup>180</sup> With a similar strategy relying on the energy-relay cascade structure, a multilayer HJ featuring  $\alpha$ -6T as the donor and SubNc and SubPc as acceptors yielded PCEs of 8.4%, among the highest in the nonfullerene organic solar cells.<sup>179</sup>

**9.3.2. Acceptor Materials.** Fullerene derivatives have served as “universal” acceptors in most best-performance HJ organic solar cells, with a variety of systematic structure–

property relationships studies focusing on the effects of fullerene structure on charge carrier dynamics and PCE. Considerable research efforts, both experimental and theoretical,<sup>364</sup> have been devoted to understanding what exactly makes fullerene derivatives such as PC<sub>61</sub>BM or PC<sub>71</sub>BM successful acceptors compatible with a variety of polymer and small-molecule donors (Table 8). Attractive properties of fullerenes include high electron affinity, near-degenerate LUMO and low-lying anion states,<sup>364</sup> high electron mobility, and 3D charge transport, as well as their ability to form nanoscale morphologies in BHJs that favor charge separation. However, they also have drawbacks including high costs, low absorption in the visible wavelength range with limited opportunities for its tunability, low stability with respect to oxidation, propensity for chemical reactions with donors, and difficulties in maintaining morphology over a long period of time. Therefore, efficient nonfullerene acceptors are highly desirable and have been a subject of intensive research. For example, Liu and Troisi<sup>364</sup> proposed four molecular designs with quasi-degenerate LUMOs and low-lying anion states. Various rotationally symmetric structures and calamitic structures featuring a central donor unit (D<sub>1</sub>), flanked by the other donor or acceptor unit (D<sub>2</sub> or A<sub>1</sub>), and terminal acceptor units A<sub>2</sub> have also been studied.<sup>988</sup> For recent reviews of nonfullerene acceptors, see refs 988–990. Most successful nonfullerene acceptors are based on PDI and DFBI derivatives in BHJs and on SubPc and SubNc derivatives in planar HJs (Table 8), yielding PCEs of up to 8.1–8.3% and 8.4%, respectively.<sup>179,991</sup> Zhong et al.<sup>991</sup> achieved PCEs of 8.3% in BHJs with a helical conjugated PDI oligomer as acceptor and PTB7-Th donor, which they considered to be a lower limit that can be surpassed by optimizing the donor structure. PCE of 8.1% was achieved with a twisted dimer acceptor DBFI-EDOT and PSEHTT donor, and the twisting between the block elements has been named a promising rational design strategy for efficient OPV acceptors (Figure 28).<sup>992</sup> Hwang et al.<sup>993</sup> recently reported a polymer acceptor PNDIS-HD, which with a polymer donor PBDTT-FTTE enabled PCEs of 7.7% in *all-polymer* solar cells.

Acceptor crystallinity has been cited as one of the important characteristics promoting charge generation.<sup>72,73</sup> For example, formation of C<sub>60</sub> crystallites with sizes of over 4 nm was linked with improved charge separation in a HJ with the NPD donor.<sup>72</sup> Another important parameter that is affected by the molecular design of the acceptor is the D–A separation. Large D–A separations have been shown to reduce recombination losses,<sup>37</sup> for example by reduction of the back transfer from the CT state to a low-lying triplet serving as a loss channel.<sup>372</sup>

### 9.3.3. High-Dielectric Constant Organic Materials.

Organic materials with high dielectric constant should have a reduced exciton binding energy (in accordance with eq 26) which promotes exciton dissociation and which makes them of interest for optoelectronic applications relying on charge photogeneration. A brief review of high-dielectric constant organic materials, which feature dielectric constants of up to 15, can be found in ref 994.

Leblebici et al.<sup>995</sup> reported a 30% increase in IQE in planar HJs containing C<sub>60</sub> as an acceptor layer and a blend of BO-ADMP with a highly polar small molecule CA as the donor. Such blending enabled raising the dielectric constant from 4.5 to 10.8, depending on the CA concentration. Torabi et al.<sup>393</sup> functionalized several PPV- and DPP-based polymers and fullerenes<sup>394</sup> with highly polar side groups and were able to

achieve dielectric constants of 5–6 without sacrificing charge carrier mobilities.

Noone et al.<sup>996</sup> examined charge generation and recombination in polymer BHJs with organic and inorganic acceptors which provided a range of dielectric environments in polymer blends. Tada et al.<sup>997</sup> incorporated perfluorinated chains into polythiophene and fullerene moieties and fabricated bilayer P3HT/PCBM solar cells with an interfacial dipole moment of tunable strength and direction, which resulted in the  $V_{oc}$  tunable between 0.3 and 0.95 V. Liu et al.<sup>395</sup> tuned the dielectric properties of polymer/fullerene blends by the addition of salt LiTFSI, which enabled reaching static dielectric constants as high as 145. Cho et al.<sup>998</sup> included dipolar side chains on PIDTT-DPP-based donor copolymers, which increased the dielectric constant from 3.9 to 5.0, reducing recombination and boosting the PCE in planar HJs with C<sub>60</sub>.

**9.3.4. Ternary Blends.** An alternative to the conventional BHJ design of organic solar cell material is ternary BHJs, in which an additional donor (D) or acceptor (A) molecule is introduced into the standard, binary blends of donor and acceptor, thus creating D<sub>1</sub>/D<sub>2</sub>/A or D/A<sub>1</sub>/A<sub>2</sub> blends.<sup>186,189,191</sup> Such additions enable tuning of open-circuit voltage ( $V_{oc}$ )<sup>999,1000</sup> and can promote a variety of processes potentially beneficial for the PCE, including FRET, cascade CT, and parallel-like CT. Increased short-circuit currents ( $J_{sc}$ ) due to additional charge transport pathways and enhanced charge photogeneration enabled by additives to the binary D:A blends were reported in a variety of BHJs.<sup>182</sup> For example, Lu et al.<sup>185</sup> obtained a PCE of 9.2% in a ternary cell with PTB7-Th and PID2 donor polymers and PC<sub>71</sub>BM acceptor. They achieved high  $J_{sc}$  and FF (Table 8) enabled by enhanced light harvesting (that utilized absorption by both polymer donors), efficient energy transfer from PID2 to PTB7, enhanced hole mobility, and reduced trap-assisted recombination.

The most efficient ternary blends to date utilize two polymer donors or a polymer and a small-molecule donor (Table 8), typically with a fullerene acceptor. An example of the latter system is a blend of PC<sub>71</sub>BM acceptor with the D–A copolymer PBDTTPD-HT and small-molecule BDT-3T-CNCOO donors, in which PCEs of up to 8.4% were achieved.<sup>1001</sup> All-small-molecule ternary blends were also demonstrated. For example, a ternary blend with BDT6T as the donor and ICBA and PC<sub>71</sub>BM as acceptors exhibited PCEs of up to 6.4%, which are higher than the PCEs of 5.7% achieved in binary blends without ICBA and 3.0% without PC<sub>71</sub>BM.<sup>192</sup> Also, PCEs of up to 8.5% were achieved in blends containing two D–A copolymer donors and a nonfullerene (DBFI-EDOT) acceptor.<sup>992</sup>

In spite of the high performance of many ternary blends (Table 8), the routes of optimizing such blends to achieve high PCEs are still under development. Mangold et al.<sup>724</sup> examined charge generation and recombination in polymer:polymer:fullerene ternary blends using various mixtures of amorphous and semicrystalline polymers. The authors concluded that the crystalline polymer in the blend ensured efficient charge generation and reduced nongeminate recombination. However, the amorphous polymer in the blend was critical in achieving higher  $V_{oc}$  and FF. Therefore, optimized morphology featuring amorphous and crystalline domains was necessary for the best PCEs. Savoie et al.<sup>189</sup> proposed a model that identifies the most promising combinations of optical bandgap, ionization potential, and composition of ternary blends. They provided a guideline for an optimal bandgap of the third component of

the blend, depending on the donor bandgap, ternary blend architecture, and device thickness. It was predicted that sensitized ternary blends (i.e., those with additional acceptors) and “parallel-type” ternary blends (i.e., those with an additional donor) are capable of PCE increases of ~40% and 20%, respectively, with respect to those in binary BHJ devices of equal thickness. Mollinger et al.<sup>1002</sup> systematically studied the energy of CT states ( $E_{CT}$ ) in ternary blends and the role of CT states in the tunable  $V_{oc}$  depending on the blend composition. They found that in systems with high miscibility and similar morphology, the trends in  $E_{CT}$  and  $V_{oc}$  could be attributed to changes in local environment. In contrast, in blends involving semicrystalline, aggregating polymers, the origin of tunable  $V_{oc}$  was more complicated due to large contribution of morphology into the  $V_{oc}$ .

**9.3.5. Kasha’s Rule Breaking Materials.** A potentially interesting idea is to utilize Kasha’s rule breaking materials in optoelectronic devices. According to Kasha’s rule, in organic optical materials, fluorescence occurs from the excited state with lowest energy.<sup>1</sup> This rule generally applies to most molecular materials and manifests, for example, in an excitation wavelength-independent PL spectrum. It also implies that, upon excitation of a higher-energy state, a picosecond time-scale internal conversion back to the lowest excited state occurs. This makes it difficult to utilize the excess energy in boosting either efficiency or the working wavelength range of optoelectronic devices. Rare exceptions to the Kasha’s rule include molecules such as azulene, in which the upper excited states are more closely spaced than the energy gap between the lowest excited state and the ground state and which exhibit intense  $S_2$ – $S_0$  fluorescence.<sup>1003</sup> A review of several classes of Kasha’s rule breaking materials can be found in ref 1004.

Kasha’s rule breaking has recently been reported in  $\alpha$ -6T encapsulated in SWCNTs.<sup>1005</sup> This extended the emission to visible wavelengths, previously not achieved in a dye-nanotube system, making the system promising for photonic applications. Charge and energy transfer from higher excited states of azulene to  $C_{60}$  and porphyrin derivatives has been extensively studied by Steer and co-workers.<sup>1003,1006–1011</sup> For example,  $S_2$ – $S_2$  energy transfer from an azulene donor to the zinc porphyrin acceptor was demonstrated, and its utility in molecular logic gates was discussed.<sup>1003</sup> Recently, an efficient electron injection from vibrationally hot azulene derivative donor to  $TiO_2$  nanoparticles was demonstrated,<sup>1012</sup> which opened up a possibility of capturing hot electrons without vibrational dissipation in PVs, potentially offering an additional strategy for improving PCEs. A recent review of the organic–inorganic materials exhibiting hot electron transfer can be found in ref 1013.

**9.3.6. Hybrids with Graphene and Carbon Nanotubes.** The potential of polymers doped with carbon nanotubes (CNTs) has been explored in PVs, in PR materials,<sup>1014</sup> and in FETs.<sup>556</sup> Yu et al.<sup>556</sup> obtained more than a factor of 20 enhancement in hole mobility when 1 wt % of boron-doped CNTs was added to a semiconducting polymer PDVT-10, reaching  $7.2 \text{ cm}^2/(\text{Vs})$  in FETs on flexible substrates. Qualitatively similar effects were obtained with other polymers, including P3HT-, PBTTT-, and DPP-based copolymers.

Ham et al.<sup>1015</sup> observed efficient exciton dissociation at the P3HT/SWCNT interfaces, and the planar HJ devices exhibited up to 2 orders of magnitude higher efficiencies per nanotube than polymer/nanotube BHJs. The inefficient BHJs were attributed to incomplete polymer dispersion, which resulted

in the formation of polymer aggregates and tube–tube junctions.

Arnold et al.<sup>1016</sup> utilized polymer-wrapped CNTs with SnPc and  $C_{60}$  acceptors in broad-band photodetectors with spectral response at <400 nm to 1600 nm. The use of CNTs enabled extension of the range of sensitivity to near-IR wavelengths, resulting in IQEs of 44% at 1155 nm.

Graphene and its derivatives, such as graphene oxide (GO) and reduced graphene oxide (rGO), have received considerable attention in the organic optoelectronics community. Their utility as an anode replacement (e.g., as an ITO substitute), cathode material, hole transport interlayer (e.g., as a PEDOT:PSS replacement) or electron extraction interlayer, and electron acceptor in BHJ solar cells and PR materials<sup>1017</sup> has been demonstrated, and challenges have been identified. For example, increasing the transparency and decreasing the sheet resistance of graphene films are necessary to improve their performance as electrodes. A better control over its work function, for example by doping, is needed for applications of graphene as a cathode material. Improving the miscibility is necessary for its use as an electron acceptor in blends. For a detailed overview, see the recent reviews in refs 1018 and 1019.

**9.3.7. Organic–Inorganic Hybrid Materials and Interfacial Phenomena.** Utilizing the best qualities of organic and inorganic materials in high-performance optoelectronic devices is one of the most promising long-term strategies for organic optoelectronics. For example, the use of inorganic oxides as interlayers in inverted OPVs has boosted the OPV performance and enabled tunable energy level matching between the inorganic electrode and organic active layers (Section 11.1.2.1).<sup>1020</sup> Kim et al.<sup>1021</sup> demonstrated PCEs of up to 10.5% in tandem cells combining polymer:fullerene and a-Si:H cells (Table 8), each of which had PCEs of <8% in a single-junction device. The performance of several organic–inorganic hybrids in solar cells, with PCEs of up to ~13–14%, and PR devices is included in Tables 8 and 7, respectively.

Theoretical efforts aiming to understand organic/inorganic hybrid materials using DFT, MBPT, GW (all for charged excitations), and BSE (for neutral excitations) and current challenges for *ab initio* methodologies are summarized in ref 1022. Renshaw and Forrest<sup>1023</sup> modeled exciton and charge transport in organic/inorganic planar HJs and derived a diode equation describing  $J$ – $V$  characteristics in such devices. The model invokes a hybrid CT exciton in which the polaron in the organic layer is localized whereas the charge carrier in the inorganic layer is delocalized over many lattice ions. In a companion publication, Panda et al.<sup>1024</sup> validated this description by modeling experimentally measured  $J$ – $V$  characteristics in several HJs.

Panahandeh-Fard et al.<sup>1025</sup> combined ultrafast spectroscopy with DFT to show the coexistence of subpicosecond electron and hole transfer at the GaAs/P3HT interface, which generated long-lived (>1 ns) hybrid interfacial states. Ambipolar CT has been observed in organic–organic HJs as well<sup>115</sup> and is a potentially promising concept for optimization of PCE in all-organic or hybrid devices. Recent advances in understanding ultrafast CT dynamics at organic/inorganic interfaces is summarized in ref 1013. Caplins et al.<sup>1026</sup> used TR-2PPE spectroscopy to observe quantum beats at metal/organic interfaces due to high-order Rydberg states (or image-potential states, IPS) that form at the interface due to the potential resulting from the image force. In CoPc/Ag(100) and NC-Ph<sub>4</sub>-CN/Ag (111), the beats persisted at >1-ps time-scales

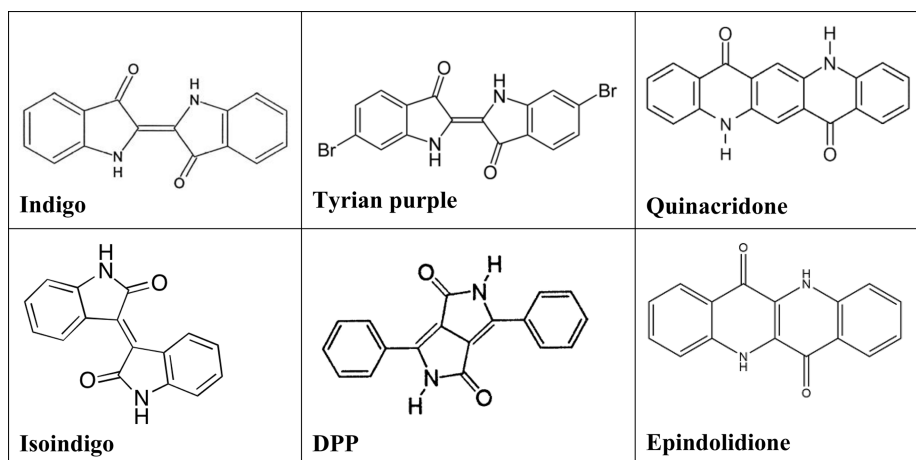


**Figure 29.** Examples of pigments utilized in organic electronics that were originally derived from (or feature building blocks originally derived from) natural products.

suggestive of long-lived coherence of electronic origin. Racke et al.<sup>1027</sup> applied core-hole clock spectroscopy to observe changes in ultrafast charge carrier dynamics in ZnO films upon adsorption of C<sub>60</sub> molecules. They demonstrated that such adsorption strongly suppressed carrier delocalization in ZnO, changing the 0.4 fs delocalization lifetime to 30 fs.

A common approach to achieving desirable optoelectronic properties in hybrid materials combines advantages of polymer processability with high-mobility and tunability of optical properties of inorganic nanocrystals (NCs), as discussed in recent review articles.<sup>1028–1031</sup> NCs and QDs have been utilized as acceptors in BHJs with a polymer donor to enhance the absorption and dielectric constant<sup>1031</sup> and in planar HJs with a SF-efficient donor to dissociate triplet excitons,<sup>23,411</sup> as well as sensitizers in PR materials to extend the sensitivity to near-IR wavelengths (Table 7).<sup>1032,1033</sup> Noone et al.<sup>996</sup> observed that in polymer:NC blends the photoinduced polaron lifetimes were an order of magnitude longer than in blends with PCBM. Bansal et al.<sup>1034</sup> studied photoinduced charge carrier dynamics in blends containing a polymer (P3HT, MEH-PPV, or various D–A copolymers) and CdS nanocrystals. The study established that acceptor crystallinity promotes charge delocalization, thus reducing the energy requirement for charge separation, a conclusion similar to that for organic–organic HJs (Section 3.3). However, the exciton binding energies were considerably lower (by several tens of eV) in organic–inorganic HJs as compared to organic–organic HJs. Yang et al.<sup>411</sup> demonstrated a solution-processed TIPS-Pn/PbS NC bilayer solar cell with a PCE of up to 4.8%. In these devices, the PbS NCs promoted dissociation of triplet excitons generated by the SF in TIPS-Pn.

Most NCs utilized in organic–inorganic hybrid optoelectronic composites involve toxic Cd- or Pb-based materials, and switching to low-toxicity earth-abundant materials such as FeS<sub>2</sub>, Cu<sub>2</sub>S, CuO, etc. is one of the important current research efforts.<sup>1031</sup>

Another potentially important approach that utilizes properties of inorganic materials in organic devices relies on harnessing plasmonic interactions to enhance light absorption in OPVs or light outcoupling in OLEDs. For example, Kulkarni et al.<sup>1035</sup> deposited an OPV benchmark blend, P3HT:PCBM, on a substrate with Ag nanoprisms and obtained a factor of 3 increase in photoinduced polaron yield. The effect was attributed to an increased optical path length due to enhanced light scattering and to the plasmonic near-field absorption

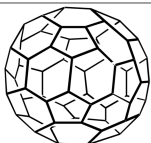
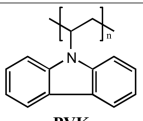
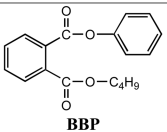
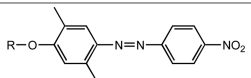
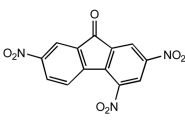
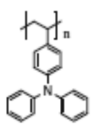
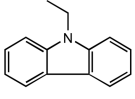
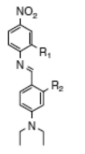
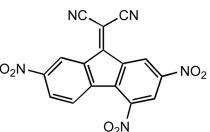
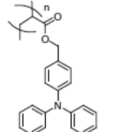
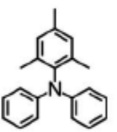
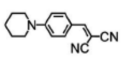
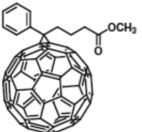
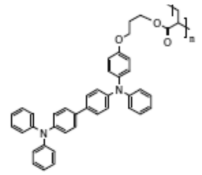
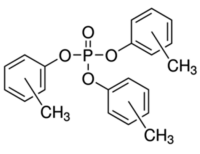
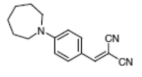
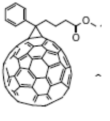
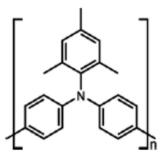
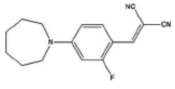
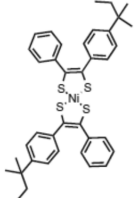
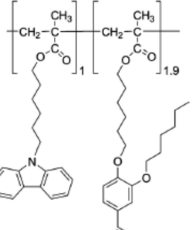
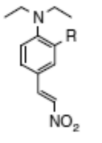
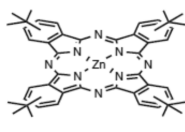
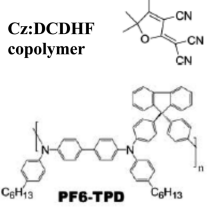
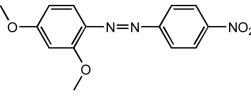
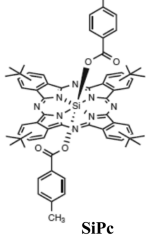
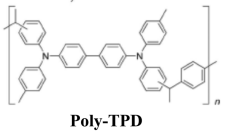
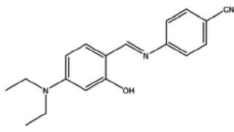
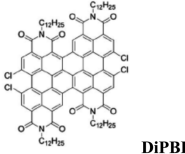
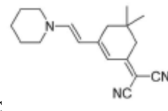
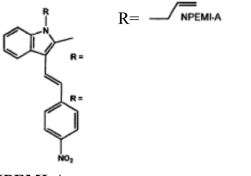
enhancement. Additional examples are given in Section 11.1.2.4.

#### 9.4. Naturally Derived and Other H-Bonded Materials

Over the past ~5 years, there has been a considerable research effort focusing on sustainable, natural product-derived materials for organic electronics.<sup>1036</sup> These include biodegradable and biocompatible substrate materials (e.g., polyester elastomers), dielectric and electrode materials, and plant- or animal-derived active layers; see recent reviews (Table S1).<sup>1037–1039</sup> Examples of the latter include carotenoids, porphyrins, and anthraquinone derivatives, with the most successful examples being the indigo and Tyrian purple dyes,<sup>1038,1040,1041</sup> as discussed below. The success of these derivatives of natural origin, and with unconventional molecular structure (Figure 29), represents a change from the traditional requirements of an organic semiconductor molecule to necessarily possess a fully  $\pi$ -conjugated core, instead shifting the focus toward the importance of H-bonding for photophysics and molecular packing.

Conjugated molecules are ubiquitous in nature, constituting many natural pigments that have been used in art, wood staining, textile dyes, etc. over the centuries.<sup>1037</sup> However, the pigments utility as organic semiconductors had been limited until very recently<sup>1042,1043</sup> (although there had been some early work on photophysics and charge carrier dynamics in carotenes<sup>1044</sup> and chlorophyll<sup>1045</sup>). The recent success of naturally derived indigo and other H-bonded dyes and pigments as organic electronic materials has been named a “paradigm shift in molecular electronics design”.<sup>1038</sup> These dyes exhibit high stability to heat degradation and chemical oxidation (which prompts their utility as textile dyes), and they possess long-range order and exhibit remarkable photophysics due to both intra- and intermolecular H-bonding. Recent work of Sariciftci and co-workers<sup>1037,1039,1042,1043,1046–1049</sup> presents evidence that H-bonded building blocks, such as indigoids (derived from indigo dye obtained from *Indigofera tinctoria* and *Isatis tinctoria* plants and traditionally used for coloring blue jeans), may offer good optoelectronic performance and stability *in spite of lack of intramolecular conjugation*. These materials owe their performance to intermolecular order that promotes charge delocalization resulting in enhanced charge transport properties. For example, the electron and hole mobility of 0.3 cm<sup>2</sup>/Vs) was reported in OFETs of Tyrian purple, a 6,6’-

Table 6. Chemical Structures of Sensitizers, Photoconductors, Plasticizers, and NLO Chromophores Utilized in High Performance PR Polymer Composites

Sensitizers	Polymers	Plasticizers	NLO chromophores
 <b>C<sub>60</sub></b>	 <b>PVK</b>	 <b>BBP</b>	 <b>DMNPAA: R=CH<sub>3</sub>,</b>
 <b>TNF</b>	 <b>PDAS</b>	 <b>ECZ</b>	 <b>HI</b>
 <b>TNFM</b>	 <b>PDAA</b>	 <b>TAA</b>	 <b>PDCST</b>
 <b>PC<sub>61</sub>BM</b>	 <b>PATPD</b>	 <b>TCP</b>	 <b>7-DCST</b>
 <b>PC<sub>85</sub>BM</b>	 <b>PTAA</b>		 <b>FDCST</b>
 <b>TT-2324</b>	 <b>Cz:DCDHf copolymer</b>		 <b>DEANST</b>
 <b>ZnPc</b>	 <b>PF6-TPD</b>		 <b>MNPA</b>
 <b>SiPc</b>	 <b>Poly-TPD</b>		 <b>Dc</b>
 <b>DiPBI</b>			 <b>P-IP-DC</b>
			 <b>NPEMI-A</b>

dibromoindigo pigment originally derived from sea snails and shellfish, and a hole mobility of  $1.5 \text{ cm}^2/(\text{Vs})$  was demonstrated in epindolidione, a structural isomer of indigo used as a yellow colored toner for printing.<sup>1042</sup> Furthermore, PCEs of up to 8.2% were obtained from D–A BHJ OPVs with indigoid donors and fullerene acceptors.<sup>1050</sup> The high performance of these dyes is coupled with high stability in air;<sup>1042</sup> for example, no degradation in Tyrian purple diode performance was reported after at least a month of continuing operation in air, and no degradation of epindolidione OFET was observed for at least 140 days of operation in air.<sup>1039</sup>

Another successful naturally derived building block is H-bonded DPP pigments. These have been used extensively in outdoor and automotive paints (e.g., in “Ferrari Red”), and they exhibited ambipolar transport in OFETs with mobilities of up to  $0.06 \text{ cm}^2/(\text{Vs})$ .<sup>1043</sup> As discussed in Section 9.2, the DPP-based D–A copolymers exhibit charge carrier mobilities of  $>10 \text{ cm}^2/(\text{Vs})$ , at least 4 orders of magnitude higher than those in traditional conjugated polymers (e.g., PPV derivatives) and on-par with molecular crystals.<sup>1052</sup>

Finally, some derivatives such as quinacridone (derived from naturally occurring acridone and widely used as a magenta colored toner for printing), in addition to ambipolar charge carrier mobilities of  $\sim 0.1 \text{ cm}^2/(\text{Vs})$ ,<sup>1042</sup> exhibited extraordinary photoconductive properties: an EQE of 10% was obtained in a single-component diode (ITO/PEDOT:PSS/quinacridone/Al), which is 3 orders of magnitude higher than that in Pn films in a similar device geometry.<sup>1046</sup> The high EQE achieved was attributed to efficient formation of CT excitons with low binding energy, which has been cited to be a common feature of H-bonded pigments.<sup>1048</sup> This is promising because of the abundance of such pigments,<sup>1053</sup> which represent a largely unexplored resource for organic optoelectronics.

H-bonds have been recognized to be ideal noncovalent interactions to construct supramolecular architectures, since they are considerably stronger than van der Waals interactions,<sup>1039</sup> and they are highly selective and directional: 1D, 2D, and 3D H-bonding-driven molecular assemblies have been demonstrated.<sup>815,1051</sup> For example, indigo and Tyrian purple (Figure 29) pigments are planar molecules with strong intermolecular H-bonding; each molecule H-bonds to four neighbor molecules. This produces highly crystalline vacuum-deposited films in which the structure is a result of the interplay between intermolecular H-bonds and  $\pi$ – $\pi$  stacking interactions. The synergy of H-bonding and  $\pi$ – $\pi$  interactions has been utilized in formation of high-mobility polymer fibers for OFETs, ordered D/A stacks for OPVs, J-aggregates for light-emitting devices, etc.<sup>815</sup> Control over pigment crystallization into macroscopic-size crystals and control over polymorphism are not simple, and they depend on the nature of the underlying substrate<sup>1049,1054</sup> and on the exact mechanism of molecular assembly.<sup>815</sup> This problem was tackled in ref 1049, and three ways of reproducing the molecular assembly into ordered crystalline structures were proposed. All three approaches use a protection/deprotection mechanism, in which functionalization with the protection group (*t*-butoxycarbonyl, or *t*-Boc) temporarily disables H-bonding, creating a latent pigment. It is then again enabled, in a controlled manner, by removal of the protecting groups (“deprotection”) using a thermal cleavage, an acid catalyzed reaction, or a substitutional reaction with amines. These methods facilitated formation of several micron-size crystallites in a wide variety of pigments tested, which led to enhanced charge transport and photo-

generation properties. Moreover, this enabled control over polymorphism, which is important, as some pigments (including a well-known CuPc) exhibit up to 5 polymorphs.<sup>1038</sup> H-bonded structures are not limited to materials of a particular class and have utilized oligomers, polymers, nanoparticles, and D/A cocrystals;<sup>1055</sup> see the comprehensive review by Gonzalez-Rodriguez and Schenning.<sup>815</sup>

### 9.5. Photorefractive Organic Amorphous Materials

There are several classes of PR organic amorphous materials, which include polymer composites, amorphous glasses, fully functionalized materials, polymer-dispersed liquid crystals (PDLCs), and other LC-containing materials. Detailed discussions of the materials of each class developed before 2004, with tables summarizing their performance, can be found in ref 220. More recent developments were reviewed in refs 628, 629, and 664. Development of PR ferroelectric LCs was summarized in ref 1056. Here the discussion will be limited to the best-performing polymer composites and glasses, arbitrarily defined as those with 2BC gain coefficients above  $150 \text{ cm}^{-1}$  and/or diffraction efficiencies above 50%, reported since 2005.

The most common composition of the best PR polymer composites is  $\sim 40$ – $60 \text{ wt } \%$  of a photoconductive polymer to provide sufficient density of charge transport sites,  $\sim 25$ – $35 \text{ wt } \%$  of a NLO chromophore to ensure a sufficient electro-optic response,  $\sim 15$ – $30 \text{ wt } \%$  of a plasticizer to facilitate chromophore orientation by lowering  $T_g$  of the material, and a small amount of a sensitizer to assist in charge generation. Examples of these constituents are shown in Table 6, and the properties of the best-performing PR polymer composites are summarized in Table 7.

Over the past decade, research efforts have focused on developing new sensitizers<sup>628,685,1057</sup> and photoconductive polymers<sup>1058,1059</sup> for PR composites. In the case of the sensitizers, the challenges include (i) promotion of charge photogeneration efficiency to increase the rate of PR grating formation without increasing the density of deep hole traps and/or (ii) extension of the PR response into the IR wavelength region (e.g., toward telecommunication wavelengths of  $\sim 1.3$  and  $1.55 \mu\text{m}$ ). (It should be noted that because of a low sensitizer concentration in typical PR materials, the improved charge photogeneration efficiency must not rely on the crystallinity of the acceptor, in contrast to organic solar cells that often take advantage of this property, unless large enhancements can be obtained with nanocrystalline acceptor domains.)

Many earlier PR polymer composites relied on fullerene derivatives as sensitizers, which promoted charge generation efficiency as a result of the fullerene forming a CT state with the polymer.<sup>220</sup> However, cw illumination of the PR composite may result in considerable accumulation of long-lived fullerene anions that serve as hole trapping and/or recombination sites<sup>632</sup> that reduce charge carrier mobility and lead to illumination history dependence of the PR performance. While this effect is not limited to fullerene sensitizers,<sup>685,1060</sup> and its extent depends on the properties of other constituents (such as the HOMO energies of the NLO chromophores<sup>603</sup>), nonfullerene sensitizers provide an opportunity to enhance the performance and eliminate this origin of irreproducible device performance. For example, Ditte et al.<sup>1057</sup> reported that a standard PVK:SCB-based PR composite sensitized with a nonfullerene sensitizer DiPBI outperformed that with PCBM,

Table 7. Photorefractive Properties of High-Performance Organic Materials

Composite (conc of the constituents, wt %) <sup>a</sup>	$T_g^b$ , °C	$\alpha_r$ , cm <sup>-1</sup> c	$d_r^d$ , μm	$\lambda_r$ , nm <sup>e</sup>	$\Gamma$ cm <sup>-1</sup> (F, V/μm)	$\tau_{\text{gr}}^{-1}$ , s <sup>-1</sup> (J, W/cm <sup>2</sup> ) <sup>g</sup>	$\eta_{\text{max}}^h$ % (E, V/μm) <sup>h</sup>	$\tau_{\text{FWM}}^{-1}$ , s <sup>-1</sup> (J, W/cm <sup>2</sup> ) <sup>i</sup>	$\Delta n$ , 10 <sup>-3</sup> (F, V/μm)	Ref
PDAS:FDCST:ECZ:PCBM (54:30:15:1)		186		532	36.5(40)		93int (50)	3 (0.344)	1.6 (40)	1066
PTAA:PDAST:AA:PCBM (44:5:35:20:0.5)		174		561	144 (45)	43 (0.052)	65int (45)	7.4 (0.052)	7.4 (0.052)	686
		384		532	128 (45)	34 (0.098)	78int (45)			
						93 (0.427)				
PVK:7-DCST:ECZ:TNF (44:35:20:1)		276	<100	532	211 (45)	-	91int (45)	9.3 (0.098)	2.0 (45)	
Poly-TPD:P-IP-DC:BBP:PCBM (54:30:15:1)	28	19	50	633	173 (70)		67int (30)	4.3 (0.17)	1.4 (45)	1067
PDAA:7-DCST:BBP:PCBM (55:40:4:1)	25	361		532	230 (60)		83int (40)	2.9 (0.12)	2.5 (50)	1059
		210		561	90 (60)		91int (50)	0.27 (0.17)	5.8 (60)	677
		129		594	70 (60)		90int (55)	0.28 (0.17)	4 (60)	
					350 (120)		90int (65)	0.45 (0.22)	3.5 (60)	
Copolymer (PVK:DCDHF):ECZ:TNF(54:45:1)	6	93	37	633	60 (63)		90int (56)	29 (0.32)	24 (120)	1068
PVK:DC:ECZ:C <sub>60</sub> (49:25:25:1)		35	110	633	40 (63)		87int (48)		2.2 (63)	676
PVK:HI:ECZ:C <sub>60</sub> (49:25:25:1)		28		633	188 (70)	6.7 (0.016) <sub>10max</sub>			2.4 (54)	1069
PVK:SCB:DIPBI (59:7:40:2:0.1) <sup>k</sup>		27	50	532	350 (76)		91int (62)		5 (76)	685
PVK:PDAST:BBP:SiPc <sup>k</sup> (<50:35:15:0.0026-0.52)	23	3-180	105	633	210 (76)	9.5 (0.32)	89int (66)	2 (1) (kick-off)	4 (76)	685
PVK:PDAST:BBP:ZnPc <sup>k</sup> (<50:35:15:0.002-0.4)	23	6-380	105	633	200 (50)	0.5 (0.32)	90int (40)	4.5 (0.2)	5 (70)	662
PATPD-CAAN:FDCST:ECZ (50:30:20)			100	532	136 (70)		90int (45)			635
PATPD:7-DCST:ECZ:C <sub>60</sub> :Alq3 (53.5:30:15:0.5:1)		160	105	532						
		45		633						
PATPD:7-DCST:ECZ:C <sub>60</sub> (54.5:25:20:0.5)		104	105	532			85-95int steady-state 56int 1 ns pulsed (95)	250 (1.2)		1064
PVK:7-DCST:TCP:PVK-CNT (49.6:34.7:14.9:0.8)		11	100	633	78 (80)		60int, 44ext (50)	3330 (4 mj/cm <sup>2</sup> )		1014
PVK:AODGST:ECZ:PbS (43:43:10:4)		27		633	211 (60)		83int, 45ext (50)	6.3 (1.5) (weighted ave)		1070
NPEMI-A:TNFM (99:1)	18		23	685	210 (75)					1071
PF6-TPD:DMNPAA:MNPAAs:fullerene <sup>k</sup> /(49:25:25:1)			106	830	32 (57)		>88int (60)	2-20 <sup>l</sup> (0.64) (preillumination)	3.4 (60)	1072
PF6-TPD:DMNPAA:MNPAAs:PCBM (40:25:25:10)	6		105	830			>95int (65)	~143 for 10%, ~50 for 50% diff.eff. (0.46)		1063
PF6-TPD:DMNPAA:MNPAAs:PC <sub>81</sub> BM (45:25:25:5)	6-7	42	106	1064	33(57)		81int (60)	28 (1)	4.3 (57)	1073
PF6-TPD:DMNPAA:MNPAAs:TT2324 (45:25:25:5)	6-7	120	106	1064	30 (57)		80int (65)	14 (1)	4.3 (57)	
PVK:DEANST:ECZ:PbS (48:25:25:2)		46	54	1310	131 (84)	~0.5 (0.05)				1033
PVK:DEANST:ECZ:PbS		69		1340	185 (93)	0.65 (0.28)				1061
PVK:DEANST:ECZ:PbSe (48:27:15:10)		8	59	1550	86 (59)		40int (60)	0.56 (0.1)	3.1	1032
PATPD:7-DCST:ECZ:DBM (49:40:10:1)	25	-	105	1550(130 fs pulse)	20 <sup>m</sup> (95)		40int (65)	29 (45 mj/cm <sup>2</sup> )	9	1062

<sup>a</sup>Composition of the photorefractive (PR) polymer composites; molecular structures of the compounds can be found in Table 6. Concentrations of the constituents are given in parentheses in wt %. All data reported were obtained in the Bragg regime (volume grating) at room temperature. <sup>b</sup>Glass transition temperature  $T_g$  of the composite. <sup>c</sup>Absorption coefficient  $\alpha$  at the wavelength of PR experiments. <sup>d</sup>Sample thickness  $d$ . <sup>e</sup>Wavelength of the PR experiments  $\lambda_r$ . <sup>f</sup>ZBC gain coefficient, measured with p-polarized writing beams,  $\Gamma$ . Shown in parentheses is the electric field  $F$ , at which the indicated  $\Gamma$  was obtained. <sup>g</sup>PR response time  $\tau_{\text{gr}}^{-1}$  obtained from fits or estimated from the 2BC dynamics. Shown in parentheses is the total light intensity of writing beams, at which the indicated value of  $\tau_{\text{gr}}^{-1}$  was obtained. <sup>h</sup>Maximal FWM diffraction efficiency  $\eta_{\text{max}}$  measured with p-polarized probe and s-polarized writing beams. External ( $\eta^{\text{ext}}$ ) or internal ( $\eta^{\text{int}}$ ) diffraction efficiency is indicated, where applicable. Shown in parentheses is the electric field  $F$  at which the indicated  $\eta$  was obtained. <sup>i</sup>PR speed  $\tau_{\text{FWM}}^{-1}$  estimated from the data or obtained from fits to formation of the PR grating measured in the FWM experiment. Shown in parentheses is the total light intensity of writing beams. Other experimental protocol details such as application of the kick-off voltage or preillumination are indicated. <sup>j</sup>Refractive

Table 7. continued

index modulation  $\Delta n$ , calculated from the diffraction efficiency, obtained at an electric field  $F$  shown in parentheses. <sup>k</sup>In these composites, the best gain, diffraction efficiency, and PR speed were achieved at slightly different sensitizer concentrations. <sup>l</sup>Seven fullerene derivatives were explored as sensitizers. Highest PR speed was achieved with PC<sub>81</sub>BM. <sup>m</sup>Net gain.

exhibiting an increase in the PR grating formation speed by a factor of  $\sim 39$  due to a  $\sim 100$  enhancement in the photocurrent.

For a detailed discussion of sensitizers, see ref 628. Briefly, nonfullerene sensitizers include fluorene-based molecules (e.g., TNF in Table 6), metal-containing complexes (e.g., phthalocyanine derivatives<sup>685</sup>), perylene bisimide (PBI) derivatives,<sup>1057</sup> graphene- and CNT-based additives,<sup>1014,1017</sup> and inorganic semiconductor QDs and nanocrystals.<sup>1032,1033,1061</sup> The latter, for example, enabled a strong PR response at 1.3 and 1.55  $\mu\text{m}$ .<sup>1032,1033,1061</sup> Such an IR response with organic sensitizers thus far has been achieved only via pulsed PR grating recording utilizing two-photon absorption (TPA) with a TPA dye acting as a sensitizer.<sup>1062</sup>

The trade-off between the PR steady-state performance and the dynamics of the PR grating formation and erasure ("PR speed") is a well-known issue, which originates from reliance of high 2BC gain and diffraction efficiency on space-charge field formation enabled by charge traps that could at the same time be detrimental for charge transport (Section 6). Because the charge trap density dramatically depends on the photophysics and concentration of the sensitizer, the requirement of high charge generation efficiency (enabled by the sensitizer) must be balanced by the requirement of high charge carrier mobility (impeded by the sensitizer-induced charge traps), and by the requirements for optimal trap densities dictated by the desirable steady-state 2BC gain or diffraction efficiency. As a result, it is commonly observed that better steady-state performance is achieved at different sensitizer concentrations than those required for the fastest dynamics.<sup>685,686,1057</sup> Nevertheless, diffraction efficiencies of  $>80\%$ , coupled with sub-100-ms PR grating formation speed, have been demonstrated in several polymer composites (Table 7), which enables holographic applications relying on the video-rate recording (Section 11.3.1).

One of the major factors limiting the PR speed has been a low hole mobility in polymers utilized in earlier PR polymer composites (e.g.,  $\mu \sim 10^{-7}$ – $10^{-6}$   $\text{cm}^2/(\text{Vs})$  in PVK). Therefore, a significant improvement in the PR speed was obtained with polymers exhibiting higher mobilities such as TPD and PTAA or PDAS derivatives ( $10^{-5}$ – $10^{-4}$   $\text{cm}^2/(\text{Vs})$  and  $10^{-4}$ – $10^{-3}$   $\text{cm}^2/(\text{Vs})$ , respectively). For example, Salvador et al.<sup>1063</sup> observed a factor of 250 higher PR speed in the PF6-TPD-based composite as compared to that based on the PVK. Internal diffraction efficiencies of  $\sim 50\%$  were achieved within  $\sim 10$ – $20$  ms in PTAA- and PF6-TPD-based PR composites at  $\sim 0.45$   $\text{W}/\text{cm}^2$  cw 532 and 830 nm excitation, respectively, at moderate electric fields (45 and 57  $\text{V}/\mu\text{m}$ ).<sup>686,1063</sup> A 56% internal (35% external) diffraction efficiency was observed with a response time of only 300  $\mu\text{s}$  using holographic recording with a single 1-ns, 532-nm pulse in a PATPD-based PR composite.<sup>1064</sup>

Regardless of challenges and of relatively low-performance photoconductive polymers which constitute the basis for current PR polymer composites, remarkable progress in PR polymer-based device technologies has been achieved (Section 11.3). Recent development of polymers with mobilities above 10  $\text{cm}^2/(\text{Vs})$  (Table 3) (including amorphous polymers with mobilities above 1  $\text{cm}^2/(\text{Vs})$ )<sup>389</sup> represents an exciting opportunity to further boost the PR speed, especially in the near-IR wavelength region. Because the PR material has to possess high optical quality, of special interest are high-mobility amorphous low-disorder polymers<sup>389</sup> and, possibly, polymers in which charge transport relies on interconnectivity of nano-

crystalline domains rather than long-range order achieved with large crystallites.<sup>1065</sup> Additional opportunities include development of nonfullerene sensitizers following guidelines similar to those outlined for highly efficient solar cells (Section 9.3.2) and an incorporation of interlayers that could potentially enhance local electric fields (Section 11.1.2.1).

## 9.6. Summary

Remarkable understanding in molecular design of organic optoelectronic materials has been achieved in the past several years, enabling impressive charge carrier mobilities of  $>10\text{ cm}^2/\text{Vs}$  and the OPV performance with PCEs  $> 8\%$ . These achievements should also enable design of novel PR organic materials with considerably faster dynamics of PR grating formation, which is awaiting realization. Design strategies have been formulated for several classes of materials depending on their function in the (opto)electronic device, as summarized in relevant parts of this section. Several nontraditional approaches highlighted in this section have not yet reached their full potential. Nevertheless, these are important for the development of next-generation optoelectronic materials, possibly utilizing synergy of organic and inorganic materials (see also Section 11.1.2) and distinct physical mechanisms (such as hot electron transfer), as well as molecular design strategies compatible with sustainable practices and green chemistry.

## 10. EFFECTS OF STRUCTURE AND MORPHOLOGY, FABRICATION, AND PROCESSING

### 10.1. Structure and Morphology

The crystallinity, morphology, and particular aspects of the microstructure of organic films are among the key factors that determine the (opto)electronic performance of organic semiconducting films. Several examples were discussed in previous sections. In this section, selected additional examples of recent computational and experimental efforts, particularly those with strong and clear manifestation of structure or morphology-related effects, are briefly discussed. For excellent comprehensive reviews of film structure characterization and correlations between structural and charge transport properties or OPV characteristics, see refs 846, 1074 and 1075.

Crystallinity has been one of the key factors enhancing (opto)electronic performance both in small-molecule and in polymer-based devices. In small-molecule FETs, higher mobilities are obtained in single crystals as compared to films (Table 3). In BHJs, crystallinity has been linked to enhanced charge photogeneration efficiencies.<sup>206,300</sup> For example, in NPDC<sub>60</sub> BHJs, the delocalization of the CT state was promoted by the nanoscale fullerene crystallinity.<sup>72</sup> In polymer-based BHJs, the acceptor crystallinity reduced the required driving energy (thus, the required D–A energy offset) for charge separation.<sup>206</sup> Various aspects of crystallinity (such as band structure, particular packing motif, enhanced photostability,<sup>35,1076,1077</sup> etc.) can play a role in determining exciton and charge carrier dynamics. In polycrystalline films, relative orientations of crystallites,<sup>746,1078</sup> their size, and the relative volume of crystalline and amorphous domains<sup>724,1065</sup> determine the (opto)electronic properties of resulting films.

**10.1.1. Crystalline Small-Molecule Materials.** Molecular packing profoundly affects intermolecular interactions, which then dictate intermolecular charge and energy transfer and exciton and charge carrier delocalization. Molecular size, rigidity, and/or the size and the nature of solubilizing groups (e.g., TES, TIPS, etc. in R-Pn) determine the packing motif, the

interaction with the substrate surface, and the solubility, which in turn influence domain size and phase segregation.<sup>846</sup> The most common examples of intermolecular interactions that contribute to molecular packing are the  $\pi$ – $\pi$  and C–H– $\pi$  interactions, commonly found in acene and thiophene derivatives. Other interactions that have been used in molecular crystal engineering are F–F and F–S (e.g., in fluorinated ADT derivatives such as diF R-ADT), and S–S in, for example, hexathiapentacene and sulfur-substituted perylene derivatives.<sup>1074</sup> Another important strategy for directional molecular packing utilizes H-bonding.<sup>815,1079</sup>

The requirements for the packing motifs depend on the application. For example, in functionalized Pn derivatives (such as R-Pn), in which packing is controlled by the side groups R, the derivatives with the 2D “brick-work”  $\pi$ -stacking yielded FET performance superior to R-Pn derivatives exhibiting other types of packing.<sup>956</sup> As can be appreciated from Table 3, most high-mobility small-molecule organic semiconductors exhibit either herringbone or 2D “brick-work” packing, with close  $\pi$ – $\pi$  stacking distances. In polycrystalline films, the best charge transport characteristics are obtained in morphologies featuring well-aligned and well-connected large crystalline grains.<sup>779,1080</sup> On the other hand, the cyano-substituted R-Pn derivatives with a 1D “sandwich-herringbone” packing exhibited a considerably better performance as acceptors in BHJs with the P3HT donor as compared to derivatives with the 2D “brick-work” or 1D “slip-stack” packing.<sup>957</sup> Finally, for R-Pn derivatives optimized for the SF, slip-stack configurations with shifts of one-two rings along the long axis and one ring along the short axis of the R-Pn molecule are desirable.<sup>160</sup>

Several studies reported systematic assessment of the electronic properties of a single compound when the molecular packing is gradually tuned. Giri et al.<sup>538</sup> tuned the  $\pi$ – $\pi$  stacking distance in TIPS-Pn films using solution shearing. The authors were able to decrease the closest  $\pi$ – $\pi$  stacking distance from 3.33 to 3.08 Å (resulting in a 3-fold increase in the transfer integral), accompanied by the (101)  $d$ -spacing decrease from 7.7 to 7.2 Å and the (010)  $d$ -spacing increase from 7.8 to 8.1 Å at the highest shearing speeds. The charge carrier mobility was not monotonic with these changes, and the maximal value of  $4.6\text{ cm}^2/\text{Vs}$  was achieved at the intermediate values of these spacings, in part due to the formation of smaller and less oriented crystallites at higher shearing speeds. The authors subsequently demonstrated<sup>953</sup> that this method enables selection of specific TIPS-Pn polymorphs, some of which exhibited hole mobilities of up to  $11\text{ cm}^2/\text{Vs}$  (Table 5). Reyes-Martinez et al.<sup>1081</sup> fabricated rubrene single-crystal FETs on an elastomeric parylene gate dielectric and studied FET mobility in response to mechanical deformation of the elastomer. They found a linear relationship between the mobility and both the tension and compression, with mobility increasing by a factor of  $\sim 2$  when the intermolecular distance ( $d$ -spacing) decreased. For additional discussion of charge transport in organic devices on flexible substrates, see ref 1082.

In spite of the developments in methods for controlling molecular packing in crystalline materials, ensuring reproducibility in the crystalline film microstructure, especially in scale-up approaches, is difficult. One of the promising solutions combines high charge carrier mobilities of small-molecule organic semiconductors with film processability of amorphous polymers, in small-molecule:polymer blends.<sup>804,805,981</sup> Mobility of up to  $43\text{ cm}^2/\text{Vs}$  was observed in a C8-BTBT:PS blend, and mobility in blade-coated diF TES-ADT:PS blends

surpassed that achieved in diF TES-ADT crystals (Table 3).<sup>571,576</sup> In diF TES-ADT:PTAA and TIPS-Pn:PTAA blends, morphology-independent charge transport was observed in TFTs, attributed to formation of highly conductive grain boundaries.<sup>804</sup> Evolution of the charge transport characteristics of the diF TES-ADT blend upon addition of the PTAA polymer can be appreciated from Figure 30, which shows

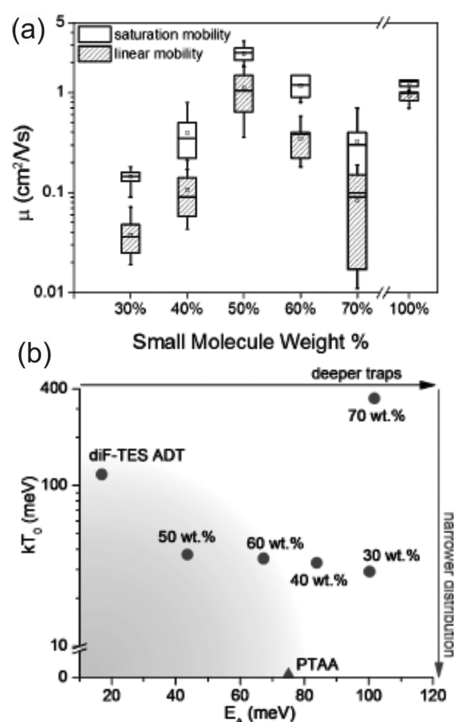


**Figure 30.** (a) Saturation and linear mobility in TFTs of small molecule:polymer (diF TES-ADT:PTAA) blends (over at least 10 devices) depending on the blend composition. (b) Trap depth ( $E_A$ ) and distribution width ( $kT_0$ ) in pristine diF TES-ADT and PTAA and their blends with various diF TES-ADT contents. Adapted with permission from ref 805. Copyright 2014 Wiley-VCH.

mobility measured in TFTs (a) and trap depth ( $E_A$ ) and distribution width ( $kT_0$ ) extracted from Arrhenius fits to the temperature dependence of the TFT characteristics (b).<sup>805</sup> Addition of PTAA resulted in the formation of deeper traps, but yielded lower trap distribution widths, an optimal combination of which (at 50 wt % of PTAA) yielded mobilities higher than those in pristine diF TES-ADT films prepared under similar conditions. This highlights blending with polymers as one of the means to decrease the energetic disorder associated with the heterogeneous environment of small-molecule polycrystalline films. An example of a spectroscopic study of blend composition-dependent molecular aggregation and the resulting photoconductive properties of small-molecule:polymer (diF TES-ADT: PMMA) blends can be found in ref 108.

**10.1.2. Polymers.** Noriega et al.<sup>1065</sup> proposed a classification of conjugated polymers into three classes based on their microstructure and crystallinity. They defined the paracrystallinity parameter  $g$  as the standard deviation of cumulative static lattice fluctuations normalized by the average value of the lattice spacing. With this definition,  $g < 1\%$  corresponds to highly crystalline materials (e.g., 0.9% in TIPS-Pn, Table 3), whereas  $g > 10\text{--}20\%$  are characteristic of

amorphous materials. Then, the three classes are (i) semi-crystalline conjugated polymers (e.g., P3HT or PBTTT) that form extended crystalline aggregates ( $g < 10\%$ ) with FET mobilities of  $0.1\text{--}1\text{ cm}^2/(\text{Vs})$  and  $\pi\text{--}\pi$  stacking distance variation causing energetic disorder with the trap depth and width of trap distributions of  $72 \pm 24\text{ meV}$ ; (ii) polymers with smaller, but well-connected aggregates ( $g = 10\text{--}15\%$ ), with trap distribution comparable to that in semicrystalline polymers of class (i); and (iii) amorphous polymers, with no aggregate formation, low mobilities ( $<0.1\text{ cm}^2/(\text{Vs})$ ), and deeper traps with wider trap distributions with energies of  $230 \pm 100\text{ meV}$ .

High-mobility D–A copolymers are the prominent examples of class (ii). In these materials, charge transport is enabled by efficient interchain charge transfer in aggregates and domain-to-domain percolation, resulting in charge carrier mobilities of over  $10\text{ cm}^2/(\text{Vs})$  (Table 3). This arrangement makes charge transport relatively insensitive to the microstructure of the amorphous regions of the films. Additionally, the large size of the conjugated molecular repeat units and close  $\pi\text{--}\pi$  stacking distances make the interchain charge transfer integrals less sensitive to the  $\pi\text{--}\pi$  stacking disorder. In these polymers the charge carrier mobility can be further improved by chain alignment. For example, Tseng et al.<sup>562</sup> used a nanogrooved substrate to facilitate growth of highly aligned densely packed fibers of PCDTPT. FET mobilities of up to  $23.7\text{ cm}^2/(\text{Vs})$  were demonstrated, which is an order of magnitude higher than those in FETs with nonpatterned substrates, without polymer alignment.

**10.1.3. Donor–Acceptor Bulk Heterojunctions.** Establishment of the optimal morphology for D/A BHJs has been a subject of intensive research, both computational (Section 3.2.2) and experimental; see a recent comprehensive review by Huang et al.<sup>1083</sup>

Maturová et al.<sup>271</sup> combined numerical modeling of charge transport and morphology of polymer:fullerene BHJs. They concluded that to achieve the best  $J\text{--}V$  characteristics, a phase separated morphology with feature sizes smaller than 50 nm is most optimal, as it supports efficient charge transport while reducing bimolecular recombination. The length scale of  $\sim 10\text{ nm}$  to match the typical exciton diffusion length has been considered an optimal domain size. However, with this requirement, it is difficult to also achieve good connectivity to electrodes to ensure optimal charge extraction.<sup>639</sup> Therefore, alternative morphologies have been examined; for example, Lyons et al.<sup>274</sup> used Monte Carlo modeling to establish the effects of domain size, purity, and interfaces on the OPV performance. They showed that the domain purity is important for good connectivity to the electrodes, and the quality of the interface plays a significant role, so that well-connected 4-nm-sized domains with sharp boundaries outperformed impure 10 nm domains with broadened interfaces.

Burke and McGehee<sup>273</sup> emphasized the importance of a three-phase morphology in BHJs containing donor, acceptor, and mixed D/A domains. Through kinetic Monte Carlo modeling of polymer:fullerene BHJs, they established that if the local charge carrier mobility is not high enough and/or the CT state is short-lived, then the three-phase structure with an energy cascade for either the electron or the hole increases the probability of charge separation and leads to high IQEs of BHJ solar cells. Westacott et al.<sup>1084</sup> combined measurements of transient absorption and optical absorption and PL spectroscopy with various techniques for structure and morphology characterization in P3HT:PCBM BHJs and P3HT/PCBM

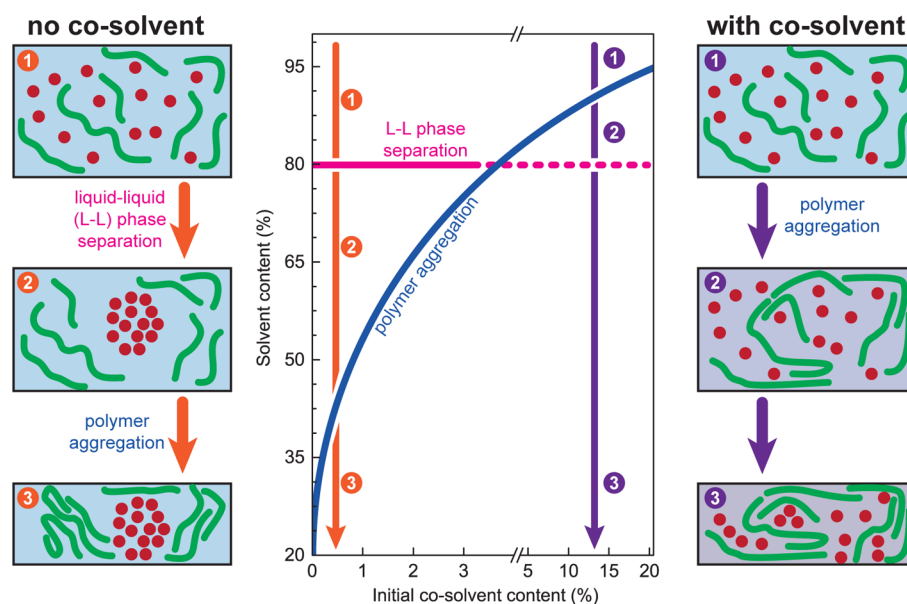


**Figure 31.** Schematic phase diagram revealing the role of cosolvent in inducing polymer aggregation at higher solvent content, which prevents large-scale liquid–liquid phase separation during drying, resulting in optimized morphologies. Adapted with permission from ref 1095. Copyright 2015 Nature Publishing Group.

planar HJs prepared using different protocols. They concluded that the intermixed D/A phase is important for exciton quenching and charge generation, but highlighted the critical importance of its coexistence with phase-pure regions, the degree of which can be controlled by the molecular weight of the polymer.

Li et al.<sup>1085</sup> examined the film morphology of BHJs containing PCBM- and DPP-based D–A copolymers (e.g., PDPPTPT) with varying lengths of solubilizing chains. The blends formed an extended polymer fibrillary network with fibril width depending on the derivative, which was correlated with the EQE. The authors concluded that short side chains and high molecular weight provide the best morphology, with the fibril width of <12 nm, enabling higher probability of excitons diffusing to the D/A interface and more than a factor of 2 improvement in PCE as compared to other derivatives.

Guo et al.<sup>398</sup> studied the effects of polymer crystallinity in BHJs of D–A copolymers (based on the PBDTTT core functionalized with various side groups) and PCBM. In this work, the ultrafast spectroscopy and optical absorption and time-resolved PL measurements were combined with GISAXS and AFM characterization. The authors concluded that higher polymer crystallinity hindered charge separation in these blends and argued that delocalized interchain excitons in these polymer donors did not lead to ultrafast charge generation. Instead, ultrafast charge separation was attributed to a high density of fullerene states energetically aligned with the donor states at the D/A interface. In another example, in AnE-PV copolymer-based ternary blends with PCBM, the polymer crystalline phase was found to be critical for efficient charge generation and suppressed nongeminate recombination.<sup>724</sup> Hwang et al.<sup>1086</sup> developed n-type NDI/PDI-selenophene random copolymers with FET mobilities of up to  $\sim 0.1 \text{ cm}^2/(\text{Vs})$ , with the highest values obtained in more crystalline samples with smaller  $\pi$ – $\pi$  stacking distances. When serving as acceptors in BHJs with the PBDTTT-CT donor, the highest PCE of 6.2% was obtained at an optimal bulk crystallinity of the acceptor polymer (quantified by the average crystalline domain

size  $L_c$  determined from the XRD), determined to be  $L_c = 5.1 \text{ nm}$ . The AFM and TEM studies of these blends revealed a phase-separated, interconnected microstructure with  $\sim 20 \text{ nm}$  domains.

## 10.2. Fabrication and Processing

Methods that enable enhanced crystallization and/or desired microstructure include optimization of the solvent, substrate surface treatment,<sup>1080,1087</sup> the use of additives,<sup>638</sup> blend composition, thermal and solvent vapor annealing, etc. (Table S1). Recent advances in solution processing methods were reviewed in refs 1088, 1089 (OFETs) and 1090, 1091 (BHJs). In this section, selected recent efforts are highlighted.

Diemer et al.<sup>1092</sup> demonstrated a vibration-assisted crystallization technique which improved charge carrier mobilities in functionalized Pn and ADT TFTs by a factor of 2–4 due to reduced charge trap density at the organic/gate dielectric interface. Yuan et al.<sup>576</sup> proposed an off-center spin-coating method which promoted formation of highly aligned crystalline grains. The method yielded the C8-BTBTB:PS TFTs with average hole mobilities of  $25 \text{ cm}^2/(\text{Vs})$ , with a maximal observed value of  $43 \text{ cm}^2/(\text{Vs})$ .

Ma et al.<sup>1093</sup> used solution shearing to manipulate the relative molecular orientation in polymer:fullerene BHJs. Using polarized soft X-ray scattering, the authors showed that slower solution-shear speed promoted the face-to-face molecular orientations of the polymer and argued that the technique should be applicable to any two-component system in which at least one of the components forms aggregates.

Zhang et al.<sup>1094</sup> developed a technique for vertical growth of nanopillars, which would enable vertical interdigitated geometry of the D/A interfaces in solar cells. Using CuPc as the donor and C<sub>60</sub> or C<sub>70</sub> as acceptors, they demonstrated up to 32% enhancement in PCE in the nanopillar geometry as compared to thin films with the same constituents, due to the increased D/A interfacial area.

Van Franeker et al.<sup>1095</sup> developed an optical system, based on measurements of optical interference, scattering, and reflectivity, for *in situ* monitoring of film casting. They examined

Table 8. High-Performance Organic Solar Cells

Material	$J_{sc}$ ( $\text{mA}/\text{cm}^2$ )	$V_{oc}$ (V)	FF	PCE <sup>b</sup> (%)	Notes <sup>c</sup>	Ref
<b>Polymer:fullerene BHJs (PCE <math>\geq</math> 8.5%)<sup>d</sup></b>						
ITO/PEDOT:PSS/PBDTTPD:PC <sub>71</sub> BM/Ca/Al	12.6	0.97	0.7	8.3 (8.5)	additives	1208
ITO/ZnO/C3-DPPTT-T:PC <sub>70</sub> BM/MoO <sub>3</sub> /Ag	23.5	0.57	0.66	8.8	Treated ZnO	1209
ITO/ZnO/PBTI3T:PC <sub>71</sub> BM/MoO <sub>3</sub> /Ag	12.8	0.85	0.76	8.4 (8.7)	2% DIO	1210
ITO/ZnO/PCBE-OH/PBDT-BT:PC <sub>71</sub> BM/MoO <sub>3</sub> /Ag	15.4	0.92	0.66	9.2 (9.4)	interlayer	1211
ITO/ZnO/PT-tt-TPD:PC <sub>71</sub> BM/MoO <sub>3</sub> /Ag	15.3	0.86	0.7	9.2	3% DIO	1212
ITO/PEDOT:PSS/PPDT2FBT:PC <sub>70</sub> BM/Al	16.3	0.79	0.73	9.2 (9.4)	CB+DPE solvent mix; 300 nm	1213
ITO/PEDOT:PSS/PBDT-TS1:PC <sub>71</sub> BM/Mg/Al	17.4	0.8	0.66	9.2 (9.5)	DIO 3%	1214
ITO/PEDOT:PSS/PBDT-TT:PC <sub>71</sub> BM/CPZ/Al	19	0.75	0.7	9.9 (10.2)	PT2NDISB CPZ interlayer	1158
ITO/ZnO/PTB7-Th:PC <sub>70</sub> BM/MoO <sub>3</sub> /Al	19.2	0.78	0.67	9.9 (10.1)	ZnO DAN substrate	1215
ITO/PEDOT:PSS/PTB7:PC <sub>71</sub> BM/MSAPBS/Al	19.3	0.76	0.68	9.7 (10.0)	interlayer	1216
ITO/ZnO/PNTz4T:PC <sub>71</sub> BM/MoO <sub>3</sub> /Ag	19.4	0.71	0.73	9.8 (10.1)	Thick film: 290 nm	1217
Ag/FPI-PEIE/PBDT-T-F-TT:PC <sub>71</sub> BM/MoO <sub>3</sub> /UTMF-Ag/TeO <sub>2</sub>	18.2	0.81	0.71	10.3 (10.5)	ITO-free; microcavity	1206
ITO/PFN/PTB7:PCBM/MoO <sub>3</sub> /Al	17.4	0.82	0.74	10.6	3% DIO, SVA	1218
<b>Tandem and triple-junction cells (PCE &gt; 10%)<sup>d</sup></b>						
ITO/PEDOT:PSS/SMPV1:PC <sub>71</sub> BM/CPE1/CPE2/M-PEDOT:PSS/SMPV1:PC <sub>71</sub> BM/CPE3/Al	7.7	1.82	0.72	10.1		1219
ITO/LZO/C <sub>60</sub> -SAM/PSEHTT:IC <sub>60</sub> BA/PEDOT-PSS/LZO/C <sub>60</sub> -SAM/PTB7:PC <sub>71</sub> BM/MoO <sub>3</sub> /Ag	10.3	1.54	0.65	10.4		1220
ITO/ZnO/P3HT:ICBA/PEDOT:PSS/ZnO/PDTP-DFBT:PC <sub>61</sub> BM/MoO <sub>3</sub> /Ag	10.1	1.53	0.68	10.6		1221
ITO/ZnO/P3HT:ICBA/Ag/MoO <sub>3</sub> /PIDTT-DFBT:PC <sub>71</sub> BM/Ag	16.1	0.88	0.65	9.2	microcavity	1205
ITO/MoO <sub>3</sub> /DTDCTB:C <sub>60</sub> /C <sub>60</sub> :Bphen/Ag/MoO <sub>3</sub> /DBP:C <sub>70</sub> /C <sub>70</sub> /buffer/Ag	9.9	1.72	0.59	10.0 (10.2)		1222
ITO/MoO <sub>3</sub> /DBP:C <sub>70</sub> /C <sub>70</sub> /Bphen:C <sub>60</sub> /Ag/MoO <sub>3</sub> /DTDCTB:C <sub>60</sub> /C <sub>60</sub> :Bphen/Ag/MoO <sub>3</sub> /DBP:C <sub>70</sub> /C <sub>70</sub> /Bphen/Ag	7.3	2.58	0.59	11.1 (11.3)		1222
ITO/ZnO/P3HT:ICBA/PEDOT:PSS/ZnO/PTB7-Th:PC <sub>71</sub> BM/WO <sub>3</sub> /PEDOT:PSS/ZnO/PDTP-DFBT:PC <sub>71</sub> BM/WO <sub>3</sub> /Al	7.3	2.26	0.64	11.0 (11.6)		1223
ITO/LZO/C <sub>60</sub> -SAM/PSEHTT:IC <sub>60</sub> BA/ICL/C <sub>60</sub> -SAM/PtB7:PC <sub>71</sub> BM/ICL/PMDPP3T:PC <sub>70</sub> BM/MoO <sub>3</sub> /Ag	7.8	2.24	0.67	11.8		1220
<b>Polymer:nonfullerene cells (PCE &gt; 6%)</b>						
ITO/PEDOT:PSS/PBDT-TT-C-T:bis-PDI-T-EG/Ca/Al	12.5	0.84	0.57	6.0 (6.1)	DIO, SVA	1224
ITO/ZnOPFFBT4T-2DT-SF-PDI2/V <sub>2</sub> O <sub>5</sub> /Al	10.7	0.98	0.57	6.0 (6.3)		1225
ITO/PEDOT:PSS/PBDT-T1:SDIPBI-S/Ca/Al	11.6	0.9	0.66	6.9 (7.2)	0.75% DIO	1226
ITO/PEDOT:PSS/PTB7-TH:ITIC/PDIN/Al	14.2	0.81	0.59	6.6 (6.8)		1227
ITO/ZnO/PTB7-Th:hPDI4/MoO <sub>3</sub> /Al	15.0	0.8	0.68	8.1 (8.3)	1% DIO	991
ITO/ZnO/PEI/PBDT-TT-FTTE:DBFI-EDOT/MoO <sub>3</sub> /Ag	13.5	0.95	0.51	6.4 (6.7)		992
ITO/ZnO/PEI/PSEHTT:DBFI-EDOT/MoO <sub>3</sub> /Ag	13.5	0.92	0.63	7.8 (8.1)		992
ITO/ZnO/PEI/PBDT-TT-FTTE:PNDIS-HD/MoO <sub>3</sub> /Ag	18.6	0.8	0.48	7.2 (7.7)	Film-aged at 25 °C for 72 h	993
<b>Small-molecule: fullerene BHJs (PCE &gt; 8.5%)</b>						
ITO/PEDOT:PSS/p-DTS(FBTTh <sub>2</sub> ) <sub>2</sub> :PC <sub>71</sub> BM/Ba/Al	15.5	0.78	0.75	9.0	Ba layer; 0.25% DIO	1122
ITO/PEDOT:PSS/DRCN7T:PC <sub>71</sub> BM/PFN/Al	14.9	0.91	0.69	9.1 (9.3)		1123
ITO/PEDOT:PSS/DRCN5T:PC <sub>71</sub> BM/PFN/Al	15.7	0.92	0.68	9.8 (10.1)	SVA	986
ITO/PEDOT:PSS/BTR:PC <sub>71</sub> BM/Ca/Al	13.6	0.9	0.74	8.9 (9.3)	SVA	1125
ITO/PEDOT:PSS/DR3TSBDT:PC <sub>71</sub> BM/ETL(fullerene)/Al	14.5	0.91	0.73	9.6 (9.9)	TA, SVA	1124
<b>Small-molecule:nonfullerene BHJs (PCE &gt; 5%), planar and mixed planar HJs (PCE &gt; 6.5%)</b>						
ITO/PEDOT:PSS/p-DTS(FBTTh <sub>2</sub> ) <sub>2</sub> :NIDCS-MO/Ca/Al	9.6	0.85	0.64	5.3 (5.44)		1228
ITO/PEDOT:PSS/DIP/SubNc/Cl <sub>6</sub> -SubPc-Cl/BCP:C <sub>60</sub> /Ag	10.1	1.04	0.67	6.9	vac	1229
ITO/ $\alpha$ -6T/SubNc/SubPc/BCP/Ag	14.55	0.96	0.61	8.4	vac	179
ITO/MoO <sub>3</sub> /DPDCTB/DPDCTB:C <sub>70</sub> (1:1.6)/C <sub>70</sub> /BCP/Ag	13.5	0.93	0.53	6.6 (6.8)	vac	1230
ITO/PEDOT:PSS/DPT/Rub/DBP/C <sub>60</sub> /C <sub>60</sub> :Bphen/Bphen/Ag	10.6	0.94	0.71	7.1 (7.5)	vac	180
ITO/MoO <sub>3</sub> /DBP:C <sub>70</sub> (1:8)/C <sub>70</sub> :C <sub>60</sub> :Bphen/Bphen/Ag	13.2	0.93	0.66	8.1	vac	1231
<b>Ternary cells (PCE &gt; 8%)</b>						
ITO/PEDOT:PSS/PTB7:SeDPPP (1:1):PC <sub>70</sub> BM/Ca/Al	18.7	0.69	0.67	8.5 (8.7)		1232
ITO/PEDOT:PSS/PBDTTPD-HT:BDT-3T-CNCOO:PC <sub>71</sub> BM/Ca/Al (60:40:100)	12.2	0.97	0.71	8.4		1001
ITO/ZnO/PEI/PSEHTT:PBDT-TT-FTTE:DFBI-EDOT/MoO <sub>3</sub> /Ag	15.5	0.91	0.60	8.4 (8.5)		992
ITO/PEDOT:PSS/PTB7:PID <sub>2</sub> :PC <sub>71</sub> BM/Ca/Al (0.9:0.1:1.5)	16.8	0.72	0.69	8.2		190
ITO/PEDOT:PSS/PTB7-Th:PID <sub>2</sub> :PC <sub>71</sub> BM/Ca/Al (0.8:0.2:1.5)	16.7	0.78	0.71	9.2		185

Table 8. continued

Material	$J_{sc}$ (mA/cm <sup>2</sup> )	$V_{oc}$ (V)	FF	PCE <sup>b</sup> (%)	Notes <sup>c</sup>	Ref
<b>Organic–inorganic hybrid cells (PCE &gt;10%)</b>						
Al/Si/Si-NR/Spiro-OMeTAD/PEDOT:PSS/Ag-grid	30.9	0.57	0.59	10.3		1233
Si/SiNW/PEDOT:PSS/Au-mesh	35.5	0.54	0.67	12.8 (13.2)		1234
Al/Cs <sub>2</sub> Co <sub>3</sub> Si/PEI/SiNW/PEDOT:PSS/Ag	32.2	0.62	0.68	13.4 (13.7)		1235
ZnO:Al/α-Si:H p-i-n/ITO/PEDOT:PSS/PDTP-DFBT:fullerene/Al/Ca	9.8	1.51	0.69	10.2 (10.5)		1021

<sup>a</sup>Solar cell characteristics averaged over many devices are given when available. The PCE values in the parentheses are the maximal PCE achieved.

<sup>b</sup>Notes regarding processing conditions or device architectures that were instrumental in obtaining the reported PCE. CB = chlorobenzene; DAN = deterministic aperiodic nanostructure; DIO = 1,8-diiodooctane; DPE = diphenyl ether; SVA = solvent vapor annealed; TA = thermally annealed; Vac = vacuum deposited. <sup>c</sup>The PCE “high-performance” cutoff set for each device category, depending the material or HJ type and the availability of data in the literature. <sup>d</sup>Device with a PCE of <10% was included as its performance relies on the high  $J_{sc}$  rather than  $V_{oc}$ .

PDPPST:PCBM BHJs processed from chloroform with and without addition of cosolvents (DIO or oDCB) at various concentrations. They concluded that the cosolvent causes the onset of polymer aggregation to occur before liquid–liquid phase separation (Figure 31). This prevents formation of large PCBM-rich domains, leading to PCEs of up to a factor of ~5 higher than in the same blends processed without the cosolvent.

Sharenko et al.<sup>938</sup> investigated the effect of the DIO additive on the charge generation dynamics and PV performance of p-DTS(FBTTh<sub>2</sub>)<sub>2</sub>:PDI BHJs. The authors used a combination of time-resolved pump–probe experiments (100 fs to 100 μs) and measurements of optical absorption and  $J$ – $V$  characteristics. It was established that the blends processed without DIO yielded structurally disordered homogeneous films which exhibited significant geminate recombination and formed CT states that recombined prior to dissociation. With the DIO, however, improvements of EQE from <7% to 37%, and in PCE from 0.13% to 3.1%, were observed due to increased structural order and phase separation.

Takacs et al.<sup>775</sup> studied blends of p-DTS(FBTTh<sub>2</sub>)<sub>2</sub> with PC<sub>61</sub>BM or PC<sub>71</sub>BM that were processed with and without DIO using polarization-dependent photoconductive AFM. They revealed a micron-scale liquid crystalline order integrated within the complex D/A BHJ structure in the best-performing BHJs with PCEs of ~7%. Perez et al.<sup>1096</sup> performed detailed evaluation of structural evolution of p-DTS(PTTh<sub>2</sub>)<sub>2</sub>:PC<sub>71</sub>BM BHJs processed with the DIO that established changes in the domain size and connectivity depending on the DIO concentration.

Chen et al.<sup>1097</sup> developed a device processing approach that eliminated the use of halogenated solvents in fabrication of polymer:fullerene BHJs. They used a 1-methylnaphthalene additive to toluene to enhance PCBM solubility, which reduced the domain size by 2 orders of magnitude and boosted the PCE from 0.02% to 6.1%.

He et al.<sup>1098</sup> developed a method that utilizes simultaneous spin coating and solvent annealing, which promoted PCBM aggregation and formation of the PTB7 edge-on crystallites. When processed using this method from combination of DCB with the 3 vol % DIO, the PTB7:PCBM BHJs exhibited PCEs of up to 9.8%.

Given that the key potential of organic electronics lies in the possibility of low-cost large-area device manufacturing, there has been a considerable effort specifically targeting methods for scale-up production of devices. Comprehensive reviews can be found in refs 1088, 1089, 1099, and 1102. Representative techniques include printing (e.g., inkjet, screen, gravure, or flexographic printing), spray deposition (e.g., ultrasonic, gas-

propelled, or electro-spray),<sup>1088,1100</sup> and other coating techniques (e.g., doctor-blade, slot-die, or knife-overedge coating).<sup>1101</sup> For example, a PCE of 6.5% was obtained in ultrasonic spray-painted pDPPST:PCBM solar cells (with a 0.13 cm<sup>2</sup> area),<sup>1103</sup> and PCEs of 7.7% (5.6%) were measured in doctor-blade-coated GEN2:PCBM/pDPPST-2:PCBM tandem cells on glass (flexible PET) substrates with a ~0.1 cm<sup>2</sup> area.<sup>1104</sup> Zhang et al.<sup>1105</sup> fabricated PBT13T:PCBM modules on glass substrates by ultrasonic (partially overlapped) spray coating, obtaining a PCE of 5.3% in a 38.5 cm<sup>2</sup> device, to be compared to 6.6% (6.1%) in a 0.09 cm<sup>2</sup> (1 cm<sup>2</sup>) device. The reduction in the PCE was mostly due to the lower FF values in the module in part due to increased series resistance in module connections. Hong et al. achieved 7.5% PCE in modules with a 4.5 cm<sup>2</sup> area fabricated by slot-die and doctor-blade coating.<sup>1106</sup>

In spite of excellent advances in this area, achieving high performance (e.g., matching the best PCEs of Table 8) in large devices that are fully R2R processed under ambient conditions remains a challenge. Issues relevant to the industrial scale fabrication and commercialization also include a long-term device stability<sup>1107</sup> and logistics related to the large-area device deployment and subsequent operation. For recent reviews of these issues, see refs 1108 and 1109.

### 10.3. Summary

It has been clearly demonstrated that optoelectronic properties dramatically depend on various aspects of film structure and morphology. Systematic studies classified organic materials by their morphological characteristics and established quantitative relationships between film or crystal structure and charge carrier mobility, charge trap characteristics, and photocurrent. Routes of optimizing morphology for various material classes have also been identified, and underlying processes that enable fabrication of organic devices with enhanced properties have been established. These have laid the foundation for understanding of how fabrication and processing conditions should be modified depending on the material and for developing new protocols that are suitable for a broad range of organic optoelectronic materials. Nevertheless, the ability to control microstructure and morphology on large areas to the level required for matching the performance of large-area devices with that of small laboratory devices needs improvement. The resolution of this issue along with that of the long-term stability will ultimately determine the usability of organic optoelectronic materials in a broad range of commercial applications. The importance of these concerns has been recognized in the literature, and the excellent progress made in this area over the past several years is encouraging.

## 11. APPLICATIONS

### 11.1. Organic Photovoltaic Cells (OPVs)

Photovoltaic (PV) cells convert light energy into electrical energy;<sup>1110</sup> many tutorials on the basic physics of the solar cell, materials considerations, and device design strategies are available; examples include refs 5, 6, 1111, and 1112. Comprehensive recent reviews of the subject are also available (Table S1).<sup>1113</sup> The main parameter that characterizes the performance of a PV cell is the power conversion efficiency (PCE)  $\eta_p$ , which under standard illumination conditions (typically AM1.5 solar spectral illumination with incident power density  $P_{\text{inc}} = 100 \text{ mW/cm}^2$ ) is given by

$$\eta_p = J_{\text{sc}} V_{\text{oc}} FF / P_{\text{inc}}$$

where  $J_{\text{sc}}$  is the short-circuit current density and  $V_{\text{oc}}$  is the open circuit voltage. The  $V_{\text{oc}}$  and  $J_{\text{sc}}$  are obtained from the  $J$ - $V$  characteristics of the solar cell under illumination at  $J = 0$  and  $V = 0$ , respectively. An excellent tutorial on how to interpret  $J$ - $V$  characteristics can be found in ref 315.  $FF$  is the fill factor, defined as

$$FF = J_m V_m / (J_{\text{sc}} V_{\text{oc}})$$

where the product  $J_m V_m$  corresponds to the maximum power.

Minnaert and Burgelman<sup>1114</sup> predicted that, in the “optimistic” scenario, the single-junction organic solar cell would reach the PCE of 15.2% with the optimum bandgap of the absorber of 1.6 eV. Kirchartz et al.<sup>1115</sup> arrived at the PCE limit of ~23% based on the optical properties of typical polymers and of ~21% in polymer:fullerene HJs. Giebink et al.<sup>1116</sup> adapted the Shockley-Quisser result (obtained using the principle of detailed balance for inorganic semiconductors) to organic solar cells, arriving at the PCE thermodynamic limit of 22–27% depending on the exciton binding energy and the free energy decrease at the HJ. Koster et al.<sup>1117</sup> analyzed the effect of CT absorption, reorganization energy, and dielectric permittivity  $\epsilon$  on the device performance, considering both geminate and nongeminate recombination. The study established, for example, that increasing  $\epsilon$  allows for smaller D–A LUMO energy offsets while enabling PCE of >20%. Würfel et al.<sup>1118</sup> explicitly included charge carrier mobility in their estimates of achievable PCEs, arriving at a ~22% maximal PCE with mobilities of >0.01  $\text{cm}^2/(\text{Vs})$  and the D–A LUMO offset of 0.2 eV. An excellent discussion and a model quantifying the entropic losses contribution to the reduced  $V_{\text{oc}}$  and the PCE can be found in ref 1119.

Impressive improvement in design of efficient D/A HJs has been achieved in the past decade, and PCEs of 10–12% have been demonstrated in several D:A systems (Table 8).<sup>1120,1121</sup> Until recently, most successful organic solar cells utilized polymer:fullerene BHJs or vacuum-deposited small-molecule-based multilayer cells, with all other classes lacking in performance. However, PCEs of above 9% were recently reported in several solution-processable small-molecule BHJs (SMBHJs),<sup>986,1122–1125</sup> and the best nonfullerene solar cells exhibit PCEs of over 8%.<sup>179,991,992</sup> Table 8 summarizes the properties of high-performance OPV devices depending on the type.

Recent research efforts focused on (i) understanding the factors that determine various parameters contributing to the PCE ( $V_{\text{oc}}$ ,  $J_{\text{sc}}$ , and  $FF$ ), (ii) optimization of material design and film morphology, and (iii) optimization of device structures to achieve better device performance. Optimization of film

morphologies toward achievement of better PCEs was briefly discussed in Section 10; the corresponding strategies were reviewed in detail in ref 1083; also see relevant references from Table S1. Examples of studies under (i) and (iii) are given below.

#### 11.1.1. Undersanding the Limiting Factors.

**11.1.1.1. Open Circuit Voltage.** Open circuit voltage not only is an important parameter for solar cell performance,<sup>1126</sup> but also is a readily measured characteristic that has been used to establish the mechanisms of charge generation<sup>390</sup> and recombination,<sup>656,1127,1128</sup> as well as to assess other device properties, such as leakage currents.<sup>657</sup> Recent review of factors impacting  $V_{\text{oc}}$  can be found in ref 1129.

In D/A HJs, earlier work suggested that the  $V_{\text{oc}}$  could be accurately determined using  $(E_A(\text{A}) - I_p(\text{D}))/e - 0.3$ , where the electron affinity  $E_A$  and ionization potential  $I_p$  are typically determined from CV measurements in solution and 0.3 eV is related to a typical exciton binding energy.<sup>206</sup> However, considerable evidence suggests that it is an oversimplified view,<sup>257,1130–1132</sup> rendering this approach unreliable in predicting  $V_{\text{oc}}$  in BHJs, especially when crystalline phases are involved.<sup>188,749</sup> The importance of including ionization potentials and activation energies of optically excited states<sup>1130</sup> and of long-range electrostatic interactions at the D/A interfaces governed by mesoscale order<sup>257</sup> into consideration for accurate predictions of the  $V_{\text{oc}}$  has been discussed in the literature. Nongeminate recombination has been determined to be a primary loss mechanism in the  $V_{\text{oc}}$  in P3HT:PCBM BHJs, and the importance of not only tailoring energy levels but also increasing charge carrier lifetimes has been emphasized.<sup>636</sup> Ray et al.<sup>332</sup> modeled  $V_{\text{oc}}$  in BHJs as an explicit function of the D/A interfacial area and showed that the  $V_{\text{oc}}$  in BHJs is always lower than that in corresponding planar HJs, regardless of morphology. In ternary blends, tunable  $V_{\text{oc}}$  has been demonstrated.<sup>1000,1002</sup>

The defects that act as charge traps<sup>1127,1131</sup> have been known to negatively impact  $V_{\text{oc}}$ . High dark currents<sup>320</sup> are also correlated with lower  $V_{\text{oc}}$ , as they often indicate strong recombination detrimental for  $V_{\text{oc}}$ . The recombination through triplet states and low-energy CT state formation are potential channels for the losses in the  $V_{\text{oc}}$ .<sup>1133,1134</sup> However, Schlenker et al.<sup>373</sup> emphasized kinetics (e.g., slow triplet state formation), and not only thermodynamics, as an important factor that determines whether the photocurrent loss via triplet states can or cannot be avoided. Burke et al.<sup>237</sup> explicitly incorporated the properties of CT states into the  $V_{\text{oc}}$  under the assumption of thermal equilibrium between the free carriers and CT states, arriving at

$$qV_{\text{oc}} = E_{\text{CT}} - \frac{\sigma_{\text{CT}}^2}{2k_{\text{B}}T} - k_{\text{B}}T \log \left( \frac{qfN_0d}{\tau_{\text{CT}}J_{\text{sc}}} \right) \quad (55)$$

where  $q$  is the elementary charge,  $E_{\text{CT}}$  is the average CT state energy,  $\sigma_{\text{CT}}$  is the standard deviation of the CT states distribution,  $f$  is the volume fraction that is mixed or interfacial,  $N_0$  is the DOS,  $d$  is the solar cell thickness,  $\tau_{\text{CT}}$  is the CT state lifetime, and  $J_{\text{sc}}$  is the short-circuit current density. They provided a quantitative breakdown of  $V_{\text{oc}}$  losses due to various factors (Figure 32) and estimated how much can be gained in the  $V_{\text{oc}}$  if various parameters in eq 55 are optimized (Table 9). This approach was utilized, for example, by Sulas et al.<sup>1135</sup> to explain the correlation between the lower  $V_{\text{oc}}$  and the higher density of CT states in polymer:PCBM blends.

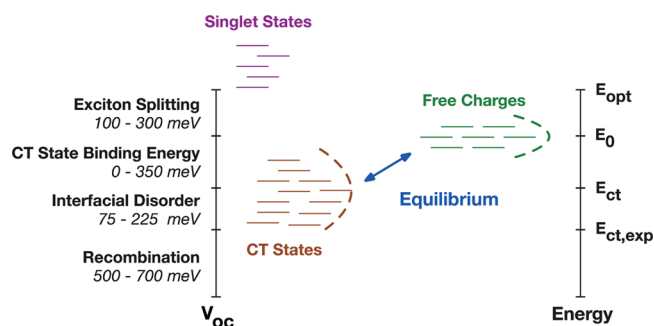


**Figure 32.** Sources of open-circuit voltage losses and corresponding characteristic energy levels in organic solar cells. Reprinted with permission from ref 237. Copyright 2015 Wiley-VCH.

**Table 9.** Potential Increases in  $V_{oc}$  That Could Be Obtained from Changing Various Parameters<sup>a</sup>

Parameter improvement strategy	$V_{oc}$ increase
Reduce volume fraction ( $f$ ) of mixed phase from 50% to 1%	100 meV
Increase CT state lifetime ( $\tau_{CT}$ ) from 100 ps to 10 ns	120 meV
Decrease interfacial disorder ( $\sigma_{CT}$ ) from 100 to 50 meV	150 meV
Decrease CT state binding energy ( $E_B$ ) from 200 to 50 meV	150 meV
Decrease number of CT states per interface from 30 to 3	60 meV

<sup>a</sup>Adapted with permission from ref 237. Copyright 2015 Wiley-VCH.

The role of charge carrier mobility and, in particular, whether high  $V_{oc}$  requires balanced or unbalanced electron and hole mobilities were studied using drift-diffusion simulations.<sup>229</sup> The result was found to be dependent on the interplay between bulk and surface recombination and, in particular, on the nature of the electrodes and whether recombination occurs through CT state formation or directly. Review of bimolecular recombination processes negatively impacting solar cell characteristics can be found in ref 641.

An interesting synergy between the properties of OPVs and OLEDs, which calls for cross-pollination between the research findings in these two areas of research,<sup>384</sup> is provided by the reciprocity conditions, which can be expressed as follows:<sup>1136,1137</sup>

$$V_{oc} = V_{oc,rad} + \frac{k_B T}{q} \ln(Q_{LED})$$

$$\Phi_{EL,norm}(E_{ph}) = EQE(E_{ph})\phi_{BB}(E_{ph}) \left( \exp\left(\frac{qV}{k_B T}\right) - 1 \right) \quad (56)$$

Here  $V_{oc,rad}$  is the upper limit of the  $V_{oc}$  (in the absence of nonradiative recombination),  $Q_{LED}$  is the LED quantum efficiency,  $\Phi_{EL,norm}$  is the electroluminescence (EL) emission normal to the surface of the device,  $E_{ph}$  is the photon energy, EQE is the external quantum efficiency of the OPV, and  $\phi_{BB}$  is the blackbody radiation spectrum. Equations 56 imply that the quantum efficiency measured in the OPV should be directly related to the EL,<sup>383</sup> if all assumptions behind the reciprocity relations are valid. For example, nonlinear recombination and space-charge field effects could invalidate this approach. However, Kirchartz et al.<sup>1137</sup> recently established that this is not the case for high-performance thin solar cells (exhibiting high mobilities, high fill factors, and minimal space-charge effects), confirming the validity of the relations of eqs 56 in these cases.

**11.1.1.2. Short-Circuit Current.** Short-circuit current  $J_{sc}$  incorporates charge generation, transport, and recombination, and contributions from these to  $J_{sc}$  have been a subject of many studies.<sup>313,314,1138–1140</sup> Shoaee et al.<sup>940</sup> observed strong correlation between the yield in photogenerated charge carriers measured on the nanosecond-microsecond time-scales using transient absorption spectroscopy and  $J_{sc}$  in various polymer:fullerene BHJs. In planar CuPc/PTCBI HJs,<sup>1141</sup> molecular order has been cited as a key factor driving the  $J_{sc}$  due to a larger exciton diffusion length in ordered systems. In planar ClAlPc/ $C_{60}$  HJs,<sup>1142</sup> improved  $\pi$ - $\pi$  interaction, enabled by ultrathin PTCDA or Pn interlayers, tuned the molecular orientation of ClAlPc, resulting in a higher  $J_{sc}$ .

Computational modeling (Section 3.2.2) enabled better understanding of the effects of temperature, light intensity, and film properties such as blend composition or film thickness on the  $J_{sc}$ .<sup>272,1143,1144</sup> For example, simulations of  $J$ - $V$  characteristics depending on the degree of nanoscale phase separation revealed  $J_{sc}$  enhancement in morphologies with finer phase separation, due to reduction in bimolecular recombination caused by lateral movement of electrons to the fullerene-rich phase.<sup>272</sup>

**11.1.1.3. Fill Factor.** Until recently the fill factor (FF) had been the least understood characteristic of the solar cell, which prompted a number of recent studies specifically addressing mechanisms that determine the FF.<sup>291,637,639,1145</sup> An overview of factors contributing to the FF can be found in ref 1146.

Charge recombination and extraction have been cited as the key factors that determine the FF. Dibb et al.<sup>291</sup> observed that in polymer:fullerene BHJs with similar  $J_{sc}$ 's and FFs, the mechanisms limiting the FF were different: enhanced non-geminate recombination in one blend and strongly electric field-dependent charge generation due to geminate recombination in the other. Bartelt et al.<sup>1147</sup> established that hole mobility of  $>0.01 \text{ cm}^2/(\text{Vs})$  is necessary for achieving FF of above 0.8 in polymer:fullerene devices and that, in an optically thick device, the minimal mobility required to achieve high FF depends on the recombination rate constant. Bartesaghi et al.<sup>639</sup> modeled the competition between the charge extraction and recombination. The authors introduced a parameter  $\theta$ , which is the ratio of extraction-to-recombination, defined as

$$\theta = \frac{\gamma G d^4}{\mu_n \mu_p V_{int}^2} \propto \frac{k_{rec}}{k_{ex}} \quad (57)$$

where  $\mu_p$  ( $\mu_n$ ) is the hole (electron) mobility,  $k_{rec}$  and  $k_{ex}$  are recombination and extraction rates, respectively, and the internal voltage  $V_{int} = (E_A(A) - I_p(D))/e - 0.4$ . The parameter  $\gamma$  is the bimolecular recombination rate coefficient,  $d$  is the active layer thickness, and  $G$  is the photogeneration rate. Then, it was demonstrated that for a variety of D-A combinations (polymer:fullerene, polymer:polymer, and small-molecule BHJs) the parameter  $\theta$  was correlated with FF (with higher  $\theta$  corresponding to a lower FF) in the 0.26–0.74 range of FFs (Figure 33). It was proposed that this figure of merit provides a way to optimize the device performance depending on the thickness, charge carrier mobilities, internal voltage, and charge generation rate.

To specifically address the performance of solar cells with low charge carrier mobilities (and resulting transport-limited photocurrent), Neher et al.<sup>318</sup> proposed a new figure of merit, a dimensionless parameter  $\alpha$  given by

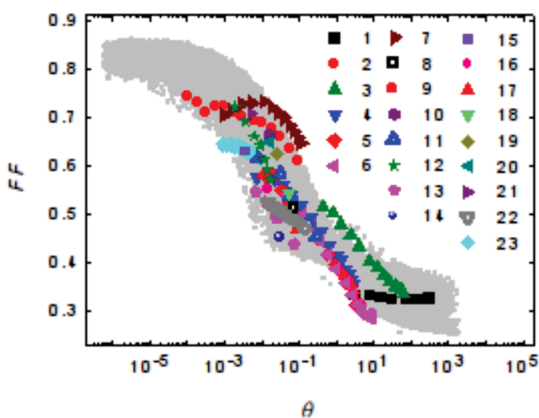


**Figure 33.** Fill factor versus parameter  $\theta$  of eq 57 for the simulated (small gray symbols) and the experimental data (large colored symbols). Numbers in the legend represent different D:A blends featuring a variety of polymer donors and both fullerene and nonfullerene acceptors. Adapted from ref 639 under Creative Commons license 4.0 (<https://creativecommons.org/licenses/by/4.0>).

$$\alpha^2 = \theta \left( \frac{V_{\text{int}}}{2V_t} \right)^2 = \frac{q^2 \gamma G d^4}{4\mu_n \mu_p (k_B T)^2} \quad (58)$$

Here  $V_t = k_B T/q$  is the thermal voltage ( $q$  is the electron charge) and other parameters are the same as in eq 57. At  $\alpha > 1$ , photocurrents are transport-limited, and the FF dramatically decreases (Figure 34). The authors derived an analytical form

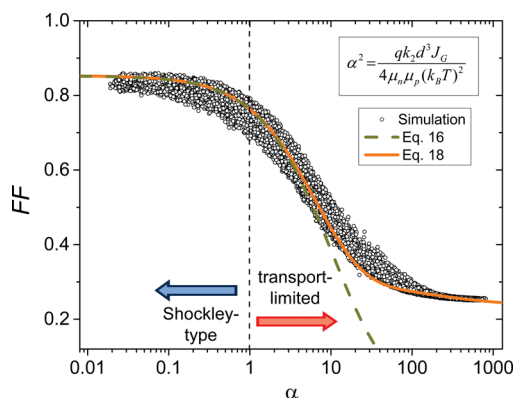


**Figure 34.** Fill factor (FF) as a function of the dimensionless parameter  $\alpha$  of eq 58. Open circles are obtained from simulated  $J$ - $V$  characteristics, and lines are obtained from analytical expressions. At  $\alpha > 1$ , photocurrents are transport-limited, leading to a progressive decrease in the FF. Reproduced from ref 318 under Creative Commons license 4.0 (<https://creativecommons.org/licenses/by/4.0>).

of  $J$ - $V$  characteristics incorporating the parameter  $\alpha$  and calculated an upper limit for the active layer thickness ( $d_{\text{max}}$ ) to achieve high FF, depending on the material properties (for  $d > d_{\text{max}}$  photocurrent is transport-limited), in particular:

$$d_{\text{max}} = \left( 400 \frac{\mu_n \mu_p}{\gamma J_{\text{sc}}} \right)^{1/3} \quad (59)$$

where  $d_{\text{max}}$  is in units of nm, mobilities are in  $\text{cm}^2/(\text{Vs})$ , the recombination rate coefficient  $\gamma$  is in  $\text{cm}^3/\text{s}$ , and the short-circuit current  $J_{\text{sc}}$  is in  $\text{mA}/\text{cm}^2$ . Although not all parameters in

eq 59 are independent, it provides a guide for the relative importance of various characteristics for the design of films with optimal film thickness. The applicability of this approach to a wide variety of high-performance organic solar cell materials is awaiting validation.

**11.1.2. Optimization of Device Design.** Reviews of historical development of OPV device architectures can be found in refs 1148 and 1149. Here selected recent examples pertaining to the optimization of the device architectures are discussed.

**11.1.2.1. Interlayers.** Thin interlayers inserted between the electrodes and the active OPV layers have been utilized to modify the work function of the electrodes and improve the quality of interfaces,<sup>1150</sup> achieve charge-carrier-selective recombination and extraction,<sup>309,1151,1152</sup> enhance exciton confinement,<sup>1153</sup> improve the thermal stability of the solar cells,<sup>1154</sup> provide energy cascading for directed exciton diffusion,<sup>1155</sup> control molecular orientation,<sup>1156</sup> etc. For a comprehensive recent review of interlayer materials for organic solar cells, see ref 1157.

For example, Liu et al.<sup>1158</sup> investigated three conjugated polymer zwitterions based on thiophene, DPP, and NDI backbones as interlayers between the active OPV layer and Ag cathode in PBDTT-TT:PCBM solar cells. The authors observed an enhancement of PCE from 3.2% with no interfacial layer to 5% with a thiophene-based interlayer and to 9.5% and 10.2% in PBDTT-TT:PCBM BHJs with the DPP- and NDI-based interlayers, respectively. The increase in performance was attributed to a combination of lowering of the work function of the cathode, increase in the built-in voltage, and efficient electron transport across the interlayer.

In conventional solar cells, indium tin oxide (ITO) is typically used as the bottom contact (anode). ITO has a high work function around 4.8 eV, which is surface-treatment-dependent, and a relatively rough surface, which leads to contact losses in devices. In order to improve the quality of the contact, a p-type PEDOT:PSS interlayer with a work function of  $\sim 5$  eV has been used. However, its acidic nature and susceptibility toward degradation under air or moisture exposure reduce the overall stability of the device. In order to resolve this issue, more stable hole-transporting interlayers such as transition metal oxides ( $\text{V}_2\text{O}_5$ ,  $\text{MoO}_3$ ,  $\text{WO}_3$ , NiO) and conjugated polyelectrolytes,<sup>1159</sup> cross-linked polymers,<sup>1160</sup> graphene oxide,<sup>1161,1162</sup> or copper thiocyanate (CuSCN)<sup>1163,1164</sup> have been utilized. For example, Treat et al.<sup>1163</sup> obtained a 17% improvement in the PCE, which reached 8.1% in a PBDTTPD:PC<sub>61</sub>BM BHJ when the PEDOT:PSS layer was replaced with the CuSCN layer. This was attributed to a higher  $V_{\text{oc}}$  achieved in devices with CuSCN, enabled by its deep valence band energy of 5.35 eV.

Lee et al.<sup>1165</sup> used an inkjet-printed combination of the graphene nanoribbons (GNRs) and carbon nanotubes (CNTs) instead of PEDOT:PSS, which improved the FF and the resulting PCE in PTB7:PC<sub>71</sub>BM BHJs. For a review of graphene-based interlayers in organic solar cells, see refs 1018 and 1019. Low-cost solutions for PEDOT:PSS replacement such as polyacrylonitrile (PAN)<sup>1166</sup> or copper iodide<sup>1167</sup> have also been proposed.

Cost-effective solutions for the ITO replacement have been actively sought after as well, using other oxides (e.g., FTO or AZO), CNTs,<sup>1168</sup> metal mesh or nanowires,<sup>1169–1173</sup> and other materials.<sup>1174,1175</sup> For example, Kim et al.<sup>1169</sup> reported a  $\text{Cu}_2\text{O}/\text{Cu}/\text{Cu}_2\text{O}$  multilayer mesh electrode grown by room-temper-

ature roll-to-roll sputtering. They demonstrated a low sheet resistance of  $\sim 15$  Ohm/square, high optical transmittance of  $\sim 89\%$ , and good mechanical flexibility.

On the cathode side, the low work-function Ca was initially used as the hole-blocking layer, followed by the Al electrode. However, due to stability issues, alternative cathode materials, e.g. inorganic salts such as LiF, CsF, or MgF in conjunction with Al, have become more common. Solution-processable electron-transporting alternatives such as ZnS,<sup>1176</sup> water/alcohol soluble polymers,<sup>1177</sup> metallophthalocyanine derivatives,<sup>1178</sup> fullerene derivatives,<sup>1179</sup> porphyrin derivatives,<sup>1180</sup> etc. have been proposed. Comprehensive reviews of the electron transporting interlayers utilized in organic solar cells can be found in refs 1157, 1177, and 1181.

Zhou et al.<sup>1182</sup> demonstrated surface modifiers based on polymers containing aliphatic amine groups that considerably reduced the work function of metals, metal oxides, and graphene. An ultrathin (sub-10-nm) layer is physisorbed on the conductor surface, and the charge-transfer character of the layer–surface interaction, as well as intrinsic dipole moments associated with the amine groups, reduce the work function. For example, the work functions of Au and ITO (5.1 and 4.6 eV, respectively, before the treatment) yielded 3.9 and 3.5 eV, respectively, after surface modification with PEIE or PEI layers. This method enables low-cost large-area deposition of air-stable electrodes from environmentally friendly solvents, which is applicable not only to solar cells, but also to OLEDs, TFTs, and potentially other optoelectronic devices.

More recently, inorganic oxide alloys In–Ga–O and Ga–Zn–Sn–O were used as solution-processable interlayers in inverted OPVs, demonstrating tunability of the energy level matching between the inorganic electrode and the organic active layer by tuning the alloy composition.<sup>1020</sup> The strategy was shown to be applicable to OPVs based on a variety of polymer-based D:A BHJs, in which the maximum PCE was obtained when the LUMO energy of the acceptor approached the energy of the conduction band minima of the oxide.

**11.1.2.2. Inverted Structure.** An alternative way of addressing the stability of solar cells related to that of the electrodes is to utilize an inverted device structure, in which the nature of charge collection is reversed.<sup>1183,1184</sup> An example of such device architecture is ITO/CBL/active layer/ABL/Au, where CBL and ABL stand for cathode and anode buffer layer, respectively. These are also commonly referred to as electron extraction layer (EEL) and hole extraction layer (HEL), respectively. Here, a high-work function metal Au replaces a low-work function Al, to achieve a better stability in air, along with other advantages related to processing and mass-production. The role of the CBL (ABL) is to transport electrons (holes), block the hole (electron) transport to the cathode (anode), adjust the energy barrier between the electrode and the active layer, and prevent physical or chemical reaction between the electrode and the active layer. The most common examples of the CBL (ABL) appearing in high-performance solar cells are ZnO or TiO<sub>2</sub> (MoO<sub>3</sub>). However, polyelectrolytes,<sup>1185,1186</sup> fullerene derivatives,<sup>1187</sup> etc. have been demonstrated as the CBL or ABL layers; see ref 1157 for a comprehensive review.

Many of the high-performance solar cells in Table 8 utilize the inverted structure, which has been shown to yield superior performance to corresponding noninverted structures due to improvements in film morphology and contact quality, leading to improved charge generation and extraction efficiencies.<sup>1091</sup>

For example, Nanova et al.<sup>1188</sup> studied the structure and properties of F<sub>4</sub>ZnPc:C<sub>60</sub> blends deposited on ultrathin layers of F<sub>4</sub>ZnPc and C<sub>60</sub> to mimic the situation in a noninverted and inverted device, respectively. The devices then were thermally annealed. The differences were observed in the typical domain size between the two cases. Most importantly, substrate-induced local fullerene ordering was observed in the inverted device, which resulted in an improved charge generation efficiency.

**11.1.2.3. Tandem Cells.** Given the constraints pertinent to charge generation and extraction (e.g., low charge carrier mobility, short exciton diffusion length, etc.), the thickness of the active OPV layer is typically restricted to  $\sim 100$ – $200$  nm, which limits optical absorption (and thus EQE). One of the ways to increase optical absorption is to combine several planar D/A HJs separated by a charge recombination layer (e.g., thin Ag or Au clusters) in a stack. Such cells also exhibit higher  $V_{oc}$  due to the addition of the photovoltage of each individual cell, with several cells exhibiting PCEs of over 11% (Table 8). Review of multijunction organic solar cells can be found in ref 1189. Review of design strategies for the interlayers between the individual cells is provided in ref 1157. Timmreck et al.<sup>1190</sup> recently reviewed reports of tandem cell efficiencies in the literature and urged adherence to strict guidelines for tandem cell characterization in order to avoid misleading and/or incorrect efficiency assessments. The authors developed a set of rules that need be followed for reliable characterization of tandem solar cells.

**11.1.2.4. Light Trapping.** Another way of improving the PCE via device architecture is to employ various optical effects, which enhance light absorption.<sup>1157,1191</sup> A theoretical description of light management in OPVs that explicitly addresses inefficient light trapping, parasitic absorption, and nonradiative recombination losses is given in ref 1119. This work also proposed a new figure of merit describing light trapping,  $\langle 1/l \rangle^{-1}$  (where  $l$  is the optical path length and the brackets designate averaging over all path lengths), and a scheme for deterministic light trapping that outperforms the Lambertian one. Experimentally, one strategy has been to utilize surface plasmon resonance to enhance light trapping by embedding metal nanoparticles in active layers<sup>1192–1195</sup> or in the interlayers,<sup>1196–1199</sup> by utilizing nanostructured metal electrodes,<sup>1200,1201</sup> or both.<sup>1202–1204</sup> Depending on the geometry of metal nanostructure incorporation in the device, the enhanced light trapping occurs via enhanced light scattering, localized surface plasmon resonance, or surface plasmon polariton,<sup>1191</sup> which increases  $J_{sc}$ .

Another strategy is to employ an ultrathin metal layer in forming the microcavity with another reflective electrode, creating a resonant structure.<sup>1205</sup> For example, in a tandem cell containing P3HT:IC<sub>60</sub>BA and PIDTT-DFBT:PC<sub>71</sub>BM stacked together using the ultrathin Ag interlayer, the PCE of 9.2% was achieved due to enhanced  $J_{sc}$ , which is comparable to PCEs in other high-performance tandem cells that rely on high  $V_{oc}$  (Table 8).

ITO-free configurations that utilize enhanced light trapping have also been proposed.<sup>1206,1207</sup> For example, Huang et al.<sup>1206</sup> used a microcavity-based device architecture formed by a thick Ag film deposited on glass or PET serving as the cathode and the ultrathin Ag film on TeO<sub>2</sub> as the anode. The enhanced light trapping resulted in up to  $\sim 11\%$  ( $\sim 10\%$ ) increase in the  $J_{sc}$  (PCE) as compared to the ITO-based device utilizing the same BHJ (PBDTT-F-TT:PC<sub>71</sub>BM) in a typical inverted architec-

Table 10. High-Performance Organic Photodetectors

Material	Spectral range (nm)	R, A/W ( $V_{\text{bias}}$ (V), wavelength (nm), intensity ( $\text{mW}/\text{cm}^2$ )) <sup>a</sup>	$J_{\text{dark}}$ ( $\mu\text{A}/\text{cm}^2$ ) ( $V_{\text{bias}}$ (V)) <sup>b</sup>	$J_{\text{ph}}/J_{\text{dark}}$ ( $V_{\text{bias}}$ (V)) <sup>c</sup>	Bandwidth (time) <sup>d</sup>	Notes <sup>e</sup>	Ref
<b>Small-molecule-based photodetectors</b>							
m-MTDATA:Ga <sub>3</sub>	200–450	0.34 (–8, 365, 1.2)		675 (–8)		BHJ, vapor	1243
m-MTDATA/NSN	300–410	0.33 (–12, 365, 1)		300 (–12)		Bilayer, vapor	1244
PFH/NSN	300–425	0.7 (–12, 365, 1)		498 (–12)		Bilayer; solution/vacuum	1244
spiroBF-TAD:spiroBF-hexaaryl	300–410	0.22 (–8, 380, 0.072)		100 (–2)	(<400 ns)	BHJ, vapor	1245
CuPc/PTCDI	525–725	0.39 (–10, 650 nm, <3)			430 MHz (720 ps)	Multilayer; vacuum	1246
Pn/C <sub>60</sub>	450–690	0.52 (–3.5, 660, 1.54)	200 (–3.5)			vacuum	1247
	500–690	0.11 (–10, 580)			80 MHz		1248
Rubrene/TCNQ	400–600	0.4 (–5, 500)				lamination	1249
Cy7-T/MeO-TPD		0.165 (–2, 850, 0.1)	0.033 (–1)		(<1 ns)		1250
Zn-met porphyrin/C <sub>60</sub>	<1350	0.07 (0, 1345, 1)			56 MHz (7 ns)	Bilayer, solution/vacuum	1251
<b>Polymer-based photodetectors</b>							
P3HT:PC <sub>61</sub> BM	400–600	0.39 (–5, 540)	0.065 (–5)		100 kHz	solution	1252
		0.24 (–5, 532, 0.19)	1 (–5)		1 MHz (40 ns)		1253
P3HT:F8TBT	400–600	0.1 (–0.5, 500)	0.004 (–0.5)			EBL, solution	1254
F8T2:PC <sub>61</sub> BM	400–500	0.67 (–10, 460, 9)	1000 (–10)		50 MHz	solution	1255
PDDTT:PC <sub>61</sub> BM	300–1450	0.17 (–0.5, 800, 0.22)	<0.001 (–1)			EBL+HBL	1256
PCPDTBT:PC <sub>71</sub> BM	300–900	0.3 (0, 80, 80)					1257
PTT:PC <sub>61</sub> BM	300–950	0.27 (–5, 800)	100 (–1)		4 MHz		1258
PCDTBT:PC <sub>71</sub> BM	400–700	0.24 (–5, 532, 0.001) D* = $3.4 \times 10^{13}$ (–5)	$1.5 \times 10^{-4}$ (–5)	>1000 (–5)		Inverted; screen-printed; PEDOT:PSS+PEIE	1239
P3HT:PC <sub>61</sub> BM:PbS	400–1450	0.16 (–5, 1220)	4 (–5)		2.5 kHz		1259

<sup>a</sup>Responsivity R in A/W. The values in parentheses represent the bias voltage in volts, the wavelength in nm, and the light intensity in  $\text{mW}/\text{cm}^2$  at which the responsivity was obtained. <sup>b</sup>Dark current density  $J_{\text{dark}}$  in  $\mu\text{A}/\text{cm}^2$ . The value in parentheses is the bias voltage in volts. <sup>c</sup>The ratio between the photocurrent and dark current at the bias voltage shown in parentheses. <sup>d</sup>Bandwidth and/or response time (given in parentheses when available) of the detector. <sup>e</sup>Notes pertaining to device preparation.

ture. The PCEs of up to 10.5% and 10.4% were achieved in ITO-free devices on glass and on PET, respectively.

## 11.2. Organic Photodetectors and Phototransistors

Discussions of earlier work on photodetectors and photoconductors can be found in refs 1148 and 1236, respectively. More recent work was reviewed in ref 741. Here a brief account of recent developments is given.

The photoconductive properties of organic semiconductors have been exploited in photodetectors in several geometries: two-terminal photodiodes and photoconductors (used both in a planar and in a sandwich-type configurations) and three-terminal photo-TFTs. The figures of merit are EQE ( $\eta_{\text{EQE}}$ ), responsivity R ( $R = \eta_{\text{EQE}}\lambda e/hc$ , where  $\lambda$  is the wavelength,  $e$  is the elementary charge,  $h$  is the Planck constant, and  $c$  is the speed of light), the signal-to-noise ratio (SNR), minimal detectable power (given by the noise-equivalent power  $NEP = S/R$ , where  $S$  is the noise spectral density), and response time or operation bandwidth. Also of importance is the wavelength range of detector sensitivity, which determines the type of application. For example, detectors with broadband sensitivity are of interest for optical remote sensing and environmental control. Detectors with a wavelength-selective response have been utilized in full-color digital cameras/camcorders, colorimetry, artificial systems mimicking human eyes, and biological imaging. UV-sensitive detectors are of interest for biological and chemical sensing, smoke and fire detection, missile warning, combustion monitoring, ozone sensing, etc. Another emerging area of interest is radiation detection.<sup>741</sup> Guo et al.<sup>960</sup> used a low-voltage photo-TFT based on diF TEG-ADT as a

humidity sensor and discussed its utility in a photocontrolled memory. Review of applications in integrated transceivers, imaging, and photosensors can be found in ref 741.

The photodiode geometry is typically similar to that of OPVs, but in contrast to OPVs, it is optimized for reverse applied fields which improve charge generation (thus, quantum efficiency) and ensure fast charge carrier collection (thus, fast response time). Also important is minimizing dark currents ( $J_{\text{dark}}$ ), as they strongly contribute to noise, which reduces the specific detectivity of the detector  $D^*$ . Under assumption of a dominant contribution of the shot noise,  $D^* = R/(2eJ_{\text{dark}})^{1/2}$  (where  $J_{\text{dark}}$  is the dark current density). In these devices, the EQE is necessarily below 100%. In photoconductors, EQE can exceed 100% when injecting contacts are used, exhibiting a photoconductive gain (defined as the ratio between the electron-hole recombination time  $\tau$  and the electron transit time) of  $>1$ .<sup>36,322,958,959,1237</sup> For example, photoconductive gains of  $\sim 20$ – $130$  have been reported in phthalocyanine, Pn, and various functionalized Pn and diF R-ADT derivatives.<sup>36,958,959,1238</sup> However, the device bandwidth is proportional to  $1/\tau$ , and therefore, there is a trade-off between the photoconductive gain and the bandwidth. For example, in the OSnNcCl<sub>2</sub> photoconductor, a photoconductive gain of  $\sim 15$  was obtained at 1064 nm, but the bandwidth was limited to the kHz range ( $<3$  kHz).<sup>1238</sup>

The photo-TFT under illumination exhibits an increase in the source-drain current with optical excitation power due to either a photovoltaic or a photoconductive effect, depending on whether the TFT is operated in the accumulation or in the

Table 11. High-Performance Organic Phototransistors

Material	R (A/W) (wavelength (nm), light intensity (mW/cm <sup>2</sup> )) <sup>a</sup>	I <sub>ph</sub> /I <sub>dark</sub> <sup>b</sup>	Mobility <sup>c</sup> (cm <sup>2</sup> /(Vs))	Notes <sup>d</sup>	Ref
<b>Small-molecule-based photo-FETs</b>					
ABT	1000 (white, 0.03)	800	0.4	BG/TC (SiO <sub>2</sub> ,OTS) (vapor)	1260
Me-ABT	12000 (white, 0.03)	6000	1.7	BG/TC (SiO <sub>2</sub> ,OTS) Single crystal	1261
A-EHDTT	>14000 (400, 0.014)	1.4 × 10 <sup>5</sup>	1.2–1.6	BG/TC (SiO <sub>2</sub> ,OTS) Single crystal	100
Py4THB	2000 (400, 0.056)	1.2 × 10 <sup>6</sup>	0.7	BG/TC (SiO <sub>2</sub> ,OTS) Single crystal	1262
4(HPBT)	2500–4300 (436, 0.068–0.03)	4 × 10 <sup>5</sup>	0.0013	BG/BC (SiO <sub>2</sub> ) (solution)	1263
diF TES-ADT	1500 (white, 0.17)	7 × 10 <sup>6</sup>	0.54	BG/TC (solution) (SiO <sub>2</sub> ,HDMS,PFBT)	961
BBDTE	9820 (365, 0.04)	10 <sup>5</sup>	1.6	BG/TC (SiO <sub>2</sub> ,OTS) Single crystal	1264
PDI-Cn	4.1 × 10 <sup>5</sup> (580, 0.007)	10	0.0004	BG/BC (SiO <sub>2</sub> ,HDMS) Drop-cast fibers	1241
<b>Polymer-based photo-FETs</b>					
PS <sub>6</sub> TPTI/ PC <sub>61</sub> BM	4808 (white, 0.107) 2200 (365, 0.043) (D* = 3.1 × 10 <sup>16</sup> )	1.7 × 10 <sup>7</sup> 7.3 × 10 <sup>7</sup>	0.12	BG/TC (SiO <sub>2</sub> )	1265
DPPSPBTSPE NW	1920 (632, 24)	10 <sup>5</sup>	24	BG/TC (SiO <sub>2</sub> ,OTS)	1266
PPhTQ	400 (white, 15)	0.5	0.09h, 0.06e	BG/BC (SiO <sub>2</sub> ,HDMS)	1267
PQBOCB	970 (white, 0.28)	1.4 × 10 <sup>4</sup>	0.13	BG/TC (SiO <sub>2</sub> )	1268
P(DPP4T-co- BDT)	4000 (white, 0.01)	6.8 × 10 <sup>5</sup>	0.047	BG/TC (SiO <sub>2</sub> )	1269
PTz	2530 (white, 0.65)	1.7 × 10 <sup>4</sup>	0.46	BG/TC (SiO <sub>2</sub> )	1270
PDPPTzBT	10 <sup>6</sup> (white, 0.0007)	10 <sup>8</sup>	1.2	BG/TC (SiO <sub>2</sub> ,PMMA)	1242

<sup>a</sup>Responsivity R in A/W. The values in parentheses represent the wavelength (in nm) and the light intensity (in mW/cm<sup>2</sup>) at which the responsivity was obtained. <sup>b</sup>The ratio of the source-drain photocurrent and dark current. <sup>c</sup>Charge carrier mobility (in cm<sup>2</sup>/(Vs)) measured in the same photo-FETs. <sup>d</sup>Device structure and device preparation notes. BG = bottom gate; BC = bottom contact; TC = top contact; HDMS = hexamethyldisilazane; OTS = octadecyltrimethoxysilane; PMMA = poly(methyl)methacrylate; PFBT = pentafluorobenzenethiol.

depletion mode (for a p-type TFT  $V_g < V_{th}$  or  $V_g > V_{th}$ , respectively). The responsivity R of the photo-TFT is often expressed as  $R = I_{ph}/P_{opt}$ , where  $I_{ph}$  is the source-drain photocurrent and  $P_{opt}$  is the incident optical power.

The performance of the best-performing organic photo-detectors is summarized in Table 10. In photodiodes, EQEs of >80% and responsivities of 0.1–0.7 A/W, with specific detectivities  $D^*$  on the order of  $(1–6) \times 10^{12}$  (cm Hz<sup>0.5</sup>/W), were achieved in the visible/NIR region. Pierre et al.<sup>1239</sup> recently reported photodiodes using screen-printed PEDOT:PSS layers modified with PEIE<sup>1182</sup> or unmodified, to serve as the cathode and anode, respectively. These devices yielded low (<nA/cm<sup>2</sup>) dark currents, resulting in specific detectivities of up to  $3.4 \times 10^{13}$  cm Hz<sup>0.5</sup>/W at a –5 V bias at 532 nm, which is comparable to that of inorganic photodiodes.

Armin et al.<sup>1240</sup> introduced the concept of “charge collection narrowing” to achieve narrow-band wavelength selectivity in BHJ photodiodes. These diodes employ considerably thicker photoactive layers (~2 μm) than typical diodes, so that  $\alpha d \gg 1$  (where  $\alpha$  is the absorption coefficient and  $d$  is the layer thickness), and the concept is based on the manipulation of collection efficiency that contributes to the EQE. In particular, only charge carriers generated by weakly absorbed light (i.e., that at wavelengths near the absorption onset) are collected and produce the photoresponse. For example, in DPP-DTT:PC<sub>71</sub>BM (PCDTBT:PC<sub>71</sub>BM) photodiodes, in which the absorption onset was observed at ~950 nm (~650 nm), the maximal EQE was obtained at ~920 nm (~670 nm) and the fwhm of <90 nm was achieved.

Fast response with operating frequencies of >100 MHz was achieved in multilayer detectors, 10–100 MHz response in vacuum-deposited bilayer detectors, and >1 MHz in solution-processed BHJs. However, the challenge remains to simultaneously optimize the EQE, bandwidth, and detectivity.

The best photo-TFTs (Table 11) are based on molecular crystals or high-mobility polymers, with several reports of responsivity of >10<sup>4</sup> A/W (which is considerably higher than the 300 A/W achieved in amorphous Si photo-TFTs) and reaching  $(4–10) \times 10^5$  A/W in PDI single fibers<sup>1241</sup> and a DPP-based D–A copolymer<sup>1242</sup> in short-channel devices at low illumination levels.

### 11.3. Photorefractive Devices and Novel Effects

Applications of PR materials include holographic 3D displays,<sup>662,663</sup> image processors (amplifiers, novelty filters, optical correlators),<sup>1271–1273</sup> imaging through turbid medium (including coherence-gated holographic imaging for medical applications),<sup>1063,1274–1276</sup> phase conjugation, optical limiting,<sup>1277</sup> non-contact surface defect control,<sup>1278,1279</sup> optical waveguiding,<sup>1280–1284</sup> temporal characterization of ultrafast pulses,<sup>1285</sup> and many others.<sup>1286</sup> Comprehensive discussions of earlier work can be found in refs 220, 628, and 629. Here the progress in applications of PR organic materials since 2012 is briefly summarized.

**11.3.1. 3D Displays.** Over the past decade, impressive progress has been made in the development of PR polymer-based 3D updatable holographic displays.<sup>662,663,677,1287</sup> Holographic recording of an image of a 2D object involves formation of the hologram (refractive index grating) in the PR material created by interfering “object” and “reference” beams (Section 6). Here the “object” beam contains amplitude and phase information about the object (e.g., using reflection or transmission through the real object or a simulated pattern using a spatial light modulator). To read off the hologram, a reading beam reproducing the wavefront of the reference beam is diffracted from the hologram, creating the image of the object. In the case of a 3D object, the object information is created using either a 3D computer model or a series of images

of a real object taken from different viewpoints and perspectives (holographic stereography). These perspectives are then optically multiplexed onto different regions of the recording medium, while keeping track of all angles and perspectives used in recording across the entire display. The image reconstruction is then performed similarly to that in real object holography.

Jolly et al.<sup>1288</sup> demonstrated proof-of-principle computer generated holograms (CGHs) directly written in the PR polymer device. Instead of holographic recording of images from various viewpoints, CGHs are calculated by computational modeling of interference between the object and the reference beam. Then, the interference pattern is, for example, displayed by the spatial light modulator and directly imaged by the medium as the intensity distribution. This method could be a cost-effective alternative to holographic stereography, featuring simpler design and a reduced footprint.

The performance of PR displays relies on high diffraction efficiency, fast video-rate recording times, and hologram persistence times depending on how long the display is expected to store the recorded information. Because optimization of all these characteristics most often involves a trade-off, additional steps have been introduced into the image recording/read-out protocols, such as voltage “kick-off” (image recording at higher voltages than image read-out, to minimize recording times and maximize persistence times)<sup>662</sup> or preillumination (image recording after the medium had been uniformly illuminated).<sup>669</sup> Blanche et al.<sup>663</sup> demonstrated an  $\sim 2$  s recording of the  $4'' \times 4''$  image in a PATPD-CAAN:FDCST:ECZ:PCBM film using a single nanosecond laser pulse to record each holographic pixel element (hogel). This writing speed enabled taking a live feed from 16 cameras of a speaker and integrating those in a real-time “telepresence” system. They also achieved a two-color reconstruction by angularly multiplexing separate holograms recorded for each wavelength (Figure 35(a)). In the follow-up work,<sup>1287</sup> Lynn et al. demonstrated an  $\sim 8$  s recording of a  $30 \text{ cm} \times 15 \text{ cm}$  image using the same laser, with an improved resolution due to a reduced hogel size ( $< 200 \mu\text{m}$ ), a display brightness of  $> 2,500 \text{ cd/m}^2$ , and the three-color gamut (Figure 35(b)) exceeding that of a standard HDTV.

One of the limitations for practical applications of PR organic materials has been the necessity of high applied electric fields and high recording light intensities to promote faster response time. Therefore, reduction of the operating voltage and light intensity, yet maintaining fast recording speed, has been a subject of intensive research. Tsujimura et al.<sup>1289</sup> obtained a  $\sim 35\%$  diffraction efficiency with the response time of 39 ms in the PDAS:ECZ:FDCST:PCBM composite at  $45 \text{ V}/\mu\text{m}$  and  $10 \text{ mW/cm}^2$  cw 532 nm writing beams, demonstrating a sub-50-ms refresh speed in the dynamic holographic images recorded in this sample. In a follow-up work, Giang et al.<sup>677</sup> obtained an over 80% diffraction efficiency in a PDAS:BBP:7-DCST:PCBM composite at  $40 \text{ V}/\mu\text{m}$  and demonstrated a dynamic hologram of an object rotating with a speed of  $0.042 \text{ rad/s}$  recorded in this material at  $25 \text{ V}/\mu\text{m}$ .

**11.3.2. Laser-Based Ultrasound.** Laser-based ultrasound (LBU) is a nondestructive technique for remote sensing, inspection, and manufacturing diagnostics for many industrial applications. In contrast to piezoelectric transducer-based systems, the LBU method allows for vibration control in surfaces of complex geometry as well as in hazardous and high temperature environments. The most common vibration detection devices are laser interferometers, which are used to

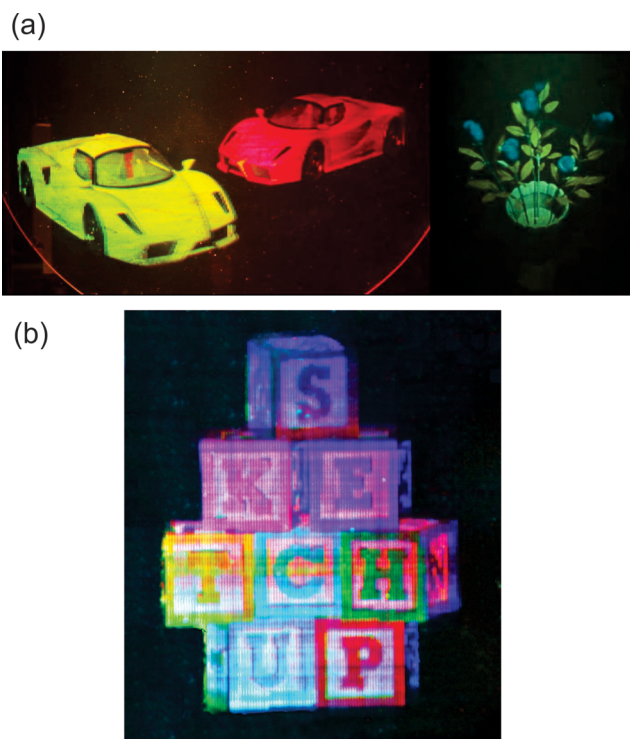


**Figure 35.** Two-colored (a) and full-color (b) rewritable holograms obtained in a PR polymer film. Part (a) is reprinted with permission from ref 663. Copyright 2010 Nature Publishing Group. Part (b) is reprinted from ref 1287 under license in *Journal of Physics: Conference Series* by IOP Publishing Ltd.

measure the small displacements produced when an ultrasonic wave reaches and distorts a surface. One such approach utilizes two-wave mixing in a PR material to combine a signal beam, distorted after reflection from the test surface in motion, with a plane-wave reference beam and to match their wavefronts for homodyne detection.<sup>1278,1279</sup> The hologram in the PR material acts as an adaptive beamsplitter, which combines the two beams with exact wavefront matching, thus allowing efficient coherent detection. A figure of merit for two-wave mixing-based homodyne detection is a noise-equivalent surface displacement amplitude defined as follows:<sup>1278</sup>

$$\delta = \frac{\lambda}{4\pi} \sqrt{\frac{hc}{2\eta\lambda}} \frac{\exp[\alpha L/2]}{\sin[\Gamma L]} \quad (60)$$

where  $\lambda$  is the wavelength,  $\eta$  is the quantum efficiency of the detector,  $\alpha$  is the absorption coefficient,  $\Gamma$  is the 2BC gain coefficient, and  $L$  is the interaction length in a PR material.

Homodyne detection systems based on several PR polymer composites, with sensitivity of  $\sim 0.1 \text{ nm}$ , have been demonstrated.<sup>1278,1279</sup> In PVK:7-DCST (or AODCST or DCDHF-6):BBP:C<sub>60</sub> (or PCBM)) the noise-equivalent surface displacement amplitude ( $\delta$ ) given by eq 60 was found to be  $\delta = (7.2 - 9.5) \times 10^{-8} \text{ nm} (\text{W/Hz})^{1/2}$ .<sup>1278,1279</sup> Zamiri et al.<sup>1279</sup> used a PR interferometer based on the PVK:AODCST:BBP:PCBM composite, with the 2BC gain coefficient  $\Gamma$  of  $60 \text{ cm}^{-1}$  at  $50 \text{ V}/\mu\text{m}$  and a  $\sim 60 \text{ ms}$  response time, to remotely determine the defect location, the defect profile, and the sample thickness in Al and steel sheets.

**11.3.3. Ultrasound-Modulated Optical Tomography.** Imaging inside the turbid medium, for example biological tissues, represents a challenge due to strong light scattering. PR

effect-based phase conjugation mirror (PCM) offers one of the potential solutions, via time-reversal “clean-up” of the beam wavefront distorted by the medium. Recently, a time-reversed ultrasonically encoded (TRUE) method for optical focusing inside the scattering medium was developed.<sup>1290,1291</sup> In this technique, a focused ultrasound beam “encodes” randomly scattered photons that propagate through the ultrasound focus with a shift frequency. The “encoded” light then interferes with a reference beam, and the interference pattern is recorded in the PR medium. The medium also serves as a PCM when the reading beam counter-propagating to the reference beam reads out the hologram, thus generating a phase-conjugated copy of the “encoded” light. In this FWM configuration, the time-reversed wavefront converges back to the ultrasound focal zone, forming an optical focus. Using the TRUE technique, the authors were able to image through media with thickness of up to 120 photon mean-free paths  $l_{\text{scat}}$  (for human skin,  $l_{\text{scat}} \sim 1$  mm) using PR polymer composite (PATPD-CAAN:FDC-ST:ECZ:PCBM) as a PCM. In a follow-up work, Suzuki et al.<sup>1292</sup> considerably simplified the setup by removing the time-reversal component and instead relying on the 2BC gain of the PR medium in a two-wave mixing experiment. They demonstrated imaging through  $\sim 94$  photon mean free paths, equivalent to  $\sim 94$  mm of breast tissue for light in the red or near-IR spectral range, with sensitivity outperforming that of inorganic PR crystals.

**11.3.4. Photonic Applications.** Several recent developments have emerged that are promising for applications of PR organic materials in photonics. Li et al.<sup>1293</sup> fabricated a PR photonic colloidal crystal using silica microspheres embedded in a PR PDLC (5CB:PMMA:C<sub>60</sub>). The optical transmission spectrum exhibited a transmission stop band (reduction in transmission in a particular wavelength range), tunable by applied electric field in the 0–3 V/ $\mu\text{m}$  range enabled by the electric field-dependent refractive index of the PDLC. In a two-wave mixing configuration, 2BC was observed, which was considerably enhanced at particular angles of incidence, correlated with those for the photonic stop band.

Abbott et al.<sup>1294</sup> demonstrated interaction of a surface plasmon polariton (SPP) with a refractive index grating. For that, they fabricated a LC cell using a rubbed PVK:C<sub>60</sub> photoconductive film of 80–150 nm thickness as an alignment layer which was deposited on a 40 nm layer of Au. The SPP was launched at the Au/PVK:C<sub>60</sub> interface, and its propagation was studied depending on the photoinduced director orientation in the LC. The latter was controlled by the space-charge field in the photoconductive layer formed by two interfering beams in the presence of an applied electric field. The authors were able to induce the SPP diffraction which could be optically controlled by changing the applied voltage, light intensity, and angle between the two interfering beams (grating pitch). In follow-up work, Daly et al.<sup>1295</sup> proposed a model describing PR grating-induced plasmon–plasmon coupling and Proctor et al.<sup>1296</sup> studied in detail the electric and PR behavior of LC cells utilizing substrates with photoconductive layers depending on the applied electric field and excitation conditions.

Xue et al.<sup>1297</sup> fabricated dye-doped LC cells on ZnSe layers and showed that the band structure of the SPP at the ZnSe/LC interface can be controlled by the photoinduced space-charge field in ZnSe. They also observed 2D diffraction patterns, which were attributed to the light-SPP coupling.

The nonlinear refractive index change in PR materials can also potentially be utilized in wave-guiding applica-

tions.<sup>1282,1283,1298</sup> One interesting possibility is realization of optical spatial solitons, which are nonlinear self-trapped wavepackets that propagate through the medium without diffraction.<sup>1299</sup> Solitons are of interest both from the fascinating physics perspective (e.g., their particle-like interactions) and for applications in waveguiding and beam steering. PR solitons are important because of several reasons, including the facts that they can be generated at low cw power and that a weak soliton beam can induce a waveguide for more intense beams at wavelengths at which the PR effect is less efficient. The PR solitons were studied extensively in PR crystals, and the soliton and its capability to guide beams at other wavelengths have been demonstrated in PR organic materials.<sup>1282,1283,1300</sup> There has been recent theoretical work on a variety of soliton types and their interaction in PR organic materials,<sup>1301–1303</sup> which is awaiting experimental realization.

#### 11.4. Other Optoelectronic Applications

Optoelectronic applications are by no means limited to those discussed above. There are also exciting applications of organic optoelectronic materials in biosensors, biomimetics, memory devices, optically switchable<sup>1304</sup> and light-emitting TFTs, etc. See recent reviews (Table S1) in, for example, refs 1037, 1039, and 1305. The most widely known optoelectronic application of organic semiconductors is organic light-emitting diodes (OLEDs). Because OLEDs do not rely on photoinduced charge carrier dynamics, detailed description of OLEDs is beyond the scope of this review; see, for example, refs 6 and 1306. However, given the large overlap in physical mechanisms and resulting issues involved in the performance of OLEDs and devices discussed above, a brief account of current trends and achievements is included below.

OLEDs have received considerable attention during the past 20 years, having reached IQEs of nearly 100%, EQEs of over 50% for monochrome OLEDs, and luminous efficacies similar to those of fluorescent tubes in white LEDs (WOLEDs). OLEDs currently represent the success story of widely commercialized applications of organic semiconductors, rapidly developing in two main directions—OLED displays and OLED lightning. Several aspects of the physics of OLEDs are still developing;<sup>1307,1308</sup> for example, Malissa et al.<sup>1307</sup> recently demonstrated that hyperfine interactions enable room-temperature control of OLED conductivity by manipulation of nuclear spin states.

Operation of an OLED is based on electroluminescence (EL), in which light emission is obtained by radiative recombination of excitons created in a solid by injection of the holes and electrons from the electrodes followed by their moving toward each other in an applied electric field. The efficiency of EL is determined by the efficiency of PL, by the charge transport properties of the material, and by effects at electric contacts. The internal EL efficiency ( $\Phi_{\text{EL}}$ ) (to be referred to as the IQE) is given by

$$\Phi_{\text{EL}} = \Phi^* \Phi_{\text{PL}} \gamma_{\text{eh}} \quad (61)$$

where  $\Phi_{\text{PL}}$  is the intrinsic quantum efficiency for radiative decay (both fluorescence and phosphorescence),  $\Phi^*$  is the fraction of excitons formed that result in radiative transitions (theoretically,  $\Phi^* = 0.25$  in fluorescent materials, assuming a random spin distribution of the injected carriers, and  $\Phi^* = 1$  in phosphorescent materials), and  $\gamma_{\text{eh}}$  is the ratio of electrons to holes (or vice versa, to maintain  $\gamma_{\text{eh}} < 1$ ) injected from the electrode. The IQE is the measure of the number of photons

emitted per electron injected, and it is based on the assumption that all the light generated is received by an external observer. The external efficiency (EQE) is a factor of  $2n^2$  smaller than the IQE, where  $n$  is the refractive index of the organic layer, unless the device architecture incorporates a structure with improved outcoupling efficiency such as an optical microcavity. Improvement of the outcoupling efficiency is one of the main challenges, and the area of research which could yield the largest improvement in OLED efficiency.<sup>6</sup>

The main requirements for OLED materials are high luminescence quantum yield in the solid state, good carrier mobility (both *n*- and *p*-type), good film-forming properties (pinhole free), good thermal and oxidative stability, and good color purity (defined by the Commission Internationale de L'Eclairage (CIE) coordinates). The first generation of OLEDs was based on fluorescent materials. In this case, the emission of light is the result of the recombination of singlet excitons, but the IQE in accordance to eq 61 is limited to 25%, which results in a maximal possible EQE of  $\sim 5\%$  (assuming the refractive index of organic layer to be  $\sim 1.7$  and no outcoupling efficiency enhancement). The second generation of OLEDs utilized phosphorescent materials where all excitons can be converted into emissive triplet states through efficient intersystem crossing. Such materials exhibited up to four times higher efficiency than fluorescent materials, relying on the presence of heavy atoms such as iridium or platinum to increase spin-orbit coupling that results in efficient intersystem crossing followed by radiative triplet decay. Highly efficient green and red electrophosphorescent emitters have been demonstrated, with IQEs approaching 100%. Reineke et al.<sup>1309</sup> reported dual emission from a single-type molecule (BzP)PB embedded in PMMA with efficient both fluorescence and phosphorescence emission. Recently, the third generation OLEDs were introduced, which use molecules exhibiting TADF (Section 2.7.2). The EQEs of nearly 20% were demonstrated,<sup>173</sup> and IQEs of nearly 100% were obtained in blue,<sup>173</sup> green,<sup>174</sup> yellow, and red<sup>172</sup> TADF-based devices.

White light-emitting diodes (WOLEDs) received considerable attention both for full-color display applications and as a potential replacement of white light incandescent sources. Detailed description of WOLED architectures and of earlier work can be found in ref 1310. Recent developments have been summarized in ref 1311. In WOLEDs, the color quality is characterized not only by the CIE coordinates, but also by the color rendering index (CRI). For high-quality white-light illumination, a stable CRI above 80 is required, which is a challenge, as most current WOLEDs have CRIs below 70.<sup>1311</sup> The broadband emission required for WOLEDs is typically provided by a number of dopants or layers combined in the WOLED using a variety of architectures, to achieve the required emission characteristics. However, fluorescent "white single polymers" have also been developed, exhibiting CRI of 85,<sup>1312</sup> although with lower EQEs as compared to those in doped or multilayer WOLEDs. Development of stable blue emitters has been one of the main challenges, which potentially could be addressed by TADF-based blue fluorescent emitters,<sup>175</sup> which have recently approached IQEs of 100%.<sup>173</sup> Simultaneous achievement of high efficiencies and stable, bias-independent white emission remains a challenge, which needs addressing via material design, device architecture, or both.

## 11.5. Summary

Impressive advances have been achieved in the performance of organic optoelectronic devices, driven by a better understanding of device physics and of fundamental properties of organic materials, as well as by improvements in fabrication procedures and device architecture. The efficiency of OPVs has been steadily increasing, and pathways to improve PCEs via engineering of properties of CT states, reduction in disorder, and controlling the morphology have been identified. As the current performance is still below the predicted thermodynamic limit of over 20%, there is a considerable potential for improvement. There has been significant progress in the development of organic photodetector/photo-TFT technology and its applications. The availability of new high-mobility materials such as D–A copolymers, which also exhibit unique photophysical properties<sup>170</sup> and promote charge separation, should further boost the performance and facilitate the optimization of the EQE, bandwidth, and detectivity. The organic PR display and imaging technology has made impressive progress; incorporation of novel photoconductive polymers and nonfullerene sensitizers into PR devices may dramatically improve the PR dynamics, bringing this technology closer to commercialization. A number of novel photonic applications of PR materials have also been demonstrated and/or predicted theoretically, which are now awaiting further developments.

## 12. SUMMARY AND OUTLOOK

The field of organic optoelectronics has experienced tremendous progress over the past 10 years, both in understanding of the fundamental physics of charge generation and transport and in material design, fabrication, and processing methods. This enabled demonstration of charge carrier mobilities of up to 40–50 cm<sup>2</sup>/(Vs) in molecular crystals and polymers and PCEs of over 10% in organic solar cells, as well as realization of novel applications such as full-color PR polymer 3D display. In spite of the remarkable advances, more work is necessary in all aspects of the field, including theoretical descriptions of charge generation and transport, experimental discovery and validation, and material design.

Theoretical models of charge generation need to be further developed to incorporate the spin-dependent dynamics, delocalization, and microscopic characteristics of the material. The origin and quantitative description of ultrafast charge generation in pristine organic materials requires further studies. In D/A HJs, understanding of how various manifestations of coherence contribute to charge separation, how the D–A character of the donor polymer and particular aspects of morphology promote charge generation with a minimal driving force, and how thermodynamics and kinetics work synergistically in determining the charge generation efficiency is necessary.

In the description of charge transport in crystalline materials, clear guidelines are necessary to distinguish between contributions of various interactions (such as electron coupling to low-frequency lattice vibrations vs high-frequency intramolecular vibrations) and to determine the dominant contribution to charge transport. Experimental evidence that directly probes and quantifies such contributions is desirable. Quantitative descriptions of charge transport in high-mobility D–A polymers are also yet to be developed and are necessary to guide further design of these materials. Given the structural

complexity of organic polycrystalline materials and blends, charge transport models that specifically take into account the microscopic structure are needed. Finally, an upper limit on charge carrier mobility in organic materials is yet to be determined.

On the materials side, design guidelines are necessary for future D–A copolymers, nonfullerene acceptors, and materials with intramolecular singlet fission. Organic acceptors for singlet fission donors are also desirable. Because many high-performance optoelectronic materials rely on the presence of crystalline phases and, in the case of BHJ solar cells, on a fine balance between the crystalline and amorphous phases, tight control of morphology and experimental procedures for an *in situ* characterization of local nanoenvironment and its contribution to device characteristics are required. This tight control over the morphology is relaxed in amorphous materials, rendering such materials with low disorder and high mobilities to be of considerable importance; these are promising candidates as a photoconductive component in the PR medium and could be a good choice for applications for which mobilities on the order of  $1 \text{ cm}^2/(\text{Vs})$  are sufficient. Several nontraditional approaches highlighted in the review may inspire future directions in the development of new-generation materials and devices. These include naturally derived sustainable materials and devices combining benefits of organic and inorganic components.

On the fabrication and processing side, more work is needed to translate the high performance obtained on laboratory devices to large-area organic devices deposited via in-air R2R processing in an industrial setting. The compatibility of processing technology with green chemistry should also be an important goal. Another critical goal is to achieve long-term stability of devices with respect to environmental and continuous use-related factors.

Although organic optoelectronic materials have been known for more than a century, the fascinating physics of their interaction with light, depending on various factors, is still being discovered every day, in single-crystal or thin-film devices and at nanoscales, down to the single-molecule level, and from femtoseconds to many seconds after photoexcitation. The potential for discovery as well as the balance between the complexity of issues involved and technologically important breakthroughs continue driving the field of organic optoelectronics toward refined models, thought-provoking discoveries, new-generation material design, commercialization of existing applications, and demonstration of novel applications. It is exciting to be a part of this fascinating journey.

## ASSOCIATED CONTENT

### Supporting Information

The Supporting Information is available free of charge on the ACS Publications website at DOI: [10.1021/acs.chemrev.6b00127](https://doi.org/10.1021/acs.chemrev.6b00127).

Extensive table summarizing recent review articles that are focused on specialized topics within the field of organic (opto)electronics (PDF)

## AUTHOR INFORMATION

### Corresponding Author

\*Phone: (541) 737-1679; e-mail: [oksana@science.oregonstate.edu](mailto:oksana@science.oregonstate.edu).

## Notes

The author declares no competing financial interest.

## Biography

Oksana Ostroverkhova received her Diploma with Honors in Physics and Optical Engineering from Kiev Taras Shevchenko National University (Kiev, Ukraine) in 1996. During her graduate studies at Case Western Reserve University (Cleveland, USA) in the group of K. D. Singer, she specialized in the photoconductive and nonlinear optical properties of polymers and liquid crystals and obtained her Ph.D. in Physics in 2001. Her postdoctoral work at Stanford University (Stanford, USA) in the group of W. E. Moerner involved physics and applications of photorefractive organic materials; there she also began her quest into single-molecule fluorescence spectroscopy of organic optoelectronic materials. The Killam Memorial Fellowship award enabled Dr. Ostroverkhova's work on ultrafast THz spectroscopy of organic semiconductors in the group of F. A. Hegmann at the University of Alberta (Edmonton, Canada). In 2005, Dr. Ostroverkhova joined Physics Department at Oregon State University (Corvallis, USA), where she is currently an Associate Professor. She is a recipient of several awards, including the NSF CAREER award and OSU Carter Award for Outstanding and Inspirational Teaching. Her current research interests are in the optoelectronic properties of organic materials spanning various time and spatial scales, in the development of sustainable (opto)electronic materials, and in utilizing optical properties of materials in entomology.

## ACKNOWLEDGMENTS

The National Science Foundation (NSF) support through NSF-DMR 1207309 and NSF-DMR 0748671 (CAREER) grants is gratefully acknowledged. The Fall 2015 teaching relief provided by the Oregon State University Faculty Release Time program has also been critical during writing of the manuscript. The author is indebted to her former mentors (K. D. Singer, W. E. Moerner, and F. A. Hegmann), long-term collaborators (J. E. Anthony, R. J. Twieg, and M. M. Haley), and many former and current students and postdoctoral researchers in her laboratory over the past 11 years.

## LIST OF ABBREVIATIONS

Ac = anthracene  
ABT = anthra[2,3-*b*]benzo[*d*]thiophene  
ADT = anthradithiophene  
A-EHDTT = anthracene substituted with two 2-ethynyl-5-hexyldithieno[3,2-*b*:2',3'-*d*] groups at the 9,10-positions  
AODCST = [2-[4-bis(2-methoxyethyl)amino]benzylidene]-malononitrile  
ARPES = angle-resolved photoemission spectroscopy  
ATOP = 1-alkyl-5-[2-(5-dialkylaminothienyl)methylene]-4-alkyl-[2,6-dioxo-1,2,5,6-tetrahydropyridine]-3-carbonitrile  
BACE = bias-assisted charge extraction  
BBDTE = (*E*)-1,2-bis(benzo[1,2-*b*:4,5-*b'*]dithiophen-2-yl)ethene  
BBP = butyl benzyl phthalate  
2BNCM = *N*-2-butyl-2,6-dimethyl-4*H*-pyridone-4-ylidene-cyanomethyl acetate  
2BC = two-beam coupling  
BDOH-PF = poly[9,9-bis(3,6-dioxahexyl)fluorene-2,7-diyl]  
BHJ = bulk heterojunction  
BO-ADPM = B,O-chelated azadipyrromethene  
BSE = Bethe–Salpeter equation  
BTBT = benzothienobenzothienophene

- BTR = benzodithiophene terthiophene rhodamine  
 BTT = [1,2-b:3,4-b:5,6-d]trithiophene  
 CA = camphoric anhydride  
 CAAN = carbaldehyde aniline  
 CARS = coherent anti-Stokes Raman scattering  
 CC2TA = 2,4-bis[3-(9H-carbazol-9-yl)-9H-carbazol-9-yl]-6-phenyl-1,3,5-triazine  
 CDCB = carbazolyl dicyanobenzene  
 CDM = correlated disorder model  
 CDT-BTZ = poly[2,6-(4,4-bis-alkyl-4H-cyclopenta-[2,1-b;3,4-b0]-dithiophene)-*alt*-4,7-(2,1,3-enzothiadiazole)]  
 CELIV = current extraction under linear increasing voltages  
 CIE = Commission Internationale de l'Éclairage  
 SCB = 4'-(*n*-pentyl)-4-cyanobiphenyl  
 CMS = charge modulation spectroscopy  
 CPZ = conjugated polymer zwitterion  
 CPE = conjugated polyelectrolyte  
 CT = charge transfer  
 CuPc = copper phthalocyanine  
 CV = cyclic voltammetry  
 Cy7-T = heptamethine cyanine dye  
 DAN = deterministic aperiodic nanostructures  
 DATT = dianthra[2,3-b:2',3'-f]thieno[3,2-b]thiophene  
 DBDC = 3-(*N,N*-di-*n*-butyl-aniline-4-yl)-1-dicyanomethylidene-2-cyclohexene  
 DBFI-EDOT = 2,5-bis(8-(17-phenyl)-7,9,16,18-tetraazabenzodifluoranthene-3,4,12,13-tetracarboxylic acid diimide)-3,4-ethylenedioxythiophene  
 DBP = tetraphenyl-dibenzoperiflanthene  
 DCB = dichlorobenzene  
 DCDHF = dicyanomethylenedihydrofuran  
 2DES = two-dimensional electron spectroscopy  
 DCVnT = dicyanovinyl-substituted oligothiophenes  
 DFT = density functional theory  
 DIO = 1,8-diiodooctane  
 diF R-ADT = difluorinated anthradithiophene derivative with side groups R  
 diCN R-ADT = dicyano-substituted anthradithiophene derivative with side groups R  
 7-DCST = 4-(azepan-1-yl)benzylidenemalononitrile  
 DMNPAA = 2,5-dimethyl-(4-*p*-nitrophenylazo)anisole  
 DNNT = dinaphto-thieno-thiophene  
 DOO-PPV = poly(dioctyloxy)phenylenevinylene  
 DOS = density of states  
 2DPP-TEG = NCS2DPP-OD-triethylene glycol  
 DPP-DTT = poly(*N*-alkyl diketopyrrolo-pyrrole dithienylthieno[3,2-*b*]thiophene)  
 DPPDBTE = poly[2,5-bis(2-decyltetradecyl)pyrrolo[3,4-*c*]pyrrole-1,4-(2H,5H)-dione-(*E*)-1,2-di(2,2'-bithiophen-5-yl)-ethene]  
 DPPDTSE = [2,5-bis(2-decyltetradecyl)pyrrolo[3,4-*c*]pyrrole-1,4-(2H,5H)-dione-(*E*)-(1,2-bis(5-(thiophen-2-yl)-selenophen-2-yl)ethene)]  
 DPP-SVS = diketopyrrolopyrrole-selenophene vinylene selenophene  
 DPT = 5,12-diphenyl tetracene  
 DRCNnT = A-D-A molecules with septithiophene backbone with 2-(1,1-dicyanomethylene)rhodamine end groups  
 DTBDT = 4,7-di-2'-thienyl-2,1,3-benzothiadiazole  
 DTDCBTB = 2-((7-(5-(dip-tolylamino)thiophen-2-yl)benzo[*c*][1,2,5]thiadiazol-4-yl)methylene)malononitrile  
 DTP = di(2-thienyl)  
 ECZ = *N*-ethylcarbazole  
 EL = electroluminescence  
 EQE = external quantum efficiency  
 ESR = electron spin resonance  
 FDCST = 4-homopiperidino-2-fluorobenzylidene malononitrile  
 FET = field-effect transistor  
 FF = fill factor  
 Fm-rubrene = bis(trifluoromethyl)dimethylrubrene  
 F2-TCNQ = difluorotetracyanoquinodimethane  
 F4-TCNQ = tetrafluorotetracyanoquinodimethane  
 F8BT = poly(9,9'-dioctylfluorene-*co*-benzothiadiazole)  
 F8 R-Pn = octafluoro pentacene derivative with side groups R  
 FRET = Förster resonant energy transfer  
 FSRs = femtosecond stimulated Raman scattering  
 FWM = four-wave mixing  
 GDM = Gaussian disorder model  
 Hex = hexacene  
 HOMO = highest occupied molecular orbital  
 4(HPBT) = 1,2,4,5-tetra(50-hexyl-[2,2']-bithiophenyl-5-vinyl)-benzene  
 HV-BT = 4,7-bis[2-(1-hexyl-4,5-dicyano-imidazol-2-yl)-vinyl]benzo[*c*]-[1,2,5]-thiadiazole  
 ICBA = indene-C(60) bisadduct  
 ICL = interconnecting layer  
 IDTBT = indacenodithiophene-*co*-benzothiadiazole  
 IF = indenofluorene  
 IQE = internal quantum efficiency  
 IRAV = infrared active vibrational modes  
 ISC = intersystem crossing  
 KFPm = Kelvin force probe microscopy  
 LUMO = lowest unoccupied molecular orbital  
 NPD = *N,N'*-bis(1-naphthyl)-*N,N'*-diphenyl-1,1'-biphenyl-4,4'-diamine  
 MBPT = many-body perturbation theory  
 Me-ABT = oligoarene 6-methyl-anthra[2,3-*b*]benzo[*d*]-thiophene  
 MeLPPP = methyl-substituted ladder-type poly(para-phenylene)  
 o-MeO-DMBI = 2-(2-methoxyphenyl)-1,3-dimethyl-2,3-dihydro-1H-benzoimidazole  
 MeO-TPD = (*N,N,N',N'*-tetrakis(4-methoxyphenyl)-benzidine)  
 MDMO-PPV = poly[2-methoxy-5-(30,70-dimethyloctyloxy)-1,4-phenylenevinylene]  
 MEH-PPV = poly[2-methoxy,5-(2'-ethyl-hexoxy)-1,4-phenylenevinylene]  
 MNPAA = 3-methoxy-(4-*p*-nitrophenylazo)anisole  
 MSAPBS = 4,4'-(((methyl(4-sulphonatobutyl)ammonio)bis(propane-3,1-diyl)) bis(dimethyl-ammoniumdiyl))bis-(butane-1-sulphonate)  
 m-MTDATA = 4,4A,4''-tris[3-methylphenyl(phenyl)-amino]triphenylamine  
 Nph = naphthalene  
 NDI = naphthalene diimide  
 NSN = silane-containing triazine derivative  
 PATPD = poly(acrylic tetraphenyldiaminobiphenyl)  
 PBDTTT-C = alkylthiophene-2-yl-substituted benzo[1,2-*b*:4,5-*b'*]-dithiophene  
 PBDTT-FTTE = poly(4,8-bis(5-(2-ethylhexyl)thiophen-2-yl)-benzo[1,2-*b*:4,5-*b'*]dithiophene-2,6-diyl-*alt*-(4-(2-ethylhexyl)-3-fluorothieno[3,4-*b*]thiophene-)-2-carboxylate-2,6-diyl)

PBTTPD-HT = copolymer with benzo[1,2-b:4,5-b']-dithiophene and thieno[3,4-c]pyrrole-4,6-dione groups  
 PBI = perylene bisimide  
 PBT = poly(2,5-bis(3-alkylthiophen-2-yl)thieno[3,2-b]-thiophene)  
 PC<sub>61</sub>BM = [6,6]-phenyl-C<sub>61</sub>-butyric acid methyl ester  
 PC<sub>71</sub>BM = [6,6]-phenyl C<sub>71</sub>-butyric acid methyl ester  
 PCE = power conversion efficiency  
 PCDTBT = poly[N-900-hepta-decanyl-2,7-carbazole-*alt*-5,5-(40,70-di-2-thienyl-20,10,30-benzothiadiazole)  
 PCDTPT = poly[4-(4,4-dihexadecyl-4Hcyclopenta[1,2-b:5,4-b']dithiophen-2-yl)-*alt*-[1,2,5]thiadiazolo[3,4-c]-pyridine]  
 PCPDTBT = poly[2,6-(4,4-bis(2-ethylhexyl)-4H-cyclopenta[2,1-b;3,4-b']-dithiophene)-*alt*-4,7-(2,1,3-benzothiadiazole)]  
 PDA = polydiacetylene  
 PDAS = poly(4-diphenylamino)styrene  
 PDBPyBT = D–A copolymer with 3,6-di(pyridin-2-yl)pyrrolo[3,4-c]pyrrole-1,4(2H, 5H)-dione acceptor  
 PDI = perylene diimide  
 PDIF-CN2 = *N,N'*-1H,1H-perfluorobutyl dicyanoperylene-carboxydiimide  
 PDPPTPT = dioxopyrrolo[3,4-c]pyrrole-1,4-diyl-*alt* -{[2,2'-(1,4-phenylene)bithiophene]-5,5'-diyl}  
 PDPP-CNTVT = Poly[2,5-bis(2-octyldecyl)pyrrolo[3,4-c] pyrrole-1,4(2 H, 5 H) -dione-(E)-[2,2'-bithiophen]-5-yl)-3-(thiophen-2-yl)acrylonitrile]  
 p-DTS(FBTTh<sub>2</sub>)<sub>2</sub> = 7,7'-(4,4-bis(2-ethylhexyl)-4H-silolo[3,2-b:4,5-b']dithiophene-2,6-diyl)bis(6-fluoro-4-(5'-hexyl[2,2'-bithiophen]-5-yl)benzo[c][1,2,5]thiadiazole)  
 PDCST = 4-piperidinobenzylidenemalononitrile  
 PDVT-10 = poly[2,5-bis(2-decyltetradecyl)pyrrolo[3,4-c]pyrrole-1,4(2H,5H)-dione-*alt*-5,5-di(thiophen-2-yl)-2,2'-(E)-2-(2-(thiophen-2-yl)vinyl)thiophene]  
 PEDOT:PSS = poly(3,4-ethylenedioxythiophene):polystyrenesulfonate  
 PEIE = polyethylenimine  
 PI = polyimide  
 PID2 = poly-3-oxothieno[3,4-*d*]isothiazole-1,1-dioxide/benzodithiophene  
 PIDTT-DFBT = poly(indacenodithieno[3,2-*b*]thiophene-difluoro-benzothiadiazole)  
 PF10TBT = poly[2,7-(9,9-didecylfluorene)-*alt*-5,5-(4',7'-di-2-thienyl-2',1',3'-benzothiadiazole)]  
 PF6-TPD = poly(*N,N'*-bis(4-hexylphenyl)-*N'*-(4-(9-phenyl-9H-fluoren-9-yl)phenyl)-4,4'-benzidine)  
 PFH = poly(9,9-dihexylfluorene-2,7-diyl)  
 PFN = poly[(9,9-bis(3'-(*N,N*-dimethylamino)propyl)-2,7-fluorene)-*alt*-2,7-(9,9-dioctylfluorene)]  
 PFO = poly(9,9-dioctylfluorene)  
 PFPE = perfluoropolyether  
 PL = photoluminescence  
 PMMA = poly(methyl)methacrylate  
 Pn = pentacene  
 p(NDI2OD-T2) = poly([*N,N'*-bis(2-octyldecyl)-naphthalene-1,4,5,8-bis(dicarboximide)-2,6-diyl]-*alt*-5,5'-(2,2'-bithiophene))  
 P3HT = poly(3-hexylthiophene)  
 P3OT = poly(3-octylthiophene)  
 PPV = poly(p-phenylenevinylene)  
 PQT-12 = poly(3,3''-didodecylquaterthiophene)  
 PR = photorefractive

PSEHTT = poly[(4,4'-bis(2-ethylhexyl)dithieno[3,2-b:2',3'-d]silole)-2,6-diyl-*alt*-(2,5-bis(3-(2-ethylhexyl)thiophen-2-yl)-thiazolo[5,4-*d*]thiazole)]  
 PSeTPTI = poly{2,5-selenophene-*alt*-2,8-(4,10-bis(2-hexyldecyl))thieno[2',3':5,6]pyrido[3,4-*g*]thieno[3,2-*c*]-isoquinoline-5,11(4H,10H)-dione}  
 PSF-BT = poly(spirobifluorene-*co*-benzothiadiazole)  
 P8T2Z-C12 = poly(tetryldodecyloctathiophene-*alt*-didodecylbithiazole)  
 PTAA = poly(triarylamine)  
 PTCDA = 3,4,9,10-perylene tetracarboxylic dianhydride  
 PTB7 = polythieno[3,4-*b*]thiophene/benzodithiophene  
 PTDPPSe = diketopyrrolopyrrole-selenophene copolymer with hybrid siloxane-solubilizing groups  
 PTZ = bithiazole-thiazolothiazole  
 PVK = poly(*N*-vinylcarbazole)  
 QY = quantum yield  
 SF = singlet fission  
 SCLC = space-charge limited current  
 SMFS = single-molecule fluorescence spectroscopy  
 SSH = Su–Schrieffer–Heeger  
 SPAD = single-photon avalanche photodiode  
 Spiro-CN = spirobifluorene derivative with two triarylamino donor and two cyano acceptor groups  
 SRH = Shockley–Read–Hall  
 STB = stilbene  
 SubNc = subnaphthalocyanine chloride  
 SubPc = subphthalocyanine chloride  
 SWCNT = single-wall carbon nanotube  
 TADF = thermally activated delayed fluorescence  
 TAT = 7,8,15,16-tetraazaterylene  
 TAS = transient absorption spectroscopy  
 Tc = tetracene  
 t-Bu BTBTB = (6,12-bis[2-(*t*-butyl)ethynyl]benzo[1,2-b:4,5-b]bis(1)benzothiothiophene  
 t-Bu-PBD = 2-(biphenyl-4-yl)-5-(4-*tert*-butylphenyl)-1,3,4-oxadiazole  
 TCDF = time-delayed-collection-field  
 TCHS = (tricyclohexylsilyl)ethynyl  
 TCNQ = tetracyanoquinodimethane  
 TDF = time-delayed fluorescence  
 TES = (triethylsilyl)ethynyl  
 TFB = poly(9,9-dioctyl-fluorene-*co*-*N*-(4-butylphenyl)-di-phenylamine)  
 TIPS = (trisopropylsilyl)ethynyl  
 THz = terahertz  
 TMTES = tetramethyltriethylsilylethynyl  
 TMTSF = tetramethyltetraselenafulvalene  
 TNF = 2,4,7-trinitro-9-fluorenone  
 TNFM = (2,4,7-trinitro-9-fluorenylidene)malononitrile  
 3TPYMB = tris[3-(3-pyridyl)mesityl]borane  
 TPV = transient photovoltage  
 TRMC = time-resolved microwave conductivity  
 TR-2PPE = time-resolved two-photon photoemission  
 TTPO = 5,6,7-trithiapentacene-13-one  
 oDCB = o-dichlorobenzene  
 ZnOOEP = zinc octakis (B-octyloxyethyl)porphyrin  
 6T = sexithiophene

## REFERENCES

- (1) Pope, M.; Swenberg, C. . *Electronic Processes in Organic Crystals and Polymers*; Oxford Science Publication: 1999.

- (2) Kohler, A.; Bassler, H. *Electronic Processes in Organic Semiconductors*; Wiley-VCH Verlag GmbH & Co. KGaA: Weinheim, Germany, 2015.
- (3) Cicoira, F.; Santato, C. *Organic Electronics: Emerging Concepts and Technologies*; Wiley-VCH: 2013.
- (4) Lanzani, G. *The Photophysics behind Photovoltaics and Photonics*; Wiley-VCH: 2012.
- (5) *Introduction to Organic Electronic and Optoelectronic Materials and Devices*; Sun, S. S., Dalton, L., Eds.; CRC Press: 2016.
- (6) Ostroverkhova, O. *Handbook of Organic Materials for Optical and (Opto)electronic Devices*; Elsevier: 2013.
- (7) Kéna-Cohen, S.; Davanço, M.; Forrest, S. Strong Exciton-Photon Coupling in an Organic Single Crystal Microcavity. *Phys. Rev. Lett.* **2008**, *101* (11), 116401.
- (8) Kéna-Cohen, S.; Forrest, S. R. Room-Temperature Polariton Lasing in an Organic Single-Crystal Microcavity. *Nat. Photonics* **2010**, *4*, 371–375.
- (9) Holmes, R. J.; Forrest, S. R. Strong Exciton-Photon Coupling in Organic Materials. *Org. Electron.* **2007**, *8* (2–3), 77–93.
- (10) Daskalakis, K. S.; Maier, S. a; Murray, R.; Kéna-Cohen, S. Nonlinear Interactions in an Organic Polariton Condensate. *Nat. Mater.* **2014**, *13* (3), 271–278.
- (11) Schröter, M.; Ivanov, S. D.; Schulze, J.; Polyutov, S. P.; Yan, Y.; Pullerits, T.; Kühn, O. Exciton–vibrational Coupling in the Dynamics and Spectroscopy of Frenkel Excitons in Molecular Aggregates. *Phys. Rep.* **2015**, *567*, 1–78.
- (12) Bardeen, C. J. The Structure and Dynamics of Molecular Excitons. *Annu. Rev. Phys. Chem.* **2014**, *65*, 127–148.
- (13) Cudazzo, P.; Sottile, F.; Rubio, A.; Gatti, M. Exciton Dispersion in Molecular Solids. *J. Phys.: Condens. Matter* **2015**, *27* (11), 113204.
- (14) Hwang, I.; Scholes, G. D. Electronic Energy Transfer and Quantum-Coherence in  $\pi$ -Conjugated Polymers. *Chem. Mater.* **2011**, *23* (3), 610–620.
- (15) Menke, S. M.; Holmes, R. J. Exciton Diffusion in Organic Photovoltaic Cells. *Energy Environ. Sci.* **2014**, *7* (2), 499.
- (16) Mikhnenko, O.; Blom, P.; Nguyen, T.-Q. T. Exciton Diffusion in Organic Semiconductors. *Energy Environ. Sci.* **2015**, *8*, 1867–1888.
- (17) Bjorgaard, J. a.; Köse, M. E. Simulations of Singlet Exciton Diffusion in Organic Semiconductors: A Review. *RSC Adv.* **2015**, *5* (11), 8432–8445.
- (18) Monahan, N.; Zhu, X.-Y. Charge Transfer–Mediated Singlet Fission. *Annu. Rev. Phys. Chem.* **2015**, *66* (1), 601–618.
- (19) Smith, M. B.; Michl, J. Recent Advances in Singlet Fission. *Annu. Rev. Phys. Chem.* **2013**, *64*, 361–386.
- (20) Smith, M. B.; Michl, J. Singlet Fission. *Chem. Rev.* **2010**, *110* (11), 6891–6936.
- (21) Chan, W. L.; Berkelbach, T. C.; Provorse, M. R.; Monahan, N. R.; Tritsch, J. R.; Hybertsen, M. S.; Reichman, D. R.; Gao, J.; Zhu, X. Y. The Quantum Coherent Mechanism for Singlet Fission: Experiment and Theory. *Acc. Chem. Res.* **2013**, *46* (6), 1321–1329.
- (22) Lee, J.; Jadhav, P.; Reusswig, P. D.; Yost, S. R.; Thompson, N. J.; Congreve, D. N.; Hontz, E.; Van Voorhis, T.; Baldo, M. a. Singlet Exciton Fission Photovoltaics. *Acc. Chem. Res.* **2013**, *46* (6), 1300–1311.
- (23) Wilson, M. W. B.; Rao, A.; Ehrler, B.; Friend, R. H. Singlet Exciton Fission in Polycrystalline Pentacene: From Photophysics toward Devices. *Acc. Chem. Res.* **2013**, *46* (6), 1330–1338.
- (24) Piland, G. B.; Burdett, J. J.; Dillon, R. J.; Bardeen, C. J. Singlet Fission: From Coherences to Kinetics. *J. Phys. Chem. Lett.* **2014**, *5* (13), 2312–2319.
- (25) Chenu, A.; Scholes, G. D. Coherence in Energy Transfer and Photosynthesis. *Annu. Rev. Phys. Chem.* **2015**, *66* (1), 69–96.
- (26) Spano, F. C.; Clark, J.; Silva, C.; Friend, R. H. Determining Exciton Coherence from the Photoluminescence Spectral Line Shape in poly(3-Hexylthiophene) Thin Films. *J. Chem. Phys.* **2009**, *130* (7), 074904.
- (27) Pingel, P.; Zen, A.; Abellón, R. D.; Grozema, F. C.; Siebbeles, L. D. a; Neher, D. Temperature-Resolved Local and Macroscopic Charge Carrier Transport in Thin P3HT Layers. *Adv. Funct. Mater.* **2010**, *20* (14), 2286–2295.
- (28) Platt, A.; Kendrick, M.; Loth, M.; Anthony, J.; Ostroverkhova, O. Temperature Dependence of Exciton and Charge Carrier Dynamics in Organic Thin Films. *Phys. Rev. B: Condens. Matter Mater. Phys.* **2011**, *84* (23), 235209.
- (29) Graus, M.; Grimm, M.; Metzger, C.; Dauth, M.; Tusche, C.; Kirschner, J.; Kummel, S.; Scholl, A.; Reinert, F. Electron-Vibration Coupling in Molecular Materials: Assignment of Vibronic Modes from Photoelectron Momentum Mapping. *Phys. Rev. Lett.* **2016**, *116* (14), 147601.
- (30) Hoffmann, S. T.; Bäessler, H.; Köhler, A. What Determines Inhomogeneous Broadening of Electronic Transitions in Conjugated Polymers? *J. Phys. Chem. B* **2010**, *114* (51), 17037–17048.
- (31) Panzer, F.; Sommer, M.; Bäessler, H.; Thelakktat, M.; Köhler, A. Spectroscopic Signature of Two Distinct H-Aggregate Species in Poly(3-Hexylthiophene). *Macromolecules* **2015**, *48*, 1543–1553.
- (32) Gigli, G.; Della Sala, F.; Lomascolo, M.; Anni, M.; Barbarella, G.; Di Carlo, a.; Lugli, P.; Cingolani, R. Photoluminescence Efficiency of Substituted Quaterthiophene Crystals. *Phys. Rev. Lett.* **2001**, *86* (1), 167–170.
- (33) Luo, Y.; Aziz, H.; Klenkler, R.; Xu, G.; Popovic, Z. D. Temperature Dependence of Photoluminescence Efficiency in Doped and Blended Organic Thin Films. *Chem. Phys. Lett.* **2008**, *458* (4–6), 319–322.
- (34) Lim, S. H.; Bjorklund, T. G.; Spano, F. C.; Bardeen, C. J. Exciton Delocalization and Superradiance in Tetracene Thin Films and Nanoaggregates. *Phys. Rev. Lett.* **2004**, *92* (10), 107402.
- (35) Shepherd, W. E. B.; Grollman, R.; Robertson, a.; Paudel, K.; Hallani, R.; Loth, M. a.; Anthony, J. E.; Ostroverkhova, O. Single-Molecule Imaging of Organic Semiconductors: Toward Nanoscale Insights into Photophysics and Molecular Packing. *Chem. Phys. Lett.* **2015**, *629*, 29–35.
- (36) Platt, A. D.; Day, J.; Subramanian, S.; Anthony, J. E.; Ostroverkhova, O. Optical, Fluorescent, and (photo)conductive Properties of High-Performance Functionalized Pentacene and Anthradithiophene Derivatives. *J. Phys. Chem. C* **2009**, *113* (31), 14006–14014.
- (37) Kendrick, M. J.; Neunzert, a.; Payne, M. M.; Purushothaman, B.; Rose, B. D.; Anthony, J. E.; Haley, M. M.; Ostroverkhova, O. Formation of the Donor-Acceptor Charge-Transfer Exciton and Its Contribution to Charge Photogeneration and Recombination in Small-Molecule Bulk Heterojunctions. *J. Phys. Chem. C* **2012**, *116* (34), 18108–18116.
- (38) Chase, D. T.; Rose, B. D.; McClintock, S. P.; Zakharov, L. N.; Haley, M. M. Indeno[1,2-B]fluorenes: Fully Conjugated Antiaromatic Analogues of Acenes. *Angew. Chem., Int. Ed.* **2011**, *50* (5), 1127–1130.
- (39) Brinkmann, M.; Graff, S.; Straupe, C.; Wittmann, J. C.; Chaumont, C.; Nuesch, F.; Aziz, a; Schaer, M.; Zuppiroli, L. Orienting Tetracene and Pentacene Thin Films onto Friction-Transferred Poly(tetrafluoroethylene) Substrate. *J. Phys. Chem. B* **2003**, *107* (38), 10531–10539.
- (40) Ostroverkhova, O.; Shcherbyna, S.; Cooke, D. G.; Egerton, R. F.; Hegmann, F. A.; Tykwinski, R. R.; Parkin, S. R.; Anthony, J. E. Optical and Transient Photoconductive Properties of Pentacene and Functionalized Pentacene Thin Films: Dependence on Film Morphology. *J. Appl. Phys.* **2005**, *98* (3), 033701.
- (41) Yamagata, H.; Norton, J.; Hontz, E.; Olivier, Y.; Beljonne, D.; Brédas, J. L.; Silbey, R. J.; Spano, F. C. The Nature of Singlet Excitons in Oligoacene Molecular Crystals. *J. Chem. Phys.* **2011**, *134* (20), 204703.
- (42) Barford, W. Exciton Transfer Integrals between Polymer Chains. *J. Chem. Phys.* **2007**, *126* (13), 134905.
- (43) Cornil, J. Influence of Interchain Interactions in the Absorption and Luminescence of Conjugated Oligomers and Polymers: A Quantum-Chemical Characterization. *J. Am. Chem. Soc.* **1998**, *120* (6), 1289–1299.
- (44) Gierschner, J.; Huang, Y.-S.; Van Aeverbeke, B.; Cornil, J.; Friend, R. H.; Beljonne, D. Excitonic versus Electronic Couplings in

Molecular Assemblies: The Importance of Non-Nearest Neighbor Interactions. *J. Chem. Phys.* **2009**, *130* (4), 044105.

(45) Clark, J.; Chang, J. F.; Spano, F. C.; Friend, R. H.; Silva, C. Determining Exciton Bandwidth and Film Microstructure in Polythiophene Films Using Linear Absorption Spectroscopy. *Appl. Phys. Lett.* **2009**, *94* (16), 163306.

(46) Hestand, N. J.; Yamagata, H.; Xu, B.; Sun, D.; Zhong, Y.; Harutyunyan, A. R.; Chen, G.; Dai, H.; Rao, Y.; Spano, F. C. Polarized Absorption in Crystalline Pentacene: Theory vs Experiment. *J. Phys. Chem. C* **2015**, *119*, 22137–22147.

(47) Spano, F. C. Modeling Disorder in Polymer Aggregates: The Optical Spectroscopy of Regioregular poly(3-Hexylthiophene) Thin Films. *J. Chem. Phys.* **2005**, *122* (23), 234701.

(48) Haedler, A. T.; Kreger, K.; Issac, A.; Wittmann, B.; Kivala, M.; Hammer, N.; Köhler, J.; Schmidt, H.-W.; Hildner, R. Long-Range Energy Transport in Single Supramolecular Nanofibres at Room Temperature. *Nature* **2015**, *523* (7559), 196–199.

(49) Wang, T.; Chan, W. L. Dynamical Localization Limiting the Coherent Transport Range of Excitons in Organic Crystals. *J. Phys. Chem. Lett.* **2014**, *5* (11), 1812–1818.

(50) Aragó, J.; Troisi, A. Dynamics of the Excitonic Coupling in Organic Crystals. *Phys. Rev. Lett.* **2015**, *114*, 026402.

(51) Ortmann, F.; Bechstedt, F.; Hannewald, K. Charge Transport in Organic Crystals: Theory and Modelling. *Phys. Status Solidi B* **2011**, *248* (3), 511–525.

(52) Picon, J. D.; Bussac, M. N.; Zuppiroli, L. Quantum Coherence and Carriers Mobility in Organic Semiconductors. *Phys. Rev. B: Condens. Matter Mater. Phys.* **2007**, *75* (23), 235106.

(53) Bittner, E. R.; Silva, C. Noise-Induced Quantum Coherence Drives Photo-Carrier Generation Dynamics at Polymeric Semiconductor Heterojunctions. *Nat. Commun.* **2014**, *5*, 3119.

(54) Yao, Y. Spin-Boson Theory for Charge Photogeneration in Organic Molecules: Role of Quantum Coherence. *Phys. Rev. B: Condens. Matter Mater. Phys.* **2015**, *91*, 045421.

(55) Tempelaar, R.; Spano, F. C.; Knoester, J.; Jansen, T. L. C. Mapping the Evolution of Spatial Exciton Coherence through Time-Resolved Fluorescence. *J. Phys. Chem. Lett.* **2014**, *5* (9), 1505–1510.

(56) Kaake, L. G.; Moses, D.; Heeger, A. J. Coherence and Uncertainty in Nanostructured Organic Photovoltaics. *J. Phys. Chem. Lett.* **2013**, *4* (14), 2264–2268.

(57) Ginsberg, N. S.; Cheng, Y.-C.; Fleming, G. R. Two-Dimensional Electronic Spectroscopy of Molecular Aggregates. *Acc. Chem. Res.* **2009**, *42* (9), 1352–1363.

(58) Bakulin, A. a.; Morgan, S. E.; Kehoe, T. B.; Wilson, M. W. B.; Chin, A. W.; Zigmantas, D.; Egorova, D.; Rao, A. Real-Time Observation of Multiexcitonic States in Ultrafast Singlet Fission Using Coherent 2D Electronic Spectroscopy. *Nat. Chem.* **2016**, *8*, 16–23.

(59) Falke, S. M.; Rozzi, C. A.; Brida, D.; Maiuri, M.; Amato, M.; Sommer, E.; De Sio, A.; Rubio, A.; Cerullo, G.; Molinari, E.; et al. Coherent Ultrafast Charge Transfer in an Organic Photovoltaic Blend. *Science (Washington, DC, U. S.)* **2014**, *344* (6187), 1001–1005.

(60) Chan, W.-L.; Ligges, M.; Zhu, X.-Y. The Energy Barrier in Singlet Fission Can Be Overcome through Coherent Coupling and Entropic Gain. *Nat. Chem.* **2012**, *4* (10), 840–845.

(61) Buchleitner, A.; Burghardt, I.; Cheng, Y.-C.; Scholes, G. D.; Schwarz, U. T.; Weber-Bargioni, A.; Wellens, T. Focus on Quantum Efficiency. *New J. Phys.* **2014**, *16* (10), 105021.

(62) Mukamel, S. Comment on “Coherence and Uncertainty in Nanostructured Organic Photovoltaics. *J. Phys. Chem. A* **2013**, *117*, 10563–10564.

(63) Wiesenhofer, H.; Beljonne, D.; Scholes, G. D.; Hennebicq, E.; Brédas, J. L.; Zojer, E. Limitations of the Förster Description of Singlet Exciton Migration: The Illustrative Example of Energy Transfer to Ketonic Defects in Ladder-Type Poly(para-Phenylenes). *Adv. Funct. Mater.* **2005**, *15* (1), 155–160.

(64) Hossein-Nejad, H.; Olaya-Castro, A.; Scholes, G. D. Phonon-Mediated Path-Interference in Electronic Energy Transfer. *J. Chem. Phys.* **2012**, *136* (2), 024112.

(65) Jumper, C. C.; Anna, J. M.; Stradomska, A.; Schins, J.; Myahkostupov, M.; Prusakova, V.; Oblinsky, D. G.; Castellano, F. N.; Knoester, J.; Scholes, G. D. Intramolecular Radiationless Transitions Dominate Exciton Relaxation Dynamics. *Chem. Phys. Lett.* **2014**, *599*, 23–33.

(66) Hildner, R.; Brinks, D.; van Hulst, N. F. Femtosecond Coherence and Quantum Control of Single Molecules at Room Temperature. *Nat. Phys.* **2011**, *7* (2), 172–177.

(67) Engel, G. S.; Calhoun, T. R.; Read, E. L.; Ahn, T.-K.; Mancal, T.; Cheng, Y.-C.; Blankenship, R. E.; Fleming, G. R. Evidence for Wavelike Energy Transfer through Quantum Coherence in Photosynthetic Systems. *Nature* **2007**, *446* (7137), 782–786.

(68) Hildner, R.; Brinks, D.; Nieder, J. B.; Cogdell, R. J.; van Hulst, N. F. Quantum Coherent Energy Transfer over Varying Pathways in Single Light-Harvesting Complexes. *Science (Washington, DC, U. S.)* **2013**, *340* (6139), 1448–1451.

(69) Fassioli, F.; Dinshaw, R.; Arpin, P. C.; Scholes, G. D. Photosynthetic Light Harvesting: Excitons and Coherence. *J. R. Soc., Interface* **2014**, *11*, 20130901.

(70) Scholes, G. D.; Smyth, C. Perspective: Detecting and Measuring Exciton Delocalization in Photosynthetic Light Harvesting. *J. Chem. Phys.* **2014**, *140* (11), 110901.

(71) Miller, W. H. Perspective: Quantum or Classical Coherence. *J. Chem. Phys.* **2012**, *136* (21), 210901.

(72) Bernardo, B.; Cheyns, D.; Verreert, B.; Schaller, R. D.; Rand, B. P.; Giebink, N. C. Delocalization and Dielectric Screening of Charge Transfer States in Organic Photovoltaic Cells. *Nat. Commun.* **2014**, *5*, 3245.

(73) Bakulin, A.; Rao, A.; Pavelyev, V. G.; van Loosdrecht, P. H. M.; Pshenichnikov, M. S.; Niedzialek, D.; Cornil, J.; Beljonne, D.; Friend, R. H. The Role of Driving Energy and Delocalized States for Charge Separation in Organic Semiconductors. *Science (Washington, DC, U. S.)* **2012**, *335* (6074), 1340–1344.

(74) Aryanpour, K.; Sheng, C. X.; Olejnik, E.; Pandit, B.; Psiachos, D.; Mazumdar, S.; Vardeny, Z. V. Evidence for Excimer Photoexcitations in an Ordered Pi-Conjugated Polymer Film. *Phys. Rev. B: Condens. Matter Mater. Phys.* **2011**, *83* (15), 155124.

(75) Stangl, T.; Wilhelm, P.; Schmitz, D.; Remmersen, K.; Henzel, S.; Jester, S.-S.; Höger, S.; Vogelsang, J.; Lupton, J. M. Temporal Fluctuations in Excimer-Like Interactions between  $\pi$ -Conjugated Chromophores. *J. Phys. Chem. Lett.* **2015**, *6*, 1321–1326.

(76) Walker, B. J.; Musser, A. J.; Beljonne, D.; Friend, R. H. Singlet Exciton Fission in Solution. *Nat. Chem.* **2013**, *5* (12), 1019–1024.

(77) Marciniak, H.; Fiebig, M.; Huth, M.; Schiefer, S.; Nickel, B.; Selmaier, F.; Lochbrunner, S. Ultrafast Exciton Relaxation in Microcrystalline Pentacene Films. *Phys. Rev. Lett.* **2007**, *99* (17), 176402.

(78) Yamagata, H.; Maxwell, D. S.; Fan, J.; Kittilstved, K. R.; Briseno, A. L.; Barnes, M. D.; Spano, F. C. Introducing a New Design Paradigm for Organic Materials. *J. Phys. Chem. C* **2014**, *118*, 28842–28854.

(79) Pac, B.; Petelenz, P. Lowest Singlet Exciton in Pentacene: Modern Calculations versus Classic Experiments. *ChemPhysChem* **2014**, *15* (13), 2801–2809.

(80) Beljonne, D.; Yamagata, H.; Brédas, J. L.; Spano, F. C.; Olivier, Y. Charge-Transfer Excitations Steer the Davydov Splitting and Mediate Singlet Exciton Fission in Pentacene. *Phys. Rev. Lett.* **2013**, *110* (22), 226402.

(81) Hestand, N. J.; Tempelaar, R.; Knoester, J.; Jansen, T. L. C.; Spano, F. C. Exciton Mobility Control through Sub-A Packing Modifications in Molecular Crystals. *Phys. Rev. B: Condens. Matter Mater. Phys.* **2015**, *91*, 195315.

(82) Sai, N.; Tiago, M. L.; Chelikowsky, J. R.; Reboledo, F. a. Optical Spectra and Exchange-Correlation Effects in Molecular Crystals. *Phys. Rev. B: Condens. Matter Mater. Phys.* **2008**, *77*, 161306.

(83) Fujita, T.; Atahan-Evrenk, S.; Sawaya, N. P. D.; Aspuru-Guzik, A. Coherent Dynamics of Mixed Frenkel and Charge-Transfer Excitons in Dinaphtho[2,3-b:2'3'-f]thieno[3,2-B]-Thiophene Thin Films: The Importance of Hole Delocalization. *J. Phys. Chem. Lett.* **2016**, *7*, 1374–1380.

- (84) Qj, D.; Su, H.; Bastjan, M.; Jurchescu, O. D.; Palstra, T. M.; Wee, A. T. S.; Rübhausen, M.; Ruydy, A. Observation of Frenkel and Charge Transfer Excitons in Pentacene Single Crystals Using Spectroscopic Generalized Ellipsometry. *Appl. Phys. Lett.* **2013**, *103* (11), 113303.
- (85) Haas, S.; Matsui, H.; Hasegawa, T. Field-Modulation Spectroscopy of Pentacene Thin Films Using Field-Effect Devices: Reconsideration of the Excitonic Structure. *Phys. Rev. B: Condens. Matter Mater. Phys.* **2010**, *82*, 161301.
- (86) Ishino, Y.; Miyata, K.; Sugimoto, T.; Watanabe, K.; Matsumoto, Y.; Uemura, T.; Takeya, J. Ultrafast Exciton Dynamics in dinaphtho-[2,3-b:2'3'-f]thieno[3,2-B]-Thiophene Thin Films. *Phys. Chem. Chem. Phys.* **2014**, *16* (16), 7501–7512.
- (87) Yamagata, H.; Maxwell, D. S.; Fan, J.; Kittilstved, K. R.; Briseno, A. L.; Barnes, M. D.; Spano, F. C. HJ-Aggregate Behaviour of Crystalline 7,8,15,16-Tetraazaterylene: Introducing a New Design Paradigm for Organic Materials. *J. Phys. Chem. C* **2014**, *118*, 28842–28854.
- (88) Yamagata, H.; Spano, F. C. Interplay between Intrachain and Interchain Interactions in Semiconducting Polymer Assemblies: The HJ-Aggregate Model. *J. Chem. Phys.* **2012**, *136* (18), 184901.
- (89) Spano, F. C. The Spectral Signatures of Frenkel Polarons in H-And J-Aggregates. *Acc. Chem. Res.* **2010**, *43* (3), 429–439.
- (90) Gierschner, J.; Park, S. Y. Luminescent Distyrylbenzenes: Tailoring Molecular Structure and Crystalline Morphology. *J. Mater. Chem. C* **2013**, *1* (37), 5818.
- (91) Spano, F. C.; Silva, C. H- and J-Aggregate Behavior in Polymeric Semiconductors. *Annu. Rev. Phys. Chem.* **2014**, *65*, 477–500.
- (92) Spano, F. C. Absorption and Emission in Oligo-Phenylene Vinylene Nanoaggregates: The Role of Disorder and Structural Defects. *J. Chem. Phys.* **2002**, *116* (13), 5877–5891.
- (93) Varghese, S.; Park, S. K.; Casado, S.; Fischer, R. C.; Resel, R.; Milián-Medina, B.; Wannemacher, R.; Park, S. Y.; Gierschner, J. Stimulated Emission Properties of Sterically Modified Distyrylbenzene-Based H-Aggregate Single Crystals. *J. Phys. Chem. Lett.* **2013**, *4* (10), 1597–1602.
- (94) Meskers, S. C. J.; Janssen, R. A. J.; Haverkort, J. E. M.; Wolter, J. H. Relaxation of Photo-Excitations in Films of Oligo- and Poly(paraphenylene Vinylene) Derivatives. *Chem. Phys.* **2000**, *260* (3), 415–439.
- (95) Spano, F. Temperature dependence exciton emission from herringbone aggregates of conjugated polymers. *J. Chem. Phys.* **2004**, *120* (16), 7643–7658.
- (96) Kistler, K. a.; Pochas, C. M.; Yamagata, H.; Matsika, S.; Spano, F. C. Absorption, Circular Dichroism, and Photoluminescence in Perylene Diimide Bichromophores: Polarization-Dependent H- and J-Aggregate Behavior. *J. Phys. Chem. B* **2012**, *116* (1), 77–86.
- (97) Paquin, F.; Yamagata, H.; Hestand, N. J.; Sakowicz, M.; Bérubé, N.; Côté, M.; Reynolds, L. X.; Haque, S. a.; Stingelin, N.; Spano, F. C.; et al. Two-Dimensional Spatial Coherence of Excitons in Semicrystalline Polymeric Semiconductors: Effect of Molecular Weight. *Phys. Rev. B: Condens. Matter Mater. Phys.* **2013**, *88* (15), 155202.
- (98) Spano, F. C.; Silvestri, L. Multiple Mode Exciton-Vibrational Coupling in H-Aggregates: Synergistic Enhancement of the Quantum Yield. *J. Chem. Phys.* **2010**, *132* (9), 094704.
- (99) Piaggi, A.; Lanzani, G.; Bongiovanni, G.; Mura, A.; Graupner, W.; Meghdadi, F.; Leising, G.; Nisoli, M. Emission Properties of Para-Hexaphenyl Polycrystalline Films. *Phys. Rev. B: Condens. Matter Mater. Phys.* **1997**, *56* (16), 10133–10137.
- (100) Kim, K. H.; Bae, S. Y.; Kim, Y. S.; Hur, J. a.; Hoang, M. H.; Lee, T. W.; Cho, M. J.; Kim, Y.; Kim, M.; Jin, J., II; et al. Highly Photosensitive J-Aggregated Single-Crystalline Organic Transistors. *Adv. Mater.* **2011**, *23* (27), 3095–3099.
- (101) Kaiser, T. E.; Scheblykin, I. G.; Thomsson, D.; Würthner, F. Temperature-Dependent Exciton Dynamics in J-Aggregates-When Disorder Plays a Role. *J. Phys. Chem. B* **2009**, *113* (48), 15836–15842.
- (102) Würthner, F.; Kaiser, T. E.; Saha-Möller, C. R. J-Aggregates: From Serendipitous Discovery to Supramolecular Engineering of Functional Dye Materials. *Angew. Chem., Int. Ed.* **2011**, *50* (15), 3376–3410.
- (103) Niles, E. T.; Roehling, J. D.; Yamagata, H.; Wise, A. J.; Spano, F. C.; Moule, A. J.; Grey, J. K. J-Aggregate Behavior in Poly-3-Hexylthiophene Nanofibers. *J. Phys. Chem. Lett.* **2012**, *3*, 259–263.
- (104) Yamagata, H.; Spano, F. C. Strong Photophysical Similarities between Conjugated Polymers and J-Aggregates. *J. Phys. Chem. Lett.* **2014**, *5* (3), 622–632.
- (105) Sung, J.; Kim, P.; Fimmel, B.; Wu, F.; Kim, D. Direct Observation of Ultrafast Coherent Exciton Dynamics in Helical  $\pi$ -Stacks of Self-Assembled Perylene Bisimides. *Nat. Commun.* **2015**, *6*, 8646.
- (106) Kang, J. H.; Da Silva Filho, D.; Bredas, J. L.; Zhu, X. Y. Shallow Trap States in Pentacene Thin Films from Molecular Sliding. *Appl. Phys. Lett.* **2005**, *86* (15), 152115.
- (107) Eggeman, A. S.; Illig, S.; Troisi, A.; Siringhaus, H.; Midgley, P. a. Measurement of Molecular Motion in Organic Semiconductors by Thermal Diffuse Electron Scattering. *Nat. Mater.* **2013**, *12* (11), 1045–1049.
- (108) Shepherd, W. E. B.; Platt, A. D.; Hofer, D.; Ostroverkhova, O.; Loth, M.; Anthony, J. E. Aggregate Formation and Its Effect on (opto)electronic Properties of Guest-Host Organic Semiconductors. *Appl. Phys. Lett.* **2010**, *97* (16), 163303.
- (109) Rawat, N.; Pan, Z.; Manning, L. W.; Lamarche, C. J.; Cour, I.; Headrick, R. L.; Waterman, R.; Woll, A. R.; Furis, M. I. Macroscopic Molecular Ordering and Exciton Delocalization in Crystalline Phthalocyanine Thin Films. *J. Phys. Chem. Lett.* **2015**, *6*, 1834–1840.
- (110) Spano, F. C. Optical Microcavities Enhance the Exciton Coherence Length and Eliminate Vibronic Coupling in J-Aggregates. *J. Chem. Phys.* **2015**, *142* (18), 184707.
- (111) Swathi, R. S.; Sebastian, K. L. Resonance Energy Transfer from a Dye Molecule to Graphene. *J. Chem. Phys.* **2008**, *129* (5), 054703.
- (112) Swathi, R. S.; Sebastian, K. L. Long Range Resonance Energy Transfer from a Dye Molecule to Graphene Has (distance)<sup>-4</sup> Dependence. *J. Chem. Phys.* **2009**, *130* (8), 086101.
- (113) Köhler, A.; Bäessler, H. What Controls Triplet Exciton Transfer in Organic Semiconductors? *J. Mater. Chem.* **2011**, *21* (12), 4003.
- (114) Shepherd, W. E. B.; Platt, A. D.; Kendrick, M. J.; Loth, M. a.; Anthony, J. E.; Ostroverkhova, O. Energy Transfer and Exciplex Formation and Their Impact on Exciton and Charge Carrier Dynamics in Organic Films. *J. Phys. Chem. Lett.* **2011**, *2* (5), 362–366.
- (115) Bakulin, A. a.; Dimitrov, S. D.; Rao, A.; Chow, P. C. Y.; Nielsen, C. B.; Schroeder, B. C.; McCulloch, I.; Bakker, H. J.; Durrant, J. R.; Friend, R. H. Charge-Transfer State Dynamics Following Hole and Electron Transfer in Organic Photovoltaic Devices. *J. Phys. Chem. Lett.* **2013**, *4* (1), 209–215.
- (116) Brédas, J.-L.; Beljonne, D.; Coropceanu, V.; Cornil, J. Charge-Transfer and Energy-Transfer Processes in Pi-Conjugated Oligomers and Polymers: A Molecular Picture. *Chem. Rev.* **2004**, *104* (11), 4971–5003.
- (117) Zhao, Y.; Liang, W. Charge Transfer in Organic Molecules for Solar Cells: Theoretical Perspective. *Chem. Soc. Rev.* **2012**, *41* (3), 1075–1087.
- (118) Baranovskii, S. D. Theoretical Description of Charge Transport in Disordered Organic Semiconductors. *Phys. Status Solidi B* **2014**, *251* (3), 487–525.
- (119) Lee, C.; Park, S.; Yang, M.; Lee, N.; Kim, N. Correlation between concentration and disorder of doped trap molecules in space charge field formation. *Chem. Phys. Lett.* **2006**, *422*, 106–110.
- (120) Johnson, B.; Kendrick, M. J.; Ostroverkhova, O. Charge Carrier Dynamics in Organic Semiconductors and Their Donor-Acceptor Composites: Numerical Modeling of Time-Resolved Photo-current. *J. Appl. Phys.* **2013**, *114* (9), 094508.
- (121) Athanasopoulos, S.; Hoffmann, S. T.; Bäessler, H.; Köhler, A.; Beljonne, D. To Hop or Not to Hop? Understanding the Temperature Dependence of Spectral Diffusion in Organic Semiconductors. *J. Phys. Chem. Lett.* **2013**, *4* (10), 1694–1700.
- (122) Jiang, Y.; Zhong, X.; Shi, W.; Peng, Q.; Geng, H.; Zhao, Y.; Shuai, Z. Nuclear Quantum Tunneling and Carrier Delocalization

Effects to Bridge the Gap between Hopping and Bandlike Behaviors in Organic Semiconductors. *Nanoscale Horiz.* **2016**, *1* (2), 53–59.

(123) Van Der Kaap, N. J.; Katsouras, I.; Asadi, K.; Blom, P. W. M.; Koster, L. J. A.; De Leeuw, D. M. Charge Transport in Disordered Semiconducting Polymers Driven by Nuclear Tunneling. *Phys. Rev. B: Condens. Matter Mater. Phys.* **2016**, *93* (14), 140206.

(124) Pelzer, K. M.; Fidler, A. F.; Griffin, G. B.; Gray, S. K.; Engel, G. S. The Dependence of Exciton Transport Efficiency on Spatial Patterns of Correlation within the Spectral Bath. *New J. Phys.* **2013**, *15*, 095019.

(125) Moix, J. M.; Khasin, M.; Cao, J. Coherent Quantum Transport in Disordered Systems: I. the Influence of Dephasing on the Transport Properties and Absorption Spectra on One-Dimensional Systems. *New J. Phys.* **2013**, *15*, 085010.

(126) Kozlov, O. V.; De Haan, F.; Kerner, R. A.; Rand, B. P.; Cheyns, D.; Pshenichnikov, M. S. Real-Time Tracking of Singlet Exciton Diffusion in Organic Semiconductors. *Phys. Rev. Lett.* **2016**, *116* (5), 057402.

(127) Najafov, H.; Lee, B.; Zhou, Q.; Feldman, L. C.; Podzorov, V. Observation of Long-Range Exciton Diffusion in Highly Ordered Organic Semiconductors. *Nat. Mater.* **2010**, *9* (11), 938–943.

(128) Irkhin, P.; Biaggio, I. Direct Imaging of Anisotropic Exciton Diffusion and Triplet Diffusion Length in Rubrene Single Crystals. *Phys. Rev. Lett.* **2011**, *107* (1), 017402.

(129) Stehr, V.; Engels, B.; Deibel, C.; Fink, R. F. Anisotropy of Singlet Exciton Diffusion in Organic Semiconductor Crystals from Ab Initio Approaches. *J. Chem. Phys.* **2014**, *140* (2), 024503.

(130) Ward, K. a.; Richman, B. R.; Biaggio, I. Nanosecond Pump and Probe Observation of Bimolecular Exciton Effects in Rubrene Single Crystals. *Appl. Phys. Lett.* **2015**, *106* (22), 223302.

(131) Lin, J. D. a.; Mikhnenko, O. V.; Chen, J.; Masri, Z.; Ruseckas, A.; Mikhailovsky, A.; Raab, R. P.; Liu, J.; Blom, P. W. M.; Loi, M. A.; et al. Systematic Study of Exciton Diffusion Length in Organic Semiconductors by Six Experimental Methods. *Mater. Horiz.* **2014**, *1* (2), 280.

(132) Mikhnenko, O. V.; Kuik, M.; Lin, J.; Van Der Kaap, N.; Nguyen, T. Q.; Blom, P. W. M. Trap-Limited Exciton Diffusion in Organic Semiconductors. *Adv. Mater.* **2014**, *26* (12), 1912–1917.

(133) Markov, D. E.; Tanase, C.; Blom, P. W. M.; Wildeman, J. Simultaneous Enhancement of Charge Transport and Exciton Diffusion in Poly(p-Phenylene Vinylene) Derivatives. *Phys. Rev. B: Condens. Matter Mater. Phys.* **2005**, *72* (4), 045217.

(134) Yang, J.; Zhu, F.; Yu, B.; Wang, H.; Yan, D. Simultaneous Enhancement of Charge Transport and Exciton Diffusion in Single-Crystal-like Organic Semiconductors. *Appl. Phys. Lett.* **2012**, *100* (10), 103305.

(135) Shen, Y.; Giebink, N. C. Monte Carlo Simulations of Nanoscale Electrical Inhomogeneity in Organic Light-Emitting Diodes and Its Impact on Their Efficiency and Lifetime. *Phys. Rev. Appl.* **2015**, *4*, 054017.

(136) Verreet, B.; Bhoolakam, A.; Brigeman, A.; Dhanker, R.; Cheyns, D.; Heremans, P.; Stesmans, A.; Giebink, N. C.; Rand, B. P. Reducing Exciton-Polaron Annihilation in Organic Planar Heterojunction Solar Cells. *Phys. Rev. B: Condens. Matter Mater. Phys.* **2014**, *90*, 115304.

(137) Deotare, P.; Chang, W.; Hontz, E.; Congreve, D.; Shi, L.; Reusswig, P.; Modtland, B.; Bahlke, M.; Lee, C.; Willard, V.; et al. Nanoscale Transport of Charge Transfer States in Organic Donor-Acceptor Blends. *Nat. Mater.* **2015**, *14*, 1130–1134.

(138) Chan, W.-L.; Ligges, M.; Jailaubekov, a.; Kaake, L.; Miaja-Avila, L.; Zhu, X.-Y. Observing the Multiexciton State in Singlet Fission and Ensuing Ultrafast Multielectron Transfer. *Science (Washington, DC, U. S.)* **2011**, *334* (6062), 1541–1545.

(139) Berkelbach, T. C.; Hybertsen, M. S.; Reichman, D. R. Microscopic Theory of Singlet Exciton Fission. II. Application to Pentacene Dimers and the Role of Superexchange. *J. Chem. Phys.* **2013**, *138* (11), 114103.

(140) Tao, G. Electronically Nonadiabatic Dynamics in Singlet Fission: A Quasi-Classical Trajectory Simulation. *J. Phys. Chem. C* **2014**, *118* (31), 17299–17305.

(141) Mirjani, F.; Renaud, N.; Gorczak, N.; Grozema, F. C. Theoretical Investigation of Singlet Fission in Molecular Dimers: The Role of Charge Transfer States and Quantum Interference. *J. Phys. Chem. C* **2014**, *118*, 14192–14199.

(142) Renaud, N.; Grozema, F. C. Intermolecular Vibrational Modes Speed Up Singlet Fission in Peryleneimide Crystals. *J. Phys. Chem. Lett.* **2015**, *6* (3), 360–365.

(143) Aryanpour, K.; Shukla, A.; Mazumdar, S. Theory of Singlet Fission in Polyenes, Acene Crystals, and Covalently Linked Acene Dimers. *J. Phys. Chem. C* **2015**, *119*, 6966–6979.

(144) Berkelbach, T. C.; Hybertsen, M. S.; Reichman, D. R. Microscopic Theory of Singlet Exciton Fission. III. Crystalline Pentacene. *J. Chem. Phys.* **2014**, *141* (7), 074705.

(145) Ramanan, C.; Smeigh, A. L.; Anthony, J. E.; Marks, T. J.; Wasielewski, M. R. Competition between Singlet Fission and Charge Separation in Solution-Processed Blend Films of 6,13-Bis-(triisopropylsilylethynyl)-Pentacene with Sterically-Encumbered Perylene-3,4:9,10-Bis(dicarboximide)s. *J. Am. Chem. Soc.* **2012**, *134*, 386–397.

(146) Herz, J.; Buckup, T.; Paulus, F.; Engelhart, J.; Bunz, U. H. F.; Motzkus, M. Acceleration of Singlet Fission in an Aza-Derivative of TIPS-Pentacene. *J. Phys. Chem. Lett.* **2014**, *5* (14), 2425–2430.

(147) Pensack, R. D.; Tilley, A. J.; Parkin, S. R.; Lee, T. S.; Payne, M. M.; Gao, D.; Jahnke, A. A.; Oblinsky, D. G.; Li, P.-F.; Anthony, J. E.; et al. Exciton Delocalization Drives Rapid Singlet Fission in Nanoparticles of Acene Derivatives. *J. Am. Chem. Soc.* **2015**, *137* (21), 6790–6803.

(148) Burdett, J. J.; Bardeen, C. J. Quantum Beats in Crystalline Tetracene Delayed Fluorescence due to Triplet Pair Coherences Produced by Direct Singlet Fission. *J. Am. Chem. Soc.* **2012**, *134* (20), 8597–8607.

(149) Bayliss, S. L.; Chepelienskii, A. D.; Sepe, A.; Walker, B. J.; Ehrler, B.; Bruzek, M. J.; Anthony, J. E.; Greenham, N. C. Geminate and Nongeminate Recombination of Triplet Excitons Formed by Singlet Fission. *Phys. Rev. Lett.* **2014**, *112* (23), 238701.

(150) Zimmerman, P. M.; Bell, F.; Casanova, D.; Head-Gordon, M. Mechanism for Singlet Fission in Pentacene and Tetracene: From Single Exciton to Two Triplets. *J. Am. Chem. Soc.* **2011**, *133* (49), 19944–19952.

(151) Burdett, J. J.; Müller, A. M.; Gosztola, D.; Bardeen, C. J. Excited State Dynamics in Solid and Monomeric Tetracene: The Roles of Superradiance and Exciton Fission. *J. Chem. Phys.* **2010**, *133* (14), 144506.

(152) Piland, G. B.; Bardeen, C. J. How Morphology Affects Singlet Fission in Crystalline Tetracene. *J. Phys. Chem. Lett.* **2015**, *6*, 1841–1846.

(153) Busby, E.; Berkelbach, T. C.; Kumar, B.; Chernikov, A.; Zhong, Y.; Hlaing, H.; Zhu, X.-Y.; Heinz, T. F.; Hybertsen, M. S.; Sfeir, M. Y.; et al. Multiphonon Relaxation Slows Singlet Fission in Crystalline Hexacene. *J. Am. Chem. Soc.* **2014**, *136* (30), 10654–10660.

(154) Lee, J.; Bruzek, M. J.; Thompson, N. J.; Sfeir, M. Y.; Anthony, J. E.; Baldo, M. a. Singlet Exciton Fission in a Hexacene Derivative. *Adv. Mater.* **2013**, *25* (10), 1445–1448.

(155) Thorsmølle, V. K.; Averitt, R. D.; Demsar, J.; Smith, D. L.; Tretiak, S.; Martin, R. L.; Chi, X.; Crone, B. K.; Ramirez, a. P.; Taylor, a. J. Morphology Effectively Controls Singlet-Triplet Exciton Relaxation and Charge Transport in Organic Semiconductors. *Phys. Rev. Lett.* **2009**, *102*, 017401.

(156) Wan, Y.; Guo, Z.; Zhu, T.; Yan, S.; Johnson, J.; Huang, L. Cooperative Singlet and Triplet Exciton Transport in Tetracene Crystals Visualized by Ultrafast Microscopy. *Nat. Chem.* **2015**, *7* (September), 785–792.

(157) Yost, S. R.; Lee, J.; Wilson, M. W. B.; Wu, T.; McMahon, D. P.; Parkhurst, R. R.; Thompson, N. J.; Congreve, D. N.; Rao, A.; Johnson, K.; et al. A Transferable Model for Singlet-Fission Kinetics. *Nat. Chem.* **2014**, *6* (6), 492–497.

- (158) Yao, Y. Coherent Dynamics of Singlet Fission Controlled by Nonlocal Electron-Phonon Coupling. *Phys. Rev. B: Condens. Matter Mater. Phys.* **2016**, *93* (11), 115426.
- (159) Tamura, H.; Huix-Rotllant, M.; Burghardt, I.; Olivier, Y.; Beljonne, D. First-Principles Quantum Dynamics of Singlet Fission: Coherent versus Thermally Activated Mechanisms Governed by Molecular Pi Stacking. *Phys. Rev. Lett.* **2015**, *115* (10), 107401.
- (160) Wang, L.; Olivier, Y.; Prezhdo, O. V.; Beljonne, D. Maximizing Singlet Fission by Intermolecular Packing. *J. Phys. Chem. Lett.* **2014**, *5*, 3345–3353.
- (161) Renaud, N.; Sherratt, P. a.; Ratner, M. a. Mapping the Relation between Stacking Geometries and Singlet Fission Yield in a Class of Organic Crystals. *J. Phys. Chem. Lett.* **2013**, *4* (7), 1065–1069.
- (162) Burdett, J. J.; Bardeen, C. J. The Dynamics of Singlet Fission in Crystalline Tetracene and Covalent Analogs. *Acc. Chem. Res.* **2013**, *46* (6), 1312–1320.
- (163) Trinh, M. T.; Zhong, Y.; Schiros, T.; Chen, Q.; Jockusch, S.; Sfeir, M. Y.; Steigerwald, M.; Nuckolls, C.; Zhu, X. Intra- to Intermolecular Singlet Fission. *J. Phys. Chem. C* **2015**, *119*, 1312–1319.
- (164) Sanders, S. N.; Kumarasamy, E.; Pun, A. B.; Trinh, M. T.; Choi, B.; Xia, J.; Taffet, E. J.; Low, J. Z.; Miller, J. R.; Roy, X.; et al. Quantitative Intramolecular Singlet Fission in Bipentacenes. *J. Am. Chem. Soc.* **2015**, *137*, 8965–8972.
- (165) Varnavski, O.; Abeyasinghe, N.; Aragó, J.; Serrano-Pérez, J. J.; Ortí, E.; López Navarrete, J. T.; Takimiya, K.; Casanova, D.; Casado, J.; Goodson, T. High Yield Ultrafast Intramolecular Singlet Exciton Fission in a Quinoidal Bithiophene. *J. Phys. Chem. Lett.* **2015**, *6*, 1375–1384.
- (166) Musser, A. J.; Al-Hashimi, M.; Maiuri, M.; Brida, D.; Heeney, M.; Cerullo, G.; Friend, R. H.; Clark, J. Activated Singlet Exciton Fission in a Semiconducting Polymer. *J. Am. Chem. Soc.* **2013**, *135* (34), 12747–12754.
- (167) Zhai, Y.; Sheng, C. Singlet Fission of Hot Excitons in  $\pi$ -Conjugated Polymers. *Philos. Trans. R. Soc., A* **2015**, *373*, 20140327.
- (168) Busby, E.; Xia, J.; Wu, Q.; Low, J. Z.; Song, R.; Miller, J. R.; Zhu, X.-Y.; Campos, L. M.; Sfeir, M. Y. A Design Strategy for Intramolecular Singlet Fission Mediated by Charge-Transfer States in Donor-acceptor Organic Materials. *Nat. Mater.* **2015**, *14*, 426–433.
- (169) Sanders, S. N.; Kumarasamy, E.; Pun, A. B.; Appavoo, K.; Steigerwald, M. L.; Campos, L. M.; Sfeir, M. Y. Exciton Correlations in Intramolecular Singlet Fission. *J. Am. Chem. Soc.* **2016**, *138*, 7289.
- (170) Aryanpour, K.; Dutta, T.; Huynh, U.; Vardeny, Z. V.; Mazumdar, S. Theory of Primary Photoexcitations in Donor-Acceptor Copolymers. *Phys. Rev. Lett.* **2015**, *115*, 267401.
- (171) Adachi, C. Third-Generation Organic Electroluminescence Materials. *Jpn. J. Appl. Phys.* **2014**, *53* (6), 060101.
- (172) Nakanotani, H.; Higuchi, T.; Furukawa, T.; Masui, K.; Morimoto, K.; Numata, M.; Tanaka, H.; Sagara, Y.; Yasuda, T.; Adachi, C. High-Efficiency Organic Light-Emitting Diodes with Fluorescent Emitters. *Nat. Commun.* **2014**, *5*, 4016.
- (173) Hirata, S.; Sakai, Y.; Masui, K.; Tanaka, H.; Lee, S. Y.; Nomura, H.; Nakamura, N.; Yasumatsu, M.; Nakanotani, H.; Zhang, Q.; et al. Highly Efficient Blue Electroluminescence Based on Thermally Activated Delayed Fluorescence. *Nat. Mater.* **2015**, *14* (3), 330–336.
- (174) Zhang, Q.; Tsang, D.; Kuwabara, H.; Hatae, Y.; Li, B.; Takahashi, T.; Lee, S. Y.; Yasuda, T.; Adachi, C. Nearly 100% Internal Quantum Efficiency in Undoped Electroluminescent Devices Employing Pure Organic Emitters. *Adv. Mater.* **2015**, *27* (12), 2096–2100.
- (175) Nishide, J.; Nakanotani, H.; Hiraga, Y.; Adachi, C. High-Efficiency White Organic Light-Emitting Diodes Using Thermally Activated Delayed Fluorescence. *Appl. Phys. Lett.* **2014**, *104* (23), 233304.
- (176) Chen, T.; Zheng, L.; Yuan, J.; An, Z.; Chen, R.; Tao, Y.; Li, H.; Xie, X.; Huang, W. Understanding the Control of Singlet-Triplet Splitting for Organic Exciton Manipulating: A Combined Theoretical and Experimental Approach. *Sci. Rep.* **2015**, *5*, 10923.
- (177) Menke, S. M.; Holmes, R. J. Energy-Cascade Organic Photovoltaic Devices Incorporating a Host-Guest Architecture. *ACS Appl. Mater. Interfaces* **2015**, *7* (4), 2912–2918.
- (178) Menke, S. M.; Luhman, W. a.; Holmes, R. J. Tailored Exciton Diffusion in Organic Photovoltaic Cells for Enhanced Power Conversion Efficiency. *Nat. Mater.* **2013**, *12* (2), 152–157.
- (179) Cnops, K.; Rand, B. P.; Cheyns, D.; Verreert, B.; Empl, M. a.; Heremans, P. 8.4% Efficient Fullerene-Free Organic Solar Cells Exploiting Long-Range Exciton Energy Transfer. *Nat. Commun.* **2014**, *5*, 3406.
- (180) Griffith, O. L.; Forrest, S. R. Exciton Management in Organic Photovoltaic Multidonor Energy Cascades. *Nano Lett.* **2014**, *14* (5), 2353–2358.
- (181) Menke, S. M.; Mullenbach, T. K.; Holmes, R. J. Directing Energy Transport in Organic Photovoltaic Cells Using Interfacial Exciton Gates. *ACS Nano* **2015**, *9* (4), 4543–4552.
- (182) Huang, J.-S.; Goh, T.; Li, X.; Sfeir, M. Y.; Bielinski, E. a.; Tomasulo, S.; Lee, M. L.; Hazari, N.; Taylor, A. D. Polymer Bulk Heterojunction Solar Cells Employing Förster Resonance Energy Transfer. *Nat. Photonics* **2013**, *7* (6), 479–485.
- (183) Lloyd, M. T.; Lim, Y. F.; Malliaras, G. G. Two-Step Exciton Dissociation in poly(3-Hexylthiophene)/fullerene Heterojunctions. *Appl. Phys. Lett.* **2008**, *92* (14), 143308.
- (184) Liu, Y.; Summers, M. a.; Edder, C.; Fréchet, J. M. J.; McGehee, M. D. Using Resonance Energy Transfer to Improve Exciton Harvesting in Organic-Inorganic Hybrid Photovoltaic Cells. *Adv. Mater.* **2005**, *17* (24), 2960–2964.
- (185) Lu, L.; Chen, W.; Xu, T.; Yu, L. High-Performance Ternary Blend Polymer Solar Cells Involving Both Energy Transfer and Hole Relay Processes. *Nat. Commun.* **2015**, *6*, 7327.
- (186) Ameri, T.; Khoram, P.; Min, J.; Brabec, C. J. Organic Ternary Solar Cells: A Review. *Adv. Mater.* **2013**, *25* (31), 4245–4266.
- (187) Coffey, D. C.; Ferguson, A. J.; Kopidakis, N.; Rumbles, G. Photovoltaic Charge Generation in Organic Semiconductors Based on Long-Range Energy Transfer. *ACS Nano* **2010**, *4* (9), 5437–5445.
- (188) Rajesh, K. R.; Paudel, K.; Johnson, B.; Hallani, R.; Anthony, J.; Ostroverkhova, O. Design of Organic Ternary Blends and Small-Molecule Bulk Heterojunctions: Photophysical Considerations. *J. Photonics Energy* **2015**, *5* (1), 057208.
- (189) Savoie, B. M.; Dunaisky, S.; Marks, T. J.; Ratner, M. a. The Scope and Limitations of Ternary Blend Organic Photovoltaics. *Adv. Energy Mater.* **2015**, *5* (3), 1400891.
- (190) Lu, L.; Xu, T.; Chen, W.; Landry, E. S.; Yu, L. Ternary Blend Polymer Solar Cells with Enhanced Power Conversion Efficiency. *Nat. Photonics* **2014**, *8*, 716.
- (191) Yang, L.; Yan, L.; You, W. Organic Solar Cells beyond One Pair of Donor-Acceptor: Ternary Blends and More. *J. Phys. Chem. Lett.* **2013**, *4* (11), 1802–1810.
- (192) Huang, T.-Y.; Patra, D.; Hsiao, Y.-S.; Chang, S.-H.; Wu, C.-G.; Ho, K.-C.; Chu, C. W. Efficient Ternary Bulk Heterojunction Solar Cells Based on Small Molecules Only. *J. Mater. Chem. A* **2015**, *3*, 10512–10518.
- (193) Lu, L.; Kelly, M. A.; You, W.; Yu, L. Status and Prospects for Ternary Organic Photovoltaics. *Nat. Photonics* **2015**, *9* (8), 491–500.
- (194) Yan, Y.; Zhao, Y. S. Organic Nanophotonics: From Controllable Assembly of Functional Molecules to Low-Dimensional Materials with Desired Photonic Properties. *Chem. Soc. Rev.* **2014**, *43* (13), 4325–4340.
- (195) Kim, H.; Whang, D. R.; Gierschner, J.; Lee, C. H.; Park, Y. High-Contrast Red – Green – Blue Tricolor Fluorescence Switching in Bicomponent Molecular Film. *Angew. Chem., Int. Ed.* **2015**, *54*, 4330–4333.
- (196) Sariciftci, N. S. *Primary Photoexcitations in Conjugated Polymers: Molecular Exciton Versus Semiconductor Band Model*; World Scientific Publishing Co. Pte. Ltd.: 1997.
- (197) Moses, D.; Dogariu, A.; Heeger, A. Ultrafast Detection of Charged Photocarriers in Conjugated Polymers. *Phys. Rev. B: Condens. Matter Mater. Phys.* **2000**, *61* (14), 9373–9379.
- (198) Hegmann, F. a.; Tykewinski, R. R.; Lui, K. P. H.; Bullock, J. E.; Anthony, J. E. Picosecond Transient Photoconductivity in Functionalized Pentacene Molecular Crystals Probed by Terahertz Pulse Spectroscopy. *Phys. Rev. Lett.* **2002**, *89* (22), 227403.

- (199) Sheng, C. X.; Tong, M.; Singh, S.; Vardeny, Z. V. Experimental Determination of the Charge/neutral Branching Ratio  $\eta$  in the Photoexcitation of  $\pi$ -Conjugated Polymers by Broadband Ultrafast Spectroscopy. *Phys. Rev. B: Condens. Matter Mater. Phys.* **2007**, *75* (8), 085206.
- (200) Yada, H.; Uchida, R.; Sekine, H.; Terashige, T.; Tao, S.; Matsui, Y.; Kida, N.; Fratini, S.; Ciuchi, S.; Okada, Y.; et al. Carrier Dynamics of Rubrene Single-Crystals Revealed by Transient Broadband Terahertz Spectroscopy. *Appl. Phys. Lett.* **2014**, *105* (14), 143302.
- (201) Ostroverkhova, O.; Cooke, D. G.; Shcherbyna, S.; Egerton, R. F.; Hegmann, F. A.; Tykewski, R. R.; Anthony, J. E. Bandlike Transport in Pentacene and Functionalized Pentacene Thin Films Revealed by Subpicosecond Transient Photoconductivity Measurements. *Phys. Rev. B: Condens. Matter Mater. Phys.* **2005**, *71* (3), 035204.
- (202) Thorsmølle, V. K.; Averitt, R. D.; Chi, X.; Hilton, D. J.; Smith, D. L.; Ramirez, a. P.; Taylor, a. J. Ultrafast Conductivity Dynamics in Pentacene Probed Using Terahertz Spectroscopy. *Appl. Phys. Lett.* **2004**, *84* (6), 891–893.
- (203) He, X.; Zhu, G.; Yang, J.; Chang, H.; Meng, Q.; Hongwu, Z.; Zhou, X.; Shi, J.; Gu, L.; Yan, D.; et al. Photogenerated Intrinsic Free Carriers in Small-Molecule Organic Semiconductors Visualized by Ultrafast Spectroscopy. *Sci. Rep.* **2015**, *5*, 17076.
- (204) Singh, S.; Pandit, B.; Basel, T. P.; Li, S.; Laird, D.; Vardeny, Z. V. Two-Step Charge Photogeneration Dynamics in Polymer/fullerene Blends for Photovoltaic Applications. *Phys. Rev. B: Condens. Matter Mater. Phys.* **2012**, *85* (20), 205206.
- (205) Savoie, B. M.; Jackson, N. E.; Chen, L. X.; Marks, T. J.; Ratner, M. A. Mesoscopic Features of Charge Generation in Organic Semiconductors. *Acc. Chem. Res.* **2014**, *47*, 3385–3394.
- (206) Dimitrov, S. D.; Durrant, J. R. Materials Design Considerations for Charge Generation in Organic Solar Cells. *Chem. Mater.* **2014**, *26* (1), 616–630.
- (207) Park, S.; Roy, A.; Beaupre, S.; Cho, S.; Coates, N.; Moon, J.; Moses, D.; Leclerc, M.; Lee, K.; Heeger, A. J. Bulk Heterojunction Solar Cells with Internal Quantum Efficiency Approaching 100%. *Nat. Photonics* **2009**, *3* (4), 297.
- (208) Hains, A. W.; Liang, Z.; Woodhouse, M. a.; Gregg, B. a. Molecular Semiconductors in Organic Photovoltaic Cells. *Chem. Rev.* **2010**, *110* (11), 6689–6735.
- (209) Deibel, C.; Strobel, T.; Dyakonov, V. Role of the Charge Transfer State in Organic Donor-Acceptor Solar Cells. *Adv. Mater.* **2010**, *22* (37), 4097–4111.
- (210) Clarke, T.; Durrant, J. Charge Carrier Photogeneration in Organic Solar Cells. *Chem. Rev.* **2010**, *110*, 6736–6767.
- (211) Gao, F.; Inganäs, O. Charge Generation in Polymer-Fullerene Bulk-Heterojunction Solar Cells. *Phys. Chem. Chem. Phys.* **2014**, *16*, 20291.
- (212) Few, S.; Frost, J. M.; Nelson, J. Models of Charge Pair Generation in Organic Solar Cells. *Phys. Chem. Chem. Phys.* **2015**, *17*, 2311–2325.
- (213) Onsager, L. Initial Recombination of Ions. *Phys. Rev.* **1938**, *54* (8), 554–557.
- (214) Tachiya, M. Breakdown of the Onsager Theory of Geminate Ion Recombination. *J. Chem. Phys.* **1988**, *89* (11), 6929.
- (215) Arkhipov, V.; Bäessler, H. In *Physics of Organic Semiconductors*; Brütting, W., Ed.; Wiley VCH: 2005.
- (216) Falkowski, K.; Stampor, W.; Grygiel, P.; Tomaszewicz, W. Sano-Tachiya-Noolandi-Hong versus Onsager Modelling of Charge Photogeneration in Organic Solids. *Chem. Phys.* **2012**, *392* (1), 122–129.
- (217) Kalinowski, J.; Stampor, W.; Di Marco, P. G. Electro-modulation of Fluorescence in a Crystalline Organic Photoconductor (thionaphthenindole). *J. Chem. Phys.* **1992**, *96* (6), 4136–4148.
- (218) Silinsh, E. A.; Čápec, V. *Organic Molecular Crystals: Interaction, Localization and Transport Phenomena*; American Institute of Physics: New York, 1994.
- (219) Lang, D. V.; Chi, X.; Siegrist, T.; Sergent, a. M.; Ramirez, a. P. Amorphouslike Density of Gap States in Single-Crystal Pentacene. *Phys. Rev. Lett.* **2004**, *93* (8), 086802.
- (220) Ostroverkhova, O.; Moerner, W. E. Organic Photorefractives: Mechanisms, Materials, and Applications. *Chem. Rev.* **2004**, *104* (7), 3267–3314.
- (221) Noolandi, J.; Hong, K. M. Theory of Photogeneration and Fluorescence Quenching. *J. Chem. Phys.* **1979**, *70* (7), 3230.
- (222) Strobel, T.; Deibel, C.; Dyakonov, V. Role of Polaron Pair Diffusion and Surface Losses in Organic Semiconductor Devices. *Phys. Rev. Lett.* **2010**, *105* (26), 266602.
- (223) Sano, H.; Tachiya, M. Partially Diffusion-Controlled Recombination. *J. Chem. Phys.* **1979**, *71* (3), 1276.
- (224) Mauzerall, D.; Ballard, S. Ionization in Solution by Photo-activated Electron Transfer. *Annu. Rev. Phys. Chem.* **1982**, *33*, 377–407.
- (225) Wojcik, M.; Tachiya, M. Accuracies of the Empirical Theories of the Escape Probability Based on Eigen Model and Braun Model Compared with the Exact Extension of Onsager Theory. *J. Chem. Phys.* **2009**, *130* (10), 104107.
- (226) Braun, C. L. Electric Field Assisted Dissociation of Charge Transfer States as a Mechanism of Photocarrier Production. *J. Chem. Phys.* **1984**, *80* (9), 4157–4161.
- (227) Petersen, A.; Ojala, A.; Kirchartz, T.; Wagner, T. a.; Würthner, F.; Rau, U. Field-Dependent Exciton Dissociation in Organic Heterojunction Solar Cells. *Phys. Rev. B: Condens. Matter Mater. Phys.* **2012**, *85* (24), 245208.
- (228) Zhang, T.; Birgersson, E.; Ananthanarayanan, K.; Yong, C. H.; Thummalakunta, L. N. S. a.; Luther, J. Analysis of a Device Model for Organic Pseudo-Bilayer Solar Cells. *J. Appl. Phys.* **2012**, *112* (8), 084511.
- (229) Tress, W.; Leo, K.; Riede, M. Optimum Mobility, Contact Properties, and Open-Circuit Voltage of Organic Solar Cells: A Drift-Diffusion Simulation Study. *Phys. Rev. B: Condens. Matter Mater. Phys.* **2012**, *85* (15), 155201.
- (230) Massip, S.; Oberhumer, P. M.; Tu, G.; Albert-Seifried, S.; Huck, W. T. S.; Friend, R. H.; Greenham, N. C. Influence of Side Chains on Geminate and Bimolecular Recombination in Organic Solar Cells. *J. Phys. Chem. C* **2011**, *115* (50), 25046–25055.
- (231) Trukhanov, V. a.; Bruevich, V. V.; Parashchuk, D. Y. Effect of Doping on Performance of Organic Solar Cells. *Phys. Rev. B: Condens. Matter Mater. Phys.* **2011**, *84* (20), 205318.
- (232) Deibel, C.; Strobel, T.; Dyakonov, V. Origin of the Efficient Polaron-Pair Dissociation in Polymer-Fullerene Blends. *Phys. Rev. Lett.* **2009**, *103* (3), 036402.
- (233) Servaites, J. D.; Savoie, B. M.; Brink, J. B.; Marks, T. J.; Ratner, M. a. Modeling Geminate Pair Dissociation in Organic Solar Cells: High Power Conversion Efficiencies Achieved with Moderate Optical Bandgaps. *Energy Environ. Sci.* **2012**, *5* (8), 8343.
- (234) Van Eersel, H.; Janssen, R. a. J.; Kemerink, M. Mechanism for Efficient Photoinduced Charge Separation at Disordered Organic Heterointerfaces. *Adv. Funct. Mater.* **2012**, *22* (13), 2700–2708.
- (235) Jones, M. L.; Chakrabarti, B.; Groves, C. Monte Carlo Simulation of Geminate Pair Recombination Dynamics in Organic Photovoltaic Devices: Multi-Exponential, Field-Dependent Kinetics and Its Interpretation. *J. Phys. Chem. C* **2014**, *118* (1), 85–91.
- (236) Mihailtchi, V. D.; Koster, L. J. a.; Hummelen, J. C.; Blom, P. W. M. Photocurrent Generation in Polymer-Fullerene Bulk Heterojunctions. *Phys. Rev. Lett.* **2004**, *93* (21), 216601.
- (237) Burke, T. M.; Sweetnam, S.; Vandewal, K.; McGehee, M. D. Beyond Langevin Recombination: How Equilibrium between Free Carriers and Charge Transfer States Determines the Open-Circuit Voltage of Organic Solar Cells. *Adv. Energy Mater.* **2015**, *5*, 1500123.
- (238) Rubel, O.; Baranovskii, S. D.; Stolz, W.; Gebhard, F. Exact Solution for Hopping Dissociation of Geminate Electron-Hole Pairs in a Disordered Hain. *Phys. Rev. Lett.* **2008**, *100* (19), 196602.
- (239) Nenashev, a. V.; Wiemer, M.; Jansson, F.; Baranovskii, S. D. Theory to Exciton Dissociation at the Interface between a Conjugated

Polymer and an Electron Acceptor. *J. Non-Cryst. Solids* **2012**, *358* (17), 2508–2511.

(240) Wojcik, M.; Tachiya, M. Long-Time Decay Kinetics of Geminate Electron-Hole Pairs in Donor-Acceptor Heterojunction Systems. *Chem. Phys. Lett.* **2012**, *537*, 58–61.

(241) Gregg, B. a. Entropy of Charge Separation in Organic Photovoltaic Cells: The Benefit of Higher Dimensionality. *J. Phys. Chem. Lett.* **2011**, *2* (24), 3013–3015.

(242) Arkhipov, V.; Emelianova, E.; Bäessler, H. Hot Exciton Dissociation in a Conjugated Polymer. *Phys. Rev. Lett.* **1999**, *82* (6), 1321–1324.

(243) Etzold, F.; Howard, I. a.; Mauer, R.; Meister, M.; Kim, T. D.; Lee, K. S.; Baek, N. S.; Laquai, F. Ultrafast Exciton Dissociation Followed by Nongeminate Charge Recombination in PCDTBT:PCBM Photovoltaic Blends. *J. Am. Chem. Soc.* **2011**, *133* (24), 9469–9479.

(244) Jailaubekov, A. E.; Willard, A. P.; Tritsch, J. R.; Chan, W.-L.; Sai, N.; Gearba, R.; Kaake, L. G.; Williams, K. J.; Leung, K.; Rossky, P. J.; et al. Hot Charge-Transfer Excitons Set the Time Limit for Charge Separation at Donor/acceptor Interfaces in Organic Photovoltaics. *Nat. Mater.* **2013**, *12* (1), 66–73.

(245) Schwarz, C.; Tscheuschner, S.; Frisch, J.; Winkler, S.; Koch, N.; Bäessler, H.; Köhler, A. Role of the Effective Mass and Interfacial Dipoles on Exciton Dissociation in Organic Donor-Acceptor Solar Cells. *Phys. Rev. B: Condens. Matter Mater. Phys.* **2013**, *87* (15), 155205.

(246) Hahn, T.; Geiger, J.; Blase, X.; Duchemin, I.; Niedzialek, D.; Tscheuschner, S.; Beljonne, D.; Bäessler, H.; Köhler, A. Does Excess Energy Assist Photogeneration in an Organic Low-Bandgap Solar Cell? *Adv. Funct. Mater.* **2015**, *25*, 1287–1295.

(247) Arkhipov, V. I.; Heremans, P.; Bäessler, H. Why Is Exciton Dissociation so Efficient at the Interface between a Conjugated Polymer and an Electron Acceptor? *Appl. Phys. Lett.* **2003**, *82* (25), 4605.

(248) Arkhipov, V. I.; Emelianova, E. V.; Bäessler, H. Dopant-Assisted Charge Carrier Photogeneration in Conjugated Polymers. *Chem. Phys. Lett.* **2003**, *372* (5–6), 886–892.

(249) Baranovskii, S. D.; Wiemer, M.; Nenashev, A.; Jansson, F.; Gebhard, F. Calculating the Efficiency of Exciton Dissociation between a Conjugated Polymer and an Electron Acceptor. *J. Phys. Chem. Lett.* **2012**, *3*, 1214–1221.

(250) Nenashev, a. V.; Wiemer, M.; Jansson, F.; Baranovskii, S. D. Theory to Exciton Dissociation at the Interface between a Conjugated Polymer and an Electron Acceptor. *J. Non-Cryst. Solids* **2012**, *358* (17), 2508–2511.

(251) Wiemer, M.; Nenashev, a. V.; Jansson, F.; Baranovskii, S. D. On the Efficiency of Exciton Dissociation at the Interface between a Conjugated Polymer and an Electron Acceptor. *Appl. Phys. Lett.* **2011**, *99*, 013302.

(252) Tscheuschner, S.; Bäessler, H.; Huber, K.; Köhler, A. A Combined Theoretical and Experimental Study of Dissociation of Charge Transfer States at the Donor–Acceptor Interface of Organic Solar Cells. *J. Phys. Chem. B* **2015**, *119* (32), 10359–10371.

(253) Körzdörfer, T.; Brédas, J.-L. Organic Electronic Materials: Recent Advances in the DFT Description of the Ground and Excited States Using Tuned Range-Separated Hybrid Functionals. *Acc. Chem. Res.* **2014**, *47*, 3284–3291.

(254) Few, S.; Frost, J.; Kirkpatrick, J.; Nelson, J. Influence of Chemical Structure on the Charge Transfer State Spectrum of a Polymer: Fullerene Complex. *J. Phys. Chem. C* **2014**, *118*, 8253–8261.

(255) Li, L. H.; Kontsevoi, O. Y.; Freeman, A. J. Orientation-Dependent Electronic Structures and Optical Properties of the P3HT:PCBM Interface: A First-Principles GW-BSE Study. *J. Phys. Chem. C* **2014**, *118* (19), 10263–10270.

(256) Duchemin, I.; Blase, X. Resonant Hot Charge-Transfer Excitations in Fullerene-Porphyrin Complexes: Many-Body Bethe-Salpeter Study. *Phys. Rev. B: Condens. Matter Mater. Phys.* **2013**, *87* (24), 245412.

(257) Poelking, C.; Tietze, M.; Elschner, C.; Olthof, S.; Hertel, D.; Baumeier, B.; Würthner, F.; Meerholz, K.; Leo, K.; Andrienko, D. Impact of Mesoscale Order on Open-Circuit Voltage in Organic Solar Cells. *Nat. Mater.* **2014**, *14* (4), 434–439.

(258) Troisi, A. How Quasi-Free Holes and Electrons Are Generated in Organic Photovoltaic Interfaces. *Faraday Discuss.* **2013**, *163*, 377.

(259) Bedard-Hearn, M. J.; Sterpone, F.; Rossky, P. J. Nonadiabatic Simulations of Exciton Dissociation in Poly-P-Phenylenevinylene Oligomers. *J. Phys. Chem. A* **2010**, *114* (29), 7661–7670.

(260) Ribeiro, L. A.; Da Cunha, W. F.; Oliveira Neto, P. H.; Gargano, R.; E Silva, G. M. Impurity Effects and Temperature Influence on the Exciton Dissociation Dynamics in Conjugated Polymers. *Chem. Phys. Lett.* **2013**, *580*, 108–114.

(261) Li, X. Polarization and Dissociation of a High Energy Photon-Excited State in Conjugated Polymers. *Phys. Lett. A* **2015**, *379* (5), 482–486.

(262) Liu, X. J.; Zhang, Y. L.; An, Z. Electron Correlation Effects on Exciton Dissociation in the Presence of an Electric Field in Polyacetylene. *Org. Electron.* **2013**, *14* (10), 2692–2697.

(263) Shin, Y. W.; Lin, X. Modeling Photoinduced Charge Transfer Across Pi-Conjugated Heterojunctions. *J. Phys. Chem. C* **2013**, *117*, 12432–12437.

(264) Gao, K.; Xie, S.; Yin, S.; Liu, D. Study on Charge-Transfer State in a Donor-Acceptor Polymer Heterojunction. *Org. Electron.* **2011**, *12* (6), 1010–1016.

(265) Caruso, D.; Troisi, A. Long-Range Exciton Dissociation in Organic Solar Cells. *Proc. Natl. Acad. Sci. U. S. A.* **2012**, *109* (34), 13498–13502.

(266) Vázquez, H.; Troisi, A. Calculation of Rates of Exciton Dissociation into Hot Charge-Transfer States in Model Organic Photovoltaic Interfaces. *Phys. Rev. B: Condens. Matter Mater. Phys.* **2013**, *88* (20), 205304.

(267) Lee, M. H.; Aragón, J.; Troisi, A. Charge Dynamics in Organic Photovoltaic Materials: Interplay between Quantum Diffusion and Quantum Relaxation. *J. Phys. Chem. C* **2015**, *119* (27), 14989–14998.

(268) Yao, Y.; Yang, W.; Zhao, Y. Exciton Dissociation in the Presence of Phonons: A Reduced Hierarchy Equations of Motion Approach. *J. Chem. Phys.* **2014**, *140* (10), 104113.

(269) Creatore, C.; Parker, M. A.; Emmott, S.; Chin, A. W. Efficient Biologically Inspired Photocell Enhanced by Delocalized Quantum States. *Phys. Rev. Lett.* **2013**, *111* (25), 253601.

(270) Heiber, M. C.; Dhinojwala, A. Estimating the Magnitude of Exciton Delocalization in Regioregular P3HT. *J. Phys. Chem. C* **2013**, *117* (42), 21627–21634.

(271) Maturová, K.; van Bavel, S. S.; Wienk, M. M.; Janssen, R. a. J.; Kemerink, M. Description of the Morphology Dependent Charge Transport and Performance of Polymer:Fullerene Bulk Heterojunction Solar Cells. *Adv. Funct. Mater.* **2011**, *21* (2), 261–269.

(272) Maturová, K.; van Bavel, S. S.; Wienk, M. M.; Janssen, R. a. J.; Kemerink, M. Morphological Device Model for Organic Bulk Heterojunction Solar Cells. *Nano Lett.* **2009**, *9* (8), 3032–3037.

(273) Burke, T. M.; McGehee, M. D. How High Local Charge Carrier Mobility and an Energy Cascade in a Three-Phase Bulk Heterojunction Enable > 90% Quantum Efficiency. *Adv. Mater.* **2014**, *26* (12), 1923–1928.

(274) Lyons, B. P.; Clarke, N.; Groves, C. The Relative Importance of Domain Size, Domain Purity and Domain Interfaces to the Performance of Bulk-Heterojunction Organic Photovoltaics. *Energy Environ. Sci.* **2012**, *5* (6), 7657.

(275) Heitzer, H. M.; Savoie, B. M.; Marks, T. J.; Ratner, M. a. Organic Photovoltaics: Elucidating the Ultra-Fast Exciton Dissociation Mechanism in Disordered Materials. *Angew. Chem., Int. Ed.* **2014**, *53* (29), 7456–7460.

(276) Shang, Y.; Li, Q.; Meng, L.; Wang, D.; Shuai, Z. Computational Characterization of Organic Photovoltaic Devices. *Theor. Chem. Acc.* **2011**, *129* (3–5), 291–301.

(277) Groves, C.; Greenham, N. C. Monte Carlo Simulations of Organic Photovoltaics. *Top. Curr. Chem.* **2013**, *352*, 257–278.

- (278) Liu, X.; Huettner, S.; Rong, Z.; Sommer, M.; Friend, R. H. Solvent Additive Control of Morphology and Crystallization in Semiconducting Polymer Blends. *Adv. Mater.* **2012**, *24* (5), 669–674.
- (279) Heiber, M. C.; Dhinojwala, A. Dynamic Monte Carlo Modeling of Exciton Dissociation in Organic Donor-Acceptor Solar Cells. *J. Chem. Phys.* **2012**, *137* (1), 014903.
- (280) Jones, M. L.; Dyer, R.; Clarke, N.; Groves, C. Are Hot Charge Transfer States the Primary Cause of Efficient Free-Charge Generation in Polymer:fullerene Organic Photovoltaic Devices? A Kinetic Monte Carlo Study. *Phys. Chem. Chem. Phys.* **2014**, *16* (38), 20310–20320.
- (281) Maqsood, I.; Cundy, L. D.; Biesecker, M.; Kimn, J.; Johnson, D.; Williams, R.; BommiSETTY, V. Monte Carlo Simulation of Förster Resonance Energy Transfer in 3D Nanoscale Organic Bulk Heterojunction Morphologies. *J. Phys. Chem. C* **2013**, *117* (41), 21086–21095.
- (282) Coehoorn, R.; Pasveer, W. F.; Bobbert, P. a.; Michels, M. a J. Charge-Carrier Concentration Dependence of the Hopping Mobility in Organic Materials with Gaussian Disorder. *Phys. Rev. B: Condens. Matter Mater. Phys.* **2005**, *72* (15), 155206.
- (283) Pasveer, W. F.; Cottaar, J.; Tanase, C.; Coehoorn, R.; Bobbert, P. a.; Blom, P. W. M.; De Leeuw, M.; Michels, M. a J. Unified Description of Charge-Carrier Mobilities in Disordered Semiconducting Polymers. *Phys. Rev. Lett.* **2005**, *94* (20), 206601.
- (284) Koster, L. J. a.; Smits, E. C. P.; Mihailetschi, V. D.; Blom, P. W. M. Device Model for the Operation of Polymer/fullerene Bulk Heterojunction Solar Cells. *Phys. Rev. B: Condens. Matter Mater. Phys.* **2005**, *72* (8), 085205.
- (285) Vervisch, W.; Biondo, S.; Riviere, G.; Duché, D.; Escoubas, L.; Torchio, P.; Simon, J. J.; Le Rouzo, J. Optical-Electrical Simulation of Organic Solar Cells: Excitonic Modeling Parameter Influence on Electrical Characteristics. *Appl. Phys. Lett.* **2011**, *98* (25), 253306.
- (286) Granero, P.; Balderrama, V. S.; Ferré-Borrull, J.; Pallarès, J.; Marsal, L. F. Two-Dimensional Finite-Element Modeling of Periodical Interdigitated Full Organic Solar Cells. *J. Appl. Phys.* **2013**, *113* (4), 043107.
- (287) Jakobsson, F. L. E.; Crispin, X.; Berggren, M. Prediction of the Current versus Voltage Behavior of Devices Based on Organic Semiconductor Guest-Host Systems. *Org. Electron.* **2009**, *10* (1), 95–106.
- (288) Set, Y. T.; Zhang, T.; Birgersson, E.; Luther, J. What Parameters Can Be Reliably Deduced from the Current-Voltage Characteristics of an Organic Bulk-Heterojunction Solar Cell? *J. Appl. Phys.* **2015**, *117* (8), 084503.
- (289) Kniepert, J.; Lange, I.; Van Der Kaap, N. J.; Koster, L. J. A.; Neher, D. A Conclusive View on Charge Generation, Recombination, and Extraction in as-Prepared and Annealed P3HT:PCBM Blends: Combined Experimental and Simulation Work. *Adv. Energy Mater.* **2014**, *4*, 1301401.
- (290) Kirchartz, T.; Pieters, B. E.; Kirkpatrick, J.; Rau, U.; Nelson, J. Recombination via Tail States in Polythiophene:fullerene Solar Cells. *Phys. Rev. B: Condens. Matter Mater. Phys.* **2011**, *83* (11), 115209.
- (291) Dibb, G. F. a.; Jamieson, F. C.; Maurano, A.; Nelson, J.; Durrant, J. R. Limits on the Fill Factor in Organic Photovoltaics: Distinguishing Nongeminate and Geminate Recombination Mechanisms. *J. Phys. Chem. Lett.* **2013**, *4* (5), 803–808.
- (292) Wehenkel, D. J.; Koster, L. J. A.; Wienk, M. M.; Janssen, R. a J. Influence of Injected Charge Carriers on Photocurrents in Polymer Solar Cells. *Phys. Rev. B: Condens. Matter Mater. Phys.* **2012**, *85* (12), 125203.
- (293) Altazin, S.; Clerc, R.; Gwoziecki, R.; Pananakakis, G.; Ghibaud, G.; Serbutoviez, C. Analytical Modeling of Organic Solar Cells and Photodiodes. *Appl. Phys. Lett.* **2011**, *99* (14), 143301.
- (294) Petersen, A.; Kirchartz, T.; Wagner, T. Charge Extraction and Photocurrent in Organic Bulk Heterojunction Solar Cells. *Phys. Rev. B: Condens. Matter Mater. Phys.* **2012**, *85* (4), 045208.
- (295) Dacuña, J.; Xie, W.; Salleo, A. Estimation of the Spatial Distribution of Traps Using Space-Charge-Limited Current Measurements in an Organic Single Crystal. *Phys. Rev. B: Condens. Matter Mater. Phys.* **2012**, *86* (11), 115202.
- (296) Dacuña, J.; Desai, A.; Xie, W.; Salleo, A. Modeling of the Effect of Intentionally Introduced Traps on Hole Transport in Single-Crystal Rubrene. *Phys. Rev. B: Condens. Matter Mater. Phys.* **2014**, *89* (24), 245302.
- (297) McNeill, C. R.; Hwang, I.; Greenham, N. C. Photocurrent Transients in All-Polymer Solar Cells: Trapping and Detrapping Effects. *J. Appl. Phys.* **2009**, *106* (2), 024507.
- (298) Blakesley, J. C.; Clubb, H. S.; Greenham, N. C. Temperature-Dependent Electron and Hole Transport in Disordered Semiconducting Polymers: Analysis of Energetic Disorder. *Phys. Rev. B: Condens. Matter Mater. Phys.* **2010**, *81* (4), 045210.
- (299) Li, Z.; Lakhwani, G.; Greenham, N. C.; McNeill, C. R. Voltage-Dependent Photocurrent Transients of PTB7:PC70BM Solar Cells: Experiment and Numerical Simulation. *J. Appl. Phys.* **2013**, *114* (3), 034502.
- (300) Paudel, K.; Johnson, B.; Thieme, M.; Haley, M. M.; Payne, M. M.; Anthony, J. E.; Ostroverkhova, O. Enhanced Charge Photo-generation Promoted by Crystallinity in Small-Molecule Donor-Acceptor Bulk Heterojunctions. *Appl. Phys. Lett.* **2014**, *105* (4), 043301.
- (301) Soci, C.; Moses, D.; Xu, Q. H.; Heeger, A. J. Charge-Carrier Relaxation Dynamics in Highly Ordered Poly(p-Phenylene Vinylene): Effects of Carrier Bimolecular Recombination and Trapping. *Phys. Rev. B: Condens. Matter Mater. Phys.* **2005**, *72* (24), 245204.
- (302) Savenije, T. J.; Ferguson, A. J.; Kopidakis, N.; Rumbles, G. Revealing the Dynamics of Charge Carriers in Polymer:fullerene Blends Using Photoinduced Time-Resolved Microwave Conductivity. *J. Phys. Chem. C* **2013**, *117* (46), 24085–24103.
- (303) Hawks, S. a.; Finck, B. Y.; Schwartz, B. J. Theory of Current Transients in Planar Semiconductor Devices: Insights and Applications to Organic Solar Cells. *Phys. Rev. Appl.* **2015**, *3*, 044014.
- (304) Kirchartz, T.; Nelson, J. Device Modelling of Organic Bulk Heterojunction Solar Cells. *Top. Curr. Chem.* **2014**, *352*, 279–324.
- (305) Schildkraut, J. S.; Buettner, A. V. Theory and Simulations of the Formation and Erasure of Space-Charge Gratings in Photoconductive Polymers. *J. Appl. Phys.* **1992**, *72*, 1888–1893.
- (306) Barker, J.; Ramsdale, C.; Greenham, N. Modeling the Current-Voltage Characteristics of Bilayer Polymer Photovoltaic Devices. *Phys. Rev. B: Condens. Matter Mater. Phys.* **2003**, *67* (7), 075205.
- (307) MacKenzie, R. C. I.; Kirchartz, T.; Dibb, G. F. a.; Nelson, J. Modeling Nongeminate Recombination in P3HT:PCBM Solar Cells. *J. Phys. Chem. C* **2011**, *115* (19), 9806–9813.
- (308) Tessler, N.; Preezant, Y.; Rappaport, N.; Roichman, Y. Charge Transport in Disordered Organic Materials and Its Relevance to Thin-Film Devices: A Tutorial Review. *Adv. Mater.* **2009**, *21* (27), 2741–2761.
- (309) Wheeler, S.; Deledalle, F.; Tokmoldin, N.; Kirchartz, T.; Nelson, J.; Durrant, J. R. Influence of Surface Recombination on Charge-Carrier Kinetics in Organic Bulk Heterojunction Solar Cells with Nickel Oxide Interlayers. *Phys. Rev. Appl.* **2015**, *4* (2), 024020.
- (310) Kirchartz, T.; Pieters, B. E.; Taretto, K.; Rau, U. Electro-Optical Modeling of Bulk Heterojunction Solar Cells. *J. Appl. Phys.* **2008**, *104* (9), 094513.
- (311) Kotlarski, J. D.; Blom, P. W. M.; Koster, L. J. a.; Lenes, M.; Slooff, L. H. Combined Optical and Electrical Modeling of Polymer:fullerene Bulk Heterojunction Solar Cells. *J. Appl. Phys.* **2008**, *103* (8), 084502.
- (312) Pettersson, L. a a; Roman, L. S.; Inganäs, O. Modeling Photocurrent Action Spectra of Photovoltaic Devices Based on Organic Thin Films Modeling Photocurrent Action Spectra of Photovoltaic Devices Based on Organic Thin Films. *J. Appl. Phys.* **2011**, *487* (1999), 487–496.
- (313) Giebink, N. C.; Wiederrecht, G. P.; Wasielewski, M. R.; Forrest, S. R. Ideal Diode Equation for Organic Heterojunctions. I. Derivation and Application. *Phys. Rev. B: Condens. Matter Mater. Phys.* **2010**, *82*, 155305.
- (314) Giebink, N. C.; Lassiter, B. E.; Wiederrecht, G. P.; Wasielewski, M. R.; Forrest, S. R. Ideal Diode Equation for Organic Hetero-

junctions. II. the Role of Polaron Pair Recombination. *Phys. Rev. B: Condens. Matter Mater. Phys.* **2010**, *82* (15), 155306.

(315) Servaites, J. D.; Ratner, M. a.; Marks, T. J. Organic Solar Cells: A New Look at Traditional Models. *Energy Environ. Sci.* **2011**, *4* (11), 4410.

(316) Arnab, S. M.; Kabir, M. Z. An Analytical Model for Analyzing the Current-Voltage Characteristics of Bulk Heterojunction Organic Solar Cells. *J. Appl. Phys.* **2014**, *115* (3), 034504.

(317) Inche Ibrahim, M. L.; Ahmad, Z.; Sulaiman, K. Analytical Expression for the Current-Voltage Characteristics of Organic Bulk Heterojunction Solar Cells. *AIP Adv.* **2015**, *5* (2), 027115.

(318) Neher, D.; Kniepert, J.; Elimelech, A.; Koster, L. J. A. A New Figure of Merit for Organic Solar Cells with Transport-Limited Photocurrents. *Sci. Rep.* **2016**, *6*, 24861.

(319) Shuttle, C. G.; Maurano, a.; Hamilton, R.; O'Regan, B.; De Mello, J. C.; Durrant, J. R. Charge Extraction Analysis of Charge Carrier Densities in a Polythiophene/fullerene Solar Cell: Analysis of the Origin of the Device Dark Current. *Appl. Phys. Lett.* **2008**, *93* (2008), 183501.

(320) Li, N.; Lassiter, B. E.; Lunt, R. R.; Wei, G.; Forrest, S. R. Open Circuit Voltage Enhancement due to Reduced Dark Current in Small Molecule Photovoltaic Cells. *Appl. Phys. Lett.* **2009**, *94* (2), 023307.

(321) Masurkar, A.; Kymissis, I. Photocurrent Measurements of Pentacene-Based Devices. *Appl. Phys. Rev.* **2015**, *2* (3), 031101.

(322) Day, J.; Platt, a. D.; Subramanian, S.; Anthony, J. E.; Ostroverkhova, O. Influence of Organic Semiconductor-Metal Interfaces on the Photoresponse of Functionalized Anthradithiophene Thin Films. *J. Appl. Phys.* **2009**, *105* (10), 103703.

(323) Fiebig, M.; Erlen, C.; Göllner, M.; Lugli, P.; Nickel, B. Spatially Resolved Photoresponse Measurements on Pentacene Thin-Film Transistors. *Appl. Phys. A: Mater. Sci. Process.* **2009**, *95*, 113–117.

(324) Barth, S.; Bäessler, H. Intrinsic Photoconduction in PPV-Type Conjugated Polymers. *Phys. Rev. Lett.* **1997**, *79* (22), 4445–4448.

(325) Moses, D.; Miranda, P. B.; Soci, C.; Heeger, A. J. Mechanism of Carrier Photoexcitation in Semiconducting Polymers: The Role of Electron Photoemission in "Photoconductivity" Measurements. *Chem. Phys. Lett.* **2001**, *350*, 531–536.

(326) Street, R. a.; Song, K. W.; Cowan, S. Influence of Series Resistance on the Photocurrent Analysis of Organic Solar Cells. *Org. Electron.* **2011**, *12* (2), 244–248.

(327) Stelzl, F. F.; Würfel, U. Modeling the Influence of Doping on the Performance of Bulk Heterojunction Organic Solar Cells: One-Dimensional Effective Semiconductor versus Two-Dimensional Donor/acceptor Model. *Phys. Rev. B: Condens. Matter Mater. Phys.* **2012**, *86* (7), 075315.

(328) Walzer, K.; Maennig, B.; Pfeiffer, M.; Leo, K. Highly Efficient Organic Devices Based on Electrically Doped Transport Layers. *Chem. Rev.* **2007**, *107*, 1233–1271.

(329) Gregg, B. A. Transport in Charged Defect-Rich Pi-Conjugated Polymers. *J. Phys. Chem. C* **2009**, *113*, 5899–5901.

(330) Maturova, K.; Kemerink, M.; Wienk, M. M.; Charrier, D. S. H.; Janssen, R. A. J. Scanning Kelvin Probe Microscopy on Bulk Heterojunction Polymer Blends. *Adv. Funct. Mater.* **2009**, *19* (9), 1379–1386.

(331) Ray, B.; Alam, M. a. Random vs Regularized OPV: Limits of Performance Gain of Organic Bulk Heterojunction Solar Cells by Morphology Engineering. *Sol. Energy Mater. Sol. Cells* **2012**, *99*, 204–212.

(332) Ray, B.; Lundstrom, M. S.; Alam, M. a. Can Morphology Tailoring Improve the Open Circuit Voltage of Organic Solar Cells? *Appl. Phys. Lett.* **2012**, *100* (1), 013307.

(333) MacKenzie, R. C. I.; Shuttle, C. G.; Chabincyn, M. L.; Nelson, J. Extracting Microscopic Device Parameters from Transient Photocurrent Measurements of P3HT:PCBM Solar Cells. *Adv. Energy Mater.* **2012**, *2* (6), 662–669.

(334) Johnson, B.; Paudel, K.; Ostroverkhova, O. Computational Modeling of Nanosecond Time-Scale Charge Carrier Dynamics in Organic Semiconductors. *MRS Online Proc. Libr.* **2015**, *1737*, DOI: 10.1557/opl.2015.501.

(335) Johnson, B.; Paudel, K.; Kendrick, M. J.; Ostroverkhova, O. Numerical Modeling of Time-Resolved Photocurrent in Organic Semiconductor Films. *Proc. SPIE* **2013**, *8830* (1), 88301S.

(336) Khelifi, S.; Decock, K.; Lauwaert, J.; Vrielinck, H.; Spoltore, D.; Piersimoni, F.; Manca, J.; Belghachi, A.; Burgelman, M. Investigation of Defects by Admittance Spectroscopy Measurements in Poly (3-hexylthiophene):(6,6)-Phenyl C61-Butyric Acid Methyl Ester Organic Solar Cells Degraded under Air Exposure. *J. Appl. Phys.* **2011**, *110* (9), 094509.

(337) Gorgolis, S.; Giannopoulou, A.; Kounavis, P. Charge Carriers Trapping States in Pentacene Films Studied by Modulated Photocurrent. *J. Appl. Phys.* **2013**, *113* (12), 123102.

(338) Vagenas, N.; Giannopoulou, a.; Kounavis, P. Density and Mobility Effects of the Majority Carriers in Organic Semiconductors under Light Excitation. *J. Appl. Phys.* **2015**, *117* (3), 033105.

(339) Set, Y. T.; Birgersson, E.; Luther, J. Predictive Mechanistic Model for the Electrical Impedance and Intensity-Modulated Photocurrent and Photovoltage Spectroscopic Responses of an Organic Bulk Heterojunction Solar Cell. *Phys. Rev. Appl.* **2016**, *5* (5), 054002.

(340) Koster, L. J. A.; Kemerink, M.; Wienk, M. M.; Maturová, K.; Janssen, R. a. J. Quantifying Bimolecular Recombination Losses in Organic Bulk Heterojunction Solar Cells. *Adv. Mater.* **2011**, *23* (14), 1670–1674.

(341) Häusermann, R.; Knapp, E.; Moos, M.; Reinke, N. a.; Flatz, T.; Ruhstaller, B. Coupled Optoelectronic Simulation of Organic Bulk-Heterojunction Solar Cells: Parameter Extraction and Sensitivity Analysis. *J. Appl. Phys.* **2009**, *106* (10), 104507.

(342) Srimath Kandada, A. R.; Petrozza, A.; Lanzani, G. Ultrafast Dissociation of Triplets in Pentacene Induced by an Electric Field. *Phys. Rev. B: Condens. Matter Mater. Phys.* **2014**, *90* (7), 075310.

(343) Hendry, E.; Schins, J. M.; Candeias, L. P.; Siebbeles, L. D. a.; Bonn, M. Efficiency of Exciton and Charge Carrier Photogeneration in a Semiconducting Polymer. *Phys. Rev. Lett.* **2004**, *92* (19), 196601.

(344) Cooke, D. G.; Krebs, F. C.; Jepsen, P. U. Direct Observation of Sub-100 Fs Mobile Charge Generation in a Polymer-Fullerene Film. *Phys. Rev. Lett.* **2012**, *108* (5), 056603.

(345) Liang, H. Y.; Cao, W. L.; Du, M.; Kim, Y.; Herman, W. N.; Lee, C. H. Ultrafast Photo-Conductivity in BAMH-PPV Polymer Thin-Films. *Chem. Phys. Lett.* **2006**, *419* (1–3), 292–296.

(346) Moses, D.; Soci, C.; Chi, X.; Ramirez, A. P. Mechanism of Carrier Photogeneration and Carrier Transport in Molecular Crystal Tetracene. *Phys. Rev. Lett.* **2006**, *97* (6), 067401.

(347) Day, J.; Subramanian, S.; Anthony, J. E.; Lu, Z.; Twieg, R. J.; Ostroverkhova, O. Photoconductivity in Organic Thin Films: From Picoseconds to Seconds after Excitation. *J. Appl. Phys.* **2008**, *103* (12), 123715.

(348) Ai, X.; Beard, M. C.; Knutsen, K. P.; Shaheen, S. E.; Rumbles, G.; Ellingson, R. J. Photoinduced Charge Carrier Generation in a Poly (3-Hexylthiophene) and Methanofullerene Bulk Heterojunction Investigated by Time-Resolved Terahertz Spectroscopy Photoinduced Charge Carrier Generation in a Poly (3-Hexylthiophene) and Methanofullerene. *J. Phys. Chem. B* **2006**, *110*, 25462–25471.

(349) Devizis, a.; Serbenta, A.; Peckus, D.; Thiessen, A.; Alle, R.; Meerholz, K.; Hertel, D.; Gulbinas, V. Electric Field Assisted Charge Carrier Photogeneration in Poly(spirobifluorene-Co-Benzothiadiazole). *J. Chem. Phys.* **2010**, *133* (16), 164904.

(350) Chasteen, S. V.; Härter, J. O.; Rumbles, G.; Scott, J. C.; Nakazawa, Y.; Jones, M.; Hörhold, H. H.; Tillman, H.; Carter, S. a. Comparison of Blended versus Layered Structures for Poly(p-Phenylene Vinylene)-Based Polymer Photovoltaics. *J. Appl. Phys.* **2006**, *99* (3), 033709.

(351) Renshaw, C. K.; Zimmerman, J. D.; Lassiter, B. E.; Forrest, S. R. Photoconductivity in Donor-Acceptor Heterojunction Organic Photovoltaics. *Phys. Rev. B: Condens. Matter Mater. Phys.* **2012**, *86* (8), 085324.

(352) Bergemann, K. J.; Liu, X.; Panda, A.; Forrest, S. R. Singlets Lead to Photogeneration in C 60 -Based Organic Heterojunctions. *Phys. Rev. B: Condens. Matter Mater. Phys.* **2015**, *92* (3), 035408.

- (353) Gehrig, D. W.; Howard, I. a.; Laquai, F. Charge Carrier Generation Followed by Triplet State Formation, Annihilation, and Carrier Recreation in PBDTTT-C:PC60 BM Photovoltaic Blends. *J. Phys. Chem. C* **2015**, *119*, 13509–13515.
- (354) Jin, Z.; Gehrig, D.; Dyer-smith, C.; Heilweil, E. J.; Bonn, M.; Turchinovich, D. Ultrafast Terahertz Photoconductivity of Photovoltaic Polymer – Fullerene Blends: A Comparative Study Correlated with Photovoltaic Device Performance. *J. Phys. Chem. Lett.* **2014**, *5*, 3662–3668.
- (355) Kaake, L. G.; Jasieniak, J. J.; Bakus, R. C.; Welch, G. C.; Moses, D.; Bazan, G. C.; Heeger, A. J. Photoinduced Charge Generation in a Molecular Bulk Heterojunction Material. *J. Am. Chem. Soc.* **2012**, *134* (48), 19828–19838.
- (356) Paudel, K.; Johnson, B.; Neunzert, a.; Thieme, M.; Purushothaman, B.; Payne, M. M.; Anthony, J. E.; Ostroverkhova, O. Small-Molecule Bulk Heterojunctions: Distinguishing between Effects of Energy Offsets and Molecular Packing on Optoelectronic Properties. *J. Phys. Chem. C* **2013**, *117* (47), 24752–24760.
- (357) Labastide, J. A.; Thompson, H. B.; Marques, S. R.; Colella, N. S.; Briseno, A. L.; Barnes, M. D. Directional Charge Separation in Isolated Organic Semiconductor Crystalline Nanowires. *Nat. Commun.* **2016**, *7*, 10629.
- (358) Paquin, F.; Latini, G.; Sakowicz, M.; Karsenti, P. L.; Wang, L.; Beljonne, D.; Stingelin, N.; Silva, C. Charge Separation in Semicrystalline Polymeric Semiconductors by Photoexcitation: Is the Mechanism Intrinsic or Extrinsic? *Phys. Rev. Lett.* **2011**, *106* (19), 197401.
- (359) Mróz, M. M.; Lüer, L.; Houarner-Rassin, C.; Anderson, H. L.; Cabanillas-Gonzalez, J. Role of Amorphous and Aggregate Phases on Field-Induced Exciton Dissociation in a Conjugated Polymer. *Phys. Rev. B: Condens. Matter Mater. Phys.* **2013**, *87* (3), 035201.
- (360) van Laarhoven, H. A.; Flipse, C. F. J.; Koeberg, M.; Bonn, M.; Hendry, E.; Orlandi, G.; Jurchescu, O. D.; Palstra, T. T. M.; Troisi, A. On the Mechanism of Charge Transport in Pentacene. *J. Chem. Phys.* **2008**, *129* (4), 044704.
- (361) Koeberg, M.; Hendry, E.; Schins, J. M.; Van Laarhoven, H. a.; Flipse, C. F. J.; Reimann, K.; Woerner, M.; Elsaesser, T.; Bonn, M. Simultaneous Ultrafast Probing of Intramolecular Vibrations and Photoinduced Charge Carriers in Rubrene Using Broadband Time-Domain THz Spectroscopy. *Phys. Rev. B: Condens. Matter Mater. Phys.* **2007**, *75* (19), 195216.
- (362) Wang, L.; Li, Q.; Shuai, Z.; Chen, L.; Shi, Q. Multiscale Study of Charge Mobility of Organic Semiconductor with Dynamic Disorders. *Phys. Chem. Chem. Phys.* **2010**, *12* (13), 3309–3314.
- (363) Smith, S. L.; Chin, A. W. Phonon-Assisted Ultrafast Charge Separation in the PCBM Band Structure. *Phys. Rev. B: Condens. Matter Mater. Phys.* **2015**, *91* (20), 201302.
- (364) Liu, T.; Troisi, A. What Makes Fullerene Acceptors Special as Electron Acceptors in Organic Solar Cells and How to Replace Them. *Adv. Mater.* **2013**, *25* (7), 1038–1041.
- (365) Ostroverkhova, O.; Cooke, D. G.; Hegmann, F. a.; Anthony, J. E.; Podzorov, V.; Gershenson, M. E.; Jurchescu, O. D.; Palstra, T. T. M. Ultrafast Carrier Dynamics in Pentacene, Functionalized Pentacene, Tetracene, and Rubrene Single Crystals. *Appl. Phys. Lett.* **2006**, *88* (16), 162101.
- (366) Tao, S.; Ohtani, N.; Uchida, R.; Miyamoto, T.; Matsui, Y.; Yada, H.; Uemura, H.; Matsuzaki, H.; Uemura, T.; Takeya, J.; et al. Relaxation Dynamics of Photoexcited Excitons in Rubrene Single Crystals Using Femtosecond Absorption Spectroscopy. *Phys. Rev. Lett.* **2012**, *109* (9), 097403.
- (367) Irkhin, P.; Najafov, H.; Podzorov, V. Steady-State Photoconductivity and Multi-Particle Interactions in High-Mobility Organic Semiconductors. *Sci. Rep.* **2015**, *5*, 15323.
- (368) Najafov, H.; Biaggio, I.; Podzorov, V.; Calhoun, M. F.; Gershenson, M. E. Primary Photoexcitations and the Origin of the Photocurrent in Rubrene Single Crystals. *Phys. Rev. Lett.* **2006**, *96* (5), 056604.
- (369) Najafov, H.; Lyu, B.; Biaggio, I.; Podzorov, V. Two Mechanisms of Exciton Dissociation in Rubrene Single Crystals. *Appl. Phys. Lett.* **2010**, *96* (18), 183302.
- (370) Mitrofanov, O.; Lang, D. V.; Kloc, C.; Wikberg, J. M.; Siegrist, T.; So, W. Y.; Sergent, M. a.; Ramirez, A. P. Oxygen-Related Band Gap State in Single Crystal Rubrene. *Phys. Rev. Lett.* **2006**, *97* (16), 166601.
- (371) Reid, O. G.; Pensack, R. D.; Song, Y.; Scholes, G. D. Rumbles, G. Charge Photogeneration in Neat Conjugated Polymers. *Chem. Mater.* **2014**, *26* (1), 561–575.
- (372) Chang, W.; Congreve, D. N.; Hontz, E.; Bahlke, M. E.; McMahon, D. P.; Reineke, S.; Wu, T. C.; Bulović, V.; Van Voorhis, T.; Baldo, M. a. Spin-Dependent Charge Transfer State Design Rules in Organic Photovoltaics. *Nat. Commun.* **2015**, *6*, 6415.
- (373) Schlenker, C. W.; Chen, K. S.; Yip, H. L.; Li, C. Z.; Bradshaw, L. R.; Ochsenbein, S. T.; Ding, F.; Li, X. S.; Gamelin, D. R.; Jen, A. K. Y.; et al. Polymer Triplet Energy Levels Need Not Limit Photocurrent Collection in Organic Solar Cells. *J. Am. Chem. Soc.* **2012**, *134* (48), 19661–19668.
- (374) Lee, M. H.; Dunitz, B. D.; Geva, E. Donor-to-Donor vs Donor-to-Acceptor Interfacial Charge Transfer States in the Phthalocyanine – Fullerene Organic Photovoltaic System. *J. Phys. Chem. Lett.* **2014**, *5*, 3810–3816.
- (375) Arkhipov, V.; Emelianova, E.; Barth, S.; Bässler, H. Ultrafast on-Chain Dissociation of Hot Excitons in Conjugated Polymers. *Phys. Rev. B: Condens. Matter Mater. Phys.* **2000**, *61* (12), 8207–8214.
- (376) Provencher, F.; Bérubé, N.; Parker, A. W.; Greetham, G. M.; Towrie, M.; Hellmann, C.; Côté, M.; Stingelin, N.; Silva, C.; Hayes, S. C. Direct Observation of Ultrafast Long-Range Charge Separation at Polymer-Fullerene Heterojunctions. *Nat. Commun.* **2014**, *5*, 4288.
- (377) Shoaee, S.; Clarke, T. M.; Huang, C.; Barlow, S.; Marder, S. R.; Heeney, M.; McCulloch, I.; Durrant, J. R. Acceptor Energy Level Control of Charge Photogeneration in Organic Donor/acceptor Blends. *J. Am. Chem. Soc.* **2010**, *132* (37), 12919–12926.
- (378) Morteani, A. C.; Sreearunothai, P.; Herz, L. M.; Friend, R. H.; Silva, C. Exciton Regeneration at Polymeric Semiconductor Heterojunctions. *Phys. Rev. Lett.* **2004**, *92* (24), 247402.
- (379) Grancini, G.; Maiuri, M.; Fazzi, D.; Petrozza, a; Egelhaaf, H.-J.; Brida, D.; Cerullo, G.; Lanzani, G. Hot Exciton Dissociation in Polymer Solar Cells. *Nat. Mater.* **2013**, *12* (1), 29–33.
- (380) Dimitrov, S. D.; Bakulin, A. a.; Nielsen, C. B.; Schroeder, B. C.; Du, J.; Bronstein, H.; McCulloch, I.; Friend, R. H.; Durrant, J. R. On the Energetic Dependence of Charge Separation in Low-Band-Gap Polymer/fullerene Blends. *J. Am. Chem. Soc.* **2012**, *134* (44), 18189–18192.
- (381) Lee, J.; Vandewal, K.; Yost, S. R.; Bahlke, M. E.; Goris, L.; Baldo, M. a.; Manca, J. V.; Voorhis, T. V. Charge Transfer State versus Hot Exciton Dissociation in Polymer-Fullerene Blended Solar Cells. *J. Am. Chem. Soc.* **2010**, *132* (34), 11878–11880.
- (382) Albrecht, S.; Vandewal, K.; Tumbleston, J. R.; Fischer, F. S. U.; Douglas, J. D.; Fréchet, J. M. J.; Ludwigs, S.; Ade, H.; Salleo, A.; Neher, D. On the Efficiency of Charge Transfer State Splitting in Polymer:fullerene Solar Cells. *Adv. Mater.* **2014**, *26* (16), 2533–2539.
- (383) Vandewal, K.; Albrecht, S.; Hoke, E. T.; Graham, K. R.; Widmer, J.; Douglas, J. D.; Schubert, M.; Mateker, W. R.; Bloking, J. T.; Burkhard, G. F.; et al. Efficient Charge Generation by Relaxed Charge-Transfer States at Organic Interfaces. *Nat. Mater.* **2014**, *13* (1), 63–68.
- (384) Vandewal, K. Interfacial Charge Transfer States in Condensed Phase Systems. *Annu. Rev. Phys. Chem.* **2016**, *67*, 113–133.
- (385) Vandewal, K.; Tvingstedt, K.; Gadisa, A.; Inganäs, O.; Manca, J. V. Relating the Open-Circuit Voltage to Interface Molecular Properties of Donor:acceptor Bulk Heterojunction Solar Cells. *Phys. Rev. B: Condens. Matter Mater. Phys.* **2010**, *81*, 125204.
- (386) Hörmann, U.; Kraus, J.; Gruber, M.; Schuhmair, C.; Linderl, T.; Grob, S.; Kapfinger, S.; Klein, K.; Stutzman, M.; Krenner, H. J.; et al. Quantification of Energy Losses in Organic Solar Cells from Temperature-Dependent Device Characteristics. *Phys. Rev. B: Condens. Matter Mater. Phys.* **2013**, *88* (23), 235307.

- (387) Pensack, R. D.; Asbury, J. B. Ultrafast Probes of Charge Transfer States in Organic Photovoltaic Materials. *Chem. Phys. Lett.* **2011**, *515* (4–6), 197–205.
- (388) Ran, N. A.; Love, J. A.; Takacs, C. J.; Sadhanala, A.; Beavers, J. K.; Collins, S. D.; Huang, Y.; Wang, M.; Friend, R. H.; Bazan, G. C.; et al. Harvesting the Full Potential of Photons with Organic Solar Cells. *Adv. Mater.* **2016**, *28* (7), 1482–1488.
- (389) Venkateshvaran, D.; Nikolka, M.; Sadhanala, A.; Lemaire, V.; Zelazny, M.; Kepa, M.; Hurhangee, M.; Kronemeijer, A. J.; Pecunia, V.; Nasrallah, I.; et al. Approaching Disorder-Free Transport in High-Mobility Conjugated Polymers. *Nature* **2014**, *515* (7527), 384–388.
- (390) Gao, F.; Tress, W.; Wang, J.; Inganäs, O. Temperature Dependence of Charge Carrier Generation in Organic Photovoltaics. *Phys. Rev. Lett.* **2015**, *114*, 128701.
- (391) Monahan, N.; Williams, K.; Kumar, B.; Nuckolls, C.; Zhu, X. Y. Direct Observation of Entropy-Driven Electron-Hole Pair Separation at an Organic Semiconductor Interface. *Phys. Rev. Lett.* **2015**, *114* (June 19), 247003.
- (392) Wang, L.; Long, R.; Prezhdov, O. V. Time-Domain Ab Initio Modeling of Photoinduced Dynamics at Nanoscale Interfaces. *Annu. Rev. Phys. Chem.* **2015**, *66* (1), 549–579.
- (393) Torabi, S.; Jahani, F.; Van Severen, I.; Kanimozhi, C.; Patil, S.; Havenith, R. W. a.; Chiechi, R. C.; Lutsen, L.; Vanderzande, D. J. M.; Cleij, T. J.; et al. Strategy for Enhancing the Dielectric Constant of Organic Semiconductors Without Sacrificing Charge Carrier Mobility and Solubility. *Adv. Funct. Mater.* **2015**, *25* (1), 150–157.
- (394) Jahani, F.; Torabi, S.; Chiechi, R. C.; Koster, L. J. A.; Hummelen, J. C. Fullerene Derivatives with Increased Dielectric Constants. *Chem. Commun.* **2014**, *50* (73), 10645–10647.
- (395) Liu, X.; Jeong, K. S.; Williams, B. P.; Vakhshouri, K.; Guo, C.; Han, K.; Gomez, E. D.; Wang, Q.; Asbury, J. B. Tuning the Dielectric Properties of Organic Semiconductors via Salt Doping. *J. Phys. Chem. B* **2013**, *117* (49), 15866–15874.
- (396) Shi, N.; Ramprasad, R. Dielectric Properties of Cu-Phthalocyanine Systems from First Principles. *Appl. Phys. Lett.* **2006**, *89* (10), 102904.
- (397) Hess, C. M.; Riley, E. a.; Reid, P. J. Dielectric Dependence of Single-Molecule Photoluminescence Intermittency: Nile Red in Poly(vinylidene Fluoride). *J. Phys. Chem. B* **2014**, *118* (29), 8905–8913.
- (398) Guo, Z.; Lee, D.; Schaller, R. D.; Zuo, X.; Lee, B.; Luo, T.; Gao, H.; Huang, L. Relationship between Interchain Interaction, Exciton Delocalization, and Charge Separation in Low-Bandgap Copolymer Blends. *J. Am. Chem. Soc.* **2014**, *136* (28), 10024–10032.
- (399) Gélinas, S.; Rao, A.; Kumar, A.; Smith, S. L.; Chin, A. W.; Clark, J.; van der Poll, T. S.; Bazan, G. C.; Friend, R. H. Ultrafast Long-Range Charge Photovoltaic Diodes. *Science (Washington, DC, U. S.)* **2014**, *343*, 512–516.
- (400) Kaake, L. G.; Moses, D.; Heeger, A. J. Charge Transfer from Delocalized Excited States in a Bulk Heterojunction Material. *Phys. Rev. B: Condens. Matter Mater. Phys.* **2015**, *91* (7), 075436.
- (401) Kaake, L.; Moses, D.; Heeger, A. Comment on “Coherence and Uncertainty in Nanostructured Organic Photovoltaics”. *J. Phys. Chem. A* **2014**, *118*, 1539.
- (402) Kaake, L.; Moses, D.; Heeger, A. Reply to “Comment on ‘Coherence and Uncertainty in Nanostructured Organic Photovoltaics’”. *J. Phys. Chem. A* **2013**, *117*, 10565.
- (403) Song, Y.; Clifton, S. N.; Pensack, R. D.; Kee, T. W.; Scholes, G. D. Vibrational Coherence Probes the Mechanism of Ultrafast Electron Transfer in Polymer–fullerene Blends. *Nat. Commun.* **2014**, *5*, 4933.
- (404) Tabachnyk, M.; Ehrler, B.; Gélinas, S.; Böhm, M. L.; Walker, B. J.; Musselman, K. P.; Friend, R. H.; Rao, A. Resonant energy transfer of triplet excitons from pentacene to PbSe nanocrystals. *Nat. Mater.* **2014**, *13*, 1033–1038.
- (405) Wu, T. C.; Thompson, N. J.; Congreve, D. N.; Hontz, E.; Yost, S. R.; Van Voorhis, T.; Baldo, M. a. Singlet Fission Efficiency in Tetracene-Based Organic Solar Cells. *Appl. Phys. Lett.* **2014**, *104* (19), 193901.
- (406) Castrucci, J. S.; Josey, D. S.; Thibau, E.; Lu, Z.-H.; Bender, T. P. Boron Subphthalocyanines as Triplet Harvesting Materials Within Organic Photovoltaics. *J. Phys. Chem. Lett.* **2015**, *6*, 3121–3125.
- (407) Thompson, N. J.; Hontz, E.; Congreve, D. N.; Bahlke, M. E.; Reineke, S.; Van Voorhis, T.; Baldo, M. a. Nanostructured Singlet Fission Photovoltaics Subject to Triplet-Charge Annihilation. *Adv. Mater.* **2014**, *26* (9), 1366–1371.
- (408) Congreve, D.; Lee, J.; Thompson, N.; Hontz, E.; Yost, S.; Reuswig, P.; Bahlke, M.; Reineke, S.; van Voorhis, T.; Baldo, M. External Quantum Efficiency above 100% in a Singlet-Exciton-Fission-Based Organic Photovoltaic Cell. *Science (Washington, DC, U. S.)* **2013**, *340*, 334–337.
- (409) Jadhav, P. J.; Mohanty, A.; Sussman, J.; Lee, J.; Baldo, M. a. Singlet Exciton Fission in Nanostructured Organic Solar Cells. *Nano Lett.* **2011**, *11* (4), 1495–1498.
- (410) Ehrler, B.; Walker, B. J.; Böhm, M. L.; Wilson, M. W. B.; Vaynzof, Y.; Friend, R. H.; Greenham, N. C. In Situ Measurement of Exciton Energy in Hybrid Singlet-Fission Solar Cells. *Nat. Commun.* **2012**, *3*, 1019.
- (411) Yang, L.; Tabachnyk, M.; Bayliss, S. L.; Bo, M. L.; Broch, K.; Greenham, N. C.; Friend, R. H.; Ehrler, B. Solution-Processable Singlet Fission Photovoltaic Devices. *Nano Lett.* **2015**, *15*, 354–358.
- (412) Rao, A.; Chow, P.; Gélinas, S.; Schlenker, C.; Li, C.; Yip, J.; Jen, A. K. Y.; Ginger, D.; Friend, R. H. The role of spin in the kinetic control of recombination in organic photovoltaics. *Nature* **2013**, *500*, 435–440.
- (413) Ostroverkhova, O.; Cooke, D. G.; Hegmann, F. a.; Tykewinski, R. R.; Parkin, S. R.; Anthony, J. E. Anisotropy of Transient Photoconductivity in Functionalized Pentacene Single Crystals. *Appl. Phys. Lett.* **2006**, *89* (19), 192113.
- (414) Day, J.; Platt, A. D.; Ostroverkhova, O.; Subramanian, S.; Anthony, J. E. Organic Semiconductor Composites: Influence of Additives on the Transient Photocurrent. *Appl. Phys. Lett.* **2009**, *94* (1), 013306.
- (415) Lee, C. H.; Yu, G.; Moses, D.; Srdanov, V.; Wei, Z.; Vardeny, Z. V. Transient and Steady-State Photoconductivity of a Solid C60 Film. *Phys. Rev. B: Condens. Matter Mater. Phys.* **1993**, *48* (11), 8506–8509.
- (416) Lane, P. A.; Cunningham, P. D.; Melinger, J. S.; Kushto, G. P.; Esenturk, O.; Heilweil, E. J. Photoexcitation Dynamics in Films of C60 and Zn Phthalocyanine with a Layered Nanostructure. *Phys. Rev. Lett.* **2012**, *108* (7), 077402.
- (417) Cabanillas-Gonzalez, J.; Virgili, T.; Gambetta, A.; Lanzani, G.; Anthopoulos, T. D.; De Leeuw, D. M. Photoinduced Transient Stark Spectroscopy in Organic Semiconductors: A Method for Charge Mobility Determination in the Picosecond Regime. *Phys. Rev. Lett.* **2006**, *96* (10), 106601.
- (418) Hendry, E.; Koeberg, M.; Schins, J.; Siebbeles, L.; Bonn, M. Ultrafast Charge Generation in a Semiconducting Polymer Studied with THz Emission Spectroscopy. *Phys. Rev. B: Condens. Matter Mater. Phys.* **2004**, *70*, 033202.
- (419) Miranda, P. B.; Moses, D.; Heeger, A. J. Ultrafast Photogeneration of Charged Polarons in Conjugated Polymer Chains. *Phys. Rev. B: Condens. Matter Mater. Phys.* **2001**, *64*, 081201.
- (420) Soti, C.; Moses, D. Terahertz Generation from Poly(p-phenylene vinylene) Photoconductive Antenna. *Synth. Met.* **2003**, *139* (3), 815–817.
- (421) Moses, D.; Okumoto, H.; Lee, C.; Heeger, A.; Ohnishi, T.; Noguchi, T. Mechanism of Carrier Generation in Poly(phenylene vinylene): Transient Photoconductivity and Photoluminescence at High Electric Fields. *Phys. Rev. B: Condens. Matter Mater. Phys.* **1996**, *54* (7), 4748–4754.
- (422) Lüer, L.; Egelhaaf, H.-J.; Oelkrug, D.; Gadermaier, C.; Cerullo, G.; Lanzani, G. Charge Carrier Photogeneration in Oligo-(phenylenevinylene) Thin Films: A Quantitative Study. *Phys. Rev. B: Condens. Matter Mater. Phys.* **2003**, *68* (15), 155313.
- (423) Hwang, I. W.; Xu, Q. H.; Soci, C.; Chen, B.; Jen, A. K. Y.; Moses, D.; Heeger, A. J. Ultrafast Spectroscopic Study of Photo-

induced Electron Transfer in an oligo(thienylenevinylene):Fullerene Composite. *Adv. Funct. Mater.* **2007**, *17* (4), 563–568.

(424) Basel, T.; Huynh, U.; Zheng, T.; Xu, T.; Yu, L.; Vardeny, Z. V. Optical, electrical, and magnetic studies of organic solar cells based on low bandgap copolymer with spin  $1/2$  radical additives. *Adv. Funct. Mater.* **2015**, *25*, 1895–1902.

(425) Cunningham, P. D.; Hayden, L. M. Carrier Dynamics Resulting from above and below Gap Excitation of P3HT and P3HT/PCBM Investigated by Optical-Pump Terahertz-Probe Spectroscopy. *J. Phys. Chem. C* **2008**, *112* (21), 7928–7935.

(426) Hendry, E.; Koeberg, M.; Schins, J. M.; Siebbeles, L. D. A.; Bonn, M. Free Carrier Photogeneration in Polythiophene versus Poly(phenylene Vinylene) Studied with THz Spectroscopy. *Chem. Phys. Lett.* **2006**, *432* (4–6), 441–445.

(427) Piris, J.; Dykstra, T. E.; Bakulin, A. a.; Van Loosdrecht, P. H. M.; Knulst, W.; Trinh, M. T.; Schins, J. M.; Siebbeles, L. D. a. Photogeneration and Ultrafast Dynamics of Excitons and Charges in P3HT/PCBM Blends. *J. Phys. Chem. C* **2009**, *113* (32), 14500–14506.

(428) Devižis, A.; Serbenta, A.; Meerholz, K.; Hertel, D.; Gulbinas, V. Ultrafast Dynamics of Carrier Mobility in a Conjugated Polymer Probed at Molecular and Microscopic Length Scales. *Phys. Rev. Lett.* **2009**, *103* (2), 027404.

(429) Cunningham, P. D.; Hayden, L. M.; Yip, H.-L.; Jen, A. K.-Y. Charge Carrier Dynamics in Metalated Polymers Investigated by Optical-Pump Terahertz-Probe Spectroscopy. *J. Phys. Chem. B* **2009**, *113* (47), 15427–15432.

(430) Graupner, W.; Cerullo, G.; Lanzani, G.; Nisoli, M.; List, E.; Leising, G.; De Silvestri, S. Direct Observation of Ultrafast Field-Induced Charge Generation in Ladder-Type Poly(Para-Phenylene). *Phys. Rev. Lett.* **1998**, *81* (15), 3259–3262.

(431) Zaushitsyn, Y.; Gulbinas, V.; Zigmantas, D.; Zhang, F.; Inganäs, O.; Sundström, V.; Yartsev, A. Ultrafast Light-Induced Charge Pair Formation Dynamics in poly[3-(2'-Methoxy-5' Octylphenyl)-thiophene]. *Phys. Rev. B: Condens. Matter Mater. Phys.* **2004**, *70* (7), 075202.

(432) Virgili, T.; Marinotto, D.; Manzoni, C.; Cerullo, G.; Lanzani, G. Ultrafast Intrachain Photoexcitation of Polymeric Semiconductors. *Phys. Rev. Lett.* **2005**, *94* (11), 117402.

(433) Brutting, W.; Adachi, C. *Physics of Organic Semiconductors*, 2nd ed.; Wiley-VCH Verlag GmbH & Co. KGaA: 2012.

(434) Coropceanu, V.; Cornil, J.; Da Silva Filho, D. a.; Olivier, Y.; Silbey, R. J.; Bredas, J.-L. Charge Transport in Organic Semiconductors. *Chem. Rev.* **2007**, *107*, 926–952.

(435) Siringhaus, H.; Sakanoue, T.; Chang, J. F. Charge-Transport Physics of High-Mobility Molecular Semiconductors. *Phys. Status Solidi B* **2012**, *249* (9), 1655–1676.

(436) Troisi, A. Charge Transport in High Mobility Molecular Semiconductors: Classical Models and New Theories. *Chem. Soc. Rev.* **2011**, *40* (5), 2347–2358.

(437) Sokolov, A. N.; Atahan-Evrenk, S.; Mondal, R.; Akkerman, H. B.; Sánchez-Carrera, R. S.; Granados-Focil, S.; Schrier, J.; Mannsfeld, S. C. B.; Zoombelt, A. P.; Bao, Z.; et al. From Computational Discovery to Experimental Characterization of a High Hole Mobility Organic Crystal. *Nat. Commun.* **2011**, *2*, 437.

(438) Yavuz, I.; Martin, B. N.; Park, J.; Houk, K. N. Theoretical Study of the Molecular Ordering, Paracrystallinity, and Charge Mobilities of Oligomers in Different Crystalline Phases. *J. Am. Chem. Soc.* **2015**, *137*, 2856–2866.

(439) Vehoff, T.; Chung, Y. S.; Johnston, K.; Troisi, A.; Yoon, D. Y.; Andrienko, D. Charge Transport in Self-Assembled Semiconducting Organic Layers: Role of Dynamic and Static Disorder. *J. Phys. Chem. C* **2010**, *114* (23), 10592–10597.

(440) Vehoff, T.; Baumeier, B.; Troisi, A.; Andrienko, D. Charge Transport in Organic Crystals: Role of Disorder and Topological Connectivity. *J. Am. Chem. Soc.* **2010**, *132* (36), 11702–11708.

(441) Schweicher, G.; Lemaure, V.; Niebel, C.; Ruzié, C.; Diao, Y.; Goto, O.; Lee, W.-Y.; Kim, Y.; Arlin, J.-B.; Karpinska, J.; et al. Bulky End-Capped [1]Benzothieno[3,2-B]benzothiophenes: Reaching

High-Mobility Organic Semiconductors by Fine Tuning of the Crystalline Solid-State Order. *Adv. Mater.* **2015**, *27*, 3066–3072.

(442) Schweicher, G.; Olivier, Y.; Lemaure, V.; Geerts, Y. H. What Currently Limits Charge Carrier Mobility in Crystals of Molecular Semiconductors? *Isr. J. Chem.* **2014**, *54* (5–6), 595–620.

(443) Stafström, S. Electron Localization and the Transition from Adiabatic to Nonadiabatic Charge Transport in Organic Conductors. *Chem. Soc. Rev.* **2010**, *39* (7), 2484–2499.

(444) Troisi, A. The Speed Limit for Sequential Charge Hopping in Molecular Materials. *Org. Electron.* **2011**, *12* (12), 1988–1991.

(445) Li, Y.; Yi, Y.; Coropceanu, V.; Br, J. Optical Conductivity and Optical Effective Mass in a High-Mobility Organic Semiconductor. *Phys. Rev. B: Condens. Matter Mater. Phys.* **2014**, *90*, 245112.

(446) Ortmann, F.; Bechstedt, F.; Hannewald, K. Charge Transport in Organic Crystals: Interplay of Band Transport, Hopping and Electron-Phonon Scattering. *New J. Phys.* **2010**, *12*, 023011.

(447) Ortmann, F.; Bechstedt, F.; Hannewald, K. Theory of Charge Transport in Organic Crystals: Beyond Holstein's Small-Polaron Model. *Phys. Rev. B: Condens. Matter Mater. Phys.* **2009**, *79* (23), 235206.

(448) Yi, H. T.; Garstein, Y. N.; Podzorov, V. Charge Carrier Coherence and Hall Effect in Organic Semiconductors. *Sci. Rep.* **2016**, *6* (1), 23650.

(449) Fukami, T.; Ishii, H.; Kobayashi, N.; Uemura, T.; Sakai, K.; Okada, Y.; Takeya, J.; Hirose, K. Correlation between Thermal Fluctuation Effects and Phase Coherence Factor in Carrier Transport of Single-Crystal Organic Semiconductors. *Appl. Phys. Lett.* **2015**, *106* (14), 143302.

(450) Ortmann, F.; Bechstedt, F.; Hannewald, K. Characteristics of Small- and Large-Polaron Motion in Organic Crystals. *J. Phys.: Condens. Matter* **2010**, *22* (46), 465802.

(451) Cheng, Y.-C.; Silbey, R. J. A Unified Theory for Charge-Carrier Transport in Organic Crystals. *J. Chem. Phys.* **2008**, *128* (11), 114713.

(452) Nan, G.; Shi, Q.; Shuai, Z.; Li, Z. Influences of Molecular Packing on the Charge Mobility of Organic Semiconductors: From Quantum Charge Transfer Rate Theory beyond the First-Order Perturbation. *Phys. Chem. Chem. Phys.* **2011**, *13* (20), 9736–9746.

(453) Shuai, Z.; Geng, H.; Xu, W.; Liao, Y.; André, J.-M. From Charge Transport Parameters to Charge Mobility in Organic Semiconductors through Multiscale Simulation. *Chem. Soc. Rev.* **2014**, *43* (8), 2662–2679.

(454) Munn, R. W.; Silbey, R. Theory of Electronic Transport in Molecular Crystals. II. Zeroth Order States Incorporating Nonlocal Linear Electron-phonon Coupling. *J. Chem. Phys.* **1985**, *83* (4), 1843.

(455) Hannewald, K.; Bobbert, P. Anisotropy Effects in Phonon-Assisted Charge-Carrier Transport in Organic Molecular Crystals. *Phys. Rev. B: Condens. Matter Mater. Phys.* **2004**, *69* (7), 075212.

(456) Hannewald, K.; Stojanović, V.; Schellekens, J.; Bobbert, P.; Kresse, G.; Hafner, J. Theory of Polaron Bandwidth Narrowing in Organic Molecular Crystals. *Phys. Rev. B: Condens. Matter Mater. Phys.* **2004**, *69* (7), 075211.

(457) Troisi, A.; Orlandi, G. Charge-Transport Regime of Crystalline Organic Semiconductors: Diffusion Limited by Thermal off-Diagonal Electronic Disorder. *Phys. Rev. Lett.* **2006**, *96* (8), 086601.

(458) Troisi, A.; Orlandi, G.; Anthony, J. E. Electronic Interactions and Thermal Disorder in Molecular Crystals Containing Cofacial Pentacene Units. *Chem. Mater.* **2005**, *17* (20), 5024–5031.

(459) Troisi, A. Dynamic Disorder in Molecular Semiconductors: Charge Transport in Two Dimensions. *J. Chem. Phys.* **2011**, *134* (3), 034702.

(460) Troisi, A. Prediction of the Absolute Charge Mobility of Molecular Semiconductors: The Case of Rubrene. *Adv. Mater.* **2007**, *19* (15), 2000–2004.

(461) Podzorov, V.; Menard, E.; Borisov, a.; Kiryukhin, V.; Rogers, J. a.; Gershenson, M. E. Intrinsic Charge Transport on the Surface of Organic Semiconductors. *Phys. Rev. Lett.* **2004**, *93*, 086602.

(462) Fratini, S.; Ciuchi, S. Bandlike Motion and Mobility Saturation in Organic Molecular Semiconductors. *Phys. Rev. Lett.* **2009**, *103* (26), 266601.

- (463) Song, L.; Shi, Q. A New Approach to Calculate Charge Carrier Transport Mobility in Organic Molecular Crystals from Imaginary Time Path Integral Simulations. *J. Chem. Phys.* **2015**, *142* (17), 174103.
- (464) Ribeiro, L., Jr.; Stafström, S. Polaron Stability in Molecular Semiconductors: Theoretical Insight into the Impact of the. *Phys. Chem. Chem. Phys.* **2015**, *17*, 8973–8982.
- (465) Shuai, Z.; Wang, L.; Li, Q. Evaluation of Charge Mobility in Organic Materials: From Localized to Delocalized Descriptions at a First-Principles Level. *Adv. Mater.* **2011**, *23* (9), 1145–1153.
- (466) Nan, G.; Yang, X.; Wang, L.; Shuai, Z.; Zhao, Y. Nuclear Tunneling Effects of Charge Transport in Rubrene, Tetracene, and Pentacene. *Phys. Rev. B: Condens. Matter Mater. Phys.* **2009**, *79* (11), 115203.
- (467) Lin, L.; Geng, H.; Shuai, Z.; Luo, Y. Theoretical Insights into the Charge Transport in Perylene Diimides Based N-Type Organic Semiconductors. *Org. Electron.* **2012**, *13* (11), 2763–2772.
- (468) Geng, H.; Peng, Q.; Wang, L.; Li, H.; Liao, Y.; Ma, Z.; Shuai, Z. Toward Quantitative Prediction of Charge Mobility in Organic Semiconductors: Tunneling Enabled Hopping Model. *Adv. Mater.* **2012**, *24*, 3568–3572.
- (469) Li, Y.; Yi, Y.; Coropceanu, V.; Brédas, J. L. Symmetry Effects on Nonlocal Electron-Phonon Coupling in Organic Semiconductors. *Phys. Rev. B: Condens. Matter Mater. Phys.* **2012**, *85* (24), 245201.
- (470) Ciuchi, S.; Fratini, S.; Mayou, D. Transient Localization in Crystalline Organic Semiconductors. *Phys. Rev. B: Condens. Matter Mater. Phys.* **2011**, *83* (8), 081202.
- (471) Zhong, X.; Zhao, Y.; Cao, J. Coherent Quantum Transport in Disordered Systems: II. Temperature Dependence of Carrier Diffusion Coefficients from the Time-Dependent Wavepacket Diffusion Method. *New J. Phys.* **2014**, *16*, 045009.
- (472) Ortmann, F.; Roche, S. Polaron Transport in Organic Crystals: Temperature Tuning of Disorder Effects. *Phys. Rev. B: Condens. Matter Mater. Phys.* **2011**, *84* (18), 180302.
- (473) Wang, L.; Beljonne, D. Flexible Surface Hopping Approach to Model the Crossover from Hopping to Band-like Transport in Organic Crystals. *J. Phys. Chem. Lett.* **2013**, *4* (11), 1888–1894.
- (474) Wang, L.; Beljonne, D. Charge Transport in Organic Semiconductors: Assessment of the Mean Field Theory in the Hopping Regime. *J. Chem. Phys.* **2013**, *139* (6), 064316.
- (475) Ciuchi, S.; Fratini, S. Electronic Transport and Quantum Localization Effects in Organic Semiconductors. *Phys. Rev. B: Condens. Matter Mater. Phys.* **2012**, *86* (24), 245201.
- (476) Jang, S.; Berkelbach, T. C.; Reichman, D. R. Coherent Quantum Dynamics in Donor-Bridge-Acceptor Systems: Beyond the Hopping and Super-Exchange Mechanisms. *New J. Phys.* **2013**, *15*, 105020.
- (477) Geng, H.; Zheng, X.; Shuai, Z.; Zhu, L.; Yi, Y. Understanding the Charge Transport and Polarities in Organic Donor-Acceptor Mixed-Stack Crystals: Molecular Insights from the Super-Exchange Couplings. *Adv. Mater.* **2015**, *27* (8), 1443–1449.
- (478) Zhu, L.; Yi, Y.; Fonari, A.; Corbin, N. S.; Coropceanu, V.; Brédas, J. L. Electronic Properties of Mixed-Stack Organic Charge-Transfer Crystals. *J. Phys. Chem. C* **2014**, *118* (26), 14150–14156.
- (479) Zech, T.; Mulet, R.; Wellens, T.; Buchleitner, A. Centrosymmetry Enhances Quantum Transport in Disordered Molecular Networks. *New J. Phys.* **2014**, *16*, 055002.
- (480) Nenashev, A.; Oelerich, J.; Baranovskii, S. D. Theoretical Tools for the Description of Charge Transport in Disordered Organic Semiconductors. *J. Phys.: Condens. Matter* **2015**, *27*, 093201.
- (481) Baranovskii, S. D. Theoretical Description of Charge Transport in Disordered Organic Semiconductors. *Phys. Status Solidi B* **2014**, *251* (3), 487–525.
- (482) Bäessler, H.; Köhler, A. Charge Transport in Organic Semiconductors. In *Top. Curr. Chem.*; Metzger, R., Ed.; **2012**; Vol. 312, pp. 1–65, DOI: 10.1007/128\_2011\_218.
- (483) Kordt, P.; van der Holst, J. J. M.; Helwi, M.; Kowalsky, W.; May, F.; Badinski, A.; Lennartz, C.; Andrienko, D. Modeling of Organic Light Emitting Diodes: From Molecular to Device Properties. *Adv. Funct. Mater.* **2015**, *25*, 1955–1971.
- (484) Coehoorn, R.; Bobbert, P. A. Effects of Gaussian Disorder on Charge Carrier Transport and Recombination in Organic Semiconductors. *Phys. Status Solidi A* **2012**, *209* (12), 2354–2377.
- (485) Knapp, E.; Häusermann, R.; Schwarzenbach, H. U.; Ruhstaller, B. Numerical Simulation of Charge Transport in Disordered Organic Semiconductor Devices. *J. Appl. Phys.* **2010**, *108* (5), 054504.
- (486) Massé, a.; Coehoorn, R.; Bobbert, P. a. Universal Size-Dependent Conductance Fluctuations in Disordered Organic Semiconductors. *Phys. Rev. Lett.* **2014**, *113* (11), 116604.
- (487) Van Mensfoort, S. L. M.; Shabro, V.; De Vries, R. J.; Janssen, R. a J.; Coehoorn, R. Hole Transport in the Organic Small Molecule Material  $\alpha$ -NPD: Evidence for the Presence of Correlated Disorder. *J. Appl. Phys.* **2010**, *107* (11), 113710.
- (488) Nenashev, A. V.; Jansson, F.; Oelerich, J. O.; Huemmer, D.; Dvurechenskii, A. V.; Gebhard, F.; Baranovskii, S. D. Advanced Percolation Solution for Hopping Conductivity. *Phys. Rev. B: Condens. Matter Mater. Phys.* **2013**, *87* (23), 235204.
- (489) Vissenberg, M. C. J. M.; Matters, M. Theory of the Field-Effect Mobility in Amorphous Organic Transistors. *Phys. Rev. B: Condens. Matter Mater. Phys.* **1998**, *57* (20), 12964.
- (490) Brondijk, J. J.; Roelofs, W. S. C.; Mathijssen, S. G. J.; Shehu, A.; Cramer, T.; Biscarini, F.; Blom, P. W. M.; De Leeuw, D. M. Two-Dimensional Charge Transport in Disordered Organic Semiconductors. *Phys. Rev. Lett.* **2012**, *109* (5), 056601.
- (491) Kronemeijer, A. J.; Pecunia, V.; Venkateshvaran, D.; Nikolka, M.; Sadhanala, A.; Moriarty, J.; Szumilo, M.; Sirringhaus, H. Two-Dimensional Carrier Distribution in Top-Gate Polymer Field-Effect Transistors: Correlation between Width of Density of Localized States and Urbach Energy. *Adv. Mater.* **2014**, *26* (5), 728–733.
- (492) Novikov, S.; Dunlap, D.; Kenkre, V.; Parris, P.; Vannikov, A. Essential Role of Correlations in Governing Charge Transport in Disordered Organic Materials. *Phys. Rev. Lett.* **1998**, *81*, 4472.
- (493) Bouhassoune, M.; Mensfoort, S. L. M. V.; Bobbert, P. a.; Coehoorn, R. Carrier-Density and Field-Dependent Charge-Carrier Mobility in Organic Semiconductors with Correlated Gaussian Disorder. *Org. Electron.* **2009**, *10* (3), 437–445.
- (494) Cottaar, J.; Coehoorn, R.; Bobbert, P. a. Scaling Theory for Percolative Charge Transport in Disordered Molecular Semiconductors. *Phys. Rev. B: Condens. Matter Mater. Phys.* **2012**, *85*, 245205.
- (495) Fishchuk, I. I.; Kadashchuk, A.; Hoffmann, S. T.; Athanasopoulos, S.; Genoe, J.; Bäessler, H.; Köhler, A. Unified Description for Hopping Transport in Organic Semiconductors Including Both Energetic Disorder and Polaronic Contributions. *Phys. Rev. B: Condens. Matter Mater. Phys.* **2013**, *88* (12), 125202.
- (496) Salleo, A.; Chen, T. W.; Völkel, A. R.; Wu, Y.; Liu, P.; Ong, B. S.; Street, R. a. Intrinsic Hole Mobility and Trapping in a Regioregular Poly(thiophene). *Phys. Rev. B: Condens. Matter Mater. Phys.* **2004**, *70* (11), 115311.
- (497) Dacuña, J.; Salleo, A. Modeling Space-Charge-Limited Currents in Organic Semiconductors: Extracting Trap Density and Mobility. *Phys. Rev. B: Condens. Matter Mater. Phys.* **2011**, *84* (19), 195209.
- (498) Street, R.; Song, K.; Northrup, J.; Cowan, S. Photoconductivity Measurements of the Electronic Structure of Organic Solar Cells. *Phys. Rev. B: Condens. Matter Mater. Phys.* **2011**, *83* (16), 165207.
- (499) Mehraeen, S.; Coropceanu, V.; Bredas, J. L. Role of Band States and Trap States in the Electrical Properties of Organic Semiconductors: Hopping versus Mobility Edge Model. *Phys. Rev. B: Condens. Matter Mater. Phys.* **2013**, *87* (19), 195209.
- (500) Olthof, S.; Mehraeen, S.; Mohapatra, S.; Barlow, S.; Coropceanu, V.; Bredas, J.-L.; Marder, S.; Kahn, A. Ultralow Doping in Organic Semiconductors: Evidence of Trap Filling. *Phys. Rev. Lett.* **2012**, *109*, 176601.
- (501) Kwiatkowski, J. J.; Jimison, L. H.; Salleo, A.; Spakowitz, A. J. A Boltzmann-Weighted Hopping Model of Charge Transport in Organic Semicrystalline Films. *J. Appl. Phys.* **2011**, *109* (11), 113720.

- (502) Park, S. K.; Varghese, S.; Kim, J. H.; Yoon, S. J.; Kwon, O. K.; An, B. K.; Gierschner, J.; Park, S. Y. Tailor-Made Highly Luminescent and Ambipolar Transporting Organic Mixed Stacked Charge-Transfer Crystals: An Isometric Donor-Acceptor Approach. *J. Am. Chem. Soc.* **2013**, *135* (12), 4757–4764.
- (503) Koster, L. J. a. Charge Carrier Mobility in Disordered Organic Blends for Photovoltaics. *Phys. Rev. B: Condens. Matter Mater. Phys.* **2010**, *81* (20), 205318.
- (504) Woellner, C. F.; Li, Z.; Freire, J. a.; Lu, G.; Nguyen, T. Q. Charge Carrier Mobility in a Two-Phase Disordered Organic System in the Low-Carrier Concentration Regime. *Phys. Rev. B: Condens. Matter Mater. Phys.* **2013**, *88* (12), 125311.
- (505) Fischer, J.; Widmer, J.; Kleemann, H.; Tress, W.; Koerner, C.; Riede, M.; Leo, K. A Charge Carrier Transport Model for Donor-Acceptor Blend Layers. *J. Appl. Phys.* **2015**, *117*, 045501.
- (506) Karl, N. Charge Carrier Transport in Organic Semiconductors. *Synth. Met.* **2003**, *133–134*, 649–657.
- (507) Pundsack, T. J.; Haugen, N. O.; Johnstone, L. R.; Frisbie, C. D.; Lidberg, R. L. Temperature Dependent c-Axis Hole Mobilities in Rubrene Single Crystals Determined by Time-of-Flight. *Appl. Phys. Lett.* **2015**, *106* (11), 113301.
- (508) Jurchescu, O. D.; Baas, J.; Palstra, T. T. M. Effect of Impurities on the Mobility of Single Crystal Pentacene. *Appl. Phys. Lett.* **2004**, *84* (16), 3061–3063.
- (509) Tao, S.; Matsuzaki, H.; Uemura, H.; Yada, H.; Uemura, T.; Takeya, J.; Hasegawa, T.; Okamoto, H. Optical Pump-Probe Spectroscopy of Photocarriers in Rubrene Single Crystals. *Phys. Rev. B: Condens. Matter Mater. Phys.* **2011**, *83* (7), 075204.
- (510) Li, Z. Q.; Podzorov, V.; Sai, N.; Martin, M. C.; Gershenson, M. E.; Di Ventra, M.; Basov, D. N. Light Quasiparticles Dominate Electronic Transport in Molecular Crystal Field-Effect Transistors. *Phys. Rev. Lett.* **2007**, *99* (1), 016403.
- (511) Podzorov, V.; Menard, E.; Rogers, J. a.; Gershenson, M. E. Hall Effect in the Accumulation Layers on the Surface of Organic Semiconductors. *Phys. Rev. Lett.* **2005**, *95* (22), 226601.
- (512) Gershenson, M. E.; Podzorov, V.; Morpurgo, a. F. Colloquium: Electronic Transport in Single-Crystal Organic Transistors. *Rev. Mod. Phys.* **2006**, *78* (3), 973–989.
- (513) Sakanoue, T.; Siringhaus, H. Band-like Temperature Dependence of Mobility in a Solution-Processed Organic Semiconductor. *Nat. Mater.* **2010**, *9* (9), 736–740.
- (514) Xie, W.; Willa, K.; Wu, Y.; Häusermann, R.; Takimiya, K.; Batlogg, B.; Frisbie, C. D. Temperature-Independent Transport in High-Mobility Dinaphtho-Thieno-Thiophene (DNTT) Single Crystal Transistors. *Adv. Mater.* **2013**, *25* (25), 3478–3484.
- (515) Ohtomo, M.; Suzuki, T.; Shimada, T.; Hasegawa, T. Band Dispersion of Quasi-Single Crystal Thin Film Phase Pentacene Monolayer Studied by Angle-Resolved Photoelectron Spectroscopy. *Appl. Phys. Lett.* **2009**, *95* (2009), 123308.
- (516) Hatch, R. C.; Huber, D. L.; Höchst, H. Electron-Phonon Coupling in Crystalline Pentacene Films. *Phys. Rev. Lett.* **2010**, *104* (4), 047601.
- (517) Jurchescu, O. D.; Popinciuc, M.; van Wees, B. J.; Palstra, T. T. M. Interface-Controlled, High-Mobility Organic Transistors. *Adv. Mater.* **2007**, *19* (5), 688–692.
- (518) Lee, S.; Koo, B.; Shin, J.; Lee, E.; Park, H.; Kim, H. Effects of Hydroxyl Groups in Polymeric Dielectrics on Organic Transistor Performance. *Appl. Phys. Lett.* **2006**, *88*, 162109.
- (519) Lin, Y.-J.; Tsao, H.-Y.; Liu, D.-S. Hall-Effect Mobility of Pentacene Films Prepared by the Thermal Evaporating Method with Different Substrate Temperature. *Appl. Phys. Lett.* **2012**, *101* (1), 013302.
- (520) Engelbrecht, S. G.; Prinz, M.; Arend, T. R.; Kersting, R. Terahertz Spectroscopy on Hole Transport in Pentacene Thin Films. *Appl. Phys. Lett.* **2014**, *105* (1), 012101.
- (521) Lee, J. Y.; Roth, S.; Park, Y. W. Anisotropic Field Effect Mobility in Single Crystal Pentacene. *Appl. Phys. Lett.* **2006**, *88* (25), 252106.
- (522) Kakuta, H.; Hirahara, T.; Matsuda, I.; Nagao, T.; Hasegawa, S.; Ueno, N.; Sakamoto, K. Electronic Structures of the Highest Occupied Molecular Orbital Bands of a Pentacene Ultrathin Film. *Phys. Rev. Lett.* **2007**, *98* (24), 247601.
- (523) Hatch, R. C.; Huber, D. L.; Höchst, H. HOMO Band Structure and Anisotropic Effective Hole Mass in Thin Crystalline Pentacene Films. *Phys. Rev. B: Condens. Matter Mater. Phys.* **2009**, *80* (8), 081411.
- (524) Germs, W. C.; Guo, K.; Janssen, R. a. J.; Kemerink, M. Unusual Thermoelectric Behavior Indicating a Hopping to Bandlike Transport Transition in Pentacene. *Phys. Rev. Lett.* **2012**, *109* (1), 016601.
- (525) Lee, B.; Chen, Y.; Fu, D.; Yi, H. T.; Czelen, K.; Najafov, H.; Podzorov, V. Trap Healing and Ultralow-Noise Hall Effect at the Surface of Organic Semiconductors. *Nat. Mater.* **2013**, *12* (12), 1125–1129.
- (526) Zhang, Y.; Qiao, J.; Gao, S.; Hu, F.; He, D.; Wu, B.; Yang, Z.; Xu, B.; Li, Y.; Shi, Y.; et al. Probing Carrier Transport and Structure-Property Relationship of Highly Ordered Organic Semiconductors at the Two-Dimensional Limit. *Phys. Rev. Lett.* **2016**, *116* (1), 016602.
- (527) Diao, Y.; Lenn, K. M.; Lee, W.; Blood-forsythe, M. A.; Xu, J.; Mao, Y.; Kim, Y.; Reinspach, J. A.; Park, S.; Xue, G.; et al. Understanding Polymorphism in Organic Semiconductor Thin Films through Nanoconfinement. *J. Am. Chem. Soc.* **2014**, *136*, 17046–17057.
- (528) James, D. T.; Frost, J. M.; Wade, J.; Nelson, J.; Kim, J. S. Controlling Microstructure of Pentacene Derivatives by Solution Processing: Impact of Structural Anisotropy on Optoelectronic Properties. *ACS Nano* **2013**, *7* (9), 7983–7991.
- (529) Siringhaus, H. 25th Anniversary Article: Organic Field-Effect Transistors: The Path beyond Amorphous Silicon. *Adv. Mater.* **2014**, *26* (9), 1319–1335.
- (530) Hegmann, F. A.; Ostroverkhova, O.; Cooke, D. G. Probing Organic Semiconductors with Terahertz Pulses. In *Photophysics of Molecular Materials: From Single Molecules to Single Crystals*; Wiley-VCH Verlag GmbH & Co. KGaA: 2006; pp 367–428.
- (531) Podzorov, V. Organic Single Crystals: Addressing the Fundamentals of Organic Electronics. *MRS Bull.* **2013**, *38* (01), 15–24.
- (532) Sundar, V. C.; Zaumseil, J.; Podzorov, V.; Menard, E.; Willett, R. L.; Someya, T.; Gershenson, M. E.; Rogers, J. a. Elastomeric Transistor Stamps: Transport in Organic Crystals. *Science* **2004**, *303*, 1644–1646.
- (533) Podzorov, V.; Menard, E.; Borissov, A.; Kiryukhin, V.; Rogers, J. a.; Gershenson, M. E. Intrinsic Charge Transport on the Surface of Organic Semiconductors. *Phys. Rev. Lett.* **2004**, *93* (8), 086602.
- (534) Machida, S.; Nakayama, Y.; Duhm, S.; Xin, Q.; Funakoshi, A.; Ogawa, N.; Kera, S.; Ueno, N.; Ishii, H. Highest-Occupied-Molecular-Orbital Band Dispersion of Rubrene Single Crystals as Observed by Angle-Resolved Ultraviolet Photoelectron Spectroscopy. *Phys. Rev. Lett.* **2010**, *104* (15), 156401.
- (535) Yamane, H.; Kosugi, N. Substituent-Induced Intermolecular Interaction in Organic Crystals Revealed by Precise Band-Dispersion Measurements. *Phys. Rev. Lett.* **2013**, *111* (8), 086602.
- (536) Illig, S.; Eggeman, A. S.; Troisi, A.; Jiang, L.; Warwick, C.; Nikolka, M.; Schweicher, G.; Yeates, S. G.; Henri Geerts, Y.; Anthony, J. E.; et al. Reducing Dynamic Disorder in Small-Molecule Organic Semiconductors by Suppressing Large-Amplitude Thermal Motions. *Nat. Commun.* **2016**, *7*, 10736.
- (537) Kubo, T.; Häusermann, R.; Tsurumi, J.; Soeda, J.; Okada, Y.; Yamashita, Y.; Akamatsu, N.; Shishido, A.; Mitsui, C.; Okamoto, T.; et al. Suppressing Molecular Vibrations in Organic Semiconductors by Inducing Strain. *Nat. Commun.* **2016**, *7*, 11156.
- (538) Giri, G.; Verploegen, E.; Mannsfeld, S. C. B.; Atahan-Evrenk, S.; Kim, D. H.; Lee, S. Y.; Becerril, H. a.; Aspuru-Guzik, A.; Toney, M. F.; Bao, Z. Tuning Charge Transport in Solution-Sheared Organic Semiconductors Using Lattice Strain. *Nature* **2011**, *480* (7378), 504–508.
- (539) Zheng, X.; Geng, H.; Yi, Y.; Li, Q.; Jiang, Y.; Wang, D.; Shuai, Z. Understanding Lattice Strain-Controlled Charge Transport in

Organic Semiconductors: A Computational Study. *Adv. Funct. Mater.* **2014**, *24* (35), 5531–5540.

(540) Emin, D. *Polarons*; Cambridge University Press: 2013.

(541) Uemura, T.; Yamagishi, M.; Soeda, J.; Takatsuki, Y.; Okada, Y.; Nakazawa, Y.; Takeya, J. Temperature Dependence of the Hall Effect in Pentacene Field-Effect Transistors: Possibility of Charge Decoherence by Molecular Fluctuations. *Phys. Rev. B: Condens. Matter Mater. Phys.* **2012**, *85*, 035313.

(542) Sakai, K.; Okada, Y.; Uemura, T.; Tsurumi, J.; Häusermann, R.; Matsui, H.; Fukami, T.; Ishii, H.; Kobayashi, N.; Hirose, K.; et al. The Emergence of Charge Coherence in Soft Molecular Organic Semiconductors via the Suppression of Thermal Fluctuations. *NPG Asia Mater.* **2016**, *8*, e252.

(543) Bakulin, A. A.; Lovrincic, R.; Yu, X.; Selig, O.; Bakker, H. J.; Rezus, Y. L. A.; Cahen, D.; Nayak, P. K.; Fonari, A.; Coropceanu, V.; et al. Mode-Selective Vibrational Modulation of Charge Transport in Organic Electronic Devices. *Nat. Commun.* **2015**, *6*, 7880.

(544) Jiang, Y.; Geng, H.; Shi, W.; Peng, Q.; Zheng, X.; Shuai, Z. Theoretical Prediction of Isotope Effects on Charge Transport in Organic Semiconductors. *J. Phys. Chem. Lett.* **2014**, *5*, 2267–2273.

(545) Jiang, Y.; Peng, Q.; Geng, H.; Ma, H.; Shuai, Z. Negative Isotope Effect for Charge Transport in Acenes and Derivatives – a Theoretical Conclusion. *Phys. Chem. Chem. Phys.* **2015**, *17* (5), 3273–3280.

(546) Xie, W.; McGarry, K. A.; Liu, F.; Wu, Y.; Ruden, P. P.; Douglas, C. J.; Frisbie, C. D. High-Mobility Transistors Based on Single Crystals of Isotopically Substituted Rubrene- D 28. *J. Phys. Chem. C* **2013**, *117* (22), 11522–11529.

(547) Xie, W.; Wang, S.; Zhang, X.; Leighton, C.; Frisbie, C. D. High Conductance 2D Transport around the Hall Mobility Peak in Electrolyte-Gated Rubrene Crystals. *Phys. Rev. Lett.* **2014**, *113* (24), 246602.

(548) Goetz, K. P.; Fonari, a.; Vermeulen, D.; Hu, P.; Jiang, H.; Diemer, P. J.; Ward, J. W.; Payne, M. E.; Day, C. S.; Kloc, C.; et al. Freezing-in Orientational Disorder Induces Crossover from Thermally-Activated to Temperature-Independent Transport in Organic Semiconductors. *Nat. Commun.* **2014**, *5*, 5642.

(549) Vukmirović, N.; Ponseca, C. S.; Némec, H.; Yartsev, A.; Sundström, V. Insights into the Charge Carrier Terahertz Mobility in Polyfluorenes from Large-Scale Atomistic Simulations and Time-Resolved Terahertz Spectroscopy. *J. Phys. Chem. C* **2012**, *116* (37), 19665–19672.

(550) Mozer, A. J.; Dennler, G.; Sariciftci, N. S.; Westerling, M.; Pivrikas, A.; Österbacka, R.; Juška, G. Time-Dependent Mobility and Recombination of the Photoinduced Charge Carriers in Conjugated Polymer/fullerene Bulk Heterojunction Solar Cells. *Phys. Rev. B: Condens. Matter Mater. Phys.* **2005**, *72* (3), 035217.

(551) Bange, S.; Schubert, M.; Neher, D. Charge Mobility Determination by Current Extraction under Linear Increasing Voltages: Case of Nonequilibrium Charges and Field-Dependent Mobilities. *Phys. Rev. B: Condens. Matter Mater. Phys.* **2010**, *81* (3), 035209.

(552) Ponseca, C. S.; Yartsev, A.; Wang, E.; Andersson, M. R.; Vithanage, D.; Sundström, V. Ultrafast Terahertz Photoconductivity of Bulk Heterojunction Materials Reveals High Carrier Mobility up to Nanosecond Time Scale. *J. Am. Chem. Soc.* **2012**, *134* (29), 11836–11839.

(553) Philippa, B.; Stolterfoht, M.; Burn, P. L.; Juška, G.; Meredith, P.; White, R. D.; Pivrikas, A. The Impact of Hot Charge Carrier Mobility on Photocurrent Losses in Polymer-Based Solar Cells. *Sci. Rep.* **2014**, *4*, 5695.

(554) Shuttle, C. G.; Hamilton, R.; Nelson, J.; O'Regan, B. C.; Durrant, J. R. Measurement of Charge-Density Dependence of Carrier Mobility in an Organic Semiconductor Blend. *Adv. Funct. Mater.* **2010**, *20*, 698–702.

(555) Nelson, J. Diffusion-Limited Recombination in Polymer-Fullerene Blends and Its Influence on Photocurrent Collection. *Phys. Rev. B: Condens. Matter Mater. Phys.* **2003**, *67* (15), 155209.

(556) Yu, K.; Lee, J. M.; Kim, J.; Kim, G.; Kang, H.; Park, B.; Kahng, Y. H.; Kwon, S.; Lee, S.; Lee, B. H.; et al. Semiconducting Polymers with Nanocrystallites Interconnected via Boron-Doped Carbon Nanotubes. *Nano Lett.* **2014**, *14*, 7100–7106.

(557) Andersson, M. L.; Hedström, S.; Persson, P. Conformation Sensitive Charge Transport in Conjugated Polymers. *Appl. Phys. Lett.* **2013**, *103* (21), 213303.

(558) Wang, S.; Ha, M.; Manno, M.; Frisbie, C. D.; Leighton, C. Hopping Transport and the Hall Effect near the Insulator-Metal Transition in Electrochemically Gated poly(3-Hexylthiophene) Transistors. *Nat. Commun.* **2012**, *3*, 1210.

(559) Asadi, K.; Kronemeijer, A. J.; Cramer, T.; Koster, L. J. A.; Blom, P. W. M.; de Leeuw, D. M. Polaron Hopping Mediated by Nuclear Tunnelling in Semiconducting Polymers at High Carrier Density. *Nat. Commun.* **2013**, *4*, 1710.

(560) Senanayak, S. P.; Ashar, a Z.; Kanimozhi, C.; Patil, S.; Narayan, K. S. Room-Temperature Bandlike Transport and Hall Effect in a High-Mobility Ambipolar Polymer. *Phys. Rev. B: Condens. Matter Mater. Phys.* **2015**, *91*, 115302.

(561) Lee, J.; Chung, J. W.; Kim, D. H.; Lee, B.-L.; Park, J.-I.; Lee, S.; Häusermann, R.; Batlogg, B.; Lee, S.-S.; Choi, I.; et al. Thin Films of Highly Planar Semiconductor Polymers Exhibiting Band-like Transport at Room Temperature. *J. Am. Chem. Soc.* **2015**, *137*, 7990–7993.

(562) Tseng, H. R.; Phan, H.; Luo, C.; Wang, M.; Perez, L. a.; Patel, S. N.; Ying, L.; Kramer, E. J.; Nguyen, T. Q.; Bazan, G. C.; et al. High-Mobility Field-Effect Transistors Fabricated with Macroscopic Aligned Semiconducting Polymers. *Adv. Mater.* **2014**, *26* (19), 2993–2998.

(563) Xu, H.; Jiang, Y.; Li, J.; Ong, B. S.; Shuai, Z.; Xu, J.-B.; Zhao, N. Spectroscopic Study of Electron and Hole Polarons in a High-Mobility Donor - Acceptor Conjugated Copolymer. *J. Phys. Chem. C* **2013**, *117*, 6835–6841.

(564) Yamashita, Y.; Hinkel, F.; Marszalek, T.; Zajackowski, W.; Pisula, W.; Baumgarten, M.; Matsui, H.; Müllen, K.; Takeya, J. Mobility Exceeding 10 Cm<sup>2</sup> /Vs in Donor-Acceptor Polymer Transistors with Band-like Charge Transport. *Chem. Mater.* **2016**, *28*, 420.

(565) Bittle, E. G.; Basham, J. I.; Jackson, T. N.; Jurchescu, O. D.; Gundlach, D. J. Mobility Overestimation due to Gated Contacts in Organic Field-Effect Transistors. *Nat. Commun.* **2016**, *7*, 10908.

(566) Wu, Y.; Chew, A. R.; Rojas, G. A.; Sini, G.; Haugstad, G.; Belianinov, A.; Kalinin, S. V.; Li, H.; Risko, C.; Brédas, J.-L.; et al. Strain Effects on the Work Function of an Organic Semiconductor. *Nat. Commun.* **2016**, *7*, 10270.

(567) Takeya, J.; Yamagishi, M.; Tominari, Y.; Hirahara, R.; Nakazawa, Y.; Nishikawa, T.; Kawase, T.; Shimoda, T.; Ogawa, S. Very High-Mobility Organic Single-Crystal Transistors with in-Crystal Conduction Channels. *Appl. Phys. Lett.* **2007**, *90* (10), 102120.

(568) Haas, S.; Stassen, A. F.; Schuck, G.; Pernstich, K. P.; Gundlach, D. J.; Batlogg, B.; Berens, U.; Kirner, H. J. High Charge-Carrier Mobility and Low Trap Density in a Rubrene Derivative. *Phys. Rev. B: Condens. Matter Mater. Phys.* **2007**, *76* (11), 115203.

(569) Kang, M. J.; Doi, I.; Mori, H.; Miyazaki, E.; Takimiya, K.; Ikeda, M.; Kuwabara, H. Alkylated Dinaphtho[2,3-b:2',3'-f]Thieno-[3,2-b]Thiophenes (Cn-DNTTs): Organic Semiconductors for High-Performance Thin-Film Transistors. *Adv. Mater.* **2011**, *23* (10), 1222–1225.

(570) Jurchescu, O. D.; Subramanian, S.; Kline, R. J.; Hudson, S. D.; Anthony, J. E.; Jackson, T. N.; Gundlach, D. J. Organic Single-Crystal Field-Effect Transistors of a Soluble Anthradithiophene. *Chem. Mater.* **2008**, *20* (21), 6733–6737.

(571) Niazi, M. R.; Li, R.; Li, E. Q.; Kirmani, A. R.; Abdelsamie, M.; Wang, Q.; Pan, W.; Payne, M. M.; Anthony, J. E.; Smilgies, D.-M.; et al. Solution-Printed Organic Semiconductor Blends Exhibiting Transport Properties on Par with Single Crystals. *Nat. Commun.* **2015**, *6*, 8598.

(572) Mei, Y.; Loth, M. a.; Payne, M.; Zhang, W.; Smith, J.; Day, C. S.; Parkin, S. R.; Heeney, M.; McCulloch, I.; Anthopoulos, T. D.; et al. High Mobility Field-Effect Transistors with Versatile Processing from

a Small-Molecule Organic Semiconductor. *Adv. Mater.* **2013**, *25* (31), 4352–4357.

(573) Okamoto, T.; Mitsui, C.; Yamagishi, M.; Nakahara, K.; Soeda, J.; Hirose, Y.; Miwa, K.; Sato, H.; Yamano, A.; Matsushita, T.; et al. V-Shaped Organic Semiconductors with Solution Processability, High Mobility, and High Thermal Durability. *Adv. Mater.* **2013**, *25* (44), 6392–6397.

(574) Zhang, L.; Fonari, A.; Liu, Y.; Hoyt, A. L.; Lee, H.; Granger, D.; Parkin, S.; Russell, T. P.; Anthony, J. E.; Bredas, J. L.; et al. Bistetracene: An Air-Stable, High-Mobility Organic Semiconductor with Extended Conjugation. *J. Am. Chem. Soc.* **2014**, *136* (26), 9248–9251.

(575) Zhang, L.; Cao, Y.; Colella, N. S.; Liang, Y.; Brédas, J. L.; Briseno, A. L. Unconventional, Chemically Stable, and Soluble Two-Dimensional Angular Polycyclic Aromatic Hydrocarbons: From Molecular Design to Device Applications. *Acc. Chem. Res.* **2015**, *48*, 500–509.

(576) Yuan, Y.; Giri, G.; Ayzner, A. L.; Zoombelt, A. P.; Mannsfeld, S. C. B.; Chen, J.; Nordlund, D.; Toney, M. F.; Huang, J.; Bao, Z. Ultra-High Mobility Transparent Organic Thin Film Transistors Grown by an off-Centre Spin-Coating Method. *Nat. Commun.* **2014**, *5*, 3005.

(577) Iino, H.; Usui, T.; Hanna, J.-I. Liquid Crystals for Organic Thin-Film Transistors. *Nat. Commun.* **2015**, *6*, 6828.

(578) Shimo, Y.; Mikami, T.; Hamao, S.; Goto, H.; Okamoto, H.; Eguchi, R.; Gohda, S.; Hayashi, Y.; Kubozono, Y. Synthesis and Transistor Application of the Extremely Extended Phenacene Molecule, [9]phenacene. *Sci. Rep.* **2016**, *6*, 21008.

(579) Okamoto, H.; Hamao, S.; Goto, H.; Sakai, Y.; Izumi, M.; Gohda, S.; Kubozono, Y.; Eguchi, R. Transistor Application of Alkyl-Substituted Picene. *Sci. Rep.* **2014**, *4* (4), 5048.

(580) Shukla, D.; Nelson, S. F.; Freeman, D. C.; Rajeswaran, M.; Ahearn, W. G.; Meyer, D. M.; Carey, J. T. Thin-Film Morphology Control in Naphthalene-Diimide-Based Semiconductors: High Mobility N-Type Semiconductor for Organic Thin-Film Transistors. *Chem. Mater.* **2008**, *20* (24), 7486–7491.

(581) Minder, N. a.; Ono, S.; Chen, Z.; Facchetti, A.; Morpurgo, A. F. Band-like Electron Transport in Organic Transistors and Implication of the Molecular Structure for Performance Optimization. *Adv. Mater.* **2012**, *24* (4), 503–508.

(582) Anthopoulos, T. D.; Singh, B.; Marjanovic, N.; Sariciftci, N. S.; Montaigne Ramil, A.; Sitter, H.; Cölle, M.; De Leeuw, D. M. High Performance N-Channel Organic Field-Effect Transistors and Ring Oscillators Based on C60 Fullerene Films. *Appl. Phys. Lett.* **2006**, *89* (21), 213504.

(583) Krupskaya, Y.; Gibertini, M.; Marzari, N.; Morpurgo, A. F. Band-Like Electron Transport with Record-High Mobility in the TCNQ Family. *Adv. Mater.* **2015**, *27* (15), 2453–2458.

(584) Naab, B. D.; Himmelberger, S.; Diao, Y.; Vandewal, K.; Wei, P.; Lussem, B.; Salleo, A.; Bao, Z. High Mobility N-Type Transistors Based on Solution-Sheared Doped 6,13-Bis(triisopropylsilyl)ethynyl-pentacene Thin Films. *Adv. Mater.* **2013**, *25* (33), 4663–4667.

(585) Xie, W.; Prabhumirashi, P. L.; Nakayama, Y.; McGarry, K. a.; Geier, M. L.; Uragami, Y.; Mase, K.; Douglas, C. J.; Ishii, H.; Hersam, M. C.; et al. Utilizing Carbon Nanotube Electrodes to Improve Charge Injection and Transport in Bis(trifluoromethyl)-Dimethyl-Rubrene Ambipolar Single Crystal Transistors. *ACS Nano* **2013**, *7* (11), 10245–10256.

(586) Li, J.; Zhao, Y.; Tan, H. S.; Guo, Y.; Di, C.-A.; Yu, G.; Liu, Y.; Lin, M.; Lim, S. H.; Zhou, Y.; et al. A Stable Solution-Processed Polymer Semiconductor with Record High-Mobility for Printed Transistors. *Sci. Rep.* **2012**, *2*, 754.

(587) Kang, I.; Yun, H.-J.; Chung, D. S.; Kwon, S.-K.; Kim, Y.-H. Record High Hole Mobility in Polymer Semiconductors via Side-Chain Engineering. *J. Am. Chem. Soc.* **2013**, *135* (40), 14896–14899.

(588) Back, J. Y.; Yu, H.; Song, I.; Kang, I.; Ahn, H.; Shin, T. J.; Kwon, S.-K.; Oh, J. H.; Kim, Y.-H. Investigation of Structure–Property Relationships in Diketopyrrolopyrrole-Based Polymer Semiconductors via Side-Chain Engineering. *Chem. Mater.* **2015**, *27* (5), 1732–1739.

(589) Shin, J.; Hong, T. R.; Lee, T. W.; Kim, A.; Kim, Y. H.; Cho, M. J.; Choi, D. H. Template-Guided Solution-Shearing Method for Enhanced Charge Carrier Mobility in Diketopyrrolopyrrole-Based Polymer Field-Effect Transistors. *Adv. Mater.* **2014**, *26* (34), 6031–6035.

(590) Chen, H.; Guo, Y.; Yu, G.; Zhao, Y.; Zhang, J.; Gao, D.; Liu, H.; Liu, Y. Highly  $\pi$ -Extended Copolymers with Diketopyrrolopyrrole Moieties for High-Performance Field-Effect Transistors. *Adv. Mater.* **2012**, *24* (34), 4618–4622.

(591) Luo, C.; Kyaw, A. K. K.; Perez, L. a.; Patel, S.; Wang, M.; Grimm, B.; Bazan, G. C.; Kramer, E. J.; Heeger, A. J. General Strategy for Self-Assembly of Highly Oriented Nanocrystalline Semiconducting Polymers with High Mobility. *Nano Lett.* **2014**, *14* (5), 2764–2771.

(592) Yun, H.-J.; Kang, S.-J.; Xu, Y.; Kim, S. O.; Kim, Y.-H.; Noh, Y.-Y.; Kwon, S.-K. Dramatic Inversion of Charge Polarity in Diketopyrrolopyrrole-Based Organic Field-Effect Transistors via a Simple Nitrile Group Substitution. *Adv. Mater.* **2014**, *26* (43), 7300–7307.

(593) Lee, J.; Han, a. R.; Yu, H.; Shin, T. J.; Yang, C.; Oh, J. H. Boosting the Ambipolar Performance of Solution-Processable Polymer Semiconductors via Hybrid Side-Chain Engineering. *J. Am. Chem. Soc.* **2013**, *135* (25), 9540–9547.

(594) Sun, B.; Hong, W.; Yan, Z.; Aziz, H.; Li, Y. Record High Electron Mobility of 6.3 cm<sup>2</sup>V<sup>-1</sup>s<sup>-1</sup> Achieved for Polymer Semiconductors Using a New Building Block. *Adv. Mater.* **2014**, *26* (17), 2636–2642, 2613.

(595) De Boer, R. W. I.; Jochemsen, M.; Klapwijk, T. M.; Morpurgo, a. F.; Niemax, J.; Tripathi, a. K.; Pflaum, J. Space Charge Limited Transport and Time of Flight Measurements in Tetracene Single Crystals: A Comparative Study. *J. Appl. Phys.* **2004**, *95* (3), 1196–1202.

(596) de Boer, R. W. I.; Gershenson, M. E.; Morpurgo, a. F.; Podzorov, V. Organic Single-Crystal Field-Effect Transistors. *Phys. Status Solidi* **2004**, *201* (6), 1302–1331.

(597) Matsubara, K.; Manaka, T.; Iwamoto, M. Band-like Transport Observed in TIPS-Pentacene Thin Film by Time-Resolved Microscopic Optical Second-Harmonic Generation Imaging. *Appl. Phys. Express* **2015**, *8* (4), 041601.

(598) Xie, H.; Alves, H.; Morpurgo, A. Quantitative Analysis of Density-Dependent Transport in Tetramethyltetraselenafulvalene Single-Crystal Transistors: Intrinsic Properties and Trapping. *Phys. Rev. B: Condens. Matter Mater. Phys.* **2009**, *80*, 245305.

(599) Liu, C.; Minari, T.; Lu, X.; Kumatani, A.; Takimiya, K.; Tsukagoshi, K. Solution-Processable Organic Single Crystals with Bandlike Transport in Field-Effect Transistors. *Adv. Mater.* **2011**, *23* (4), 523–526.

(600) Kaake, L. G.; Barbara, P. F.; Zhu, X. Y. Intrinsic Charge Trapping in Organic and Polymeric Semiconductors: A Physical Chemistry Perspective. *J. Phys. Chem. Lett.* **2010**, *1* (3), 628–635.

(601) Carr, J. a.; Chaudhary, S. The Identification, Characterization and Mitigation of Defect States in Organic Photovoltaic Devices: A Review and Outlook. *Energy Environ. Sci.* **2013**, *6* (12), 3414.

(602) Salleo, A. Electronic Traps in Organic Semiconductors. *Organic Electronics: Emerging Concepts and Technologies* **2013**, 341–382.

(603) Ostroverkhova, O.; Singer, K. D. Space-Charge Dynamics in Photorefractive Polymers. *J. Appl. Phys.* **2002**, *92* (4), 1727–1743.

(604) Krellner, C.; Haas, S.; Goldmann, C.; Pernstich, K. P.; Gundlach, D. J.; Batlogg, B. Density of Bulk Trap States in Organic Semiconductor Crystals: Discrete Levels Induced by Oxygen in Rubrene. *Phys. Rev. B: Condens. Matter Mater. Phys.* **2007**, *75* (24), 245115.

(605) Mastrogianni, D. D. T.; Mayer, J.; Wan, A. S.; Vishnyakov, A.; Neimark, A. V.; Podzorov, V.; Feldman, L. C.; Garfunkel, E. Oxygen Incorporation in Rubrene Single Crystals. *Sci. Rep.* **2014**, *4*, 4753.

(606) Kalb, W. L.; Mattenberger, K.; Batlogg, B. Oxygen-Related Traps in Pentacene Thin Films: Energetic Position and Implications for Transistor Performance. *Phys. Rev. B: Condens. Matter Mater. Phys.* **2008**, *78* (3), 035334.

- (607) Nicolai, H. T.; Kuik, M.; Wetzelaer, G. a. H.; de Boer, B.; Campbell, C.; Risko, C.; Brédas, J. L.; Blom, P. W. M. Unification of Trap-Limited Electron Transport in Semiconducting Polymers. *Nat. Mater.* **2012**, *11* (10), 882–887.
- (608) Goldmann, C.; Gundlach, D. J.; Batlogg, B. Evidence of Water-Related Discrete Trap State Formation in Pentacene Single-Crystal Field-Effect Transistors. *Appl. Phys. Lett.* **2006**, *88* (6), 063501.
- (609) Jurchescu, O. D.; Baas, J.; Palstra, T. T. M. Electronic Transport Properties of Pentacene Single Crystals upon Exposure to Air. *Appl. Phys. Lett.* **2005**, *87* (5), 052102.
- (610) Nasrallah, I.; Banger, K. K.; Vaynzof, Y.; Payne, M. M.; Too, P.; Jongman, J.; Anthony, J. E.; Sirringhaus, H. Effect of Ozone on the Stability of Solution-Processed Anthradithiophene-Based Organic Field-Effect Transistors. *Chem. Mater.* **2014**, *26*, 3914–3919.
- (611) Street, R. a.; Krakaris, A.; Cowan, S. R. Recombination through Different Types of Localized States in Organic Solar Cells. *Adv. Funct. Mater.* **2012**, *22* (21), 4608–4619.
- (612) Ando, M.; Kehoe, T. B.; Yoneya, M.; Ishii, H.; Kawasaki, M.; Duffy, C. M.; Minakata, T.; Phillips, R. T.; Sirringhaus, H. Evidence for Charge-Trapping Inducing Polymorphic Structural-Phase Transition in Pentacene. *Adv. Mater.* **2015**, *27* (1), 122–129.
- (613) Najafov, H.; Mastrogiovanni, D.; Garfunkel, E.; Feldman, L. C.; Podzorov, V. Photon-Assisted Oxygen Diffusion and Oxygen-Related Traps in Organic Semiconductors. *Adv. Mater.* **2011**, *23* (8), 981–985.
- (614) Kalb, W. L.; Haas, S.; Krellner, C.; Mathis, T.; Batlogg, B. Trap Density of States in Small-Molecule Organic Semiconductors: A Quantitative Comparison of Thin-Film Transistors with Single Crystals. *Phys. Rev. B: Condens. Matter Mater. Phys.* **2010**, *81* (15), 155315.
- (615) Jaquith, M.; Muller, E. M.; Marohn, J. a. Time-Resolved Electric Force Microscopy of Charge Trapping in Polycrystalline Pentacene. *J. Phys. Chem. B* **2007**, *111* (27), 7711–7714.
- (616) Jaquith, M. J.; Anthony, J. E.; Marohn, J. a. Long-Lived Charge Traps in Functionalized Pentacene and Anthradithiophene Studied by Time-Resolved Electric Force Microscopy. *J. Mater. Chem.* **2009**, *19* (34), 6116.
- (617) Muller, E. M.; Marohn, J. a. Microscopic Evidence for Spatially Inhomogeneous Charge Trapping in Pentacene. *Adv. Mater.* **2005**, *17* (11), 1410–1414.
- (618) Tachiya, M.; Seki, K. Theory of Bulk Electron-Hole Recombination in a Medium with Energetic Disorder. *Phys. Rev. B: Condens. Matter Mater. Phys.* **2010**, *82* (8), 085201.
- (619) Christ, N.; Kettlitz, S. W.; Züfle, S.; Valouch, S.; Lemmer, U. Nanosecond Response of Organic Solar Cells and Photodiodes: Role of Trap States. *Phys. Rev. B: Condens. Matter Mater. Phys.* **2011**, *83* (19), 195211.
- (620) Seki, K.; Marumoto, K.; Tachiya, M. Bulk Recombination in Organic Bulk Heterojunction Solar Cells under Continuous and Pulsed Light Irradiation. *Appl. Phys. Express* **2013**, *6*, 051603.
- (621) Hofacker, A.; Oelerich, J. O.; Nenashev, A. V.; Gebhard, F.; Baranovskii, S. D. Theory to Carrier Recombination in Organic Disordered Semiconductors. *J. Appl. Phys.* **2014**, *115* (22), 223713.
- (622) Street, R. A. Localized State Distribution and Its Effect on Recombination in Organic Solar Cells. *Phys. Rev. B: Condens. Matter Mater. Phys.* **2011**, *84* (7), 075208.
- (623) MacKenzie, R. C. I.; Shuttle, C. G.; Dibb, G. F.; Treat, N.; Von Hauff, E.; Robb, M. J.; Hawker, C. J.; Chabiny, M. L.; Nelson, J. Interpreting the Density of States Extracted from Organic Solar Cells Using Transient Photocurrent Measurements. *J. Phys. Chem. C* **2013**, *117* (24), 12407–12414.
- (624) Abbaszadeh, D.; Kunz, A.; Wetzelaer, G. A. H.; Michels, J. J.; Crăciun, N. I.; Koynov, K.; Lieberwirth, I.; Blom, P. W. M. Elimination of Charge Carrier Trapping in Diluted Semiconductors. *Nat. Mater.* **2016**, *15*, 628–633.
- (625) Oh, J. W.; Lee, C.; Kim, N. The Effect of Trap Density on the Space Charge Formation in Polymeric Photorefractive Composites. *J. Chem. Phys.* **2009**, *130* (13), 134909.
- (626) Tsujimura, S.; Fujihara, T.; Sassa, T.; Kinashi, K.; Sakai, W.; Ishibashi, K.; Tsutsumi, N. Enhanced Photoconductivity and Trapping Rate through Control of Bulk State in Organic Triphenylamine-Based Photorefractive Materials. *Org. Electron.* **2014**, *15* (12), 3471–3475.
- (627) Fujihara, T.; Mamiya, J.; Kawamoto, M.; Sassa, T. Dark Current and Light Illumination Effects on Grating Formation during Periodic Long-Term Operation in Photorefractive Polymers. *J. Appl. Phys.* **2014**, *115* (2), 023109.
- (628) Köber, S.; Salvador, M.; Meerholz, K. Organic Photorefractive Materials and Applications. *Adv. Mater.* **2011**, *23* (41), 4725–4763.
- (629) Lynn, B.; Blanche, P. A.; Peyghambarian, N. Photorefractive Polymers for Holography. *J. Polym. Sci., Part B: Polym. Phys.* **2014**, *52* (3), 193–231.
- (630) Grunnet-Jepsen, a; Thompson, C. L.; Twieg, R. J.; Moerner, W. E. High Performance Photorefractive Polymer with Improved Stability. *Appl. Phys. Lett.* **1997**, *70* (12), 1515.
- (631) Däubler, T.; Bittner, R.; Meerholz, K.; Cimrová, V.; Neher, D. Charge Carrier Photogeneration, Trapping, and Space-Charge Field Formation in PVK-Based Photorefractive Materials. *Phys. Rev. B: Condens. Matter Mater. Phys.* **2000**, *61* (20), 13515–13527.
- (632) Grunnet-Jepsen, A.; Wright, D.; Smith, B.; Bratcher, M. S.; DeClue, M. S.; Siegel, J. S.; Moerner, W. E. Spectroscopic Determination of Trap Density in C 60 -Sensitized Photorefractive Polymers. *Chem. Phys. Lett.* **1998**, *291*, 553–561.
- (633) Herlocker, J. a; Fuentes-Hernandez, C.; Ferrio, K. B.; Hendrickx, E.; Blanche, P.-A.; Peyghambarian, N.; Kippelen, B.; Zhang, Y.; Wang, J. F.; Marder, S. R. Stabilization of the Response Time in Photorefractive Polymers. *Appl. Phys. Lett.* **2000**, *77* (15), 2292.
- (634) Thomas, J.; Fuentes-Hernandez, C.; Yamamoto, M.; Cammack, K.; Matsumoto, K.; Walker, G. a.; Barlow, S.; Kippelen, B.; Meredith, G.; Marder, S. R.; et al. Bistriarylamine Polymer-Based Composites for Photorefractive Applications. *Adv. Mater.* **2004**, *16* (22), 2032–2036.
- (635) Christenson, C. W.; Thomas, J.; Blanche, P.; Voorakaranam, R.; Norwood, R. a; Yamamoto, M.; Peyghambarian, N. Grating Dynamics in a Photorefractive Polymer with Alq(3) Electron Traps. *Opt. Express* **2010**, *18* (9), 9358–9365.
- (636) Credgington, D.; Hamilton, R.; Atienzar, P.; Nelson, J.; Durrant, J. R. Non-Geminate Recombination as the Primary Determinant of Open-Circuit Voltage in Polythiophene:fullerene Blend Solar Cells: An Analysis of the Influence of Device Processing Conditions. *Adv. Funct. Mater.* **2011**, *21* (14), 2744–2753.
- (637) Credgington, D.; Jamieson, F. C.; Walker, B.; Nguyen, T. Q.; Durrant, J. R. Quantification of Geminate and Non-Geminate Recombination Losses within a Solution-Processed Small-Molecule Bulk Heterojunction Solar Cell. *Adv. Mater.* **2012**, *24* (16), 2135–2141.
- (638) Kyaw, A. K. K.; Wang, D. H.; Luo, C.; Cao, Y.; Nguyen, T.-Q.; Bazan, G. C.; Heeger, A. J. Effects of Solvent Additives on Morphology, Charge Generation, Transport, and Recombination in Solution-Processed Small-Molecule Solar Cells. *Adv. Energy Mater.* **2014**, *4* (7), 1301469.
- (639) Bartesaghi, D.; Pérez, I. D. C.; Kniepert, J.; Roland, S.; Turbiez, M.; Neher, D.; Koster, L. J. A. Competition between Recombination and Extraction of Free Charges Determines the Fill Factor of Organic Solar Cells. *Nat. Commun.* **2015**, *6*, 7083.
- (640) Kuik, M.; Wetzelaer, G.-J. a H.; Nicolai, H. T.; Craciun, N. I.; De Leeuw, D. M.; Blom, P. W. M. 25Th Anniversary Article: Charge Transport and Recombination in Polymer Light-Emitting Diodes. *Adv. Mater.* **2014**, *26* (4), 512–531.
- (641) Lakhwani, G.; Rao, A.; Friend, R. H. Bimolecular Recombination in Organic Photovoltaics. *Annu. Rev. Phys. Chem.* **2014**, *65*, 557–581.
- (642) Proctor, C. M.; Kuik, M.; Nguyen, T.-Q. Charge Carrier Recombination in Organic Solar Cells. *Prog. Polym. Sci.* **2013**, *38* (12), 1941–1960.
- (643) Roland, S.; Schubert, M.; Collins, B. A.; Kurpiers, J.; Chen, Z.; Facchetti, A.; Ade, H.; Neher, D. Fullerene-Free Polymer Solar Cells with Highly Reduced Bimolecular Recombination and Field-

Independent Charge Carrier Generation. *J. Phys. Chem. Lett.* **2014**, *5* (16), 2815–2822.

(644) Deibel, C.; Baumann, A.; Dyakonov, V. Polaron Recombination in Pristine and Annealed Bulk Heterojunction Solar Cells. *Appl. Phys. Lett.* **2008**, *93* (16), 163303.

(645) Hilczler, M.; Tachiya, M. Unified Theory of Geminate and Bulk Electron-Hole Recombination in Organic Solar Cells. *J. Phys. Chem. C* **2010**, *114*, 6808.

(646) Heiber, M. C.; Baumbach, C.; Dyakonov, V.; Deibel, C. Encounter-Limited Charge-Carrier Recombination in Phase-Separated Organic Semiconductor Blends. *Phys. Rev. Lett.* **2015**, *114*, 136602.

(647) Heiber, M. C.; Nguyen, T.-Q.; Deibel, C. Charge Carrier Concentration Dependence of Encounter-Limited Bimolecular Recombination in Phase-Separated Organic Semiconductor Blends. *Phys. Rev. B: Condens. Matter Mater. Phys.* **2016**, *93* (20), 205204.

(648) Rappaport, N.; Solomesch, O.; Tessler, N. The Interplay between Space Charge and Recombination in Conjugated Polymer/molecule Photocells. *J. Appl. Phys.* **2005**, *98*, 033714.

(649) Tzabari, L.; Tessler, N. Shockley–Read–Hall Recombination in P3HT:PCBM Solar Cells as Observed under Ultralow Light Intensities. *J. Appl. Phys.* **2011**, *109* (6), 064501.

(650) Kniepert, J.; Schubert, M.; Blakesley, J.; Neher, D. Photo-generation and Recombination in P3HT: PCBM Solar Cells Probed by Time Delayed Collection Field Experiments. *J. Phys. Chem. Lett.* **2011**, *2*, 700–705.

(651) Wetzelaer, G. J. a H.; Van Der Kaap, N. J.; Koster, J. A.; Blom, P. W. M. Quantifying Bimolecular Recombination in Organic Solar Cells in Steady State. *Adv. Energy Mater.* **2013**, *3* (9), 1130–1134.

(652) Kuik, M.; Koster, L.; Wetzelaer, G.; Blom, P. Trap-Assisted Recombination in Disordered Organic Semiconductors. *Phys. Rev. Lett.* **2011**, *107*, 256805.

(653) Kirchartz, T.; Nelson, J. Meaning of Reaction Orders in Polymer:fullerene Solar Cells. *Phys. Rev. B: Condens. Matter Mater. Phys.* **2012**, *86* (16), 165201.

(654) Shuttle, C. G.; O'Regan, B.; Ballantyne, a. M.; Nelson, J.; Bradley, D. D. C.; De Mello, J.; Durrant, J. R. Experimental Determination of the Rate Law for Charge Carrier Decay in a Polythiophene: Fullerene Solar Cell. *Appl. Phys. Lett.* **2008**, *92* (9), 093311.

(655) Shuttle, C. G.; Hamilton, R.; O'Regan, B. C.; Nelson, J.; Durrant, J. R. Charge-Density-Based Analysis of the Current–voltage Response of Polythiophene/fullerene Photovoltaic Devices. *Proc. Natl. Acad. Sci. U. S. A.* **2010**, *107* (38), 16448–16452.

(656) Mandoc, M. M.; Kooistra, F. B.; Hummelen, J. C.; de Boer, B.; Blom, P. W. M. Effect of Traps on the Performance of Bulk Heterojunction Organic Solar Cells. *Appl. Phys. Lett.* **2007**, *91* (26), 263505.

(657) Proctor, C. M.; Nguyen, T.-Q. Effect of Leakage Current and Shunt Resistance on the Light Intensity Dependence of Organic Solar Cells. *Appl. Phys. Lett.* **2015**, *106* (8), 083301.

(658) Koster, L. J. A.; Mihaileti, V. D.; Ramaker, R.; Blom, P. W. M. Light Intensity Dependence of Open-Circuit Voltage of Polymer:fullerene Solar Cells. *Appl. Phys. Lett.* **2005**, *86* (12), 123509.

(659) Tzabari, L.; Zayats, V.; Tessler, N. Exciton Annihilation as Bimolecular Loss in Organic Solar Cells. *J. Appl. Phys.* **2013**, *114* (15), 154514.

(660) Devir-Wolfman, A. H.; Khachatryan, B.; Gautam, B. R.; Tzabary, L.; Keren, A.; Tessler, N.; Vardeny, Z. V.; Ehrenfreund, E. Short-Lived Charge-Transfer Excitons in Organic Photovoltaic Cells Studied by High-Field Magneto-Photocurrent. *Nat. Commun.* **2014**, *5*, 4529.

(661) Gautam, B. R.; Nguyen, T. D.; Ehrenfreund, E.; Vardeny, Z. V. Magnetic Field Effect on Excited-State Spectroscopies of  $\pi$ -Conjugated Polymer Films. *Phys. Rev. B: Condens. Matter Mater. Phys.* **2012**, *85* (20), 205207.

(662) Tay, S.; Blanche, P.; Voorakaranam, R.; Tunç, a V.; Lin, W.; Rokutanda, S.; Gu, T.; Flores, D.; Wang, P.; Li, G.; et al. An Updatable Holographic Three-Dimensional Display. *Nature* **2008**, *451* (7179), 694–698.

(663) Blanche, P.; Bablumian, a; Voorakaranam, R.; Christenson, C.; Lin, W.; Gu, T.; Flores, D.; Wang, P.; Hsieh, W.-Y.; Kathaperumal, M.; et al. Holographic Three-Dimensional Telepresence Using Large-Area Photorefractive Polymer. *Nature* **2010**, *468* (7320), 80–83.

(664) Blanche, P.-A., Ed. *Photorefractive Organic Materials and Applications*; Springer International Publishing: 2016.

(665) Lee, C.; Yang, M.; Lee, N. S.; Kim, N. Monte Carlo Simulation of Trap Effects on Space-Charge Field Formation. *Chem. Phys. Lett.* **2006**, *418* (1–3), 54–58.

(666) Moerner, W. E.; Silence, S. M.; Hache, F.; Bjorklund, G. C. Orientationally Enhanced Photorefractive Effect in Polymers. *J. Opt. Soc. Am. B* **1994**, *11* (2), 320.

(667) Schildkraut, J. S.; Cui, Y. Zero-Order and First-Order Theory of the Formation of Space-Charge Gratings in Photoconductive Polymers. *J. Appl. Phys.* **1992**, *72*, 5055–5060.

(668) Kulikovskiy, L.; Neher, D.; Mecher, E.; Meerholz, K.; Hörhold, H.-H.; Ostroverkhova, O. Photocurrent Dynamics in a Poly(phenylene Vinylene)-Based Photorefractive Composite. *Phys. Rev. B: Condens. Matter Mater. Phys.* **2004**, *69* (12), 125216.

(669) Mecher, E.; Gallego-Gómez, F.; Tillmann, H.; Hörhold, H.-H.; Hummelen, J. C.; Meerholz, K. Near-Infrared Sensitivity Enhancement of Photorefractive Polymer Composites by Pre-Illumination. *Nature* **2002**, *418* (6901), 959–964.

(670) Gather, M. C.; Mansurova, S.; Meerholz, K. Determining the Photoelectric Parameters of an Organic Photoconductor by the Photoelectromotive-Force Technique. *Phys. Rev. B: Condens. Matter Mater. Phys.* **2007**, *75* (16), 165203.

(671) Mansurova, S.; Meerholz, K.; Sliwinski, E.; Hartwig, U.; Buse, K. Enhancement of Charge Carrier Transport by Doping PVK-Based Photoconductive Polymers with LiNbO<sub>3</sub> Nanocrystals. *Phys. Rev. B: Condens. Matter Mater. Phys.* **2009**, *79* (17), 174208.

(672) Samiullah, M. The Role of Diffusion of Excitons in Organic Photorefractive Materials. *J. Appl. Phys.* **2010**, *107* (11), 113525.

(673) Blanche, P.-A.; Lynn, B.; Churin, D.; Kieu, K.; Norwood, R. A.; Peyghambarian, N. Diffraction Response of Photorefractive Polymers over Nine Orders of Magnitude of Pulse Duration. *Sci. Rep.* **2016**, *6*, 29027.

(674) Ostroverkhova, O.; Stickrath, A.; Singer, K. D. Electric Field-Induced Second Harmonic Generation Studies of Chromophore Orientational Dynamics in Photorefractive Polymers. *J. Appl. Phys.* **2002**, *91* (12), 9481–9486.

(675) Ostroverkhova, O.; He, M.; Twieg, R. J.; Moerner, W. E. Role of Temperature in Controlling Performance of Photorefractive Organic Glasses. *ChemPhysChem* **2003**, *4* (7), 732–744.

(676) Herrera-Ambriz, V. M.; Maldonado, J. L.; Rodríguez, M.; Castro-Beltrán, R.; Ramos-Ortiz, G.; Magaña-Vergara, N. E.; Meneses-Nava, M. A.; Barbosa-García, O.; Santillan, R.; Farfán, N.; et al. Highly Efficient Photorefractive Organic Polymers Based on Benzonitrile Schiff Bases Nonlinear Chromophores. *J. Phys. Chem. C* **2011**, *115* (48), 23955–23963.

(677) Giang, H. N.; Kinashi, K.; Sakai, W.; Tsutsumi, N. Photorefractive Response and Real-Time Holographic Application of a poly(4-(diphenylamino)benzyl Acrylate)-Based Composite. *Polym. J.* **2014**, *46* (1), 59–66.

(678) Zhang, L.; Shi, J.; Yang, Z.; Huang, M.; Chen, Z.; Gong, Q.; Cao, S. Photorefractive Properties of Polyphosphazenes Containing Carbazole-Based Multifunctional Chromophores. *Polymer* **2008**, *49* (8), 2107–2114.

(679) Gallego-Gómez, F.; del Monte, F.; Meerholz, K. Optical Gain by a Simple Photoisomerization Process. *Nat. Mater.* **2008**, *7* (6), 490–497.

(680) Gallego-Gómez, F.; del Monte, F.; Meerholz, K. Mechanisms for High-Performance and Non-Local Photoisomerization Gratings in a Sol-Gel Material. *Adv. Funct. Mater.* **2013**, *23* (30), 3770–3781.

(681) Tsutsumi, N.; Kinashi, K.; Sakai, W.; Nishide, J.; Kawabe, Y.; Sasabe, H. Real-Time Three-Dimensional Holographic Display Using a Monolithic Organic Compound Dispersed Film. *Opt. Mater. Express* **2012**, *2* (8), 1003.

- (682) Tsutsumi, N.; Kinashi, K.; Ogo, K.; Fukami, T.; Yabuhara, Y.; Kawabe, Y.; Tada, K.; Fukuzawa, K.; Kawamoto, M.; Sassa, T.; et al. Updatable Holographic Diffraction of Monolithic Carbazole-Azobenzene Compound in Poly(methyl Methacrylate) Matrix. *J. Phys. Chem. C* **2015**, *119* (32), 18567–18572.
- (683) Wu, P.; Sun, S. Q.; Baig, S.; Wang, M. R. Nanoscale Optical Reinforcement for Enhanced Reversible Holography. *Opt. Express* **2012**, *20* (3), 3091.
- (684) Ishii, N.; Kato, T.; Abe, J. A Real-Time Dynamic Holographic Material Using a Fast Photochromic Molecule. *Sci. Rep.* **2012**, *2*, 819.
- (685) Gallego-Gómez, F.; Quintana, J. a.; Villalvilla, J. M.; Díaz-García, M. a.; Martín-Gomis, L.; Fernández-Lázaro, F.; Sastre-Santos, Á. Phthalocyanines as Efficient Sensitizers in Low-Tg Hole-Conducting Photorefractive Polymer Composites. *Chem. Mater.* **2009**, *21* (13), 2714–2720.
- (686) Tsutsumi, N.; Kinashi, K.; Masumura, K.; Kono, K. Photorefractive Performance of Poly (Triarylamine) -Based Polymer Composites: An Approach from the Photoconductive Properties. *J. Polym. Sci., Part B: Polym. Phys.* **2015**, *53* (7), 502–508.
- (687) Lakowicz, J. R. *Principles of Fluorescence Spectroscopy*, 3rd ed.; 2006.
- (688) Hadziioannou, G.; Malliaras, G. *Semiconducting Polymers: Chemistry, Physics and Engineering*; Wiley-VCH: 2006.
- (689) Saito, T.; Kobayashi, T. Real-Time Spectroscopy of Excited States in Azobenzene. *Opt. Mater. (Amsterdam, Neth.)* **2003**, *21* (1–3), 301–305.
- (690) Virgili, T.; Cerullo, G.; Lüer, L.; Lanzani, G.; Gadermaier, C.; Bradley, D. D. C. Understanding Fundamental Processes in poly(9,9-Diocyfluorene) Light-Emitting Diodes via Ultrafast Electric-Field-Assisted Pump-Probe Spectroscopy. *Phys. Rev. Lett.* **2003**, *90* (24), 247402.
- (691) Tani, M.; Herrmann, M.; Sakai, K. Generation and Detection of THz Pulsed Radiation with Photoconductive Antennas. *Meas. Sci. Technol.* **2002**, *13*, 1739–1745.
- (692) Huber, R.; Kübler, C.; Tübel, S.; Leitenstorfer, A.; Vu, Q. T.; Haug, H.; Köhler, F.; Amann, M. C. Femtosecond Formation of Coupled Phonon-Plasmon Modes in InP: Ultrabroadband THz Experiment and Quantum Kinetic Theory. *Phys. Rev. Lett.* **2005**, *94* (2), 027401.
- (693) Pensack, R. D.; Banyas, K. M.; Asbury, J. B. Temperature-Independent Vibrational Dynamics in an Organic Photovoltaic Material. *J. Phys. Chem. B* **2010**, *114* (38), 12242–12251.
- (694) Jeong, K. S.; Pensack, R. D.; Asbury, J. B. Vibrational Spectroscopy of Electronic Processes in Emerging Photovoltaic Materials. *Acc. Chem. Res.* **2013**, *46* (7), 1538–1547.
- (695) Elliott, A. B. S.; Horvath, R.; Gordon, K. C. Vibrational Spectroscopy as a Probe of Molecule-Based Devices. *Chem. Soc. Rev.* **2012**, *41*, 1929.
- (696) Pensack, R. D.; Scholes, G. D. Managing Complex Photo-physical Pathways for Solar Energy Conversion. *J. Phys. Chem. Lett.* **2014**, *5* (13), 2380–2381.
- (697) Onda, K.; Yamochi, H.; Koshihara, S. Y. Diverse Photoinduced Dynamics in an Organic Charge-Transfer Complex Having Strong Electron-Phonon Interactions. *Acc. Chem. Res.* **2014**, *47* (12), 3494–3503.
- (698) Miranda, P. B.; Moses, D.; Heeger, A. J. Ultrafast Photo-generation of Charged Polarons on Conjugated Polymer Chains in Dilute Solution. *Phys. Rev. B: Condens. Matter Mater. Phys.* **2004**, *70* (8), 085212.
- (699) Meskers, S.; van Hal, P.; Spiering, a.; Hummelen, J.; van der Meer, a.; Janssen, R. Time-Resolved Infrared-Absorption Study of Photoinduced Charge Transfer in a Polythiophene-Methanofullerene Composite Film. *Phys. Rev. B: Condens. Matter Mater. Phys.* **2000**, *61* (15), 9917–9920.
- (700) Yang, Q.; Muntwiler, M.; Zhu, X. Y. Charge Transfer Excitons and Image Potential States on Organic Semiconductor Surfaces. *Phys. Rev. B: Condens. Matter Mater. Phys.* **2009**, *80* (11), 115214.
- (701) Zhu, X.-Y.; Yang, Q.; Muntwiler, M. Charge-Transfer Excitons at Organic Semiconductor Surfaces and Interfaces. *Acc. Chem. Res.* **2009**, *42* (11), 1779–1787.
- (702) Varene, E.; Bogner, L.; Bronner, C.; Tegeder, P. Ultrafast Exciton Population, Relaxation, and Decay Dynamics in Thin Oligothiophene Films. *Phys. Rev. Lett.* **2012**, *109* (20), 207601.
- (703) Dutton, G. J.; Robey, S. W. Non-Fullerene Acceptors: Exciton Dissociation with PTCDA versus C 60. *Phys. Chem. Chem. Phys.* **2015**, *17*, 15953–15962.
- (704) Kim, J. W.; Park, H.; Zhu, X. Charge Transport and Separation Dynamics at the C60/GaAs(001) Interface. *J. Phys. Chem. C* **2014**, *118* (6), 2987–2991.
- (705) Dutton, G. J.; Robey, S. W. Exciton Dynamics at CuPc/C60 Interfaces: Energy Dependence of Exciton Dissociation. *J. Phys. Chem. C* **2012**, *116* (36), 19173–19181.
- (706) Milne, C. J.; Penfold, T. J.; Chergui, M. Recent Experimental and Theoretical Developments in Time-Resolved X-Ray Spectroscopies. *Coord. Chem. Rev.* **2014**, *277*, 44–68.
- (707) Arion, T.; Neppel, S.; Roth, F.; Shavorskiy, A.; Bluhm, H.; Hussain, Z.; Gessner, O.; Eberhardt, W. Site-Specific Probing of Charge Transfer Dynamics in Organic Photovoltaics. *Appl. Phys. Lett.* **2015**, *106* (12), 121602.
- (708) Kaake, L. G.; Jailaubekov, A.; Williams, K. J.; Zhu, X. Y. Probing Ultrafast Charge Separation at Organic Donor/acceptor Interfaces by a Femtosecond Electric Field Meter. *Appl. Phys. Lett.* **2011**, *99* (8), 083307.
- (709) Taguchi, D.; Shino, T.; Chen, X.; Zhang, L.; Li, J.; Weis, M.; Manaka, T.; Iwamoto, M. Analyzing Carrier Lifetime of Double-Layer Organic Solar Cells by Using Optical Electric-Field-Induced Second-Harmonic Generation Measurement. *Appl. Phys. Lett.* **2011**, *98* (13), 133507.
- (710) Tapping, P. C.; Kee, T. W. Optical Pumping of Poly (3-Hexylthiophene) Singlet Excitons Induces Charge Carrier Generation Ground State Bleaching. *J. Phys. Chem. Lett.* **2014**, *5*, 1040–1047.
- (711) Busby, E.; Carroll, E. C.; Chinn, E. M.; Chang, L.; Moulé, A. J.; Larsen, D. S. Excited-State Self-Trapping and Ground-State Relaxation Dynamics in poly(3-Hexylthiophene) Resolved with Broadband Pump-Dump-Probe Spectroscopy. *J. Phys. Chem. Lett.* **2011**, *2* (21), 2764–2769.
- (712) Clark, J.; Nelson, T.; Tretiak, S.; Cirimi, G.; Lanzani, G. Femtosecond Torsional Relaxation. *Nat. Phys.* **2012**, *8* (3), 225–231.
- (713) Gadermaier, C.; Cerullo, G.; Sansone, G.; Leising, G.; Scherf, U.; Lanzani, G. Time-Resolved Charge Carrier Generation from Higher Lying Excited States in Conjugated Polymers. *Phys. Rev. Lett.* **2002**, *89* (11), 117402.
- (714) Gaab, K. M.; Bardeen, C. J. Anomalous Exciton Diffusion in the Conjugated Polymer MEH-PPV Measured Using a Three-Pulse Pump-Dump-Probe Anisotropy Experiment. *J. Phys. Chem. A* **2004**, *108* (49), 10801–10806.
- (715) Musser, A. J.; Liebel, M.; Schnedermann, C.; Wende, T.; Kehoe, T. B.; Rao, A.; Kukura, P. Evidence for Conical Intersection Dynamics Mediating Ultrafast Singlet Exciton Fission. *Nat. Phys.* **2015**, *11*, 352–357.
- (716) Collini, E. Spectroscopic Signatures of Quantum-Coherent Energy Transfer. *Chem. Soc. Rev.* **2013**, *42* (12), 4932–4947.
- (717) Wells, N. P.; Blank, D. a. Correlated Exciton Relaxation in poly(3-Hexylthiophene). *Phys. Rev. Lett.* **2008**, *100* (8), 086403.
- (718) Tekavec, P. F.; Lott, G. A.; Marcus, A. H. Fluorescence-Detected Two-Dimensional Electronic Coherence Spectroscopy by Acousto-Optic Phase Modulation. *J. Chem. Phys.* **2007**, *127* (21), 214307.
- (719) Aeschlimann, M.; Brixner, T.; Fischer, A.; Kramer, C.; Melchior, P.; Pfeiffer, W.; Schneider, C.; Struber, C.; Tuchscherer, P.; Voronine, D. V. Coherent Two-Dimensional Nanoscopy. *Science (Washington, DC, U. S.)* **2011**, *333* (6050), 1723–1726.
- (720) Nardin, G.; Autry, T. M.; Silverman, K. L.; Cundiff, S. T. Multidimensional Coherent Photocurrent Spectroscopy of a Semiconductor Nanostructure. *Opt. Express* **2013**, *21* (23), 28617–28627.

- (721) Fuller, F. D.; Ogilvie, J. P. Experimental Implementations of Two-Dimensional Fourier Transform Electronic Spectroscopy. *Annu. Rev. Phys. Chem.* **2015**, *66* (1), 667–690.
- (722) Karki, K. J.; Widom, J. R.; Seibt, J.; Moody, I.; Lonergan, M. C.; Pullerits, T.; Marcus, A. H. Coherent Two-Dimensional Photocurrent Spectroscopy in a PbS Quantum Dot Photocell. *Nat. Commun.* **2014**, *5*, 5869.
- (723) Li, H.; Bristow, A. D.; Siemens, M. E.; Moody, G.; Cundiff, S. T. Unraveling Quantum Pathways Using Optical 3D Fourier-Transform Spectroscopy. *Nat. Commun.* **2013**, *4*, 1390.
- (724) Mangold, H.; Bakulin, A. a.; Howard, I. a.; Kästner, C.; Egbe, D. a M.; Hoppe, H.; Laquai, F. Control of Charge Generation and Recombination in Ternary Polymer/polymer:fullerene Photovoltaic Blends Using Amorphous and Semi-Crystalline Copolymers as Donors. *Phys. Chem. Chem. Phys.* **2014**, *16*, 20329.
- (725) Vaynzof, Y.; Bakulin, A. a.; Gélinas, S.; Friend, R. H. Direct Observation of Photoinduced Bound Charge-Pair States at an Organic-Inorganic Semiconductor Interface. *Phys. Rev. Lett.* **2012**, *108* (24), 246605.
- (726) Coates, N. E.; Moses, D.; Heeger, A. J. Photocarrier Relaxation through the Manifold of Localized States in a Polymer-Fullerene Bulk Heterojunction Material. *Appl. Phys. Lett.* **2011**, *98* (10), 102103.
- (727) Diesinger, H.; Panahandeh-Fard, M.; Wang, Z.; Baillargeat, D.; Soci, C. Enhancing Photocurrent Transient Spectroscopy by Electromagnetic Modeling. *Rev. Sci. Instrum.* **2012**, *83* (5), 053103.
- (728) Hertel, D.; Bäessler, H. Photoconduction in amorphous organic solids. *ChemPhysChem* **2008**, *9*, 666–688.
- (729) Hegmann, F. A.; Ostroverkhova, O.; Gao, J.; Barker, L.; Tykwinski, R. R.; Bullock, J. E.; Anthony, J. E. Picosecond Transient Photoconductivity in Organic Molecular Crystals. *Proc. SPIE* **2004**, *5352*, 196–207.
- (730) Moses, D.; Wang, J.; Yu, G.; Heeger, a. Temperature-Independent Photoconductivity in Thin Films of Semiconducting Polymers: Photocarrier Sweep-Out Prior to Deep Trapping. *Phys. Rev. Lett.* **1998**, *80* (12), 2685–2688.
- (731) Street, R. A.; Cowan, S.; Heeger, A. J. Experimental Test for Geminate Recombination Applied to Organic Solar Cells. *Phys. Rev. B: Condens. Matter Mater. Phys.* **2010**, *82*, 121301.
- (732) Kokil, A.; Yang, K.; Kumar, J. Techniques for Characterization of Charge Carrier Mobility in Organic Semiconductors. *J. Polym. Sci., Part B: Polym. Phys.* **2012**, *50* (15), 1130–1144.
- (733) Wen, Y. G.; Liu, Y. Q.; Guo, Y. L.; Yu, G.; Hu, W. P. Experimental Techniques for the Fabrication and Characterization of Organic Thin Films for Field-Effect Transistors. *Chem. Rev.* **2011**, *111* (5), 3358–3406.
- (734) Tessler, N. Experimental Techniques and the Underlying Device Physics. *J. Polym. Sci., Part B: Polym. Phys.* **2014**, *52* (17), 1119–1152.
- (735) Chen, Y.; Yi, H. T.; Podzorov, V. High-Resolution Ac Measurements of the Hall Effect in Organic Field-Effect Transistors. *Phys. Rev. Appl.* **2016**, *5* (3), 034008.
- (736) Quintana, J. A.; Boj, P. G.; Villalvilla, J. M.; Díaz-García, M. a.; Ortiz, J.; Martín-Gomis, L.; Fernández-Lázaro, F.; Sastre-Santos, Á. Determination of the Glass Transition Temperature of Photorefractive Polymer Composites from Photoconductivity Measurements. *Appl. Phys. Lett.* **2008**, *92* (4), 041101.
- (737) Quintana, J. A.; Villalvilla, J. M.; Peña, A. D. La; Segura, J. L.; Díaz-García, M. a. Singular Temperatures Connected to Charge Transport Mechanism Transitions in Perylene Bisimides from Steady-State Photocurrent Measurements. *J. Phys. Chem. C* **2015**, *119*, 14023–14028.
- (738) Shakya, P.; Desai, P.; Kreouzis, T.; Gillin, W. P.; Tuladhar, S. M.; Ballantyne, a M.; Nelson, J. The Effect of Applied Magnetic Field on Photocurrent Generation in Poly-3-hexylthiophene:[6,6]-Phenyl C61-Butyric Acid Methyl Ester Photovoltaic Devices. *J. Phys.: Condens. Matter* **2008**, *20* (45), 452203.
- (739) Liphardt, M.; Goonesekera, A.; Ducharme, S.; Takacs, J. M.; Zhang, L. Effect of Beam Attenuation on Photorefractive Grating Erasure. *J. Opt. Soc. Am. B* **1996**, *13* (10), 2252.
- (740) Ostroverkhova, O.; Moerner, W. E.; He, M.; Twieg, R. J. High-Performance Photorefractive Organic Glass with near-Infrared Sensitivity. *Appl. Phys. Lett.* **2003**, *82* (21), 3602–3604.
- (741) Baeg, K. J.; Binda, M.; Natali, D.; Caironi, M.; Noh, Y. Y. Organic Light Detectors: Photodiodes and Phototransistors. *Adv. Mater.* **2013**, *25* (31), 4267–4295.
- (742) Hwang, I.; McNeill, C. R.; Greenham, N. C. Drift-Diffusion Modeling of Photocurrent Transients in Bulk Heterojunction Solar Cells. *J. Appl. Phys.* **2009**, *106* (9), 094506.
- (743) Hu, L.; Liu, X.; Dalgleish, S.; Matsushita, M. M.; Yoshikawa, H.; Awaga, K. Organic Optoelectronic Interfaces with Anomalous Transient Photocurrent. *J. Mater. Chem. C* **2015**, *3*, 5122–5135.
- (744) Gorgolis, S.; Giannopoulou, A.; Anastassopoulos, D.; Kounavis, P. Impact of Pentacene Film Thickness on the Photoresponse Spectra: Determination of the Photocarrier Generation Mechanism. *J. Appl. Phys.* **2012**, *112* (1), 013101.
- (745) Credginton, D.; Kim, Y.; Labram, J.; Anthopoulos, T. D.; Durrant, J. R. Analysis of Recombination Losses in a Pentacene/C. J. *Phys. Chem. Lett.* **2011**, *2* (21), 2759–2763.
- (746) Schubert, M.; Collins, B. a.; Mangold, H.; Howard, I. a.; Schindler, W.; Vandewal, K.; Roland, S.; Behrends, J.; Kraffert, F.; Steyrleuthner, R.; et al. Correlated Donor/acceptor Crystal Orientation Controls Photocurrent Generation in All-Polymer Solar Cells. *Adv. Funct. Mater.* **2014**, *24* (26), 4068–4081.
- (747) Albrecht, S.; Tumbleston, J. R.; Janietz, S.; Dumsch, I.; Allard, S.; Scherf, U.; Ade, H.; Neher, D. Quantifying Charge Extraction in Organic Solar Cells: The Case of Fluorinated PCPDTBT. *J. Phys. Chem. Lett.* **2014**, *5* (7), 1131–1138.
- (748) O'Regan, B. C.; Bakker, K.; Kroeze, J.; Smit, H.; Sommeling, P.; Durrant, J. R. Measuring Charge Transport from Transient Photovoltage Rise Times. A New Tool to Investigate Electron Transport in Nanoparticle Films. *J. Phys. Chem. B* **2006**, *110* (34), 17155–17160.
- (749) Lange, I.; Kniepert, J.; Pingel, P.; Dumsch, I.; Allard, S.; Janietz, S.; Scherf, U.; Neher, D. Correlation between the Open Circuit Voltage and the Energetics of Organic Bulk Heterojunction Solar Cells. *J. Phys. Chem. Lett.* **2013**, *4* (22), 3865–3871.
- (750) Lange, I.; Blakesley, J. C.; Frisch, J.; Vollmer, A.; Koch, N.; Neher, D. Band Bending in Conjugated Polymer Layers. *Phys. Rev. Lett.* **2011**, *106* (21), 216402.
- (751) Lee, M. J.; Chen, Z.; Pietro, R.; Heeney, M.; Sirringhaus, H. Electrooptical Spectroscopy of Uniaxially Aligned Polythiophene Films in Field-Effect Transistors. *Chem. Mater.* **2013**, *25* (10), 2075–2082.
- (752) Chin, X. Y.; Yin, J.; Wang, Z.; Caironi, M.; Soci, C. Mapping Polarons in Polymer FETs by Charge Modulation Microscopy in the Mid-Infrared. *Sci. Rep.* **2014**, *4*, 3626.
- (753) Brown, P.; Thomas, D.; Köhler, A.; Wilson, J.; Kim, J.-S.; Ramsdale, C.; Sirringhaus, H.; Friend, R. Effect of Interchain Interactions on the Absorption and Emission of poly(3-Hexylthiophene). *Phys. Rev. B: Condens. Matter Mater. Phys.* **2003**, *67* (6), 064203.
- (754) Di Pietro, R.; Sirringhaus, H. High Resolution Optical Spectroscopy of Air-Induced Electrical Instabilities in N-Type Polymer Semiconductors. *Adv. Mater.* **2012**, *24* (25), 3367–3372.
- (755) Di Pietro, R.; Fazzi, D.; Kehoe, T. B.; Sirringhaus, H. Spectroscopic Investigation of Oxygen- and Water-Induced Electron Trapping and Charge Transport Instabilities in N-Type Polymer Semiconductors. *J. Am. Chem. Soc.* **2012**, *134* (36), 14877–14889.
- (756) Dalton, L. R.; Sullivan, P. a.; Bale, D. H. Electric Field Poled Organic Electro-Optic Materials: State of the Art and Future Prospects. *Chem. Rev.* **2010**, *110* (1), 25–55.
- (757) Lim, E.; Iwamoto, M. Analysis of Carrier Transport of Organic Devices by Using Nonlinear Optical Polarization. *J. Nanosci. Nanotechnol.* **2015**, *15* (3), 1973–1983.
- (758) Iwamoto, M.; Manaka, T.; Taguchi, D. Modeling and Visualization of Carrier Motion in Organic Films by Optical Second Harmonic Generation and Maxwell-Displacement Current. *J. Phys. D: Appl. Phys.* **2015**, *48* (37), 373001.

- (759) Anglin, T. C.; Sohrabpour, Z.; Massari, A. M. Nonlinear Spectroscopic Markers of Structural Change during Charge Accumulation in Organic Field-Effect Transistors. *J. Phys. Chem. C* **2011**, *115* (41), 20258–20266.
- (760) Anglin, T. C.; Lane, A. P.; Massari, A. M. Real-Time Structural Evolution at the Interface of an Organic Transistor during Thermal Annealing. *J. Mater. Chem. C* **2014**, *2* (17), 3390–3400.
- (761) O'Brien, D. B.; Massari, A. M. Simulated Vibrational Sum Frequency Generation from a Multilayer Thin Film System with Two Active Interfaces. *J. Chem. Phys.* **2013**, *138* (15), 154708.
- (762) O'Brien, D. B.; Massari, A. M. Experimental Evidence for an Optical Interference Model for Vibrational Sum Frequency Generation on Multilayer Organic Thin Film Systems. II. Consideration for Higher Order Terms. *J. Chem. Phys.* **2015**, *142* (2), 024704.
- (763) O'Brien, D. B.; Massari, A. M. Experimental Evidence for an Optical Interference Model for Vibrational Sum Frequency Generation on Multilayer Organic Thin Film Systems. I. Electric Dipole Approximation. *J. Chem. Phys.* **2015**, *142* (2), 024703.
- (764) Anglin, T. C.; Massari, A. M. Polarization-Multiplexed Vibrational Sum Frequency Generation for Comprehensive Simultaneous Characterization of Interfaces. *Opt. Lett.* **2012**, *37* (10), 1754.
- (765) Bittle, E. G.; Brill, J. W.; Anthony, J. E. Electro-Optic Measurement of Carrier Mobility in an Organic Thin-Film Transistor. *Appl. Phys. Lett.* **2010**, *97* (1), 013302.
- (766) Matsui, H.; Hasegawa, T. Visualization of Accumulated Charge Density in Operating Organic Thin-Film Transistors. *Appl. Phys. Lett.* **2009**, *95* (22), 223301.
- (767) Valeur, B. *Molecular Fluorescence: Principles and Applications*; Wiley VCH: 2001.
- (768) Sauer, M.; Hofkens, J.; Enderlein, J. Basic Principles of Fluorescence Spectroscopy. In *Handbook of Fluorescence Spectroscopy and Imaging: From Single Molecules to Ensembles*; Wiley-VCH Verlag GmbH & Co. KGaA: 2011; pp 1–30.
- (769) Kytka, M.; Gisslen, L.; Gerlach, A.; Heinemeyer, U.; Kováč, J.; Scholz, R.; Schreiber, F. Optical Spectra Obtained from Amorphous Films of Rubrene: Evidence for Predominance of Twisted Isomer. *J. Chem. Phys.* **2009**, *130* (21), 214507.
- (770) Tavazzi, S.; Borghesi, A.; Papagni, A.; Spearman, P.; Silvestri, L.; Yassar, A.; Camposo, A.; Polo, M.; Pisignano, D. Optical Response and Emission Waveguiding in Rubrene Crystals. *Phys. Rev. B: Condens. Matter Mater. Phys.* **2007**, *75* (24), 245416.
- (771) Roden, J.; Eisfeld, A.; Dvok, M.; Bnermann, O.; Stienkemeier, F. Vibronic Line Shapes of PTCDA Oligomers in Helium Nanodroplets. *J. Chem. Phys.* **2011**, *134* (5), 054907.
- (772) van Dijk, M. a.; Tchebotareva, a L.; Orrit, M.; Lippitz, M.; Berciaud, S.; Lasne, D.; Cognet, L.; Lounis, B. Absorption and Scattering Microscopy of Single Metal Nanoparticles. *Phys. Chem. Chem. Phys.* **2006**, *8* (30), 3486–3495.
- (773) Gaiduk, A.; Yorulmaz, M.; Ruijgrok, P.; Orrit, M. Room-Temperature Detection of a Single Molecule's Absorption by Photothermal Contrast. *Science (Washington, DC, U. S.)* **2010**, *330* (6002), 353–357.
- (774) Groves, C.; Reid, O. G.; Ginger, D. S. Heterogeneity in Polymer Solar Cells: Local Morphology and Performance in Organic Photovoltaics Studied with Scanning Probe Microscopy. *Acc. Chem. Res.* **2010**, *43* (5), 612–620.
- (775) Takacs, C. J.; Collins, S. D.; Love, J. a.; Mikhailovsky, A. a.; Wynands, D.; Bazan, G. C.; Nguyen, T.-Q.; Heeger, A. J. Mapping Orientational Order in a Bulk Heterojunction Solar Cell with Polarization-Dependent Photoconductive Atomic Force Microscopy. *ACS Nano* **2014**, *8* (8), 8141–8151.
- (776) Giridharagopal, R.; Rayermann, G. E.; Shao, G.; Moore, D. T.; Reid, O. G.; Tillack, A. F.; Masiello, D. J.; Ginger, D. S. Submicrosecond Time Resolution Atomic Force Microscopy for Probing Nanoscale Dynamics. *Nano Lett.* **2012**, *12* (2), 893–898.
- (777) Coffey, D. C.; Ginger, D. S. Time-Resolved Electrostatic Force Microscopy of Polymer Solar Cells. *Nat. Mater.* **2006**, *5* (9), 735–740.
- (778) Gao, J.; Thomas, A. K.; Yang, J.; Aldaz, C.; Yang, G.; Qin, Y.; Grey, J. K. Polythiethylene–Vinylene Structure–Function Correlations Revealed from Resonance Raman Spectroscopy and Photocurrent Imaging. *J. Phys. Chem. C* **2015**, *119*, 8980–8990.
- (779) Naden, A. B.; Loos, J.; MacLaren, D. a. Structure-Function Relations in diF-TES-ADT Blend Organic Field Effect Transistors Studied by Scanning Probe Microscopy. *J. Mater. Chem. C* **2014**, *2* (2), 245–255.
- (780) Puntambekar, K.; Dong, J.; Haugstad, G.; Frisbie, C. D. Structural and Electrostatic Complexity at a Pentacene/insulator Interface. *Adv. Funct. Mater.* **2006**, *16* (7), 879–884.
- (781) Mathijssen, S. G. J.; Kemerink, M.; Sharma, A.; Cölle, M.; Bobbert, P. a.; Janssen, R. a J.; De Leeuw, D. M. Charge Trapping at the Dielectric of Organic Transistors Visualized in Real Time and Space. *Adv. Mater.* **2008**, *20* (5), 975–979.
- (782) Giridharagopal, R.; Shao, G.; Groves, C.; Ginger, D. S. New SPM Techniques for Analyzing OPV Materials. *Mater. Today* **2010**, *13* (9), 50–56.
- (783) Liscio, A.; Palermo, V.; Samori, P. Nanoscale Quantitative Measurement of the Potential of Charged Nanostructures by Electrostatic and Kelvin Probe Force Microscopy: Unraveling Electronic Processes in Complex Materials. *Acc. Chem. Res.* **2010**, *43* (4), 541–550.
- (784) Palermo, V.; Palma, M.; Samori, P. Electronic Characterization of Organic Thin Films by Kelvin Probe Force Microscopy. *Adv. Mater.* **2006**, *18* (2), 145–164.
- (785) Liscio, A. Scanning Probe Microscopy beyond Imaging: A General Tool for Quantitative Analysis. *ChemPhysChem* **2013**, *14* (6), 1283–1292.
- (786) Barth, C.; Foster, A. S.; Henry, C. R.; Shluger, A. L. Recent Trends in Surface Characterization and Chemistry with High-Resolution Scanning Force Methods. *Adv. Mater.* **2011**, *23* (4), 477–501.
- (787) Palermo, V.; Ridolfi, G.; Talarico, A. M.; Favaretto, L.; Barbarella, G.; Camaioni, N.; Samori, P. A Kelvin Probe Force Microscopy Study of the Photogeneration of Surface Charges in All-Thiophene Photovoltaic Blends. *Adv. Funct. Mater.* **2007**, *17* (3), 472–478.
- (788) Collins, L.; Okatan, M. B.; Li, Q.; Kravchenko, I. I.; Lavrik, N. V.; Kalinin, S. V.; Rodriguez, B. J.; Jesse, S. Quantitative 3D-KPFM Imaging with Simultaneous Electrostatic Force and Force Gradient Detection. *Nanotechnology* **2015**, *26* (17), 175707.
- (789) Garcia, R.; Herruzo, E. T. The Emergence of Multifrequency Force Microscopy. *Nat. Nanotechnol.* **2012**, *7* (4), 217–226.
- (790) Lekkala, S.; Marohn, J. A.; Loring, R. F. Electric Force Microscopy of Semiconductors: Theory of Cantilever Frequency Fluctuations and Noncontact Friction. *J. Chem. Phys.* **2013**, *139* (18), 184702.
- (791) Ng, T. N.; Silveira, W. R.; Marohn, J. A. Dependence of Charge Injection on Temperature, Electric Field, and Energetic Disorder in an Organic Semiconductor. *Phys. Rev. Lett.* **2007**, *98* (6), 066101.
- (792) Lekkala, S.; Hoepker, N.; Marohn, J. A.; Loring, R. F. Charge Carrier Dynamics and Interactions in Electric Force Microscopy. *J. Chem. Phys.* **2012**, *137* (12), 124701.
- (793) Smieska, L. M.; Pozdin, V. A.; Luria, J. L.; Hennig, R. G.; Hines, M. A.; Lewis, C. A.; Marohn, J. A. Following Chemical Charge Trapping in Pentacene Thin Films by Selective Impurity Doping and Wavelength Resolved Electric Force Microscopy. *Adv. Funct. Mater.* **2012**, *22* (24), 5096–5106.
- (794) Tello, M.; Chiesa, M.; Duffy, C. M.; Siringhaus, H. Charge Trapping in Intergrain Regions of Pentacene Thin Film Transistors. *Adv. Funct. Mater.* **2008**, *18* (24), 3907–3913.
- (795) Giridharagopal, R.; Ginger, D. S. Characterizing Morphology in Bulk Heterojunction Organic Photovoltaic Systems. *J. Phys. Chem. Lett.* **2010**, *1* (7), 1160–1169.
- (796) Musumeci, C.; Salzmann, I.; Bonacchi, S.; Röthel, C.; Duhm, S.; Koch, N.; Samori, P. The Relationship between Structural and Electrical Characteristics in Perylenecarboxydiimide-Based Nano-architectures. *Adv. Funct. Mater.* **2015**, *25* (17), 2501–2510.

- (797) Mativetsky, J. M.; Loo, Y.-L.; Samori, P. Elucidating the Nanoscale Origins of Organic Electronic Function by Conductive Atomic Force Microscopy. *J. Mater. Chem. C* **2014**, *2* (17), 3118.
- (798) Dante, M.; Peet, J.; Nguyen, T.-Q. Nanoscale Charge Transport and Internal Structure of Bulk Heterojunction Conjugated Polymer/ Fullerene Solar Cells by Scanning Probe Microscopy. *J. Phys. Chem. C* **2008**, *112*, 7241.
- (799) Pingree, L. S. C.; Reid, O. G.; Ginger, D. S. Imaging the Evolution of Nanoscale Photocurrent Collection Networks During Annealing of P3HT: PCBM Solar Cells Networks During Annealing of P3HT: PCBM Solar Cells. *Nano Lett.* **2009**, *9* (8), 2946–2952.
- (800) Moerman, D.; Sebaihi, N.; Kaviyil, S. E.; Leclère, P.; Lazzaroni, R.; Douhéret, O. Towards a Unified Description of the Charge Transport Mechanisms in Conductive Atomic Force Microscopy Studies of Semiconducting Polymers. *Nanoscale* **2014**, *6*, 10596.
- (801) Uttiya, S.; Miozzo, L.; Fumagalli, E. M.; Bergantin, S.; Ruffo, R.; Parravicini, M.; Papagni, a.; Moret, M.; Sassella, a. Connecting Molecule Oxidation to Single Crystal Structural and Charge Transport Properties in Rubrene Derivatives. *J. Mater. Chem. C* **2014**, *2* (21), 4147.
- (802) Wood, D.; Hancox, I.; Jones, T. S.; Wilson, N. R. Quantitative Nanoscale Mapping with Temperature Dependence of the Mechanical and Electrical Properties of poly(3-Hexythiophene) by Conductive Atomic Force Microscopy. *J. Phys. Chem. C* **2015**, *119* (21), 11459–11467.
- (803) Hourani, W.; Rahimi, K.; Botiz, I.; Koch, F. P. V.; Reiter, G.; Lienherth, P.; Heiser, T.; Bubendorff, J.-L.; Simon, L. Anisotropic Charge Transport in Large Single Crystals of  $\pi$ -Conjugated Organic Molecules. *Nanoscale* **2014**, *6* (9), 4774–4780.
- (804) Hunter, S.; Anthopoulos, T. D. Observation of Unusual, Highly Conductive Grain Boundaries in High-Mobility Phase Separated Organic Semiconducting Blend Films Probed by Lateral-Transport Conductive-AFM. *Adv. Mater.* **2013**, *25* (31), 4320–4326.
- (805) Hunter, S.; Chen, J.; Anthopoulos, T. D. Microstructural Control of Charge Transport in Organic Blend Thin-Film Transistors. *Adv. Funct. Mater.* **2014**, *24* (38), 5969–5976.
- (806) Stipe, B. C.; Rezaei, M. A.; Ho, W. Single-Molecule Vibrational Spectroscopy and Microscopy. *Science (Washington, DC, U. S.)* **1998**, *280* (5370), 1732.
- (807) Qiu, X. H.; Nazin, G. V.; Ho, W. Vibronic States in Single Molecule Electron Transport. *Phys. Rev. Lett.* **2004**, *92* (20), 206102.
- (808) Skomski, D.; Jo, J.; Tempas, C. D.; Kim, S.; Lee, D.; Tait, S. L. High-Fidelity Self-Assembly of Crystalline and Parallel-Oriented Organic Thin Films by  $\pi$ - $\pi$  Stacking from a Metal Surface. *Langmuir* **2014**, *30* (33), 10050–10056.
- (809) Skomski, D.; Tait, S. L. Interfacial Organic Layers for Chemical Stability and Crystalline Ordering of Thiophene and Carboxyl Films on a Metal Surface. *J. Phys. Chem. C* **2014**, *118* (3), 1594–1601.
- (810) Kunkel, D. A.; Hooper, J.; Simpson, S.; Miller, D. P.; Routaboul, L.; Braunstein, P.; Doudin, B.; Beniwal, S.; Dowben, P.; Skomski, R.; et al. Self-Assembly of Strongly Dipolar Molecules on Metal Surfaces. *J. Chem. Phys.* **2015**, *142* (10), 101921.
- (811) Kintigh, J. T.; Hodgson, J. L.; Singh, A.; Pramanik, C.; Larson, A. M.; Zhou, L.; Briggs, J. B.; Noll, B. C.; Kheirkhahi, E.; Pohl, K.; et al. A Robust, High-Temperature Organic Semiconductor. *J. Phys. Chem. C* **2014**, *118*, 26955–26963.
- (812) Glowatzki, H.; Heimel, G.; Vollmer, A.; Wong, S. L.; Huang, H.; Chen, W.; Wee, A. T. S.; Rabe, J. P.; Koch, N. Impact of Fluorination on Initial Growth and Stability of Pentacene on Cu(111). *J. Phys. Chem. C* **2012**, *116* (14), 7726–7734.
- (813) Huang, Y.; Chen, W.; Bussolotti, F.; Niu, T.; Wee, A.; Ueno, N.; Kera, S. Impact of Molecule-Dipole Orientation on Energy Level Alignment at the Submolecular Scale. *Phys. Rev. B: Condens. Matter Mater. Phys.* **2013**, *87*, 085205.
- (814) Mali, K. S.; Schwab, M. G.; Feng, X.; Müllen, K.; De Feyter, S. Structural Polymorphism in Self-Assembled Networks of a Triphenylene Based Macrocycle. *Phys. Chem. Chem. Phys.* **2013**, *15* (30), 12495–12503.
- (815) González-Rodríguez, D.; Schenning, A. P. H. J. Hydrogen-Bonded Supramolecular  $\pi$ -Functional Materials. *Chem. Mater.* **2011**, *23* (3), 310–325.
- (816) Zhao, X.; Watkins, D. L.; Galindo, J. F.; Shewmon, N. T.; Roitberg, A. E.; Xue, J.; Castellano, R. K.; Perry, S. S. Hydrogen Bond Directed Assembly of Oligothiophene/fullerene Superstructures on Au(111). *Org. Electron.* **2015**, *19*, 61–69.
- (817) Hirsch, B. E.; McDonald, K. P.; Flood, A. H.; Tait, S. L. Living on the Edge: Tuning Supramolecular Interactions to Design Two-Dimensional Organic Crystals near the Boundary of Two Stable Structural Phases. *J. Chem. Phys.* **2015**, *142* (10), 101914.
- (818) Wang, J.; Dougherty, D. B. Extrinsic Origins of Electronic Disorder in 2D Organic Crystals. *J. Vac. Sci. Technol. B Microelectron. Nanom. Struct.* **2014**, *32* (3), 030601.
- (819) Roelofs, C. W. S.; Charrier, D. S. H.; Dzwilewski, A.; Janssen, R. A. J.; De Leeuw, D. M.; Kemerink, M. Scanning Tunneling Microscopy on Organic Field-Effect Transistors Based on Intrinsic Pentacene. *Appl. Phys. Lett.* **2014**, *104* (26), 263301.
- (820) Qiu, A. X. H.; Nazin, G. V.; Ho, W. Vibrationally Resolved Fluorescence Excited with Submolecular Precision. *Science (Washington, DC, U. S.)* **2003**, *299* (5606), 542–546.
- (821) Huan, Q.; Jiang, Y.; Zhang, Y. Y.; Ham, U.; Ho, W. Spatial Imaging of Individual Vibronic States in the Interior of Single Molecules. *J. Chem. Phys.* **2011**, *135* (1), 014705.
- (822) Qiu, X. H.; Nazin, G. V.; Ho, W. Mechanisms of Reversible Conformational Transitions in a Single Molecule. *Phys. Rev. Lett.* **2004**, *93* (19), 196806.
- (823) Nazin, G. V.; Qiu, X. H.; Ho, W. Charging and Interaction of Individual Impurities in a Monolayer Organic Crystal. *Phys. Rev. Lett.* **2005**, *95* (16), 166103.
- (824) Wu, S.; Nazin, G.; Ho, W. Intramolecular Photon Emission from a Single Molecule in a Scanning Tunneling Microscope. *Phys. Rev. B: Condens. Matter Mater. Phys.* **2008**, *77* (20), 205430.
- (825) Yu, A.; Li, S.; Czap, G.; Ho, W. Single-Molecule Rotational and Vibrational Spectroscopy and Microscopy with the Scanning Tunneling Microscope. *J. Phys. Chem. C* **2015**, *119* (26), 14737–14741.
- (826) Zhao, J.; Feng, M.; Dougherty, D. B.; Sun, H.; Petek, H. Molecular Electronic Level Alignment at Weakly Coupled Organic Film/Metal Interfaces. *ACS Nano* **2014**, *8* (10), 10988–10997.
- (827) Menard, E.; Marchenko, A.; Podzorov, V.; Gershenson, M. E.; Fichou, D.; Rogers, J. A. Nanoscale Surface Morphology and Rectifying Behavior of a Bulk Single-Crystal Organic Semiconductor. *Adv. Mater.* **2006**, *18* (12), 1552–1556.
- (828) Kemerink, M.; Alvarado, S. F.; Muller, P.; Koenraad, P. M.; Salemin, H.; Wolter, J.; Janssen, R. Scanning Tunneling Spectroscopy on Organic Semiconductors: Experiment and Model. *Phys. Rev. B: Condens. Matter Mater. Phys.* **2004**, *70*, 045202.
- (829) Taber, B. N.; Kislitsyn, D. A.; Gervasi, C. F.; Mannsfeld, S. C. B.; Zhang, L.; Briseno, A. L.; Nazin, G. V. Adsorption-Induced Conformational Isomerization of Alkyl-Substituted Thiophene Oligomers on Au(111): Impact on the Interfacial Electronic Structure. *ACS Appl. Mater. Interfaces* **2015**, *7* (28), 15138–15142.
- (830) Kislitsyn, D. A.; Taber, B. N.; Gervasi, C. F.; Mannsfeld, S. C. B.; Zhang, L.; Briseno, A. L.; Nazin, G. V. Coverage-Dependent Self-Assembly Regimes of Alkyl-Substituted Thiophene Oligomers on Au(111): Scanning Tunneling Microscopy and Spectroscopy. *J. Phys. Chem. C* **2015**, *119* (48), 26959–26967.
- (831) Ilyas, N.; Monti, O. L. A. Interplay of Local and Global Interfacial Electronic Structure of a Strongly Coupled Dipolar Organic Semiconductor. *Phys. Rev. B: Condens. Matter Mater. Phys.* **2014**, *90* (12), 125435.
- (832) Milan, D. C.; Villalvilla, J. M.; Díaz-García, M. A.; Untiedt, C. Comparing the Distribution of the Electronic Gap of an Organic Molecule with Its Photoluminescence Spectrum. *Appl. Phys. Lett.* **2013**, *102* (16), 163307.
- (833) Lackinger, M.; Janson, M. S.; Ho, W. Localized Interaction of Single Porphyrin Molecules with Oxygen Vacancies on TiO<sub>2</sub>(110). *J. Chem. Phys.* **2012**, *137* (23), 234707.

- (834) Li, S.; Yuan, D.; Yu, A.; Czap, G.; Wu, R.; Ho, W. Rotational Spectromicroscopy: Imaging the Orbital Interaction between Molecular Hydrogen and an Adsorbed Molecule. *Phys. Rev. Lett.* **2015**, *114* (20), 206101.
- (835) Jiang, Y.; Huan, Q.; Fabris, L.; Bazan, G. C.; Ho, W. Submolecular Control, Spectroscopy and Imaging of Bond-Selective Chemistry in Single Functionalized Molecules. *Nat. Chem.* **2013**, *5* (1), 36–41.
- (836) Ham, U.; Ho, W. Spin Splitting Unconstrained by Electron Pairing: The Spin-Vibronic States. *Phys. Rev. Lett.* **2012**, *108* (10), 106803.
- (837) Brede, J.; Atodiresei, N.; Caciuc, V.; Bazarnik, M.; Al-Zubi, A.; Blügel, S.; Wiesendanger, R. Long-Range Magnetic Coupling between Nanoscale Organic–metal Hybrids Mediated by a Nanoskyrmion Lattice. *Nat. Nanotechnol.* **2014**, *9* (12), 1018–1023.
- (838) Chakrabarti, S.; Pal, A. J. On the Valve Nature of a Monolayer of Aligned Molecular Magnets in Tunneling Spin-Polarized Electrons: Towards Organic Molecular Spintronics. *Appl. Phys. Lett.* **2014**, *104* (1), 013305.
- (839) Brede, J.; Wiesendanger, R. Spin-Resolved Imaging and Spectroscopy of Individual Molecules with Sub-Molecular Spatial Resolution. *MRS Bull.* **2014**, *39* (7), 608–613.
- (840) Fei, X.; Wu, G.; Lopez, V.; Lu, G.; Gao, H. J.; Gao, L. Spin-Dependent Conductance in Co/C60/Co/Ni Single-Molecule Junctions in the Contact Regime. *J. Phys. Chem. C* **2015**, *119* (21), 11975–11981.
- (841) Moore, A. M.; Mantooth, B. A.; Donhauser, Z. J.; Yao, Y.; Tour, J. M.; Weiss, P. S. Real-Time Measurements of Conductance Switching and Motion of Single Oligo(phenylene Ethynylene) Molecules. *J. Am. Chem. Soc.* **2007**, *129* (34), 10352–10353.
- (842) Kemiktarak, U.; Ndukum, T.; Schwab, K. C.; Ekinci, K. L. Radio-Frequency Scanning Tunneling Microscopy. *Nature* **2007**, *450* (7166), 85–88.
- (843) Loth, S.; Eitzkorn, M.; Lutz, C. P.; Eigler, D. M.; Heinrich, A. J. Measurement of Fast Electron Spin Relaxation Times with Atomic Resolution. Supplement. *Science (Washington, DC, U. S.)* **2010**, *329* (5999), 1628–1630.
- (844) Cocker, T.; Jelic, V.; Gupta, M.; Molesky, S.; Burgess, J.; De Los Reyes, G.; Titova, L.; Tsui, Y.; Freeman, M. R.; Hegmann, F. A. An Ultrafast Terahertz Scanning Tunneling Microscope. *Nat. Photonics* **2013**, *7* (8), 620–625.
- (845) Barbara, P. F.; Adams, D. M.; O'Connor, D. B. Characterization of Organic Thin Film Materials With Near-Field Scanning Optical Microscopy (Nsom). *Annu. Rev. Mater. Sci.* **1999**, *29* (1), 433–469.
- (846) Rivnay, J.; Mannsfeld, S. C. B.; Miller, C. E.; Salleo, A.; Toney, M. F. Quantitative Determination of Organic Semiconductor Microstructure from the Molecular to Device Scale. *Chem. Rev.* **2012**, *112* (10), 5488–5519.
- (847) Schubert, M.; Dolfen, D.; Frisch, J.; Roland, S.; Steyrlleuthner, R.; Stiller, B.; Chen, Z.; Scherf, U.; Koch, N.; Facchetti, A.; et al. Influence of Aggregation on the Performance of All-Polymer Solar Cells Containing Low-Bandgap Naphthalenediimide Copolymers. *Adv. Energy Mater.* **2012**, *2*, 369–380.
- (848) Kuehn, S.; Pingel, P.; Breusing, M.; Fischer, T.; Stumpe, J.; Neher, D.; Elsaesser, T. High-Resolution near-Field Optical Investigation of Crystalline Domains in Oligomeric PQT-12 Thin Films. *Adv. Funct. Mater.* **2011**, *21* (5), 860–868.
- (849) Huang, L.; Liao, Q.; Shi, Q.; Fu, H.; Ma, J.; Yao, J. Rubrene Micro-Crystals from Solution Routes: Their Crystallography, Morphology and Optical Properties. *J. Mater. Chem.* **2010**, *20* (1), 159.
- (850) Karki, K.; Nambodiri, M.; Khan, T. Z.; Materny, A. Pump-Probe Scanning near Field Optical Microscopy: Sub-Wavelength Resolution Chemical Imaging and Ultrafast Local Dynamics. *Appl. Phys. Lett.* **2012**, *100* (15), 153103.
- (851) Nambodiri, M.; Khan, T.; Karki, K.; Kazemi, M. M.; Bom, S.; Flachenecker, G.; Nambodiri, V.; Materny, A. Nonlinear Spectroscopy in the near-Field: Time Resolved Spectroscopy and Sub-wavelength Resolution Non-Invasive Imaging. *Nanophotonics* **2014**, *3* (1–2), 61–73.
- (852) Akselrod, G. M.; Deotare, P. B.; Thompson, N. J.; Lee, J.; Tisdale, W. a.; Baldo, M. a.; Menon, V. M.; Bulović, V. Visualization of Exciton Transport in Ordered and Disordered Molecular Solids. *Nat. Commun.* **2014**, *5*, 3646.
- (853) Sharifzadeh, S.; Wong, C. Y.; Wu, H.; Cotts, B. L.; Kronik, L.; Ginsberg, N. S.; Neaton, J. B. Relating the Physical Structure and Optoelectronic Function of Crystalline TIPS-Pentacene. *Adv. Funct. Mater.* **2015**, *25*, 2038–2046.
- (854) Oklobia, O.; Shafai, T. S. A Quantitative Study of the Formation of PCBM Clusters upon Thermal Annealing of P3HT/PCBM Bulk Heterojunction Solar Cell. *Sol. Energy Mater. Sol. Cells* **2013**, *117*, 1–8.
- (855) Riisness, I.; Carach, C.; Gordon, M. J. Spatially Resolved Spectral Mapping of Phase Mixing and Charge Transfer Excitons in Bulk Heterojunction Solar Cell Films. *Appl. Phys. Lett.* **2012**, *100* (7), 073308.
- (856) Sinwani, M.; Tischler, Y. R. Raman and Photoluminescence Properties of Red and Yellow Rubrene Crystals. *J. Phys. Chem. C* **2014**, *118* (26), 14528–14533.
- (857) Polli, D.; Grancini, G.; Clark, J.; Celebrano, M.; Virgili, T.; Cerullo, G.; Lanzani, G. Nanoscale Imaging of the Interface Dynamics in Polymer Blends by Femtosecond Pump-Probe Confocal Microscopy. *Adv. Mater.* **2010**, *22* (28), 3048–3051.
- (858) Sciascia, C.; Celebrano, M.; Binda, M.; Natali, D.; Lanzani, G.; Cabanillas-Gonzalez, J. R. Electric Field and Charge Distribution Imaging with Sub-Micron Resolution in an Organic Thin-Film Transistor. *Org. Electron.* **2012**, *13* (1), 66–70.
- (859) Grancini, G.; Polli, D.; Fazzi, D.; Cabanillas-gonzalez, J.; Cerullo, G.; Lanzani, G. Transient Absorption Imaging of P3HT:PCBM Photovoltaic Blend. *J. Phys. Chem. Lett.* **2011**, *2* (9), 1099–1105.
- (860) Cabanillas-Gonzalez, J.; Grancini, G.; Lanzani, G. Pump-Probe Spectroscopy in Organic Semiconductors: Monitoring Fundamental Processes of Relevance in Optoelectronics. *Adv. Mater.* **2011**, *23* (46), 5468–5485.
- (861) Wong, C. Y.; Cotts, B. L.; Wu, H.; Ginsberg, N. S. Exciton Dynamics Reveal Aggregates with Intermolecular Order at Hidden Interfaces in Solution-Cast Organic Semiconducting Films. *Nat. Commun.* **2015**, *6*, 5946.
- (862) Wong, C. Y.; Penwell, S. B.; Cotts, B. L.; Noriega, R.; Wu, H.; Ginsberg, N. S. Revealing Exciton Dynamics in a Small-Molecule Organic Semiconducting Film with Subdomain Transient Absorption Microscopy. *J. Phys. Chem. C* **2013**, *117* (42), 22111–22122.
- (863) Grancini, G.; Biasiucci, M.; Mastria, R.; Scotognella, F.; Tassone, F.; Polli, D.; Gigli, G.; Lanzani, G. Dynamic Microscopy Study of Ultrafast Charge Transfer in a Hybrid P3HT/Hyperbranched CdSe Nanoparticle Blend for Photovoltaics. *J. Phys. Chem. Lett.* **2012**, *3*, 517–523.
- (864) Thompson, M. A.; Lew, M. D.; Moerner, W. E. Extending Microscopic Resolution with Single-Molecule Imaging and Active Control. *Annu. Rev. Biophys.* **2012**, *41* (1), 321–342.
- (865) von Diezmann, A.; Lee, M. Y.; Lew, M. D.; Moerner, W. E. Correcting Field-Dependent Aberrations with Nanoscale Accuracy in Three-Dimensional Single-Molecule Localization Microscopy. *Optica* **2015**, *2* (11), 985.
- (866) Penwell, S. B.; Ginsberg, L. D. S.; Ginsberg, N. S. Bringing Far-Field Subdiffraction Optical Imaging to Electronically Coupled Optoelectronic Molecular Materials Using Their Endogenous Chromophores. *J. Phys. Chem. Lett.* **2015**, *6*, 2767–2772.
- (867) Lupton, J. M. Single-Molecule Spectroscopy for Plastic Electronics: Materials Analysis from the Bottom-Up. *Adv. Mater.* **2010**, *22* (15), 1689–1721.
- (868) Kozankiewicz, B.; Orrit, M. Single-Molecule Photophysics, from Cryogenic to Ambient Conditions. *Chem. Soc. Rev.* **2014**, *43* (4), 1029–1043.

- (869) Brinks, D.; Hildner, R.; van Dijk, E. M. H. P.; Stefani, F. D.; Nieder, J. B.; Hernando, J.; van Hulst, N. F. Ultrafast Dynamics of Single Molecules. *Chem. Soc. Rev.* **2014**, *43* (8), 2476–2491.
- (870) Bolinger, J.; Traub, M.; Brazard, J.; Adachi, T.; Barbara, P.; Vanden Bout, D. Conformation and Energy Transfer in Single Conjugated Polymers. *Acc. Chem. Res.* **2012**, *45* (11), 1992–2001.
- (871) Vogelsang, J.; Lupton, J. M. Solvent Vapor Annealing of Single Conjugated Polymer Chains: Building Organic Optoelectronic Materials from the Bottom up. *J. Phys. Chem. Lett.* **2012**, *3* (11), 1503–1513.
- (872) Wöll, D.; Braeken, E.; Deres, A.; De Schryver, F. C.; Uji-i, H.; Hofkens, J. Polymers and Single Molecule Fluorescence Spectroscopy, What Can We Learn? *Chem. Soc. Rev.* **2009**, *38* (2), 313–328.
- (873) Kulzer, F.; Xia, T.; Orrit, M. Single Molecules as Optical Nanoprobes for Soft and Complex Matter. *Angew. Chem., Int. Ed.* **2010**, *49* (5), 854–866.
- (874) Hania, P. R.; Thomsson, D.; Scheblykin, I. G. Host Matrix Dependent Fluorescence Intensity Modulation by an Electric Field in Single Conjugated Polymer Chains. *J. Phys. Chem. B* **2006**, *110* (51), 25895–25900.
- (875) Habuchi, S.; Onda, S.; Vacha, M. Molecular Weight Dependence of Emission Intensity and Emitting Sites Distribution within Single Conjugated Polymer Molecules. *Phys. Chem. Chem. Phys.* **2011**, *13* (5), 1743–1753.
- (876) Schindler, F.; Lupton, J. M. Single Chromophore Spectroscopy of MEH-PPV: Homing-in on the Elementary Emissive Species in Conjugated Polymers. *ChemPhysChem* **2005**, *6* (5), 926–934.
- (877) Lin, H.; Tian, Y.; Zapadka, K.; Persson, G.; Thomsson, D.; Mirzov, O.; Larsson, P. O.; Widengren, J.; Scheblykin, I. G. Fate of Excitations in Conjugated Polymers: Single-Molecule Spectroscopy Reveals Nonemissive “Dark” Regions in MEH-PPV Individual Chains. *Nano Lett.* **2009**, *9* (12), 4456–4461.
- (878) Vogelsang, J.; Adachi, T.; Brazard, J.; Vanden Bout, D. a.; Barbara, P. F. Self-Assembly of Highly Ordered Conjugated Polymer Aggregates with Long-Range Energy Transfer. *Nat. Mater.* **2011**, *10* (12), 942–946.
- (879) Steiner, F.; Vogelsang, J.; Lupton, J. M. Singlet-Triplet Annihilation Limits Exciton Yield in poly(3-Hexylthiophene). *Phys. Rev. Lett.* **2014**, *112* (13), 137402.
- (880) Thiessen, A.; Vogelsang, J.; Adachi, T.; Steiner, F.; Vanden Bout, D.; Lupton, J. M. Unraveling the Chromophoric Disorder of poly(3-Hexylthiophene). *Proc. Natl. Acad. Sci. U. S. A.* **2013**, *110* (38), E3550–E3556.
- (881) Adachi, T.; Vogelsang, J.; Lupton, J. M. Unraveling the Electronic Heterogeneity of Charge Traps in Conjugated Polymers by Single-Molecule Spectroscopy. *J. Phys. Chem. Lett.* **2014**, *5* (3), 573–577.
- (882) Honmou, Y.; Hirata, S.; Komiyama, H.; Hiyoshi, J.; Kawauchi, S.; Iyoda, T.; Vacha, M. Single-Molecule Electroluminescence and Photoluminescence of Polyfluorene Unveils the Photophysics behind the Green Emission Band. *Nat. Commun.* **2014**, *5*, 4666.
- (883) Vosch, T.; Fron, E.; Hotta, J. I.; Deres, A.; Uji-i, H.; Idrissi, A.; Yang, J.; Kim, D.; Puhl, L.; Haeuseler, A.; et al. Synthesis, Ensemble, and Single Molecule Characterization of a Diphenyl-Acetylene Linked Peryleneimide Trimer. *J. Phys. Chem. C* **2009**, *113* (27), 11773–11782.
- (884) Yoo, H.; Yang, J.; Yousef, A.; Wasielewski, M. R.; Kim, D. Excimer Formation Dynamics of Intramolecular Pi-Stacked Peryleneimides Probed by Single-Molecule Fluorescence Spectroscopy. *J. Am. Chem. Soc.* **2010**, *132* (11), 3939–3944.
- (885) Yoo, H.; Bahng, H. W.; Wasielewski, M. R.; Kim, D. Polymer Matrix Dependence of Conformational Dynamics within a  $\pi$ -Stacked Peryleneimide Dimer and Trimer Revealed by Single Molecule Fluorescence Spectroscopy. *Phys. Chem. Chem. Phys.* **2012**, *14* (6), 2001–2007.
- (886) Wustholz, K. L.; Sluss, D. R. B.; Kahr, B.; Reid, P. J. Applications of Single-Molecule Microscopy to Problems in Dyed Composite Materials. *Int. Rev. Phys. Chem.* **2008**, *27* (2), 167–200.
- (887) Lord, S. J.; Conley, N. R.; Lee, H. L. D.; Nishimura, S. Y.; Pomerantz, A. K.; Willets, K. a.; Lu, Z.; Wang, H.; Liu, N.; Samuel, R.; et al. DCDHF Fluorophores for Single-Molecule Imaging in Cells. *ChemPhysChem* **2009**, *10* (1), 55–65.
- (888) Tian, Y.; Navarro, P.; Orrit, M. Single Molecule as a Local Acoustic Detector for Mechanical Oscillators. *Phys. Rev. Lett.* **2014**, *113* (13), 135505.
- (889) Kol’chenko, M. a.; Nicolet, a. L.; Galouzis, M. D.; Hofmann, C.; Kozankiewicz, B.; Orrit, M. Single Molecules Detect Ultra-Slow Oscillators in a Molecular Crystal Excited by Ac Voltages. *New J. Phys.* **2009**, *11*, 023037.
- (890) Bartko, A. P.; Dickson, R. M. Imaging Three-Dimensional Single Molecule Orientations. *J. Phys. Chem. B* **1999**, *103* (51), 11237–11241.
- (891) Zhang, G.; Xiao, L.; Zhang, F.; Wang, X.; Jia, S. Single Molecules Reorientation Reveals the Dynamics of Polymer Glasses Surface. *Phys. Chem. Chem. Phys.* **2010**, *12* (10), 2308–2312.
- (892) Wirtz, A. C.; Hofmann, C.; Groenen, E. J. J. Stretched Polyethylene Films Probed by Single Molecules. *J. Phys. Chem. B* **2006**, *110*, 21623–21629.
- (893) Wallace, P. M.; Sluss, D. R. B.; Dalton, L. R.; Robinson, B. H.; Reid, P. J. Single-Molecule Microscopy Studies of Electric-Field Poling in Chromophore-Polymer Composite Materials. *J. Phys. Chem. B* **2006**, *110* (1), 75–82.
- (894) Werley, C. a.; Moerner, W. E. Single-Molecule Nanoprobes Explore Defects in Spin-Grown Crystal. *J. Phys. Chem. B* **2006**, *110* (38), 18939–18944.
- (895) Banasiewicz, M.; Wiacek, D.; Kozankiewicz, B. Structural Dynamics of 2,3-Dimethylnaphthalene Crystals Revealed by Fluorescence of Single Terrylene Molecules. *Chem. Phys. Lett.* **2006**, *425* (1–3), 94–98.
- (896) Jung, C.; Hellriegel, C.; Platschek, B.; Wöhrle, D.; Bein, T.; Michaelis, J.; Bräuchle, C. Simultaneous Measurement of Orientational and Spectral Dynamics of Single Molecules in Nanostructured Host-Guest Materials. *J. Am. Chem. Soc.* **2007**, *129* (17), 5570–5579.
- (897) Hofmann, C.; Nicolet, A.; Kol’chenko, M. a.; Orrit, M. Towards Nanoprobes for Conduction in Molecular Crystals: Dibenzoterrylene in Anthracene Crystals. *Chem. Phys.* **2005**, *318* (1–2), 1–6.
- (898) Cichos, F.; von Borczyskowski, C.; Orrit, M. Power-Law Intermittency of Single Emitters. *Curr. Opin. Colloid Interface Sci.* **2007**, *12* (6), 272–284.
- (899) Riley, E. a.; Hess, C. M.; Reid, P. J. Photoluminescence Intermittency from Single Quantum Dots to Organic Molecules: Emerging Themes. *Int. J. Mol. Sci.* **2012**, *13* (10), 12487–12518.
- (900) Ishitobi, H.; Kai, T.; Fujita, K.; Sekkat, Z.; Kawata, S. On Fluorescence Blinking of Single Molecules in Polymers. *Chem. Phys. Lett.* **2009**, *468* (4–6), 234–238.
- (901) Riley, E. a.; Hess, C. M.; Whitham, P. J.; Reid, P. J. Beyond Power Laws: A New Approach for Analyzing Single Molecule Photoluminescence Intermittency. *J. Chem. Phys.* **2012**, *136* (18), 184508.
- (902) Schmidt, R.; Krasselt, C.; Göhler, C.; Von Borczyskowski, C. The Fluorescence Intermittency for Quantum Dots Is Not Power-Law Distributed: A Luminescence Intensity Resolved Approach. *ACS Nano* **2014**, *8* (4), 3506–3521.
- (903) Galland, C.; Ghosh, Y.; Steinbrück, A.; Sykora, M.; Hollingsworth, J. a.; Klimov, V. I.; Htoon, H. Two Types of Luminescence Blinking Revealed by Spectroelectrochemistry of Single Quantum Dots. *Nature* **2011**, *479* (7372), 203–207.
- (904) Zhao, J.; Nair, G.; Fisher, B. R.; Bawendi, M. G. Challenge to the Charging Model of Semiconductor-Nanocrystal Fluorescence Intermittency from off-State Quantum Yields and Multiexciton Blinking. *Phys. Rev. Lett.* **2010**, *104* (15), 157403.
- (905) Rosen, S.; Schwartz, O.; Oron, D. Transient Fluorescence of the off State in Blinking CdSe/CdS/ZnS Semiconductor Nanocrystals Is Not Governed by Auger Recombination. *Phys. Rev. Lett.* **2010**, *104* (15), 157404.

- (906) Riley, E. a; Bingham, C.; Bott, E. D.; Kahr, B.; Reid, P. J. Two Mechanisms for Fluorescence Intermittency of Single Violamine R Molecules. *Phys. Chem. Chem. Phys.* **2011**, *13* (5), 1879–1887.
- (907) Haase, M.; Hübner, C. G.; Nolde, F.; Müllen, K.; Basché, T. Photoblinking and Photobleaching of Rylene Diimide Dyes. *Phys. Chem. Chem. Phys.* **2011**, *13* (5), 1776–1785.
- (908) Frantsuzov, P. A.; Volkán-Kacsó, S.; Janko, B. Universality of the Fluorescence Intermittency in Nanoscale Systems: Experiment and Theory. *Nano Lett.* **2013**, *13* (2), 402–408.
- (909) Hoogenboom, J. P.; Hernando, J.; García-Parajó, M. F.; Van Hulst, N. F. Memory in Single Emitter Fluorescence Blinking Reveals the Dynamic Character of Nanoscale Charge Tunneling. *J. Phys. Chem. C* **2008**, *112* (9), 3417–3422.
- (910) Wilma, K.; Issac, A.; Chen, Z.; Würthner, F.; Hildner, R.; Köhler, J. Tracing Single Electrons in a Disordered Polymer Film at Room Temperature. *J. Phys. Chem. Lett.* **2016**, *7*, 1478–1483.
- (911) Tretiak, S.; Saxena, a; Martin, R. L.; Bishop, a R. Conformational Dynamics of Photoexcited Conjugated Molecules. *Phys. Rev. Lett.* **2002**, *89* (9), 097402.
- (912) Da Como, E.; Borys, N. J.; Strohrriegl, P.; Walter, M. J.; Lupton, J. M. Formation of a Defect-Free Pi-Electron System in Single Beta-Phase Polyfluorene Chains. *J. Am. Chem. Soc.* **2011**, *133* (11), 3690–3692.
- (913) Lippitz, M.; Hübner, C. G.; Christ, T.; Eichner, H.; Bordat, P.; Herrmann, A.; Müllen, K.; Basché, T. Coherent Electronic Coupling versus Localization in Individual Molecular Dimers. *Phys. Rev. Lett.* **2004**, *92* (10), 103001.
- (914) Steiner, F.; Bange, S.; Vogelsang, J.; Lupton, J. M. Spontaneous Fluctuations of Transition Dipole Moment Orientation in OLED Triplet Emitters. *J. Phys. Chem. Lett.* **2015**, *6*, 999–1004.
- (915) Aggarwal, a V.; Thiessen, A.; Idelson, A.; Kalle, D.; Würsch, D.; Stangl, T.; Steiner, F.; Jester, S.-S.; Vogelsang, J.; Höger, S.; et al. Fluctuating Exciton Localization in Giant  $\pi$ -Conjugated Spoked-Wheel Macrocycles. *Nat. Chem.* **2013**, *5* (11), 964–970.
- (916) Thiessen, A.; Würsch, D.; Jester, S.-S.; Aggarwal, A. V.; Bange, S.; Vogelsang, J.; Höger, S.; Lupton, J. M. Exciton Localization in Extended  $\pi$ -Electron Systems: Comparison of Linear and Cyclic Structures. *J. Phys. Chem. B* **2015**, *119*, 9949–9958.
- (917) Adachi, T.; Vogelsang, J.; Lupton, J. M. Chromophore Bending Controls Fluorescence Lifetime in Single Conjugated Polymer Chains. *J. Phys. Chem. Lett.* **2014**, *5* (12), 2165–2170.
- (918) Hernando, J.; Van Dijk, E. M. H. P.; Hoogenboom, J. P.; García-López, J. J.; Reinhoudt, D. N.; Crego-Calama, M.; García-Parajó, M. F.; Van Hulst, N. F. Effect of Disorder on Ultrafast Exciton Dynamics Probed by Single Molecule Spectroscopy. *Phys. Rev. Lett.* **2006**, *97* (21), 216403.
- (919) Yoo, H.; Furumaki, S.; Yang, J.; Lee, J. E.; Chung, H.; Oba, T.; Kobayashi, H.; Rybtchinski, B.; Wilson, T. M.; Wasielewski, M. R.; et al. Excitonic Coupling in Linear and Trefoil Trimer Perylenediimide Molecules Probed by Single-Molecule Spectroscopy. *J. Phys. Chem. B* **2012**, *116* (42), 12878–12886.
- (920) Schindler, F.; Lupton, J. M. Electrothermal Manipulation of Individual Chromophores in Single Conjugated Polymer Chains: Controlling Intrachain Fret, Blinking, and Spectral Diffusion. *Nano Lett.* **2010**, *10* (7), 2683–2689.
- (921) Stangl, T.; Bange, S.; Schmitz, D.; Würsch, D.; Höger, S.; Vogelsang, J.; Lupton, J. M. Temporal Switching of Homo-FRET Pathways in Single-Chromophore Dimer Models of  $\pi$ -Conjugated Polymers. *J. Am. Chem. Soc.* **2013**, *135* (1), 78–81.
- (922) Nicolet, a. a. L.; Kol'chenko, M. a.; Hofmann, C.; Kozankiewicz, B.; Orrit, M. Nanoscale Probing of Charge Transport in an Organic Field-Effect Transistor at Cryogenic Temperatures. *Phys. Chem. Chem. Phys.* **2013**, *15* (12), 4415.
- (923) Backer, A. S.; Moerner, W. E. Extending Single-Molecule Microscopy Using Optical Fourier Processing. *J. Phys. Chem. B* **2014**, *118*, 8313–8329.
- (924) Lew, M. D.; Moerner, W. E. Azimuthal Polarization Filtering for Accurate, Precise, and Robust Single-Molecule Localization Microscopy. *Nano Lett.* **2014**, *14* (11), 6407–6413.
- (925) Backer, A. S.; Moerner, W. E. Determining the Rotational Mobility of a Single Molecule from a Single Image: A Numerical Study. *Opt. Express* **2015**, *23* (4), 4255.
- (926) Winterhalder, M. J.; Zumbusch, a; Lippitz, M.; Orrit, M. Toward Far-Field Vibrational Spectroscopy of Single Molecules at Room Temperature. *J. Phys. Chem. B* **2011**, *115* (18), 5425–5430.
- (927) Brinks, D.; Hildner, R.; Stefani, F. D.; van Hulst, N. F. Coherent Control of Single Molecules at Room Temperature. *Faraday Discuss.* **2011**, *153*, 51.
- (928) Basché, T. Photothermal Contrast Reaches Single-Molecule Sensitivity. *Angew. Chem., Int. Ed.* **2011**, *50* (16), 3602–3604.
- (929) Celebrano, M.; Kukura, P.; Renn, A.; Sandoghdar, V. Single-Molecule Imaging by Optical Absorption. *Nat. Photonics* **2011**, *5* (2), 95–98.
- (930) Singh, A.; Calbris, G.; Van Hulst, N. F. Vectorial Nanoscale Mapping of Optical Antenna Fields by Single Molecule Dipoles. *Nano Lett.* **2014**, *14* (8), 4715–4723.
- (931) Wientjes, E.; Renger, J.; Curto, A. G.; Cogdell, R.; van Hulst, N. F. Strong Antenna-Enhanced Fluorescence of a Single Light-Harvesting Complex Shows Photon Antibunching. *Nat. Commun.* **2014**, *5*, 4236.
- (932) Lee, K.; Chen, X.; Eghlidi, H.; Renn, A.; Sandoghdar, V.; Gotzinger, S. A Planar Dielectric Antenna for Directional Single-Photon Emission and near-Unity Collection Efficiency. *Nat. Photonics* **2011**, *5*, 166–169.
- (933) Khatua, S.; Orrit, M. Toward Single-Molecule Microscopy on a Smart Phone. *ACS Nano* **2013**, *7* (10), 8340–8343.
- (934) Wei, Q.; Qi, H.; Luo, W.; Tseng, D.; Ki, S. J.; Wan, Z.; Göröcs, Z.; Bentolila, L. A.; Wu, T. T.; Sun, R.; et al. Fluorescent Imaging of Single Nanoparticles and Viruses on a Smart Phone. *ACS Nano* **2013**, *7* (10), 9147–9155.
- (935) Dicker, G.; de Haas, M.; Siebbeles, L. Signature of Exciton Annihilation in the Photoconductance of Regioregular poly(3-Hexylthiophene). *Phys. Rev. B: Condens. Matter Mater. Phys.* **2005**, *71*, 155205.
- (936) Dimitrov, S. D.; Wheeler, S.; Niedzialek, D.; Schroeder, B. C.; Utzat, H.; Frost, J. M.; Yao, J.; Gillett, A.; Tuladhar, P. S.; McCulloch, I.; et al. Polaron Pair Mediated Triplet Generation in Polymer/fullerene Blends. *Nat. Commun.* **2015**, *6*, 6501.
- (937) Singh, S.; Vardeny, Z. V. Ultrafast Transient Spectroscopy of Polymer/fullerene Blends for Organic Photovoltaic Applications. *Materials* **2013**, *6* (3), 897–910.
- (938) Sharenko, A.; Gehrig, D.; Laquai, F.; Nguyen, T.-Q. The Effect of Solvent Additive on the Charge Generation and Photovoltaic Performance of a Solution-Processed Small Molecule:Perylene Diimide Bulk Heterojunction Solar Cell. *Chem. Mater.* **2014**, *26*, 4109–4118.
- (939) Kumar, A.; Pace, G.; Bakulin, A. a.; Fang, J.; Ho, P. K. H.; Huck, W. T. S.; Friend, R. H.; Greenham, N. C. Donor–acceptor Interface Modification by Zwitterionic Conjugated Polyelectrolytes in Polymer Photovoltaics. *Energy Environ. Sci.* **2013**, *6* (5), 1589.
- (940) Shoaee, S.; Subramaniyan, S.; Xin, H.; Keiderling, C.; Tuladhar, P. S.; Jamieson, F.; Jenekhe, S. a.; Durrant, J. R. Charge Photogeneration for a Series of Thiazolo-Thiazole Donor Polymers Blended with the Fullerene Electron Acceptors PCBM and ICBA. *Adv. Funct. Mater.* **2013**, *23* (26), 3286–3298.
- (941) Frolov, S.; Kloc, C.; Batlogg, B.; Wohlgenannt, M.; Jiang, X.; Vardeny, Z. Excitation Dynamics in Single Molecular Crystals of  $\alpha$ -Hexathiophene from Femtoseconds to Milliseconds. *Phys. Rev. B: Condens. Matter Mater. Phys.* **2001**, *63* (20), 205203.
- (942) Savenije, T. J.; Murthy, D. H. K.; Gunz, M.; Gorenflot, J.; Siebbeles, L. D. a.; Dyakonov, V.; Deibel, C. Absence of Postnanosecond Charge Carrier Relaxation in Poly(3-hexylthiophene)/Fullerene Blends. *J. Phys. Chem. Lett.* **2011**, *2* (12), 1368–1371.
- (943) Zhong, C.; Huang, F.; Cao, Y.; Moses, D.; Heeger, A. J. Role of Localized States on Carrier Transport in Bulk Heterojunction Materials Comprised of Organic Small Molecule Donors. *Adv. Mater.* **2014**, *26* (15), 2341–2345.

- (944) Raimondo, L.; Laicini, M.; Spearman, P.; Tavazzi, S.; Borghesi, A. Effect of Static and Dynamic Disorder on Exciton Mobility in Oligothiophenes. *J. Chem. Phys.* **2006**, *125* (2), 024702.
- (945) Najafov, H.; Biaggio, I.; Chuang, T. K.; Hatalis, M. K. Exciton Dissociation by a Static Electric Field Followed by Nanoscale Charge Transport in PPV Polymer Films. *Phys. Rev. B: Condens. Matter Mater. Phys.* **2006**, *73* (12), 125202.
- (946) Inal, S.; Schubert, M.; Sellinger, A.; Neher, D. The Relationship between the Electric Field-Induced Dissociation of Charge Transfer Excitons and the Photocurrent in Small Molecular/polymeric Solar Cells. *J. Phys. Chem. Lett.* **2010**, *1* (6), 982–986.
- (947) Tvingstedt, K.; Vandewal, K.; Zhang, F.; Inganäs, O. On the Dissociation Efficiency of Charge Transfer Excitons and Frenkel Excitons in Organic Solar Cells: A Luminescence Quenching Study. *J. Phys. Chem. C* **2010**, *114* (49), 21824–21832.
- (948) Nayak, P. K.; Narasimhan, K. L.; Cahen, D. Separating Charges at Organic Interfaces: Effects of Disorder, Hot States, and Electric Field. *J. Phys. Chem. Lett.* **2013**, *4*, 1707–1717.
- (949) Scholz, R.; Kobitski, a. Y.; Vragović, I.; Wagner, H. P.; Zahn, D. R. T. Time-Resolved Photoluminescence in  $\alpha$ -PTCDA Single Crystals: Evidence for Recombination via Frenkel Excitons, Charge Transfer States, and Excimers. *Org. Electron.* **2004**, *5* (1–3), 99–105.
- (950) Hoffmann, S. T.; Jaiser, F.; Hayer, A.; Bäessler, H.; Unger, T.; Athanasopoulos, S.; Neher, D.; Köhler, A. How Do Disorder, Reorganization, and Localization Influence the Hole Mobility in Conjugated Copolymers? *J. Am. Chem. Soc.* **2013**, *135* (5), 1772–1782.
- (951) Reid, O. G.; Malik, J. A. N.; Latini, G.; Dayal, S.; Kopidakis, N.; Silva, C.; Stingelin, N.; Rumbles, G. The Influence of Solid-State Microstructure on the Origin and Yield of Long-Lived Photogenerated Charge in Neat Semiconducting Polymers. *J. Polym. Sci., Part B: Polym. Phys.* **2012**, *50* (1), 27–37.
- (952) Mei, J.; Diao, Y.; Appleton, A.; Fang, L.; Bao, Z. Integrated Materials Design of Organic Semiconductors for Field-Effect Transistors. *J. Am. Chem. Soc.* **2013**, *135*, 6724–6746.
- (953) Giri, G.; Li, R.; Smilgies, D.-M.; Li, E. Q.; Diao, Y.; Lenn, K. M.; Chiu, M.; Lin, D. W.; Allen, R.; Reinspach, J.; et al. One-Dimensional Self-Confinement Promotes Polymorph Selection in Large-Area Organic Semiconductor Thin Films. *Nat. Commun.* **2014**, *5*, 3573.
- (954) Ostroverkhova, O. Photophysical and Photoconductive Properties of Organic Semiconductor Composites. In *Organic Electronics: Emerging Concepts and Technologies*; Cicoira, F., Santato, C., Eds.; Wiley-VCH Verlag GmbH & Co. KGaA: 2013; ch. 10.
- (955) Torricelli, F.; Colalongo, L.; Raiteri, D.; Kovács-Vajna, Z. M.; Cantatore, E. Ultra-High Gain Diffusion-Driven Organic Transistor. *Nat. Commun.* **2016**, *7*, 10550.
- (956) Anthony, J. E. Functionalized Acenes and Heteroacenes for Organic Electronics. *Chem. Rev.* **2006**, *106* (12), 5028–5048.
- (957) Lim, Y.-F.; Shu, Y.; Parkin, S. R.; Anthony, J. E.; Malliaras, G. G. Soluble N-Type Pentacene Derivatives as Novel Acceptors for Organic Solar Cells. *J. Mater. Chem.* **2009**, *19* (19), 3049.
- (958) Gao, J.; Hegmann, F. a. Bulk Photoconductive Gain in Pentacene Thin Films. *Appl. Phys. Lett.* **2008**, *93* (22), 223306.
- (959) Lehnher, D.; Gao, J.; Hegmann, F. a.; Tykewinski, R. R. Synthesis and Electronic Properties of Conjugated Pentacene Dimers. *Org. Lett.* **2008**, *10* (21), 4779–4782.
- (960) Guo, W.; Liu, Y.; Huang, W.; Payne, M. M.; Anthony, J.; Katz, H. E. Solution-Processed Low-Voltage Organic Phototransistors Based on an Anthradithiophene Molecular Solid. *Org. Electron.* **2014**, *15* (11), 3061–3069.
- (961) Kim, J.; Cho, S.; Kim, Y.-H.; Park, S. K. Highly-Sensitive Solution-Processed 2,8-Difluoro-5,11-Bis(triethylsilylethynyl) Anthradithiophene (diF-TESADT) Phototransistors for Optical Sensing Applications. *Org. Electron.* **2014**, *15* (9), 2099–2106.
- (962) Lim, B. T.; Cho, J.; Cheon, K. H.; Shin, K.; Chung, D. S. Photoconductive Behaviors of Difluorinated 5,11-Bis-(triethylsilylethynyl) Anthradithiophene. *Org. Electron.* **2015**, *18*, 113–117.
- (963) Purushothaman, B.; Parkin, S. R.; Kendrick, M. J.; David, D.; Ward, J. W.; Yu, L.; Stingelin, N.; Jurchescu, O. D.; Ostroverkhova, O.; Anthony, J. E. Synthesis and Charge Transport Studies of Stable, Soluble Hexacenes. *Chem. Commun.* **2012**, *48*, 8261.
- (964) Payne, M. M.; Parkin, S. R.; Anthony, J. E.; Kuo, C. C.; Jackson, T. N. Organic Field-Effect Transistors from Solution-Deposited Functionalized Acenes with Mobilities as High as 1 cm<sup>2</sup>/Vs. *J. Am. Chem. Soc.* **2005**, *127* (14), 4986–4987.
- (965) Zhang, L.; Walker, B.; Liu, F.; Colella, N.; Mannsfeld, S.; Watkins, J.; Nguyen, T.-Q.; Briseno, A. L. Triisopropylsilylethynyl-functionalized dibenzo[def,mno]chrysene: a solution-processed small molecule for bulk heterojunction solar cells. *J. Mater. Chem.* **2012**, *22*, 4266–4268.
- (966) Cao, Y.; Liang, Y.; Zhang, L.; Osuna, S.; Hoyt, A. L. M.; Briseno, A. L.; Houk, K. N. Why Bistetracenes Are Much Less Reactive than Pentacenes in Diels-Alder Reactions with Fullerenes. *J. Am. Chem. Soc.* **2014**, *136* (30), 10743–10751.
- (967) Song, C.; Swager, T. M. Conducting Polymers Containing Peri-Xanthenoxanthenes via Oxidative Cyclization of Binaphthols. *Macromolecules* **2009**, *42* (5), 1472–1475.
- (968) Kobayashi, N.; Sasaki, M.; Nomoto, K. Stable Peri-Xanthenoxanthene Thin-Film Transistors with Efficient Carrier Injection. *Chem. Mater.* **2009**, *21* (3), 552–556.
- (969) Wang, L.; Duan, G.; Ji, Y.; Zhang, H. Electronic and Charge Transport Properties of Peri-Xanthenoxanthene: The Effects of Heteroatoms and Phenyl Substitutions. *J. Phys. Chem. C* **2012**, *116* (43), 22679–22686.
- (970) Lv, N.; Xie, M.; Gu, W.; Ruan, H.; Qiu, S. Synthesis, Properties, and Structures of Functionalized Peri-Xanthenoxanthene. *Org. Lett.* **2013**, *15* (10), 2382–2385.
- (971) Wang, L.; Duan, G.; Ji, Y.; Zhang, H. Electronic and Charge Transport Properties of Peri-Xanthenoxanthene: The Effects of Heteroatoms and Phenyl Substitutions. *J. Phys. Chem. C* **2012**, *116* (43), 22679–22686.
- (972) Song, C.; Swager, T. M. Conducting Polymers Containing Peri-Xanthenoxanthenes via Oxidative Cyclization of Binaphthols. *Macromolecules (Washington, DC, U. S.)* **2009**, *42*, 1472–1475.
- (973) Yoneya, N.; Ono, H.; Ishii, Y.; Himori, K.; Hirai, N.; Abe, H.; Yumoto, A.; Kobayashi, N.; Nomoto, K. Flexible Electrophoretic Display Driven by Solution-Processed Organic Thin-Film Transistors. *J. Soc. Inf. Disp.* **2012**, *20*, 143–147.
- (974) Liess, A.; Huang, L.; Arjona-Esteban, A.; Lv, A.; Gsänger, M.; Stepanenko, V.; Stolte, M.; Würthner, F. Organic Thin Film Transistors Based on Highly Dipolar Donor-Acceptor Polymethine Dyes. *Adv. Funct. Mater.* **2015**, *25* (1), 44–57.
- (975) Ostroverkhova, O.; Gubler, U.; Wright, D.; Moerner, W. E.; He, M.; Twieg, R. J. Recent Advances in Understanding and Development of Photorefractive Organic Glasses. *Adv. Funct. Mater.* **2002**, *12*, 1727–1743.
- (976) Würthner, F.; Yao, S.; Schilling, J.; Wortmann, R.; Redi-Abshiro, M.; Mecher, E.; Gallego-Gomez, F.; Meerholz, K. ATOP Dyes. Optimization of a Multifunctional Merocyanine Chromophore for High Refractive Index Modulation in Photorefractive Materials. *J. Am. Chem. Soc.* **2001**, *123* (12), 2810–2824.
- (977) Yi, Z.; Wang, S.; Liu, Y. Design of High-Mobility Diketopyrrolopyrrole-Based  $\pi$ -Conjugated Copolymers for Organic Thin-Film Transistors. *Adv. Mater.* **2015**, *27*, 3589–3606.
- (978) Lei, T.; Wang, J. Y.; Pei, J. Design, Synthesis, and Structure-Property Relationships of Isoindigo-Based Conjugated Polymers. *Acc. Chem. Res.* **2014**, *47* (4), 1117–1126.
- (979) Nielsen, C. B.; Turbiez, M.; McCulloch, I. Recent Advances in the Development of Semiconducting DPP-Containing Polymers for Transistor Applications. *Adv. Mater.* **2013**, *25* (13), 1859–1880.
- (980) Zhang, X.; Bronstein, H.; Kronemeijer, A. J.; Smith, J.; Kim, Y.; Kline, R. J.; Richter, L. J.; Anthopoulos, T. D.; Sirringhaus, H.; Song, K.; et al. Molecular Origin of High Field-Effect Mobility in an

Indacenodithiophene-Benzothiadiazole Copolymer. *Nat. Commun.* **2013**, *4*, 2238.

(981) Smith, J.; Zhang, W.; Sougrat, R.; Zhao, K.; Li, R.; Cha, D.; Amassian, A.; Heeney, M.; McCulloch, I.; Anthopoulos, T. D. Solution-Processed Small Molecule-Polymer Blend Organic Thin-Film Transistors with Hole Mobility Greater than 5 Cm<sup>2</sup>/Vs. *Adv. Mater.* **2012**, *24* (18), 2441–2446.

(982) Hachmann, J.; Olivares-Amaya, R.; Jinich, A.; Appleton, A. L.; Blood-Forsythe, M. a.; Seress, L. R.; Román-Salgado, C.; Treppe, K.; Atahan-Evrenk, S.; Er, S.; et al. Lead Candidates for High-Performance Organic Photovoltaics from High-Throughput Quantum Chemistry – the Harvard Clean Energy Project. *Energy Environ. Sci.* **2014**, *7* (2), 698.

(983) Scharber, M. C.; Mühlbacher, D.; Koppe, M.; Denk, P.; Waldauf, C.; Heeger, A. J.; Brabec, C. J. Design Rules for Donors in Bulk-Heterojunction Solar Cells - Towards 10% Energy-Conversion Efficiency. *Adv. Mater.* **2006**, *18* (6), 789–794.

(984) Mohamed, S.; Demeter, D.; Laffitte, J.-A.; Blanchard, P.; Roncali, J. Structure-Properties Relationships in Triarylamine-Based Donor-Acceptor Molecules Containing Naphtyl Groups as Donor Material for Organic Solar Cells. *Sci. Rep.* **2015**, *5*, 9031.

(985) Love, J. a.; Nagao, I.; Huang, Y.; Kuik, M.; Gupta, V.; Takacs, C. J.; Coughlin, J. E.; Qi, L.; Van Der Poll, T. S.; Kramer, E. J.; et al. Silaindacenodithiophene-Based Molecular Donor: Morphological Features and Use in the Fabrication of Compositionally Tolerant, High-Efficiency Bulk Heterojunction Solar Cells. *J. Am. Chem. Soc.* **2014**, *136* (9), 3597–3606.

(986) Kan, B.; Li, M.; Zhang, Q.; Liu, F.; Wan, X.; Wang, Y.; Ni, W.; Long, G.; Yang, X.; Feng, H.; et al. A Series of Simple Oligomer-like Small Molecules Based on Oligothiophenes for Solution-Processed Solar Cells with High Efficiency. *J. Am. Chem. Soc.* **2015**, *137*, 3886–3893.

(987) Fan, H.; Zhu, X. Development of Small-Molecule Materials for High-Performance Organic Solar Cells. *Sci. China: Chem.* **2015**, *58* (6), 922–936.

(988) Nielsen, C. B.; Holliday, S.; Chen, H.; Cryer, S. J.; McCulloch, I. Non-Fullerene Electron Acceptors for Use in Organic Solar Cells. *Acc. Chem. Res.* **2015**, *48*, 2803–2812.

(989) Lin, Y.; Zhan, X. Non-Fullerene Acceptors for Organic Photovoltaics: An Emerging Horizon. *Mater. Horiz.* **2014**, *1* (5), 470–488.

(990) Zhan, C.; Yao, J. More than Conformational “Twisting” or “Coplanarity”: Molecular Strategies for Designing High-Efficiency Nonfullerene Organic Solar Cells. *Chem. Mater.* **2016**, *28*, 1948–1964.

(991) Zhong, Y.; Trinh, M. T.; Chen, R.; Purdum, G. E.; Khlyabich, P. P.; Sezen, M.; Oh, S.; Zhu, H.; Fowler, B.; Zhang, B.; et al. Molecular Helices as Electron Acceptors in High-Performance Bulk Heterojunction Solar Cells. *Nat. Commun.* **2015**, *6*, 8242.

(992) Hwang, Y.-J.; Li, H.; Courtright, B. A. E.; Subramanian, S.; Jenekhe, S. A. Nonfullerene Polymer Solar Cells with 8.5% Efficiency Enabled by a New Highly Twisted Electron Acceptor Dimer. *Adv. Mater.* **2016**, *28*, 124–131.

(993) Hwang, Y.-J.; Courtright, B. A. E.; Ferreira, A. S.; Tolbert, S. H.; Jenekhe, S. A. 7.7% Efficient All-Polymer Solar Cells. *Adv. Mater.* **2015**, *27*, 4578–4584.

(994) Camaioni, N.; Po, R. Pushing the Envelope of the Intrinsic Limitation of Organic Solar Cells. *J. Phys. Chem. Lett.* **2013**, *4* (11), 1821–1828.

(995) Leblebici, S. Y.; Chen, T. L.; Olalde-Velasco, P.; Yang, W.; Ma, B. Reducing Exciton Binding Energy by Increasing Thin Film Permittivity: An Effective Approach to Enhance Exciton Separation Efficiency in Organic Solar Cells. *ACS Appl. Mater. Interfaces* **2013**, *5* (20), 10105–10110.

(996) Noone, K. M.; Subramanian, S.; Zhang, Q.; Cao, G.; Jenekhe, S. A.; Ginger, D. S. Photoinduced Charge Transfer and Polaron Dynamics in Polymer and Hybrid Photovoltaic Thin Films: Organic vs Inorganic Acceptors. *J. Phys. Chem. C* **2011**, *115* (49), 24403–24410.

(997) Tada, A.; Geng, Y.; Wei, Q.; Hashimoto, K.; Tajima, K. Tailoring Organic Heterojunction Interfaces in Bilayer Polymer Photovoltaic Devices. *Nat. Mater.* **2011**, *10* (6), 450–455.

(998) Cho, N.; Schlenker, C. W.; Kesting, K. M.; Koelsch, P.; Yip, H. L.; Ginger, D. S.; Jen, A. K. Y. High-Dielectric Constant Side-Chain Polymers Show Reduced Non-Geminate Recombination in Heterojunction Solar Cells. *Adv. Energy Mater.* **2014**, *4* (10), 1301857.

(999) Khlyabich, P. P.; Burkhart, B.; Thompson, B. C. Efficient Ternary Blend Bulk Heterojunction Solar Cells with Tunable Open-Circuit Voltage. *J. Am. Chem. Soc.* **2011**, *133* (37), 14534–14537.

(1000) Street, R. a.; Davies, D.; Khlyabich, P. P.; Burkhart, B.; Thompson, B. C. Origin of the Tunable Open-Circuit Voltage in Ternary Blend Bulk Heterojunction Organic Solar Cells. *J. Am. Chem. Soc.* **2013**, *135* (3), 986–989.

(1001) Zhang, Y.; Deng, D.; Lu, K.; Zhang, J.; Xia, B.; Zhao, Y.; Fang, J.; Wei, Z. Synergistic Effect of Polymer and Small Molecules for High-Performance Ternary Organic Solar Cells. *Adv. Mater.* **2015**, *27* (6), 1071–1076.

(1002) Mollinger, S. A.; Vandewal, K.; Salero, A. Microstructural and Electronic Origins of Open-Circuit Voltage Tuning in Organic Solar Cells Based on Ternary Blends. *Adv. Energy Mater.* **2015**, *5*, 1501335.

(1003) Yeow, E. K. L.; Steer, R. P. Dynamics of Electronic Energy Transfer from the S<sub>2</sub> State of Azulene to the S<sub>2</sub> State of Zinc Porphyrin. *Phys. Chem. Chem. Phys.* **2003**, *5* (1), 97–105.

(1004) Itoh, T. Fluorescence and Phosphorescence from Higher Excited States of Organic Molecules. *Chem. Rev.* **2012**, *112* (8), 4541–4568.

(1005) Yanagi, K.; Kataura, H. Carbon Nanotubes: Breaking Kasha’s Rule. *Nat. Photonics* **2010**, *4* (4), 200–201.

(1006) Maiti, M.; Danger, B. R.; Steer, R. P. Photophysics of Soret-Excited Tetrapyrroles in Solution. IV. Radiationless Decay and Triplet-Triplet Annihilation Investigated Using Tetrphenylporphyrinato Sn(IV). *J. Phys. Chem. A* **2009**, *113* (42), 11318–11326.

(1007) Yeow, E. K. L.; Steer, R. P. Energy Transfer Involving Higher Electronic States: A New Direction for Molecular Logic Gates. *Chem. Phys. Lett.* **2003**, *377* (3–4), 391–398.

(1008) Velate, S.; Liu, X.; Steer, R. P. Does the Radiationless Relaxation of Soret-Excited Metalloporphyrins Follow the Energy Gap Law? *Chem. Phys. Lett.* **2006**, *427* (4–6), 295–299.

(1009) Tétreault, N.; Muthyala, R. S.; Liu, R. S. H.; Steer, R. P. Control of the Photophysical Properties of Polyatomic Molecules by Substitution and Solvation: The Second Excited Singlet State of Azulene. *J. Phys. Chem. A* **1999**, *103*, 2524–2531.

(1010) Liu, X.; Yeow, E. K. L.; Velate, S.; Steer, R. P. Photophysics and Spectroscopy of the Higher Electronic States of Zinc Metalloporphyrins: A Theoretical and Experimental Study. *Phys. Chem. Chem. Phys.* **2006**, *8* (11), 1298–1309.

(1011) Maiti, M.; Steer, R. P. Is Soret-Excited ZnTPP Quenched by Electron Transfer in Chlorinated Solvents? *Chem. Phys. Lett.* **2009**, *482* (4–6), 254–258.

(1012) Myahkostupov, M.; Pagba, C. V.; Gundlach, L.; Piotrowiak, P. Vibrational State Dependence of Interfacial Electron Transfer: Hot Electron Injection from the S<sub>1</sub> State of Azulene into TiO<sub>2</sub> Nanoparticles. *J. Phys. Chem. C* **2013**, *117*, 20485–20493.

(1013) Nieto-Pescador, J.; Abraham, B.; Gundlach, L. Photoinduced Ultrafast Heterogeneous Electron Transfer at Molecule – Semiconductor Interfaces. *J. Phys. Chem. Lett.* **2014**, *5*, 3498–3507.

(1014) Lingam, N. K.; Kalghatgi, S.; Winiarz, J. G. Enhanced Photorefractivity in a Polymeric Composite Photosensitized with Carbon Nanotubes Grafted to a Photoconductive Polymer. *J. Appl. Phys.* **2011**, *109* (2), 023106.

(1015) Ham, M. H.; Paulus, G. L. C.; Lee, C. Y.; Song, C.; Kalantar-Zadeh, K.; Choi, W.; Han, J. H.; Strano, M. S. Evidence for High-Efficiency Exciton Dissociation at Polymer/Single-Walled Carbon Nanotube Interfaces in Planar Nano-Heterojunction Photovoltaics. *ACS Nano* **2010**, *4* (10), 6251–6259.

(1016) Arnold, M. S.; Zimmerman, J. D.; Renshaw, C. K.; Xu, X.; Lunt, R. R.; Austin, C. M.; Forrest, S. R. Broad Spectral Response

Using Carbon Nanotube/organic semiconductor/C60 Photodetectors. *Nano Lett.* **2009**, *9* (9), 3354–3358.

(1017) Chantharasupawong, P.; Christenson, C. W.; Philip, R.; Zhai, L.; Winiarz, J.; Yamamoto, M.; Tetard, L.; Nair, R. R.; Thomas, J. Photorefractive Performances of a Graphene-Doped PATPD/7-DCST/ECZ Composite. *J. Mater. Chem. C* **2014**, *2* (36), 7639.

(1018) Manzano-Ramírez, A.; López-Naranjo, E. J.; Soboyejo, W.; Meas-Vong, Y.; Vilquin, B. A Review on the Efficiency of Graphene-Based BHJ Organic Solar Cells. *J. Nanomater.* **2015**, *2015*, 406597.

(1019) Liu, J.; Durstock, M.; Dai, L. Graphene Oxide Derivatives as Hole- and Electron-Extraction Layers for High-Performance Polymer Solar Cells. *Energy Environ. Sci.* **2014**, *7* (4), 1297.

(1020) Zhou, N.; Kim, M.-G.; Loser, S.; Smith, J.; Yoshida, H.; Guo, X.; Song, C.; Jin, H.; Chen, Z.; Yoon, S. M.; et al. Amorphous Oxide Alloys as Interfacial Layers with Broadly Tunable Electronic Structures for Organic Photovoltaic Cells. *Proc. Natl. Acad. Sci. U. S. A.* **2015**, *112* (26), 7897–7902.

(1021) Kim, J.; Hong, Z.; Li, G.; Song, T.; Chey, J.; Lee, Y. S.; You, J.; Chen, C.-C.; Sadana, D. K.; Yang, Y. 10.5% Efficient Polymer and Amorphous Silicon Hybrid Tandem Photovoltaic Cell. *Nat. Commun.* **2015**, *6*, 6391.

(1022) Draxl, C.; Nabok, D.; Hannewald, K. Organic/Inorganic Hybrid Materials: Challenges for Ab Initio Methodology. *Acc. Chem. Res.* **2014**, *47*, 3225–3232.

(1023) Renshaw, C. K.; Forrest, S. R. Excited State and Charge Dynamics of Hybrid Organic/inorganic Heterojunctions. I. Theory. *Phys. Rev. B: Condens. Matter Mater. Phys.* **2014**, *90* (4), 045302.

(1024) Panda, A.; Renshaw, C. K.; Oskooi, A.; Lee, K.; Forrest, S. R. Excited State and Charge Dynamics of Hybrid Organic/inorganic Heterojunctions. II. Experiment. *Phys. Rev. B: Condens. Matter Mater. Phys.* **2014**, *90* (4), 045302.

(1025) Panahandeh-Fard, M.; Yin, J.; Kurniawan, M.; Wang, Z.; Leung, G.; Sum, T. C.; Soci, C. Ambipolar Charge Photogeneration and Transfer at GaAs/P3HT Heterointerfaces. *J. Phys. Chem. Lett.* **2014**, *5* (7), 1144–1150.

(1026) Caplins, B. W.; Suich, D. E.; Shearer, A. J.; Harris, C. B. Quantum Beats at the Metal/organic Interface. *J. Electron Spectrosc. Relat. Phenom.* **2015**, *198*, 20–25.

(1027) Racke, D. a.; Kelly, L. L.; Kim, H.; Schulz, P.; Sigdel, A.; Berry, J. J.; Graham, S.; Nordlund, D.; Monti, O. L. a. Disrupted Attosecond Charge Carrier Delocalization at a Hybrid Organic/Inorganic Semiconductor Interface. *J. Phys. Chem. Lett.* **2015**, *6*, 1935–1941.

(1028) Zhao, L.; Lin, Z. Crafting Semiconductor Organic-Inorganic Nanocomposites via Placing Conjugated Polymers in Intimate Contact with Nanocrystals for Hybrid Solar Cells. *Adv. Mater.* **2012**, *24* (32), 4353–4368.

(1029) Jung, J.; Yoon, Y. J.; He, M.; Lin, Z. Organic-Inorganic Nanocomposites Composed of Conjugated Polymers and Semiconductor Nanocrystals for Photovoltaics. *J. Polym. Sci., Part B: Polym. Phys.* **2014**, *52* (24), 1641–1660.

(1030) Freitas, J. N.; Gonçalves, A. S.; Nogueira, A. F. A Comprehensive Review of the Application of Chalcogenide Nanoparticles in Polymer Solar Cells. *Nanoscale* **2014**, *6* (12), 6371–6397.

(1031) Gao, F.; Ren, S.; Wang, J. The Renaissance of Hybrid Solar Cells: Progresses, Challenges, and Perspectives. *Energy Environ. Sci.* **2013**, *6* (7), 2020.

(1032) Roy Choudhury, K.; Sahoo, Y.; Prasad, P. N. Hybrid Quantum-Dot-Polymer Nanocomposites for Infrared Photorefractivity at an Optical Communication Wavelength. *Adv. Mater.* **2005**, *17* (23), 2877–2881.

(1033) Zhu, J.; Kim, W. J.; He, G. S.; Seo, J.; Yong, K.-T.; Lee, D.; Cartwright, A. N.; Cui, Y.; Prasad, P. N. Enhanced Photorefractivity in a Polymer/nanocrystal Composite Photorefractive Device at Telecommunication Wavelength. *Appl. Phys. Lett.* **2010**, *97* (26), 263108.

(1034) Bansal, N.; Reynolds, L. X.; MacLachlan, a.; Lutz, T.; Ashraf, R. S.; Zhang, W.; Nielsen, C. B.; McCulloch, I.; Rebois, D. G.; Kirchartz, T.; et al. Influence of Crystallinity and Energetics on Charge

Separation in Polymer-Inorganic Nanocomposite Films for Solar Cells. *Sci. Rep.* **2013**, *3*, 1531.

(1035) Kulkarni, A. P.; Noone, K. M.; Munechika, K.; Guyer, S. R.; Ginger, D. S. Plasmon-Enhanced Charge Carrier Generation in Organic Photovoltaic Films Using Silver Nanoprisms. *Nano Lett.* **2010**, *10* (4), 1501–1505.

(1036) Meredith, P.; Bettinger, C.; Irimia-Vladu, M.; Mostert, A.; Schwenn, P. Electronic and Optoelectronic Materials and Devices Inspired by Nature. *Rep. Prog. Phys.* **2013**, *76*, 034501.

(1037) Irimia-Vladu, M.; Sariciftci, N.; Bauer, S. Exotic Materials for Bio-Organic Electronics. *J. Mater. Chem.* **2011**, *21* (5), 1350.

(1038) Irimia-Vladu, M. “Green” Electronics: Biodegradable and Biocompatible Materials and Devices for Sustainable Future. *Chem. Soc. Rev.* **2014**, *43* (2), 588–610.

(1039) Glowacki, E. D.; Irimia-Vladu, M.; Bauer, S.; Sariciftci, N. S. Hydrogen-Bonds in Molecular Solids – from Biological Systems to Organic Electronics. *J. Mater. Chem. B* **2013**, *1* (31), 3742.

(1040) Glowacki, E. D.; Voss, G.; Leonat, L.; Irimia-Vladu, M.; Bauer, S.; Sariciftci, N. S. Indigo and Tyrian Purple—from Ancient Natural Dyes to Modern Organic Semiconductors. *Isr. J. Chem.* **2012**, *52*, 540–551.

(1041) Irimia-Vladu, M.; Glowacki, E. D.; Troshin, P. a.; Schwabegger, G.; Leonat, L.; Susarova, D.; Krystal, O.; Ullah, M.; Kanbur, Y.; Bodea, M.; et al. Indigo-A Natural Pigment for High Performance Ambipolar Organic Field Effect Transistors and Circuits. *Adv. Mater.* **2012**, *24*, 375–380.

(1042) Glowacki, E.; Voss, G.; Sariciftci, N. 25th Anniversary Article: Progress in Chemistry and Applications of Functional Indigos for Organic Electronics. *Adv. Mater.* **2013**, *25*, 6783–6800.

(1043) Glowacki, E. D.; Coskun, H.; Blood-Forsythe, M. a.; Monkowius, U.; Leonat, L.; Grzybowski, M.; Gryko, D.; White, M. S.; Aspuru-Guzik, A.; Sariciftci, N. S. Hydrogen-Bonded Diketopyrrolopyrrole (DPP) Pigments as Organic Semiconductors. *Org. Electron.* **2014**, *15* (12), 3521–3528.

(1044) Ehrenfreund, E.; Moses, D.; Heeger, A. J. Doped Beta-Carotene Films: Spinless Charge Storage Stabilized by Structural Relaxation. *Chem. Phys. Lett.* **1992**, *196*, 84–90.

(1045) Kamat, P. V.; Chauvet, J.-P.; Fessenden, R. W. Photoelectrochemistry in Particulate Systems. 4. Photosensitization of a TiO<sub>2</sub> Semiconductor with a Chlorophyll Analogue. *J. Phys. Chem.* **1986**, *90*, 1389–1394.

(1046) Glowacki, E. D.; Leonat, L.; Irimia-Vladu, M.; Schwödiauer, R.; Ullah, M.; Sitter, H.; Bauer, S.; Sariciftci, N. S. Intermolecular Hydrogen-Bonded Organic Semiconductors-Quinacridone versus Pentacene. *Appl. Phys. Lett.* **2012**, *101* (2), 023305.

(1047) Glowacki, E. D.; Voss, G.; Demirak, K.; Havlicek, M.; Sünger, N.; Okur, A. C.; Monkowius, U.; Gąsiorowski, J.; Leonat, L.; Sariciftci, N. S. A Facile Protection-Deprotection Route for Obtaining Indigo Pigments as Thin Films and Their Applications in Organic Bulk Heterojunctions. *Chem. Commun. (Cambridge, U. K.)* **2013**, *49* (54), 6063–6065.

(1048) Glowacki, E. D.; Romanazzi, G.; Yumusak, C.; Coskun, H.; Monkowius, U.; Voss, G.; Burian, M.; Lechner, R. T.; Demitri, N.; Redhammer, G. J.; et al. Epindolidione-Versatile and Stable Hydrogen-Bonded Pigments for Organic Field-Effect Transistors and Light-Emitting Diodes. *Adv. Funct. Mater.* **2015**, *25*, 776–787.

(1049) Sytnyk, M.; Daniel, E.; Yakunin, S.; Voss, G.; Scho, W.; Krieger, D.; Stangl, J.; Trotta, R.; Gollner, C.; Tollabimazraehno, S.; et al. Hydrogen-Bonded Organic Semiconductor Micro- And Nanocrystals: From Colloidal Syntheses to (Opto-)Electronic Devices. *J. Am. Chem. Soc.* **2014**, *136* (47), 16522–16532.

(1050) Deng, Y.; Liu, J.; Wang, J.; Liu, L.; Li, W.; Tian, H.; Zhang, X.; Xie, Z.; Geng, Y.; Wang, F. Dithienocarbazole and Isoindigo Based Amorphous Low Bandgap Conjugated Polymers for Efficient Polymer Solar Cells. *Adv. Mater.* **2014**, *26* (3), 471–476.

(1051) Gospodinova, N.; Tomšik, E. Hydrogen-Bonding versus  $\pi$ - $\pi$  Stacking in the Design of Organic Semiconductors: From Dyes to Oligomers. *Prog. Polym. Sci.* **2015**, *43*, 33–47.

- (1052) Guo, X.; Facchetti, A.; Marks, T. J. Imide- and Amide-Functionalized Polymer Semiconductors. *Chem. Rev.* **2014**, *114*, 8943–9021.
- (1053) Hao, Z.; Iqbal, A. Some Aspects of Organic Pigments. *Chem. Soc. Rev.* **1997**, *26* (3), 203.
- (1054) Irimia-Vladu, M.; Glowacki, E.; Sariciftci, N. S.; Bauer, S. Natural Materials for Organic Electronics. In *Small Organic Molecules on Surfaces* (Sitter, H. et al, Eds.), Springer Series in Materials Science, **2013**, *173*, 295–318.
- (1055) Black, H. T.; Lin, H.; Bélanger-Gariépy, F.; Perepichka, D. Supramolecular Control of Organic P/n-Heterojunctions by Complementary Hydrogen Bonding. *Faraday Discuss.* **2014**, *174*, 297–312.
- (1056) Sasaki, T.; Naka, Y. Photorefractive Effect in Ferroelectric Liquid Crystals. *Opt. Rev.* **2014**, *21* (2), 99–109.
- (1057) Ditte, K.; Jiang, W.; Schemme, T.; Denz, C.; Wang, Z. Innovative Sensitizer DiPBI Outperforms PCBM. *Adv. Mater.* **2012**, *24* (16), 2104–2108.
- (1058) Thomas, J.; Christenson, C. W.; Blanche, P. A.; Yamamoto, M.; Norwood, R. a.; Peyghambarian, N. Photoconducting Polymers for Photorefractive 3D Display Applications. *Chem. Mater.* **2011**, *23* (3), 416–429.
- (1059) Moon, I. K.; Choi, J.; Kim, N. High-Performance Photorefractive Composite Based on Non-Conjugated Main-Chain, Hole-Transporting Polymer. *Macromol. Chem. Phys.* **2013**, *214* (4), 478–485.
- (1060) Van Steenwinkel, D.; Hendrickx, E. Persoons, a. Dynamics and Steady-State Properties of Photorefractive poly(N-Vinylcarbazole)-Based Composites Sensitized with (2,4,7-Trinitro-9-Fluorenylidene)-Malononitrile in a 0 - 3 Wt% Range. *J. Chem. Phys.* **2001**, *114* (21), 9557–9564.
- (1061) Roy Choudhury, K.; Sahoo, Y.; Jang, S.; Prasad, P. N. Efficient Photosensitization and High Optical Gain in a Novel Quantum-Dot-Sensitized Hybrid Photorefractive Nanocomposite at a Telecommunications Wavelength. *Adv. Funct. Mater.* **2005**, *15* (5), 751–756.
- (1062) Tay, S.; Thomas, J.; Eralp, M.; Li, G.; Norwood, R. a.; Schülzgen, A.; Yamamoto, M.; Barlow, S.; Walker, G. a.; Marder, S. R.; et al. High-Performance Photorefractive Polymer Operating at 1550 Nm with near-Video-Rate Response Time. *Appl. Phys. Lett.* **2005**, *87* (17), 171105.
- (1063) Salvador, M.; Prauzner, J.; Köber, S.; Meerholz, K.; Turek, J. J.; Jeong, K.; Nolte, D. D. Three-Dimensional Holographic Imaging of Living Tissue Using a Highly Sensitive Photorefractive Polymer Device. *Opt. Express* **2009**, *17* (14), 11834–11849.
- (1064) Eralp, M.; Thomas, J.; Tay, S.; Li, G.; Schülzgen, a.; Norwood, R. a.; Yamamoto, M.; Peyghambarian, N. Submillisecond Response of a Photorefractive Polymer under Single Nanosecond Pulse Exposure. *Appl. Phys. Lett.* **2006**, *89* (11), 114105.
- (1065) Noriega, R.; Rivnay, J.; Vandewal, K.; Koch, F. P. V.; Stingelin, N.; Smith, P.; Toney, M. F.; Salleo, A. A General Relationship between Disorder, Aggregation and Charge Transport in Conjugated Polymers. *Nat. Mater.* **2013**, *12* (11), 1038–1044.
- (1066) Tsujimura, S.; Kinashi, K.; Sakai, W.; Tsutsumi, N. Recent Advances in Photorefractivity of poly(4-Diphenylaminostyrene) Composites: Wavelength Dependence and Dynamic Holographic Images. *Jpn. J. Appl. Phys.* **2014**, *53*, 082601.
- (1067) Kinashi, K.; Wang, Y.; Sakai, W.; Tsutsumi, N. Optimization of Photorefractivity Based on poly(N-Vinylcarbazole) Composites: An Approach from the Perspectives of Chemistry and Physics. *Macromol. Chem. Phys.* **2013**, *214* (16), 1789–1797.
- (1068) Gallego-Gómez, F.; Álvarez-Santos, J. C.; Rodríguez-Redondo, J. L.; Font-Sanchis, E.; Villalvilla, J. M.; Sastre-Santos, Á.; Díaz-García, M. a.; Fernández-Lázaro, F. Millisecond Photorefractivity with Novel Dicyanomethylenedihydrofuran-Containing Polymers. *J. Mater. Chem.* **2012**, *22* (24), 12220.
- (1069) Maldonado, J. L.; Ponce-de-León, Y.; Ramos-Ortiz, G.; Rodríguez, M.; Meneses-Nava, M. a.; Barbosa-García, O.; Santillán, R.; Farfán, N. High Diffraction Efficiency at Low Electric Field in Photorefractive Polymers Doped with Arylimine Chromophores. *J. Phys. D: Appl. Phys.* **2009**, *42* (7), 075102.
- (1070) Moon, J.-S.; Liang, Y.; Stevens, T. E.; Monson, T. C.; Huber, D. L.; Mahala, B. D.; Winiarz, J. G. Off-Resonance Photosensitization of a Photorefractive Polymer Composite Using PbS Nanocrystals. *J. Phys. Chem. C* **2015**, *119* (24), 13827–13835.
- (1071) Angelone, R.; Ciardelli, F.; Colligiani, A.; Greco, F.; Masi, P.; Romano, A.; Ruggieri, G. The Relevance of the Collaborative Effect in Determining the Performances of Photorefractive Polymer Materials. *ChemPhysChem* **2010**, *11*, 460–465.
- (1072) Köber, S.; Gallego-Gomez, F.; Salvador, M.; Kooistra, F. B.; Hummelen, J. C.; Aleman, K.; Mansurova, S.; Meerholz, K. Influence of the Sensitizer Reduction Potential on the Sensitivity of Photorefractive Polymer Composites. *J. Mater. Chem.* **2010**, *20* (29), 6170.
- (1073) Köber, S.; Prauzner, J.; Salvador, M.; Kooistra, F. B.; Hummelen, J. C.; Meerholz, K. 1064-Nm Sensitive Organic Photorefractive Composites. *Adv. Mater.* **2010**, *22* (12), 1383–1386.
- (1074) Mas-Torrent, M.; Rovira, C. Role of Molecular Order and Solid-State Structure in Organic Field-Effect Transistors. *Chem. Rev.* **2011**, *111* (8), 4833–4856.
- (1075) Liu, F.; Gu, Y.; Shen, X.; Ferdous, S.; Wang, H. W.; Russell, T. P. Characterization of the Morphology of Solution-Processed Bulk Heterojunction Organic Photovoltaics. *Prog. Polym. Sci.* **2013**, *38* (12), 1990–2052.
- (1076) Soon, Y. W.; Shoaee, S.; Ashraf, R. S.; Bronstein, H.; Schroeder, B. C.; Zhang, W.; Fei, Z.; Heeney, M.; McCulloch, I.; Durrant, J. R. Material Crystallinity as a Determinant of Triplet Dynamics and Oxygen Quenching in Donor Polymers for Organic Photovoltaic Devices. *Adv. Funct. Mater.* **2014**, *24* (10), 1474–1482.
- (1077) Heumueller, T.; Mateker, W. R.; Sachs-Quintana, I. T.; Vandewal, K.; Bartelt, J. a.; Burke, T. M.; Ameri, T.; Brabec, C. J.; McGehee, M. D. Reducing Burn-in Voltage Loss in Polymer Solar Cells by Increasing the Polymer Crystallinity. *Energy Environ. Sci.* **2014**, *7*, 2974.
- (1078) Li, R.; Ward, J. W.; Smilgies, D. M.; Payne, M. M.; Anthony, J. E.; Jurchescu, O. D.; Amassian, A. Direct Structural Mapping of Organic Field-Effect Transistors Reveals Bottlenecks to Carrier Transport. *Adv. Mater.* **2012**, *24* (41), 5553–5558.
- (1079) Schulze, B. M.; Shewmon, N. T.; Zhang, J.; Watkins, D. L.; Mudrick, J. P.; Cao, W.; Bou Zerdan, R.; Quartararo, A. J.; Ghiviriga, I.; Xue, J.; et al. Consequences of Hydrogen Bonding on Molecular Organization and Charge Transport in Molecular Organic Photovoltaic Materials. *J. Mater. Chem. A* **2014**, *2* (5), 1541–1549.
- (1080) Gundlach, D. J.; Royer, J. E.; Park, S. K.; Subramanian, S.; Jurchescu, O. D.; Hamadani, B. H.; Moad, a J.; Kline, R. J.; Teague, L. C.; Kirillov, O.; et al. Contact-Induced Crystallinity for High-Performance Soluble Acene-Based Transistors and Circuits. *Nat. Mater.* **2008**, *7* (3), 216–221.
- (1081) Reyes-Martinez, M. a.; Crosby, A. J.; Briseno, A. L. Rubrene Crystal Field-Effect Mobility Modulation via Conducting Channel Wrinkling. *Nat. Commun.* **2015**, *6*, 6948.
- (1082) Yao, Y.; Dong, H.; Hu, W. Charge Transport in Organic and Polymeric Semiconductors for Flexible and Stretchable Devices. *Adv. Mater.* **2016**, *28*, 4513.
- (1083) Huang, Y.; Kramer, E. J.; Heeger, A. J.; Bazan, G. C. Bulk Heterojunction Solar Cells: Morphology and Performance Relationships. *Chem. Rev.* **2014**, *114* (14), 7006–7043.
- (1084) Westacott, P.; Tumbleston, J. R.; Shoaee, S.; Fearn, S.; Bannock, J. H.; Gilchrist, J. B.; Heutz, S.; DeMello, J.; Heeney, M.; Ade, H.; et al. On the Role of Intermixed Phases in Organic Photovoltaic Blends. *Energy Environ. Sci.* **2013**, *6* (9), 2756.
- (1085) Li, W.; Hendriks, K. H.; Furlan, A.; Roelofs, W. S. C.; Meskers, S. C. J.; Wienk, M. M.; Janssen, R. a J. Effect of the Fibrillar Microstructure on the Efficiency of High Molecular Weight Diketopyrrolopyrrole-Based Polymer Solar Cells. *Adv. Mater.* **2014**, *26* (10), 1565–1570.
- (1086) Hwang, Y.-J.; Earmme, T.; Courtright, B. a E.; Eberle, F. N.; Jenekhe, S. a. N-Type Semiconducting Naphthalene Diimide-Perylene Diimide Copolymers: Controlling Crystallinity, Blend Morphology, and Compatibility Toward High-Performance All-Polymer Solar Cells. *J. Am. Chem. Soc.* **2015**, *137*, 4424–4434.

- (1087) Kline, R. J.; Hudson, S. D.; Zhang, X.; Gundlach, D. J.; Moad, A. J.; Jurchescu, O. D.; Jackson, T. N.; Subramanian, S.; Anthony, J. E.; Toney, M. F.; et al. Controlling the Microstructure of Solution-Processable Small Molecules in Thin-Film Transistors through Substrate Chemistry. *Chem. Mater.* **2011**, *23* (5), 1194–1203.
- (1088) Ward, J. W.; Lampert, Z. a.; Jurchescu, O. D. Versatile Organic Transistors by Solution Processing. *ChemPhysChem* **2015**, *16* (6), 1118–1132.
- (1089) Shaw, L.; Bao, Z. The Large-Area, Solution-Based Deposition of Single-Crystal Organic Semiconductors. *Isr. J. Chem.* **2014**, *54* (5–6), 496–512.
- (1090) Pivrikas, A.; Neugebauer, H.; Sariciftci, N. Influence of Processing Additives to Nano-Morphology and Efficiency of Bulk-Heterojunction Solar Cells: A Comparative Review. *Sol. Energy* **2011**, *85*, 1226–1237.
- (1091) Etxebarria, I.; Ajuria, J.; Pacios, R. Polymer:fullerene Solar Cells: Materials, Processing Issues, and Cell Layouts to Reach Power Conversion Efficiency over 10%, a Review. *J. Photonics Energy* **2015**, *5* (1), 057214.
- (1092) Diemer, P. J.; Lyle, C. R.; Mei, Y.; Sutton, C.; Payne, M. M.; Anthony, J. E.; Coropceanu, V.; Brédas, J. L.; Jurchescu, O. D. Vibration-Assisted Crystallization Improves Organic/dielectric Interface in Organic Thin-Film Transistors. *Adv. Mater.* **2013**, *25* (48), 6956–6962.
- (1093) Ma, W.; Reinspach, J.; Zhou, Y.; Diao, Y.; McAfee, T.; Mannsfeld, S. C. B.; Bao, Z.; Ade, H. Tuning Local Molecular Orientation-Composition Correlations in Binary Organic Thin Films by Solution Shearing. *Adv. Funct. Mater.* **2015**, *25*, 3131–3137.
- (1094) Zhang, Y.; Diao, Y.; Lee, H.; Mirabito, T. J.; Johnson, R. W.; Puodziukynaitė, E.; John, J.; Carter, K. R.; Emrick, T.; Mannsfeld, S. C. B.; et al. Intrinsic and Extrinsic Parameters for Controlling the Growth of Organic Single-Crystalline Nanopillars in Photovoltaics. *Nano Lett.* **2014**, *14*, 5547–5554.
- (1095) van Franeker, J. J.; Turbiez, M.; Li, W.; Wienk, M. M.; Janssen, R. a. J. A Real-Time Study of the Benefits of Co-Solvents in Polymer Solar Cell Processing. *Nat. Commun.* **2015**, *6*, 6229.
- (1096) Perez, L. a.; Rogers, J. T.; Brady, M. a.; Sun, Y.; Welch, G. C.; Schmidt, K.; Toney, M. F.; Jinnai, H.; Heeger, A. J.; Chabynyc, M. L.; et al. The Role of Solvent Additive Processing in High Performance Small Molecule Solar Cells. *Chem. Mater.* **2014**, *26*, 6531–6541.
- (1097) Chen, K.-S.; Yip, H.-L.; Schlenker, C. W.; Ginger, D. S.; Jen, A. K.-Y. Halogen-Free Solvent Processing for Sustainable Development of High Efficiency Organic Solar Cells. *Org. Electron.* **2012**, *13* (12), 2870–2878.
- (1098) He, Z.; Liu, F.; Wang, C.; Chen, J.; He, L.; Nordlund, D.; Wu, H.; Russell, T. P.; Cao, Y. Simultaneous Spin-Coating and Solvent Annealing: Manipulating the Active Layer Morphology to a Power Conversion Efficiency of 9.6% in Polymer Solar Cells. *Mater. Horiz.* **2015**, *2*, 592–597.
- (1099) Arias, A. C.; MacKenzie, J. D.; McCulloch, I.; Rivnay, J.; Salleo, A. Materials and Applications for Large Area Electronics: Solution-Based Approaches. *Chem. Rev.* **2010**, *110* (1), 3–24.
- (1100) Reale, A.; La Notte, L.; Salamandra, L.; Polino, G.; Susanna, G.; Brown, T. M.; Brunetti, F.; Di Carlo, a. Spray Coating for Polymer Solar Cells: An Up-to-Date Overview. *Energy Technol.* **2015**, *3*, 385–406.
- (1101) Krebs, F. C. Fabrication and Processing of Polymer Solar Cells: A Review of Printing and Coating Techniques. *Sol. Energy Mater. Sol. Cells* **2009**, *93* (4), 394–412.
- (1102) Pastorelli, F.; Schmidt, T. M.; Hösel, M.; Søndergaard, R. R.; Jørgensen, M.; Krebs, F. C. The Organic Power Transistor: Roll-to-Roll Manufacture, Thermal Behavior, and Power Handling When Driving Printed Electronics. *Adv. Eng. Mater.* **2016**, *18* (1), 51–55.
- (1103) Tait, J.; Wong, C.; Cheyng, D.; Turbiez, M.; Rand, B.; Heremans, P. Ultrasonic Spray Coating of 6.5% Efficient Diketopyrrolopyrrole-Based Organic Photovoltaics. *IEEE J. Photovoltaics* **2014**, *4* (6), 1538.
- (1104) Li, N.; Baran, D.; Spyropoulos, G.; Zhang, H.; Berny, S.; Turbiez, M.; Ameri, T.; Krebs, F.; Brabec, C. Environmentally Printing Efficient Organic Tandem Solar Cells with High Fill Factors: A Guideline towards 20% Power Conversion Efficiency. *Adv. Energy Mater.* **2014**, *4*, 1400084.
- (1105) Zhang, T.; Chen, Z.; Yang, D.; Wu, F.; Zhao, X.; Yang, X. Fabricating High Performance Polymer Photovoltaic Modules by Creating Large-Scale Uniform Films. *Org. Electron.* **2016**, *32*, 126–133.
- (1106) Hong, S.; Kang, H.; Kim, G.; Lee, S.; Kim, S.; Lee, J.-H.; Lee, J.; Yi, M.; Kim, J.; Back, H.; et al. A Series Connection Architecture for Large-Area Organic Photovoltaic Modules with a 7.5% Module Efficiency. *Nat. Commun.* **2016**, *7*, 10279.
- (1107) Angmo, D.; Krebs, F. C. Over 2 Years of Outdoor Operational and Storage Stability of ITO-Free, Fully Roll-to-Roll Fabricated Polymer Solar Cell Modules. *Energy Technol.* **2015**, *3*, 774–783.
- (1108) Krebs, F. C.; Espinosa, N.; Hösel, M.; Søndergaard, R. R.; Jørgensen, M. 25th Anniversary Article: Rise to Power - OPV-Based Solar Parks. *Adv. Mater.* **2014**, *26* (1), 29–39.
- (1109) Cheng, P.; Zhan, X. Stability of Organic Solar Cells: Challenges and Strategies. *Chem. Soc. Rev.* **2016**, *45*, 2544–2582.
- (1110) Polman, A.; Knight, M.; Garnett, E. C.; Ehrler, B.; Sinke, W. C. Photovoltaic Materials – Present Efficiencies and Future Challenges. *Science (Washington, DC, U. S.)* **2016**, *352*, aad4424.
- (1111) Mazziro, K. a.; Luscombe, C. K. The Future of Organic Photovoltaics. *Chem. Soc. Rev.* **2015**, *44* (1), 78–90.
- (1112) Deibel, C.; Dyakonov, V. Polymer-Fullerene Bulk Heterojunction Solar Cells. *Rep. Prog. Phys.* **2010**, *73*, 096401.
- (1113) Dou, L.; You, J.; Hong, Z.; Xu, Z.; Li, G.; Street, R. a.; Yang, Y. 25th Anniversary Article: A Decade of Organic/polymeric Photovoltaic Research. *Adv. Mater.* **2013**, *25* (46), 6642–6671.
- (1114) Minnaert, B.; Burgelman, M. Efficiency Potential of Organic Bulk Heterojunction Solar Cells. *Prog. Photovoltaics* **2007**, *15* (8), 741–748.
- (1115) Kirchartz, T.; Taretto, K.; Rau, U. Efficiency Limits of Organic Bulk Heterojunction Solar Cells. *J. Phys. Chem. C* **2009**, *113* (41), 17958–17966.
- (1116) Giebink, N. C.; Wiederrecht, G. P.; Wasielewski, M. R.; Forrest, S. R. Thermodynamic Efficiency Limit of Excitonic Solar Cells. *Phys. Rev. B: Condens. Matter Mater. Phys.* **2011**, *83* (19), 195326.
- (1117) Koster, J.; Shaheen, S.; Hummelen, J. Pathways to a New Efficiency Regime for Organic Solar Cells. *Adv. Energy Mater.* **2012**, *2*, 1246–1253.
- (1118) Würfel, U.; Neher, D.; Spies, A.; Albrecht, S. Impact of Charge Transport on Current–voltage Characteristics and Power-Conversion Efficiency of Organic Solar Cells. *Nat. Commun.* **2015**, *6*, 6951.
- (1119) Rau, U.; Paetzold, U. W.; Kirchartz, T. Thermodynamics of Light Management in Photovoltaic Devices. *Phys. Rev. B: Condens. Matter Mater. Phys.* **2014**, *90* (3), 035211.
- (1120) Mishra, A.; Bäuerle, P. Small Molecule Organic Semiconductors on the Move: Promises for Future Solar Energy Technology. *Angew. Chem., Int. Ed.* **2012**, *51*, 2020–2067.
- (1121) Scharber, M.; Sariciftci, N. Efficiency of Bulk-Heterojunction Organic Solar Cells. *Prog. Polym. Sci.* **2013**, *38* (12), 1929–1940.
- (1122) Gupta, V.; Kyaw, A. K. K.; Wang, D. H.; Chand, S.; Bazan, G. C.; Heeger, A. J. Barium: An Efficient Cathode Layer for Bulk-Heterojunction Solar Cells. *Sci. Rep.* **2013**, *3*, 1965.
- (1123) Zhang, Q.; Kan, B.; Liu, F.; Long, G.; Wan, X.; Chen, X.; Zuo, Y.; Ni, W.; Zhang, H.; Li, M.; et al. Small-Molecule Solar Cells with Efficiency over 9%. *Nat. Photonics* **2014**, *9* (1), 35–41.
- (1124) Kan, B.; Zhang, Q.; Li, M.; Wan, X.; Ni, W.; Long, G.; Wang, Y.; Yang, X.; Feng, H.; Chen, Y. Solution-Processed Organic Solar Cells Based on Dialkylthiol-Substituted Benzodithiophene Unit with Efficiency near 10%. *J. Am. Chem. Soc.* **2014**, *136* (44), 15529–15532.
- (1125) Sun, K.; Xiao, Z.; Lu, S.; Zajackowski, W.; Pisula, W.; Hanssen, E.; White, J. M.; Williamson, R. M.; Subbiah, J.; Ouyang, J.; et al. A Molecular Nematic Liquid Crystalline Material for High-Performance Organic Photovoltaics. *Nat. Commun.* **2015**, *6*, 6013.

- (1126) Vandewal, K.; Tvingstedt, K.; Gadisa, A.; Inganäs, O.; Manca, J. V. On the Origin of the Open-Circuit Voltage of Polymer–fullerene Solar Cells. *Nat. Mater.* **2009**, *8* (11), 904–909.
- (1127) Garcia-Belmonte, G.; Bisquert, J. Open-Circuit Voltage Limit Caused by Recombination through Tail States in Bulk Heterojunction Polymer–Fullerene Solar Cells. *Appl. Phys. Lett.* **2010**, *96* (11), 113301.
- (1128) Cowan, S.; Roy, A.; Heeger, A. J. Recombination in Polymer–Fullerene Bulk Heterojunction Solar Cells. *Phys. Rev. B: Condens. Matter Mater. Phys.* **2010**, *82*, 245207.
- (1129) Elumalai, N. K.; Uddin, A. Open Circuit Voltage of Organic Solar Cells: An in-Depth Review. *Energy Environ. Sci.* **2016**, *9* (2), 391–410.
- (1130) Zhu, X. Y. How to Draw Energy Level Diagrams in Excitonic Solar Cells. *J. Phys. Chem. Lett.* **2014**, *5* (13), 2283–2288.
- (1131) Ripolles, T. S.; Guerrero, A.; Garcia-Belmonte, G. Polymer Defect States Modulate Open-Circuit Voltage in Bulk-Heterojunction Solar Cells. *Appl. Phys. Lett.* **2013**, *103* (24), 243306.
- (1132) Chen, S.; Tsang, S. W.; Lai, T. H.; Reynolds, J. R.; So, F. Dielectric Effect on the Photovoltage Loss in Organic Photovoltaic Cells. *Adv. Mater.* **2014**, *26* (35), 6125–6131.
- (1133) Westenhoff, S.; Howard, I. a.; Hodgkiss, J. M.; Kirov, K. R.; Bronstein, H. a.; Williams, C. K.; Greenham, N. C.; Friend, R. H. Charge Recombination in Organic Photovoltaic Devices with High Open-Circuit Voltages. *J. Am. Chem. Soc.* **2008**, *130* (41), 13653–13658.
- (1134) Veldman, D.; Meskers, S. C. J.; Janssen, R. a J. The Energy of Charge-Transfer States in Electron Donor-Acceptor Blends: Insight into the Energy Losses in Organic Solar Cells. *Adv. Funct. Mater.* **2009**, *19* (12), 1939–1948.
- (1135) Sulas, D. B.; Yao, K.; Intemann, J. J.; Williams, S. T.; Li, C. Z.; Chueh, C. C.; Richards, J. J.; Xi, Y.; Pozzo, L. D.; Schlenker, C. W.; et al. Open-Circuit Voltage Losses in Selenium-Substituted Organic Photovoltaic Devices from Increased Density of Charge-Transfer States. *Chem. Mater.* **2015**, *27* (19), 6583–6591.
- (1136) Rau, U. Reciprocity Relation between Photovoltaic Quantum Efficiency and Electroluminescent Emission of Solar Cells. *Phys. Rev. B: Condens. Matter Mater. Phys.* **2007**, *76* (8), 085303.
- (1137) Kirchartz, T.; Nelson, J.; Rau, U. Reciprocity between Charge Injection and Extraction and Its Influence on the Interpretation of Electroluminescence Spectra in Organic Solar Cells. *Phys. Rev. Appl.* **2016**, *5* (5), 054003.
- (1138) Kaake, L. G.; Sun, Y.; Bazan, G. C.; Heeger, A. J. Fullerene Concentration Dependent Bimolecular Recombination in Organic Photovoltaic Films. *Appl. Phys. Lett.* **2013**, *102* (13), 133302.
- (1139) Marsh, R. a.; Groves, C.; Greenham, N. C. A Microscopic Model for the Behavior of Nanostructured Organic Photovoltaic Devices. *J. Appl. Phys.* **2007**, *101* (8), 083509.
- (1140) Liedtke, M.; Sperlich, A.; Kraus, H.; Baumann, A.; Deibel, C.; Wirix, M. J. M.; Loos, J.; Cardona, C. M.; Dyakonov, V. Triplet Exciton Generation in Bulk-Heterojunction Solar Cells Based on Endohedral Fullerenes. *J. Am. Chem. Soc.* **2011**, *133* (23), 9088–9094.
- (1141) Rim, S.-B.; Fink, R. F.; Schöneboom, J. C.; Erk, P.; Peumans, P. Effect of Molecular Packing on the Exciton Diffusion Length in Organic Solar Cells. *Appl. Phys. Lett.* **2007**, *91* (17), 173504.
- (1142) Cho, S. W.; Demasi, a.; Preston, a. R. H.; Smith, K. E.; Piper, L. F. J.; Chauhan, K. V.; Jones, T. S. Probing the Effect of Relative Molecular Orientation on the Photovoltaic Device Performance of an Organic Bilayer Heterojunction Using Soft X-Ray Spectroscopies. *Appl. Phys. Lett.* **2012**, *100* (26), 263302.
- (1143) Nelson, J.; Choulis, S. a.; Durrant, J. R. Charge Recombination in Polymer/fullerene Photovoltaic Devices. *Thin Solid Films* **2004**, *451–452*, 508–514.
- (1144) Monestier, F.; Simon, J.-J.; Torchio, P.; Escoubas, L.; Flory, F.; Bailly, S.; de Bettignies, R.; Guillerez, S.; Defranoux, C. Modeling the Short-Circuit Current Density of Polymer Solar Cells Based on P3HT:PCBM Blend. *Sol. Energy Mater. Sol. Cells* **2007**, *91* (5), 405–410.
- (1145) Wu, L.; Zang, H.; Hsiao, Y. C.; Zhang, X.; Hu, B. Origin of the Fill Factor Loss in Bulk-Heterojunction Organic Solar Cells. *Appl. Phys. Lett.* **2014**, *104* (15), 153903.
- (1146) Qi, B.; Wang, J. Fill Factor in Organic Solar Cells. *Phys. Chem. Chem. Phys.* **2013**, *15*, 8972.
- (1147) Bartelt, J. A.; Lam, D.; Burke, T. M.; Sweetnam, S. M.; McGehee, M. D. Charge-Carrier Mobility Requirements for Bulk Heterojunction Solar Cells with High Fill Factor and External Quantum Efficiency > 90%. *Adv. Energy Mater.* **2015**, *5* (15), 1500577.
- (1148) Peumans, P.; Yakimov, A.; Forrest, S. R. Small Molecular Weight Organic Thin-Film Photodetectors and Solar Cells. *J. Appl. Phys.* **2003**, *93* (7), 3693–3723.
- (1149) Rand, B. P.; Genoe, J.; Heremans, P.; Poortmans, J. Solar Cells Utilizing Small Molecular Weight Organic Semiconductors. *Prog. Photovoltaics* **2007**, *15* (8), 659–676.
- (1150) Jia, X.; Shen, L.; Yao, M.; Liu, Y.; Yu, W.; Guo, W.; Ruan, S. Highly Efficient Low-Bandgap Polymer Solar Cells with Solution-Processed and Annealing-Free Phosphomolybdic Acid as Hole-Transport Layers. *ACS Appl. Mater. Interfaces* **2015**, *7* (9), 5367–5372.
- (1151) Lv, L.; Teng, F.; Yin, Y.; Hou, Y.; Hu, Y. Self-Assembled TiO<sub>2</sub> Nanorods as Electron Extraction Layer for High-Performance Inverted Polymer Solar Cells. *Chem. Mater.* **2015**, *27*, 44–52.
- (1152) Jo, S. B.; Kim, M.; Sin, D. H.; Lee, J.; Kim, H. G.; Ko, H.; Cho, K. Carrier-Selectivity-Dependent Charge Recombination Dynamics in Organic Photovoltaic Cells with a Ferroelectric Blend Interlayer. *Adv. Energy Mater.* **2015**, *5* (19), 1500802.
- (1153) Hahn, T.; Saller, C.; Weigl, M.; Bauer, I.; Unger, T.; Köhler, A.; Strohhriegel, P. Organic Solar Cells with Crosslinked Polymeric Exciton Blocking Layer. *Phys. Status Solidi A* **2015**, *212* (10), 2162–2168.
- (1154) Chambon, S.; Murat, Y.; Wantz, G.; Hirsch, L.; Tardy, P. Lanthanum Hexaboride As Novel Interlayer for Improving the Thermal Stability of P3HT:PCBM Organic Solar Cells. *ACS Appl. Mater. Interfaces* **2015**, *7* (45), 25334–25340.
- (1155) Mueller, C. J.; Brendel, M.; Ruckdeschel, P.; Pflaum, J.; Thelakkat, M. Diketopyrrolopyrroles with a Distinct Energy Level Cascade for Efficient Charge Carrier Generation in Organic Solar Cells. *Adv. Energy Mater.* **2015**, *5* (21), 1500914.
- (1156) Song, H. J.; Lee, E. J.; Kim, D. H.; Moon, D. K.; Lee, S. Solution-Processed Interlayer of N-Type Small Molecules for Organic Photovoltaic Devices: Enhancement of the Fill Factor due to Ordered Orientation. *Sol. Energy Mater. Sol. Cells* **2015**, *141*, 232–239.
- (1157) Chueh, C.-C.; Li, C.-Z.; Jen, A. K.-Y. Recent Progress and Perspective in Solution-Processed Interfacial Materials for Efficient and Stable Polymer and Organometal Perovskite Solar Cells. *Energy Environ. Sci.* **2015**, *8* (4), 1160–1189.
- (1158) Liu, Y.; Page, Z. a.; Russell, T. P.; Emrick, T. Finely Tuned Polymer Interlayers Enhance Solar Cell Efficiency. *Angew. Chem., Int. Ed.* **2015**, *54*, 11485–11489.
- (1159) Zhou, H.; Zhang, Y.; Mai, C.-K.; Collins, S. D.; Nguyen, T.-Q.; Bazan, G. C.; Heeger, A. J. Conductive Conjugated Polyelectrolyte as Hole-Transporting Layer for Organic Bulk Heterojunction Solar Cells. *Adv. Mater.* **2014**, *26* (5), 780–785.
- (1160) Tsai, C.-E.; Liao, M.-H.; Chen, Y.-L.; Cheng, S.-W.; Lai, Y.-Y.; Cheng, Y.-J.; Hsu, C.-S. Triarylamine-Based Crosslinked Hole-Transporting Material with an Ionic Dopant for High-Performance PEDOT:PSS-Free Polymer Solar Cells. *J. Mater. Chem. C* **2015**, *3* (24), 6158–6165.
- (1161) Smith, C. T. G.; Rhodes, R. W.; Beliatas, M. J.; Imalka Jayawardena, K. D. G.; Rozanski, L. J.; Mills, C. A.; Silva, S. R. P. Graphene Oxide Hole Transport Layers for Large Area, High Efficiency Organic Solar Cells. *Appl. Phys. Lett.* **2014**, *105* (7), 073304.
- (1162) Murray, I. P.; Lou, S. J.; Cote, L. J.; Loser, S.; Kadleck, C. J.; Xu, T.; Szarko, J. M.; Rolczynski, B. S.; Johns, J. E.; Huang, J.; et al. Graphene Oxide Interlayers for Robust, High-Efficiency Organic Photovoltaics. *J. Phys. Chem. Lett.* **2011**, *2* (24), 3006–3012.
- (1163) Treat, N. D.; Yaacobi-Gross, N.; Faber, H.; Perumal, A. K.; Bradley, D. D. C.; Stingelin, N.; Anthopoulos, T. D. Copper

Thiocyanate: An Attractive Hole Transport/extraction Layer for Use in Organic Photovoltaic Cells. *Appl. Phys. Lett.* **2015**, *107* (1), 013301.

(1164) Yaacobi-Gross, N.; Treat, N. D.; Pattanasattayavong, P.; Faber, H.; Perumal, A. K.; Stingelin, N.; Bradley, D. D. C.; Stavrinou, P. N.; Heeney, M.; Anthopoulos, T. D. High-Efficiency Organic Photovoltaic Cells Based on the Solution-Processable Hole Transporting Interlayer Copper Thiocyanate (CuSCN) as a Replacement for PEDOT:PSS. *Adv. Energy Mater.* **2015**, *5* (3), 1401529.

(1165) Lee, S. J.; Kim, J.-Y.; Kim, H. P.; Kim, D.; da Silva, W. J.; Schneider, F. K.; bin Mohd Yusoff, A. R.; Jang, J. An Organic Photovoltaic Featuring Graphene Nanoribbons. *Chem. Commun.* **2015**, *51*, 9185–9188.

(1166) Noh, Y. J.; Park, S. M.; Yeo, J. S.; Kim, D. Y.; Kim, S. S.; Na, S. I. Efficient PEDOT:PSS-Free Polymer Solar Cells with an Easily Accessible Polyacrylonitrile Polymer Material as a Novel Solution-Processable Anode Interfacial Layer. *ACS Appl. Mater. Interfaces* **2015**, *7* (45), 25032–25038.

(1167) Mohamed, S. a.; Gasiorowski, J.; Hingerl, K.; Zahn, D. R. T.; Scharber, M. C.; Obayya, S. S. a.; El-Mansy, M. K.; Sariciftci, N. S.; Egbe, D. a. M.; Stadler, P. CuI as Versatile Hole-Selective Contact for Organic Solar Cell Based on Anthracene-Containing PPE–PPV. *Sol. Energy Mater. Sol. Cells* **2015**, *143*, 369–374.

(1168) Dabera, G. D. M. R.; Prabhath, M. R. R.; Lai, K. T.; Jayawardena, K. D. G. I.; Sam, F. L. M.; Rozanski, L. J.; Adikaari, A. A. D. T.; Silva, S. R. P. Does Electronic Type Matter When Single-Walled Carbon Nanotubes Are Used for Electrode Applications? *Adv. Funct. Mater.* **2015**, *25* (28), 4520–4530.

(1169) Kim, D.-J.; Kim, H.-J.; Seo, K.-W.; Kim, K.-H.; Kim, T.-W.; Kim, H.-K. Indium-Free, Highly Transparent, Flexible Cu<sub>2</sub>O/Cu/Cu<sub>2</sub>O Mesh Electrodes for Flexible Touch Screen Panels. *Sci. Rep.* **2015**, *5*, 16838.

(1170) Mohl, M.; Dombovari, A.; Vajtai, R.; Ajayan, P. M.; Kordas, K. Self-Assembled Large Scale Metal Alloy Grid Patterns as Flexible Transparent Conductive Layers. *Sci. Rep.* **2015**, *5*, 13710.

(1171) Kim, I.; Kwak, S. W.; Ju, Y.; Park, G. Y.; Lee, T. M.; Jang, Y.; Choi, Y. M.; Kang, D. Roll-Offset Printed Transparent Conducting Electrode for Organic Solar Cells. *Thin Solid Films* **2015**, *580*, 21–28.

(1172) Ye, S.; Rathmell, A. R.; Chen, Z.; Stewart, I. E.; Wiley, B. J. Metal Nanowire Networks: The next Generation of Transparent Conductors. *Adv. Mater.* **2014**, *26* (39), 6670–6687.

(1173) Wang, B. Y.; Yoo, T. H.; Lim, J. W.; Sang, B. I.; Lim, D. S.; Choi, W. K.; Hwang, D. K.; Oh, Y. J. Enhanced Light Scattering and Trapping Effect of Ag Nanowire Mesh Electrode for High Efficient Flexible Organic Solar Cell. *Small* **2015**, *11* (16), 1905–1911.

(1174) Machui, F.; Hösel, M.; Li, N.; Spyropoulos, G. D.; Ameri, T.; Sondergaard, R. R.; Jørgensen, M.; Scheel, A.; Gaiser, D.; Kreul, K.; et al. Cost Analysis of Roll-to-Roll Fabricated ITO Free Single and Tandem Organic Solar Modules Based on Data from Manufacture. *Energy Environ. Sci.* **2014**, *7*, 2792.

(1175) Gentle, A. R.; Yambem, S. D.; Smith, G. B.; Burn, P. L.; Meredith, P. Optimized Multilayer Indium-Free Electrodes for Organic Photovoltaics. *Phys. Status Solidi A* **2015**, *212* (2), 348–355.

(1176) Kuwabara, T.; Nakamoto, M.; Kawahara, Y.; Yamaguchi, T.; Takahashi, K. Characterization of ZnS-Layer-Inserted Bulk-Heterojunction Organic Solar Cells by Ac Impedance Spectroscopy. *J. Appl. Phys.* **2009**, *105* (12), 124513.

(1177) Huang, F.; Wu, H.; Cao, Y. Water/alcohol Soluble Conjugated Polymers as Highly Efficient Electron Transporting/injection Layer in Optoelectronic Devices. *Chem. Soc. Rev.* **2010**, *39* (7), 2500–2521.

(1178) Jia, T.; Han, J.; Zhou, W.; Wang, L.; Wu, M.; Chen, W.; Chen, Y.; Li, F.; Wang, Y. Application of a Water-Soluble Metallophthalocyanine Derivative as a Cathode Interlayer for the Polymer Solar Cells. *Sol. Energy Mater. Sol. Cells* **2015**, *141*, 93–100.

(1179) Zhang, Z.-G.; Li, H.; Qi, B.; Chi, D.; Jin, Z.; Qi, Z.; Hou, J.; Li, Y.; Wang, J. Amine Group Functionalized Fullerene Derivatives as Cathode Buffer Layers for High Performance Polymer Solar Cells. *J. Mater. Chem. A* **2013**, *1* (34), 9624.

(1180) Kesters, J.; Verstappen, P.; Kelchtermans, M.; Lutsen, L.; Vanderzande, D.; Maes, W. Porphyrin-Based Bulk Heterojunction Organic Photovoltaics: The Rise of the Colors of Life. *Adv. Energy Mater.* **2015**, *5* (13), 1500218.

(1181) Zeng, H.; Zhu, X.; Liang, Y.; Guo, X. Interfacial Layer Engineering for Performance Enhancement in Polymer Solar Cells. *Polymers (Basel, Switz.)* **2015**, *7* (2), 333–372.

(1182) Zhou, Y.; Fuentes-hernandez, C.; Shim, J.; Meyer, J.; Giordano, A. J.; Li, H.; Winget, P.; Papadopoulos, T.; Cheun, H.; Kim, J.; et al. A Universal Method to Produce Low-Work Function Electrodes for Organic Electronics. *Science (Washington, DC, U. S.)* **2012**, *336*, 327–332.

(1183) Liang, Z.; Zhang, Q.; Jiang, L.; Cao, G. ZnO Cathode Buffer Layers for Inverted Polymer Solar Cells. *Energy Environ. Sci.* **2015**, *8*, 3442–3476.

(1184) Hau, S. K.; Yip, H.-L.; Jen, A. K.-Y. A Review on the Development of the Inverted Polymer Solar Cell Architecture. *Polym. Rev.* **2010**, *50* (4), 474–510.

(1185) Puodziukynaite, E.; Wang, H.-W.; Lawrence, J.; Wise, A. J.; Russell, T. P.; Barnes, M. D.; Emrick, T. Azulene Methacrylate Polymers: Synthesis, Electronic Properties, and Solar Cell Fabrication. *J. Am. Chem. Soc.* **2014**, *136* (31), 11043–11049.

(1186) Yang, T.; Wang, M.; Duan, C.; Hu, X.; Huang, L.; Peng, J.; Huang, F.; Gong, X. Inverted Polymer Solar Cells with 8.4% Efficiency by Conjugated Polyelectrolyte. *Energy Environ. Sci.* **2012**, *5* (8), 8208.

(1187) Li, C. Z.; Chang, C. Y.; Zang, Y.; Ju, H. X.; Chueh, C. C.; Liang, P. W.; Cho, N.; Ginger, D. S.; Jen, A. K. Y. Suppressed Charge Recombination in Inverted Organic Photovoltaics via Enhanced Charge Extraction by Using a Conductive Fullerene Electron Transport Layer. *Adv. Mater.* **2014**, *26* (36), 6262–6267.

(1188)anova, D.; Scherer, M.; Schell, F.; Zimmermann, J.; Glaser, T.; Kast, A. K.; Krekeler, C.; Pucci, A.; Kowalsky, W.; Schröder, R. R.; et al. Why Inverted Small Molecule Solar Cells Outperform Their Noninverted Counterparts. *Adv. Funct. Mater.* **2015**, *25*, 6511–6518.

(1189) Adebajo, O.; Maharjan, P.; Adhikary, P.; Wang, M.; Yang, S.; Qiao, Q. Triple Junction Polymer Solar Cells. *Energy Environ. Sci.* **2013**, *6* (11), 3150.

(1190) Timmreck, R.; Meyer, T.; Gilot, J.; Seifert, H.; Mueller, T.; Furlan, A.; Wienk, M. M.; Wynands, D.; Hohl-Ebinger, J.; Warta, W.; et al. Characterization of Tandem Organic Solar Cells. *Nat. Photonics* **2015**, *9* (8), 478–479.

(1191) Choy, W. C. H.; Sha, W. E. I.; Li, X.; Zhang, D. Multi-Physical Properties of Plasmonic Organic Solar Cells. *Prog. Electromagn. Res.* **2014**, *146*, 25–46.

(1192) Chen, H. C.; Chou, S. W.; Tseng, W. H.; Chen, I. W. P.; Liu, C. C.; Liu, C.; Liu, C. L.; Chen, C. H.; Wu, C. I.; Chou, P. T. Large AuAg Alloy Nanoparticles Synthesized in Organic Media Using a One-Pot Reaction: Their Applications for High-Performance Bulk Heterojunction Solar Cells. *Adv. Funct. Mater.* **2012**, *22* (19), 3975–3984.

(1193) Li, X.; Choy, W. C. H.; Lu, H.; Sha, W. E. I.; Ho, A. H. P. Efficiency Enhancement of Organic Solar Cells by Using Shape-Dependent Broadband Plasmonic Absorption in Metallic Nanoparticles. *Adv. Funct. Mater.* **2013**, *23* (21), 2728–2735.

(1194) Park, H.; Il; Lee, S.; Lee, J. M.; Nam, S. A.; Jeon, T.; Han, S. W.; Kim, S. O. High Performance Organic Photovoltaics with Plasmonic-Coupled Metal Nanoparticle Clusters. *ACS Nano* **2014**, *8* (10), 10305–10312.

(1195) Wang, D.; Park, K.; Seo, J.; Seifert, J.; Jeon, J.; Kim, J.; Park, J.; Park, O.; Heeger, A. Enhanced Power Conversion Efficiency in PCDTBT/PC70BM Bulk Heterojunction Photovoltaic Devices with Embedded Silver Nanoparticle Clusters. *Adv. Energy Mater.* **2011**, *1*, 766–770.

(1196) Choi, H.; Ko, S.-J.; Choi, Y.; Joo, P.; Kim, T.; Lee, B. R.; Jung, J.-W.; Choi, H. J.; Cha, M.; Jeong, J.-R.; et al. Versatile Surface Plasmon Resonance of Carbon-Dot-Supported Silver Nanoparticles in Polymer Optoelectronic Devices. *Nat. Photonics* **2013**, *7* (9), 732–738.

(1197) Ko, S.-J.; Choi, H.; Lee, W.; Kim, T.; Lee, B. R.; Jung, J.-W.; Jeong, J.-R.; Song, M. H.; Lee, J. C.; Woo, H. Y.; et al. Highly Efficient

Plasmonic Organic Optoelectronic Devices Based on a Conducting Polymer Electrode Incorporated with Silver Nanoparticles. *Energy Environ. Sci.* **2013**, *6* (6), 1949.

(1198) Baek, S.-W.; Noh, J.; Lee, C.-H.; Kim, B.; Seo, M.-K.; Lee, J.-Y. Plasmonic Forward Scattering Effect in Organic Solar Cells: A Powerful Optical Engineering Method. *Sci. Rep.* **2013**, *3*, 1726.

(1199) Baek, S. W.; Park, G.; Noh, J.; Cho, C.; Lee, C. H.; Seo, M. K.; Song, H.; Lee, J. Y. Au@Ag Core-Shell Nanocubes for Efficient Plasmonic Light Scattering Effect in Low Bandgap Organic Solar Cells. *ACS Nano* **2014**, *8* (4), 3302–3312.

(1200) Lim, D. C.; Kim, K.-D.; Park, S.-Y.; Hong, E. M.; Seo, H. O.; Lim, J. H.; Lee, K. H.; Jeong, Y.; Song, C.; Lee, E.; et al. Towards Fabrication of High-Performing Organic Photovoltaics: New Donor-Polymer, Atomic Layer Deposited Thin Buffer Layer and Plasmonic Effects. *Energy Environ. Sci.* **2012**, *5*, 9803–9807.

(1201) Niesen, B.; Rand, B. P.; Van Dorpe, P.; Cheyns, D.; Tong, L.; Dmitriev, A.; Heremans, P. Plasmonic Efficiency Enhancement of High Performance Organic Solar Cells with a Nanostructured Rear Electrode. *Adv. Energy Mater.* **2013**, *3* (2), 145–150.

(1202) Li, X.; Choy, W. C. H.; Huo, L.; Xie, F.; Sha, W. E. I.; Ding, B.; Guo, X.; Li, Y.; Hou, J.; You, J.; et al. Dual Plasmonic Nanostructures for High Performance Inverted Organic Solar Cells. *Adv. Mater.* **2012**, *24* (22), 3046–3052.

(1203) Yang, X.; Chueh, C. C.; Li, C. Z.; Yip, H. L.; Yin, P.; Chen, H.; Chen, W. C.; Jen, A. K. Y. High-Efficiency Polymer Solar Cells Achieved by Doping Plasmonic Metallic Nanoparticles into Dual Charge Selecting Interfacial Layers to Enhance Light Trapping. *Adv. Energy Mater.* **2013**, *3* (5), 666–673.

(1204) Yao, K.; Salvador, M.; Chueh, C.-C.; Xin, X.-K.; Xu, Y.-X.; DeQuilettes, D. W.; Hu, T.; Chen, Y.; Ginger, D. S.; Jen, A. K.-Y. A General Route to Enhance Polymer Solar Cell Performance Using Plasmonic Nanoprisms. *Adv. Energy Mater.* **2014**, *4*, 1400206.

(1205) Zuo, L.; Chueh, C.-C.; Xu, Y.-X.; Chen, K.-S.; Zang, Y.; Li, C.-Z.; Chen, H.; Jen, A. K.-Y. Microcavity-Enhanced Light-Trapping for Highly Efficient Organic Parallel Tandem Solar Cells. *Adv. Mater.* **2014**, *26* (39), 6778–6784.

(1206) Huang, J.; Li, C.-Z.; Chueh, C.-C.; Liu, S.-Q.; Yu, J.-S.; Jen, A. K.-Y. 10.4% Power Conversion Efficiency of ITO-Free Organic Photovoltaics Through Enhanced Light Trapping Configuration. *Adv. Energy Mater.* **2015**, *5*, 1500406.

(1207) Guo, F.; Kubis, P.; Przybilla, T.; Spiecker, E.; Hollmann, A.; Langner, S.; Forberich, K.; Brabec, C. J. Nanowire Interconnects for Printed Large-Area Semitransparent Organic Photovoltaic Modules. *Adv. Energy Mater.* **2015**, *5*, 1401779.

(1208) Cabanetos, C.; El Labban, A.; Bartelt, J. A.; Douglas, J. D.; Mateker, W. R.; Fréchet, J. M. J.; McGehee, M. D.; Beaujuge, P. M. Linear Side Chains in benzo[1,2-b:4,5-B']dithiophene-thieno[3,4-C]pyrrole-4,6-Dione Polymers Direct Self-Assembly and Solar Cell Performance. *J. Am. Chem. Soc.* **2013**, *135* (12), 4656–4659.

(1209) Ashraf, R. S.; Meager, I.; Nikolka, M.; Kirkus, M.; Planells, M.; Schroeder, B. C.; Holliday, S.; Hurchangee, M.; Nielsen, C. B.; Siringhaus, H.; et al. Chalcogenophene Comonomer Comparison in Small Band Gap Diketopyrrolopyrrole-Based Conjugated Polymers for High-Performing Field-Effect Transistors and Organic Solar Cells. *J. Am. Chem. Soc.* **2015**, *137* (3), 1314–1321.

(1210) Guo, X.; Zhou, N.; Lou, S. J.; Smith, J.; Tice, D. B.; Hennek, J. W.; Ortiz, R. P.; Navarrete, J. T. L.; Li, S.; Strzalka, J.; et al. Polymer Solar Cells with Enhanced Fill Factors. *Nat. Photonics* **2013**, *7* (10), 825–833.

(1211) Subbiah, J.; Purushothaman, B.; Chen, M.; Qin, T.; Gao, M.; Vak, D.; Scholes, F. H.; Chen, X.; Watkins, S. E.; Wilson, G. J.; et al. Organic Solar Cells Using a High-Molecular-Weight Benzodithiophene-Benzothiadiazole Copolymer with an Efficiency of 9.4%. *Adv. Mater.* **2015**, *27* (4), 702–705.

(1212) Kim, J.-H.; Park, J. B.; Jung, I. H.; Grimsdale, A. C.; Yoon, S. C.; Yang, H.; Hwang, D.-H. Well-Controlled thieno[3,4-C]pyrrole-4,6-(5H)-Dione Based Conjugated Polymers for High Performance Organic Photovoltaic Cells with the Power Conversion Efficiency Exceeding 9%. *Energy Environ. Sci.* **2015**, *8*, 2352–2356.

(1213) Nguyen, T. L.; Choi, H.; Ko, S.-J.; Uddin, M. a.; Walker, B.; Yum, S.; Jeong, J.-E.; Yun, M. H.; Shin, T. J.; Hwang, S.; et al. Semi-Crystalline Photovoltaic Polymers with Efficiency Exceeding 9% in a ~ 300 Nm Thick Conventional Single-Cell Device. *Energy Environ. Sci.* **2014**, *7* (9), 3040–3051.

(1214) Ye, L.; Zhang, S.; Zhao, W.; Yao, H.; Hou, J. Highly Efficient 2D-Conjugated Benzodithiophene-Based Photovoltaic Polymer with Linear Alkylthio Side Chain. *Chem. Mater.* **2014**, *26* (12), 3603–3605.

(1215) Chen, J.-D.; Cui, C.; Li, Y.-Q.; Zhou, L.; Ou, Q.-D.; Li, C.; Li, Y.; Tang, J.-X. Polymer Solar Cells: Single-Junction Polymer Solar Cells Exceeding 10% Power Conversion Efficiency. *Adv. Mater.* **2015**, *27* (6), 1132.

(1216) Ouyang, X.; Peng, R.; Ai, L.; Zhang, X.; Ge, Z. Efficient Polymer Solar Cells Employing a Non-Conjugated Small-Molecule Electrolyte. *Nat. Photonics* **2015**, *9* (8), 520–524.

(1217) Vohra, V.; Kawashima, K.; Kakara, T.; Koganezawa, T.; Osaka, I.; Takimiya, K.; Murata, H. Efficient Inverted Polymer Solar Cells Employing Favourable Molecular Orientation. *Nat. Photonics* **2015**, *9* (6), 403–408.

(1218) He, Z.; Xiao, B.; Liu, F.; Wu, H.; Yang, Y.; Xiao, S.; Wang, C.; Russell, T. P.; Cao, Y. Single-Junction Polymer Solar Cells with High Efficiency and Photovoltage. *Nat. Photonics* **2015**, *9* (3), 174–179.

(1219) Liu, Y.; Chen, C.-C.; Hong, Z.; Gao, J.; Yang, Y. M.; Zhou, H.; Dou, L.; Li, G.; Yang, Y. Solution-Processed Small-Molecule Solar Cells: Breaking the 10% Power Conversion Efficiency. *Sci. Rep.* **2013**, *3*, 3356.

(1220) Yusoff, A. R. b. M.; Kim, D.; Kim, H. P.; Shneider, F. K.; da Silva, W. J.; Jang, J. High Efficiency Solution Processed Polymer Inverted Triple-Junction Solar Cell Exhibiting Conversion Efficiency of 11.83%. *Energy Environ. Sci.* **2015**, *8*, 303–316.

(1221) You, J.; Dou, L.; Yoshimura, K.; Kato, T.; Ohya, K.; Moriarty, T.; Emery, K.; Chen, C.; Gao, J.; Li, G.; et al. A Polymer Tandem Solar Cell with 10.6% Power Conversion Efficiency. *Nat. Commun.* **2013**, *4*, 1446.

(1222) Che, X.; Xiao, X.; Zimmerman, J. D.; Fan, D.; Forrest, S. R. High-Efficiency, Vacuum-Deposited, Small-Molecule Organic Tandem and Triple-Junction Photovoltaic Cells. *Adv. Energy Mater.* **2014**, *4*, 1400568.

(1223) Chen, C.-C.; Chang, W.-H.; Yoshimura, K.; Ohya, K.; You, J.; Gao, J.; Hong, Z.; Yang, Y. An Efficient Triple-Junction Polymer Solar Cell Having a Power Conversion Efficiency Exceeding 11%. *Adv. Mater.* **2014**, *26* (32), 5670–5677.

(1224) Zhang, X.; Zhan, C.; Yao, J. Non-Fullerene Organic Solar Cells with 6.1% Efficiency through Fine-Tuning Parameters of the Film-Forming Process. *Chem. Mater.* **2015**, *27*, 166–173.

(1225) Zhao, J.; Li, Y.; Lin, H.; Liu, Y.; Jiang, K.; Mu, C.; Ma, T.; Lin Lai, J. Y.; Hu, H.; Yu, D.; et al. High-Efficiency Non-Fullerene Organic Solar Cells Enabled by a Difluorobenzothiadiazole-Based Donor Polymer Combined with a Properly Matched Small Molecule Acceptor. *Energy Environ. Sci.* **2015**, *8* (2), 520–525.

(1226) Sun, D.; Meng, D.; Cai, Y.; Fan, B.; Li, Y.; Jiang, W.; Huo, L.; Sun, Y.; Wang, Z. Non-Fullerene-Acceptor-Based Bulk-Heterojunction Organic Solar Cells with Efficiency over 7%. *J. Am. Chem. Soc.* **2015**, *137* (34), 11156–11162.

(1227) Lin, Y.; Wang, J.; Zhang, Z.; Bai, H.; Li, Y.; Zhu, D.; Zhan, X. An Electron Acceptor Challenging Fullerenes for Efficient Polymer Solar Cells. *Adv. Mater.* **2015**, *27* (7), 1170–1174.

(1228) Kwon, O. K.; Park, J.; Kim, D. W.; Park, S. K.; Park, S. Y. An All-Small-Molecule Organic Solar Cell with High Efficiency Non-fullerene Acceptor. *Adv. Mater.* **2015**, *27*, 1951–1956.

(1229) Cnops, K.; Zango, G.; Genoe, J.; Heremans, P.; Martínez-Díaz, M. V.; Torres, T.; Cheyns, D. Energy Level Tuning of Non-Fullerene Acceptors in Organic Solar Cells. *J. Am. Chem. Soc.* **2015**, *137*, 8991–8997.

(1230) Chen, Y. H.; Lin, L. Y.; Lu, C. W.; Lin, F.; Huang, Z. Y.; Lin, H. W.; Wang, P. H.; Liu, Y. H.; Wong, K. T.; Wen, J.; et al. Vacuum-Deposited Small-Molecule Organic Solar Cells with High Power Conversion Efficiencies by Judicious Molecular Design and Device Optimization. *J. Am. Chem. Soc.* **2012**, *134* (33), 13616–13623.

- (1231) Xiao, X.; Bergemann, K. J.; Zimmerman, J. D.; Lee, K.; Forrest, S. R. Small-Molecule Planar-Mixed Heterojunction Photovoltaic Cells with Fullerene-Based Electron Filtering Buffers. *Adv. Energy Mater.* **2014**, *4*, 1301557.
- (1232) Yang, Y.; Chen, W.; Dou, L.; Chang, W.-H.; Duan, H.-S.; Bob, B.; Li, G.; Yang, Y. High-Performance Multiple-Donor Bulk Heterojunction Solar Cells. *Nat. Photonics* **2015**, *9* (3), 190–198.
- (1233) He, L.; Jiang, C.; Rusli; Lai, D.; Wang, H. Highly Efficient Si-Nanorods/organic Hybrid Core-Sheath Heterojunction Solar Cells. *Appl. Phys. Lett.* **2011**, *99* (2), 021104.
- (1234) Park, K.-T.; Kim, H.-J.; Park, M.-J.; Jeong, J.-H.; Lee, J.; Choi, D.-G.; Lee, J.-H.; Choi, J.-H. 13.2% Efficiency Si nanowire/PEDOT:PSS Hybrid Solar Cell Using a Transfer-Imprinted Au Mesh Electrode. *Sci. Rep.* **2015**, *5*, 12093.
- (1235) Zhang, Y.; Cui, W.; Zhu, Y.; Zu, F.; Liao, L.; Lee, S.-T.; Sun, B. High Efficiency Hybrid PEDOT:PSS/nanostructured Silicon Schottky Junction Solar Cells by Doping-Free Rear Contact. *Energy Environ. Sci.* **2015**, *8* (1), 297–302.
- (1236) Weiss, D. S.; Abkowitz, M. Advances in Organic Photoconductor Technology. *Chem. Rev.* **2010**, *110* (1), 479–526.
- (1237) Agostinelli, T.; Caironi, M.; Natali, D.; Sampietro, M.; Biagioni, P.; Finazzi, M.; Duò, L. Space Charge Effects on the Active Region of a Planar Organic Photodetector. *J. Appl. Phys.* **2007**, *101*, 114504.
- (1238) Campbell, I. H.; Crone, B. K. A near Infrared Organic Photodiode with Gain at Low Bias Voltage. *Appl. Phys. Lett.* **2009**, *95* (26), 263302.
- (1239) Pierre, A.; Deckman, I.; Lechêne, P. B.; Arias, A. C. High Detectivity All-Printed Organic Photodiodes. *Adv. Mater.* **2015**, *27*, 6411–6417.
- (1240) Armin, A.; Jansen-van Vuuren, R. D.; Kopidakis, N.; Burn, P. L.; Meredith, P. Narrowband Light Detection via Internal Quantum Efficiency Manipulation of Organic Photodiodes. *Nat. Commun.* **2015**, *6*, 6343.
- (1241) El Gemayel, M.; Treier, M.; Musumeci, C.; Li, C.; Müllen, K.; Samori, P. Tuning the Photoresponse in Organic Field-Effect Transistors. *J. Am. Chem. Soc.* **2012**, *134* (4), 2429–2433.
- (1242) Wang, H.; Cheng, C.; Zhang, L.; Liu, H.; Zhao, Y.; Guo, Y.; Hu, W.; Yu, G.; Liu, Y. Inkjet Printing Short-Channel Polymer Transistors with High-Performance and Ultrahigh Photoresponsivity. *Adv. Mater.* **2014**, *26* (27), 4683–4689.
- (1243) Su, Z. S.; Li, W. L.; Chu, B.; Li, T. L.; Zhu, J. Z.; Zhang, G.; Yan, F.; Li, X.; Chen, Y. R.; Lee, C. S. High Response Organic Ultraviolet Photodetector Based on Blend of 4,4'-Tri-(2-Methylphenyl Phenylamino) Triphenylamine and Tris-(8-Hydroxyquinoline) Gallium. *Appl. Phys. Lett.* **2008**, *93*, 103309.
- (1244) Li, H. G.; Wu, G.; Chen, H. Z.; Wang, M. Spectral Response Tuning and Realization of Quasi-Solar-Blind Detection in Organic Ultraviolet Photodetectors. *Org. Electron.* **2011**, *12* (1), 70–77.
- (1245) Lin, H. W.; Ku, S. Y.; Su, H. C.; Huang, C. W.; Lin, Y. T.; Wong, K. T.; Wu, C. C. Highly Efficient Visible-Blind Organic Ultraviolet Photodetectors. *Adv. Mater.* **2005**, *17* (20), 2489–2493.
- (1246) Peumans, P.; Bulovic, V.; Forrest, S. R. Efficient, High-Bandwidth Organic Multilayer Photodetectors. *Appl. Phys. Lett.* **2000**, *76*, 3855–3857.
- (1247) Lee, J.; Jadhav, P.; Baldo, M. A. High Efficiency Organic Multilayer Photodetectors Based on Singlet Exciton Fission. *Appl. Phys. Lett.* **2009**, *95* (3), 033301.
- (1248) Tsai, W.-W.; Chao, Y.-C.; Chen, E.-C.; Zan, H.-W.; Meng, H.-F.; Hsu, C.-S. Increasing Organic Vertical Carrier Mobility for the Application of High Speed Bilayered Organic Photodetector. *Appl. Phys. Lett.* **2009**, *95* (21), 213308.
- (1249) Alves, H.; Pinto, R. M.; Maçôas, E. S. Photoconductive Response in Organic Charge Transfer Interfaces with High Quantum Efficiency. *Nat. Commun.* **2013**, *4*, 1842.
- (1250) Zhang, H.; Jenatsch, S.; De Jonghe, J.; Nüesch, F.; Steim, R.; Véron, A. C.; Hany, R. Transparent Organic Photodetector Using a Near-Infrared Absorbing Cyanine Dye. *Sci. Rep.* **2015**, *5*, 9439.
- (1251) Zimmerman, J. D.; Diev, V. V.; Hanson, K.; Lunt, R. R.; Yu, E. K.; Thompson, M. E.; Forrest, S. R. Porphyrin-tape/C60 Organic Photodetectors with 6.5% External Quantum Efficiency in the near Infrared. *Adv. Mater.* **2010**, *22* (25), 2780–2783.
- (1252) Tedde, S. F.; Kern, J.; Sterzl, T.; Fürst, J.; Lugli, P.; Hayden, O.; Furst, J.; Lugli, P.; Hayden, O. Fully Spray Coated Organic Photodiodes. *Nano Lett.* **2009**, *9* (3), 980–983.
- (1253) Punke, M.; Valouch, S.; Kettlitz, S. W.; Gerken, M.; Lemmer, U. Optical Data Link Employing Organic Light-Emitting Diodes and Organic Photodiodes as Optoelectronic Components. *J. Lightwave Technol.* **2008**, *26* (7), 816–823.
- (1254) Keivanidis, P. E.; Khong, S.-H.; Ho, P. K. H.; Greenham, N. C.; Friend, R. H. All-Solution Based Device Engineering of Multilayer Polymeric Photodiodes: Minimizing Dark Current. *Appl. Phys. Lett.* **2009**, *94* (17), 173303.
- (1255) Hamasaki, T.; Morimune, T.; Kajii, H.; Minakata, S.; Tsuruoka, R.; Nagamachi, T.; Ohmori, Y. Fabrication and Characteristics of Polyfluorene Based Organic Photodetectors Using Fullerene Derivatives. *Thin Solid Films* **2009**, *518* (2), 548–550.
- (1256) Gong, X.; Tong, M.; Xia, Y.; Cai, W.; Moon, J. S.; Cao, Y.; Yu, G.; Shieh, C.-L.; Nilsson, B.; Heeger, A. J. High-Detectivity Polymer Photodetectors with Spectral Response from 300 Nm to 1450 Nm. *Science* **2009**, *325* (5948), 1665–1667.
- (1257) Peet, J.; Kim, J. Y.; Coates, N. E.; Ma, W. L.; Moses, D.; Heeger, A. J.; Bazan, G. C. Efficiency Enhancement in Low-Bandgap Polymer Solar Cells by Processing with Alkane Dithiols. *Nat. Mater.* **2007**, *6*, 497–500.
- (1258) Yao, Y.; Liang, Y.; Shrotriya, V.; Xiao, S.; Yu, L.; Yang, Y. Plastic near-Infrared Photodetectors Utilizing Low Band Gap Polymer. *Adv. Mater.* **2007**, *19* (22), 3979–3983.
- (1259) Rauch, T.; Boberl, M.; Tedde, S.; Furst, J.; Kovalenko, M.; Hesser, G.; Lemmer, U.; Heiss, W.; Hayden, O. Near-Infrared Imaging with Quantum Dot-Sensitized Organic Photodiodes. *Nat. Photonics* **2009**, *3*, 332–336.
- (1260) Guo, Y.; Du, C.; Di, C.; Zheng, J.; Sun, X.; Wen, Y.; Zhang, L.; Wu, W.; Yu, G.; Liu, Y. Field Dependent and High Light Sensitive Organic Phototransistors Based on Linear Asymmetric Organic Semiconductor. *Appl. Phys. Lett.* **2009**, *94* (14), 143303.
- (1261) Guo, Y.; Du, C.; Yu, C.; Di, C. A.; Jiang, S.; Xi, H.; Zheng, J.; Yan, S.; Yu, C.; Hu, W.; et al. High-Performance Phototransistors Based on Organic Microribbons Prepared by a Solution Self-Assembly Process. *Adv. Funct. Mater.* **2010**, *20* (6), 1019–1024.
- (1262) Sun Kim, Y.; Bae, S. Y.; Kim, K. H.; Lee, T. W.; Hur, J. a.; Hoang, M. H.; Cho, M. J.; Kim, S.-J.; Kim, Y.; Kim, M.; et al. Highly Sensitive Phototransistor with Crystalline Microribbons from New  $\pi$ -Extended Pyrene Derivative via Solution-Phase Self-Assembly. *Chem. Commun. (Cambridge, U. K.)* **2011**, *47*, 8907–8909.
- (1263) Cho, M. Y.; Kim, S. J.; Han, Y. D.; Park, D. H.; Kim, K. H.; Choi, D. H.; Joo, J. Highly Sensitive, Photocontrolled, Organic Thin-Film Transistors Using Soluble Star-Shaped Conjugated Molecules. *Adv. Funct. Mater.* **2008**, *18* (19), 2905–2912.
- (1264) Zhao, G.; Liu, J.; Meng, Q.; Ji, D.; Zhang, X.; Zou, Y. High-Performance UV-Sensitive Organic Phototransistors Based on Benzo [1, 2- B: 4, 5- B' ] Dithiophene Dimers Linked with Unsaturated Bonds. *Adv. Electron. Mater.* **2015**, *1*, 1500071.
- (1265) Qi, Z.; Cao, J.; Li, H.; Ding, L.; Wang, J. High-Performance Thermally Stable Organic Phototransistors Based on PSeTPTI/PC61BM for Visible and Ultraviolet Photodetection. *Adv. Funct. Mater.* **2015**, *25*, 3138–3146.
- (1266) Um, H. A.; Lee, D. H.; Heo, D. U.; Yang, D. S.; Shin, J.; Baik, H.; Cho, M. J.; Choi, D. H. High Aspect Ratio Conjugated Polymer Nanowires for High Performance Field-Effect Transistors and Phototransistors. *ACS Nano* **2015**, *9* (5), 5264–5274.
- (1267) Li, M.; An, C.; Marszalek, T.; Guo, X.; Long, Y.-Z.; Yin, H.; Gu, C.; Baumgarten, M.; Pisula, W.; Müllen, K. Phenanthrene Condensed Thiadiazoloquinoline Donor–Acceptor Polymer for Phototransistor Applications. *Chem. Mater.* **2015**, *27*, 2218–2223.

- (1268) Li, H.; Wu, Y.; Wang, X.; Kong, Q.; Fu, H. A Self-Assembled Ultrathin Crystalline Polymer Film for High Performance Phototransistors. *Chem. Commun.* **2014**, 50 (75), 11000.
- (1269) Ma, L.; Yi, Z.; Wang, S.; Liu, Y.; Zhan, X. Highly Sensitive Thin Film Phototransistors Based on a Copolymer of Benzodithiophene and. *J. Mater. Chem. C* **2015**, 3, 1942–1948.
- (1270) Liu, Y.; Dong, H.; Jiang, S.; Zhao, G.; Shi, Q.; Tan, J.; Jiang, L.; Hu, W.; Zhan, X. High Performance Nanocrystals of a Donor-Acceptor Conjugated Polymer. *Chem. Mater.* **2013**, 25, 2649–2655.
- (1271) Halvorson, C.; Kraabel, B.; Heeger, a. J.; Volodin, B. L.; Meerholz, K.; Sandalphon, S.; Peyghambarian, N. Optical Computing by Use of Photorefractive Polymers. *Opt. Lett.* **1995**, 20 (1), 76.
- (1272) Goonesekera, A.; Wright, D.; Moerner, W. E. Image Amplification and Novelty Filtering with a Photorefractive Polymer. *Appl. Phys. Lett.* **2000**, 76 (23), 3358–3360.
- (1273) Volodin, B. L.; Kippelen, B.; Meerholz, K.; Javidi, B.; Peyghambarian, N. A Polymeric Optical Pattern-Recognition System for Security Verification. *Nature* **1996**, 383, 58–60.
- (1274) Li, G.; Eralp, M.; Thomas, J.; Tay, S.; Schülzgen, A.; Norwood, R. a.; Peyghambarian, N. All-Optical Dynamic Correction of Distorted Communication Signals Using a Photorefractive Polymeric Hologram. *Appl. Phys. Lett.* **2005**, 86 (16), 161103.
- (1275) Salvador, M.; Prauzner, J.; Köber, S.; Meerholz, K. Beam Walk-off Suppression in Photorefractive Polymer-Based Coherence Domain Holography. *Appl. Phys. B: Lasers Opt.* **2011**, 102 (4), 803–807.
- (1276) Hwang, J.; Choi, J.; Kim, C.; Kim, W.; Oh, J.; Kim, N. Coherence Gated Three-Dimensional Imaging System Using Organic Photorefractive Holography. *Bull. Korean Chem. Soc.* **2014**, 35 (3), 938–940.
- (1277) Gubler, U.; He, M.; Wright, D.; Roh, Y.; Twieg, R.; Moerner, W. E. Monolithic Photorefractive Organic Glasses with Large Coupling Gain and Strong Beam Fanning. *Adv. Mater.* **2002**, 14 (4), 313–317.
- (1278) Klein, M. B.; Bacher, G. D.; Grunnet-Jepsen, A.; Wright, D.; Moerner, W. E. Homodyne Detection of Ultrasonic Surface Displacements Using Two-Wave Mixing in Photorefractive Polymers. *Opt. Commun.* **1999**, 162 (1), 79–84.
- (1279) Zamiri, S.; Reitingner, B.; Portenkirchner, E.; Berer, T.; Font-Sanchis, E.; Burgholzer, P.; Sariciftci, N. S.; Bauer, S.; Fernández-Lázaro, F. Laser Ultrasonic Receivers Based on Organic Photorefractive Polymer Composites. *Appl. Phys. B: Lasers Opt.* **2014**, 114 (4), 509–515.
- (1280) Andrzej, W.; Paweł, M.; Edward, N. Semiconductor–LC Layer Boundary and Photonic Structures. *Mol. Cryst. Liq. Cryst.* **2012**, 559 (1), 186–193.
- (1281) Ren, X. K.; Yang, D. Y.; Zhang, T. H.; Zhang, S.; Zhou, L.; Tian, J. G.; Xu, J. J. Polymeric Photorefractive Surface Waves. *Opt. Commun.* **2010**, 283 (19), 3792–3797.
- (1282) Chen, Z.; Asaro, M.; Ostroverkhova, O.; Moerner, W. E.; He, M.; Twieg, R. J. Self-Trapping of Light in an Organic Photorefractive Glass. *Opt. Lett.* **2003**, 28 (24), 2509–2511.
- (1283) Asaro, M.; Sheldon, M.; Chen, Z.; Ostroverkhova, O.; Moerner, W. E. Soliton-Induced Waveguides in an Organic Photorefractive Glass. *Opt. Lett.* **2005**, 30 (5), 519–521.
- (1284) Fujihara, T.; Sassa, T.; Muto, T.; Umegaki, S.; Wada, T. Surface Waves in Photorefractive Polymer Films. *Opt. Express* **2009**, 17 (16), 14150–14155.
- (1285) Nau, D.; Christ, A.; Giessen, H.; Wagner, A.; Euteneuer, A.; Salvador, M.; Mecher, E.; Meerholz, K. Femtosecond Properties of Photorefractive Polymers. *Appl. Phys. B: Lasers Opt.* **2009**, 95 (1), 31–35.
- (1286) Oh, J.-W.; Choi, J.; Kim, N. Tunable Color Filter with Surface Plasmon Resonance Using Organic Photorefractive Composite. *Appl. Opt.* **2009**, 48 (17), 3160–3164.
- (1287) Lynn, B.; Blanche, P.; Bablumian, a; Rankin, R.; Voorakaranam, R.; Hilaire, P. S.; LaComb, L.; Yamamoto, M.; Peyghambarian, N. Recent Advancements in Photorefractive Holographic Imaging. *J. Phys. Conf. Ser.* **2013**, 415, 012050.
- (1288) Jolly, S.; Bove, V. M. Direct Optical Fringe Writing of Diffraction Specific Coherent Panoramagrams in Photorefractive Polymer for Updatable Three-Dimensional Holographic Display. *J. Phys. Conf. Ser.* **2013**, 415, 012054.
- (1289) Tsujimura, S.; Kinashi, K.; Sakai, W.; Tsutsumi, N. High-Speed Photorefractive Response Capability in Triphenylamine Polymer-Based Composites. *Appl. Phys. Express* **2012**, 5 (6), 064101.
- (1290) Yang, Q.; Xu, X.; Lai, P.; Xu, D.; Wang, L. V. Time-Reversed Ultrasonically Encoded Optical Focusing Using Two Ultrasonic Transducers for Improved Ultrasonic Axial Resolution. *J. Biomed. Opt.* **2013**, 18 (11), 110502.
- (1291) Lai, P.; Xu, X.; Liu, H.; Suzuki, Y.; Wang, L. V. Reflection-Mode Time-Reversed Ultrasonically Encoded Optical Focusing into Turbid Media. *Nat. Photonics* **2011**, 5, 154–157.
- (1292) Suzuki, Y.; Lai, P.; Xu, X.; Wang, L. High-Sensitivity Ultrasound-Modulated Optical Tomography with a Photorefractive Polymer. *Opt. Lett.* **2013**, 38 (6), 899–901.
- (1293) Li, S.; Fu, M.; Zhang, Y.; Duan, J.; He, D.; Wang, Y. Photorefractive Photonic Crystals Fabricated with PMMA and SCB Based Materials Using Three-Dimensional Colloidal Crystals. *J. Mater. Chem. C* **2013**, 1 (33), 5072.
- (1294) Abbott, S.; Daly, K. R.; D'Alessandro, G.; Kaczmarek, M.; Smith, D. C. A Hybrid Liquid Crystal Photorefractive System for the Photorefractive Coupling of Surface Plasmon Polaritons. *J. Opt. Soc. Am. B* **2012**, 29 (8), 1947–1958.
- (1295) Daly, K. R.; Abbott, S. B.; Smith, D. C.; D'Alessandro, G. Optimization of Plasmon–plasmon Coupling in Photorefractive Layered Media. *J. Opt. Soc. Am. B* **2013**, 30 (8), 2090.
- (1296) Proctor, M.; Bateman, J.; Daly, K.; Herrington, M.; Buchnev, O.; Podoliak, N.; Alessandro, G. D.; Kaczmarek, M. Light-activated modulation and coupling in integrated polymer–liquid crystal systems. *J. Opt. Soc. Am. B* **2014**, 31 (12), 3144–3152.
- (1297) Xue, T.; Zhao, H.; Meng, C.; Fu, J.; Zhang, J. Impact of Surface Plasmon Polaritons on Photorefractive Effect in Dye Doped Liquid Crystal Cells with ZnSe Interlayers. *Opt. Express* **2014**, 22 (17), 20964–20972.
- (1298) Fujihara, T.; Umegaki, S.; Hara, M.; Sassa, T. Formation Speed and Formation Mechanism of Self-Written Surface Wave-Based Waveguides in Photorefractive Polymers. *Opt. Mater. Express* **2012**, 2 (6), 849.
- (1299) Chen, Z.; Segev, M.; Christodoulides, D. Optical Spatial Solitons: Historical Overview and Recent Advances. *Rep. Prog. Phys.* **2012**, 75, 086401.
- (1300) Peccianti, M.; Brzdękiewicz, K. a; Assanto, G. Nonlocal Spatial Soliton Interactions in Nematic Liquid Crystals. *Opt. Lett.* **2002**, 27 (16), 1460–1462.
- (1301) Jiang, Q.; Su, Y.; Ji, X.; Xie, S. Grey–grey Separate Spatial Soliton Pairs in a Biased Series Photorefractive Polymer Circuit. *Opt. Commun.* **2012**, 285 (3), 338–340.
- (1302) Tan, Z.; Tian, B.; Jiang, Y.; Wang, P.; Li, M. Dynamics of the Manakov Solitons in Biased Guest-Host Photorefractive Polymer. *Commun. Theor. Phys.* **2013**, 60, 150–158.
- (1303) Su, Y.; Jiang, Q.; Ji, X.; Xie, S. Bright-Dark Manakov Solitons in Biased Guest-Host Photorefractive Polymer. *Commun. Theor. Phys.* **2012**, 57, 281–284.
- (1304) Gemayel, M. El; Börjesson, K.; Herder, M.; Duong, D. T.; Hutchison, J. a; Ruzié, C.; Schweicher, G.; Salleo, A.; Geerts, Y.; Hecht, S.; et al. Optically Switchable Transistors by Simple Incorporation of Photochromic Systems into Small-Molecule Semiconducting Matrices. *Nat. Commun.* **2015**, 6, 6330.
- (1305) Dong, H.; Zhu, H.; Meng, Q.; Gong, X.; Hu, W. Organic Photoreponse Materials and Devices. *Chem. Soc. Rev.* **2012**, 41 (5), 1754.
- (1306) Minaev, B.; Baryshnikov, G.; Agren, H. Principles of Phosphorescent Organic Light Emitting Devices. *Phys. Chem. Chem. Phys.* **2014**, 16 (5), 1719–1758.
- (1307) Malissa, H.; Kavand, M.; Waters, D. P.; van Schooten, K. J.; Burn, P. L.; Vardeny, Z. V.; Saam, B.; Lupton, J. M.; Boehme, C. Room-Temperature Coupling between Electrical Current and Nuclear

Spins in OLEDs. *Science (Washington, DC, U. S.)* **2014**, *345* (6203), 1487.

(1308) Nguyen, T. D.; Hukic-Markosian, G.; Wang, F.; Wojcik, L.; Li, X.-G.; Ehrenfreund, E.; Vardeny, Z. V. Isotope Effect in Spin Response of Pi-Conjugated Polymer Films and Devices. *Nat. Mater.* **2010**, *9* (4), 345–352.

(1309) Reineke, S.; Seidler, N.; Yost, S. R.; Prins, F.; Tisdale, W. a.; Baldo, M. a. Highly Efficient, Dual State Emission from an Organic Semiconductor. *Appl. Phys. Lett.* **2013**, *103* (9), 093302.

(1310) D'Andrade, B. W.; Forrest, S. R. White Organic Light-Emitting Devices for Solid-State Lighting. *Adv. Mater.* **2004**, *16* (18), 1585–1595.

(1311) Zhang, B.; Liu, L.; Xie, Z. Recent Advances in White Organic Light-Emitting Materials and Devices (WOLEDs). *Isr. J. Chem.* **2014**, *54*, 897–917.

(1312) Wang, Q.; Ding, J.; Ma, D.; Cheng, Y.; Wang, L. Highly Efficient Single-Emitting-Layer White Organic Light-Emitting Diodes with Reduced Efficiency Roll-Off. *Appl. Phys. Lett.* **2009**, *94* (10), 103503.